Riccardo Manfredi
Roberto Pozzi Mucelli
Editors

MRI of the Female and Male Pelvis

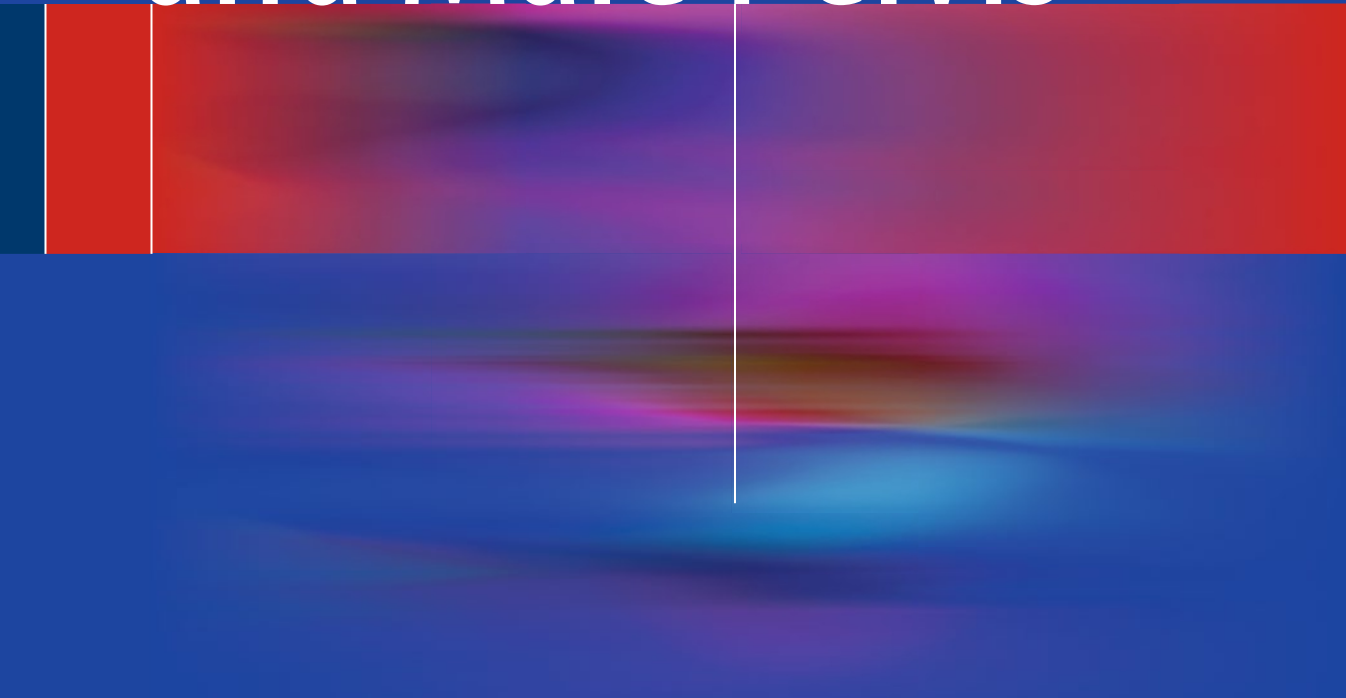

Springer

MRI of the Female and Male Pelvis

Riccardo Manfredi • Roberto Pozzi Mucelli
Editors

MRI of the Female and Male Pelvis

Springer

Editors
Riccardo Manfredi
Department of Radiology
University of Verona
"G.B. Rossi" University Hospital
Verona
Italy

Roberto Pozzi Mucelli
Department of Radiology
University of Verona
"G.B. Rossi" University Hospital
Verona
Italy

ISBN 978-3-319-09658-2 ISBN 978-3-319-09659-9 (eBook)
DOI 10.1007/978-3-319-09659-9
Springer Cham Heidelberg New York Dordrecht London

Library of Congress Control Number: 2014957394

© Springer International Publishing Switzerland 2015
This work is subject to copyright. All rights are reserved by the Publisher, whether the whole or part of the material is concerned, specifically the rights of translation, reprinting, reuse of illustrations, recitation, broadcasting, reproduction on microfilms or in any other physical way, and transmission or information storage and retrieval, electronic adaptation, computer software, or by similar or dissimilar methodology now known or hereafter developed. Exempted from this legal reservation are brief excerpts in connection with reviews or scholarly analysis or material supplied specifically for the purpose of being entered and executed on a computer system, for exclusive use by the purchaser of the work. Duplication of this publication or parts thereof is permitted only under the provisions of the Copyright Law of the Publisher's location, in its current version, and permission for use must always be obtained from Springer. Permissions for use may be obtained through RightsLink at the Copyright Clearance Center. Violations are liable to prosecution under the respective Copyright Law.
The use of general descriptive names, registered names, trademarks, service marks, etc. in this publication does not imply, even in the absence of a specific statement, that such names are exempt from the relevant protective laws and regulations and therefore free for general use.
While the advice and information in this book are believed to be true and accurate at the date of publication, neither the authors nor the editors nor the publisher can accept any legal responsibility for any errors or omissions that may be made. The publisher makes no warranty, express or implied, with respect to the material contained herein.

Printed on acid-free paper

Springer is part of Springer Science+Business Media (www.springer.com)

Contents

1 Magnetic Resonance Imaging of Congenital Malformation of the Uterus

Valerio Di Paola, Eugenio Oliboni, Daniela Avolio, Riccardo Manfredi, and Roberto Pozzi Mucelli

1.1 Introduction

Female genital tract anomalies are common deviations from normal anatomy with an estimated prevalence of 1–3 % in the general population and even higher in selected populations such as recurrent aborters [1, 2].

Their occurrence could be associated with a variety of clinical presentations ranging between life-threatening complications, severe health problems in the adolescence, and reproductive problems, although in most of them they are asymptomatic [1–3].

Due to their high prevalence and possible impact on the reproductive health of women, congenital uterine malformations of the female genital tract are a challenge for the therapeutic decision-making process.

The diagnosis of Mullerian duct anomalies (MDA) is based upon the clinical presentation, physical examination, and subsequent imaging work-up with different imaging methods available, namely, sonography and magnetic resonance (MR) imaging, among them MR imaging takes a leading role, especially in complex uterine malformation [1–4].

1.2 Epidemiology

Congenital malformations of the uterus frequency vary widely owing to different patient populations, non-standardized classification systems, and differences in diagnostic data acquisition. Because normal pregnancies can occur in women with MDA and the anomalies are discovered in most cases of patients presenting with infertility, the reported prevalence of MDA in the general population is probably underestimated. The overall published data suggest a prevalence range of uterovaginal anomalies of 1–3 % in the general population, among women with normal and abnormal fertility [5–7].

While conceiving is a minor problem for the majority of women with MDA, the risk of pregnancy loss is truly associated with MDA, and its prevalence in women with repeated miscarriage is considered to be in the order of 3 %. No racial predilection is reported in the literature [5, 8, 9].

1.3 Clinical Presentation

MDA may become clinically evident at different ages depending on their specific characteristics and associated disorders. In the newborn/infant age, an initial presentation of a palpable abdominal or pelvic mass due to a utero and/or vaginal obstruction causing intraluminal fluid retention can be discovered.

V. Di Paola (✉)• E. Oliboni
D. Avolio • R. Manfredi • R.P. Mucelli
Department of Radiology, University of Verona,
Piazzale Scuro, Verona, Italy
e-mail: dipaola.valerio@libero.it

R. Manfredi, R. Pozzi Mucelli (eds.), *MRI of the Female and Male Pelvis*,
DOI 10.1007/978-3-319-09659-9_1,

In adolescent age group a delayed menarche or primary amenorrhea with/without a fluid retention in the uterus (hematometra) and/or vagina (hematocolpos) may present as a painful intra-abdominal tumor. Some patients also have cyclical pain.

In childbearing age, MDA can present with various problems of infertility, repeated spontaneous abortions, premature delivery, fetal intrauterine growth retardation, and difficulties during delivery. The defective embryological development can also be associated with congenital malformations of other organ systems. Most frequently, renal malformations like renal agenesis or ectopia can occur. Much less frequent are bony malformations – most of them occur in a complex of varying symptoms – like abnormal scapula, supernumerary or fused ribs, vertebral malsegmentation, fusion of the vertebral column (i.e., Klippel-Feil syndrome), and radiocarpal hypoplasia.

Other malformations such as cardiac defects have been described, but it remains unclear if some of the associated malformations are caused in the same development field or if early exposure to teratogenic agents was causative [7, 9].

The literature does not show increased mortality for patients carrying an MDA compared to the general population, whereas the morbidity may be increased in some specific types of MDA causing obstructed Mullerian systems with the presence of hematosalpinx (retention of blood in the fallopian tubes), hematocolpos (retention of blood in the vagina), and retrograde menses causing the potential problem of endometriosis [5].

1.4 Embryology

The understanding of the embryogenesis of the urogenital female tract is of paramount importance to understand the pathogenesis of the different types of MDA.

The female reproductive system develops from the two-paired Mullerian ducts (synonym: paramesonephric duct) that start off in the embryonal mesoderm lateral to each Wolffian duct (synonym: mesonephric duct). The paired Mullerian ducts develop in medial and caudal directions, and the cranial part remains non-fused and forms the fallopian tubes. The caudal part fuses to a single canal forming the uterus and the upper two thirds of the vagina. This is called lateral fusion.

In a process called vertical fusion, the intervening midline septum of both ducts undergoes regression. The caudal part of the vagina arises from the sinovaginal bulb and fuses with the lower fused Mullerian ducts.

The ovaries originate from the gonadal ridge, a completely different tissue than the mesoderm, forming both the urinary and genital systems. Hence, associated malformations of the kidney, but not of the ovaries, are frequently observed together with MDA.

Pathogenesis of MDA can be basically classified into the presence of agenesis, hypoplasia, and defects in vertical and lateral fusion of the paired ducts [5].

1.5 Classes of Mullerian Duct Anomalies (MDA)

The first attempt to classify female congenital anomalies goes back to the beginning of the nineteenth century; Strassmann described septate and bicornuate uterus and some subgroups of the disorders in 1907. However, the first classification system for categorization of congenital uterine malformations was that of the American Fertility Society (AFS) published in 1988, mostly based on the previous work of Buttram and Gibbons [3, 4].

Then other classification systems followed, but the AFS classification is still the most broadly used, widely accepted among specialists.

The American Fertility Society introduced a classification system that stratifies MDA into seven different classes of uterine anomalies (Fig. 1.1).

1.5.1 Class I Anomalies: Dysgenesis

Dysgenesis (segmental agenesis and variable hypoplasia) of the Mullerian ducts (uterus and

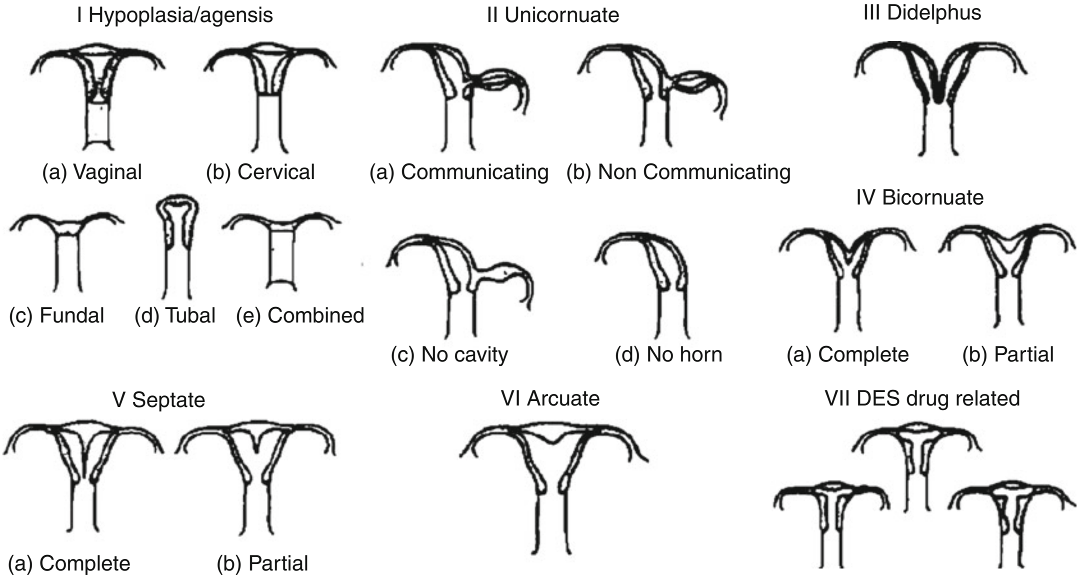

Fig. 1.1 Classification system of Mullerian duct anomalies by the American Fertility Society

upper 2/3 of the vagina) (Fig. 1.1). Mayer-Rokitansky-Küster-Hauser syndrome is the most common form of Class I anomaly and includes agenesis of uterus and vagina [5, 9, 10].

1.5.2 Class II Anomalies: Unicornuate Uterus

Unicornuate uterus is the result of partial or complete hypoplasia of one Mullerian duct (Fig. 1.1) [11]. Unicornuate uterus may be isolated (35 %) or associated with a contralateral rudimentary horn. The rudimentary horn presents with or without communication to the endometrial cavity and may be associated with or without endometrium, which is also called no cavity rudimentary horn. In patients with cavity non-communicating rudimentary horn, dysmenorrhea and hematometra may occur. Surgical resection either to relieve symptomatic pain or to reduce the risk of potential ectopic pregnancy is justified. As with every obstructed system, the risk of endometriosis is also increased with a non-communicating rudimentary horn. Renal malformations are common with unicornuate uterus and occur mostly on the same side as the rudimentary horn could be found [5].

1.5.3 Class III Anomalies: Uterus Didelphys

Uterus didelphys is a result of complete non-fusion of the Mullerian ducts forming a complete uterine duplication with no communication between each other (Fig. 1.1).

Uterus didelphys may be associated with a longitudinal (75 %) or, more rarely, with a transverse vaginal septum, the latter causing obstructive hematometrocolpos.

Endometriosis as a result of retrograde menstruation may also occur in these conditions. A nonobstructive uterus didelphys is usually asymptomatic [5].

1.5.4 Class IV Anomalies: Bicornuate Uterus

Bicornuate uterus is the result of incomplete fusion of the cranial parts of the Mullerian ducts (Fig. 1.1) [5–9, 12]. Two uterine cavities with normal zonal anatomy can be depicted. The leading imaging feature is a fundal cleft greater than 1 cm of the external uterine contour that helps to distinguish bicornuate uterus from septate uterus.

Extension of the intervening fundal cleft to the internal cervical os characterizes the complete bicornuate uterus with a single cervix (bicornuate, unicollis uterus), whereas variants of partial bicornuate uterus exist if the cleft is of variable length. Bicornuate uterus may be associated with a duplicated cervix (bicornuate bicollis uterus), as well as with a longitudinal vaginal septum that coexists in up to 25 % of bicornuate uterus. Nevertheless, a degree of communication is always present between both uterine cavities.

Still controversial is the need for surgical intervention and this is probably only necessary in specific cases.

A higher rate of cervical incompetence seems to be associated with bicornuate uterus [13].

1.5.5 Class V Anomalies: Septate Uterus

Septate uterus is a result of partial or complete non-regression or the midline uterovaginal septum (Fig. 1.1) [12, 13]. The main imaging feature is that the external contour of the uterine fundus may be either convex or mildly concave (<1 cm) and not with a cleft greater than 1 cm, the latter defining a bicornuate or didelphic uterus.

Septate uterus is the most common Mullerian duct anomaly and is unfortunately associated with the poorest reproductive outcome. Because of different treatment options, septate uterus must be differentiated from bicornuate and didelphic uterus. A widely accepted definition – empirically established during laparoscopy procedures – states that a uterus is septate if the outer contour of the uterine fundus is only mildly concave in the presence of a septum. The cutoff of concavity is 1 cm; deeper concavity is associated with bicornuate uterus and uterus didelphys.

In a complete septate uterus, the septum extends to the external cervical os. In 25 % of septate uteri, the septum extends even further into the upper part of the vagina.

Obstetric outcome seems not to be correlated with the length of the septum. The septum may be composed of muscle or fibrous tissue and is not a reliable means of distinguishing septate and bicornuate uteri.

Resection of the septum by hysteroscopic metroplasty is indicated and may improve the reproductive outcome significantly [5].

1.5.6 Class VI Anomalies: Arcuate Uterus

Arcuate uterus is the result of a near-complete regression of the uterovaginal septum forming a mild and broad saddle-shaped indentation of the fundal endometrium (Fig. 1.1).

Differentiation from bicornuate uterus is based on the complete fundal unification; however, a broad-based septate uterus is difficult to distinguish from an arcuate uterus. There is much controversy as to whether an arcuate uterus should be considered a real anomaly or an anatomic variant. MRI may detect this abnormality, but, typically, it is not clinically significant because arcuate uterus has no significant negative effects on pregnancy outcome [5].

1.5.7 Class VII Anomalies

DES-exposed uterus (Fig. 1.1). DES (synthetic estrogen, diethylstilbestrol, 1948–1971) may induce abnormal myometrial hypertrophy in the fetal uterus forming small T-shaped endometrial cavities, as well as increase the risk of developing a clear cell carcinoma of the vagina.

The characteristic uterine abnormalities must be categorized in the group of complex uterine anomalies and may occur with or without the exposure of DES [5–10, 12–14].

1.6 Diagnosis of Uterine Anomalies

Diagnosis of uterine anomalies should be based on diagnostic modalities that could determine the anatomical status of the female genital tract on an objective way.

The ideal diagnostic method should provide objective and measurable information on the anatomical status of the uterus in a noninvasive way [1–10, 12–15].

The available diagnostic methods that can be used in the investigation of the patient are as follows.

1.6.1 Gynecological Examination

It should be noticed that gynecological examination is very important in the diagnostic work-up of the patients with congenital malformations.

Vaginal malformations (aplasia, septum) and some cervical malformations could be diagnosed objectively mainly with inspection. Furthermore, palpation through the vagina and/or the rectum (in cases of vaginal aplasia) could provide useful but not always objective information [1].

1.6.2 Two-Dimensional Ultrasound (2D US)

This approach provides objective and, importantly, measurable information for the cervix, the uterine cavity, the uterine wall, and the external contour of the uterus. It is very popular and accessible, noninvasive, but its accuracy highly depends on the experience of the examiner and on the examination methodology followed.

Endovaginal US has the advantage of improved spatial resolution [1–10, 12–16].

1.6.3 Sonohysterography (SHG)

Compared to 2D US, this method has the additional advantage of offering a better imaging of the uterine cavity, thus enhancing the accuracy in identifying the anatomy of the female genital tract and especially that of the uterus.

With infusion of saline into the endometrial canal, sonohysterography provides improved delineation of the endometrium and internal uterine morphology; however, it shares limitations similar to those of conventional endovaginal US and can only help evaluate patent endometrial canal [17].

1.6.4 Hysterosalpingography (HSG)

HSG is indicated in the early stages of evaluation of the infertile couple. The examination provides a morphologic assessment of the endometrial and endocervical canal and supplies important information regarding tubal patency.

Characterization of uterine anomalies can be difficult; however, there can be considerable overlap in findings, notably with regard to differentiation of a septate from a bicornuate uterus.

The major limitations of the procedure are the ability to characterize only patent canals and the inability to evaluate the external uterine contour adequately.

HSG also entails exposure to ionizing radiation in these typically young women [12, 16–18].

1.6.5 Three-Dimensional Ultrasound (3D US)

3D US provides an ideal, objective, and measurable representation of the examined organs. It provides information on the cervix, the uterine cavity, the uterine wall, the external contour of the uterus, and the other structures with the exception of tubes. Theoretically, it seems to be an ideal method for the diagnostic approach of the uterus [19–21], but has limited application in clinical practice.

1.6.6 Magnetic Resonance Imaging (MR)

MR imaging has a reported accuracy of up to 100 % in the evaluation of Mullerian duct anomalies.

It is a very useful diagnostic tool, since it can provide clear delineation of internal and external uterine anatomy in multiple imaging planes and, most importantly, reliable depiction of the external uterine contour. Complex anomalies and secondary diagnoses such as endometriosis can often be optimally characterized noninvasively.

Although it is more expensive than US, its greater accuracy makes it more trusted by many gynecologists [12, 17–22].

1.6.7 Hysteroscopy (HYS)

Hysteroscopy is the gold standard for the examination of the cervical canal and the uterine cavity. However, as it does not provide information on the myometrial layer, hysteroscopy alone could not be used for the differential diagnosis between different groups.

Nowadays, with the use of normal saline as distension medium and the miniaturization of the rigid scopes, hysteroscopy has become a minimally invasive screening tool, well tolerated by the patients and feasible for gynecologists [1].

1.6.8 Laparoscopy and Hysteroscopy (Lap/Hys)

The combined application of these endoscopic techniques is thought to be the gold standard in the investigation of women with congenital malformations and especially the uterine ones.

However, the diagnosis is mainly based on the subjective impression of the clinician performing them, and this is thought to be a limitation in the objective estimation of the anomaly [1].

1.7 Imaging Findings in MDA

Once an MDA is suggested based on evidence from the patient history and physical examination, the next diagnostic step includes different imaging work-ups in order to detect and specify MDA and to guide further treatment options.

Before US and MRI were capable of visualizing MDA with a high accuracy, imaging of MDA was limited to hysterosalpingography (HSG). Since the diagnostic imaging properties of MDA include mainly the configuration of the endometrial cavity and the external uterine contour, HSG is able to depict only certain types of MDA, whereas it fails in other cases and stays nonspecific for precise diagnosis, the latter mainly due to the lack of the visualization of the outer uterine contour. Because of this drawback, HSG did not provide diagnoses with high degrees of confidence, and US and MRI soon began to play a larger role in assessment and treatment of patients. As HSG provides, besides the morphological, also the functional information of tubal patency, it is still used in the primary imaging work-up in case of infertility clarification.

Nowadays, the first imaging modalities in the MDA assessment include pelvic US – transabdominal US (performed with a 2.5- to 5-MHz probe, for evaluation of the entire abdomen, especially for associated renal malformations) and transvaginal US (performed with a 5- to 8-MHz endovaginal probe, for better delineation of the uterus, vagina, and ovaries) – and MRI. Newer techniques, such as 3D US, even further improved the imaging diagnostics by giving better information about the external contour of the uterus and its volume [5, 16, 17].

1.8 Magnetic Resonance Imaging (MRI)

Magnetic resonance imaging (MRI) is today considered standard in the evaluation of MDA and accepted as the leading imaging modality for further surgical planning. MRI provides high-resolution images of the entire uterine anatomy (internal and external contour), as well as of secondary findings like renal malformations.

Among the three major imaging methods, MRI has the best accuracy in the evaluation of uterine anomalies (up to 100 % has been reported) [5, 8, 16, 17, 23, 24].

1.8.1 MRI Technique [11, 17, 25]

Patients should be scheduled to undergo RM examination possibly in the second half of the menstrual cycle, during the follicular and secretory phase when the thickness of the endometrium is increased, thus permitting to better depict the normal zonal anatomy of the uterus. No specific patient preparation is necessary but patients should have an empty urinary bladder; an intramuscular antispasmodic drug could be administered some minutes prior the examination in order to reduce the motion artifacts related to the bowel peristalsis.

At moment, the gold standard for MR imaging of pelvic region is a high-field magnet such as a 1.5 T magnet with a phased array surface coil, but 3 T magnets could be used too [26, 27]. Standard pelvic MR imaging protocols include axial T1-weighted and T2-weighted images. T2-weighted imaging is essential for evaluation of uterine anatomy.

T2 RARE sequences have the best spatial resolution and are those to prefer in order to evaluate the presence of MDA, even if the acquisition time is longer than T2-weighted *half-Fourier* sequences.

Sagittal sections are best suited to image the uterus point for proper assessment of the uterine fundal contour. In addition it is mandatory to perform axial or coronal oblique sections, depending on uterine lie, parallel to the endometrial cavity resulting in a long-axis view of the uterus.

An additional oblique sequence obtained perpendicular to the cervical results in a short-axis view and allows accurate assessment of the cervix, demonstrating, if present, duplication or septation.

Because this series is pivotal in the evaluation of MDA, it is best performed earlier in the examination, prior to bladder filling, which often displaces consequently the uterus.

A coronal T2-weighted sequence, with a large field of view to enable assessment of the kidneys should be performed in addiction [12, 17].

T1-weighted sequences are mainly helpful to evaluate the presence of any associated pathologies such as ovarian disease; they should be obtained both without and with fat saturation in order to better demonstrate the presence of hemorrhage within the endometrial cavity (hematometra) and/or vagina (hematocolpos).

3D T2-weighted sequences are quick and provide submillimeter section thickness allowing multiplanar reconstruction, thus could be used in pediatric patients to significantly reduce imaging time.

Contrast material is not necessary to evaluate the presence and type of MDA and is not used in standard examination; Gadolinium-enhanced imaging is reserved for assessment of incidentally discovered additional disease.

1.8.2 Specific MRI Findings

1.8.2.1 Class I: Mullerian Agenesis and Hypoplasia

Variable degrees of early failure to form the Mullerian ducts prior to fusion occur in approximately 10 % of uterine congenital anomalies. Complete vaginal agenesis is the common presentation (Mayer-Rokitansky-Küster- Hauser syndrome) (Figs. 1.1 and 1.2) [11, 24–29].

Ninety percent of patients have associated uterine agenesis, and 10 % have a small rudimentary uterus (Fig. 1.3). Uterine agenesis manifests as lack of visualization of a discernible uterus on MRI.

Hypoplastic uteri are small, low-signal-intensity, soft-tissue remnants on T2-weighted images with diminished zonal anatomy even if an endometrial segment is present (Fig. 1.3).

Vaginal agenesis is best characterized on the axial plane with no normal vaginal tissue insinuated between the urethra and rectum (Fig. 1.2) [24].

1.8.2.2 Class II: Unicornuate Uterus

Failure of one Mullerian duct to elongate while the other develops normally results in the unicornuate uterus and accounts for approximately 20 % of Mullerian duct anomalies (Fig. 1.1). A unicornuate uterus may be isolated, manifesting in 35 % of patients, although it is usually associated with variable degrees of a rudimentary uterine horn (Figs. 1.4 and 1.5) [17].

A noncavitary rudimentary horn without associated endometrium is seen in 33 % of cases, and that with an endometrial segment is seen in 32 %.

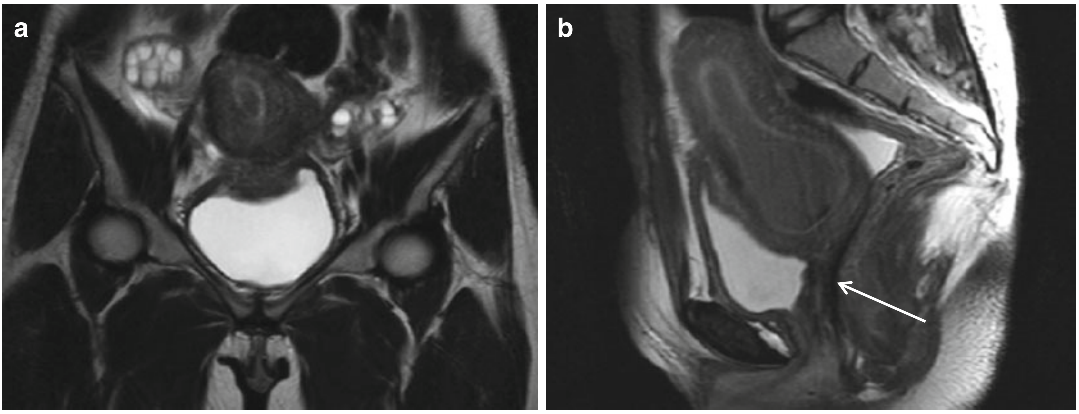

Fig. 1.2 Vaginal agenesis (Ia). Fast spin-echo T2-weighted images on coronal (TR/TE 3310/94) (**a**) and sagittal plane (TR/TE 4070/94) (**b**) show normal uterus with cervix and no vaginal cavity (*arrow* in **b**)

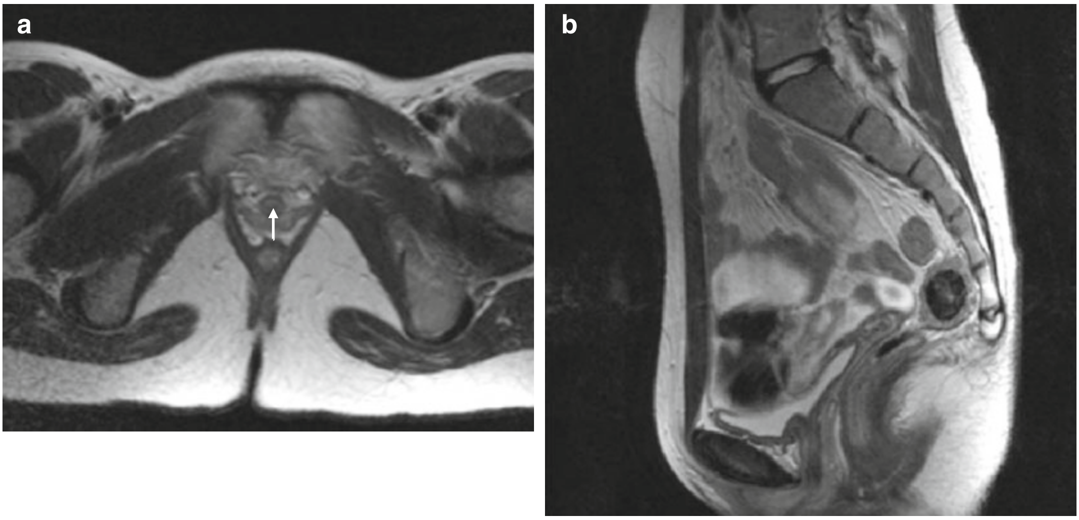

Fig. 1.3 Uterine hypoplasia (I). Fast spin-echo T2-weighted images on axial (TR/TE 3000/108) (**a**) and sagittal plane (TR/TE 3310/94) (**b**) show uterine hypoplasia. Small uterine remnant demonstrating lack of normal zonal anatomy. The vagina is normal in configuration with normal vaginal tissue between urethra and rectum (*arrow* in **a**)

A cavitary rudimentary horn is designated "communicating" if there is communication with the endometrium of the contralateral horn (10 % of cases) and "non-communicating" if there is no such communication (22 % of cases) (Figs. 1.4 and 1.5) [22].

As with uterus didelphys, the manifestation is usually incidental unless a non-communicating rudimentary horn is present. Dysmenorrhea with hematometra may manifest at menarche in this subgroup.

In addition, the incidence of endometriosis is increased in this subgroup, similar to the case in an obstructed uterus didelphys [30].

Resection of the non-communicating horn is indicated, not only for symptomatic relief but also because ectopic pregnancy may occur in the rudimentary horn.

Resection of a communicating horn is also a consideration, because pregnancies that develop in the rudimentary horn rarely yield viable offspring.

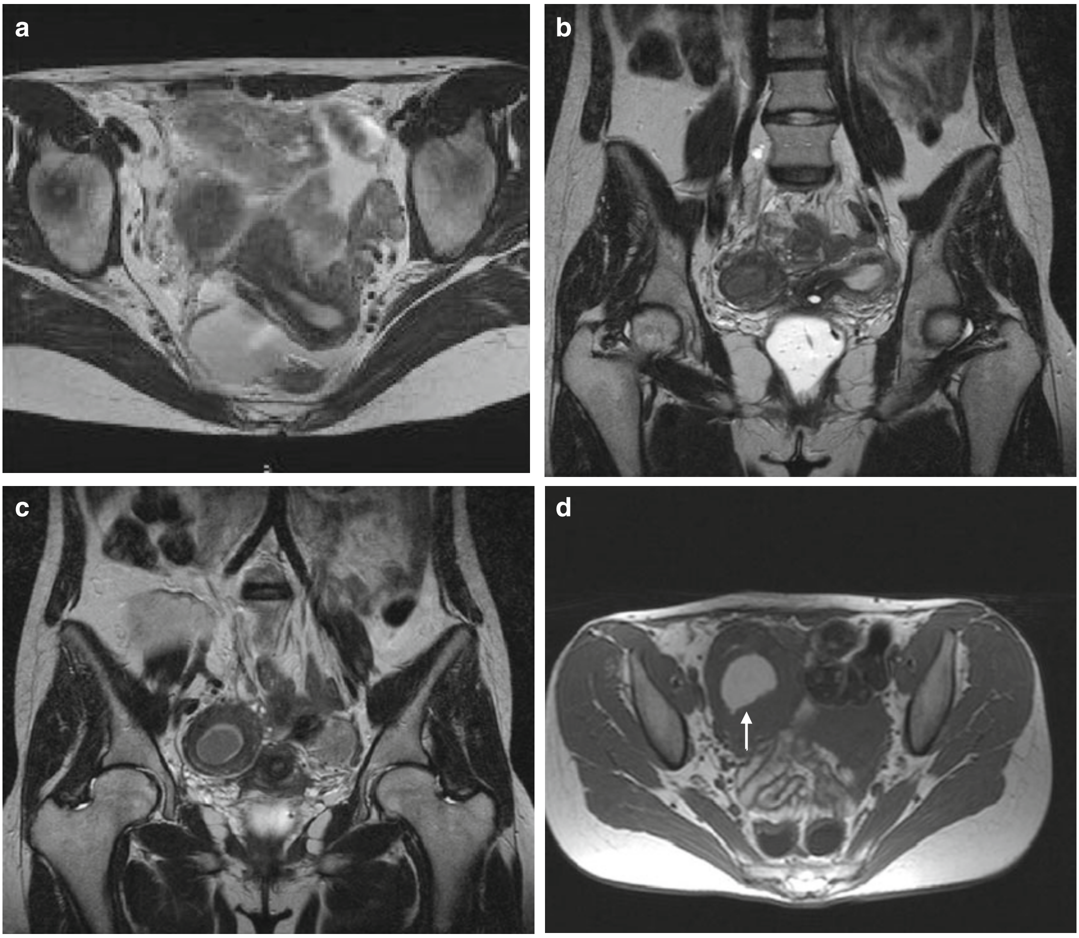

Fig. 1.4 Non-communicating unicornuate uterus (II b). Fast spin-echo T2-weighted images on axial (TR/TE 3000/108) (**a**) and coronal plane (TR/TE 3310/94) (**b**, **c**); fast spin-echo T1-weighted images on axial (TR/TE 550/12) (**d**) show unicornuate uterus with non-communicating rudimentary horn that contains endometrium. No communication with the cavity of normal left uterine horn. This cavity communicates with a normal cervix; the image (**b**) shows Naboth cyst of the cervix uteri. A large area of hematometra within the non-communicating horn is seen (*arrow* in **d**)

Surgical intervention in a rudimentary horn without associated endometrium is rarely indicated.

Renal abnormalities are more commonly associated with unicornuate uterus than with other Mullerian duct anomalies and have been reported in 40 % of these patients. The anomaly is always ipsilateral to the rudimentary horn.

Renal agenesis is the most commonly reported abnormality, occurring in 67 % of cases.

Ectopic kidney, horseshoe kidney, cystic renal dysplasia, and duplicated collecting systems have also been described.

On MR images, the unicornuate uterus appears curved and elongated, with the external uterine contour assuming a banana shape. Uterine volume is reduced, and the configuration of the uterus is asymmetric. Normal myometrial zonal anatomy is maintained. The endometrium may be uniformly narrow or may assume a bullet shape, tapering at the apex. The endometrial-to-myometrial width and ratio are reported to be normal.

The appearance of the rudimentary horn is variable. When the endometrium is absent, the horn is of low signal intensity, with loss of normal

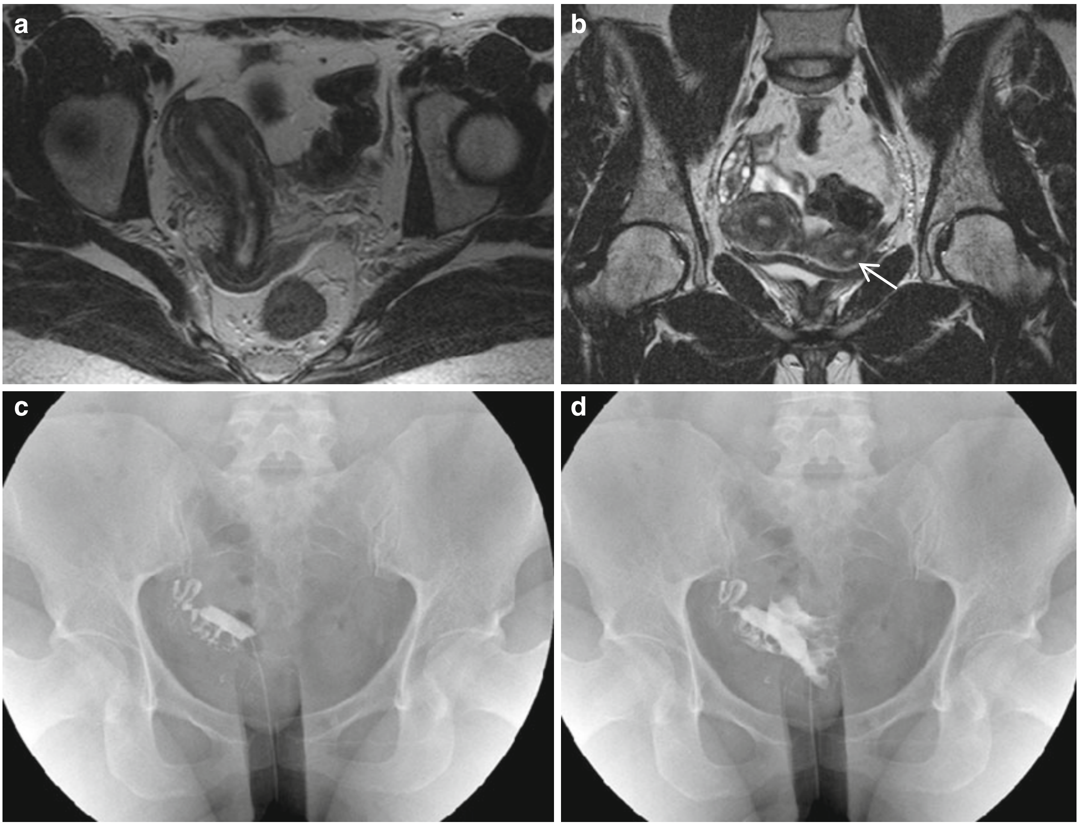

Fig. 1.5 Unicornuate communicating uterus (IIa). Fast spin-echo T2-weighted images on axial (TR/TE 2800/110) (**a**) and coronal plane (TR/TE 3310/93) (**b**) show unicornuate uterus with a communicating rudimentary left uterine horn (*arrow* in **b**). Hysterosalpingography images (**c**, **d**) demonstrated the filling of only the main uterine cavity; however, the lack of hematometra at MRI imaging allows excluding non-communicating uterus

zonal anatomy [31]. When the endometrium is present, zonal anatomy may be preserved [12, 17–24].

1.8.2.3 Class III: Uterus Didelphys

Uterus didelphys, which constitutes approximately 5 % of Mullerian duct anomalies, is the result of nearly complete failure of fusion of the Mullerian ducts (Fig. 1.1). Each Mullerian duct develops its own hemiuterus and cervix and demonstrates normal zonal anatomy with a minor degree of fusion at the level of the cervices. No communication is present between the duplicated endometrial cavities (Figs. 1.6, 1.7, and 1.8).

A longitudinal vaginal septum is associated in 75 % of these anomalies.

Longitudinal vaginal septa may be complicated by defects in vertical fusion that result in a transverse vaginal septum and subsequent hematometrocolpos.

Nonobstructive uterus didelphys is usually asymptomatic, while uterus didelphys with unilateral vaginal obstruction may become symptomatic at menarche and manifest as dysmenorrhea.

Endometriosis and pelvic adhesions have an increased prevalence and are reported to be secondary to retrograde menstrual flow in the subset of patients with obstruction. MR imaging demonstrates two separate uteri with widely divergent apices, two separate cervices, and usually an upper vaginal longitudinal septum (Figs. 1.6, 1.7, and 1.8). In each uterus, the endometrial-to-myometrial width and ratio are preserved, as is normal uterine zonal anatomy.

An obstructed unilateral vaginal septum may cause apparent marked deformity of the

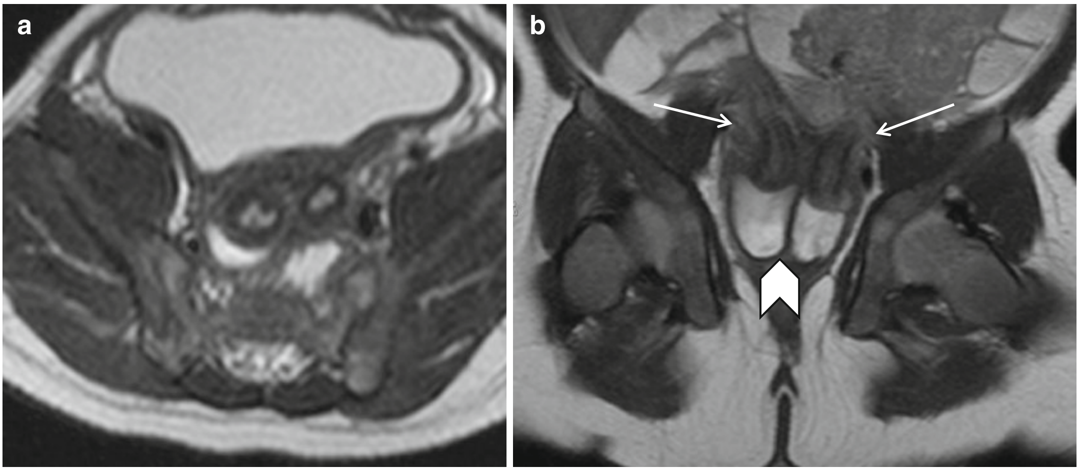

Fig. 1.6 Didelphys uterus (III). Fast spin-echo T2-weighted images on sagittal (TR/TE 4530/90) (**a**) and coronal plane (TR/TE 3310/93) (**b**) show two separate cervices and two divergent uterine horns (*arrows* in **b**) and duplication of the proximal vagina well defined by presence of fluid (*arrowheads* in **b**)

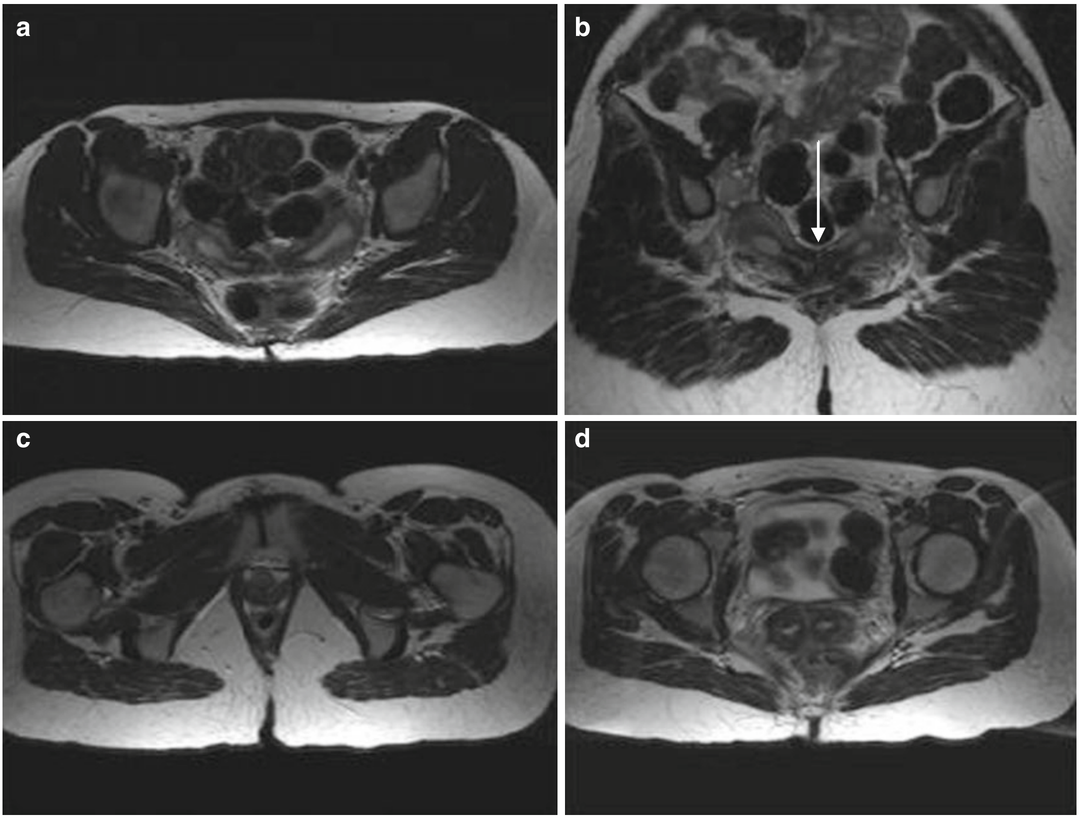

Fig. 1.7 Didelphys uterus (III). Fast spin-echo T2-weighted images on axial (TR/TE 2800/110) (**a**, **c**, **d**) and coronal plane (TR/TE 4070/94) (**b**) show two divergent horns with duplicated cervices in close apposition but no evidence of fusion. It is appreciable wide divergence of uterine horns without communication of endometrial cavities and presence of septum (*arrow* in **b**). No longitudinal septum is seen in the vagina (**c**)

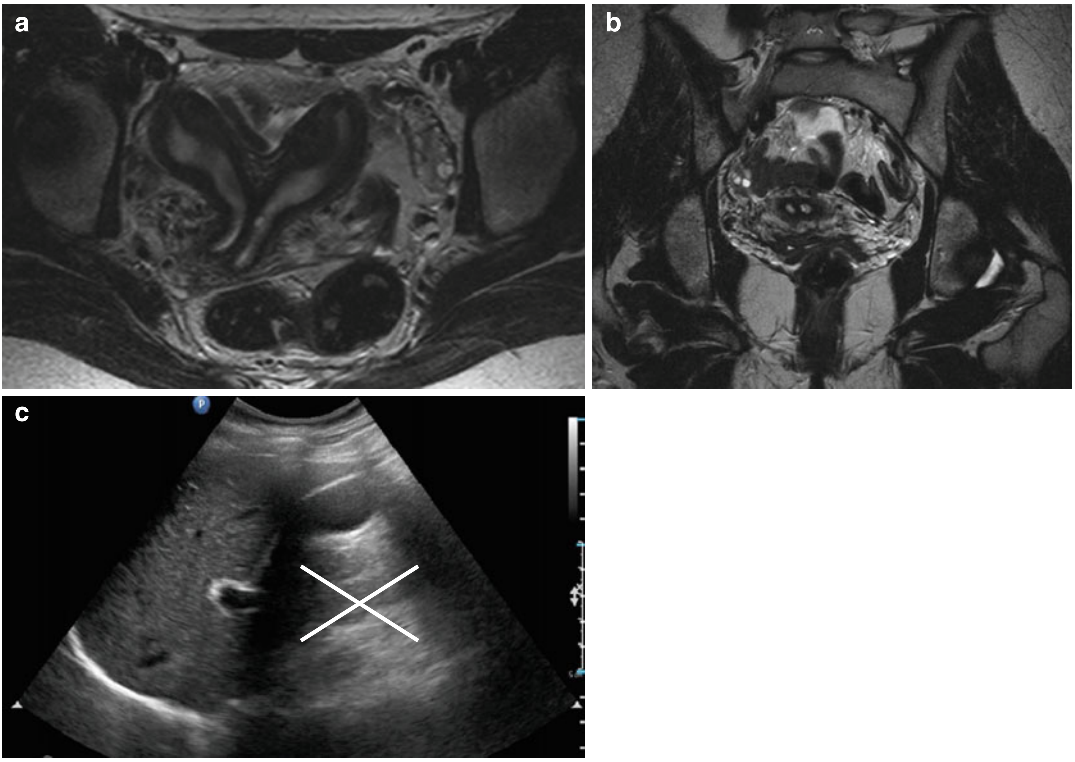

Fig. 1.8 Didelphys uterus (III). Fast spin-echo T2-weighted images on axial (TR/TE 4070/94) (**a**) and coronal plane (TR/TE 3310/93) (**b**) show complete duplication of uterine horns, which result non-communicating. (**c**) US examination demonstrated the associated agenesis of the right kidney

uterus according to the degree of associated hematometrocolpos [17, 24, 32].

1.8.2.4 Class IV: Bicornuate Uterus

The bicornuate uterus results from incomplete fusion of the uterovaginal horns at the level of the fundus and accounts for approximately 10 % of Mullerian duct anomalies (Fig. 1.1). Patients with a bicornuate uterus and no extrauterine infertility issues usually have little difficulty conceiving.

A bicornuate uterus consists of two symmetric cornua that are fused caudally, with communication of the endometrial cavities – most often at the level of the uterine isthmus (Figs. 1.9 and 1.10).

The intervening cleft of the complete bicornuate uterus extends to the internal cervical os (bicornuate unicollis) (Figs. 1.9 and 1.10), while the cleft of a partial bicornuate configuration is of variable length (Figs. 1.11 and 1.12).

A bicornuate bicollis uterus is associated with a duplicated cervix, although a degree of communication is maintained between the two horns. At least six variations of the bicornuate uterus have been described in the literature. Longitudinal upper vaginal septa are reported to coexist in 25 % of bicornuate uteri.

On MR images, the bicornuate uterus demonstrates a cleft of at least 1.0 cm of the external fundal uterine contour. The horns demonstrate normal uterine zonal anatomy. The endometrial-to-myometrial ratio and width are normal in appearance. Superimposed leiomyomas and adenomyosis are well demonstrated [12, 17–24].

1.8.2.5 Class V: Septate Uterus

The septate uterus is the most common Mullerian duct anomaly (Fig. 1.1). This anomaly composes approximately 55 % of Mullerian duct anomalies and is associated with some of the poorest reproductive outcomes.

On MR images, the septate uterus is generally normal in size. The endometrial cavities appear smaller than in uteri with a normal configuration (Figs. 1.13 and 1.14). The external uterine

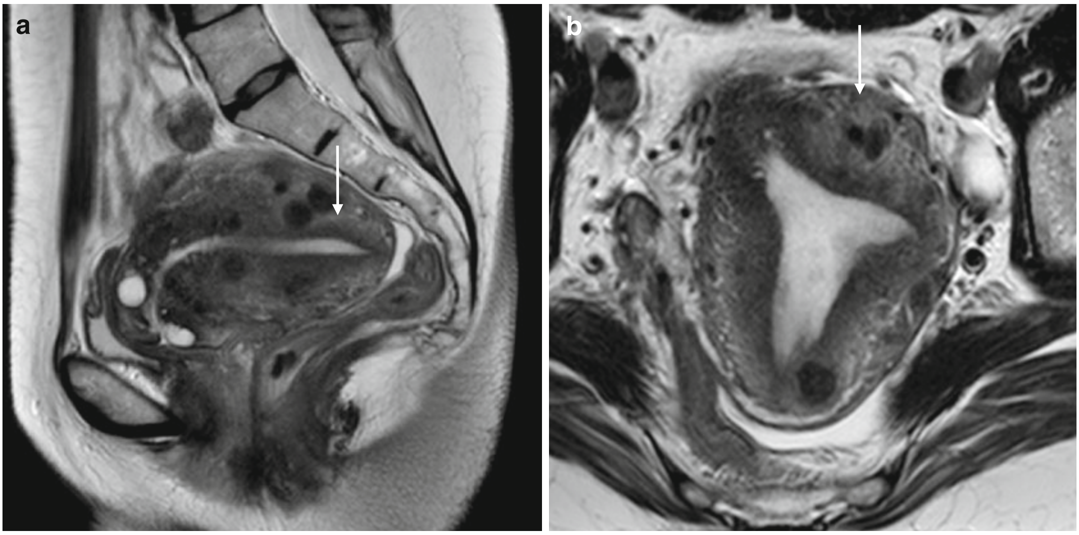

Fig. 1.9 Partial bicornuate uterus (IV). Fast spin-echo T2-weighted images on sagittal plane (TR/TE 4530/90) (**a**) and on axial plane (TR/TE 4070/94) (**b**) show a unique uterine cavity with abnormal uterine contour (*arrow*)

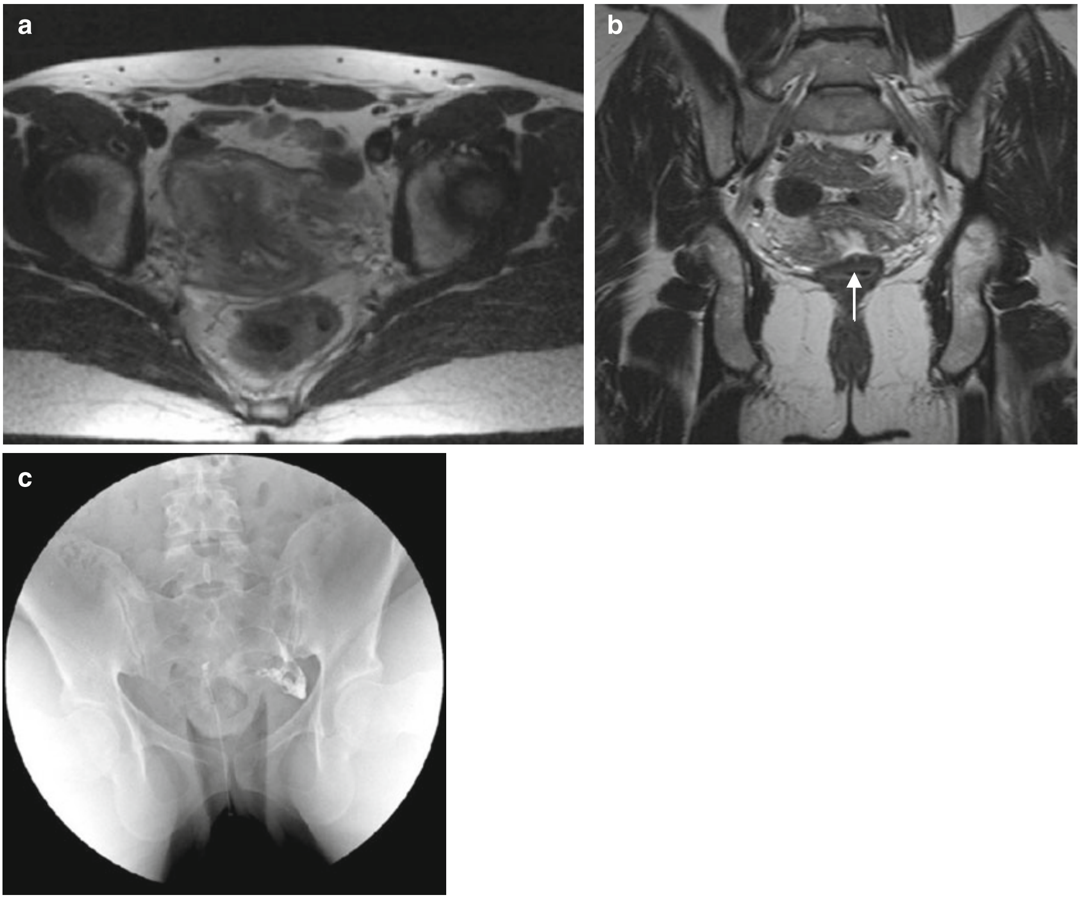

Fig. 1.10 Partial bicornuate uterus (IV b). Fast spin-echo T2-weighted images on axial (TR/TE 4070/94) (**a**) and coronal plane (TR/TE 3300/108) (**b**) show large notch between two separate uterine horns and the communication with a solitary cervix (*arrow*). Hysterosalpingography (HSG) image of the same patients (**c**) shows normal opacization only of the left horn

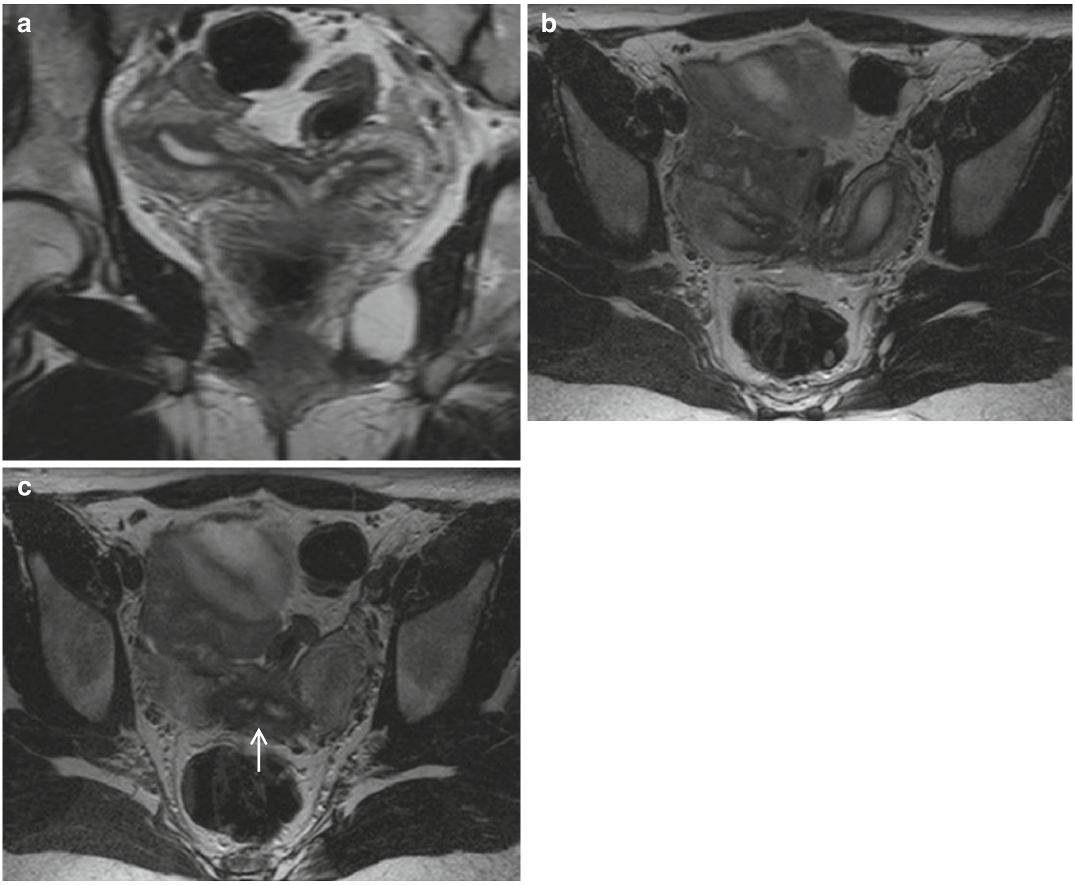

Fig. 1.11 Complete bicornuate uterus (IVa). Fast spin-echo T2-weighted images on coronal (TR/TE 4070/94) (**a**) and axial plane (TR/TE 3070/108) (**b**, **c**) demonstrate wide divergence of uterine horns, with communication of endometrial cavities in the cervix (*arrow* in **c**)

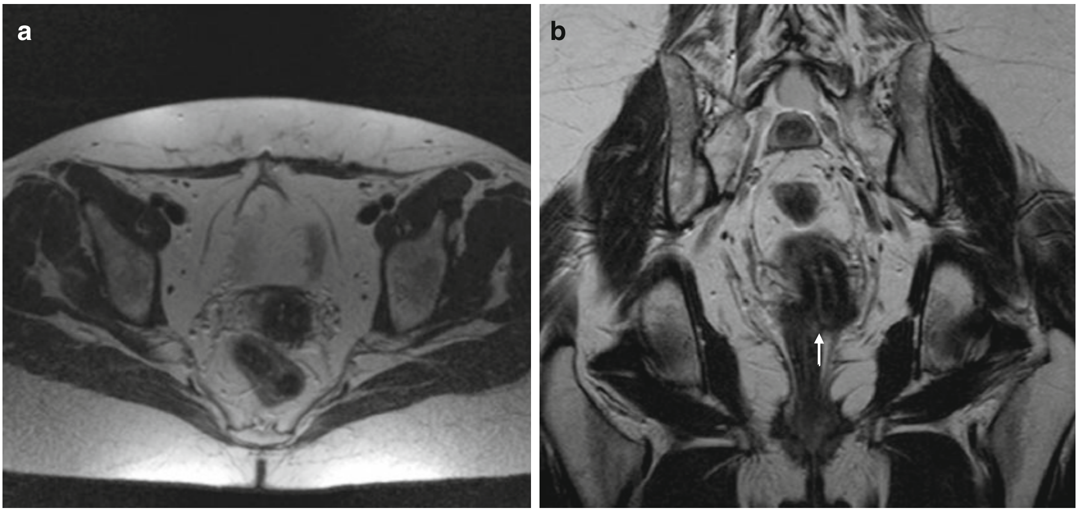

Fig. 1.12 Complete bicornuate uterus (IVa). Fast spin-echo T2-weighted images on axial (TR 2800/TE 110) (**a**) and coronal plane (TR/TE 4070/94) (**b**) demonstrate two uterine horns with communication of endometrial cavities within the lower uterine body (*arrow* in **b**) and two duplicated cervices

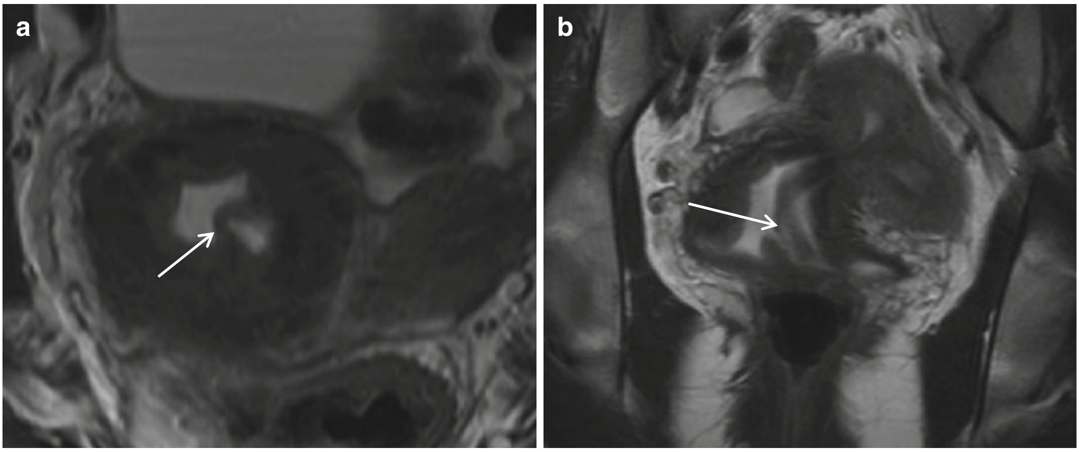

Fig. 1.13 Complete septate uterus (Va). Fast spin-echo T2-weighted images on axial (TR 2820/TE110) (**a**) and coronal plane (**b**) (TR/TE 4070/94) show a normal-sized uterus with the presence of a low-signal-intensity complete fibrous septum (*arrows* in **a** and **b**)

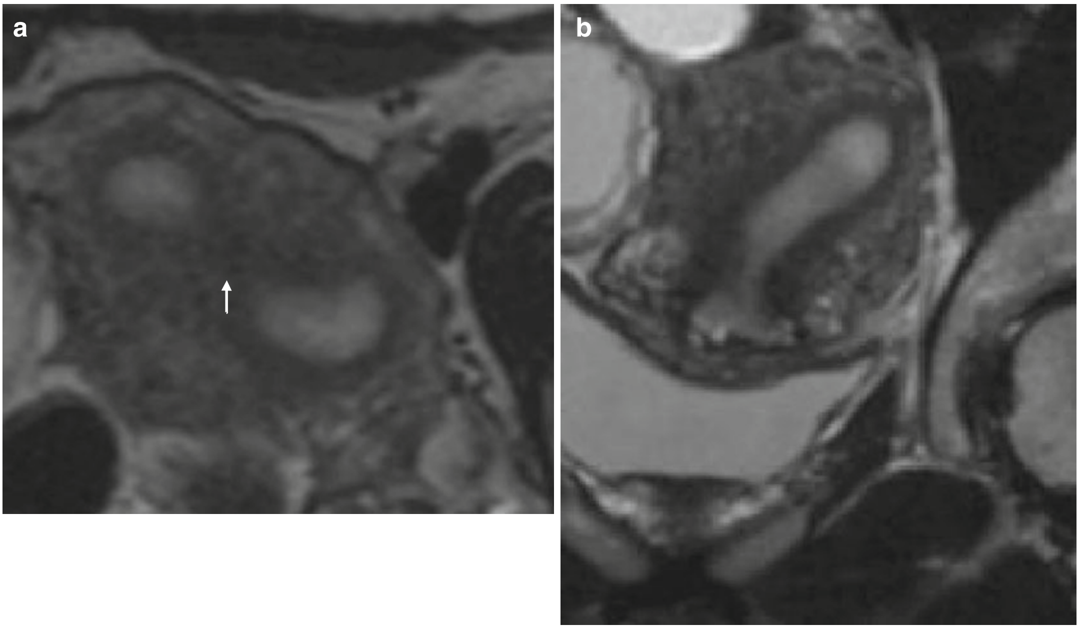

Fig. 1.14 Partial septate uterus (Vb). Fast spin-echo T2-weighted images on axial (TR 2820/TE 110) (**a**) and coronal plane (**b**) (TR/TE 4000/94) show the septum dividing the uterine cavity is of uniform low signal intensity, consistent with fibrous tissue surrounded by myometrium (*arrow* in **a**). The septum does not extend onto the cervical os

contour is united and may be convex, flat, or mildly concave.

The fundal segment of the septum is isointense to myometrium in all septa, partial or complete (Figs. 1.13 and 1.14). In complete septa, the inferior segment of the septum is usually a low-signal linear band on T2-weighted images, corresponding to the more fibrous component. This band more often is absent in partial septa, which are uniformly isointense to myometrium.

The presence of leiomyomas and adenomyosis that can arise in the septum corroborates the myometrial composition of the septum [12, 17–24].

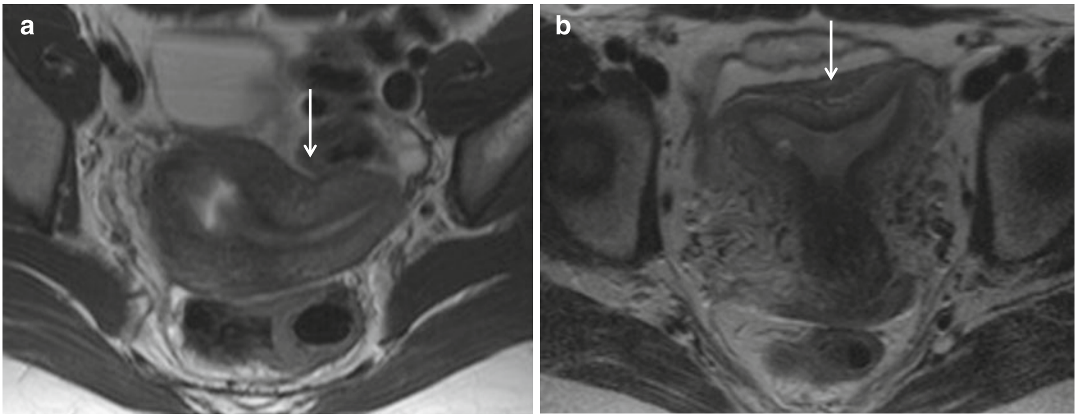

Fig. 1.15 Arcuate uterus (VI). Fast spin-echo T2-weighted image on axial plane (TR/TE 4070/94) (**a**, **b**) in two different patients shows a mild indentation of uterine profile (*arrows*), with the normal myometrial signal intensity. The lack of low signal intensity allows to exclude the presence of fibrous septum and then of a septate uterus

1.8.2.6 Class VI: Arcuate Uterus

The arcuate uterus is characterized by a mild indentation of the endometrium at the uterine fundus as a result of near-complete resorption of the uterovaginal septum (Fig. 1.1). Classification has been problematic, because it remains unclear whether this variant should be classified as a true anomaly or as an anatomic variant of normal. On revision of the classification by the American Fertility Society, a separate class was designated because the arcuate uterus can be distinguished from a bicornuate uterus on the basis of its complete fundal unification (Fig. 1.15).

Data regarding the reproductive outcomes of patients with an arcuate uterus are extremely limited and widely disparate.

On MR images, the normal external uterine contour is maintained. The myometrial fundal indentation is smooth and broad, and the signal intensity of this region is isointense to normal myometrium. No low-signal-intensity fibrous component is appreciated (Fig. 1.15) [12, 17–24]. A defining depth to differentiate a prominent arcuate from a mild septum has not been established.

1.8.2.7 Class VII: DES-Exposed Uterus

DES is a synthetic estrogen that was introduced in 1948 and prescribed for women experiencing recurrent spontaneous abortions, premature deliveries, and other pregnancy complications. By increasing the synthesis of placental steroidal hormones, DES was thought to decrease the frequency of pregnancy loss.

In utero exposure to DES was shown to be associated with clear cell carcinoma of the vagina, and use of the drug was abruptly discontinued in 1971.

Structural anomalies of the uterine corpus, cervix, and vagina were subsequently described and shown to affect reproductive potential. DES has been shown to interfere with embryologic development of the mesenchyme of the genital tract.

However, it should be noted that not all women exposed to DES have reproductive problems.

The amount of the drug ingested, as well as when the drug was taken during the gestation, has clinical implications. If the drug was taken very early in the first trimester or after 22 weeks gestation, structural abnormalities are not likely to occur [14–17].

Moreover, the characteristic spectrum of uterine abnormalities associated with DES exposure has been reported in women without a history of exposure to the medication. As such, the morphologic changes may represent a rare Mullerian anomaly of the uterus that may be expressed because of or induced by exposure to DES.

A T-shaped configuration of the endometrial cavity is the most commonly associated abnormality, seen in 31 % of exposed women (Fig. 1.1).

Other uterine corpus anomalies include a small hypoplastic uterus, constriction bands, a widened lower uterine segment, a narrowed fundal segment of the endometrial canal, irregular endometrial margins, and intraluminal filling defects.

Anomalies of the fallopian tube include foreshortening, sacculations, and fimbrial deformities with fimbrial stenosis. Cervical anomalies occur in 44 % of cases and include hypoplasia anterior cervical ridge, cervical collar, and pseudopolyps. On MR images, uterine hypoplasia, the T configuration of the endometrial cavity, and constriction bands can be demonstrated.

The characteristic T configuration is best delineated with optimized imaging parallel to the long axis of the uterus. Constriction bands are characterized by focal thickening of the junctional zone, which makes the endometrial cavity narrow and irregular [12, 17–24].

Conclusions

Mullerian duct anomalies encompass a wide spectrum of clinical and imaging findings, and while many of the anomalies will be diagnosed initially at HSG or two-dimensional US, further imaging with MR and, potentially, three-dimensional US will often be required for a definitive diagnosis. MR imaging currently is the study of choice because of its high accuracy and detailed elaboration of uterovaginal and ovarian anatomy. Laparoscopy and hysteroscopy are then reserved for women in whom interventional therapy is being undertaken, thus reducing health-care expenditures and sparing women invasive diagnostic procedures [17].

References

1. Grimbizis GF, Campo R (2012) Clinical approach for the classification of congenital uterine malformations. Gynecol Surg 9:119–129
2. Grimbizis GF, Campo R (2010) Congenital malformations of the female genital tract: the need for a new classification system. Fertil Steril 94:401–4017
3. American Fertility Society (1988) The AFS classification of adnexal adhesions, distal tubal occlusion, tubal occlusion secondary to tubal ligation, tubal pregnancies, Mullerian anomalies and intrauterine adhesions. Fertil Steril 49:944–955
4. Buttram VC, Gibbons WE (1979) Mullerian anomalies: a proposed classification (an analysis of 144 cases). Fertil Steril 32:40–46
5. Baert AL, Knauth M, Sartor K, Kubik-Huch R (2007) MR and CT of the female pelvis. Congenital malformation of the uterus: 50–59
6. Nahum GG (1998) Uterine anomalies. How common are they, and what is their distribution among subtypes? J Reprod Med 43:877–888
7. Acien P, Acien MI (2011) The history of female genital tract malformation classifications and proposal of an updated system. Hum Reprod Update 17:693–705
8. Saleem SN (2003) MR imaging diagnosis of uterovaginal anomalies: current state of the art. Radiographics 23:e13
9. Pittock ST, Babovic-Vuksanovic D, Lteif A (2005) Mayer-Rokitansky-Kuster-Hauser anomaly and its associated malformations. Am J Med Genet A 135: 314–316
10. Oppelt P, Renner SP, Kellermann A, Brucker S, Hauser GA, Ludwig KS, Strissel PL, Strick R, Wallwiener D, Beckmann MW (2006) Clinical aspects of Mayer–Rokitansky–Kuester–Hauser syndrome: recommendations for clinical diagnosis and staging. Hum Reprod 21:792–797
11. Junqueira BL et al (2009) Müllerian duct anomalies and mimics in children and adolescents: correlative intraoperative assessment with clinical imaging. Radiographics 29:1085–1103
12. Pellerito JS, McCarthy SM, Doyle MB, Glickman MG, DeCherney AH (1992) Diagnosis of uterine anomalies: relative accuracy of MR imaging, endovaginal sonography, and hysterosalpingography. Radiology 183:795–800
13. Reuter KL, Daly DC, Cohen SM (1989) Septate versus bicornuate uteri: errors in imaging diagnosis. Radiology 172:749–752
14. van Gils AP, Than RT, Falke TH, Peters AA (1989) Abnormalities of the uterus and cervix after diethylstilbestrol exposure: correlation of findings on MR and hysterosalpingography. AJR Am J Roentgenol 153:1235–1238
15. Mazouni C, Girard G, Deter R, Haumonte J-B, Blanc B, Bretelle F (2008) Diagnosis of Mullerian anomalies in adults: evaluation of practice. Fertil Steril 89:219–222
16. Dee Olpin J, Heilbrun M (2009) Imaging of Mullerian duct anomalies. Clin Obstet Gynecol 52:40–56
17. Troiano RN, McCarthy SM (2004) Mullerian duct anomalies: imaging and clinical issues. Radiology 233:19–34
18. Braun P, Grau FV, Pons RM, Enguix DP (2005) Is hysterosalpingography able to diagnose all uterine malformations correctly? A retrospective study. Eur J Radiol 53:274–279
19. Bermejo C, Ten Martinez P, Cantarero R, Diaz D, Perez Pedregosa J, Barro E, Labrador E, Ruiz Lopez L (2010) Three-dimensional ultrasound in the diagnosis of Mullerian duct anomalies and concordance in the magnetic resonance imaging. Ultrasound Obstet Gynecol 35:593–601

20. Ghi T, Casadio P, Kuleva M, Perrone AM, Savelli L, Giunchi S, Meriggiola C, Gubbini G, Pilu G, Pelusi C, Pelusi G (2009) Accuracy of three-dimensional ultrasound in diagnosis and classification of congenital uterine anomalies. Fertil Steril 92:808–813
21. Jurkovic D (2002) Three-dimensional ultrasound in gynecology: a critical evaluation. Ultrasound Obstet Gynecol 19:109–117
22. Carrington BM, Hricak H, Nuruddin RN, Secaf E, Laros RK Jr, Hill EC (1990) Mullerian duct anomalies: MR imaging evaluation. Radiology 176: 715–720
23. Church DG, Vancil JM, Vasanawala SS (2009) Magnetic resonance imaging for uterine and vaginal anomalies. Curr Opin Obstet Gynecol 21:379–389
24. Robert N, Troiano MD (2003) Magnetic resonance imaging of mullerian duct anomalies of the uterus. Top Magn Reson Imaging 14(4):269–280
25. Olson MC, Posniak HV, Tempany CM, Dudiak CM (1992) MR imaging of the female pelvic region. Radiographics 12(3):445–465
26. Behr SC, Courtier JL, Qayyum A (2012) Imaging of müllerian duct anomalies. Radiographics 32:E233–E250
27. Epilman M, Dinan D, Gee MS, Servaes S, Lee EY, Darge K (2013) Mullerian duct and related anomalies in children and adolescents. Magn Reson Imaging Clin N Am 21(4):773–789
28. Kaufman RH, Adam E, Hatch EE et al (2000) Continued follow-up of pregnancy outcomes in diethylstilbestrol-exposed offspring. Obstet Gynecol 96:483–489
29. Fedele L, Dorta M, Brioschi D, Giudici MN, Candiani GB (1990) Magnetic resonance imaging in Mayer-Rokitansky-Kuster-Hauser syndrome. Obstet Gynecol 16:593–596
30. Brody JM, Koelliker SL, Frishman GN (1998) Unicornuate uterus: imaging appearance, associated anomalies, and clinical applications. AJR Am J Roentgenol 171:1341–1347
31. Fedele L, Bianchi S, Agnoli B, Tozzi L, Vignali M (1996) Urinary tract anomalies associated with unicornuate uterus. J Urol 155:847–848
32. Madureira AJ, Mariz CM, Bernardes JC, Ramos IM (2006) Uterus didelphys with obstructing hemivaginal septum and ipsilateral renal agenesis. Radiology 239: 602–606

MRI of Endometrial Carcinoma

2

Matteo Bonatti, Lisa Zantedeschi, Flavia Dal Corso, Riccardo Manfredi, and Roberto Pozzi Mucelli

2.1 Epidemiology

Endometrial cancer (EC) represents the most common gynecological malignancy in developed countries [1] and is the fourth most common cancer, after breast, lung, and colorectal cancer [2]. About 290,000 new cases of endometrial cancer are annually diagnosed worldwide [3], leading to approximately 74,000 deaths per year [4], and 47,000 new cases of EC are diagnosed yearly in the United States only [4]. The incidence of EC is ten times higher in North America and Europe than in less developed countries, because of a higher prevalence of risk factors among these populations [5], and it is rising parallel to the increase of life expectancy [2] and to the increase in the prevalence of obesity [6].

Endometrial cancer predominantly affects postmenopausal women [2], with 95 % of the cases diagnosed in women >40 years of age [7], and shows an incidence peak between 55 and 65 years [8]. Besides age, the main risk factors for developing endometrial carcinoma are correlated to an excessive and prolonged estrogenic stimulation [9] and include obesity, estrogen-only substituting therapy, early menarche, late menopause, nulliparity, and Stein-Leventhal syndrome [4]. Estrogenic hyperstimulation increases the mitotic activity of endometrial cells, i.e., the number of DNA replications, increasing therefore the possibility of replication errors, which may lead to the somatic mutations that are responsible for the generation of a malignant phenotype [10–12]. Among the abovementioned ones, another well-known risk factor for the development of EC is the administration of tamoxifen, an antiestrogenic drug used as an adjuvant treatment in patients affected by breast cancer. In the endometrium, tamoxifen shows a paradox estrogenic-like effect that is responsible for its oncogenetic effect [4]. Hereditary nonpolyposis colorectal cancer (HNPCC) disease represents another risk factor for the development of EC and may induce it in young women. Moreover a significant association has been also highlighted between endometrial cancer and diabetes mellitus [8].

2.2 Presentation and Diagnosis

Abnormal uterine bleeding (intermenstrual or postmenopausal) is the most frequent presenting symptom of endometrial carcinoma, and it is

---

M. Bonatti (✉)
Department of Radiology, University of Verona,
Piazzale L.A. Scuro 10, Verona 37134, Italy

Department of Radiology, Bolzano General Hospital,
5 Boehler Street, Bolzano 39100, Italy
e-mail: matteobonatti@hotmail.com

L. Zantedeschi • F.D. Corso • R. Manfredi
R.P. Mucelli
Department of Radiology, University of Verona,
Piazzale L.A. Scuro 10, Verona 37134, Italy
e-mail: lisazantedeschi@yahoo.it;
flaviadalcorso@yahoo.it; riccardo.manfredi@univr.it;
roberto.pozzimucelli@univr.it

R. Manfredi, R. Pozzi Mucelli (eds.), *MRI of the Female and Male Pelvis*,
DOI 10.1007/978-3-319-09659-9_2, © Springer International Publishing Switzerland 2015

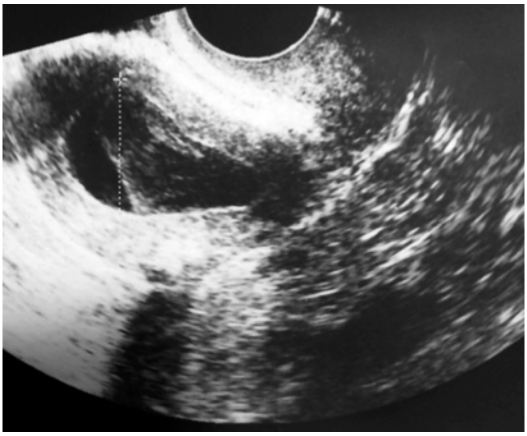

Fig. 2.1 Transvaginal sonography showing a pathologically thickened endometrial cavity (*line*) secondary to the presence of an endometrial carcinoma

appreciable in about 90 % of the cases [13]. Abnormal uterine bleeding usually manifests early in the disease history and leads women to seek a gynecologist; as a consequence, in developed countries 75 % of the cases of EC are early diagnosed (at stage I). In postmenopausal women, endometrial carcinoma is responsible for 8–10 % of the cases of uterine bleeding, whereas its prevalence as a cause of abnormal uterine bleeding in pre- and perimenopausal women is extremely lower, and this difference may lead to some diagnostic delay in this patient population. On the other hand, about 10 % of EC are clinically asymptomatic, and these neoplasms are usually detected because of the presence of atypical cells at cervical smear or because of abnormal findings during pelvic ultrasound [8]. Finally, only a minority of EC are detected in very advanced stages because of symptoms correlated to metastatic disease.

In a patient presenting with abnormal uterine bleeding, first of all an accurate physiological and pharmacological anamnesis must be performed. After that, transvaginal ultrasound (TV-US) represents the first-line imaging modality; in postmenopausal women, the finding of an endometrial thickness >5–7 mm is considered pathological and requires further investigations. The use of a 7 mm cutoff value enables to identify patients affected by EC with a sensitivity >95 % (Fig. 2.1). On the other hand, no definite cutoff values exist for endometrial thickness in premenopausal women in which the suspicion of endometrial carcinoma should be mainly clinical.

If, because of clinical data or ultrasound findings, the presence of an endometrial carcinoma is suspected, histological evaluation is mandatory. To date, endometrial biopsy represents the most widely used technique for assessing the presence of EC and has largely replaced dilatation and curettage because of its lower cost, little or no need of anesthesia, and less traumatism. However, endometrial biopsy shows only a fair accuracy in assessing tumor type and grade: for example, up to 30 % of grade 1 tumors at endometrial biopsy will be upgraded to grade 2 or 3 on hysterectomy specimen.

2.3 Pathological Findings

The large majority of endometrial neoplasms arises from the endometrial glandular epithelium and is represented by adenocarcinomas of endometrioid type (75–85 %) (Fig. 2.2a) [8]. Endometrioid-type EC usually develops in the setting of a hypertrophic endometrium and often show a polypoid appearance; these lesions may be further subdivided into four subtypes according to their prevalent histologic aspects (with squamous differentiation and villoglandular, secretory, or ciliated cells). Moreover, every subtype can show three different grades of differentiation, from grade 1, well differentiated neoplasms, to grade 3, poorly or undifferentiated neoplasms [8]. Grade 1 endometrioid EC are constituted by well-formed glands, with no more than 5 % of solid non-squamous areas, whereas solid non-squamous areas represent 6–50 % of the mass in grade 2 neoplasms and more than 50 % of it in grade 3 ones [2, 14].

Another 20–25 % of endometrial neoplasms are constituted by endometrial adenocarcinomas that are grouped together under the “non-endometrioid” diction (Fig. 2.2b) that comprises serous carcinomas, clear-cell carcinomas, mixed carcinomas, squamous-cell carcinomas, transitional-cell carcinomas, small-cell carcinomas, and undifferentiated carcinomas. All these neoplasms have a highly aggressive behavior, which makes unnecessary the definition of a grade; in particular, serous carcinoma is the most aggressive subtype of endometrial carcinoma and shows prognosis similar to ovarian carcinoma.

In a small percentage of cases, the endometrium may also be involved by tumors of stromal origin (Fig. 2.2c), which include endometrial sarcoma, mixed Müllerian tumor, and leiomyosarcoma, that are characterized by a highly aggressive behavior and by an extremely poor prognosis [8].

It is important to notice that mixed epithelial-stromal tumors exist and that they may lead to some errors in preoperative histological evaluation because only one of the two components might be sampled during endometrial biopsy.

2.4 Tumor Spread

The most common way of diffusion of endometrial carcinoma is direct infiltration of adjacent structures. In particular, EC, which arises within

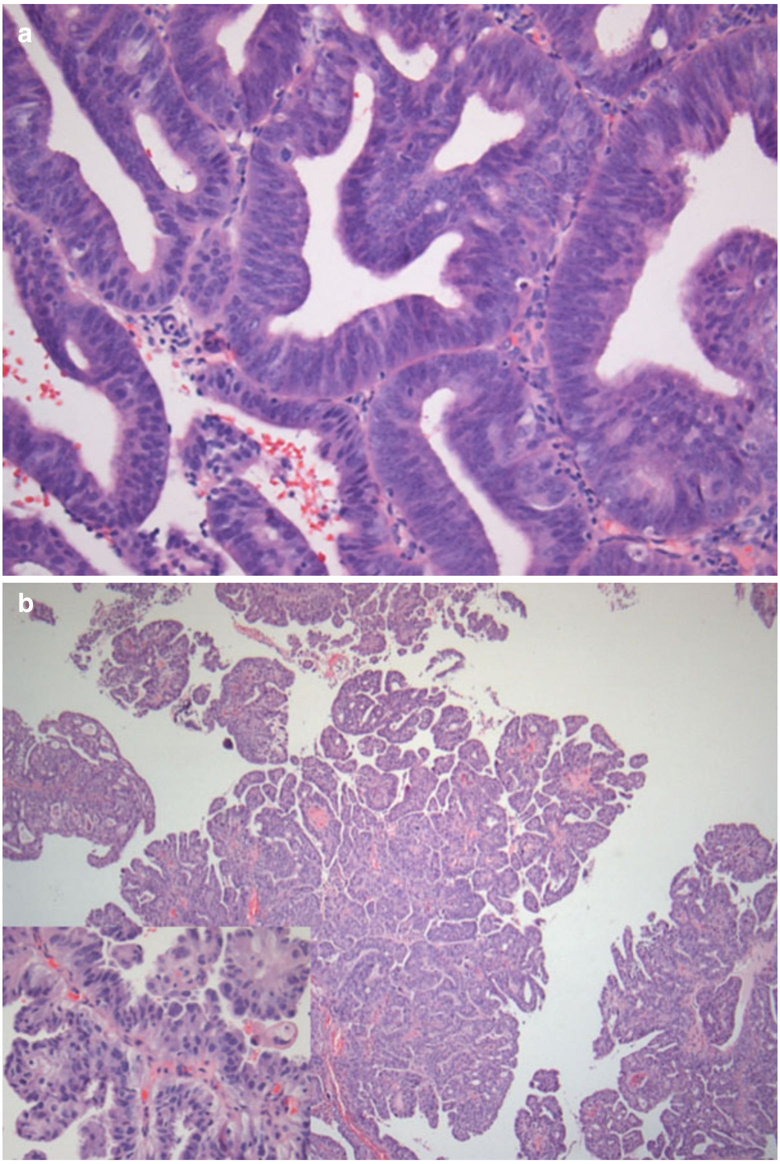

Fig. 2.2 (**a–c**) Different pathological appearances of endometrial cancer. G1 endometrioid-type endometrial carcinoma (**a**) is characterized by an overall conservation of endometrial glandular appearance with the presence of nuclear atypia, nuclear overlays, and an increased number of mitosis; the stroma is markedly reduced and atypical glands are densely packed. Serous-type endometrial carcinoma (**b**) shows a papillary architecture with more evident nuclear atypia (*box*). Endometrial stroma sarcoma (**c**) is characterized by glandular rarefaction (*lower portion*), in comparison with the physiological endometrium (*upper portion*), secondary to an abnormal expansion of endometrial stroma. At high magnification (*box*) the atypical stromal proliferation is clearly appreciable

Fig. 2.2 (continued)

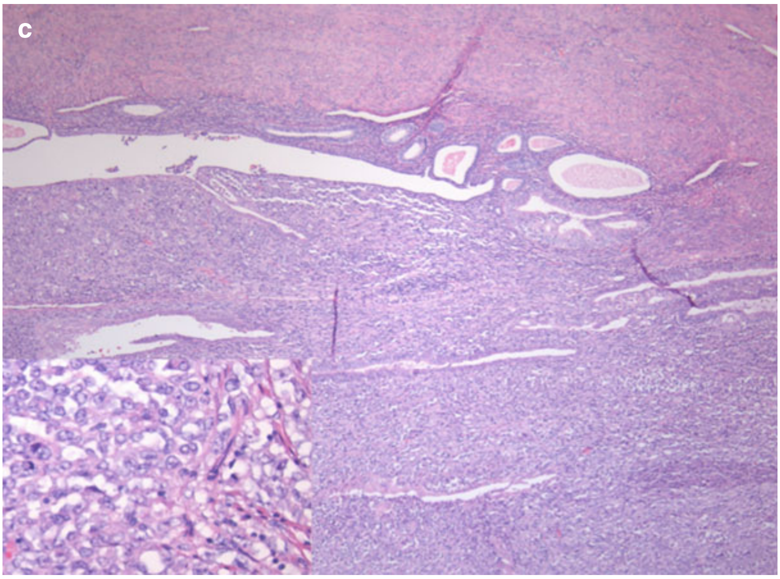

the endometrium, usually begins its spread by infiltrating the superficial myometrium (i.e., the junctional zone). The neoplasm may then advance infiltrating deeper myometrial portions, usually by means of a wide infiltrating front. In advanced stages, EC may also reach the serosa and extend to peritoneal cavity and to adjacent organs. A less common way of direct spread of EC involves cervical epithelium and cervical stroma with possible extension to vaginal walls [15, 16].

The second most common way of diffusion of EC involves the lymphatic pathways that lead to the parametrial, paracervical, and obturator lymph nodes, in case of tumors of the middle and lower uterine portions, and to the common iliac and para-aortic lymph nodes, in case of neoplasms involving the uterine fundus and tubaric angles [15–17]. Inguinal nodes may also be involved by means of a spread along the round ligament following adnexal or pelvic sidewall tumor involvement. The probability of lymphatic spread is minimal for neoplasms confined to the inner myometrial portion and increases parallel to the depth of myometrial infiltration [18, 19]. Moreover, the presence of cervical stromal infiltration and the histologic diagnosis of non-endometrioid-type EC are also associated with a significantly increased risk of nodal metastases.

Tumor extension to the uterine cornua and to Fallopian tubes provides another route of spread to adnexal structures and the peritoneal cavity; this kind of spread is obviously more common for tumors involving the uterine fundus and tubaric angles than for the ones involving the uterine body or neck [15, 16, 20].

Distant hematogenous metastases usually occur late in the biological history of EC, usually in locally advanced cases or in histological subtypes with poor prognosis, and mainly involve the lungs, liver, and bone marrow [8].

2.5 Tumor Staging

Since 1988, the FIGO (International Federation of Gynecology and Obstetrics) defines formal staging of endometrial carcinoma subdividing the neoplasms into four main stages (stage I, tumor confined to the corpus uteri; stage II, tumor involving cervical stroma; stage III, local/regional tumor spread; and stage IV, tumor invading other organs/structures) according to surgical and pathological data acquired after complete abdominal hysterectomy with bilateral salpingo-oophorectomy, pelvic and retroperitoneal lymphadenectomy, omentectomy or omental biopsies, and peritoneal washing [21, 22].

Table 2.1 The 2009 FIGO staging system of endometrial carcinoma and corresponding MRI features

Stage	FIGO description	MRI features
IA	No/less than half myometrial invasion	Myometrium shows normal signal intensity profoundly to the neoplasm >50 % of its thickness
IB	Equal to/more than half myometrial invasion	Myometrium shows normal signal intensity profoundly to the neoplasm <50 % of its thickness but serosa hypointense rim is preserved
II	Cervical stroma infiltration	Interruption/signal intensity alteration of cervical stroma hypointense ring
IIIA	Serosa infiltration and/or adnexal involvement	Interruption/signal intensity alteration of serosa hypointense rim and/or presence of an adnexal mass
IIIB	Vaginal and/or parametrial involvement	Signal intensity alteration extending to the vagina and/or to the parametria
IIIC1	Pelvic lymph node metastases	Pathologically enlarged (>10 mm in minimum diameter) pelvic lymph nodes
IIIC2	Para-aortic lymph node metastases	Pathologically enlarged (>10 mm in minimum diameter) retroperitoneal lymph nodes
IVA	Bladder and/or bowel mucosa infiltration	Loss of cleavage plans between the neoplasm and the bladder and/or the bowel walls that appear thickened
IVB	Distant metastases (including inguinal lymph nodes)	Pathologically enlarged (>10 mm in minimum diameter) inguinal lymph nodes or other distant metastases (often not comprised in MRI scans)

The 2009 revision (Table 2.1) of the 1988 FIGO classification of endometrial carcinoma is the one actually in use; it maintained the four main stages (I–IV) of differentiation, but simplified some further subdivisions. Stage I is actually subdivided into two substages (vs. 3 substages in the previous classification): Stage IA is characterized by myometrial infiltration <50 % of its thickness, and stage IB by myometrial infiltration >50 % of its thickness; no more difference is made between EC that exclusively involve the endometrium and EC that also infiltrate the inner half of the myometrium. Stage II actually has no substages (vs. 2 substages in the previous classification): cervical mucosa infiltration is no longer considered a staging parameter, whereas cervical stromal infiltration remains its unique characteristic. Stage III maintained three substages: stage IIIA is characterized by serosa and/or adnexal infiltration, stage IIIB by vaginal and/or parametrial involvement, and stage IIIC by nodal metastases. Two differences exist between the 1988 and 2009 classification of stage III: positive peritoneal cytology is no more considered a staging criteria (previously it was included in stage IIIA), and stage IIIC has been further subdivided into IIIC1 (pelvic nodal involvement) and IIIC2 (lomboaortic nodal involvement). No differences exist between the 1988 and 2006 classification of stage IV that maintained two substages: stage IVA, characterized by bladder and/or rectal infiltration, and stage IVB, showing distant metastases (including inguinal lymph nodes).

2.6 Prognosis

The prognosis of a patient affected by EC is overall better than for other gynecological malignancies, but it depends on the histological type, tumor grade, and tumor stage.

Non-endometrioid-type EC is associated with an overall poor prognosis; indeed, although representing only about 20 % of the cases, non-endometrioid EC account for more than 50 % of all recurrences and deaths for endometrial carcinoma [23]. On the other hand, endometrioid-type EC show an extremely variable prognosis, depending on the tumor grade and stage; for example, the prevalence of nodal metastases, which are correlated with a poor prognosis, is significantly higher in patients affected by G2–G3 endometrioid-type EC than in patients affected by G1 ones.

Besides tumor type and grade, the 5-year survival rates (5 years) of endometrial carcinoma are also strictly correlated with tumor stage at the time of diagnosis. Stage IA EC show a 5 years of about 89.6 %, stage IB ones of 77.6 %, and stage II of 70.2 %. The 5 year survival rates of EC significantly decrease for stage III neoplasms, to about 49.2 %; the presence of nodal metastases is associated with 5 years of 57 % for pelvic nodal involvement only (stage IIIC1) and 49 % for para-aortic nodal involvement (stage IIIC2) [24]. Stage IV EC is associated with an extremely poor prognosis, with a 5 years of 18.7 %.

The patient's overall physical performance status and age are also strictly correlated with prognosis [25].

2.7 Treatment

The standard surgical treatment for endometrial carcinoma implies laparotomy and comprises complete hysterectomy with bilateral salpingo-oophorectomy, pelvic and retroperitoneal lymphadenectomy, omentectomy or omental biopsies, and peritoneal washing. Nowadays, however, the improvements in preoperatory staging techniques, namely, ultrasound (US), magnetic resonance (MR), and computed tomography (CT), and in surgical techniques have determined an increase in the request of less invasive treatment approaches. Currently, laparoscopy and robotic surgery approach are preferred over laparotomy in the large majority of cases, and a recent publication by the Gynecologic Oncology Group (GOG), the LAP2 study, has shown that laparoscopy provides equivalent results in terms of disease-free survival and overall survival, compared with laparotomy, with the advantage of shorter hospital stay, less use of painkillers, lower rate of complications, and improved quality of life [24]. Moreover, despite the surgical approach, nowadays the extent of surgery must also be modulated according to histological data and to preoperative staging findings; for example, lymphadenectomy, which is burdened by significant complication rates and postoperative morbidity, has shown no benefits in terms of survival and recurrence-free rates in patients affected by low-risk (grade 1, stage IA) EC [26–28], whereas it remains crucial for improving the prognosis in high-risk patients [29–31].

Adjuvant chemotherapy is usually administered to all patients affected by non-endometrioid-type EC or by endometrioid-type G2–G3 ones and to patients affected by FIGO stage II to IV neoplasms. Patients affected by surgically unresectable EC and patients showing absolute clinical contraindications to surgery may benefit from radiation therapy in order to reduce bleeding risk; however, maximal surgical debulking should be performed also in case of unresectable neoplasms in order to increase life expectancy. In case of hemorrhage, uterine artery embolization may be useful for reducing and/or stopping blood loss.

Therefore, in the era of individualized treatments, an accurate preoperative staging is crucial in order to tailor the best surgical approach for each patient. Many imaging modalities are actually available for locoregional staging of endometrial carcinoma, but magnetic resonance imaging must be considered the imaging modality of choice, thanks to its panoramicity, high tissue contrast resolution, and reproducibility [32–36].

2.8 The Role of MRI in Endometrial Carcinoma

MRI is not indicated for diagnosing endometrial carcinoma; indeed, although recent studies have demonstrated that apparent diffusion coefficient (ADC) values can reliably differentiate benign from malignant endometrial lesions [37, 38], hysteroscopy with endometrial biopsy remains the gold standard for this aim. On the other hand, nowadays MRI plays a well-defined role in the preoperative workup of patients with histologically proven EC [31, 39–43].

The main aims of preoperative MRI staging of endometrial carcinoma are the assessment of "T" stage (i.e., the quantification of the depth of myometrial infiltration, the identification of cervical stromal infiltration, and the assessment of extrauterine spread) and the definition of "N" stage

Table 2.2 Risk stratification for the presence of nodal metastases and for recurrence of endometrial carcinoma (EC), according to MRI and pathology data

	MRI stage	Histological type	Histological grade
Low-risk EC	T1a	Type 1	G1–G2
Intermediate-risk EC	T1a	Type 1	G3
Intermediate-risk EC	T1b	Type 1	G1–G2
High-risk EC	T1b	Type 1	G3
High-risk EC	T≥2	Type 1	G1–G2–G3
High-risk EC	Every T	Type 2	G3

(i.e., the identification of nodal metastases). MRI offers an overall high accuracy (81–92 %) [43, 44] in the definition of the "T" stage of endometrial carcinoma, which is significantly higher in comparison to CT, PET/CT, and transvaginal ultrasound [33–35, 45–48], but still lower than intraoperative pathological evaluation of frozen sections [49, 50]. Recent works report a high accuracy of MRI (89–97 %) [51, 52] also in the evaluation of the "N" stage of endometrial carcinoma. Such promising results, however, must be critically evaluated because of the influence of low pretest probability of nodal metastases in endometrial carcinoma (about 20 %). Indeed, the sensitivity of MRI in identifying nodal metastases, as reported in the same abovementioned studies, ranges from 55 to 67 %. However, despite the unsatisfactory sensitivity of MRI in directly recognizing nodal metastases, the MRI information about the "T" stage and, in particular, about the depth of myometrial infiltration and the presence of cervical stromal infiltration, in association with pathologic information about the tumor type and grade, enables to confidently predict the risk of nodal metastases, subdividing endometrial carcinoma into three groups (low, intermediate, and high risk) (Table 2.2) with consequent therapeutic implications [30, 36, 40].

The secondary aims of preoperative MRI in EC are the evaluation of pelvic anatomy and the recognition of eventual pelvic comorbidities; the latter information, in particular, can be extremely helpful for a correct surgical planning. For example, the identification of coexistent large pelvic masses (Fig. 2.3) or of voluminous uterine fibromas might advise against a laparoscopic or transvaginal approach.

Nowadays, an extremely important means that enables to increase the quality of MRI staging of endometrial carcinoma and to improve diagnostic skills is the institution of radiological-surgical-pathological-oncological tumor boards in which each case can be preoperatively collegially discussed and postoperative feedbacks can be obtained.

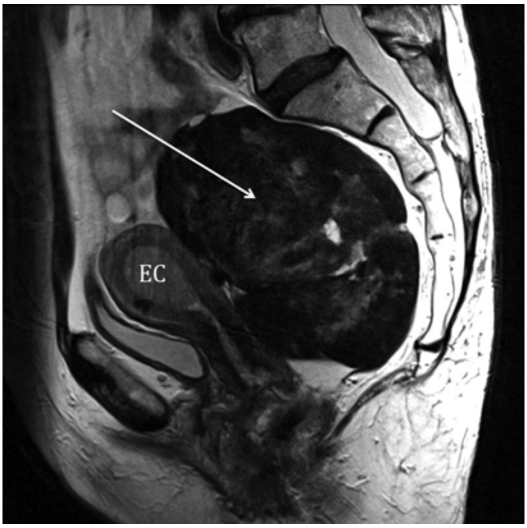

Fig. 2.3 Incidental MRI findings. Sagittal TSE T2-weighted image (TR/TE 2,400/76 ms) showing an endometrial carcinoma with polypoid appearance (*EC*). Dorsally to the uterus, in the presacral region, a large rounded T2-hypointense mass (*arrow*) is clearly recognizable. In this case, because of the coexistence of the pre sacral mass, laparotomy has been preferred to a laparoscopy. At pathology the presacral mass has been classified as a solitary fibrous tumor of the mesorectum

2.9 Technical Requirements

MRI of the uterus must be performed on high field magnets (1.5 T or more) using multichannel (four or more channels) phased array body coils,

Table 2.3 Suggested MRI protocol for the study of endometrial carcinoma

Pulse sequence	Orientation	Region	TR/TE (ms)	Fov (mm)	Voxel size (mm)
TSE T1 weighted	Axial	Abdomen	730/10	350×260	5×1×1
FS TSE T2 weighted	Axial	Abdomen	7,700/83	400×400	5×1×1
TSE T2 weighted	Sagittal, axial, coronal	Uterus	2,400/76	230×230	4×0.5×0.7
EPI diffusion weighted (*b*=0, 500, 1,000)	Sagittal, axial, coronal	Uterus	3,100/98	250×250	5×2×2
CE TSE T1 weighted	Sagittal, axial, coronal	Uterus	660/9.5	250×250	4×0.8×0.9

Fov field of view, *TSE* turbo spin echo, *FS* fat saturated, *EPI* echo planar imaging, *CE* contrast enhanced

in order to warrant an adequate signal-to-noise ratio. Recent studies have demonstrated that 3 T magnets do not increase MRI accuracy in staging endometrial carcinoma in comparison with 1.5 T ones [53, 54]. Moreover, the use of endorectal or endovaginal coils is not indicated because of their lower panoramicity in comparison with body coils [54].

The patient must fast at least 4–6 h before the examination, and 20 mg of hyoscine butylbromide should be intramuscularly administered 5 min before the patients enters the scanning room; alternatively, if hyoscine butylbromide is contraindicated, 5 mg of glucagon may be intravenously administered just before the beginning of the examination, but its effect might not last for the entire examination time.

An adequate bladder filling is essential in order to obtain high-quality images: in fact, a completely void bladder produces a bundling of the pelvic structures, thereby increasing the difficulties in recognizing the physiological cleavage planes, whereas an overfilled bladder stimulates bowel peristalsis, therefore increasing motion artifacts, and reduces the quality of T2-weighted and diffusion-weighted images. Intermediate bladder repletion may be obtained by suggesting the patient to void about 60 min before the examination and to hold urine from that time on.

The patient is usually positioned supine on the MR table with the arms lying down along her body, but prone position can be also considered in claustrophobic patients. MRI sequences for the study of the uterus can be acquired in free breathing, but the patient must be accurately instructed to maintain regular superficial breathing during the whole examination time, reducing the movements of the abdomen as much as possible.

MRI sequences are usually acquired using anteroposterior phase encoding, in case of sagittal images, and using laterolateral phase encoding in case of axial and coronal images. The placement of a presaturation bar over the anterior abdominal wall significantly increases image quality by reducing breathing-related motion artifacts. In order to further reduce abdominal wall motion artifacts, sagittal images may be acquired using a feet to head phase codification, with 100 % phase oversampling (50 % cranial and 50 % caudal to the region of interest).

2.10 MRI Protocol

Our suggested MRI protocol for the study of endometrial carcinoma is presented in Table 2.3 and is based on T2-weighted sequences, diffusion-weighted sequences, and pre- and post-contrast T1-weighted sequences.

First of all, large field of view (350×350 mm) TSE T1-weighted images must be acquired, according to the axial plane, from femoral heads to renal hila; these images play a fundamental role in the identification of enlarged lymph nodes, in the evaluation of the interface between the uterus and periuterine fat, and as a roadmap for the precise positioning of subsequent sequences.

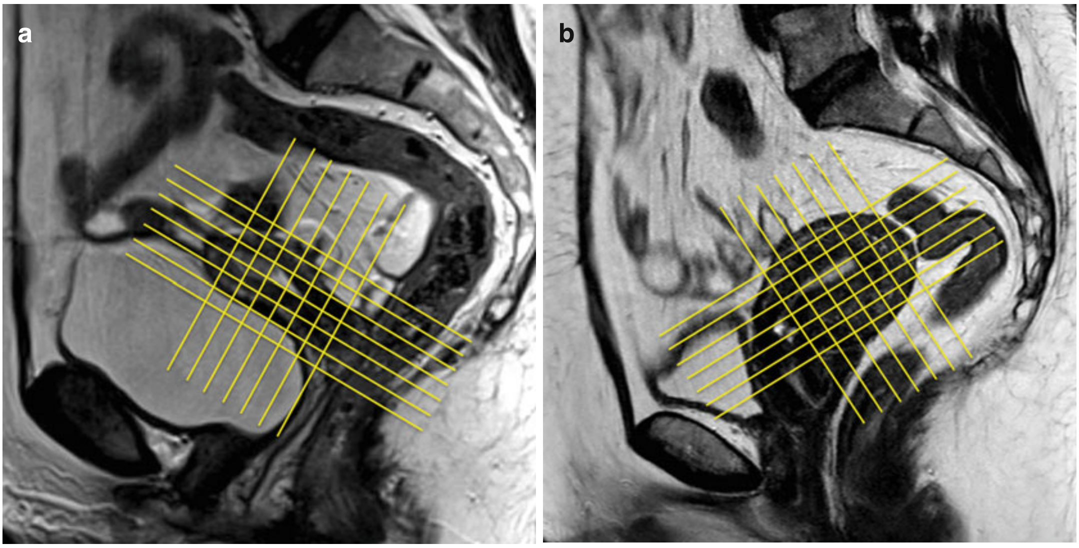

Fig. 2.4 (**a**, **b**) MR scanning plans for the study of the endometrium. The *yellow lines* on these sagittal TSE T2-weighted images (TR/TE 2,400/76 ms) show the correct orientation of uterine scanning plans. In order to avoid possible staging errors, MRI scanning planes must be always orientated orthogonal to the endometrial longer axis, on the sagittal, axial, and coronal planes, despite the uterine position, like in these two cases representing both an anteroflexed (**a**) and a retroflexed (**b**) uterus

On the other hand, native T1-weighted images are not able to differentiate the different uterine structures, and also endometrial carcinoma, because of their low intrinsic tissue contrast resolution. Optionally or in addition to the abovementioned TSE T1-weighted images, the acquisition of large field of view axial fat-saturated T2-weighted RARE (rapid acquisition with relaxation enhancement) images, even from femoral heads to renal hila, may increase the accuracy of MRI in identifying retroperitoneal enlarged lymph nodes; in fact, the long repetition time of these sequences generates a "flow void" artifact into the lumen of blood vessels that therefore appear hypointense and thus can be easily differentiated from lymph nodes, which show an intermediate signal intensity/hyperintensity on these sequences and show up within the hypointense "saturated" abdominal fat.

All subsequent imaging sequences must be acquired using small fields of view (about 250 × 250 mm, depending on the patient's size) and large matrix, in order to warrant a high spatial resolution, according to the three orthogonal planes (parasagittal, para-coronal, and para-axial) of longest endometrial axis (Fig. 2.4a, b).

TSE T2-weighted images play a central role in staging endometrial carcinoma because of their high soft tissue contrast resolution in association with their high spatial resolution that warrants an excellent anatomical detail. On TSE T2-weighted images, the physiological uterine wall stratification (the endometrium, the myometrium with the junctional zone, and the serosa), the cervical structures (mucosa and stroma), the vagina, and adjacent organs and structures are clearly recognizable, and it is possible to carefully differentiate endometrial carcinoma from the abovementioned structures. Therefore, TSE T2-weighted images are crucial for local staging of EC.

Contrast-enhanced (CE) TSE T1-weighted images must be acquired after i.v. administration of 0.05–0.1 mmol/Kg of gadolinium chelates. They are extremely useful for local staging of neoplasms that appear isointense in comparison to adjacent structures on T2-weighted images and in elderly women, in which the disappearance of junctional zone reduces the signal-to-noise ratio between the neoplasm and the myometrium.

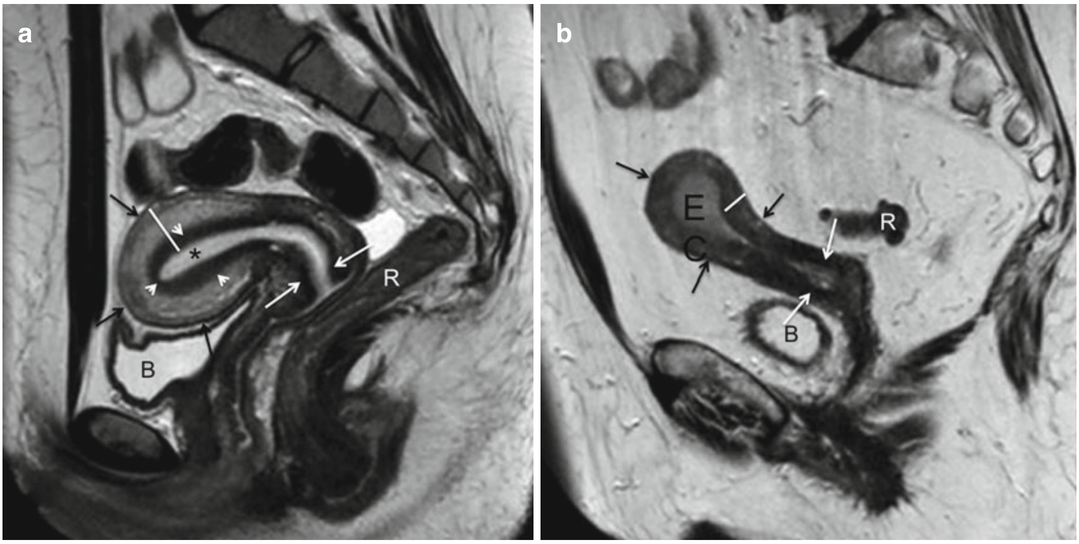

Fig. 2.5 (**a**, **b**) Pre- and postmenopausal uterus. Sagittal TSE T2-weighted images (TR/TE 2,400/76 ms) demonstrating uterine anatomy in a premenopausal (**a**) and in a postmenopausal (**b**) woman. The hyperintense endometrium (*star*) shows a physiological thickness in case "a", whereas it appears pathologically thickened (23 mm) in case "b" as a consequence of the presence of an endometrial neoplasm (*EC*). The overall myometrial thickness is highlighted with a white line and is normal in both cases; in premenopausal women (case "a") the hypointense junctional zone (white *arrowheads*) can be clearly differentiated from the outer myometrial portion, whereas in postmenopausal women (case "b") this distinction disappears. The thin hypointense rim delimitating the uterus from periuterine fat (*black arrows*) represents the serosa. Cervical stroma is also well recognizable and appears as a thin, markedly hypointense rim (*white arrows*); cervical stroma prosecutes directly with the junctional zone in premenopausal women (case "a"). Urinary bladder (*B*) and rectum (*R*) are clearly recognizable and also the fatty cleavage planes between these structures and the uterus

Diffusion-weighted images are collecting increasing consensuses for MRI staging of endometrial carcinoma; indeed, technical developments have made it possible to obtain high-b-value diffusion-weighted images with an adequate spatial resolution in short acquisition times. Diffusion-weighted images are extremely useful for identifying small endometrial carcinomas, which may be often barely recognizable on conventional MRI sequences, and for quantifying the depth of myometrial infiltration; indeed, their high sensitivity in identifying hypercellular tissues is useful for the recognition of small neoplastic spicule within the myometrial layer.

2.11 Normal Uterine Anatomy

As mentioned before, uterine anatomy is best depicted on TSE T2-weighted images (Fig. 2.5a, b). In premenopausal women (Fig. 2.5a), the uterine wall shows four well-defined different layers on T2-weighted MR images that reduce to three with progressive aging (Fig. 2.5b). Going from the center to the periphery, the innermost layer is constituted by the endometrium, which shows high signal intensity on T2-weighted images and presents a physiologic thickness variable from 1 to 7 mm, according to the patient's age and phase of the menstrual cycle. The following layer is the so-called junctional zone, or intermediate layer. The junctional zone appears hypointense on T2-weighted images and is constituted by the innermost portion of the myometrium; it has not a precise correspondence on pathological specimens, and its MRI differentiation from the outer portion of the myometrium is due to its relatively lower water content. In postmenopausal age the junctional zone shows a progressive increase in its water content, and, consequently, its signal intensity on T2-weighted images becomes substantially isointense to the outer portion of the

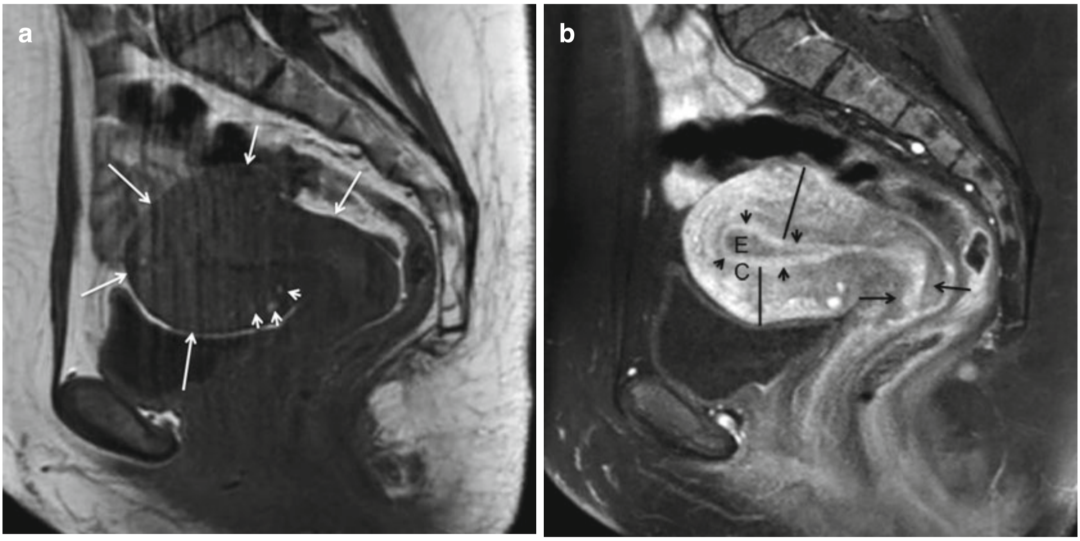

Fig. 2.6 (**a**, **b**) Uterine anatomy on T1-weighted images. Pre-contrast sagittal TSE T1-weighted image (TR/TE 730/10 ms) (**a**) doesn't clearly display uterine stratification, but the interface between uterus and abdominal fat, represented by the thin hypointense serosa (*white arrows*), is well delimitable. Some focal hyperintense spots (*white arrowheads*) can be highlighted within uterine wall on the pre-contrast T1-weighted image, representing adenomyosis foci. After i.v. administration of gadolinium chelates, fat-saturated TSE T1-weighted image (TR/TE 660/9.5 ms) (**b**) clearly depicts uterine anatomy. In this case of a postmenopausal woman, the endometrium (*black arrowheads*) shows an early and uniform enhancement and can be differentiated both from the myometrium, showing a delayed and more heterogeneous enhancement (*black lines*), and from the endoluminal neoplasm (*EC*) that appears hypovascular compared to the adjacent structures. Cervical stroma (*black arrows*) appears as a hypointense ring

myometrium [42]. The outer layer of the myometrium shows intermediate signal intensity on T2-weighted images, both on pre- and postmenopausal women. The overall myometrial thickness is usually between 14 and 21 mm and shows a progressive reduction with patient's aging; it is crucial to remember that the myometrium becomes progressively thinner approaching the tubaric angles. The outermost layer of the uterine wall that can sometimes be barely recognizable appears as a thin T2-hypointense line and is constituted by the uterine serosa. Cervical structures are also well depicted on T2-weighted images. Cervical mucosa shows the same signal intensity of the endometrium, but appears thinner, whereas cervical stroma appears markedly hypointense on T2-weighted images.

On native T1-weighted images, uterine stratification cannot be appreciated because the endometrium and myometrium show similar T1 relaxation times (Fig. 2.6a), but after i.v. administration of gadolinium chelates the above-described four uterine layers can be differentiated thanks to their different contrast material uptake (Fig. 2.6b). The enhancement dynamic differs according to the menstrual period, and three main enhancement patterns can be found: postmenopausal women and women in the proliferative phase of their menstrual cycle show a rapid sub-endometrial enhancement followed by a complete myometrial enhancement, women in the secretive phase of their menstrual cycle show a vivid enhancement of the junctional layer followed by a complete myometrial enhancement, while women in their menstrual period show a diffuse and homogeneous endometrial enhancement. Uterine serosa is usually not recognizable on post-contrast T1-weighted images, whereas it is clearly appreciable on pre-contrast ones. Cervical stroma is also recognizable on post-contrast images only and is represented by a hypointense ring, whereas cervical mucosa shows an enhancement pattern analogous to the endometrium.

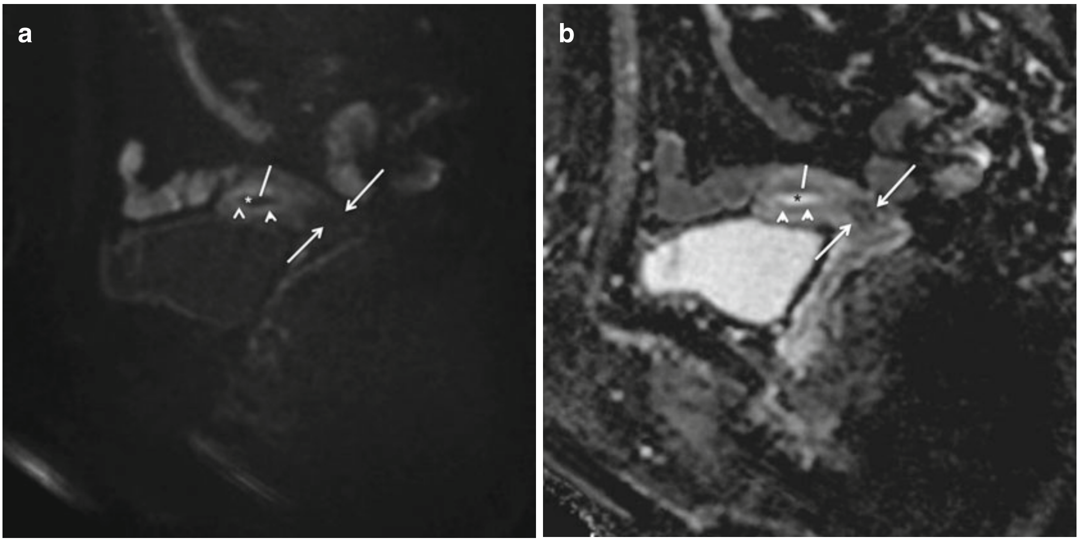

Fig. 2.7 (**a**, **b**) Uterine anatomy on diffusion-weighted imaging. Sagittal diffusion-weighted image (DWI) (TR/TE 3,100/98 ms, $b = 1{,}000$ s/mm^2) (**a**) and corresponding apparent diffusion coefficient (ADC) map (**b**) are displayed. Endometrium (*star*) appears hypointense on DWI and hyperintense on ADC, compared to the myometrium (*white lines*). Within the myometrium, junctional zone (*white arrowheads*) appears hyperintense on DWI and hypointense an ADC, compared to the outer myometrial portions. Cervical stroma appears markedly hypointense both on DWI and on ADC, and the serosa cannot be visualized nor on DWI or on ADC maps

On diffusion-weighted images (Fig. 2.7a) uterine stratification is not precisely recognizable, but anyway the endometrium can be clearly differentiated from the myometrium thanks to its lower signal intensity; moreover, the junctional zone may sometimes appear slightly hyperintense compared to the outer myometrium. Conversely, on ADC maps (Fig. 2.7b) the endometrium appears hyperintense and is surrounded by the hypointense junctional zone, which shows lower signal intensity even if compared with the outer myometrial portion. Cervical stroma appears hypointense both on diffusion-weighted images and on ADC maps.

On parasagittal images (Fig. 2.5a) the uterus is sectioned along its longest axis and uterine stratification can be recognized; they are extremely useful because adjacent organs, in particular the urinary bladder (B) and rectum (R), are always included in the scanning plan, and the evaluation of the physiological cleavage fat plans in vesicouterine and rectouterine pouches is therefore made possible. On the other hand, para-axial images (Fig. 2.8a) are the most accurate for precisely showing uterine stratification and for evaluating the relations between EC and the uterine wall. Finally, the main advantage of para-coronal images (Fig. 2.8b) resides in the possibility of correctly evaluating tubaric angles.

2.12 MRI Appearance of Endometrial Carcinoma

Endometrial carcinoma may show two main growth patterns. Type 1 (endometrioid) EC often shows a prevalently exophytic endoluminal “polypoid” growth with only a subsequent myometrial involvement characterized by a broad front of infiltration, whereas type 2 (non-endometrioid) EC usually shows a mainly infiltrative growth pattern ab initio.

On T2-weghted images endometrial carcinoma appears hyperintense compared to the adjacent junctional zone and to the myometrium and hypointense compared to the physiological endometrium in the majority of the cases [55] (Fig. 2.9a); however, lesions iso- or hypointense compared to the junctional zone and the myometrium may also be found. In our recent experience

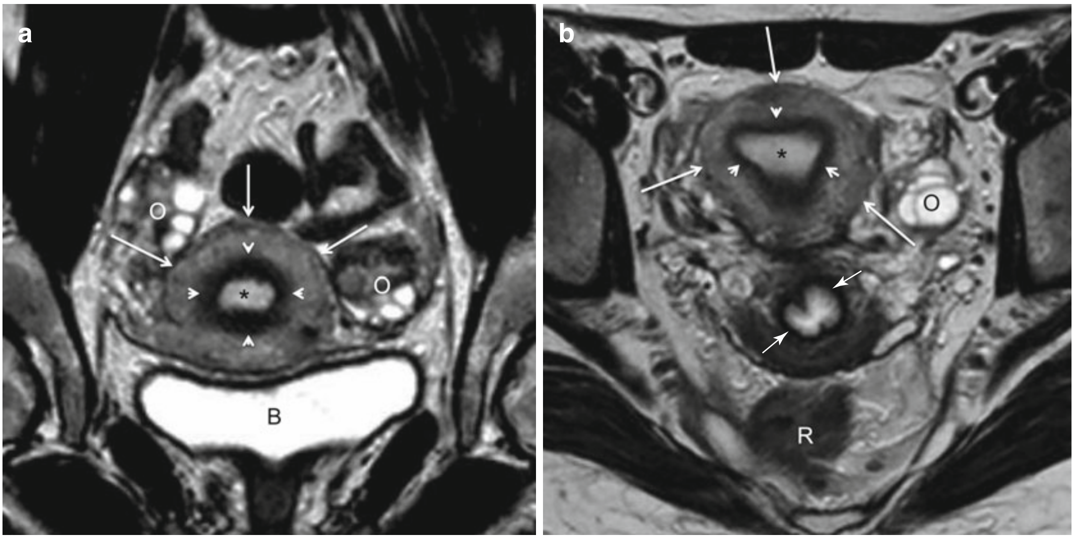

Fig. 2.8 (**a**, **b**) Uterine anatomy on T2-weighted images. Uterine axial TSE T2-weighted image (TR/TE 2,400/76 ms) (**a**) exactly depicts uterine stratification in this premenopausal woman. The endometrium (*star*) appears hyperintense, the junctional zone (*white arrowheads*) appears markedly hypointense, the outer myometrium shows intermediate signal intensity, and the serosa is recognizable as a thin hypointense rim (*white arrows*). The same findings can be highlighted on uterine coronal TSE T2-weighted image (TR/TE 2,400/76 ms) (**b**); incidentally, an axial scan of cervical channel is included in this image: notice the marked hypointensity of the cervical stromal ring (*black arrows*). An important finding on coronal images (**c**) is that the physiological myometrial thickness at tubaric angles (*white lines*) is lower compared to the other uterine portions; this must be kept in mind when staging neoplasms involving tubaric angles. The urinary bladder (*B*), ovaries (*O*), and rectum (*R*) are also recognizable in these images

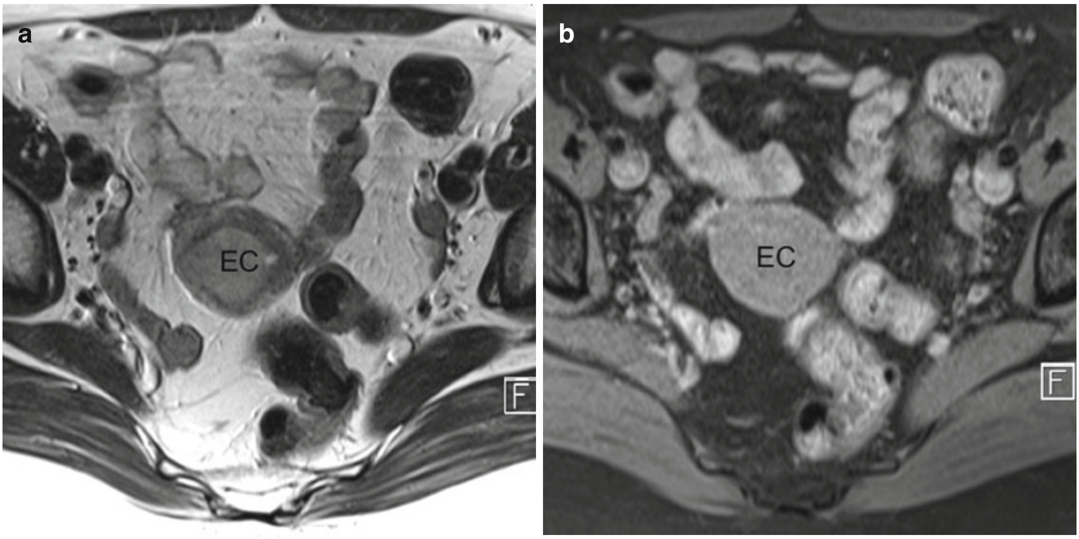

Fig. 2.9 (**a**–**e**) Typical MRI features of endometrial carcinoma. Typically, endometrial carcinoma (*EC*) appears slightly hyperintense compared to the adjacent myometrium on T2-weighted images (TR/TE 2,400/76 ms) (**a**). On native T1-weighted images (TR/TE 730/10 ms) (**b**) endometrial carcinoma is not distinguishable from the normal uterine structures, whereas on post-contrast T1-weighted images (TR/TE 660/9.5 ms) (**c**) it appears hypointense compared to the adjacent myometrium. On diffusion-weighted images (TR/TE 3,100/98 ms, $b = 1{,}000$ s/mm^2) (**d**) endometrial carcinoma appears hyperintense compared to the adjacent myometrium, whereas on the relative apparent diffusion coefficient (ADC) map (**e**) it appears hypointense as a consequence of true diffusion restriction

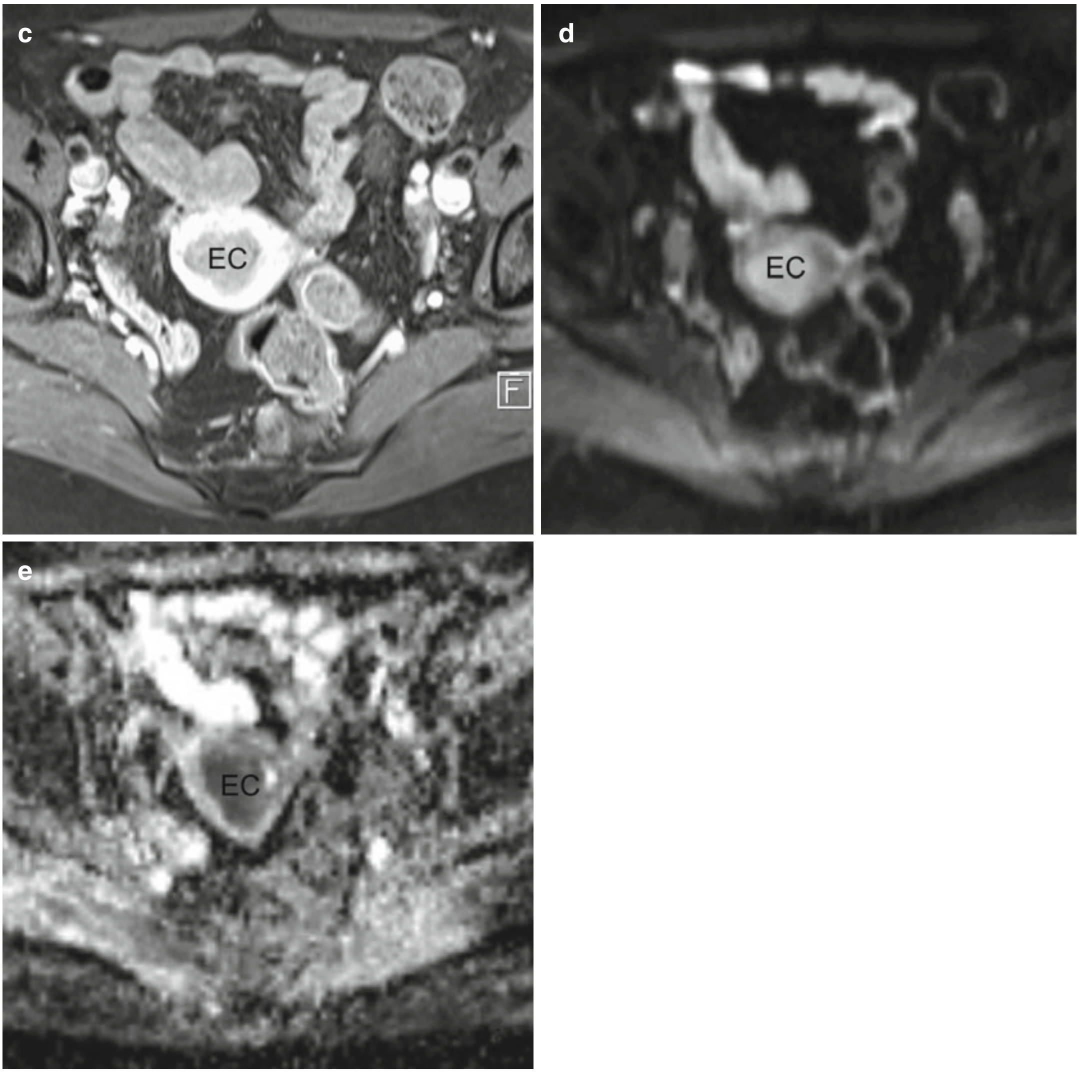

Fig. 2.9 (continued)

regarding 56 consecutive cases of endometrial carcinoma, the neoplasms appeared hyperintense compared to the junctional zone and to the myometrium on T2-weighted images in 86 % of the cases, isointense in 10 %, and hypointense in 4 %. In case of no macroscopic visible lesions in the setting of a histologically proven endometrial carcinoma, the finding of an irregularly thickened endometrium can be referred to as an indirect sign of the presence of the neoplasm.

On native T1-weighted images endometrial carcinoma is not recognizable because it appears isointense to the adjacent physiological endometrium and to the myometrium (Fig. 2.9b), but on post-contrast T1-weighted images the neoplasm becomes hypointense compared to the physiological endometrium and to the myometrium (Fig. 2.9c). The highest contrast-to-noise ratio between the neoplasm and the myometrium is reached about 3 min after contrast material injection, when the myometrium appears uniformly hyperintense, whereas post-contrast T1-weighted images acquired earlier might obscure the neoplasm and be the cause of false-negative findings.

On diffusion-weighted images, endometrial carcinoma appears hyperintense compared to both the physiological endometrium and the myometrium (Fig. 2.9d) as a consequence of its high cellularity that reduces the Brownian motions of water molecules. The highest signal-to-noise ratio between the neoplasm and myometrium is reached on high-b-value images ($b = 500$–1,000 s/mm^2), when the influence of the T2-relaxation time virtually disappears. The hyperintensity on diffusion-weighted images corresponds to a hypointensity on ADC maps (Fig. 2.9e), indicating a true diffusion restriction instead of a T2 shine-through artifact.

2.13 MRI Staging of Endometrial Carcinoma

MRI staging of endometrial carcinoma refers to the 2009 FIGO classification (Table 2.1), which subdivides the neoplasm into four main stages with a total of nine substages. In order to perform a complete locoregional MRI staging, four main imaging parameters must be sequentially evaluated.

2.13.1 Depth of Myometrial Infiltration

The depth of myometrial infiltration is the first parameter that must be evaluated when staging endometrial carcinoma. The 2009 FIGO endometrial carcinoma staging system differentiates neoplasms with an infiltration of less than 50 % of myometrial thickness (stage IA) from the ones with an infiltration of more than 50 % of it (stage IB).

Magnetic resonance imaging accuracy in differentiating stage IA from stage IB tumors ranges from 66 to 88 %, according to different series [7, 32, 52, 56–58], with possible errors mainly in the sense of an overstaging. A fundamental assumption in order to correctly evaluate the depth of myometrial infiltration is the availability of technically correct performed examinations, with imaging sequences accurately orientated according to endometrial longer axis.

The quantification of the depth of myometrial infiltration can be typically performed both on T2-weighted images and on contrast-enhanced T1-weighted images, with an overall slightly higher accuracy for the second compared to the first ones [59]; recent evidences, however, are showing that high-spatial-resolution diffusion-weighted images, in association with TSE T2-weighted images, might warrant even a higher accuracy for this aim [60]. As a matter of fact, the evaluation of the depth of myometrial infiltration should be performed on the images that offer the highest signal-to-noise ratio in the single case in exam; for example, in relatively young patients, when the junctional zone is still recognizable, T2-weighted images usually offer the highest accuracy for evaluation of the depth of myometrial infiltration.

First of all sagittal images should be evaluated in order to understand the neoplasm's location and shape; the depth of myometrial infiltration can also be calculated on sagittal images, but, usually, axial images warrant a higher accuracy. The percentage of myometrial infiltration can be easily calculated (Fig. 2.10) by subtracting the

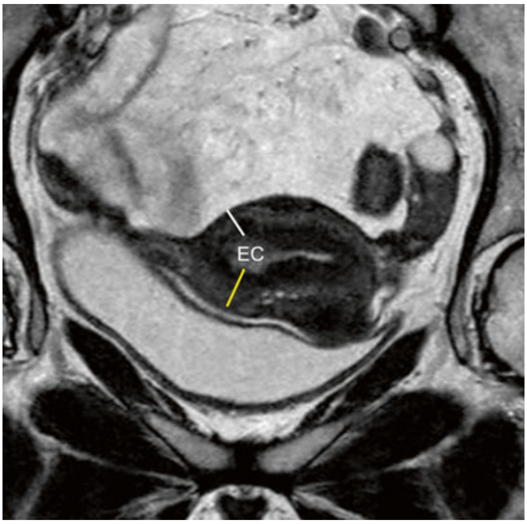

Fig. 2.10 Quantification of the depth of myometrial infiltration. The percentage of myometrial infiltration can be calculated by dividing the disease-free myometrial thickness (*white line*) in the site of uterine wall involved by endometrial carcinoma (*EC*) for the physiological myometrial thickness in an analogue uninvolved position (*yellow line*) and by multiplying the obtained value by 100. On this axial TSE T2-weighted image (TR/TE 2,400/76 ms), the calculated percentage of myometrial infiltration is about 30 % (<50 %, stage Ia)

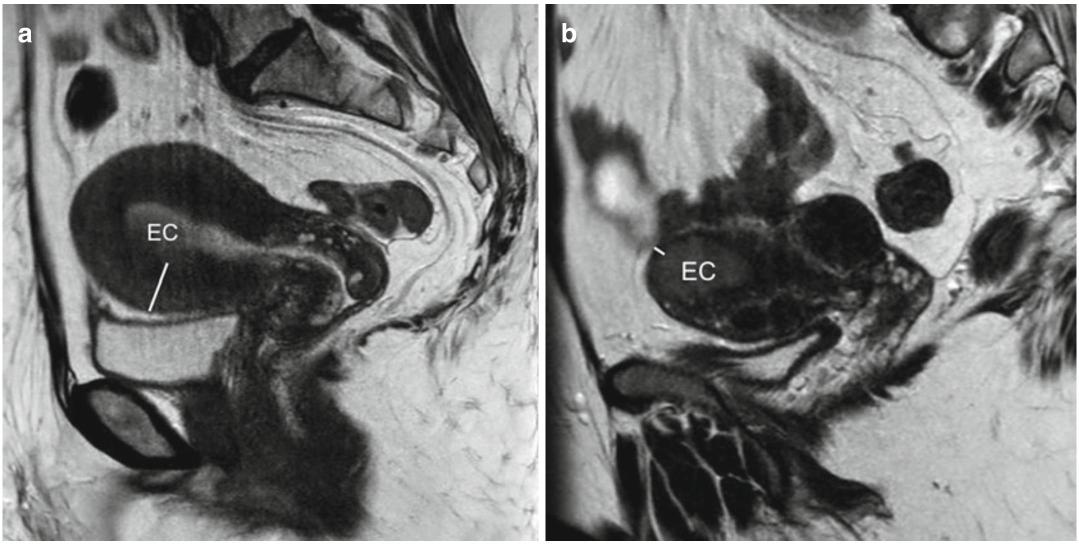

Fig. 2.11 (**a**, **b**) Stage Ia vs. stage IB endometrial Carcinoma on TSE sagittal eT2-weighted images (TR/TE 2,400/76 ms). (**a**) Shows an endometrial carcinoma (*EC*) infiltrating the myometrium for less than 50 % of its thickness (*white line*) (stage Ia), whereas (**b**) shows an endometrial carcinoma (*EC*) infiltrating the myometrium for more than 50 % of its thickness (*white line*) (stage IB). In both cases the hypointense serosa lining the uterus is clearly recognizable, excluding extrauterine spread

minimal thickness of uninvolved myometrium in the site of the neoplasm from the overall thickness of normal myometrium, measured in an analogue uninvolved position (i.e., if the neoplasm involves the ventral uterine wall, the normal myometrium thickness should be measured in the dorsal uterine wall, whereas if the neoplasm involves the right tubaric angle, the normal myometrium thickness should be measured in the contralateral tubaric angle); the minimal thickness of uninvolved myometrium must be divided for the thickness of normal myometrium and multiplied by 100. Endometrial carcinoma is classified as T1a if it infiltrates less than 50 % of myometrial thickness (Figs. 2.11a and 2.12a, b) and as T1b if it infiltrates more than 50 % of myometrial thickness (Figs. 2.11b and 2.12c, d). It is important to keep in mind that endometrial carcinoma may cause compressive alterations on the involved uterine wall, particularly in case of large polypoid lesions, reducing therefore the physiological uterine wall thickness; in patients in which the junctional zone is still recognizable, the absence of a complete interruption of the junctional zone by the tumor is always associated with a myometrial infiltration of less than 50 % (Fig. 2.13).

2.13.2 Cervical Stromal Infiltration

The relation between the neoplasm and cervical stroma is the second parameter that must be accurately evaluated when staging endometrial carcinoma. Despite the older ones, in the new 2009 FIGO guidelines the presence of cervical mucosa infiltration, which may also be a consequence of seeding after endometrial biopsy, does not influence the staging of EC, whereas a neoplasm showing cervical stromal infiltration is classified as stage II.

The accuracy of MRI in diagnosing cervical stromal infiltration ranges from 82 to 97 %, according to different series [7, 32, 44, 45], with possible errors mainly in the sense of an understaging.

T2-weighted images, thanks to their high anatomical detail, are the most accurate for evaluating the presence of cervical stroma infiltration. If EC reaches the hypointense stromal ring causing

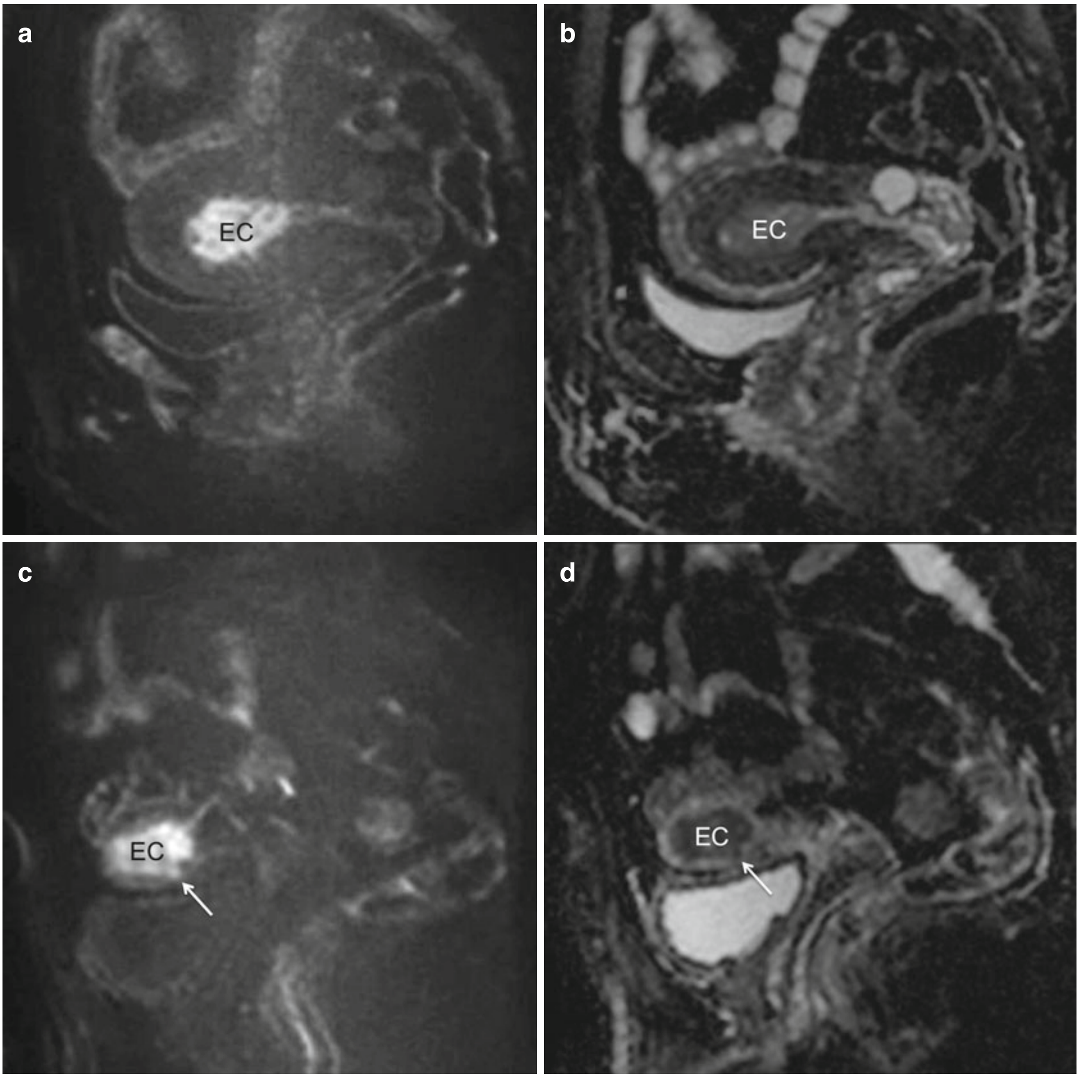

Fig. 2.12 (**a–d**) Stage Ia vs. stage Ib endometrial carcinoma on DW images (TR/TE 3,100/98 ms, b = 1,000 s/mm2) and ADC maps. Endometrial carcinoma (*EC*) is clearly recognizable as a hyperintense lesion on DW images (**a**, **c**) with a corresponding hypointensity on ADC maps (**b**, **d**). (**a**, **b**) show a neoplasm infiltrating less than 50 % of myometrial thickness (stage Ia), whereas (**c**, **d**) show a neoplasm infiltrating more than 50 % of myometrial thickness (*arrow*) (stage Ib)

an alteration in its physiologic hypointensity (Fig. 2.14a) and/or a complete interruption, the presence of infiltration must be strongly suspected; in these cases further T2-weighted axial images, orientated according cervical channel longest axis, should be acquired in order to confirm the finding (Fig. 2.14b). It is important to notice that cervical stroma infiltration may be also present in case of extremely small tumors, even infiltrating less than 50 % of myometrial thickness, if they originate in the adjacency of uterine neck (Fig. 2.15).

2.13.3 Extrauterine Growth

Once the entity of intrauterine (myometrial and cervical) spread of the endometrial carcinoma is

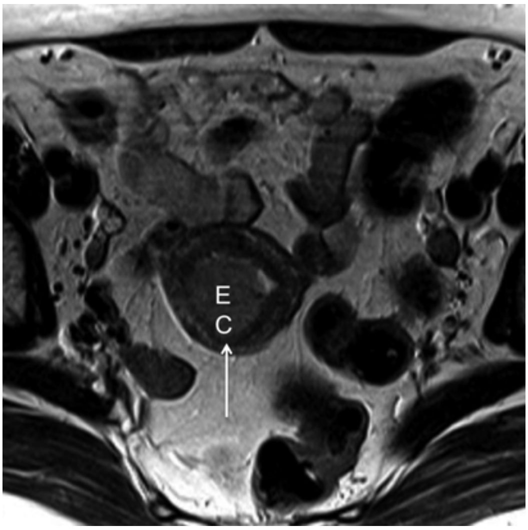

Fig. 2.13 Risk of overstaging the depth of myometrial infiltration. On this axial TSE T2-weighted image (TR/TE 2,400/76 ms), a large polypoid endometrial carcinoma (*EC*) is clearly appreciable. The calculated percentage of myometrial infiltration exceeds 50 %, but it is important to notice that the junctional zone shows no interruptions in the site involved by the neoplasm. Therefore, the >50 % reduction of myometrial thickness in that site must be considered a consequence of compression and not of infiltration by the neoplasm. In such conditions the neoplasm must be classified as MRI stage Ia, despite the measured values of myometrial infiltration

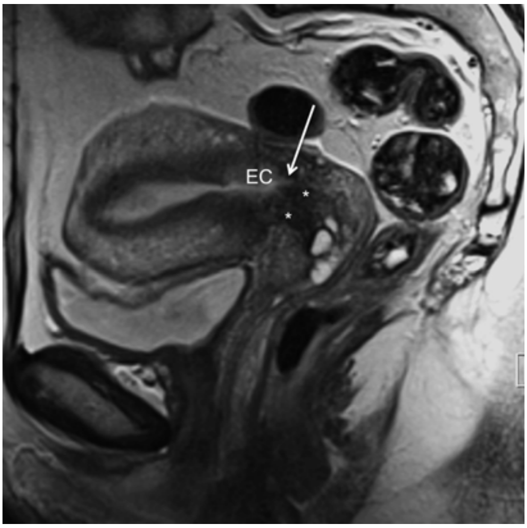

Fig. 2.15 Cervical stromal infiltration (stage II) in a small endometrial carcinoma. Sagittal TSE T2-weighted image (TR/TE 2,400/76 ms) shows a small endometrial carcinoma (*EC*) infiltrating less than 50 % of myometrial thickness. Although it has small dimensions, the neoplasm reaches the cervical structures (*arrow*) causing a focal signal intensity alteration in the physiologically hypointense cervical stroma (*stars*). The neoplasm must be classified as stage II

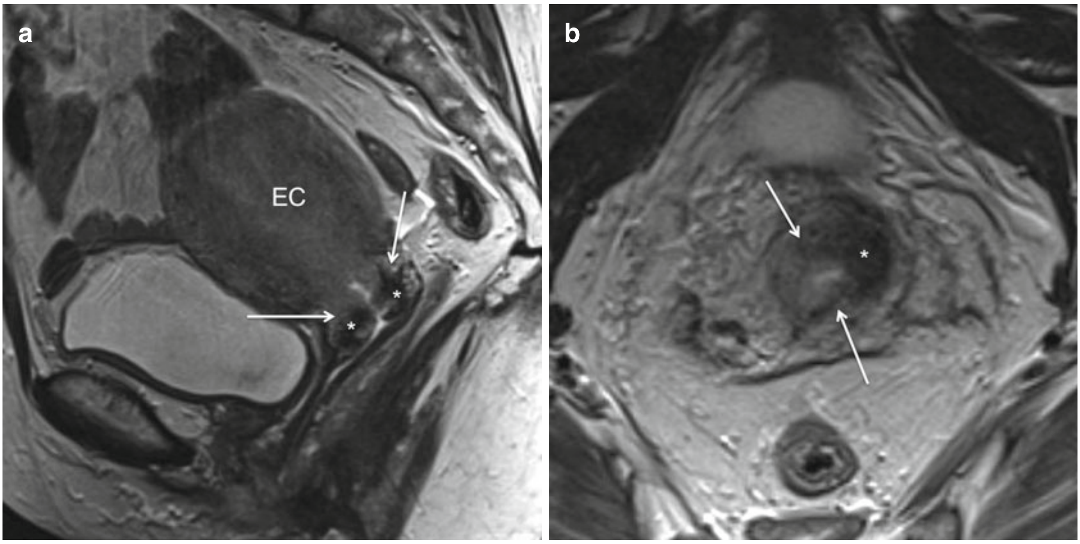

Fig. 2.14 (**a**, **b**) Cervical stromal infiltration (stage II). Sagittal TSE T2-weighted image (TR/TE 2,400/76 ms) (**a**) shows a large endometrial carcinoma (EC), infiltrating more than 50 % of myometrial thickness, which reaches the cervical structures (*arrows*) and interrupts the physiological hypointensity of cervical stroma (*arrows*). Axial TSE T2-weighted image (TR/TE 2,400/76 ms) (**b**) acquired according to the main axis of cervical channel confirms the finding by showing a complete interruption (*arrows*) of the physiologically hypointense of cervical stroma ring (*star*). The neoplasm must be classified as stage II

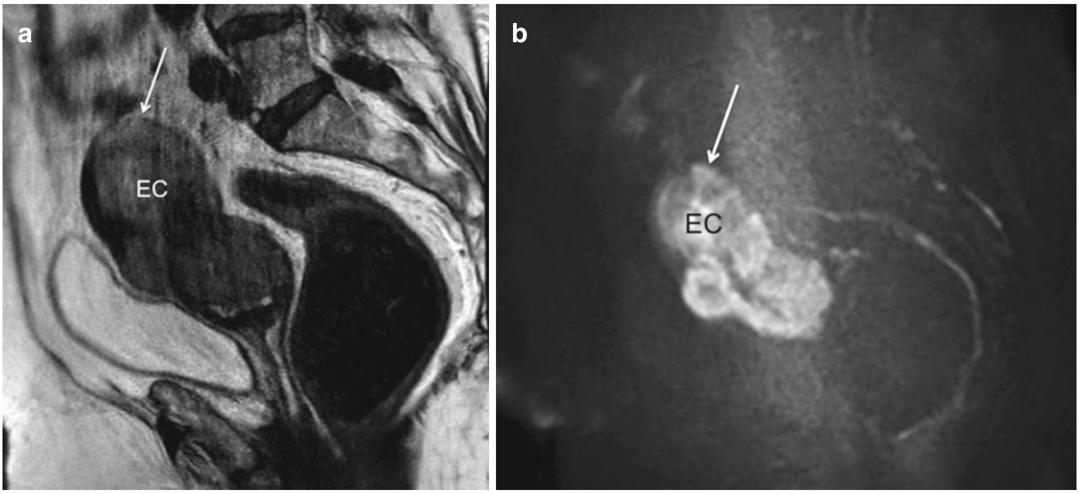

Fig. 2.16 (**a**, **b**) Serosa infiltration (stage IIIA). Sagittal TSE T2-weighted image (TR/TE 2,400/76 ms) (**a**) shows a large endometrial carcinoma (*EC*) diffusely infiltrating the myometrium; of the uterine fundus and determining a focal interruption of the hypointense serosa (*arrow*) representing an indirect sign of infiltration. Sagittal diffusion-weighted image ($b = 1{,}000$ s/mm^2) confirms the neoplastic nature if the signal intensity alteration (*arrow*)

assessed, extrauterine spread must be evaluated. Nowadays the finding of an extrauterine spreading EC is an extremely rare eventuality in developed countries. The finding of extrauterine spread classifies the neoplasm as stage III or IV, according to the 2009 FIGO staging system; in particular, neoplasms infiltrating the serosa uteri and/or spreading to the adnexa are classified as stage IIIA, neoplasms infiltrating the vagina or the parametria are classified as stage IIIB, while neoplasms infiltrating adjacent pelvic organs, in particular the bladder and the rectum, are classified as stage IVA.

Given the rarity of extrauterine spread of endometrial carcinomas in the magnetic resonance era, no data can be found in the literature about the accuracy of MRI in diagnosing it.

The evaluation of extrauterine spread is usually performed on the highly anatomical TSE T2-weighted images, on different planes according to the involved organs and structures. Diffusion-weighted and post-contrast T1-weighted images may be useful, in addition to T2-weighted images, in order to increase diagnostic confidence. In particular, DWI may help in distinguishing neoplastic infiltration from peritumoral edema.

Serosa uteri infiltration (Fig. 2.16a, b) is best highlighted on TSE T2-weighted images, on sagittal, axial, or coronal plane according to neoplasm location. The first sign of infiltration is represented by the absence of a cleavage plane between the hyperintense neoplastic tissue and the hypointense serosa; the subsequent step is represented by an alteration in the serosa signal intensity, which becomes progressively hyperintense, whereas if the infiltration becomes more extended, a complete interruption of the abovementioned hypointense line becomes appreciable, with subsequent infiltration of the T2-hyperintense periuterine fat responsible of a spiculated uterine-periuterine interface.

Ovaries are usually involved by endometrial carcinoma as a consequence of trans-tubaric seeding, but they may also be reached because of hematogenous seeding. Trans-tubaric adnexal involvement should be strongly suspected if a patient affected by an endometrial carcinoma involving one of the tubaric angles shows the presence of an ipsilateral expansive adnexal mass (Fig. 2.17a, b); MRI, however, cannot warrant a differential diagnosis between adnexal involvement by endometrial carcinoma and primitive solid adnexal neoplasm.

The presence of vaginal infiltration represents an extremely rare eventuality and can be usually best highlighted on sagittal TSE T2-weighted

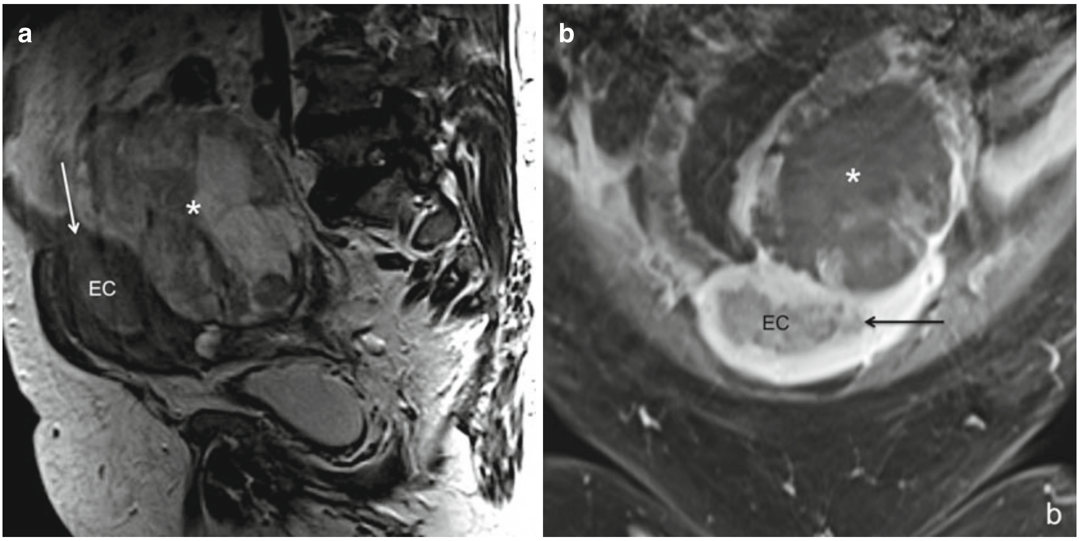

Fig. 2.17 (**a**, **b**) Adnexal involvement (stage IIIA). Sagittal TSE T2-wieghted image (TR/TE 2,400/76 ms) (**a**) shows an endometrial carcinoma (*EC*) extending to the left tubaric angle (*arrow*); in that site the neoplasm infiltrates the myometrium for more than 50 %. Posteriorly to the uterus a large inhomogeneous expansive mass (*star*) with a wide zone of hyperintensity on T2-weighted images is clearly recognizable. Post-contrast fat-saturated axial TSE T1-weighted image (TR/TE 660/9.5 ms) confirms the extension of endometrial carcinoma (*EC*) to the left tubaric angle (*arrow*) and shows the pertinence of the abovementioned expansive mass (*star*) to the left ovary. The expansive mass shows a vascularized peripheral zone and a central avascular portion, indicating necrosis; at histology it was diagnosed as a localization of endometrial carcinoma

images; the caudal growth of endometrial carcinoma that usually appears hyperintense compared to the adjacent structures progressively obliterates vaginal fornices and produces a thickening of vaginal walls, which therefore lose their physiological hypointensity. Diffusion-weighted images may increase the confidence in diagnosing vaginal infiltration by showing the presence of hyperintense neoplastic tissue within the thickened vaginal walls.

Parametrial infiltration also represents an extremely rare event and can be best evaluated on the coronal and the axial TSE T2-weighted images in which the neoplastic tissue appears relatively hypointense compared to the hyperintense parametrial fatty tissue. Differently from cervical carcinoma, endometrial carcinoma shows parametrial infiltration only in anecdotic extremely advanced cases.

The most advanced stage of local extrauterine growth is represented by the involvement of adjacent anatomical structures, in particular the bladder and the rectum (stage IVA). Sagittal TSE T2-weighted images are usually the most accurate for the detection of bladder and/or rectum infiltration by showing a complete loss of the fatty cleavage plane between the neoplastic tissue and the adjacent organ and a concomitant wall thickening. Axial TSE T2-weighted images might be useful for confirming the finding, but in case of doubt, the repetition of the same MRI sequences after the patient emptied his/her bladder and/or rectum may increase the confidence in the diagnosis.

2.13.4 Nodal Involvement

After the evaluation of the “T” stage, the “N” stage must also be considered. The presence of endoabdominal nodal metastases classifies the neoplasm as stage IIIC, which is further subdivided into stage IIIC1, in case of pelvic nodal involvement only, and stage IIIC2, in case of para-aortic lymph node involvement, independently to the pelvic nodal status. On the other

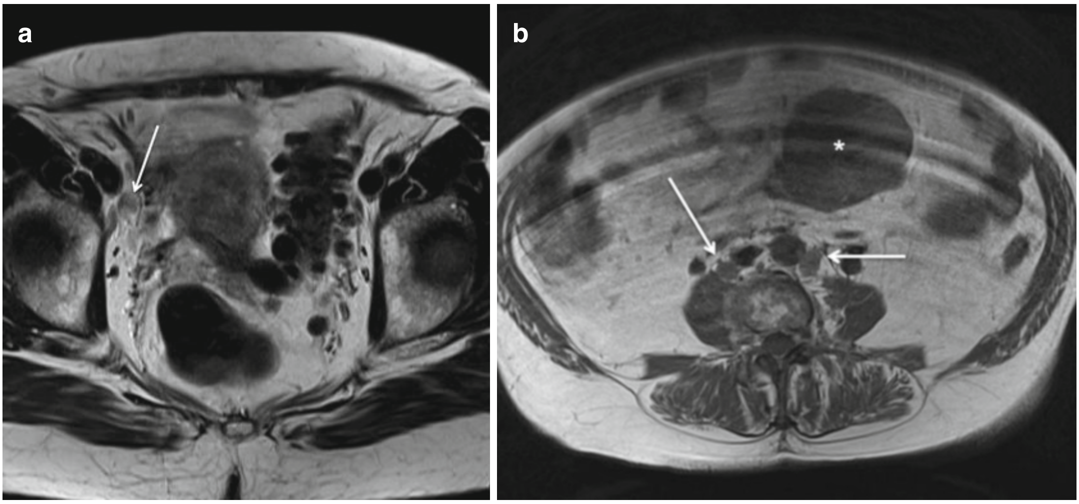

Fig. 2.18 (**a**, **b**) Nodal involvement (stage IIIC/IVB). Axial TSE T2-weighted image (TR/TE 2,400/76 ms) (**a**) shows a 12 mm large, rounded, internal obturator lymph node (*arrow*), which showed to be metastatic at pathology. Axial TSE T1-weighted image (TR/TE 730/10 ms) shows retroperitoneal lymphadenopathies (*arrows*) in a patient affected by a locally advanced endometrial carcinoma with left ovary involvement (*star*)

hand, inguinal lymph nodes are considered "distant" metastatic sites (stage IVB). The uterine neck and body first drain to the parametrial, paracervical, and obturator lymph nodes, whereas the uterine fundus and tubaric angles first drain to the common iliac and para-aortic lymph nodes.

Although some optimistic articles appeared in the literature, it must be kept in mind that, to date, MRI shows an unsatisfactory performance in the identification of abdominopelvic metastatic lymph nodes: indeed, despite accuracy values of about 80–90 %, sensitivity values do not exceed 60 % [42, 61]. Indeed, nowadays the only universally recognized MRI criterion for recognizing metastatic lymph nodes is a diameter >1 cm (Fig. 2.18a, b). As a matter of fact, such an approach leads to a double problem: firstly, "micrometastases" do not produce a sufficient nodal enlargement to reach the 10 mm-diameter cutoff, causing therefore a loose in the methodic sensitivity, whereas, secondly, inflammatory lymph nodes may often enlarge over the 10 mm-diameter cutoff, causing therefore a loose in the methodic specificity. In order to increase the diagnostic performance of MRI in recognizing nodal metastases, some additional features may be evaluated. Rounded shape, lost of fatty hilum, and spiculated margins, for example, are significantly associated with nodal metastases, but the evaluation is limited by low interobserver agreement. The recognition of necrotic tissue, which appears markedly hyperintense on T2-weighted images, without diffusion coefficient restriction, within an enlarged lymph node is virtually pathognomonic for nodal metastases, but it represents a rare eventuality in endometrial carcinoma, whereas the low apparent diffusion coefficient values of metastatic lymph nodes shows a significant overlap with ADC of inflammatory ones [62]. Moreover, with the experimentation of superparamagnetic contrast material stopped, there are to date no other effective means for diagnosing nodal metastases apart from the "morphodimensional" one.

Lymph nodes must be evaluated on large field of view TSE T1-weighted images, on which they appear hypointense in comparison to adjacent hyperintense intra-abdominal fat, and/or on large field of view T2-weighted RARE images, on which they appear hyperintense in comparison to adjacent saturated intra-abdominal fat. Both these imaging sequences are acquired on the true axial plane from femoral heads to renal hila in order to include all the possible abdominopelvic nodal metastatic sites. Moreover, diffusion-weighted images acquired in the pelvis may offer additional aid in recognizing nodal structures in that region.

2.14 Pitfalls in MRI Staging of Endometrial Carcinoma

MRI offers an overall high accuracy in local staging of endometrial carcinoma, but there are some well-known pitfalls that a radiologist must know [7].

First of all, the most important assumption for correctly staging EC is a technically unexceptionable MR examination, which means an examination with as few motion artifacts as possible and with imaging sequences acquired according to the correct axis. The first step when evaluating an MR examination for staging EC is to check the correctness of scanning planes because MR images acquired with inclinations not orthogonal to endometrial axis are the primary cause of error in the evaluation of the depth of myometrial infiltration.

Uterine morphological anomalies and the presence of large fibroids may increase the difficulty in correctly evaluating both the depth of myometrial infiltration and the presence of cervical stromal infiltration because distorting the physiological uterine morphology.

Tumors involving tubaric angles must be carefully evaluated because myometrial thickness in that location is physiologically thinner than in the remaining uterus and, therefore, the depth of myometrial infiltration might be overestimated. It is crucial to keep the myometrial thickness of the uninvolved contralateral tubaric angle as a reference.

Large polypoid tumors with a prevalent exophytic growth are often responsible of compressive alterations against uterine walls that result thinned that may lead to an overestimation of the depth of myometrial infiltration. The evaluation of junctional zone integrity, if visible, can be useful for excluding deep myometrial infiltration in these cases.

Operative maneuvers performed on the cervix in the days before MR examination, e.g., curettage, often cause signal intensity alterations that may lead to interpretation dilemmas; these alterations, however, are usually limited to cervical mucosa, without cervical stromal involvement, and, therefore, do not generate staging errors.

Conclusions

Endometrial carcinoma represents a common pathology in developed countries, with a prevalence that is going to increase parallel to the increase of population aging and of obesity.

The standard treatment of endometrial carcinoma is constituted by a wide surgical debulking, but it has been proven that such an approach is inordinate in patients affected by low-recurrence-risk neoplasms; therefore, in the era of individualized therapies, MRI plays a fundamental role in the preoperative staging of endometrial carcinoma in order to tailor the best surgical approach for each patient.

MRI staging of endometrial carcinoma is based on high-resolution T2-weighted and contrast-enhanced T1-weighted images, but diffusion-weighted imaging is showing increasing consensus thanks to its high tissue contrast resolution. MRI sequence acquisition plans must be accurately oriented according to the endometrial longer axis in order to prevent staging errors.

MRI offers a high accuracy in preoperative "T" staging of endometrial carcinoma; the most important parameters that must be carefully evaluated because implicating significant differences in patients' outcome are the depth of myometrial infiltration and cervical stromal infiltration.

MRI offers an unsatisfactory sensitivity in preoperative "N" staging of endometrial carcinoma, with this evaluation being based on volumetric parameters only. However, histological data, if combined with MRI data about "T" stage, can accurately predict the risk of nodal metastases and help in treatment planning.

References

1. Pathiraja P, Dhar S, Haldar K (2013) Serous endometrial intraepithelial carcinoma: a case series and literature review. Cancer Manag Res 5:117–122

2. Hamm B, Forstner R, Beinder E (2007) MRI and CT of the female pelvis. Springer, Berlin Heidelberg New York
3. Brinton LA, Felix AS (2014) Menopausal hormone therapy and risk of endometrial cancer. J Steroid Biochem Mol Biol 142:83–89
4. Rizner TL (2013) Estrogen biosynthesis, phase I and phase II metabolism, and action in endometrial cancer. Mol Cell Endocrinol 381(1–2):124–139
5. Hill HA, Eley JW, Harlan LC, Greenberg RS, Barrett RJ 2nd, Chen VW (1996) Racial differences in endometrial cancer survival: the black/white cancer survival study. Obstet Gynecol 88(6):919–926
6. Cheung MR (2013) African American race and low income neighborhoods decrease cause specific survival of endometrial cancer: a SEER analysis. Asian Pac J Cancer Prev 14(4):2567–2570
7. Foti PV, Farina R, Coronella M, Ruggeri C, Palmucci S, Montana A, Milone P, Zarbo G, Caltabiano R, Lanzafame S et al (2013) Endometrial carcinoma: MR staging and causes of error. Radiol Med 118(3):487–503
8. Hulse PA, Carrington BM, Carrington BM (2004) MRI manual of pelvic cancer. Taylor & Francis Independence (KY)
9. Epplein M, Reed SD, Voigt LF, Newton KM, Holt VL, Weiss NS (2008) Risk of complex and atypical endometrial hyperplasia in relation to anthropometric measures and reproductive history. Am J Epidemiol 168(6):563–570; discussion 71–6
10. Akhmedkhanov A, Zeleniuch-Jacquotte A, Toniolo P (2001) Role of exogenous and endogenous hormones in endometrial cancer: review of the evidence and research perspectives. Ann N Y Acad Sci 943:296–315
11. Blouin K, Nadeau M, Mailloux J, Daris M, Lebel S, Luu-The V, Tchernof A (2009) Pathways of adipose tissue androgen metabolism in women: depot differences and modulation by adipogenesis. Am J Physiol Endocrinol Metab 296(2):E244–E255
12. Sonoda Y, Barakat RR (2006) Screening and the prevention of gynecologic cancer: endometrial cancer. Best Pract Res Clin Obstet Gynaecol 20(2):363–377
13. Myriokefalitaki E, D'Costa D, Smith M, Ahmed AS (2013) Primary bone metastasis as initial presentation of endometrial cancer (stage IVb). Arch Gynecol Obstet 288(4):739–746
14. Saibene A, Robbins e Cotran VK (2010) Le basi patologiche delle malattie. Patologia generale. Elsevier. Milano
15. Amant F, Cadron I, Fuso L, Berteloot P, de Jonge E, Jacomen G, Van Robaeys J, Neven P, Moerman P, Vergote I (2005) Endometrial carcinosarcomas have a different prognosis and pattern of spread compared to high-risk epithelial endometrial cancer. Gynecol Oncol 98(2):274–280
16. Creasman WT, Morrow CP, Bundy BN, Homesley HD, Graham JE, Heller PB (1987) Surgical pathologic spread patterns of endometrial cancer. A Gynecologic Oncology Group Study. Cancer 60(8 Suppl):2035–2041
17. Willis G, Misas JE, Byrne W, Podczaski E (2011) Nodal metastasis in endometrial cancer. Eur J Gynaecol Oncol 32(3):259–263
18. Han SS, Lee SH, Kim DH, Kim JW, Park NH, Kang SB, Song YS (2010) Evaluation of preoperative criteria used to predict lymph node metastasis in endometrial cancer. Acta Obstet Gynecol Scand 89(2):168–174
19. Larson DM, Connor GP, Broste SK, Krawisz BR, Johnson KK (1996) Prognostic significance of gross myometrial invasion with endometrial cancer. Obstet Gynecol 88(3):394–398
20. Stewart CJ, Doherty DA, Havlat M, Koay MH, Leung YC, Naran A, O'Brien D, Ruba S, Salfinger S, Tan J (2013) Transtubal spread of endometrial carcinoma: correlation of intra-luminal tumour cells with tumour grade, peritoneal fluid cytology, and extra-uterine metastasis. Pathology 45(4):382–387
21. Renaud MC, Le T, Le T, Bentley J, Farrell S, Fortier MP, Giede C, Kupets R, Plante M, Power P et al (2013) Epidemiology and investigations for suspected endometrial cancer. J Obst Gynaecol Can 35(4): 380–383
22. Zamani F, Goodarzi S, Hallaji F, Zamiri A, Deilami T, Malek M, Modarress Gilani M (2012) Diagnostic value of pelvic MRI for assessment of the depth of myometrial invasion and cervical involvement in endometrial cancer: comparison of new versus old FIGO staging. Iran J Radiol 9(4):202–208
23. Frei Bonel KA, Kinkel K (eds) (2007) MRI and CT of the female pelvis
24. Colombo N, Preti E, Landoni F, Carinelli S, Colombo A, Marini C, Sessa C (2013) Endometrial cancer: ESMO Clinical Practice Guidelines for diagnosis, treatment and follow-up. Ann Oncol 24 Suppl 6:vi33–vi38
25. Panici PB, Basile S, Salerno MG, Di Donato V, Marchetti C, Perniola G, Palagiano A, Perutelli A, Maneschi F, Lissoni AA et al (2014) Secondary analyses from a randomized clinical trial: age as the key prognostic factor in endometrial carcinoma. Am J Obstet Gynecol 210(4):363.e1–363.e10
26. ASTEC Study Group, Kitchener H, Swart AM, Qian Q, Amos C, Parmar MK (2009) Efficacy of systematic pelvic lymphadenectomy in endometrial cancer (MRC ASTEC trial): a randomised study. Lancet 373(9658):125–136
27. May K, Bryant A, Dickinson HO, Kehoe S, Morrison J (2010) Lymphadenectomy for the management of endometrial cancer. Cochrane Database Syst Rev (1):CD007585
28. Galaal K, Bryant A, Fisher AD, Al-Khaduri M, Kew F, and Lopes AD (2012) Laparoscopy versus laparotomy for the management of early stage endometrial cancer. Cochrane Database Syst Rev (9):CD006655.
29. Bats AS, Bensaid C, Huchon C, Scarabin C, Nos C, Lecuru F (2010) Current indications of lymphadenectomy in endometrial cancer. Gynecol Obstet Fertil 38(12):754–759
30. Todo Y, Kato H, Kaneuchi M, Watari H, Takeda M, Sakuragi N (2010) Survival effect of para-aortic lymphadenectomy in endometrial cancer (SEPAL study): a retrospective cohort analysis. Lancet 375(9721): 1165–1172
31. Kang WD, Kim CH, Cho MK, Kim JW, Kim YH, Choi HS, Kim SM (2009) Lymphadenectomy for low-risk

endometrial cancer based on preoperative and intraoperative assessments. Int J Gynecol Cancer 19(4): 657–661

32. Antonsen SL, Jensen LN, Loft A, Berthelsen AK, Costa J, Tabor A, Qvist I, Hansen MR, Fisker R, Andersen ES et al (2013) MRI, PET/CT and ultrasound in the preoperative staging of endometrial cancer – a multicenter prospective comparative study. Gynecol Oncol 128(2):300–308
33. Brocker KA, Alt CD, Eichbaum M, Sohn C, Kauczor HU, Hallscheidt P (2011) Imaging of female pelvic malignancies regarding MRI, CT, and PET/CT: part 1. Strahlenther Onkol 187(10):611–618
34. Zerbe MJ, Bristow R, Grumbine FC, Montz FJ (2000) Inability of preoperative computed tomography scans to accurately predict the extent of myometrial invasion and extracorporeal spread in endometrial cancer. Gynecol Oncol 78(1):67–70
35. Rubtsova NA, Novicova EG, Sinitsyn VE, Vostrov AN, Stepanov SO (2012) Endometrial cancer: preoperative staging. The informative value of ultrasound study versus magnetic resonance imaging. Vestn Rentgenol Radiol 2012 Jul–Aug; (4):33–41
36. Ortoft G, Dueholm M, Mathiesen O, Hansen ES, Lundorf E, Moller C, Marinovskij E, Petersen LK (2013) Preoperative staging of endometrial cancer using TVS, MRI, and hysteroscopy. Acta Obstet Gynecol Scand 92(5):536–545
37. Bharwani N, Miquel ME, Sahdev A, Narayanan P, Malietzis G, Reznek RH, Rockall AG (2011) Diffusion-weighted imaging in the assessment of tumour grade in endometrial cancer. Br J Radiol 84(1007):997–1004
38. Takeuchi M, Matsuzaki K, Nishitani H (2009) Diffusion-weighted magnetic resonance imaging of endometrial cancer: differentiation from benign endometrial lesions and preoperative assessment of myometrial invasion. Acta Radiol 50(8):947–953
39. Abu Freij M, Saleh H, Rawlins H, Duncan T, Nieto J (2011) The use of MRI for selecting patients with endometrial cancer and significant co-morbidities for vaginal hysterectomy. Arch Gynecol Obstet 283(5):1097–1101
40. Kang S, Kang WD, Chung HH, Jeong DH, Seo SS, Lee JM, Lee JK, Kim JW, Kim SM, Park SY et al (2012) Preoperative identification of a low-risk group for lymph node metastasis in endometrial cancer: a Korean gynecologic oncology group study. J Clin Oncol 30(12):1329–1334
41. Loubeyre P, Undurraga M, Bodmer A, Petignat P (2011) Non-invasive modalities for predicting lymph node spread in early stage endometrial cancer? Surg Oncol 20(2):e102–e108
42. Manfredi R, Mirk P, Maresca G, Margariti PA, Testa A, Zannoni GF, Giordano D, Scambia G, Marano P (2004) Local-regional staging of endometrial carcinoma: role of MR imaging in surgical planning. Radiology 231(2):372–378
43. Patel S, Liyanage SH, Sahdev A, Rockall AG, Reznek RH (2010) Imaging of endometrial and cervical cancer. Insights Imaging 1(5–6):309–328
44. Shin KE, Park BK, Kim CK, Bae DS, Song SY, Kim B (2011) MR staging accuracy for endometrial cancer based on the new FIGO stage. Acta Radiol 52(7):818–824
45. Celik C, Ozdemir S, Kiresi D, Emlik D, Tazegul A, Esen H (2010) Evaluation of cervical involvement in endometrial cancer by transvaginal sonography, magnetic resonance imaging and frozen section. J Obstet Gynaecol 30(3):302–307
46. Connor JP, Andrews JI, Anderson B, Buller RE (2000) Computed tomography in endometrial carcinoma. Obstet Gynecol 95(5):692–696
47. Weber G, Merz E, Bahlmann F, Mitze M, Weikel W, Knapstein PG (1995) Assessment of myometrial infiltration and preoperative staging by transvaginal ultrasound in patients with endometrial carcinoma. Ultrasound Obstet Gynecol 6(5):362–367
48. Frei KA, Kinkel K (2001) Staging endometrial cancer: role of magnetic resonance imaging. J Magn Reson Imaging 13(6):850–855
49. Furukawa N, Takekuma M, Takahashi N, Hirashima Y (2010) Intraoperative evaluation of myometrial invasion and histological type and grade in endometrial cancer: diagnostic value of frozen section. Arch Gynecol Obstet 281(5):913–917
50. Kisu I, Banno K, Lin LY, Ueno A, Abe T, Kouyama K, Okuda S, Masugi Y, Umene K, Nogami Y et al (2013) Preoperative and intraoperative assessment of myometrial invasion in endometrial cancer: comparison of magnetic resonance imaging and frozen sections. Acta Obstet Gynecol Scand 92(5):525–535
51. Kitajima K, Suenaga Y, Ueno Y, Kanda T, Maeda T, Takahashi S, Ebina Y, Miyahara Y, Yamada H, Sugimura K (2013) Value of fusion of PET and MRI for staging of endometrial cancer: comparison with F-FDG contrast-enhanced PET/CT and dynamic contrast-enhanced pelvic MRI. Eur J Radiol 2013;82(10): 1672–1676. doi: 10.1016/j.ejrad.2013.05.005. Epub 2013 May 30
52. Ren C, Xue HD, Li S, Zhang J, Pan WD, Sun ZY, Fang HY, Sun HY, Jin ZY (2012) Clinical application of magnetic resonance imaging in preoperative evaluation of endometrial cancer. Zhongguo Yi Xue Ke Xue Yuan Xue Bao 34(5):455–460
53. Dogan D, Inan N, Sarisoy HT, Gumustas S, Akansel G, Muezzinoglu B, Yucesoy I, Demirci A (2013) Preoperative evaluation of myometrial invasion in endometrial carcinoma: diagnostic performance of 3T MRI. Abdom Imaging 38(2):388–396
54. Hori M, Kim T, Murakami T, Imaoka I, Onishi H, Nakamoto A, Nakaya Y, Tomoda K, Tsutsui T, Enomoto T et al (2009) MR imaging of endometrial carcinoma for preoperative staging at 3.0T: comparison with imaging at 1.5T. J Magn Reson Imaging 30(3):621–630
55. Manfredi R, Gui B, Maresca G, Fanfani F, Bonomo L (2005) Endometrial cancer: magnetic resonance imaging. Abdom Imaging 30(5):626–636
56. Duncan KA, Drinkwater KJ, Frost C, Remedios D, Barter S (2012) Staging cancer of the uterus: a national audit of MRI accuracy. Clin Radiol 67(6):523–530

57. Wu WJ, Yu MS, Su HY, Lin KS, Lu KL, Hwang KS (2013) The accuracy of magnetic resonance imaging for preoperative deep myometrium assessment in endometrial cancer. Taiwan J Obstet Gynecol 52(2): 210–214
58. McComiskey MH, McCluggage WG, Grey A, Harley I, Dobbs S, Nagar HA (2012) Diagnostic accuracy of magnetic resonance imaging in endometrial cancer. Int J Gynecol Cancer 22(6):1020–1025
59. Wu LM, Xu JR, Gu HY, Hua J, Haacke EM, Hu J (2013) Predictive value of T2-weighted imaging and contrast-enhanced MR imaging in assessing myometrial invasion in endometrial cancer: a pooled analysis of prospective studies. Eur Radiol 23(2): 435–449
60. Beddy P, Moyle P, Kataoka M, Yamamoto AK, Joubert I, Lomas D, Crawford R, Sala E (2012) Evaluation of depth of myometrial invasion and overall staging in endometrial cancer: comparison of diffusion-weighted and dynamic contrast-enhanced MR imaging. Radiology 262(2):530–537
61. Haldorsen IS, Husby JA, Werner HM, Magnussen IJ, Rorvik J, Helland H, Trovik J, Salvesen OO, Espeland A, Salvesen HB (2012) Standard 1.5-T MRI of endometrial carcinomas: modest agreement between radiologists. Eur Radiol 22(7):1601–1611
62. Rechichi G, Galimberti S, Oriani M, Perego P, Valsecchi MG, Sironi S (2013) ADC maps in the prediction of pelvic lymph nodal metastatic regions in endometrial cancer. Eur Radiol 23(1):65–74

Uterine Cervix

3

Claudia Schenk, Federica Spagnolli, Arianna Rossi,
Riccardo Manfredi, and Roberto Pozzi Mucelli

3.1 Anatomy of the Cervix

The cervix represents the inferior part of the uterus, which communicates superiorly with the isthmus uteri and inferiorly with the vagina. It has a cylindrical shape and is 2.5 cm long. It consists of the supravaginal canal (endocervix) and of the intravaginal portion that projects into the vagina (ectocervix). The vagina surrounds the cervix creating the fornix. The part of the cervix, which is visible from the vagina, is called portio; in its centre, there is the external uterine orifice. This orifice is circular and tight in childless women, stretched in women who have already delivered [1].

Unlike the uterine corpus, the wall of the cervix consists mostly of firm connective tissue; the muscular portion accounts for less than 10 % of the cervical wall and consists primarily of smooth muscle cells in a circular arrangement. The mucosa of the anterior and posterior walls of the cervical canal is irregular because of the underlying smooth muscle cells, which give a typical palm-like configuration to the walls (plicae palmatae).

The cervical canal is lined by mucus-producing columnar epithelium, which contains numerous gland-like units, called crypts.

The ectocervix is coated with non-keratinizing squamous epithelium. The squamocolumnar junction is located in the ectocervix, at the level of the external os during childhood and pregnancy. In the menopausal period, it is located along the cervical canal [2].

The vascularization of the cervix is provided by the uterine and the ovarian arteries. The uterine arteries originate from the anterior branch of the internal iliac artery, run through the parametria and cross the ureters about 2 cm lateral to the uterine cervix. At the level of the internal os of the cervical canal, the uterine arteries divide into an ascending and a descending branch. The uterine veins are connected to vaginal, rectal and vesical veins, which drain the venous blood into the hypogastric veins.

The lymphatic drainage of the cervix is provided by lymphatic vessels reaching the obturator, the iliac and the promontory lymph nodes. Lymphatic vessels from the cervix communicate with lymphatic vessels of the corpus uteri, which reach the para-aortic, the preaortic and the superior medial superficial inguinal lymph nodes.

C. Schenk (✉) • F. Spagnolli • A. Rossi
R. Manfredi • R.P. Mucelli
Department of Radiology,
G.B. Rossi, University Hospital,
Piazzale Ludovico Antonio Scuro,
10, Verona 37134, Italy
e-mail: schenk.claudia@yahoo.it;
riccardo.manfredi@univr.it;
roberto.pozzimucelli@univr.it

R. Manfredi, R. Pozzi Mucelli (eds.), *MRI of the Female and Male Pelvis*,
DOI 10.1007/978-3-319-09659-9_3,

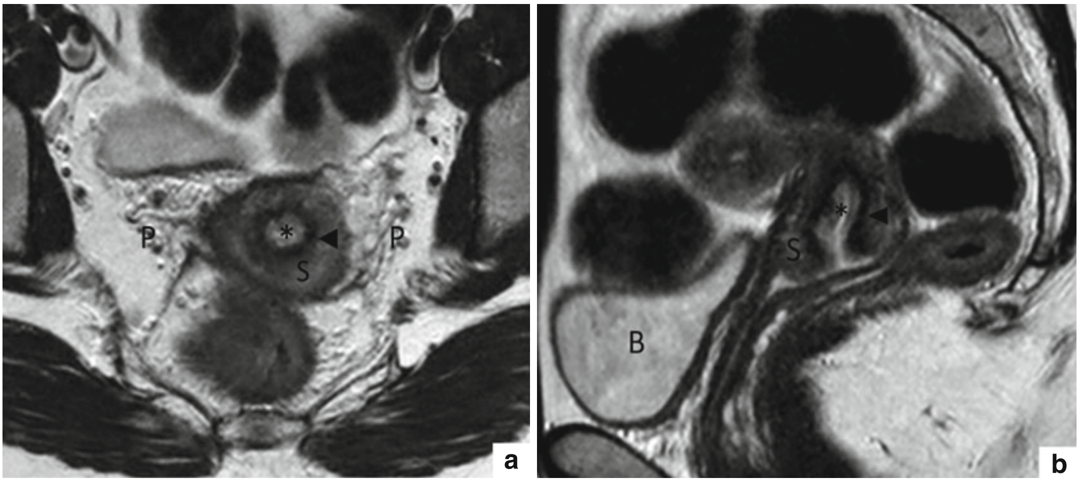

Fig. 3.1 Normal cervical anatomy. (**a**, **b**) T2w TSE images in axial (TR 5,130 ms, TE 108 ms) and sagittal (TR 6,040 ms, TE 90 ms) orientation showing the normal appearance of the cervical anatomy at MRI: endocervix (*asterisk*), inner stromal ring (*black arrowhead*) and outer cervical stroma (*S*). Parametrial tissue (*P*). Urinary bladder (*B*)

3.2 Normal Appearance of the Uterine Cervix at MRI

Contrary to the uterine corpus, the morphological appearance of the uterine cervix is only little influenced by woman's age, phase of menstrual cycle or hormonal therapies [3].

The normal zonal anatomy of the cervix is well visible on T2-weighted images. It is possible to distinguish three different anatomic zones: the endocervix, the inner stroma and the outer stroma (Fig. 3.1).

The central endocervical mucosa shows high signal intensity on T2-weighted images, due to the presence of cervical mucus, particularly during the periovulatory phase. During menopausal age, the cervical epithelium atrophies and the production of mucus diminishes; consequently the thickness and the signal intensity of the endocervical mucosa is reduced [4].

The middle layer corresponds to the inner layer of fibromuscular cervical stroma, which is often contiguous to the junctional zone of the uterine corpus. It is characterized by low signal intensity on T2-weighted images, due to the large amount of fibroblasts and smooth muscle cells and less vascularized connective tissue compared to the outer cervical stroma.

The outer layer of the cervix, corresponding to the outer cervical stroma, has low to intermediate signal intensity on T2-weighted images, due to the lower concentration of smooth muscle cells; it is often contiguous to the outer myometrium [5].

On unenhanced T1-weighted images, the cervix appears as a homogeneous cylinder-shaped structure of intermediate signal intensity; the single layers are not distinguishable.

After endovenous administration of contrast agent, both endocervical epithelium and parametrium show rapid contrast enhancement, followed by a progressive increase of the signal intensity of the outer stroma, whereas the compact stroma of the intermediate layer remains hypointense.

The paracervical tissue is composed of less dense stroma; consequently it has moderate to high signal intensity on T2-weighted images, whereas it demonstrates intermediate signal intensity on T1-weighted images.

3.3 Imaging Technique

3.3.1 Patient Preparation

Before scanning it is important to gather the gynaecologic anamnesis of the patient with information about her symptoms, hormonal status, menstrual

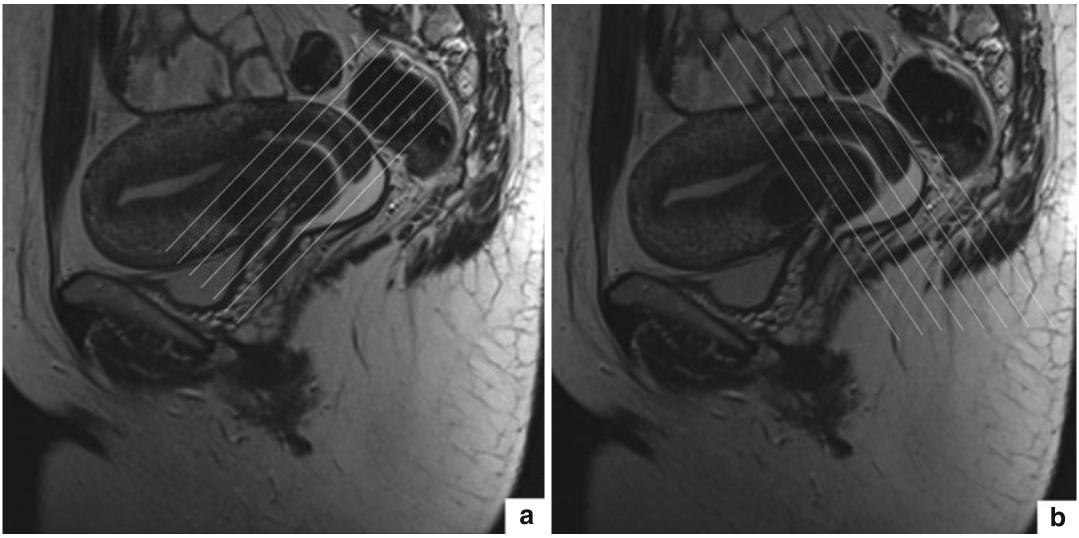

Fig. 3.2 T2w TSE images in sagittal orientation (TR 6,040 ms, TE 90 ms). Example for positioning of the imaging slices in an MRI cervical examination along the short (**a**) and long (**b**) axis of the uterine cervix

cycle, eventual hormone therapy, pregnancies, previous surgery or chemoradiotherapy.

A 4-h fasting is required for contrast medium injection and for reduction of bowel peristalsis. Motion artefacts caused by peristalsis are also reduced by the administration of a spasmolytic agent, such as butyl scopolamine bromide (Buscopan) administered preferentially intramuscularly at a dose of 20 mg few minutes before scanning (in alternative: glucagon 2 mg endovenously).

The urinary bladder should be moderately filled in order to straighten an anteflexed uterus.

If vaginal infiltration is suspected, it would be helpful to distend the vagina with gel for better delineation of the fornices.

The application of contrast medium is usually not necessary, apart from selected cases, in which a low molecular paramagnetic gadolinium-based contrast agent is administered at a dose of 0.5–1 mmol/kg body weight.

3.3.2 Patient Positioning, Scan Planes and Sequences

The patient is positioned supine with the arms lying along her sides.

The use of body phased array surface coils, covering from mid symphysis pubis to renal hilum, is important in order to obtain a high signal to noise ratio, high signal homogeneity, high spatial resolution and rapid acquisitions. A relative disadvantage is that subcutaneous fat shows high signal intensity, which may accentuate motion artefacts in sequences obtained without breath hold. Thus, it is important to employ presaturation bands, anteriorly and above to the region of interest, in order to reduce the signal from the moving abdominal wall. Other strategies to reduce motion artefacts are respiratory triggering or breath-hold acquisitions with very fast sequences, large measurements and the correct phase encoding direction.

The imaging area must comprehend not only the pelvis but also the abdomen up to the renal hilum for the evaluation of para-aortic lymph nodes.

The best sequences for the depiction of cervical carcinoma are turbo spin echo (TSE) T2-weighted sequences without fat saturation, which are characterized by high soft tissue contrast. They are first acquired in the sagittal plane, parallel to the long uterine axis (covering the uterus and vagina to the pelvic floor), then parallel to the short axis of the cervical canal (from the fundus uteri to the pelvic floor) and finally perpendicularly to this, parallel to the long axis of the cervical canal (Fig. 3.2).

Table 3.1 Standard protocol for the cervix study at 1.5 T

	Orientation	TR ms	TE ms	ST mm	FOV cm	Matrix px	Imaging area	Rationale
T2w TSE	True axial (Short cervical axis)	5,130	108	4	320	320×85	Pelvis	Evaluation of stromal ring integrity and cervical infiltration
T2w TSE	True sagittal (Long uterine axis)	6,040	90	3	330	448×80	Pelvis	Evaluation of vaginal invasion
T2w TSE	True coronal (Long cervical axis)	3,870	101	3	320	320×65	Pelvis	Evaluation of parametrial pelvic floor infiltration
T1w SE	Axial	550	9.3	4	320	256×80	Kidneys to pelvis	Evaluation of pelvic floor muscles
T2w BH TRUE-FISP	Axial	5.65	2.83	3	380	512×80	Kidneys to pelvis	Evaluation of lymph nodes and ureters

Angulated images are important for the optimal depiction of the cervical stromal ring (axial planes) and for the evaluation of the relationship of the cervix with contiguous structures: axial and coronal planes and in particular the coronal planes parallel to the long axis of the endocervical canal. Additional angulated images perpendicular to the uterus or vagina may be useful in suspected infiltration of these structures.

Lymph node metastases are best evaluated with high-resolution respiratory-triggered T2 axial sequences, which are also useful in case of ureteral involvement.

DWI-weighted sequences may also be helpful in the detection of the cervical cancer itself, lymph node metastases and the peritoneal dissemination of tumours, as their ADC values are lower than those of normal tissues.

Intravenous contrast medium injection is usually not necessary, neither in benign lesions nor in primary staging of cervical cancer, which, at T2-weighted images, is usually well delineated from the surrounding tissue.

The administration of contrast material agents instead is helpful if cervical cancer is not seen at T2-weighted sequences and in patient candidates to trachelectomy. The injection of contrast agents may be useful even in those conditions, in cases where rectal, urinary bladder or vaginal infiltration by the tumour or endometriosis is suspected or in the differentiation between tumour recurrence and inflammatory, post-actinic or postoperative changes at follow-up examinations.

3.3.3 Standard Protocol for the Cervix Study at 1.5 T

Table 3.1.

3.3.4 Optional Protocol for the Cervix Study at 1.5 T

Table 3.2.

3.4 Non-neoplastic Diseases

3.4.1 Cervical Pregnancy

Cervical pregnancy is rare, occurring in 0.15 % of ectopic pregnancies [6]. Anyway, its incidence is increasing, probably due to the more frequent abortions. The causative process for cervical pregnancy is still not well comprehended. Well-known risk factors include uterine and cervix surgery, leiomyoma, anatomic malformations such as uterus septate, atrophic endometrium and

Table 3.2 Optional protocol for the cervix study at 1.5 T

	Orientation	TR ms	TE ms	ST mm	FOV cm	Matrix px	Imaging area	Rationale
T1w SE FS Pre-post Gd	Axial Coronal Sagittal	550	9.3	4	320	256×80	Kidneys to pelvis	Evaluation of tumour, therapy complications and fistulas
T1w 3D GRE FS Pre-post Gd	Volumetric	4.89	2.4	2.5	400	320×80	Kidneys to pelvis	Evaluation of tumour and therapy complications
DWI EPI FS b 0–500-1,000 (s/mm^2)	Axial Sagittal	2,100	81	7	400	144×100	Kidneys to pelvis	Evaluation of tumour
T1w GRE FS	Axial	822	4.93	4	320	256×91	Pelvis	Evaluation of cervical endometriosis

multiparity. It is a painless condition manifesting as bleeding after a period of amenorrhea. At the physical examination findings consist of an enlarged cervix with a dilated cervical external ostium [7].

At MRI the mass, made of decidua and chorionic villa with variable amount of blood at different stages of degradation, shows heterogeneous signal on both T1- and T2-weighted sequences with a low-signal-intensity margin on T2-weighted images and variable contrast enhancement after administration of gadolinium-based contrast material [3, 8]

3.4.2 Uterine Cervicitis

The ectocervix and the endocervix are, respectively, lined by squamous and columnar (glandular) epithelium and are therefore affected by different pathogens including *Trichomonas vaginalis*, *Candida albicans* and herpes simplex virus (mostly HSV type 2), which invade the ectocervical squamous epithelium, and *Neisseria gonorrhoeae* and *Chlamydia trachomatis* which affect the glandular endocervical epithelium causing mucopurulent infections [3, 7, 8].

Clinical manifestations of acute cervicitis are tenacious, jelly-like, yellow or turbid vaginal discharge, sensation of pelvic pressure or discomfort. Chronic inflammation instead may be completely asymptomatic but may cause epithelial erosion followed by atypical reparation processes with formation of retention cysts, which are demonstrated at MRI with low signal intensity on T1- and high signal intensity on T2-weighted sequences without enhancement after gadolinium-based contrast material administration [3, 8].

3.4.3 Nabothian Cysts

Nabothian cysts are a common finding in the cervix and represent mucous retention cysts localized in the deep cervical glandular epithelium caused by proliferation of the squamous epithelium in response to chronic flogosis with obstruction of the crypts, which consequently fill with mucus secreted by the columnar epithelium [3, 7, 9].

A subtype of nabothian cysts are the so-called tunnel clusters which are characterized by multicystic dilatation of the endocervical glands. They can be found in about 8 % of adult women, 40 % of whom are pregnant, almost exclusively multigravida and older than 30 years. Therefore, tunnel cluster seems to be the result of a stimulatory process occurring during pregnancy [8, 9].

Nabothian cysts are usually discovered incidentally, measuring from few millimetres to several centimetres and can easily be evaluated by visual inspection. Large cysts in the deeper cervical stroma may cause an unexplained enlargement of the cervix [8].

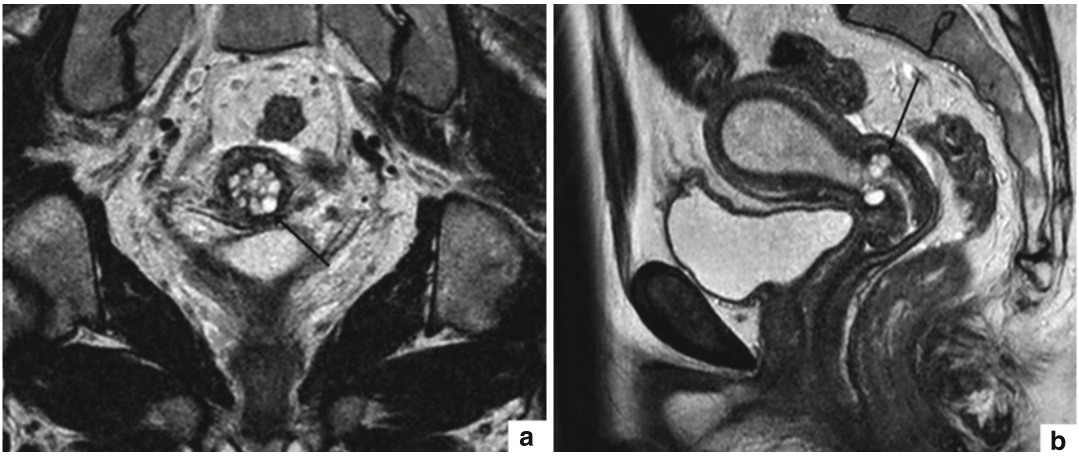

Fig. 3.3 Nabothian cysts. T2w TSE images in coronal (TR 3,870 ms, TE 101 ms) (**a**) and sagittal (TR 6,040 ms, TE 90 ms) (**b**) orientation showing multiple, round- to oval-shaped, well-circumscribed, hyperintense cystic formations (*arrow*)

At MRI they appear as single or multiple circumscribed superficial round- to oval-shaped lesions with smooth margins. Their proteinaceous content determines the intermediate or slightly high signal intensity on T1-weighted sequences and the prominent homogeneous high signal intensity on T2-weighted images. There is no enhancement after administration of intravenous contrast material [3, 8–10] (Fig. 3.3).

The most important differential diagnosis consists in adenoma malignum, a well-differentiated adenocarcinoma of the cervix associated with cystic portions. The presence of solid tissue between the cysts suggests the malignant nature of this lesion [3].

3.4.4 Cervical Polyps

Cervical polyps are the most common benign lesions of the cervix and are due to inflammatory and metaplastic processes occurring above all in the endocervical canal. They may range in size from a few millimetre sessile lesions to huge pedicled masses of 5 cm, protruding through the cervical orifice. They are soft masses arising from the mucosa and made of loose fibromyxoid connective stroma, blood vessels and dilated glands. Malignant degeneration is uncommon [3, 7].

They typically occur in perimenopausal women (especially in the fifth decade). The presenting symptoms include menorrhagia, intermenstrual or postmenopausal vaginal bleeding, contact bleeding and vaginal discharge. The diagnosis is made by hysteroscopy [3, 8].

At MRI cervical polyps are depicted as heterogeneous intermediate to high-signal-intensity masses with a hypointense central fibrous core and intratumoural cysts. After contrast medium injection the mass frequently shows a delayed lattice-like enhancement with outlining of the cystic spaces [3, 6, 8].

3.4.5 Endometriosis

Cervical endometriosis is rare and usually affects the endocervical canal or the portio. The retrocervical region and the posterior fornices instead are frequently affected by deeply infiltrating endometriosis with associated alterations of the uterosacral ligaments at their cervical insertions [3, 8].

The solid components of endometriosis, consisting of predominant muscular hyperplasia with associated fibrosis surrounding foci of endometrial tissue, show low signal intensity on both T1- and T2-weighted sequences and show pronounced

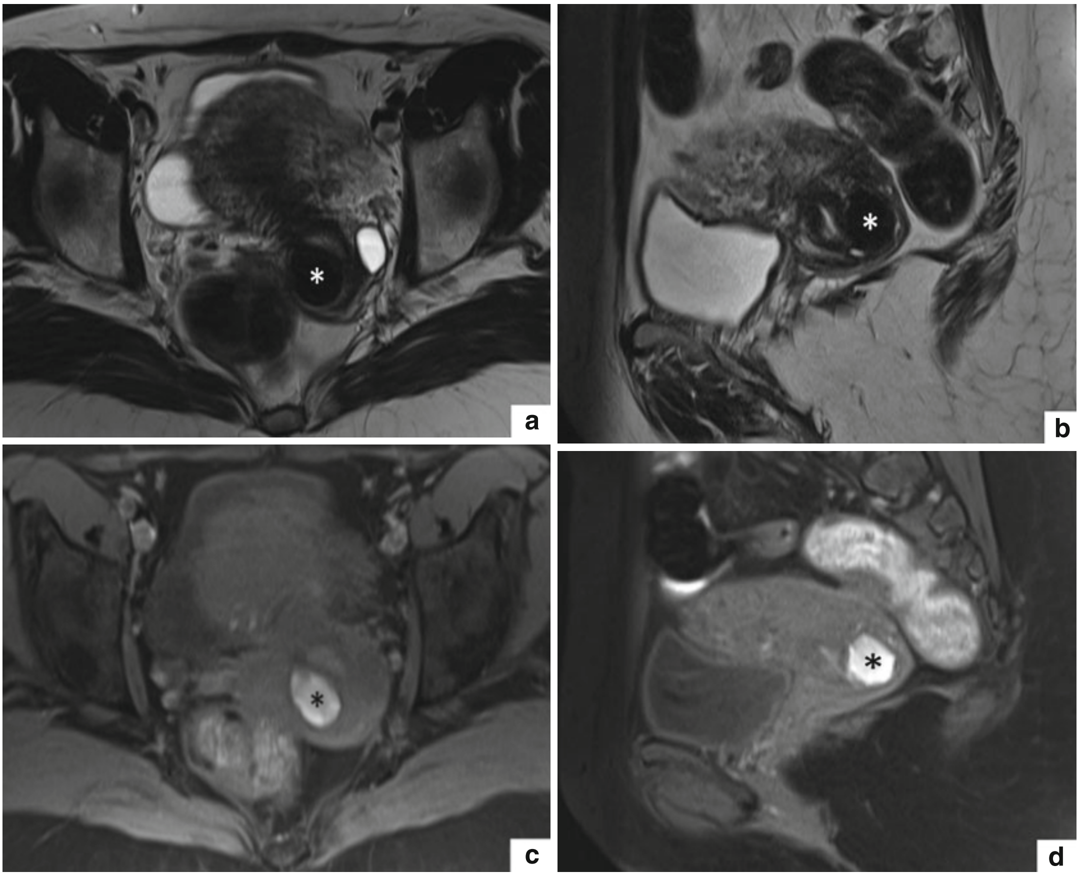

Fig. 3.4 Endometriosic cyst with haemorrhagic content in the posterior outer cervical stroma. T2w TSE images in axial (TR 5,130 ms, TE 108 ms) (**a**) and sagittal orientation (TR 6,040 ms, TE 90 ms) (**b**) and T1w TSE FS images in axial (TR 660 TE 9.5) (**c**) and sagittal orientation (TR 660, TE 9.5) (**d**) show a round-shaped, well-defined cystic lesion (*asterisk*) in the posterior outer cervical stroma. Its content shows low signal intensity on T2w TSE images (**a**, **b**) and high signal intensity on T1w TSE FS images (**c**, **d**), due to the presence of intracystic haemorrhagic material

contrast enhancement after contrast medium injection. These lesions usually contain haemorrhagic material which gives rise to the development of cystic components with high T1-signal intensity and variable T2-signal intensity [3] (Fig. 3.4).

More often it happens that an adenomyosic polypoid mass of the corpus uterine, covered by endometrial mucosa and smooth muscle layers resembling myometrium, protrudes into the cervical canal; it appears as ill-defined hypointense mass with some hyperintense cystic spots on T2-weighted images [3, 11].

3.5 Epithelial Neoplasms

3.5.1 Cervical Cancer

3.5.1.1 Introduction

Cervical cancer represents the second most common malignancy in women after breast cancer, is the most common malignant pathology affecting the female genital tract and one of the most frequent causes of death in women [4, 8, 12, 13]. The average age at diagnosis is 30–50 years, with a first peak between 35 and 45 years and a second one between 65 and 75 years [14–16].

In most cases, cervical cancer is due to the infection of the cervical epithelium by oncogenic human papillomaviruses (HPV), in particular HPV 16 and 18, which represent the high-risk types. Thus, there are many other risk factors for developing cervical carcinoma, i.e. sex at an early age, many different sexual partners, poor genital hygiene, frequent other genital infections, multiple pregnancies, immunosuppression and long-term use of oral contraceptives [3].

Typically these tumours arise from the unstable transformation zone of the uterine cervix at the junction of the squamous epithelium of the portio and the columnar epithelium of the cervical canal. Eighty to ninety percent of these tumours are squamous cell carcinomas followed by adenocarcinomas (5–10 %). Other rare histologic types of cervical cancer include adenosquamous carcinomas, small cell carcinomas and neuroendocrine tumours [3, 8, 17].

In early stages, cervical carcinomas are frequently asymptomatic. They become evident when the tumour has reached the stage of an invasive ulcerating cancer and are mainly represented by irregular or heavy vaginal bleeding, postcoital bleeding. Some patients present with a watery, mucoid, or purulent and malodorous vaginal discharge, which is a nonspecific finding. Advanced cervical tumour presents with pelvic and back pain due to infiltration of the adjacent anatomic structures, unilateral oedema of the leg caused by disturbance of the lymphatic drainage and increase in body circumference in case of peritoneal seeding [3]. Anyway, nowadays most cervical cancers are discovered in an early stage thanks to screening programmes with Pap test.

The final diagnosis of carcinoma of the uterine cervix is based upon histologic evaluation of a cervical biopsy.

3.5.1.2 Roles of MR Imaging

MRI is the method of choice for pretreatment evaluation of tumour extent in patients with FIGO stage IB or greater (stage 0 and IA cannot be assessed with this imaging method), giving important information about:

- Tumour volume
- Depth of stromal invasion
- Extension into the lower uterine segment
- Involvement of other contiguous anatomic structures and lymph nodes

Furthermore, MRI plays an important role in:

- Demonstrating complications of the disease itself and treatment complications
- Determining the feasibility of the uterus preserving surgery and in planning radio- and/or chemotherapy
- Monitoring response and detection of tumour recurrence [3, 15, 17, 18]

3.5.1.3 General Appearance of Cervical Cancer on MRI

Cervical carcinoma can demonstrate a wide variety of morphologic appearances and may be endocervical with a barrel shape or exophytic infiltrating [19].

Cervical tumours are best seen on T2-weighted MRI images as they show a high soft tissue contrast resolution and allow better differentiation of the tumour from the normal fibrocervical stroma, the surrounding tissues and organs. In fact, cervical cancer usually develops as a focal lesion from the mucosal layer of the cervix with a higher signal intensity on T2-weighted sequences in comparison to the low-signal-intensity cervical stroma [3, 14, 17, 18] (Fig. 3.5a, b).

On T1-weighted images, cervical cancer is usually isointense to the cervical stroma, and its identification is much more difficult compared to T2-weighted images. These sequences, instead, permit a better depiction of the parametrial tissue infiltration, since this tissue contains more fat and therefore shows a high signal intensity while the tumour itself presents a low signal intensity. T1-weighted sequences are used furthermore for the staging of lymph nodes [3] (Fig. 3.5c).

In those particular cases where gadolinium-based contrast medium is applied (patients with positive histological outcome for cervical cancer but the tumour is not detectable on T2-weighted images or patients candidate for trachelectomy), cervical carcinomas show an early enhancement within the first 15–30 s. Small tumours enhance homogeneously while large tumours often present necrotic changes and may or may not enhance. Anyway, they are often surrounded by an enhancing rim [3, 14, 17] (Fig. 3.5d, e).

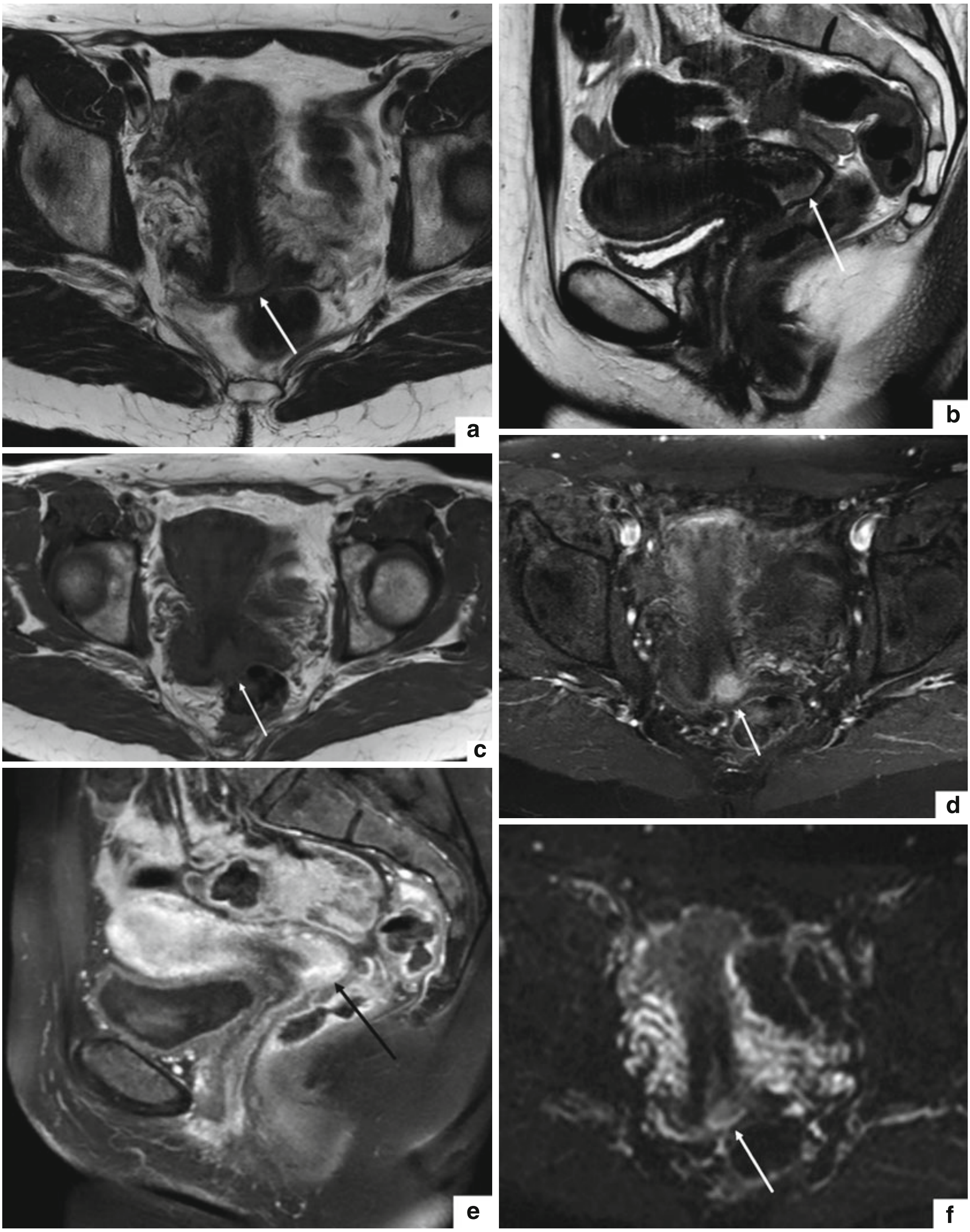

Fig. 3.5 Cervical cancer (FIGO stage IB1). T2w TSE images in axial (TR 5,130 ms, TE 108 ms) (**a**) and sagittal (TR 6,040 ms, TE 90 ms) (**b**) orientation show an area of high signal intensity in the left posterior portion of the uterine cervix attributable to cervical cancer (*arrows*). On T1w TSE image in axial orientation (TR 550 ms, TE 9.3 ms) (**c**), the tumour (*arrow*) is represented by an area of altered signal intensity which results nearly isointense to the signal intensity of the outer cervical stroma. T1w TSE FS images after administration of contrast material (TR 4.89 ms, TE 2.4 ms) in axial (**d**) and sagittal orientation (**e**) show a marked enhancement of the neoplastic process (*arrows*). Furthermore, on diffusion-weighted images (TR 2,100 ms, TE 81 ms) with B0 (**f**), B150 (**g**) and B300 (**h**) values, the pathological process demonstrates a progressive increase of signal intensity (*arrows*). On the ADC map (**i**), the tumoural process shows low signal intensity

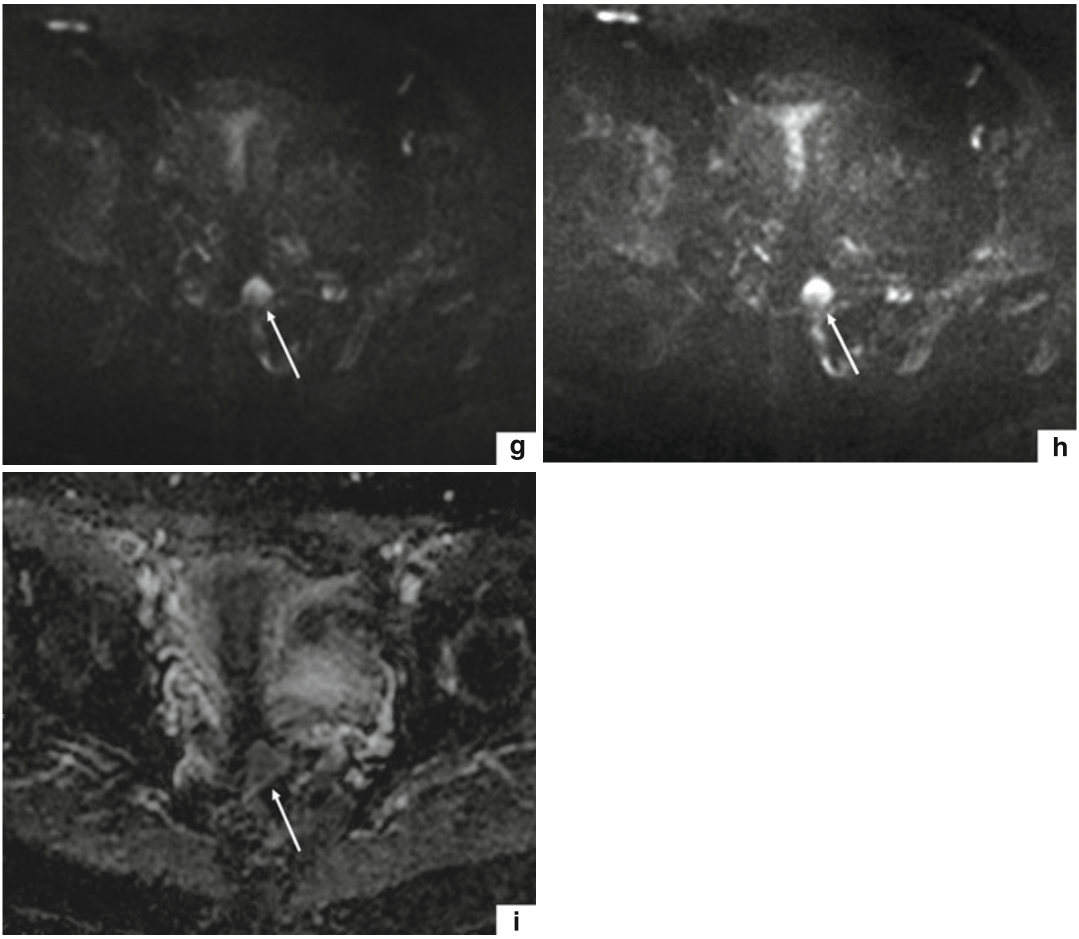

Fig. 3.5 (continued)

Diffusion-weighted imaging (DWI) is a functional imaging technique whose contrast is derived from differences in the restriction of the movement of water molecules in intercellular spaces and gives information about water mobility, tissue cellularity and integrity of cellular membranes [20, 21]. Cervical malignancies are characterized by a larger cell diameter and a denser cellularity, which restricts water diffusion [21]. Therefore, on DWI uterine cancers appear as hyperintense lesions and obvious in contrast to the dark background and are therefore better discernable from the surrounding normal cervical tissue as with usual T2-weighted sequences [18, 21] (Fig. 3.5f–h).

DWI can provide a quantitative measurement of apparent diffusion coefficient (ADC) value, which is influenced by nuclear-to-cytoplasm ratio and cellular densities in solid tissues [22]. The ADC values of cervical carcinoma are significantly lower than the median ADC values of benign lesions or normal cervical tissue and enable better delineation of the tumour boundaries [18, 22, 23]. According to some authors, the ADC values seem to correlate with the histological grade of cervical cancer: in their studies, poorly (G3) differentiated tumours showed lower ADC values in comparison to well- (G1) and moderately (G2) differentiated tumours [20–22]. Moreover, the ADC values of squamous cell carcinoma seem to be significantly lower than those of adenocarcinomas [21, 22] (Fig. 3.5i).

Table 3.3 TNM classification and FIGO staging of cervical cancer [3, 4]

TNM	FIGO	Criteria
0	0	No evidence of primary tumour
T1	I	Cervical carcinoma strictly confined to cervix uteri
T1A	IA	Invasive carcinoma diagnosed only by microscopy. Stromal invasion with a maximum depth of 5 mm and a horizontal spread of 7 mm or less
T1a1	IA1	Stromal invasion 3 mm or less in depth and 7 mm or less in horizontal spread
T1a2	IA2	Measured stromal invasion more than 3 mm and not more than 5 mm in depth with a horizontal spread 7 mm or less
T1b	IB	Stromal invasion greater than 5 mm in depth or greater than 7 mm in diameter or clinical visible lesion confined to the cervix
T1b1	IB1	Clinically visible lesion no greater than 4 cm in size
T1b2	IB2	Clinically visible lesion greater than 4 cm in size
T2	II	Carcinoma extending beyond the cervix, not involving the pelvic sidewall or the lower third of the vagina
T2a	IIA	Tumour involves the upper two thirds of the vagina
T2b	IIB	Tumour with parametrial invasion
T3	III	Tumour involves the lower third of the vagina or extends to the pelvic sidewall or causes hydronephrosis or non-functioning kidney
T3a	IIIA	Tumour involves the lower third of the vagina, no extension to the pelvic wall
T3b	IIIB	Tumour extends to the pelvic sidewall and/or causes hydronephrosis or non-functioning kidney
T4	IV	Tumour extends beyond the true pelvis and/or invades the mucosa of the bladder or rectum
	IVA	Invasion of the mucosa of the bladder or rectum
M1	IVB	Metastatic spread to distant organs

3.5.1.4 Local Tumour Staging

The most widely used staging system for cervical cancer is the “Federation Internationale de Gynécologie and Obstétrique” (FIGO) classification (Table 3.3), which is only based on clinical examination (physical examination, colposcopy, cystoscopy, sigmoidoscopy, etc.) [8, 15].

Stages 0 and IA represent the precursor stages of cervical cancer (CIN, CIS and microinvasive cancer) and are not evaluable with clinical exams nor with MRI as they do not change the normal cervical appearance. However, on dynamic MRI, microinvasive disease may be detected as a strongly enhancing area on early arterial phase images. Anyway, colposcopy and conization are the best methods for evaluation of these early cancer stages [3, 17].

Stage IB1 is the earliest stage of cervical cancer detectable by MRI and is defined as clinically invasive tumour, confined to the cervix, without invasion of the parametria or the vagina. On T2-weighted images, the tumour can be depicted as a high-signal-intensity mass completely surrounded by the low signal intensity of the fibrocervical stroma [3, 8] (Fig. 3.6). An intact low-signal-intensity cervical stroma excludes parametrial infiltration with a negative predictive value of 94–100 % [14, 17–19].

As large IB2 cancers tend to obstruct the cervical canal, they are often associated with hydro- or haematometra. Hydrometra is defined as fluid collection within the uterine cavity and is characterized by low signal intensity on T1-weighted images and high signal intensity on T2-weighted images. Haematometra instead represents the collection of blood within the uterine cavity and therefore it shows high signal intensity on both, T1- and T2-weighted images [3] (Fig. 3.12).

In stage IIA, the tumour invades the upper two thirds of the vagina; the lower third of the vagina and the parametria are spared. On T2-weighted images, the invasion of the vaginal wall, which normally shows low signal intensity, is represented by a hyperintense segmental lesion or disruption [3, 8, 14, 18] (Figs. 3.7 and 3.8).

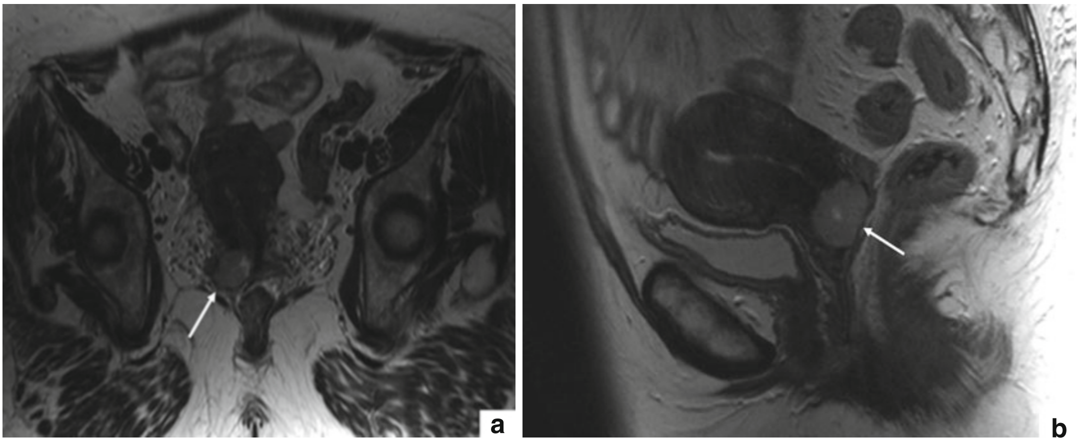

Fig. 3.6 Cervical carcinoma FIGO stage IB1. T2w TSE images in axial (TR 5,130 ms, TE 108 ms) (**a**) and sagittal (TR 6,040 ms, TE 90 ms) (**b**) orientation show a hyperintense cervical mass (*arrows*) completely surrounded by the hypointense stromal ring without infiltration of the surrounding tissues

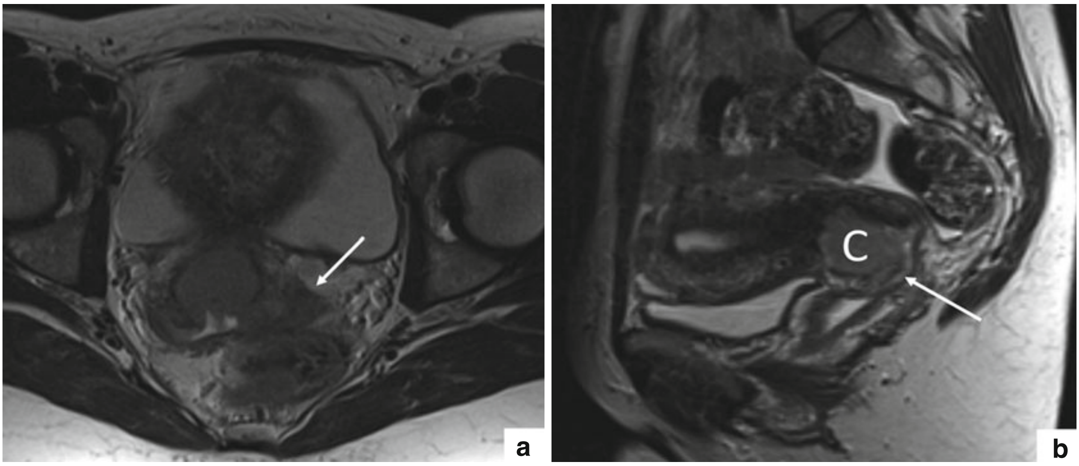

Fig. 3.7 Cervical carcinoma FIGO stage IIA. T2w TSE images in axial (TR 5,130 ms, TE 108 ms) (**a**) and sagittal (TR 6,040, TE 90) (**b**) orientation show a hyperintense cervical mass (*C*) extending to the anterior-lateral fornix on the left side (*arrows*)

Stage IIB tumour is defined as cervical cancer with infiltration of the parametrial tissue, without extension to the pelvic sidewall (Figs. 3.9, 3.10, 3.11 and 3.12). In this stage the tumour is seen as high-signal-intensity mass on T2-weighted images with unsharp and irregular margins, disrupting the hypointense cervical stroma and invading the parametrial tissue. This results in focal thickening of the infiltrated vesicouterine/rectouterine ligaments or retraction and dislocation of the cervix to the side of tumour invasion [3, 14].

In stage IIIA, the tumour invades the lower third of the vagina, without extension to the pelvic sidewall (Fig. 3.13). On MRI, this stage is characterized by a hyperintense disruption associated with continuous/discontinuous thickening of the vaginal wall. This stage is even characterized by a high risk for metastatic spread to superficial inguinal lymph nodes [3, 8, 14, 18, 19].

Stage IIIB is defined as tumour extension to the pelvic sidewall. On T2-weighted images, the

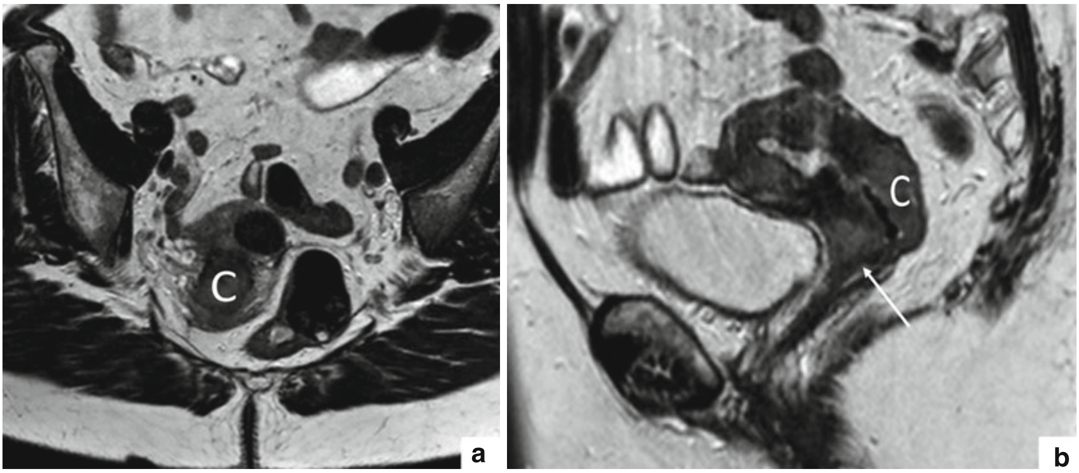

Fig. 3.8 Cervical cancer FIGO stage IIA. T2w TSE images in axial (TR 5,130 ms, TE 108 ms) (**a**) and sagittal (TR 6,040 ms, TE 90 ms) (**b**) orientation show a cervical mass extending to the anterior and posterior portion of the uterine portio (*C*) and along the anterior wall of the upper third of the vagina (*arrow*)

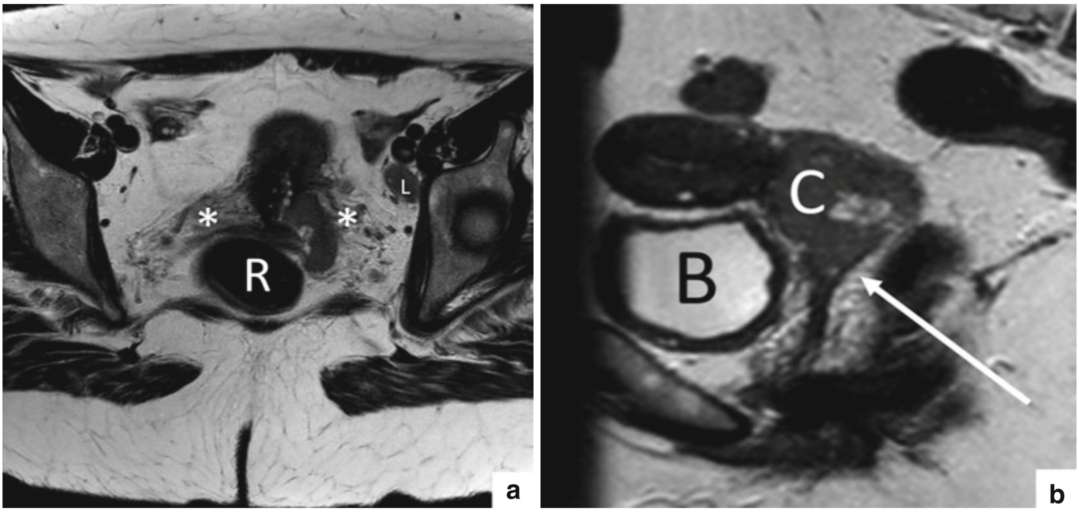

Fig. 3.9 Cervical cancer FIGO stage IIB. T2w TSE images in axial (TR 5,130 ms, TE 108 ms) (**a**) and sagittal (TR 6,040 ms, TE 90 ms) (**b**) orientation show the presence of a cervical mass (*C*) infiltrating the parametria (*asterisk*) on both sides without reaching the pelvic side walls. The neoplastic process extends furthermore to the anterior wall of the upper third of the vagina (*arrow*). There is no rectal (*R*) or urinary bladder (*B*) infiltration visible. Presence of a pathologic lymph node (*L*) in the left obturator region

pelvic sidewall infiltration is characterized by a high-signal-intensity tumour mass localized in the intermediate signal intensity of the pelvic musculature and of the low signal intensity of the cortical bone or as thickening of the iliac vascular walls. Another sign of pelvic sidewall infiltration is the tumour-related reduction of the hyperintense lateral lipid lamella on T1-weighted images. Hydronephrosis due to tumoural ureteral infiltration and obstruction is classified as IIIB disease as well [3, 6, 8, 14, 18, 19].

Stage IVA is characterized by tumour infiltration of the urinary bladder or the rectal mucosa (Figs. 3.14 and 3.15). In these cases, MRI shows

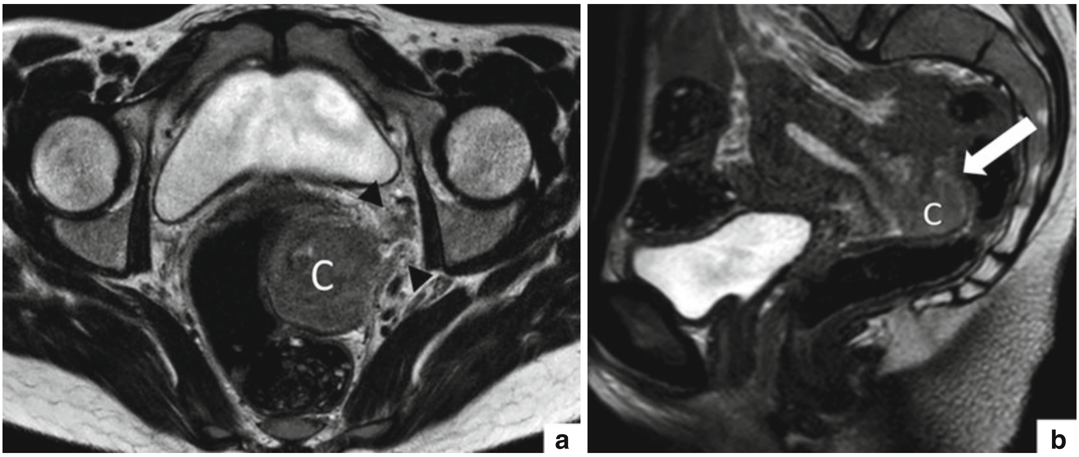

Fig. 3.10 Cervical carcinoma FIGO stage IIB. T2w TSE images in axial (TR 5,130 ms, TE 108 ms) (**a**) and sagittal (TR 6,040 ms, TE 90 ms) (**b**) orientation show a cervical mass (*C*) which extends to the left-sided parametrial tissue (*black arrowheads* in **a**) without reaching the pelvic side wall. It coexists infiltration of the posterior vaginal fornix (*white arrow* in **b**)

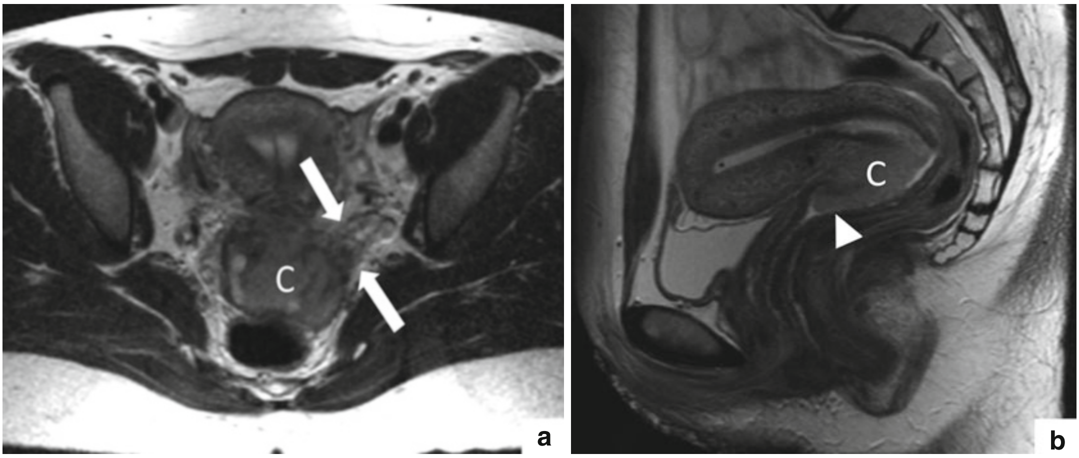

Fig. 3.11 Cervical carcinoma FIGO stage IIB. T2w TSE images in axial (TR 5,130 ms, TE 108 ms) (**a**) and sagittal (TR 6,040 ms, TE 90 ms) (**b**) orientation show a hyperintense mass in the anterior portion of the cervix (*C*) with infiltration of the left-sided fornix and parametrial tissue (*arrows* in **a**). The pelvic sidewall is spared. The tumour determines furthermore infiltration of the anterior wall of the upper third of the vagina (*arrowhead* in **b**)

a sensitivity of 91 % for invasion of the urinary bladder and 75 % for rectal involvement [15].

Bladder infiltration is suggested by focal or diffuse disruption of the normal low-signal-intensity posterior bladder wall on T2-weighted sequences, by a nodular or irregular bladder wall, by a mass protruding into the lumen of the bladder or by the presence of bullous oedema, which can be depicted as hyperintense thickening of the urinary bladder wall [6, 14, 19].

Direct rectal infiltration is rare because of the presence of the intervening pouch of Douglas. It usually occurs via the uterosacral ligaments and appears as segmental thickening, loss of the anterior rectal wall and segmental disruption of the low-signal-intensity rectal wall by tumour tissue with high signal intensity on T2-weighted images. Rectal invasion may also be suggested by prominent strands between the tumour and the rectal wall [15, 17].

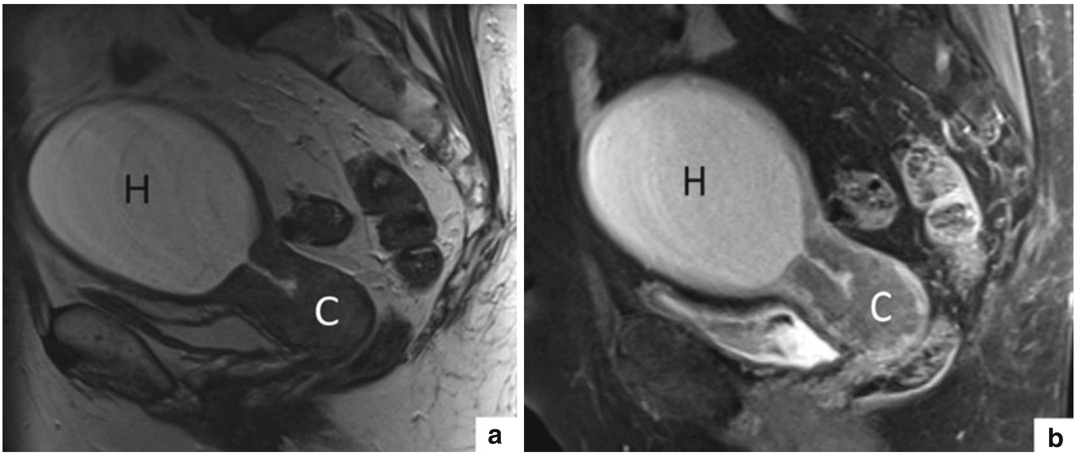

Fig. 3.12 Haematometra and cervical cancer FIGO stage IIB. T2w TSE image (TR 6,040 ms, TE 90 ms) (**a**) and T1 GRE FS image after administration of gadolinium-based contrast medium (TR 4.89 ms, TE 2.4 ms) (**b**) in sagittal orientation show a neoplastic pseudopolyp (*C*) protruding into the vaginal fornix. The proliferative process determines obstruction of the cervical canal with formation of a haematometra (*H*) and dilatation of the uterine cavity

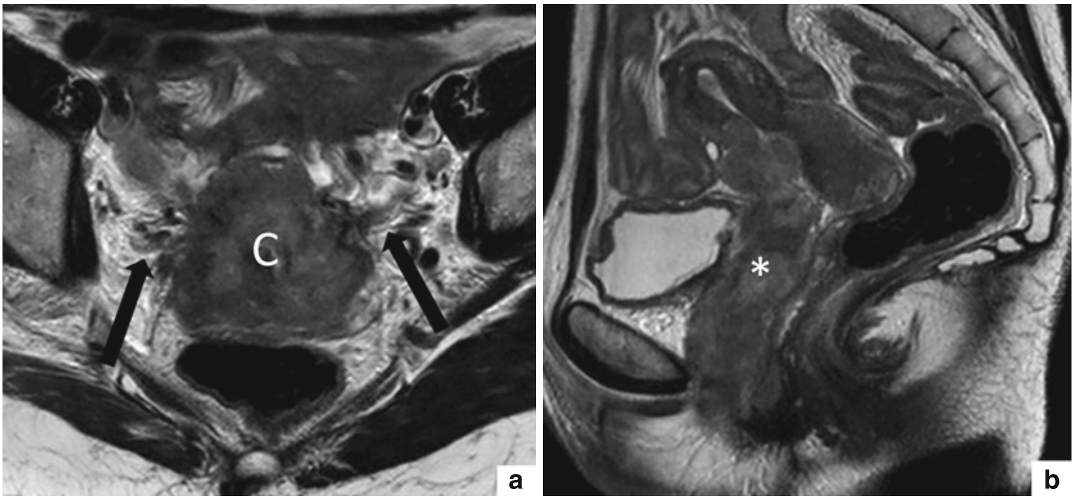

Fig. 3.13 Cervical cancer FIGO stage IIIA. T2w TSE images in axial (TR 5,130 ms, TE 108 ms) (**a**) and sagittal (TR 6,040 ms, TE 90 ms) (**b**) orientation show a cervical mass (*C*) infiltrating the inferior third of the corpus uteri, the parametria on both sides without extension to the pelvic sidewalls (*black arrows* in **a**) and the anterior wall of the vagina until its lower third (*asterisk* in **b**)

Both conditions are often associated with the development of fistulas, which, on T2-weighted images, are seen as hyperintense, filiform tubular or serpiginous structures within the tumour mass extending towards the bladder or the rectum. In case of contrast medium application, on T1-weighted post-contrast MR images, fistulas can be depicted as enhancing structures, due to the enhancement of the surrounding granulation tissue, with a non-enhancing filiform lumen [3, 8, 14, 24].

Stage IVB cervical tumour is characterized by the presence of distant metastases [3, 17].

3.5.1.5 Lymph Node Staging

The earliest tumour stage associated with lymph node metastases is stage IB and the risk increases with increasing depth of tumour invasion [3].

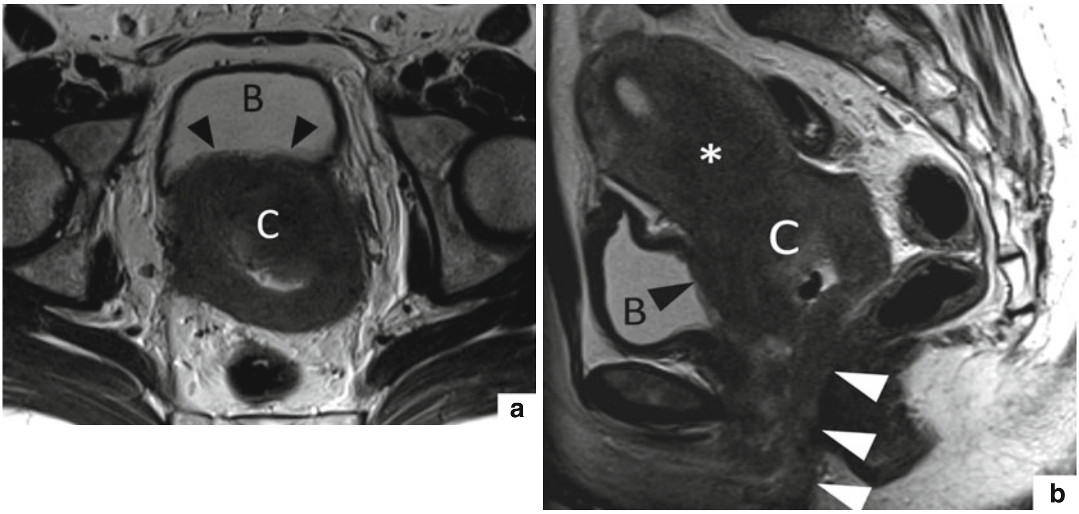

Fig. 3.14 Cervical carcinoma FIGO stage IVA. T2w images in axial (TR 5,130 ms, TE 108 ms) (**a**) and sagittal (TR 6,040 ms, TE 90 ms) (**b**) orientation show an extensive neoplastic process of the uterine cervix with infiltration of the corpus uteri (*asterisk*), the vagina and the vulva (*white arrowheads*). The tumour invades furthermore the posterior wall of the urinary bladder (*B*) (*black arrowheads*), neoplastic process (*C*)

The radiologic evaluation of lymph nodes is mainly based on their size and shape: parametrial lymph nodes have to be considered as suspicious, when they present a short axis of 1 cm or more, spherical morphology, irregular margins, signal intensity similar to the primary tumour, inhomogeneous contrast enhancement and central necrosis, which is highly predictive for metastatic disease [3, 6, 16, 18, 19, 24]. Some authors, however, suggest that a spherical lymph node should already be considered as suspicious if its short axis exceeds 5–7 mm [3].

Cervical cancer spreads first to the parametrial nodes, then to the lymph nodes along the internal and external iliac vessels, to the lymph nodes in the presacral area and the lymph nodes situated along the common iliac artery and in the para-aortic area, which are already considered as distant metastases [3, 15].

Lymph node metastases of cervical cancer can even affect the supraclavicular, the parabronchial and the axillary lymph nodes [3].

The presence of lymph node metastases is associated with a poor prognosis with decreased disease-free survival, increased incidence of tumour recurrence and marked decrease in survival rates [6, 17].

3.5.1.6 Distant Metastases

Haematogenous spread of cervical cancer to other organs occurs very late and is mainly seen in patients with local tumour recurrence [3].

The most common affected organ is the lung, where metastases appear as solitary or multiple parenchymal solid nodules, which are eventually associated with hilar and mediastinal adenopathy and pleural lesions or effusions. Rare findings include endobronchial obstruction, pulmonary lymphangiomatosis carcinomatosa and pericardial metastases [3, 8, 13].

Abdominal metastases occur in the liver (especially in patients with recurrent cervical tumour), the pancreas, the spleen, the adrenal glands, the kidneys and the gastrointestinal tract (rare). Metastases in the peritoneal cavity are suggested by ascites (unspecific sign), irregular contour of the liver caused by focal lesions, peritoneal thickening and nodularity and soft tissue masses. Abdominal metastases are often associated with abdominal pain and increase in abdominal circumference [3, 13].

Skeletal metastases occur mainly in patients with tumour recurrence, affect primarily the bony pelvis, the lumbar and other vertebral bodies, the ribs and the extremities and present typically an

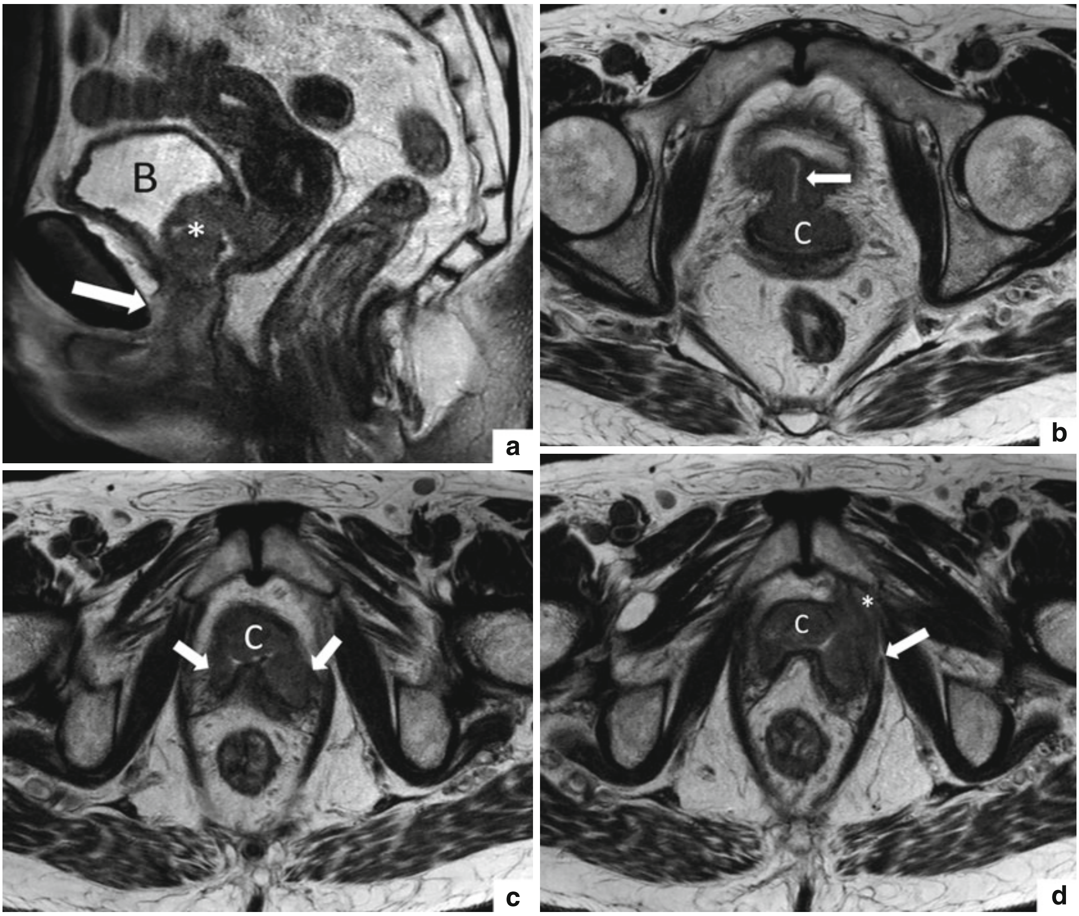

Fig. 3.15 Cervical cancer FIGO stage IVA. T2w TSE image in sagittal orientation (TR 6,040 ms, TE 90 ms) (**a**) shows the cervical neoplasm with infiltration of the anterior wall of the vagina (*arrow*), the posterior wall of the urinary bladder (*asterisk*, urinary bladder *B*). T2w TSE image in axial orientation (TR 5,130 ms, TE 108 ms) (**b**) shows a fine hyperintense tubular structure, attributable to a small fistula, in the cervical tumour mass (*C*) extending towards the urinary bladder (*arrow*). T2w TSE image in axial orientation (TR 5,130 ms, TE 108 ms) (**c**) shows bilateral infiltration of the parametrial tissue (*arrows*) by the tumour mass (*C*). T2w TSE image in axial orientation (TR 5,130 ms, TE 108 ms) (**d**) shows the neoplastic cervical process (*C*) which invades the left pelvic sidewall and the homolateral levator ani (*arrow*) and obturatorius muscles (*asterisk*)

osteolytic character. On T1-weighted MR images, bone metastases are visible as hypointense lesions within the skeletal bone marrow, while on T2-weighted and on fat-saturated T1-weighted images after contrast material administration, they appear as hyperintense lesions [3].

3.5.1.7 Uterine Cervical Carcinoma After Therapy

Findings After Surgery

Radical hysterectomy (Fig. 3.16) with associated pelvic lymphadenectomy represents the standard surgery for stage IB and IIA disease. The uterus and the upper third of the vagina are absent, and the residual vaginal stump is represented by an elongated, rectangular structure, which is well delimitated from the surrounding fatty tissue between rectum and urinary bladder and shows a smooth end. The normal residual vaginal wall can be visualized as smooth, low-signal-intensity muscular wall on T2-weighted images. In some cases, fibrotic scar tissue is present at the vaginal vault showing an intermediate to low signal intensity on T1- and T2-weighted images.

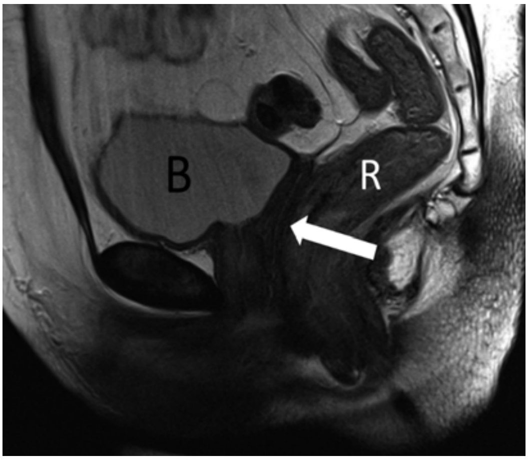

Fig. 3.16 T2w image in sagittal orientation (TR 6,040 ms, TE 90 ms) shows the normal female pelvic anatomy after radical hysterectomy with absence of the uterus and the upper third of the vagina. The vaginal stump is visible as elongated, rectangular structure (*arrow*) located between the urinary bladder (*B*) and the rectum (*R*)

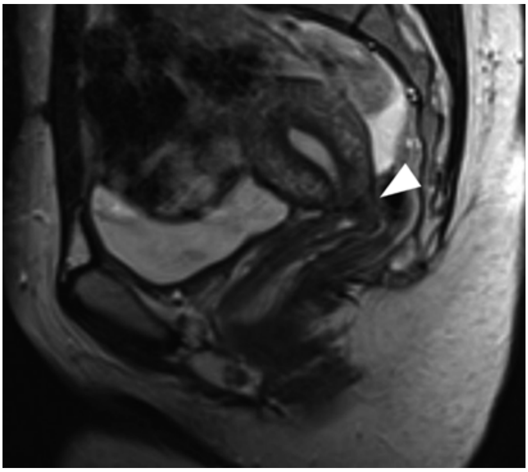

Fig. 3.17 T2w TSE image in sagittal orientation (TR 6,040 ms, TE 90 ms) shows the normal female pelvic anatomy after trachelectomy with preservation of the uterus and end-to-end anastomosis between the corpus uteri and the vaginal vault (*arrowhead*)

Metallic clips can be appreciated as small signal voids [3, 8, 13, 16].

Radical trachelectomy (Fig. 3.17) is usually performed in young women with stage IA or small stage IB1 tumours who wish to preserve their fertility. This surgical intervention consists in proximal vaginotomy, cervical resection and paracervical and paravaginal dissection, and the corpus uteri is preserved. An end-to-end anastomosis between the corpus uteri and the vaginal vault is performed, and a cerclage suture is placed to maintain competency and therefore fertility potential. Trachelectomy is furthermore associated with bilateral pelvic lymphadenectomy. In some cases, there will be an extension of the posterior wall of the vagina appearing as a neo-posterior vaginal fornix. Common changes after trachelectomy in the pelvis include lymphoceles and exaggeration of the pelvic venous plexus. Recurrence of cervical cancer in this type of surgery develops at the anastomotic site [3, 17, 25].

Pelvic exenteration is performed in patients with a central pelvic tumour recurrence and is characterized by hysterectomy, colpectomy and removal of the urinary bladder (anterior exenteration) or of the urinary bladder and the rectosigmoid (complete exenteration). In case of a supralevator exenteration, a part of the levator plate will be resected. A translevator exenteration instead is represented by vulvectomy and resection of the levator muscle, urogenital diaphragm and vulvoperineal soft tissue [3].

The complications of surgery consist in lymphocele, vesicovaginal and ureteral fistula, injury to the urinary bladder, ureteral damage, pelvic infection and haemorrhage [3, 13]

Up to 2 years after surgical therapy, the scar tissue might show a high signal intensity on T2-weighted images due to inflammatory processes and neovascularization. In this period of time, the differentiation between scar tissue and tumour recurrence is very difficult [24]; in fact, the only way to recognize a tumour recurrence in follow-up MRI exams during this period is the appearance and/or increase in volume of pathologic solid tissue at the site of surgical intervention.

Findings After Chemoradiotherapy

MRI is the first-line radiological modality for follow-up after combined chemoradiotherapy, which is performed as primary therapy in patients with cervical cancer in advanced stages.

A positive response to this therapy is characterized by a significant decrease in tumour

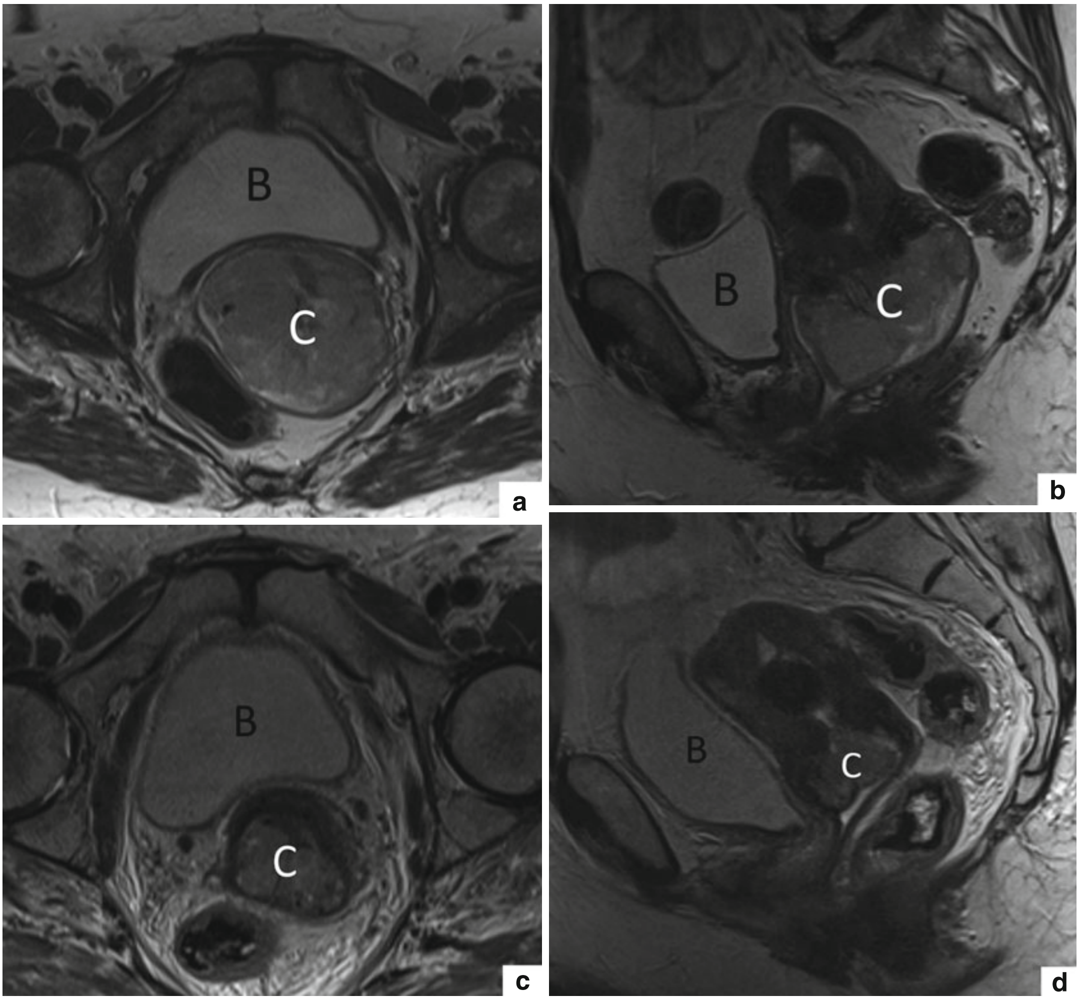

Fig. 3.18 T2w TSE images in axial (TR 5,130 ms, TE 108 ms) and sagittal orientation (TR 6,040 ms, TE 90 ms) show a cervical cancer (FIGO stage IIb) before (**a**, **b**) and after (**c**, **d**) combined chemoradiotherapy with evident reduction in tumour size. Cervical cancer (*C*), urinary bladder (*B*)

volume and signal intensity on T2-weighted images (Fig. 3.18). The typical signs of a tumour-free cervix are the reconstitution of the normal zonal anatomy with presence of homogeneous low-signal-intensity cervical stroma and the return of the normal anatomy of the proximal vagina [3, 13, 19].

Other changes, which are primarily induced by radiotherapy, are represented by wall thickening of the urinary bladder and rectum with or without increased signal intensity on T2-weighted images, symmetric thickening of the uterosacral ligament, presacral space widening and alteration of its signal intensity on both, T1- and T2-weighted sequences, high signal intensity of the skeletal muscle on T2-weighted sequences and high signal intensity of the bone marrow on T1-weighted images [18, 19].

Complications of radiation therapy consist in rectovesical fistulas, post-actinic radiogenic colitis, rectal and ureteral stricture and sacral insufficiency fractures [3, 13, 19].

3.5.1.8 Recurrence of Cervical Cancer

Approximately 30 % of women treated for invasive cervical cancer die of residual or recurrent disease. Tumour recurrence is defined as local tumour regrowth, development of lymph node or distant metastases after a tumour-free period of at least 6 months. In case of cervical cancer, recurrence usually occurs within 2 years after the diagnosis [3, 13, 15].

The risk factors for recurrence of cervical carcinoma are represented by histologic features of the tumour, tumour size, depth of stromal invasion and nodal status at presentation [13].

The sensitivity of MRI in detection of recurrent pelvic disease is 90 % [15].

On MRI, the tumour:

- May present a nodular appearance with irregular borders, due to tumour extensions and desmoplastic reactions and extension to the surrounding anatomic structures
- May show a diffuse growth

The most frequent site of tumour recurrence is the pelvis, either in a central position or at the sidewall.

Central recurrence of cervical cancer is usually located in the preserved cervix or vaginal cuff and is indicated by loss of the low-signal-intensity linear configuration of the vaginal vault and the presence of a soft tissue mass with blurred margins and high signal intensity on T2-weighted MR images [17, 24].

Compared to scar tissue and muscle, the recurrent neoplasm shows a higher signal intensity on T2-weighted images and an earlier and more evident enhancement on T1-weighted images after administration of gadolinium-based contrast medium. The maximum tumour enhancement occurs between 45 and 90 s after the contrast medium application [3, 13, 17].

If the carcinoma extends anteriorly, it may lead to encasement of the ureters with ureteral obstruction or infiltration of the urinary bladder wall with obstruction of the ureteral orifices with development of hydronephrosis.

Posterior tumour growth instead determines infiltration of the presacral space, of the os sacrum or of the perirectal space and rectum. Rectal infiltration of the recurrent neoplasm occurs in about 17 % of cases and involves most frequently the rectosigmoid junction. The remaining colon and the small intestine can be involved in presence of an advanced cervical cancer recurrence with development of adhesions of small bowel loops or intestinal obstruction [3, 13].

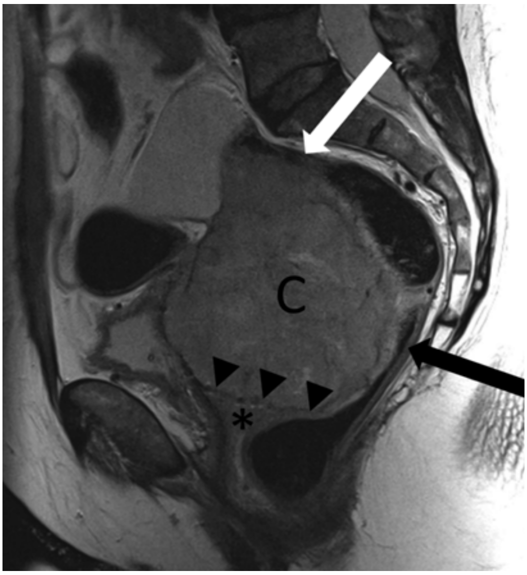

Fig. 3.19 Tumour recurrence after radical hysterectomy in cervical cancer. T2w TSE image in sagittal orientation (TR 6,040 ms, TE 90 ms) shows a huge, tumour mass (*C*) with pseudocapsule (*arrowheads*), originating from the vaginal stump (*asterisk*) and extending towards the promontorium. The neoplastic process infiltrates the proximal sigma (*white arrow*) and the anterior wall of the rectum (*black arrow*)

The pelvic sidewall is the second most frequent site of tumour recurrence and the preferred region of lymph node metastases. It can be infiltrated by a central tumour recurrence with lateral extension as well [3, 13].

After surgery, tumour recurrence occurs most frequently in the operative bed, especially at the vaginal stump, and at the resection margins. After radical hysterectomy, most cervical carcinomas show supravaginal recurrence (20 %) at the roof of the vaginal stump and in the rectovaginal space, between the bladder and rectum [3] (Fig. 3.19).

After primary chemoradiotherapy, local recurrence of cervical cancer is represented by a new tumour in the cervix, infiltration of the vagina or recurrence in the parametria with extension to cervix and vagina. A large recurrent tumour in the cervix may determine an obstruction of the internal os with resultant hydro- or pyometra [3].

Pelvic exenteration is only performed in young patients, with low comorbidity and only a central pelvic tumour recurrence without peritoneal disease, vessel encasement, involvement of the pelvic sidewall or nodal metastases. In case of tumour recurrence of the pelvic sidewall, the primary therapy consists in chemoradiotherapy. Lymph node metastases are usually treated by radiotherapy and haematogenous distant metastases by chemotherapy [3].

3.5.2 Adenoma Malignum or Minimal Deviation Adenocarcinoma

Adenoma malignum is an extremely well-differentiated mucinous adenocarcinoma of the cervix, and its prevalence is about 3 % of all cervical adenocarcinomas. It is very often associated with Peutz-Jeghers syndrome and mucinous tumours of the ovary. The most common initial symptom is watery vaginal discharge. Other nonspecific clinical presentations include abdominal pain, vaginal bleeding and abnormal Papanicolaou test. Its prognosis is very unfavourable, as it disseminates early to the peritoneal cavity and presents poor response to radio- or chemotherapy. Moreover this kind of malignancy is associated with vaginal, parametrial and bladder invasion and ovarian and lymph node metastases [6, 8, 9, 17].

MRI demonstrates a multicystic nodular or annular mass with solid tissue components, extending from the endocervical glands to the deep cervical stroma. The cystic portions have irregular and rough walls and are hypointense on T1-weighted images and hyperintense on T2-weighted images with intervening low-signal septations. The solid components instead show obvious enhancement after administration of gadolinium-based contrast medium [6, 9, 10, 17].

This tumour has to be differentiated from nabothian cysts, florid endocervical hyperplasia and well-differentiated adenocarcinoma [3, 8, 17].

3.6 Neuroendocrine Tumours

Small cell carcinoma is a rare primary tumour of the uterine cervix and accounts only 0.5–6 % of all cervical cancers. This tumour is extremely aggressive with early spread to the whole body. In most cases, they present with unspecific symptoms. MRI signal intensity of neuroendocrine tumours of the cervix is nonspecific with low signal intensity on T1-weighted sequences and slightly heterogeneous high signal intensity on T2-weighted images. After administration of gadolinium-based contrast agent, they show an evident enhancement. They are frequently accompanied by extensive lymphadenopathy and parametrial invasion [8, 26].

3.6.1 Malignant Melanoma

One to three percent of malignant melanomas develop in the female genital tract. Anyway, primary malignant melanoma of the uterine cervix is extremely rare. In fact, the cervix is usually involved secondarily as result of local extension from the vagina or vulva or as a result of haematogenous spread from primary melanoma located somewhere else in the body. Prognosis of this pathology is very poor as it is very often diagnosed at an advanced stage with most patients dying within 3 years [27].

On MRI, these lesions present a high signal intensity on T1-weighted images which varies according to the content of melanin. On T2-weighted images instead, the malignant melanoma shows low signal intensity. The signal intensity can furthermore be altered by intralesional haemorrhages, which occur quite often [3].

The malignant melanoma can be very easily identified at clinical examination (visual inspection) because of its characteristic black colour [8]. The treatment consists above all in radical hysterectomy, pelvic lymphadenectomy and partial vaginectomy. Radiotherapy may be useful as adjuvant therapy or in the palliation of an inoperable patient [27].

3.6.2 Metastases

Metastatic involvement of the uterine cervix is most commonly due to contiguous infiltration from other primary malignancies in the pelvis, colorectal cancer and urinary bladder carcinoma being the most frequent primary sites. The uterine cervix may also be infiltrated by peritoneal implants or ovarian cancer. On MRI, contiguous metastatic disease manifests as mass disrupting the hypointense fibrous cervical stroma with heterogeneous enhancement on post-contrast T1-weighted sequences [6].

Haematogenous dissemination of metastatic disease to the uterine cervix is rare and may occur from primary sites in the breast, gastrointestinal tract, ovary, skin and kidney. These metastases may be mass like and are characterized by heterogeneously enhancing masses disrupting the low signal intensity of the cervical stroma. Infiltrative metastases instead manifest as bulky enlargement of the cervix with abnormal signal and heterogeneous enhancement [3, 6].

3.7 Nonepithelial Neoplasms

3.7.1 Malignant Lymphoma

Malignant lymphoma of the cervix is uncommon and occurs only in 2 % of all primary extra nodal malignant lymphomas. In fact, usually it is due to secondary infiltration by advanced lymphoma from other sites. The majority of primary cervicouterine lymphomas are represented by B-cell NHL. The age of presentation of primary cervical lymphoma varies from 20 to 80 years with a mean age of 40–59 years. The most frequent presenting signs are vaginal bleeding, spotting or discharge, dyspareunia, perianal discomfort, urinary retention, abdominal mass or constitutional symptoms.

On MRI, it is characterized by a bulky, ill-defined, homogeneous mass with low signal intensity on T1-weighted images and a high signal intensity on T2-weighted images, similar to that of cervical squamous cell carcinoma. After administration of gadolinium-based contrast material, the mass enhances homogeneously and can be better delineated from surrounding tissues. Necrosis is uncommon and typically there is no infiltration of the surrounding anatomic structures [3, 6, 8, 28, 29].

Prognosis of cervical lymphoma is very favourable, even in advanced disease, as it shows a good response to combined chemo- and radiotherapy [28, 29].

3.7.2 Cervical Leiomyoma

Leiomyoma of the uterine cervix is very rare and accounts for less than 10 % of all leiomyomas of the uterus [8]. Clinical symptoms of this disease are mainly due to mass effect with abdominal distension, hyper- or dysmenorrhea and intra-abdominal blood accumulation [8, 30].

Typical leiomyoma are made of whorls of smooth muscle cells with various amount of collagen, that is little or absent in the cellular type. Scattered adipocytes in a typical leiomyoma are relatively common findings, but sometimes they are prominent and the lesion is called lipoleiomyoma [30].

On MRI, typical, not degenerated, leiomyomas appear as well-defined, circumscribed masses with low signal intensity on T1- and T2-weighted images and homogeneous enhancement after contrast material application. They do not have a true capsule but are surrounded by a pseudocapsule that sometimes is visible as a thin rim of hyperintensity on T2-weighted and post-contrast images [6, 31].

Moreover, leiomyomas may present different kinds of degeneration:

- Hyaline degeneration (most common) with hypointense signal on T2-weighted images and lack of enhancement
- Cystic degeneration (advanced stage of intratumoural oedema) with small or large, well-defined cystic spaces, demonstrating low signal intensity on T1-weighted images, high signal intensity on T2-weighted images and no enhancement on post-contrastographic T1-weighted sequences.
- Myxoid degeneration with marked high signal intensity on T2-weighted sequences with late and gradual enhancement

- Red degeneration caused by venous thrombosis with high signal intensity on T1-weighted images and lack of enhancement of the entire mass. The thrombosed veins may be visible as hyperintense rim surrounding the tumour on T1-weighted images [6, 8]

Four percent of degenerated fibroids have calcifications which are visible as signal voids on all MRI sequences [6].

Rarely leiomyomas may degenerate into leiomyosarcomas: irregular borders, pelvic sidewall or vascular invasion, haemorrhagic necrosis and rapidly increasing size are suggestive of sarcomatous transformation [6, 8, 31].

References

1. Magnaldi S, Travan L (2006) Dall'anatomia all'immagine. Poletto, Milan
2. Mariuzzi GM (2007) Anatomia patologica e correlazioni anatomo-cliniche. Piccin, Padova
3. Hamm B, Forstner R (2007) MRI and CT of the female pelvis. Springer, Berlin
4. Ragozzino A (2010) Imaging RM, nella donna – Syllabus. Idelson-Gnocchi, Napoli
5. Siegelman ES (2005) Body MRI. Elsevier Saunders, London
6. Rezvani M, Shaaban A (2010) Imaging of cervical pathology. Top Magn Reson Imaging 21:261–271
7. Vinay K, Abul A, Nelson F (2006) Pathologic basis of diseases: Robbins Cotran. 7th edn. Elsevier, Milan
8. Okamoto Y, Tanaka YO, Nishida M, Tsunoda H, Yoshikawa H, Itai Y (2003) MR imaging of the uterine cervix: imaging-pathologic correlation. Radiographics 23:425–445; quiz 534-5
9. Park SB, Lee JH, Lee YH et al (2013) Adenoma malignum of the uterine cervix: imaging features with clinicopathologic correlation. Acta Radiol 54: 113–120
10. Oguri H, Maeda N, Izumiya C, Kusume T, Yamamoto Y, Fukaya T (2004) MRI of endocervical glandular disorders: three cases of a deep nabothian cyst and three cases of a minimal-deviation adenocarcinoma. Magn Reson Imaging 22:1333–1337
11. Siegelman ES, Oliver ER (2012) MR imaging of endometriosis: ten imaging pearls. Radiographics 32:1675–1691
12. Choi HJ, Kim SH, Seo SS et al (2006) MRI for pretreatment lymph node staging in uterine cervical cancer. AJR Am J Roentgenol 187:W538–W543
13. Jeong YY, Kang HK, Chung TW, Seo JJ, Park JG (2003) Uterine cervical carcinoma after therapy: CT and MR imaging findings. Radiographics 23:969–981; discussion 81
14. Nicolet V, Carignan L, Bourdon F, Prosmanne O (2000) MR imaging of cervical carcinoma: a practical staging approach. Radiographics 20:1539–1549
15. Reznek RH, Sahdev A (2005) MR imaging in cervical cancer: seeing is believing. The 2004 Mackenzie Davidson Memorial Lecture. Br J Radiol 78(Spec No 2):S73–S85
16. Collettini F, Hamm B (2011) Uterine cervical cancer: preoperative staging with magnetic resonance imaging. Radiologe 51:589–595
17. Sala E, Wakely S, Senior E, Lomas D (2007) MRI of malignant neoplasms of the uterine corpus and cervix. AJR Am J Roentgenol 188:1577–1587
18. Testa AC, Di Legge A, De Blasis I et al (2014) Imaging techniques for the evaluation of cervical cancer. Best Pract Res Clin Obstet Gynaecol 28:741–768
19. Engin G (2006) Cervical cancer: MR imaging findings before, during, and after radiation therapy. Eur Radiol 16:313–324
20. Whittaker CS, Coady A, Culver L, Rustin G, Padwick M, Padhani AR (2009) Diffusion-weighted MR imaging of female pelvic tumors: a pictorial review. Radiographics 29:759–774; discussion 74-78
21. Kuang F, Ren J, Zhong Q, Liyuan F, Huan Y, Chen Z (2013) The value of apparent diffusion coefficient in the assessment of cervical cancer. Eur Radiol 23:1050–1058
22. Liu Y, Bai R, Sun H, Liu H, Wang D (2009) Diffusion-weighted magnetic resonance imaging of uterine cervical cancer. J Comput Assist Tomogr 33:858–862
23. McVeigh PZ, Syed AM, Milosevic M, Fyles A, Haider MA (2008) Diffusion-weighted MRI in cervical cancer. Eur Radiol 18:1058–1064
24. Testa AC, Di Legge A, Virgilio B et al (2014) Which imaging technique should we use in the follow up of gynaecological cancer? Best Pract Res Clin Obstet Gynaecol 28:769–791
25. Sahdev A, Jones J, Shepherd JH, Reznek RH (2005) MR imaging appearances of the female pelvis after trachelectomy. Radiographics 25:41–52
26. Yang DH, Kim JK, Kim KW, Bae SJ, Kim KH, Cho KS (2004) MRI of small cell carcinoma of the uterine cervix with pathologic correlation. AJR Am J Roentgenol 182:1255–1258
27. Yucesoy G, Kus E, Cakiroglu Y, Muezzinoglu B, Yildiz K, Yucesoy I (2009) Primary malignant melanoma of the cervix: report of a case. Arch Gynecol Obstet 279:573–575
28. Marin C, Seoane JM, Sanchez M, Ruiz Y, Garcia JA (2002) Magnetic resonance imaging of primary lymphoma of the cervix. Eur Radiol 12:1541–1545
29. Thyagarajan MS, Dobson MJ, Biswas A (2004) Case report: appearance of uterine cervical lymphoma on MRI: a case report and review of the literature. Br J Radiol 77:512–515
30. Terada T (2011) Huge lipoleiomyoma of the uterine cervix. Arch Gynecol Obstet 283:1169–1171
31. Deshmukh SP, Gonsalves CF, Guglielmo FF, Mitchell DG (2012) Role of MR imaging of uterine leiomyomas before and after embolization. Radiographics 32:E251–E281

Endometriosis

4

Simona Mautone, Salvatore Belluardo,
Valerio Di Paola, Luigi Romano, Giovanni Foti,
Riccardo Manfredi, and Roberto Pozzi Mucelli

4.1 Endometriosis

Endometriosis is defined as the presence of endometrial tissue, composed of both glandular and stromal elements, outside of the uterine cavity.

Originally, endometriosis was further classified as endometriosis "interna" (referred to as endometrial tissue within the uterine musculature) and "externa" (endometrial tissue in all other sites). Currently, adenomyosis has replaced the term endometriosis "interna."

Several systems have been used to stage the extension of the disease. The most common staging system used is the American Fertility Society (AFS) classification. It divides the disease into minimal, mild, moderate or severe, based on the presence of ovarian or peritoneal endometriosis (subdivided into superficial or deep), adhesions, and posterior cul-de-sac obliteration [1]. The AFS classification is the most commonly used, but it has poor correlation with severity of the disease and poor prognostic value of response to treatment. We consider the anatomic subdivision of pelvic endometriosis into three forms: the adenomyosis, the tubo-ovarian lesions (localized in the ovaries and tubes), and the deep pelvic endometriosis, defined by the invasion of endometrial tissue at least 5 mm beneath the peritoneal surface. There are also superficial peritoneal lesions, or noninvasive implants, well recognized at laparoscopy [2, 3], but usually not detectable with imaging.

4.1.1 Epidemiology

The real prevalence of endometriosis is difficult to determine since laparoscopy or surgery is required to make a definitive diagnosis [4]. Endometriosis is found especially in women of childbearing age, involved with an incidence of 10 % [5] and a peak of incidence between 24 and 29 years. Anyway it is not uncommon between adolescents (in most cases related to obstructive Mullerian duct anomalies of the cervix or vagina) [6], and about 5 % of cases are seen in postmenopausal women, related to hormone replacement therapy [7].

4.1.2 Pathogenesis

The pathogenesis of endometriosis is complex and still debated, probably multifactorial. Up to

---

S. Mautone (✉) • S. Belluardo • V. Di Paola
R. Manfredi • R. Pozzi Mucelli
Dipartimento di Radiologia di Verona,
Azienda Ospedaliera Universitaria di Verona,
Policlinico "G. B. Rossi", P.le L.A. Scuro 10,
Verona 37100, Italy
e-mail: simonamautone@gmail.com;
totibelluardo@alice.it; dipaola.valerio@libero.it;
rmanfredi@univr.it; roberto.pozzimucelli@univr.it

L. Romano • G. Foti
Dipartimento di Radiologia,
Ospedale "Sacro Cuore – Don Calabria",
V. don Sempreboni 5, Verona, Negrar, Italy

R. Manfredi, R. Pozzi Mucelli (eds.), *MRI of the Female and Male Pelvis*,
DOI 10.1007/978-3-319-09659-9_4, © Springer International Publishing Switzerland 2015

now, three principal theories have been proposed.

4.1.2.1 Metastatic Theory [8]

It is the most widely accepted theory that endometriosis results from a retrograde menstruation transporting endometrial tissue from the uterine cavity into the peritoneal cavity, where endometrial cells implant.

Actually, a retrograde menstruation has been observed in up to 90 % of normal women during the menstrual period [9], but endometrial tissue is normally resorbed by the abdominal cavity. Instead in case of endometriosis, the equilibrium between retrograde menstruation and resorption of endometrial tissue in the abdominal cavity is altered and leads to development of endometriosic lesions. Further evidence of this theory is suggested by the major frequency in women with obstructive anomalies of Mullerian duct development and with consequently excessive retrograde flow [6] and by the anatomic locations of the disease in the dependent pelvic areas [10]. Furthermore, the risk of endometriosis seems to be dependent on the amount of menstrual flow.

The metastatic spread can happen also by vascular and lymphatic channels or iatrogenically during surgery.

4.1.2.2 Metaplastic Theory [11]

It suggests the metaplastic differentiation of the Müllerian remnant tissue or peritoneal cells of serosal surfaces into functioning endometrial cells. The demonstration of endometriosis in women lacking functional eutopic endometrium (e.g., Turner syndrome, uterine agenesis) supports this theory [12].

4.1.2.3 Induction Theory

This is a combination of both first two theories. It suggests that substances released from shed endometrium induce undifferentiated mesenchyma to form endometriosic tissue [6].

Regardless of these theories, there is growing evidence suggesting that a genetic component plays a role in endometriosis with significant familial clustering and first-degree relatives of women with endometriosis having a sevenfold greater chance of having endometriosis [13].

Table 4.1 Symptoms related to anatomic location of endometriosic implants

Anatomic location	Symptoms
Pouch of douglas, torus uterinus, USLs, rectovaginal septum	Dyspareunia
Bowel	Dyschezia, catamenial diarrhea, rectal bleeding, constipation, intestinal occlusion
Ureteral stenosis	Urinary obstruction, flank pain
Bladder	Urgency, frequent urination, hematuria
Pleura – lung	Hemophthysis, chest pain, shortness of breath
Brain	Perimenstrual headaches, seizures, subarachnoid hemorrhage
Skin	Catamenial bleeding, tenderness

4.1.3 Signs and Symptoms

Endometriosis is frequently asymptomatic; it could be associated with a wide variety of symptoms, none of these pathognomonic, thus making the diagnosis difficult.

The most important clinical manifestations are pelvic pain and infertility. Endometriosis was detected at surgery in 19 % of women with chronic pelvic pain. Patients usually have cyclic symptoms related to bleeding and inflammation of menses; common symptoms are dysmenorrhea, back pain, dyspareunia, and rectal discomfort. However, clinical manifestations are related to implant's location and are listed in the Table 4.1.

Infertility may be the presenting complaint of endometriosis, with or without pelvic pain. It is estimated that 30–50 % of women with endometriosis are infertile, and 20 % of infertile women have endometriosis [14]. The pathogenic mechanism is debated. It could be related to repeated episodes of bleedings causing a chronic inflammatory state, which can lead not only to anatomic alterations induced by fibrosis and adhesions, but also to bio-humoral changes [15].

Of the three forms, deep pelvic endometriosis is thought to contribute most often to clinical symptoms. Then, in case of ovarian endometrioma with chronic and severe pelvic pain, associated deep pelvic endometriosis lesions are generally present, often multifocal and with intestinal infiltration [16].

4.1.4 Diagnosis

The lack of specific symptoms makes the diagnosis of endometriosis difficult and, often, very late. Diagnosis is made harder because the first-line imaging study, usually transvaginal or transabdominal ultrasound (US) [17], has a high sensitivity for adnexal lesions but a poor accuracy for other locations, especially for deep pelvic endometriosis, frequently giving false-negative results [17]. Above transabdominal and transvaginal US, several techniques have been used: magnetic resonance (MR) imaging and, in case of suspected bowel endometriosis, transrectal ultrasonography (US), rectal endoscopic sonography, and double barium contrast enema (DBCE). When the urinary system is involved, MR urography and cystography could be employed.

The reference standard for the diagnosis of pelvic endometriosis remains laparoscopy with histological confirmation.

In this chapter, we would highlight the role of magnetic resonance (MR) imaging in the diagnosis of endometriosis. This technique has already been demonstrated as a successful diagnostic tool to investigate the tubo-ovarian endometriosis, with a sensitivity, specificity, and accuracy of 90, 98, and 96 %, respectively [18], but also for deep endometriosis, with a sensitivity and specificity of 90 and 91 %, respectively [19].

4.2 Uterine Adenomyosis

Adenomyosis is a common non-neoplastic uterine disease defined by the presence of ectopic endometrial tissue within the myometrium, due to the invagination of endometrium in the myometrium at a depth of at least 2.5 mm below the basal layer of the endometrium. This process leads to hyperplasia and hypertrophy of the smooth muscle [20].

Adenomyosis can be either *focal* (one or several foci in the myometrium) or *diffuse* (numerous foci spread throughout the myometrium), and it is often asymmetric, predominating in the posterior uterine corpus. More controversial is the distinction between *superficial* (simple thickening of the junctional zone seen on MRI or lesions not extending beyond one third of the depth of the myometrium) and *deep forms* (penetrating deeper than one third of the myometrium). Although it has been accepted that uterine adenomyosis results from the direct invasion of the endometrium into the myometrium, and in such cases no direct relationship between the adenomyosis and the endometrium is proved histologically. Rather the disease appears to be the result of the invasion of endometrium-like structures (presumably endometriosis) from outside the uterus, disrupting the uterine serosa. This case has been named by some authors as "*external*" (or "extrinsic") adenomyosis, connected to lesions of deep pelvic endometriosis [21] extending to the uterine myometrium, frequently sparing the endometrial-myometrial junctional zone. The definition of this form as "external" adenomyosis or DPE involving the uterus is still debated; however, it practically does not affect therapy.

Furthermore, in some cases adenomyosis is present in the myometrium completely isolated from both the endometrium and the serosa. Such a difference would postulate a new hypothesis that adenomyosis is composed of multiple heterogeneous subtypes [22].

4.2.1 Imaging Features of Adenomyosis

4.2.1.1 Ultrasonography

The transvaginal ultrasonography (TVUS) is usually the first-line investigation in cases of suspected adenomyosis. The transabdominal ultrasonography has a poor sensitivity (53–89 %) but a good specificity (97 %). The combination of transabdominal and transvaginal ultrasonography (TVUS) increases the diagnostic accuracy.

The direct signs of adenomyosis are:

1. Anechoic subendometrial microcysts in the myometrium (2–4 mm) that can be distinguished from vascular images on

Doppler sonography because they are not vascularized (pathognomonic sign). This cystic space corresponds to ectopic dilated endometrial glands into the myometrium; if they are hemorrhagic, their content shows greater echogenicity.

2. Inhomogeneous appearance of the myometrium with hyperechoic linear striations (correlated to its hypertrophy).
3. Small hyperechoic subendometrial nodules, pseudonodular hypoechoic zones with indistinct contours and no mass effect on the endometrium.
4. A poorly defined or thickened endometrial-myometrial junctional zone (JZ).

The indirect signs of adenomyosis are:

1. The uterus is enlarged, rounded with regular contours.
2. Asymmetric thickening of the myometrium, especially in case of focal adenomyosis, results from reactive hyperplasia and hypertrophy of the smooth muscle fibers around the ectopic endometrial glands.
3. Linear pattern of vascularization on Doppler sonography, crossing the myometrium within the adenomyosic lesion (opposed to the leiomyoma).
4. A poorly defined or thickened endometrial-myometrial junctional zone (JZ).

4.2.1.2 Magnetic Resonance Imaging (MRI)

Pelvic MRI is the second-line investigation, and it offers the best performance when there is any doubt over diagnosis and in terms of looking for any pathology associated with adenomyosis.

Pelvic MRI is superior to TVUS in terms of sensibility and specificity for both focal and diffuse adenomyosis.

The MRI signs of adenomyosis can be classified into direct and indirect.

The *direct MRI signs* of adenomyosis are:

1. On T2-weighted images, typical adenomyosis appears as an ill-demarcated low-signal-intensity area (Fig. 4.1a, c, e, f), owing to abundant smooth muscle proliferation, with or without punctuate high-signal-intensity foci scattered throughout the lesion or high-signal-intensity linear striations extending from the endometrium. Hyperintense foci could be present on T1-weighted images, more evident with fat saturation, corresponding to small areas of hemorrhage (Fig. 4.1b, d).
2. An important sign of adenomyosis is the presence of subendometrial microcysts, related to the presence of endometrial glands within the myometrium. MRI reveals round cystic foci varying from 2 to 7 mm in diameter, hyperintense on T2-weighted sequence, embedded within the myometrium, and usually located within the JZ. Sometimes, at the end of the menstrual period, hemorrhagic foci within cystic cavities are recognizable and appear as high-signal-intensity spot on T1-weighted images owing to the T1-shortening effects of methemoglobin. This hemorrhagic content is not found routinely because adenomyotic endometrium, like the basalis endometrium, seldom responds to hormonal stimuli with cyclic changes, but it is less common than in endometriosis. Susceptibility-weighted imaging (gradient echo – GRE sequences) is sensitive for old hemorrhagic foci, which appear as spotty signal voids owing to the T2*-shortening effects of accumulated hemosiderin.

At diffusion-weighted images, adenomyosis has low to intermediate signal intensity, a finding consistent with its benign, non-neoplastic nature. Because adenomyosis may show various degrees of enhancement after administration of contrast medium, dynamic study does not contribute to diagnostic accuracy. However, additional MR angiographic GRE sequences are recommended in patients with adenomyosis in whom uterine artery embolization is planned.

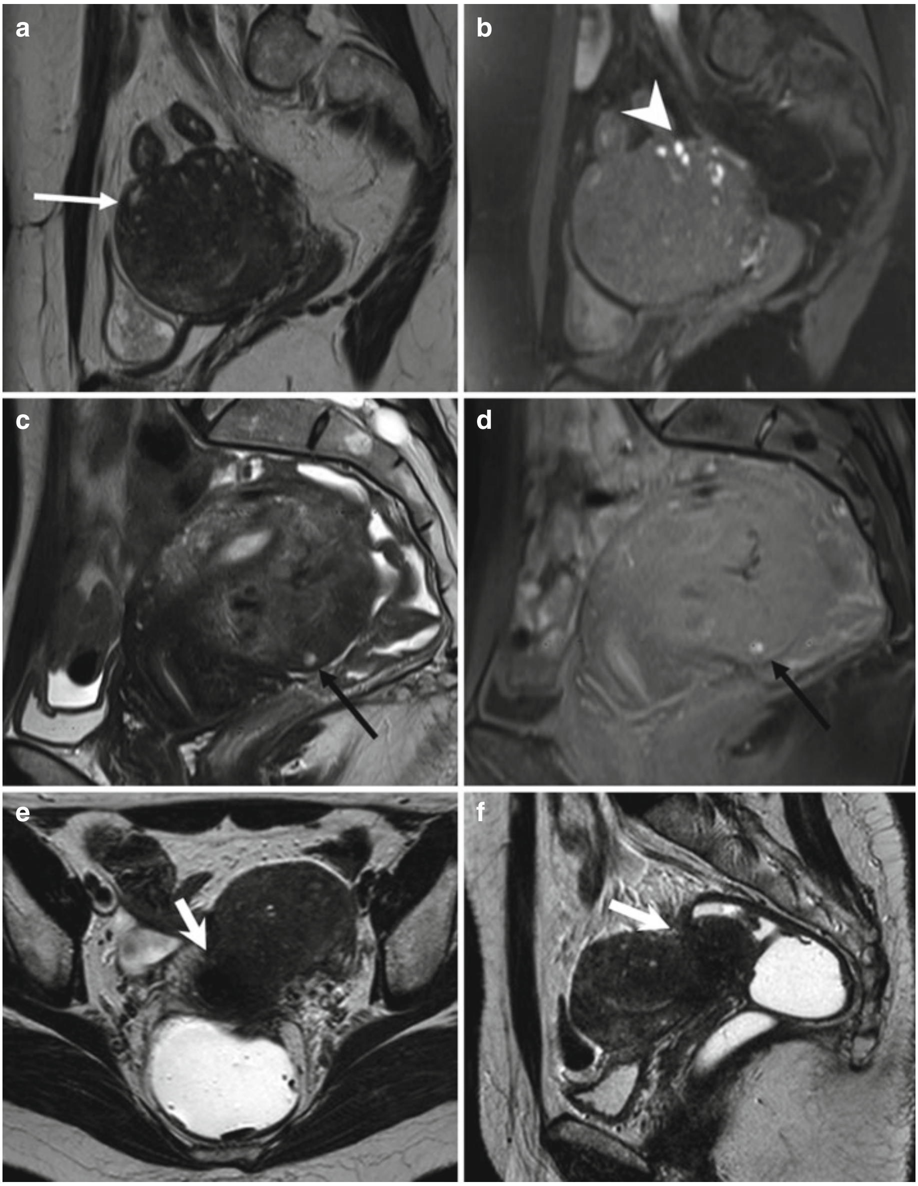

Fig. 4.1 Diffuse adenomyosis. Sagittal (**a**, **c**, **f**) and axial (**e**) T2-weighted FSE images. Sagittal T1-weighted FS-GRE image (**b**, **d**). **a** (TR 4670 TE 94), **b** (TR 369, TE 10). The uterus is markedly enlarged, especially in the posterior portion, with regular contours and a thickened and poorly recognizable endometrial-myometrial junctional zone (JZ). On T2-weighted images this low-signal-intensity area contains multiple small foci hyperintense (**a**: *arrow*), which represent ectopic endometrial glands and small subendometrial cysts. The high-signal-intensity spots on T1-weighted fat-saturated image (**b**: *arrowhead*) correspond to multiple area of hemorrhage within the ectopic endometrial tissue. **c** (TR 3870 TE 100), **d** (TR 369, TE 10). The uterus is retroflexed and markedly enlarged in its posterior portion, with hyperintense spots in both T1- and T2-weighted images (*black arrow*). These findings are consistent with adenomyosis. **e** (TR 4530 TE 90), **f** (TR 5390 TE 113). Also in this case the uterus is enlarged, and the JZ is thickened. Moreover a heterogeneous hypointense nodule on T2-weighted images is recognizable in the pouch of Douglas (*short arrows*), suggestive of deep pelvic endometriosis (DPE) location. Obliteration of the fat tissue plan and invasion of both the posterior uterine surface and anterior rectosigmoid wall are present

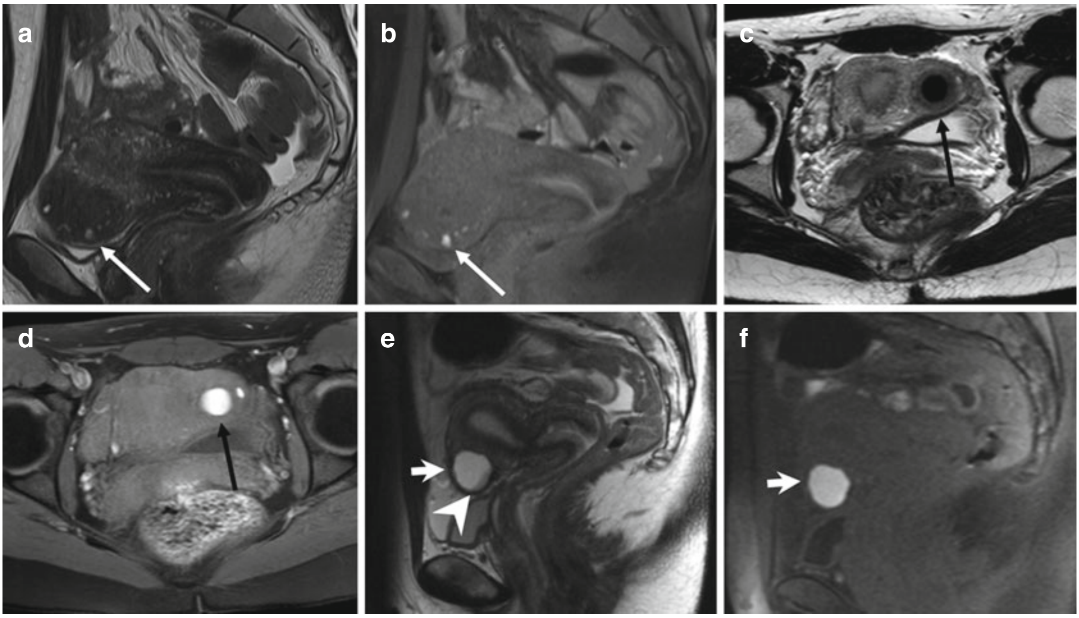

Fig. 4.2 Focal adenomyosis (**a**, **b**). Sagittal T2-weighted (**a**: TR 4070, TE 94) and FS-T1-weighted (**b**: TR 629, TE 10) images. The uterus is anteverted. A focal myometrial thickening is recognizable on the anterior uterine wall (*arrows*). This area is heterogeneously hypointense on T2-weighted image, with hyperintense foci on both T1- and T2-weighted sequences, findings consistent with focal uterine adenomyosis. Adenomyotic cysts. Two cases. (**c**, **d**) Axial T2-weighted FSE MR image (**c**: TR 3252, TE 100) and axial T1-weighted fat-suppressed image (**d**: TR 629, TE 10) show a rounded well-defined intramyometrial lesion (*black arrow*), located near the left uterine horn. This lesion shows a very low signal intensity on T2-weighted sequence (**c**) and high signal intensity on T1-weighted image (**d**), related to its hemorrhagic content. (**e**, **f**) Sagittal T2-weighted FSE MR image (**e**: TR 4530, TE 90) shows another adenomyotic cyst, located in the subserosal layer of the anterior uterine wall, with inhomogeneous high signal intensity content (*short arrow*) and contextual-dependent fluid-fluid level (*arrowhead*). This cyst retains high signal intensity on T1-weighted fat-suppressed MR image (**f**: TR 328, TE 11), due to its hemorrhagic content

The indirect signs of adenomyosis are secondary to the reactive hyperplasia of the myometrium provoked by endometrial invasion and include:

1. Globular aspect of the enlarged uterus with regular contours.
2. Asymmetric thickening of the myometrial walls (more common of the posterior wall).
3. Thickening of endometrial-myometrial junctional zone (JZ: Fig. 4.1). Generally, a JZ thickness of greater than 12 mm is the accepted criterion in establishing the presence of adenomyosis (JZ ≥12 mm). Also the greatest JZ thickness to total myometrium ratio >40–50 % is considered [23]. However, adenomyosis can be excluded if the JZ thickness is 8 mm or less [24]. Anyway, from 20 to 30 % of patients will not have a visible or measurable endometrial-myometrial junctional zone during their reproductive cycle [25].

4.2.2 Atypical Morphologic Appearances of Adenomyosis

4.2.2.1 Adenomyoma

Adenomyoma is an atypical morphologic appearance of adenomyosis and is rarer than both focal and diffuse adenomyosis. It is composed of a focal consolidation of adenomyotic glands and appears as a poorly defined nodular lesion with extensive muscular response (Fig. 4.2a, b). It may be intramyometrial, subserosal, and possibly even intracavitary. Like adenomyosis, adenomyoma usually shows heterogeneous low signal intensity on T2-weighted images and may be indistinguishable from degenerated leiomyomas and from aggressive uterine neoplasms such as uterine sarcomas. Relatively low signal intensity at diffusion-weighted imaging with high ADC value is suggestive of its benign nature.

4.2.2.2 Adenomyotic Cyst

Adenomyotic cyst (cystic adenomyosis) is a rare variation of adenomyosis that appears as an intramyometrial endometrioma-like lesion, hyperintense on T1-weighted images, surrounded by adenomyotic tissue with low signal intensity on T2-weighted images (Fig. 4.2c–f). A subserosal adenomyotic cyst may mimic an ovarian tumor. The finding of continuity with the myometrium is suggestive of its uterine origin [26].

4.2.3 Malignant Transformation of Adenomyotic Lesions

Malignant transformation of adenomyosis is quite rare and may manifest as a predominantly intramyometrial mass. Imaging findings of an adenomyotic cyst with malignant transformation are similar to those of an endometrioma with malignant transformation. High-signal-intensity hemorrhagic fluid in the adenomyotic cyst on T1-weighted images may mask the enhancement of malignant mural nodules; therefore, contrast-enhanced subtraction imaging may be useful for detection of malignant transformation. Dynamic contrast-enhanced imaging may have greater accuracy than T2-weighted imaging when adenomyosis and endometrial cancer coexist [27]. Diffusion-weighted imaging can demonstrate the malignant foci as areas of high signal intensity.

4.2.4 Differential Diagnosis

Various benign and malignant conditions may mimic adenomyosis: physiologic myometrial contraction, myometrial involvement by deep pelvic endometriosis, leiomyomas, low-grade endometrial stromal sarcoma, and myometrial metastases.

Transient myometrial contraction is a physiologic phenomenon that may mimic focal adenomyosis because it determines focal pseudo-thickening of the junctional zone. This aspect usually disappears on subsequent images or at cine MR images, instead of focal adenomyosis that persists.

Myometrial contractions in the pregnant uterus are commonly seen and usually do not represent a diagnostic dilemma.

To differentiate physiologic myometrial contractions from focal adenomyosis, rapid T2-weighted sequences can be repeated and should be correlated with other views. Useful to eliminate physiologic uterine contractions is the injection of an antiperistaltic drug, if no contraindications are present.

4.3 Ovarian Endometriosis

The most common location of endometriosis is the ovary, where small and shallow endometrial implants develop, leading to adjacent para-ovarian scarring and adhesions. An ovarian enlargement could be present, attributable to repeated episodes of hemorrhage within a deep implant, resulting in endometriosic cysts, also defined as *endometriomas* (multiloculated cystic lesions). They may completely replace normal ovarian tissue. From the anatomo-pathological point of view, endometriosic cyst walls are generally thick and fibrotic with common areas of discoloration and dense fibrous adhesions. The cyst lining can vary from smooth and pale to shaggy and brown. Their contents can be watery or, more typically, composed of thick, dark, degenerated blood products, depending on the presence and dating of bleeding. This appearance is called “chocolate cyst.”

4.3.1 Ultrasonography

Pelvic ultrasound (especially TVUS) is the method of choice to identify endometriomas, defined as benign ovarian neoplasms persisting

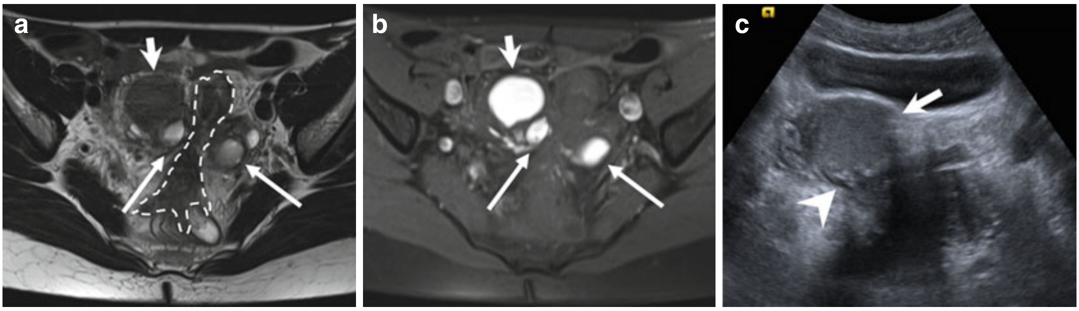

Fig. 4.3 "Kissing ovaries" and bowel adhesions due to endometriosis. Axial T2-weighted FSE MR image (**a**: TR 4070, TE 94) shows small bilateral ovarian cysts of intermediate signal intensity (*arrows*) and one right-sided ovarian cyst (*short arrow*) with marked "T2-shading effect" (low signal intensity). Correspondent axial T1-weighted fat-suppressed MR image (**b**: TR 351, TE 10) shows bilateral T1-hyperintense endometriomas (*arrows* and *short arrow*), confirming the hemorrhagic nature of the cystic content. Adhesions between bilateral endometriomas bring the ovaries closer to the midline ("kissing ovaries" sign). Furthermore there is tight contact with obliteration of the fat tissue plane between ovarian masses and the interposed sigmoid colon (**a**: *dashed line*), due to adhesions related to endometriosis. Transverse transabdominal sonogram (**c**) demonstrates the right-sided endometrioma (*short arrow*) with diffuse low-level internal echoes and focal wall hyperechoic nodularities (*arrowhead*)

after 3 months. They typically appear as multilocular cysts with diffuse low-level internal echoes and hyperechoic foci in their walls (Fig. 4.3c). Internal thin or thick septations may be present. However, unilocular cysts were found in 43 % of endometriomas. The echogenic wall foci differ from true wall nodules because they are more echogenic and smaller than malignant wall nodules. Although the pathological basis of their formation has not been established, it is postulated that they form as cholesterol deposits accumulating in the endometrioma's wall.

The endometriomas vary between 30 and 59 mm in maximum diameter in 81 % of cases. The positive predictive value of sonography to predict ovarian endometriosis was evaluated at 75 % when criteria such as diffuse low-level internal echoes and absent neoplastic features were used [28]. The color Doppler imaging shows the absent flow within the lesion. The presence of hyperechoic foci alone at the surface of the ovary is not a sign for endometriosis.

Differential diagnosis includes ovarian functional cysts, mature cystic teratoma, cystadenoma, fibroma, tubo-ovarian abscess, and ovarian carcinoma. The functional cysts, such as corpus luteum or hemorrhagic follicular cysts, will disappear or decrease in size at short-time follow-up. Ovarian cancer can be difficult to exclude if wall irregularities or nodules are present; absence of color Doppler flux within the cyst helps to confirm the benign nature of the lesion. Whenever sonographic features of ovarian masses are uncertain or indeterminate, MRI is the imaging modality of choice to rule out malignancy.

4.3.2 MRI Findings

Superficial peritoneal ovarian endometriosis, not visible at TVUS, can be only rarely detected by MRI, using fat-suppression techniques, as hemorrhagic superficial foci [2]. Their signal intensity is quite variable [3].

Instead *endometriomas* have typical MRI features, and this technique has a sensitivity and specificity reported of 90 and 98 %, respectively, in the definitive diagnosis [29]. Endometrioma appears as a cystic mass with internal high signal intensity on T1-weighted images, also with fat suppression (Figs. 4.3, 4.4, and 4.5). The walls are usually thickened, and, frequently, loss of the interface between lesion and adjacent organs is present (Fig. 4.3).

Use of chemically selective T1-weighted fat-suppressed sequences is mandatory to visualize smaller endometriomas and to differentiate endometriomas from mature cystic teratomas

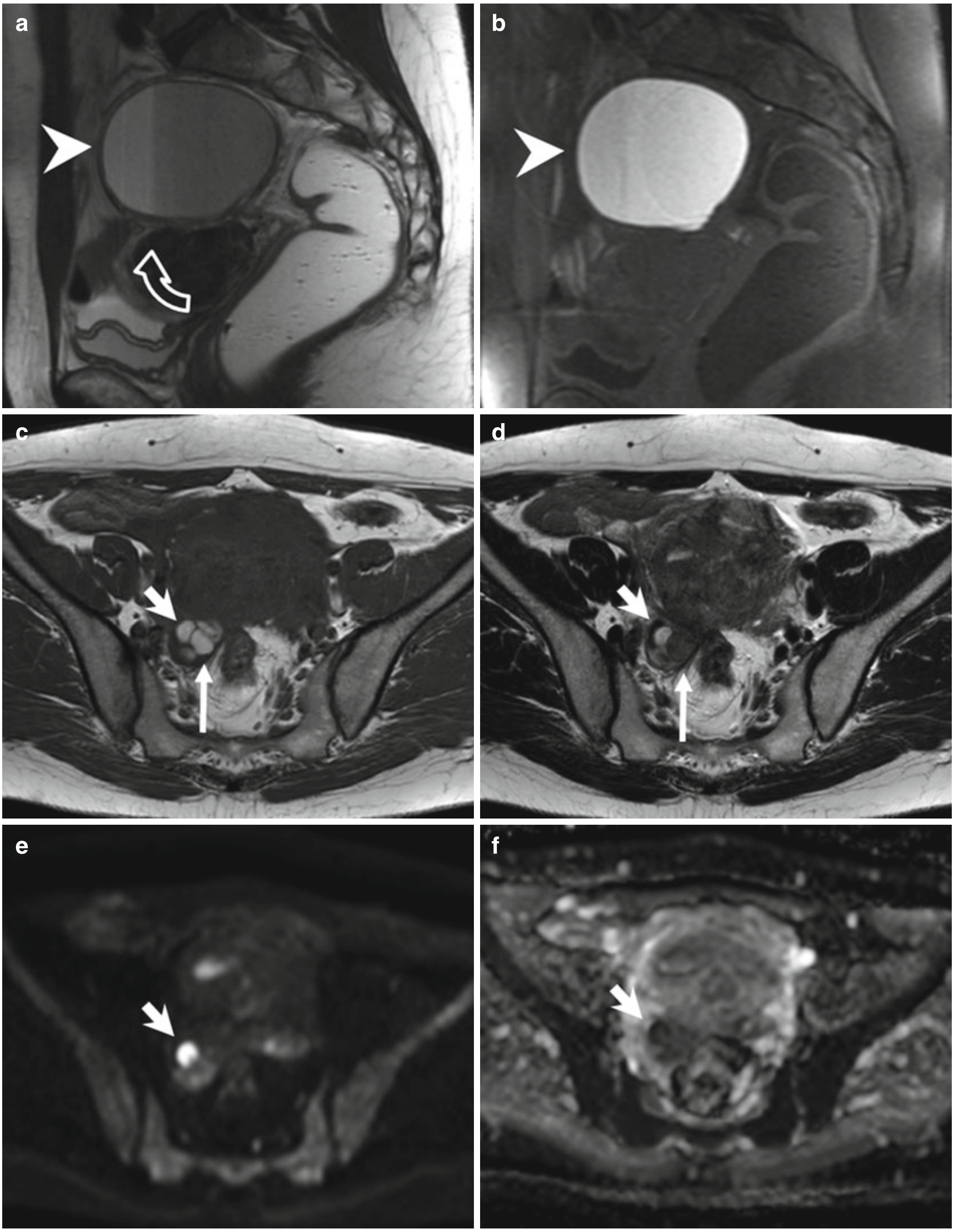

Fig. 4.4 Large endometrioma (**a**, **b**). Sagittal T2- (**a**: TR 4530, TE 90) and T1-FS-weighted (**b**: TR 328, TE 11) images show a large adnexal cystic lesion (*arrowheads*) with fluid-fluid level (**a**: *curved arrow*). The dependent component appears hyperintense on T1-weighted image with fat suppression (**b**) and shows a marked T2-shading effect (hypointensity on T2-weighted image). Small endometriomas (**c**–**f**). Axial T1-weighted FSE MR image (**c**: TR 640, TE 10) shows multiple small T1-hyperintense cystic lesions in the right ovary. Axial T2-weighted FSE MR image (**d**: TR 3652, TE 100) at the same level shows marked T2 shading (hypointensity) in the posteromedial cystic lesion of the right adnexa (*long arrows*), instead of the anterolateral cyst (*short arrows*), hyperintense on both T1- and T2-weighted images. Furthermore only the anterolateral cyst (*short arrows*) presents a restricted diffusion, seen in almost half of endometriomas: in the correspondent diffusion-weighted MR image obtained with *b* value of 800 s/mm^2 (**e**: TR 7198, TE 69), it shows high signal intensity (*short arrow*) with low signal intensity on the ADC map (**f**: TR 7198, TE 69)

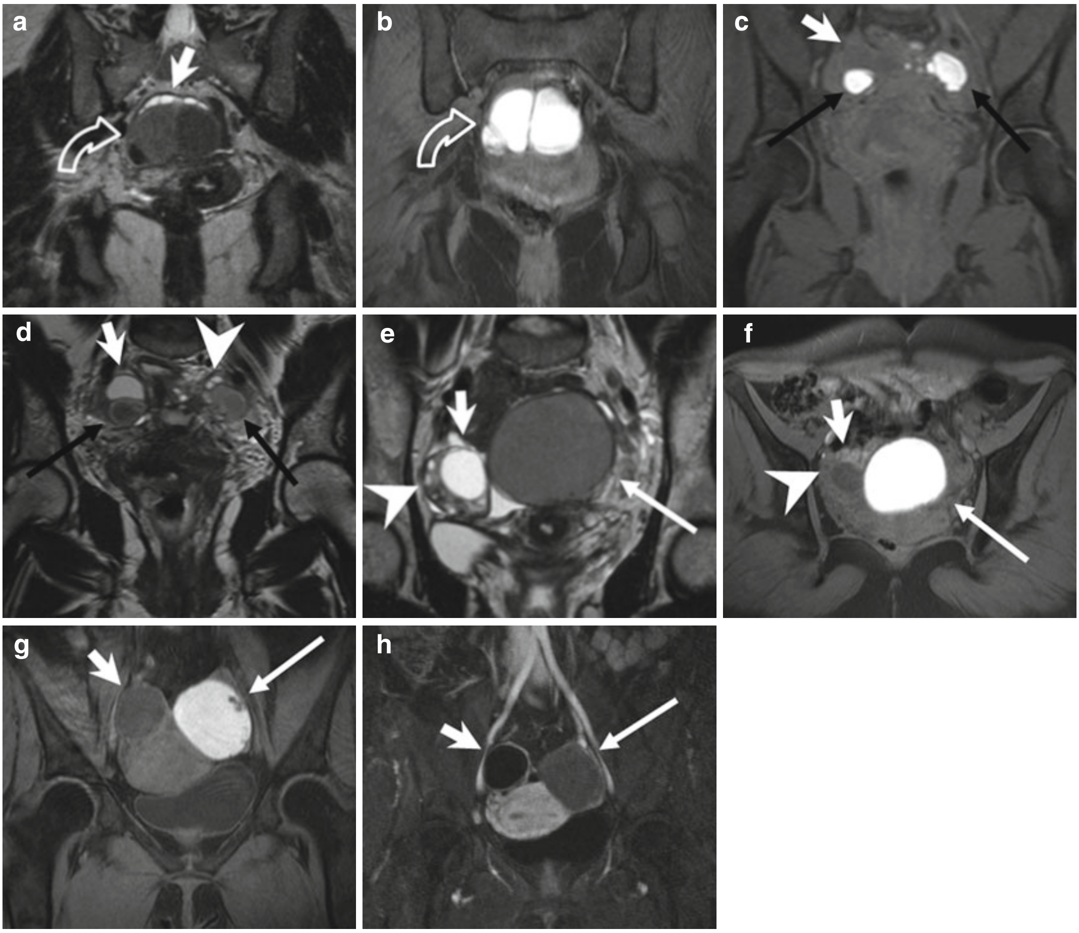

Fig. 4.5 Endometriomas (**a**, **b**) Coronal T2-weighted FSE (**a**: TR 5390, TE 113) and fat-suppressed T1-weighted (**b**: TR 440, TE 4.9) FSE MR images show multiloculated adnexal cystic mass with a "coffee bean" appearance (*curved arrow*). These cystic formations present high signal intensity on T1-weighted fat-suppressed MR image (**b**) and marked "T2-shading effect" with consequent lower signal intensity than the adjacent functional ovarian follicles on T2-weighted image (**a**: *short arrow*). Bilateral endometriomas (**c**, **d**). Coronal fat-suppressed T1-weighted FSE image (**c**: TR 597, TE 11) and T2-weighted FSE image (**d**: TR 3520, TE 89). Bilateral endometriomas (*black arrows*), hyperintense on T1-weighted sequence, present the typical "shading sign" on the T2-weighted image (**d**: *black arrows*). Furthermore a hypointense functional cyst (*short arrow*) is present in the right adnexa and multiple ovarian follicles in the left (*arrowhead*), both hypointense on T1- and hyperintense on the T2-weighted images. (**e**–**h**) Endometrioma of the left ovary. Coronal T2-weighted FSE (**e**: TR 5390, TE 113), axial T1- (**f**: TR 493, TE 4.9) and coronal T1-weighted with fat suppression (**g**: TR 440, TE 4.9) MR images show the two ovaries adjacent to the midline (the "kissing ovaries sign"). A functional cyst (*short arrow*) and multiple ovarian follicles (*arrowhead*) are recognizable in the right ovary, both hyperintense on T2- and hypointense on T1-weighted images. In the left ovary an endometrioma presents some parietal nodules (**g**: *arrow*), feature suspected for malignant degeneration. The coronal contrast-enhanced T1-weighted fat-suppressed MR image (**h**: TR 3.7, TE 1.3) demonstrates no contrast uptake within the parietal nodules (*arrow*), ruling out the suspect of malignant degeneration

(hypointense after fat saturation, due to their fat content).

Gradual decrease of signal intensity at T2-weighted image has been described as "T2-shading" sign and is due to chronic bleeding with high concentrations of iron and protein inside the endometriomas (Figs. 4.4a, d and 4.5a, d, e). Adnexal mass with high signal intensity on T1-weighted fat-saturated sequences and signal intensity lower than that of simple fluid on T2-weighted images helps to establish a diagnosis of endometrioma, with a specificity greater than 90 %.

The differential diagnosis with functional hemorrhagic cysts is not always simple. The functional cysts do not demonstrate (or demonstrate less) T2-shading sign and disappear at follow-up imaging. Bilaterality and multifocality of adnexal lesions, along the other characteristics above discussed, can help establish the diagnosis of endometrioma. Bilateral endometriomas occur in more than 50 % of cases, often associated with interovarian adhesions, described as "kissing ovaries" sign (Figs. 4.3 and 4.5e–h). When atypical features of endometriomas are present, such as localized wall thickening, the use of intravenous contrast media is mandatory: the absent enhancement confirms the benign nature of the disease.

At contrast-enhanced T1 sequences (Fig. 4.5h), the peripheral hypointense rim of the endometrioma, representing the thick fibrous capsule, usually shows intense enhancement. Instead the enhancement of solid nodules within a hemorrhagic ovarian cyst has been described in case of ovarian cancer arising within endometrioma [30].

Diffusion-weighted imaging (DWI) with quantitative assessment of apparent diffusion coefficient values (ADC) has often been incorporated into pelvic MR imaging protocols (Fig. 4.4e, f), even though the presence of restricted diffusion and low ADC value within an adnexal lesion does not have a high positive predictive value or specificity for the diagnosis of ovarian malignancy. Benign hemorrhagic ovarian cysts, endometriomas, and solid endometrial implants, as well as benign mature cystic teratomas, also can demonstrate restricted diffusion [31–33].

During pregnancy, increased progesterone levels promote hypertrophy of the endometrial stromal cells and formation of the vascular decidual lining of the uterus. Endometrial stromal cells within endometriomas may also respond to hormonal changes forming vascularized mural nodules. Decidualized endometriosis can mimic ovarian cancer at US and MR imaging. An MR imaging feature specific for decidualized endometriosis is the T2 hyperintensity of the mural nodules, isointense to the thickened decidualized endometrium, and with a broad base. After the end of the pregnancy, decidualized endometriosis has been reported to either resolve or regress to uncomplicated endometriomas (Fig. 4.6) [34].

4.3.3 Malignancies Arising in Endometriomas

Women with endometriosis are at risk for developing both clear cell and endometrioid subtypes of epithelial ovarian cancer. An estimated 2.5 % of women with endometriosis develop an ovarian cancer that usually manifests at an earlier stage, with a lower grade and a better prognosis than ovarian malignancies in women with no endometriosis [33, 35].

Endometriosis is one of several benign causes of an abnormal cancer antigen 125 (CA-125) level; thus, an elevated biomarker value alone is not specific for endometriosis-associated ovarian cancer.

The MR imaging features suggestive of malignant endometriomas are the increase in size and, more specific, the development of enhancing mural nodules.

Dynamic subtraction MR imaging is useful in depicting small contrast-enhanced nodules within the hyperintense endometrioma on T1-weighted images. Normal adjacent ovarian parenchyma, intracystic coagulate, inflammation, and decidual change of the endometrium in an endometrioma during pregnancy should be differentiated from malignant transformation. The adjacent ovarian parenchyma may be mistaken for a contrast-enhanced solid malignant component in an endometrioma. An extracystic crescent-shaped

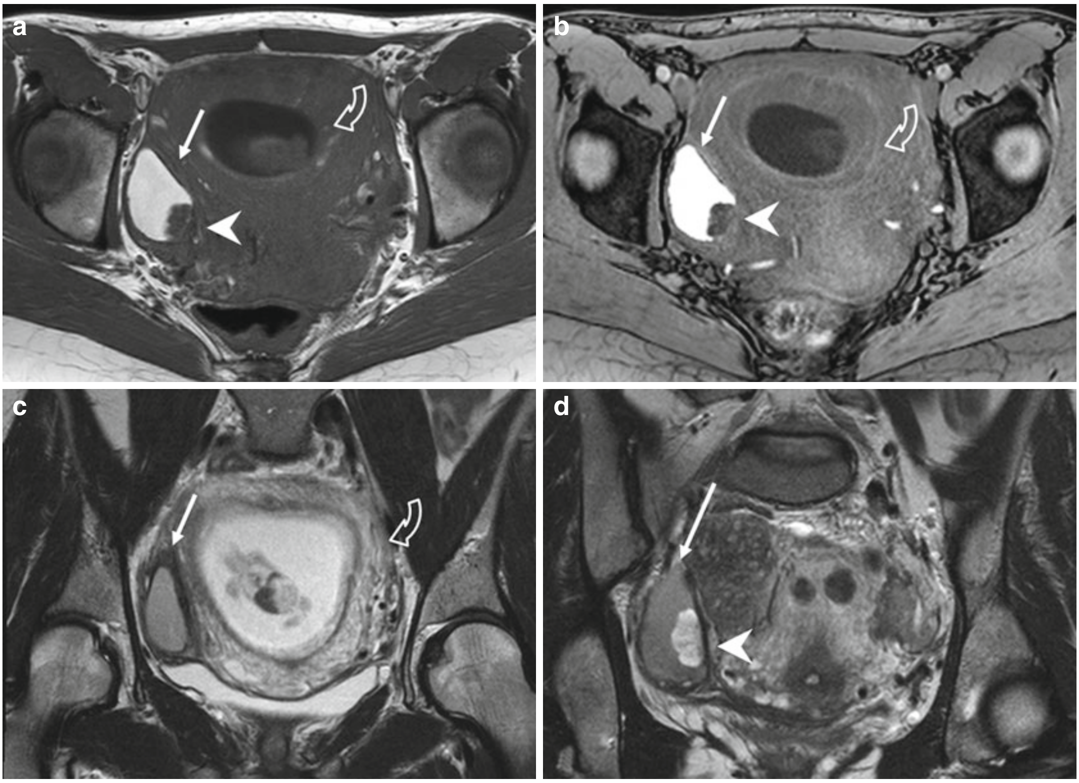

Fig. 4.6 Endometrioma with mural nodule due to decidual reaction of pregnancy (**a**–**d**). Axial T1-weighted (**a**: TR 642, TE 10), FS-T1-weighted (**b**:TR 5,8 TE 2,8), and T2-weighted images (**c**, **d**: TR 4251, TE 100) of a pregnant woman show an enlarged gravidic uterus (*curved arrows* due to decidual reaction due to pregnancy) and a hyperintense cystic lesion (*arrows*) in the right ovary. In the posterior part of this cystic formation, a mural nodule (*arrowheads*) is visible, hypointense on the T1-weighted images, and hyperintense on the T2-weighted sequence. It is a decidualized endometriosis location, related to the hypertrophy of the endometrial stromal cells in the endometrioma. It was due to the increased progesterone levels during pregnancy, and it completely regressed on the MRI images obtained 6 weeks postpartum, when only the endometrioma remained visible

portion, which may contain follicles, is the characteristic finding in such cases [33, 35].

4.3.4 Endometriosis of the Fallopian Tubes

Endometriosis is a frequent cause of dilated fallopian tubes; 30 % of women with endometriosis show tubal involvement at laparoscopy. The fallopian tubes are involved by endometrial implants in 6 % and by adhesions in 24 % of cases.

Tubal endometriosis can be divided into two forms, on the basis of implant location: the *serosal/subserosal* and the *intraluminal* forms. Both types of tubal endometriosis can be either unilateral or bilateral. The most common *serosal* or *subserosal* endometriosis is characterized by implantation of endometrial tissue on the peritoneal surface of the fallopian tubes. Recurrent hemorrhages within the serosal implants presumably result in fibrosis and scarring, leading to peritubal adhesions, obstruction of the tube, and hydrosalpinx.

The *intraluminal endometriosis* is less common and involves ectopic implantation of endometrium on the mucosal surface of the tube lumen. Cyclic hemorrhage of the implants can cause distention of the fallopian tube with blood, resulting in a hematosalpinx. Hematosalpinx has been reported to be one of the indicators of pelvic endometriosis, and it may be the only imaging finding indicative of endometriosis. However,

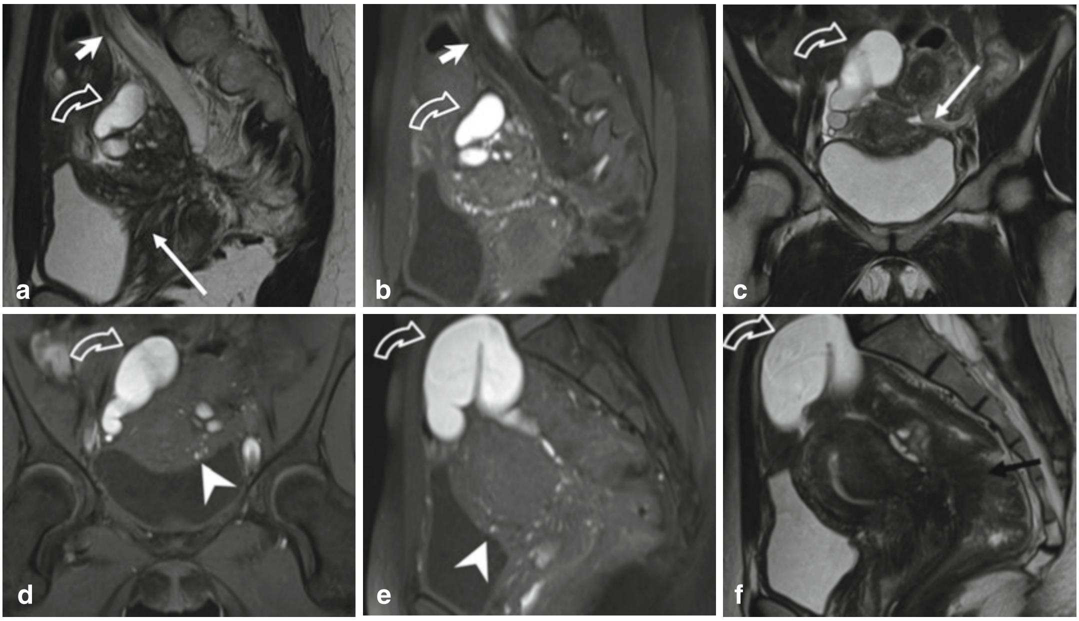

Fig. 4.7 Extensive deeply infiltrating endometriosis involving the urinary system. Sagittal (**a**, **f**) and coronal (**c**) T2-weighted MR images (TR 4670, TE 94). Sagittal (**b**, **e**) and coronal (**d**) T1-weighted fat-suppressed images (TR 369, TE 10). A deep pelvic lesion involves both the anterior and the posterior pelvic compartment; it is located over the bladder dome (**a**, **c**: *arrows*) with obliteration of the vesicouterine pouch (*extrinsic bladder endometriosis*). Also the distal portion of the left ureter is encased by the endometriosic lesion, with an upstream ureteral dilatation (**a**, **b**: *short arrows*). Intralesional small hyperintense foci on T1-weighted images (**d**, **e**: *arrowheads*) represent microhemorrhages in the ectopic endometrial glands. Bilateral hematosalpinx (*tubal endometriosis: curved arrows*), more evident on the right fallopian tube, coexists. Also obliteration of the pouch of Douglas and infiltration of the anterior rectal wall (**f**: *black arrow*) are present

hematosalpinx is not specific for endometriosis and may have other causes, such as tubal pregnancy, tumors, and tubal torsion. So an accurate assessment of the patient's history is important.

Hematosalpinx appears on MRI as a hyperintense distention of the fallopian tube on fat-saturated T1- and T2-weighted images (Fig. 4.7). Low T2 signal intensity (T2-shading sign), often seen in endometriomas, is not characteristic of tubal endometriosis, maybe because tubal dilation is most commonly secondary to serosal/subserosal endometrial implants [32, 36, 37].

4.4 Deep Pelvic Endometriosis

Deep pelvic endometriosis (DPE) is defined as a subperitoneal invasion that exceeds 5 mm in depth in the retroperitoneal space or in the pelvic organ wall. DPE affects more frequently the rectovaginal septum and the uterosacral ligaments (69.2 %), vagina (14.5 %), alimentary tract (9.9 %), urinary tract (6.4 %), and other extraperitoneal pelvic sites [38].

From a clinical point of view, although peritoneal endometriosis can be asymptomatic, DPE is symptomatic in up to 75 % of cases. The symptoms are not specific, so an early diagnosis is a major challenge, as it can help to avoid mutilating surgery, enhance fertility, and improve quality of life [39–41].

From a pathological point of view, the endometrial glands and stroma infiltrate the adjacent fibromuscular tissue and elicit smooth muscle proliferation and fibrous reaction, with the development of solid tissue and nodules. In visceral organs the implants adhere to the serosal surface and can invade the muscular layers, eliciting smooth muscle proliferation, with consequent strictures and obstructions.

4.4.1 Diagnosis

Laparoscopy represents the gold standard in diagnosing and treating endometriosis because it provides a direct visualization of lesions that conduct to the most conservative surgical approach. However the laparoscopy cannot reach the subperitoneal plane, especially in presence of deep pelvic lesions with extensive adhesions and cul-de-sac obliteration. Because the standard treatment for DPE is complete surgical excision, presurgical diagnosis and accurate knowledge of location of the lesions are essential prerequisites for successful outcome. So in the preoperative assessment, a complete depiction of all pelvic planes with panoramic imaging techniques is extremely important. Several techniques have been used, including transabdominal, transvaginal, and transrectal ultrasonography (US), rectal endoscopic sonography, DBCE computed tomography (CT), and magnetic resonance (MR) imaging.

4.4.1.1 Ultrasonography

Transabdominal and transvaginal ultrasonography (US) is usually the first imaging technique used to diagnose endometriosis. The diagnosis of endometriomas and bladder endometriosis is reliable; recent studies have emphasized their role also in identifying deep endometriosis, especially when located in the rectal wall and retrocervical space [42]. However, their accuracy may vary depending on the lesions' location and the operator's experience.

Rectal endoscopic US with high-frequency probes has been recommended for diagnosing the depth of rectal wall infiltration [43–45], but it has poor penetration for the detection of other pelvic lesions, due to its small field of view. As in women with intestinal lesions, unifocal isolated localization accounts for only 21 % [46], and the ideal imaging method should be able to diagnose at least the associated pelvic lesions.

4.4.1.2 Double-Barium Contrast Enema (DBCE)

Double-barium contrast enema (DBCE) is rapidly available and low cost [47–50], and it has already been described as a valuable imaging tool in the preoperative diagnosis and quantification of bowel wall infiltration by endometriosic lesions. It demonstrates the extrinsic mass effect with the mucosal fine crenulation (Fig. 4.8f) and, if present, the stenosis of the lumen, findings highly suggestive of the presence of bowel endometriosis.

4.4.1.3 Multidetector Computed Tomography (MDCT)

MDCT has higher spatial resolution than MRI, but it involves radiation exposure and iodinated contrast medium administration to women of reproductive age, without the characterization of the hemoglobin degradation products, as MRI permits. MDCT identifies only aspecific signs, and it is generally employed in the acute complications of endometriosis, such as intestinal occlusion (Fig. 4.11f).

4.4.1.4 Magnetic Resonance Imaging (MRI)

MR imaging demonstrates high accuracy in the evaluation of DPE [19] and permits a complete survey of the anterior and posterior compartments of the pelvis. It is a noninvasive method with high spatial resolution and good tissue characterization.

The MRI diagnosis of DPE is established by the coexistence of *signal intensity abnormality* and *morphologic abnormalities* [19].

The *signal intensity* of DPE lesions is strictly related to the anatomo-pathological features. The acellular regions of fibrous tissue and smooth muscle proliferation have intermediate signal intensity on T1-weighted MR images and low signal intensity on T2-weighted images [51]. So the solid endometriosic lesions appear as hypointense masses on T2-weighted images with irregular indistinct or stellate margins, or as irregular hypointense soft tissue thickening, with or without nodular aspect. In particular, the involvement of such structures as uterosacral ligaments (USLs) and vaginal, rectal, or bladder walls may be suspected when they have a hypointense thickened, with or without nodular appearance on T2-weighted images [52].

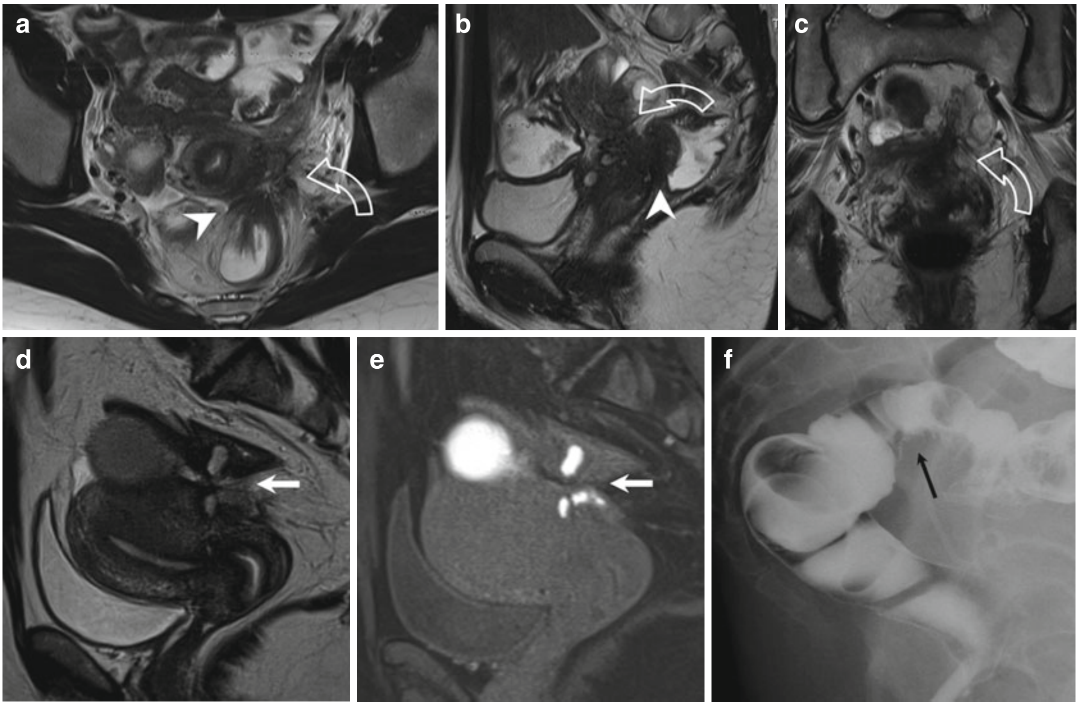

Fig. 4.8 Deep pelvic endometriosis (DPE). Two cases. (**a**–**c**) Axial (**a**), sagittal (**b**), and coronal (**c**) T2-weighted FSE images (TR 4670, TE 94) show a endometriosic lesion with stellate morphology (*curved arrow*), dishomogeneously hypointense, involving the left torus uterinus, the homolateral uterosacral ligament, the posterior wall of the uterine cervix and the anterior wall of the rectum (*arrowhead*). An obliteration of the Pouch of Douglas is present, with speculated low-signal-intensity strandings that obscure organ interfaces (adhesions). (**d**–**f**) Sagittal T2-weighted FSE images (**d**: TR 4670, TE 94), fat-saturated T1-weighted image (**e**: TR 369, TE 10) and double-barium contrast enema (DBCE: **f**). The lesion (*arrows*) presents some hemorrhagic components, hyperintense on T1-weighted images. It involves the posterior uterine wall and the above bowel with obliteration of the fat tissue plan between them. The involvement of the sigmoid colon is confirmed by the DBCE (**e**): it presents a focal irregular mucosal fine crenulation (*black arrow*) and a mild luminal stenosis

The presence of punctate foci of high signal intensity on T1-weighted images, more evident in the fat-suppressed sequences (Figs. 4.7d, e and 4.8e), represents regions of hemorrhage, because the ectopic endometrium responds to hormonal stimulation like basal endometrium. These hemorrhagic foci, hyperintense on T1-weighted images, may be distinguished from flow-related phenomena in the pelvic venous system.

Moreover intermingled hyperintense foci on T2-weighted images may be visible, for the presence of dilated ectopic endometrial glands (Figs. 4.7a and 4.9a).

Some masses of endometriosis are composed of a large proportion of glandular material with little fibrotic reaction, resulting in high-signal-intensity masses on T2-weighted images.

DPE can affect the anterior or the posterior compartment. The less frequently encountered anterior DPE is characterized by endometrial implants located anterior to the uterus [31], instead of the more frequent posterior DPE, characterized by lesions located posterior to the uterus.

The *morphologic abnormalities* vary according to the anatomic locations of endometriosis in the posterior and anterior compartment.

4.5 Endometriosis of the Anterior Compartment

It includes endometrial implants within the vesicouterine pouch, vesicovaginal septum, bladder (detrusor muscle), ureters, urethra, and, more

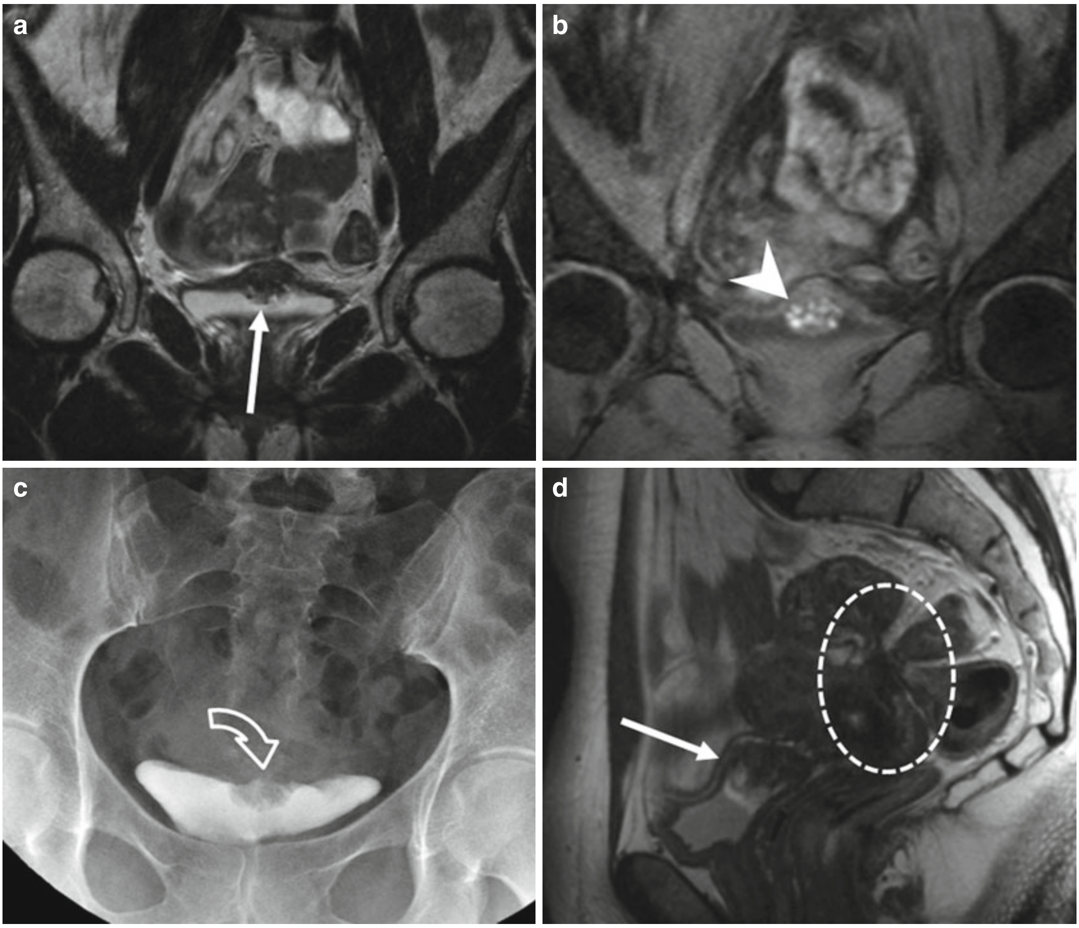

Fig. 4.9 Intrinsic bladder endometriosis (**a**–**d**). Coronal (**a**) and sagittal- (**d**) T2-weighted FSE MR images (TR 5390, TE 113); coronal fat-suppressed T1-weighted FSE image (**b**: TR 493, TE 4.9). A well-defined nodule is recognizable in the supero-posterior bladder wall (*arrows*); it infiltrates the bladder's dome and projects into the lumen (*intrinsic endometriosis*). On T1-weighted image (**b**), small-intermingled hyperintense foci are present within the nodule (*arrowhead*), finding consistent with bloody content within the ectopic endometrial glands. This aspect is crucial for the differential diagnosis between bladder endometriosis and bladder cancer. The excretory urographic study (**c**) shows the corresponding filling defect on the bladder's dome (*curved arrow*); this radiographic appearance is nonspecific for intrinsic bladder endometriosis and requires endoscopy and biopsy to rule out malignancy. Endometriosis of the posterior compartment coexists (**d**: *dashed circle*), with partial obliteration of the pouch of Douglas, infiltration of the posterior uterine surface and of the anterior rectosigmoid wall (*deep pelvic endometriosis*)

rarely, in the anterior pelvic wall (discussed in the *unusual locations*).

Endometriosis of the urinary tract is associated with lesions in other pelvic locations in up to 50–75 % of cases; it represents 0.2–2.5 % of all cases of endometriosis, with a frequency ratio of 40:5:1 for the bladder, ureters, and kidneys, respectively.

It has been showed that patients with ureteral and bladder endometriosis have more advanced stages of the disease (stages III and IV according to the 1996 American Society of Reproductive Medicine criteria) than patients without urinary system involvement.

- *Vesicouterine pouch* lesions are characterized by hypointense tissue on T2-weighted images, with or without nodular appearance, located on the anterior uterine surface, forming an obtuse angle with the vesical wall (Figs. 4.7a–c and 4.9d). The resulting extensive adhesions between the peritoneum of the bladder fold and the uterus determine anteflexion of the uterus and obliteration of the vesicouterine pouch with the disappearance of the intervesicouterine fat [53].

The diagnosis is easier when the lesion is nodular, whereas it could be more difficult in case of plaque-like lesion [54].

- *Bladder* endometriosis can be seen at MRI as localized or diffuse hypointense thickening of the vesical wall on T2-weighted images with irregular margins that replaces the normal signal of detrusor muscle (Figs. 4.7 and 4.9). Eventually, intermingled hyperintense foci may be observed on T2-weighted (Fig. 4.7a, c) and T1-weighted fat-suppressed (Fig. 4.7d, e) images, findings that correspond to the dilated endometrial glands and blood content, respectively.

  The endometriosic implants of the bladder are more frequently confined to the serosal surface ("extrinsic" involvement: Fig. 4.7), but they can infiltrate the muscular layer appearing as mural masses projecting into the lumen ("intrinsic" involvement: Fig. 4.9) [3].

  Differential diagnosis: bladder endometriosis, appearing as localized wall thickening with occasional protrusion inside the bladder lumen, mimics bladder cancer [55]. Subserosal anterior leiomyoma of the uterus with extrinsic compression of the bladder is another differential diagnosis. The presence of intralesional hyperintense foci on T1-weighted images helps in the differential diagnosis.
- The *ureteral* involvement is usually unilateral, in its pelvic portion, and it is more frequently extrinsic (75–80 %) with endometrial tissue originating from adjacent structures that compress the ureter from the outside or that invade the adventitia and the surrounding connective tissue. The intrinsic involvement of the ureters is more rare (20–25 %) and is characterized by the presence of endometrial tissue in the muscular and/or mucosal layer of the ureter [56]. Ureteral endometriosis appears as irregular hypointense nodules on T2-weighted images with obliteration of the fat tissue plan between nodule and ureter (Fig. 4.10d). Retractile adhesions may be visible as periureteral hypointense lines with angular deviation. Ureteral involvement may result in luminal narrowing with upstream dilatation of the ureter (Figs. 4.7a, b and 4.10a, b), hydronephrosis, and impairment of renal function, observed in up to 30 % of cases [57]. Findings at intravenous pyelography or MR urography are nonspecific and usually correspond to hydronephrosis with a stricture of the distal ureter. It is important to identify the ureter's involvement because it requires ureteral diversion or reimplantation surgery, with the presence of the urologist needed during surgical treatment.
- The *vesicovaginal septum* can be affected with a cystic lesion that resembles an endometrioma.
- *Urethral* endometriosis usually develops as contiguous extension from bladder lesions, while isolated forms are not reported in literature [53].

4.6 Endometriosis of the Posterior Compartment

It can involve the pouch of Douglas, the torus uterinus, the uterosacral ligaments (USLs), the vagina, the posterior vaginal fornix, the rectovaginal septum, and the bowel wall.

- Deep solid lesions involving the *pouch of Douglas* usually appear as ill-defined, hypointense tissue thickening on T2-weighted images, with possible hyperintense foci on T1-weighted sequences, reflecting the blood content (Fig. 4.8e). A partial or complete cul-de-sac obliteration can occur [58].
- The *torus uterinus* is a small transverse thickening that binds the insertion of both USLs on the posterior wall of the uterus. It is not clearly visible at MRI in absence of pathological thickening; it is frequently involved in endometriosis appearing as a mass or a thickening in the upper middle portion of the posterior cervix (Figs. 4.8a and 4.10d), forming an arciform abnormality. Uterine retroversion or

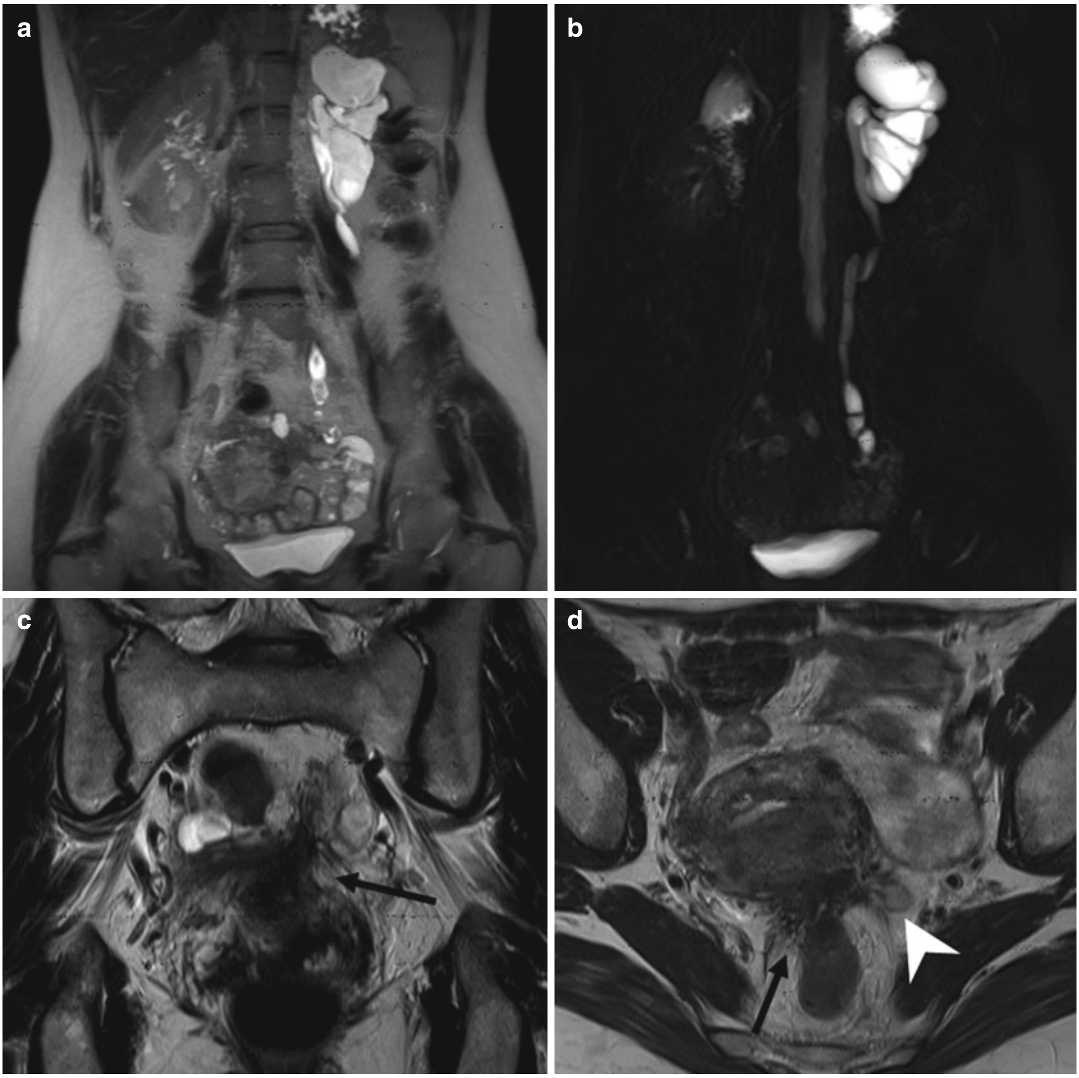

Fig. 4.10 Deep pelvic endometriosis involving the left ureter. Coronal (**a**, **c**: TR 4670, TE 94) and axial (**d**: TR 4070, TE 94) T2-weighted images; magnetic resonance urography (**b**: T2-haste thick slab, TR 6000, TE 754). There is a dilation of the left ureter and calyceal system (**a**, **b**) caused by a deep infiltrating lesion located in the posterior pelvic compartment (**c**, **d**: *black arrows*). The distal portion of the left ureter (**d**: *arrowhead*) is encased by the endometriosic lesion, with an upstream dilation of the urinary system. The lesion is poorly marginated, presents a stellate morphology, and involves also the posterior uterine surface and the anterior bowel wall

angular rectal attraction is often associated, reflecting the fibrotic component [59].

- The *uterosacral ligaments (USLs)* are normally visible at MR imaging as thin semicircular hypointense cords that originate from the lateral margin of the uterine cervix, directed dorso-cranially toward the sacrum. Normally, if visible, they appear thin and regular. When the USLs are involved by endometriosis, more frequently in their proximal part, their fibrotic thickening or the presence of a nodule within the ligaments, with regular or stellate margins (Figs. 4.8a and 4.10d), makes the ligaments palpable at physical examination. False-negative or false-positive results are possible when a retroflexed uterus, adhesions, or endometriomas mask the origin or the proximal part of the USL or in case of frozen pelvis [60].

Furthermore, thickened USLs due to endometriosis may be distinguished from the consequences of preview surgery.

- *Rectovaginal septum (RVS)* lesions account for 10 % of cases, and they consist of a nodule or a mass that passes through the lower border of the posterior lip of the cervix with attraction of the vaginal fornix. RVS lesions are usually associated with cul-de-sac obliteration and are, in most cases, secondary to involvement of the peritoneum of the pouch of Douglas. This is related to the embryogenetic origin of the RVS that originates from the fusion of the two layers of the peritoneal cul-de-sac extending downward between the rectum and the vaginal wall to the level of levator ani muscle.
- The involvement of the *cervix* appears as a thickening or a mass, hypointense on T2-weighted images, obliterating the posterior vaginal or cervical wall (Figs. 4.7f and 4.8a, b). Errors can occur, especially in case of retroflexed uterus or frozen pelvis. The retrocervical area is a virtual extraperitoneal space behind the cervix, situated above the rectovaginal septum. Here the *posterior vaginal fornix* is the larger recess located posterior to the cervix, and normally it appears as a curved regular cavity. Its involvement in endometriosis account for 65 % of cases and appears as an upward attraction of the vaginal fornix toward the lesion [38].
- The *parametrium* consists of connective tissue forming a sheet containing the blood vessels, the ureter and the inferior hypogastric plexus, extending from the lateral surface of the cervix and vagina to the lateral pelvic wall in the frontal plane [61, 62]. Signs of parametral involvement are the presence of a low-signal-intensity area in the paracervical or paravaginal region on T2-weighted images and a pelvic wall or ureteral involvement [63].
- 5–27 % of women with pelvic endometriosis present *intestinal* localizations. The bowel endometriosis most commonly affects the rectosigmoid junction (70–85 %) [3, 64]. Less frequent sites are the appendix, cecum, and distal ileum [3, 65].

The implants are usually superficial, localized to the serosa on the antimesenteric edge of the bowel, but they can erode the subserosal layers, causing thickening and fibrosis of the muscularis propria. The implanted tissue only rarely invades the mucosa that is almost always intact; this is why the colonoscopy is often false negative. In response to cyclic hemorrhage, an inflammatory response can cause adhesions, bowel strictures, and gastrointestinal obstruction.

To identify the intestinal lesions in the MRI study, we considered both *direct* and *indirect* signs. The *direct* signs consist of parietal nodules or plaques with low signal intensity on T2-weighted images and high signal foci on T1-weighted images (Figs. 4.7f and 4.8). The *indirect* signs include adhesions between the lesion, uterus, and/or adjacent organs (Fig. 4.3) with strands of hypointense tissue on T2-weighted images in the pelvic adipose tissue, abnormal angulations of bowel loops, and retroverted fixation of the uterus with obliteration of the posterior cul-de-sac (Figs. 4.7, 4.8, 4.9d, and 4.10c, d) [58].

The presence of hypointense parietal thickening on T2-weighted images (Figs. 4.7f and 4.8b), with or without intermingled hemorrhagic foci hyperintense on T1-weighted images, causes the disappearance of the hypointense signal of the anterior bowel wall and obliteration of the fat tissue plan. In most cases, the rectum is attracted toward the torus uterinus with involvement of the USL and obliteration of the cul-de-sac.

MR imaging has a good sensitivities and specificities, of 76.5–88.3 % and 76–80 %, respectively, in the diagnosis of rectosigmoid colon involvement [19, 42, 66, 67].

There is not consensus concerning the indications of gadolinium administration in the diagnosis of DPE. Use of contrast-enhanced MRI is primarily required to identify solid enhancing nodules in the endometriosic cysts, when malignant transformation is suspected. Contrast medium is also useful to define the extent of glandular tissue, fibrosis, and active inflammatory reaction [38] incited by micro- or macroscopic endometrial implants. However gadolinium is usually not administered because implants of DPE can enhance, but it is neither sensitive nor specific [68]. Furthermore, an accurate preoperative evaluation of endometriosis extension has been demonstrated even without use of contrast agent [69, 70].

Opacification of rectum with air [64], water enema [71], or US gel [70] improves diagnostic capabilities of pelvic MRI, because it reaches a better contrast between the lumen and the wall of the rectus and a better delineation of the rectovaginal septum [43, 70]. Anyway with the MRI study, it is difficult to determine the depth of bowel wall infiltration and to differentiate lesions limited to the serosa from lesions that invade the muscular wall.

Differential diagnosis: radiographic findings of intestinal endometriosis may mimic a colon carcinoma as endometriosis causes marked overgrowth of the external muscular layer, producing an eccentric or a circumferential lesion, with crenulated appearance at BDCE. Unlike colonic carcinoma, endometriosis does not cause mucosal ulceration, and the mucosa is intact. Furthermore, the US and CT appearance are nonspecific, and they do not help in the differential diagnosis. MRI is a good tool in the differentiation between tumors and endometriosis in selected cases, thanks to the peculiar MRI signal intensity of endometriosic implants [72]. The differential diagnosis of the gastrointestinal implants includes also metastatic disease, in particular drop metastasis from an upper abdominal malignancy.

4.7 Complications of Endometriosis

The endometriosic implants can lead to a number of complications.

Adhesions represent a very common and clinically important complication and can result in intestinal obstruction (Fig. 4.11f). They occasionally can be identified on MRI as speculated low-signal-intensity strandings that obscure organ interfaces (Figs. 4.7a, 4.8a, 4.9d, and 4.10c, d). Indirect signs of adhesions include angulation of bowel loops (Fig. 4.9d), too large changes in bowel diameter with peritoneal nodules, fixed posterior displacement of uterus and ovaries, elevation of the posterior vaginal fornix, loculated fluid collections, and hydrosalpinx [3].

Frozen pelvis is due to the extension of endometriosis to multiple adjacent pelvic structures, with a block of tissue that simulates a carcinoma [19]. Rupture of an endometrioma can lead to *hemoperitoneum. Ascites* can be a consequence of the rupture of endometriosic implant and subsequent peritoneal irritation. *Adnexal torsion* can be due to an endometrioma acting as a leading mass [73]. *Malignant transformation* is rare (<1 % cases of endometriosis), and long-standing ovarian endometrioma is most likely to undergo this change rather than extraovarian endometriosis [33, 35]. In fact, 75 % of malignant transformation arises from ovary and only 25 % from extraovarian lesions (endometrioid tumors and sarcomas) (Fig. 4.12).

4.8 Rare Locations of Endometriosis

Although extrapelvic endometriosis has been reported to affect almost all organs except the heart and the spleen, the most frequent location is in the abdominal wall [74].

4.8.1 Parietal Endometriosis

The principal risk factor for parietal endometriosis is antecedent abdominopelvic surgery [75–77], due to the iatrogenic seeding of endometrial cells within the scar tissue.

Parietal endometriosis of the abdomen is a rare finding, described in the rectus abdominis, umbilicus, sites of hysterectomy or cesarean scars, and puncture sites of amniocentesis or trocar for laparoscopy [75, 78, 79]. Solid endometriosis developing in *cesarean section scars*, after cesarean section, appears with hemorrhagic signal intensity in the context of the myometrium along the surgical scar (Fig. 4.11a, b) [80]. Endometriosis occurring on *episiotomy scars* has very a similar pathophysiology [81].

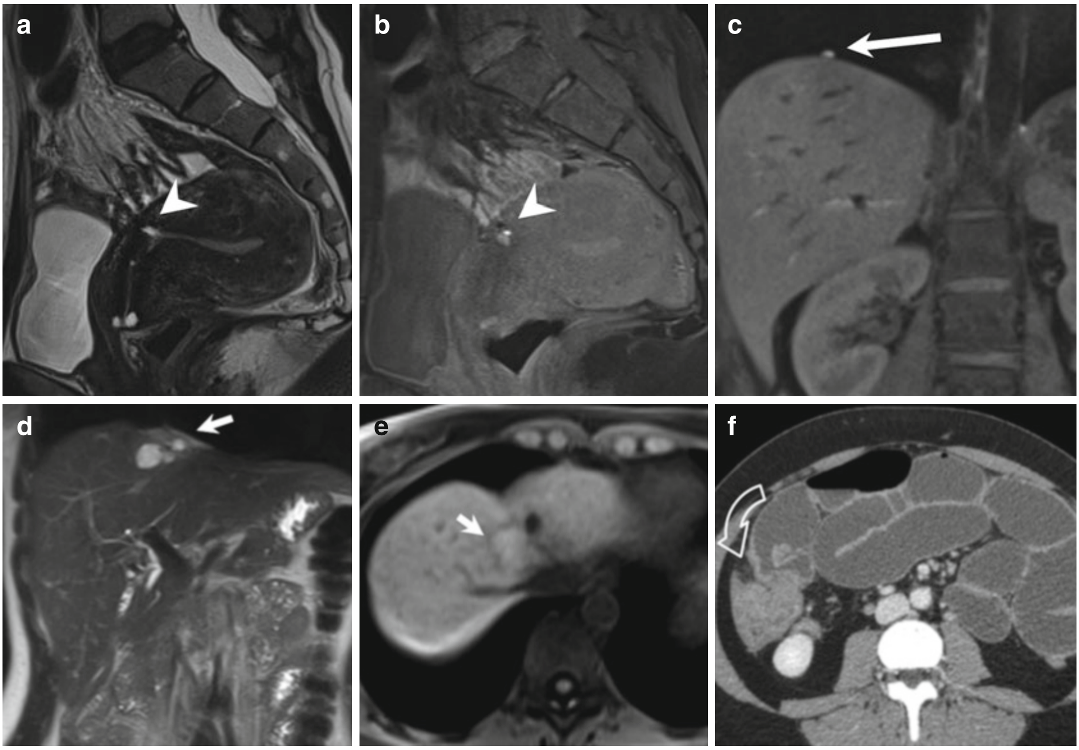

Fig. 4.11 Unusual locations. Endometriosis of the cesarean scar (**a**, **b**). Sagittal T2-weighted FSE images (**a**: TR 4670, TE 94) and T1-weighted FS-GRE image (**b**: TR 369, TE 10). Woman with previous cesarean section presents an endometriosic lesion (*arrowheads*) in the context of the myometrium, along the surgical scar. This lesion presents hyperintense foci on the T1-FS-weighted image, due to its hemorrhagic content. Diaphragmatic location (**c**: TR 541, TE 6.3). A millimetric hyperintense nodule on T1-weighted FS-GRE image (*arrow*) is recognizable on the right emidiaphragm, over the liver. (**d**, **e**) Diaphragmatic/hepatic locations. In this patient the right emidiaphragm is focally irregular and thickened (*arrow*) due to previous surgery for endometriosic location. In this site a multiloculated lesion, hyperintense on the T2- (**d**: TR 1300, TE 88) and T1-weighted (**e**: TR 761, TE 5.9) images is recognizable. The anatomo-pathological examination after surgery demonstrated was an endometriosic lesion. MDCT technique axial image after intravenous contrast medium administration during portal phase (**f**) of a patient with endometriosis and bowel occlusion. The small bowel is dilated by fluid, and solid tissue is recognizable on the right flank (*curved arrow*). The patient underwent surgery, and the solid tissue was demonstrated as endometriosic lesion adherent to bowel walls, causing occlusion

4.8.2 Inguinal Endometriosis

It is more frequently located through the canal of Nuck, which, if patent, creates a communication between the peritoneal cavity and the inguinal canal [82]. The canal of Nuck is an embryological remnant of the peritoneovaginal canal; in women the round ligament extends toward the subcutaneous tissue in this canal up to the labia majora. Endometriosis locations in the canal of Nuck are extremely rare and appear on MRI as fibrohemorrhagic lesions in proximity to the inguinal ring (Fig. 4.13c, d). In these cases, the clinical presentation is pathognomonic with a palpable inguinal mass intermittently painful following the menstrual cycle [83, 84]. The intra- and extraperitoneal portion of the round ligament, hernia sacs, and postoperative scars of the abdominal wall has been cited as regions of endometrial involvement in the groin.

4.8.3 Round Ligament Endometriosis

The round ligaments of the uterus originate at the uterine horns, where the uterus and the uterine

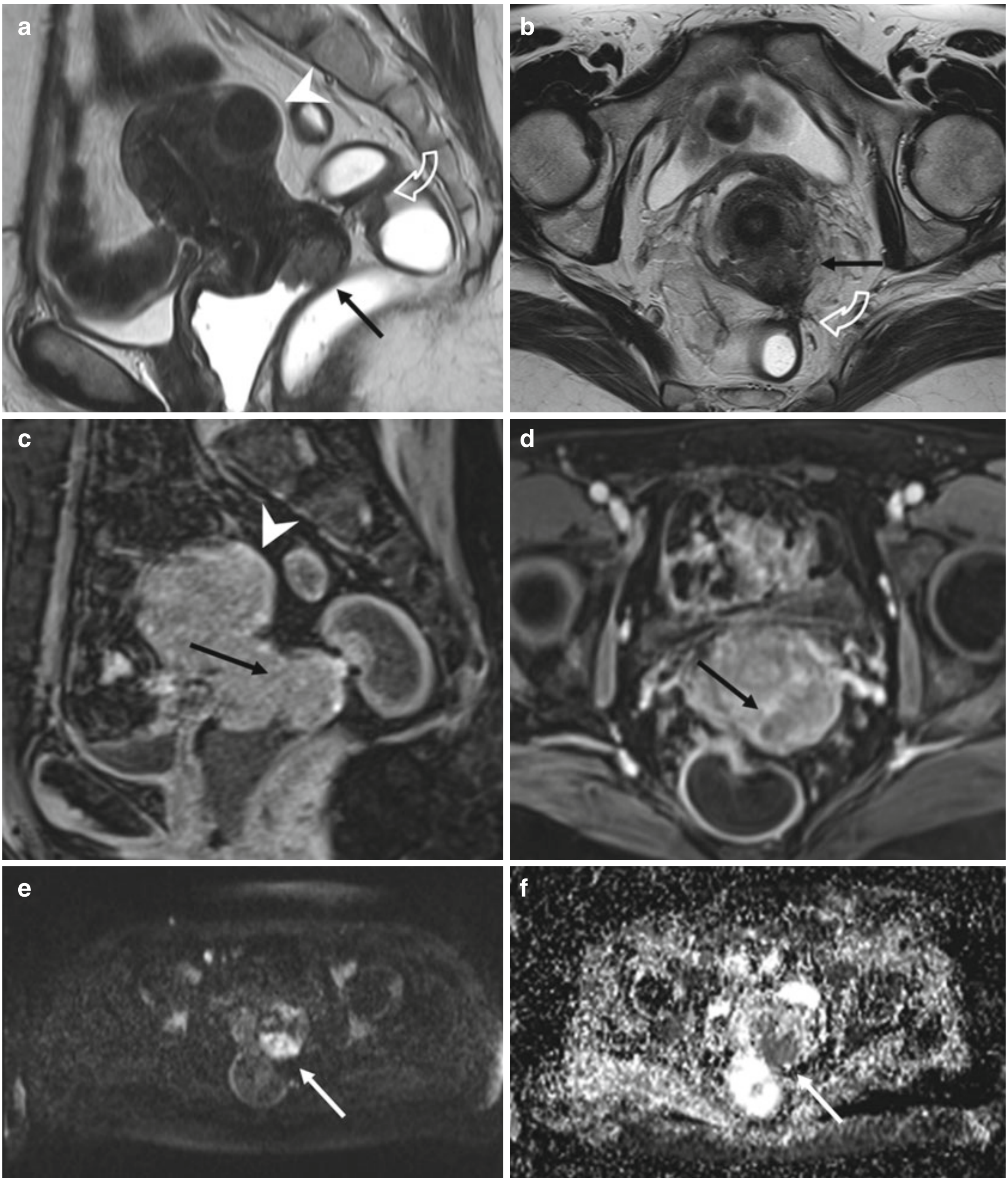

Fig. 4.12 Malignant transformation in endometriosis. Sagittal (**a**: TR 3857, TE 100) and axial (**b**: TR 3652, TE 100) T2-weighted MR images show a cervical lesion in the posterior fornix (*arrows*) in a patient with endometriosis of the posterior compartment (*curved arrows*). It exhibits enhancement on the T1-weighted image after contrast medium administration (**c**, **d**: TR 5.8, TE 2.8), and it shows restricted diffusion on diffusion-weighted ($b = 1{,}000$ s/mm^2) images (**e**) and apparent diffusion coefficient (ADC) maps (**f**). Also a subserosal leiomyoma of the posterior uterine wall is recognizable (*arrowheads*)

tube meet. These ligaments pass through the inguinal canals and enter the labium majus. The function of the round ligament is to maintain the anteversion of the uterus. Endometriosis of the round ligaments, either in their intra- or extra-peritoneal portions, is a rare event (0.3–0.6 %) [85]. It is located on the right side in more than 90 % of cases, probably due to the barrier to the menstrual flow reflux provided by the sigmoid colon on the left side [86]. On MRI, the round ligaments are thin structures with a fibrous signal intensity, anterior to the external iliac vessels.

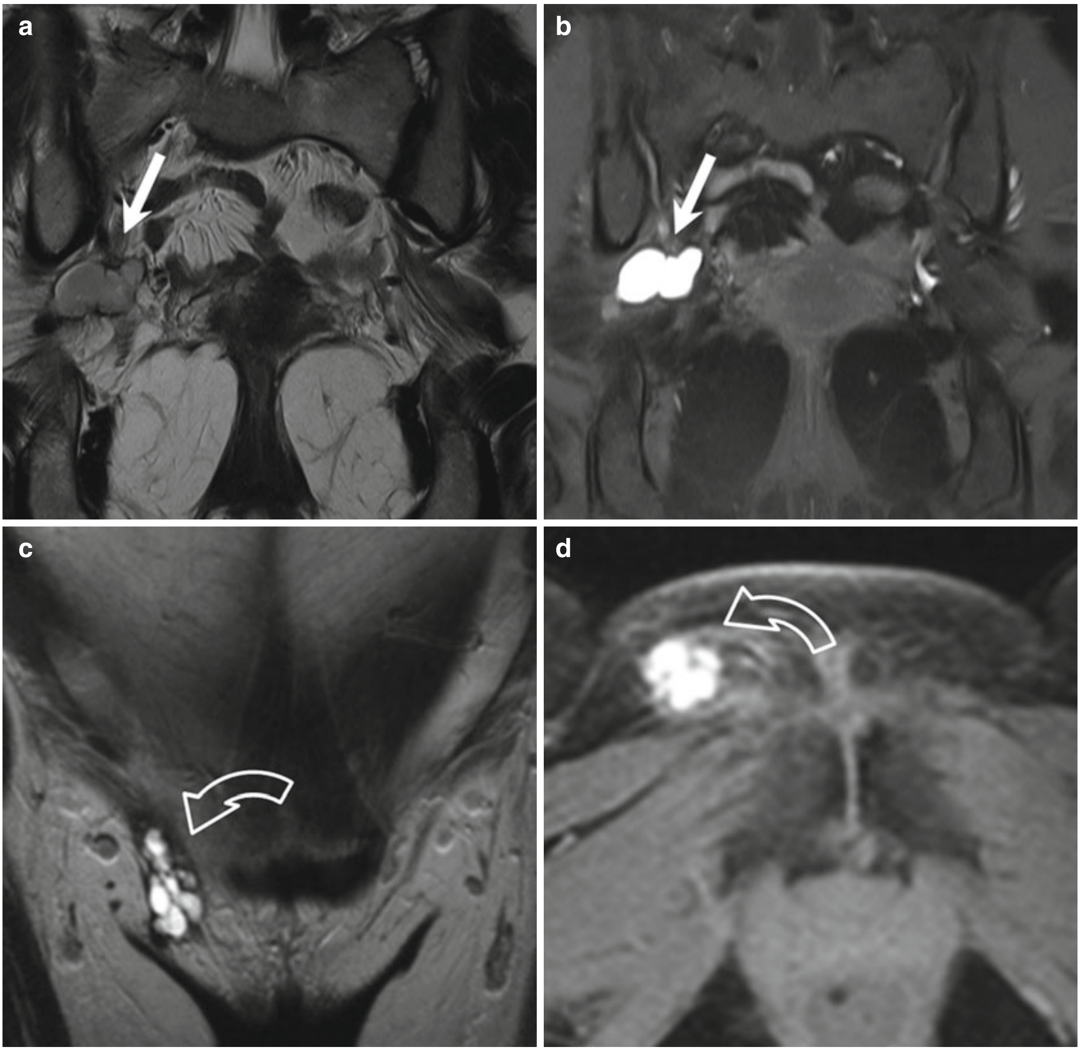

Fig. 4.13 Unusual locations. (**a**, **b**) Endometriosis of the ischiatic foramen. Coronal T2- (**a**: TR 5390, TE 113) and FS-T1-weighted (**b**: TR 369, TE 10) images. Woman with catamenial sciatica presents an endometriosic lesion in the ischiatic foramen (*arrows*), markedly hyperintense on T1-weighted sequence (**b**). (**c**, **d**) Endometriosis of the nuck canal. Coronal T2- (**c**: TR 5390, TE 113) and axial FS-T1-weighted (**d**: TR 822, TE 4.9) images. Woman with a painful palpable right inguinal mass presents a lesion near the right inguinal ring (*curved arrow*), multiloculated, with hemorrhagic content, hyperintense on T1- and T2-weighed images. It is an endometriosic location in the Nuck canal, where the round ligament extends toward the subcutaneous tissue. The round ligament is not involved. (**e**, **f**) Endometriosis of the right round ligament. Axial T2- (**e**: TR 5130, TE 108) and T1-weighted (**f**: TR 550, TE 9.3) images. The right round ligament appears thickened (*arrowhead*), irregular, hypointense in all pulsed sequences due to its fibrous thickening

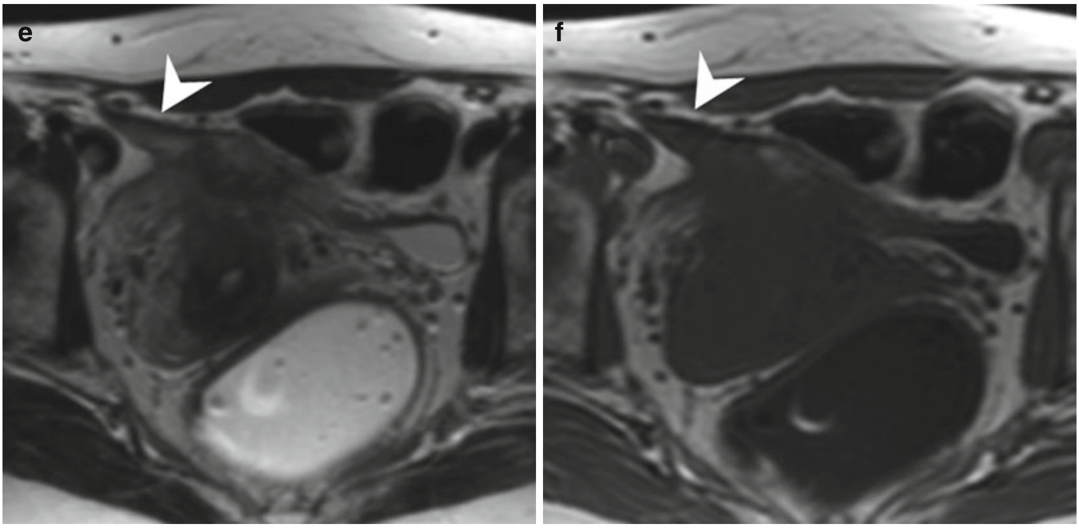

Fig. 4.13 (continued)

When involved by endometriosis, they appear as thickened, irregular, and with or without nodular appearance (Fig. 4.13e, f).

4.8.4 Sciatic Nerve Endometriosis (Cyclical Sciatica)

Cyclic sciatica due to implantation of endometrial tissue in the sciatic nerve in the region of the sciatic notch is a very unusual form of sciatica. It manifests as cyclic episodes of pain in the distribution of the sciatic nerve that coincide with menstruation. If not treated, a sensorimotor mononeuropathy of the sciatic nerve can develop [87]. MR imaging may show a focal mass-like lesion centered around the sciatic nerve, commonly in the area of the greater sciatic notch. This mass-like lesion often exhibits high signal intensity on T1-weighted images (more evident in the fat-suppressed T1-weighted images) and mixed signal intensity on T2-weighted images, depending upon the quantity, age, and proportion of hemorrhagic tissue (Fig. 4.13a, b).

4.8.5 Hepatic Endometriosis

Liver involvement by endometriosis is rare. Only 18 cases are reported in the English literature. The pathogenesis is unknown; the blood/lymphatic dissemination, similar to the cancer metastasis, is the presumed pathway for intraparenchymal hepatic lesions [88, 89]. The imaging features of hepatic endometriosis are variable and depend on its response to the hormonal changes during menstrual cycles [90]. There is no magnetic resonance imaging (MRI)-specific characteristics, but most commonly it presents as well-defined lobulated cystic lesions (Fig. 4.11d, e) with possible solid components and septations [91, 92].

4.8.6 Thoracic Endometriosis (*Diaphragm, Pleura, Pericardium, and Lung*)

Endometriosis of the thorax is a clinical entity that includes the presence of ectopic endometrial tissue in the *diaphragm*, in the *pleura*, and rarely in the *pericardium. Diaphragmatic endometriosis* is a rare entity, often asymptomatic, in up to 90 % of cases associated with severe pelvic endometriosis. The most plausible theory about this condition is based on retrograde menstruation and subsequent transportation of viable cells in peritoneal fluid from the pelvis up the right paracolic gutter to the right hemidiaphragm. Here the cells are blocked by the falciform ligament and infiltrate the right half of the muscle and then the left side, thus demonstrating its asymmetric distribution on the diaphragm. The lesions may be hide behind the right hepatic lobe (*perihepatic endometriosis:* Fig. 4.11c–e). Catamenial pneumothorax is the most common clinical expression [93].

4.8.7 Nasal Mucosa Endometriosis

It is an exceptional localization (two cases reported in the literature). The clinical symptoms are catamenial nasal tumefaction, pain, and epistaxis, and the endoscopic biopsy allows the diagnosis [94, 95].

References

1. Revised American Fertility Society classification of endometriosis: 1985 (1985) Fertil Steril 43(3):351–352
2. Brosens I et al (2004) Diagnosis of endometriosis: pelvic endoscopy and imaging techniques. Best Pract Res Clin Obstet Gynaecol 18(2):285–303
3. Woodward PJ, Sohaey R, Mezzetti TP Jr (2001) Endometriosis: radiologic-pathologic correlation. Radiographics 21(1):193–216; questionnaire 288–294
4. Spaczynski RZ, Duleba AJ (2003) Diagnosis of endometriosis. Semin Reprod Med 21(2):193–208
5. Vigano P et al (2004) Endometriosis: epidemiology and aetiological factors. Best Pract Res Clin Obstet Gynaecol 18(2):177–200
6. Olive DL, Henderson DY (1987) Endometriosis and mullerian anomalies. Obstet Gynecol 69(3 Pt 1):412–415
7. Clement PB (1990) Pathology of endometriosis. Pathol Annu 25(Pt 1):245–295
8. Halme J et al (1984) Retrograde menstruation in healthy women and in patients with endometriosis. Obstet Gynecol 64(2):151–154
9. Liu DT, Hitchcock A (1986) Endometriosis: its association with retrograde menstruation, dysmenorrhoea and tubal pathology. Br J Obstet Gynaecol 93(8):859–862
10. Jenkins S, Olive DL, Haney AF (1986) Endometriosis: pathogenetic implications of the anatomic distribution. Obstet Gynecol 67(3):335–338
11. Dunselman GA, Groothuis PG (2004) Etiology of endometriosis: hypotheses and facts. Gynecol Obstet Invest 57(1):42–43
12. Kurman RJ (2011) Diseases of the peritoneum. In: Blaustein's pathology of the female genital tract, 6th edn. Springer, New York/London
13. Kashima K et al (2004) Familial risk among Japanese patients with endometriosis. Int J Gynaecol Obstet 84(1):61–64
14. Rogers PA et al (2013) Defining future directions for endometriosis research: workshop report from the 2011 World Congress of Endometriosis in Montpellier, France. Reprod Sci 20(5):483–499
15. Carvalho LF et al (2013) From conception to birth – how endometriosis affects the development of each stage of reproductive life. Minerva Ginecol 65(2):181–198
16. Chapron C et al (2012) Ovarian endometrioma: severe pelvic pain is associated with deeply infiltrating endometriosis. Hum Reprod 27(3):702–711
17. Gauche Cazalis C et al (2012) Preoperative imaging of deeply infiltrating endometriosis in: transvaginal sonography, rectal endoscopic sonography and magnetic resonance imaging. Gynecol Obstet Fertil 40(11):634–641
18. Saba L et al (2012) MRI and "tenderness guided" transvaginal ultrasonography in the diagnosis of recto-sigmoid endometriosis. J Magn Reson Imaging 35(2):352–360
19. Bazot M et al (2004) Deep pelvic endometriosis: MR imaging for diagnosis and prediction of extension of disease. Radiology 232(2):379–389
20. Siegler AM, Camilien L (1994) Adenomyosis. J Reprod Med 39(11):841–853
21. Levy G et al (2013) An update on adenomyosis. Diagn Interv Imaging 94(1):3–25
22. Kishi Y et al (2012) Four subtypes of adenomyosis assessed by magnetic resonance imaging and their specification. Am J Obstet Gynecol 207(2):114 e1-7
23. Bazot M et al (2001) Ultrasonography compared with magnetic resonance imaging for the diagnosis of adenomyosis: correlation with histopathology. Hum Reprod 16(11):2427–2433
24. Reinhold C et al (1996) Diffuse adenomyosis: comparison of endovaginal US and MR imaging with histopathologic correlation. Radiology 199(1):151–158
25. Novellas S et al (2011) MRI characteristics of the uterine junctional zone: from normal to the diagnosis of adenomyosis. AJR Am J Roentgenol 196(5):1206–1213
26. Takeuchi M, Matsuzaki K, Nishitani H (2010) Manifestations of the female reproductive organs on MR images: changes induced by various physiologic states. Radiographics 30(4):1147
27. Utsunomiya D et al (2004) Endometrial carcinoma in adenomyosis: assessment of myometrial invasion on T2-weighted spin-echo and gadolinium-enhanced T1-weighted images. AJR Am J Roentgenol 182(2):399–404
28. Patel MD et al (1999) Endometriomas: diagnostic performance of US. Radiology 210(3):739–745
29. Togashi K et al (1991) Endometrial cysts: diagnosis with MR imaging. Radiology 180(1):73–78
30. Wu TT et al (2004) Magnetic resonance imaging of ovarian cancer arising in endometriomas. J Comput Assist Tomogr 28(6):836–838
31. Coutinho AC Jr et al (2011) Pelvic applications of diffusion magnetic resonance images. Magn Reson Imaging Clin N Am 19(1):133–157
32. Siegelman ES, Oliver ER (2012) MR imaging of endometriosis: ten imaging pearls. Radiographics 32(6):1675–1691

33. McDermott S et al (2012) MR imaging of malignancies arising in endometriomas and extraovarian endometriosis. Radiographics 32(3):845–863
34. Takeuchi M, Matsuzaki K, Nishitani H (2008) Magnetic resonance manifestations of decidualized endometriomas during pregnancy. J Comput Assist Tomogr 32(3):353–355
35. Takeuchi M et al (2006) Malignant transformation of pelvic endometriosis: MR imaging findings and pathologic correlation. Radiographics 26(2):407–417
36. Kim MY et al (2009) MR Imaging findings of hydrosalpinx: a comprehensive review. Radiographics 29(2):495–507
37. Rezvani M, Shaaban AM (2011) Fallopian tube disease in the nonpregnant patient. Radiographics 31(2):527–548
38. Del Frate C et al (2006) Deep retroperitoneal pelvic endometriosis: MR imaging appearance with laparoscopic correlation. Radiographics 26(6):1705–1718
39. Redwine DB, Wright JT (2001) Laparoscopic treatment of complete obliteration of the cul-de-sac associated with endometriosis: long-term follow-up of en bloc resection. Fertil Steril 76(2):358–365
40. Darai E et al (2005) Feasibility and clinical outcome of laparoscopic colorectal resection for endometriosis. Am J Obstet Gynecol 192(2):394–400
41. Darai E et al (2005) Fertility after laparoscopic colorectal resection for endometriosis: preliminary results. Fertil Steril 84(4):945–950
42. Abrao MS et al (2007) Comparison between clinical examination, transvaginal sonography and magnetic resonance imaging for the diagnosis of deep endometriosis. Hum Reprod 22(12):3092–3097
43. Kinkel K et al (1999) Magnetic resonance imaging characteristics of deep endometriosis. Hum Reprod 14(4):1080–1086
44. Chapron C et al (1998) Results and role of rectal endoscopic ultrasonography for patients with deep pelvic endometriosis. Hum Reprod 13(8):2266–2270
45. Fedele L et al (1998) Transrectal ultrasonography in the assessment of rectovaginal endometriosis. Obstet Gynecol 91(3):444–448
46. Chapron C et al (2003) Anatomical distribution of deeply infiltrating endometriosis: surgical implications and proposition for a classification. Hum Reprod 18(1):157–161
47. Faccioli N et al (2008) Barium enema evaluation of colonic involvement in endometriosis. AJR Am J Roentgenol 190(4):1050–1054
48. Rock JA (1995) The revised American Fertility Society classification of endometriosis: reproducibility of scoring. ZOLADEX Endometriosis Study Group. Fertil Steril 63(5):1108–1110
49. Prystowsky JB et al (1988) Gastrointestinal endometriosis. Incidence and indications for resection. Arch Surg 123(7):855–858
50. Landi S et al (2004) Preoperative double-contrast barium enema in patients with suspected intestinal endometriosis. J Am Assoc Gynecol Laparosc 11(2):223–228
51. Siegelman ES, Outwater EK (1999) Tissue characterization in the female pelvis by means of MR imaging. Radiology 212(1):5–18
52. Loubeyre P et al (2009) Anatomic distribution of posterior deeply infiltrating endometriosis on MRI after vaginal and rectal gel opacification. AJR Am J Roentgenol 192(6):1625–1631
53. Coutinho A Jr et al (2011) MR imaging in deep pelvic endometriosis: a pictorial essay. Radiographics 31(2):549–567
54. Savelli L et al (2009) Diagnostic accuracy and potential limitations of transvaginal sonography for bladder endometriosis. Ultrasound Obstet Gynecol 34(5):595–600
55. Kinkel K et al (2006) Diagnosis of endometriosis with imaging: a review. Eur Radiol 16(2):285–298
56. Frachet O et al (2006) Ureteral obstruction from endometriosis: a case report and review of the literature. J Gynecol Obstet Biol Reprod (Paris) 35 (5 Pt 1):500–503
57. Perez-Utrilla Perez M et al (2009) Urinary tract endometriosis: clinical, diagnostic, and therapeutic aspects. Urology 73(1):47–51
58. Kataoka ML et al (2005) Posterior cul-de-sac obliteration associated with endometriosis: MR imaging evaluation. Radiology 234(3):815–823
59. Kinkel K. (2005) Management of endometriosis. Informa Healthcare, Philadelphia, pp 448–451
60. Bazot M et al (2011) Value of thin-section oblique axial T2-weighted magnetic resonance images to assess uterosacral ligament endometriosis. Hum Reprod 26(2):346–353
61. Ercoli A et al (2005) Terminologia Anatomica versus unofficial descriptions and nomenclature of the fasciae and ligaments of the female pelvis: a dissection-based comparative study. Am J Obstet Gynecol 193(4):1565–1573
62. Touboul C et al (2008) The lateral infraureteral parametrium: myth or reality? Am J Obstet Gynecol 199(3):242 e1-6
63. Bazot M et al (2012) The value of MRI in assessing parametrial involvement in endometriosis. Hum Reprod 27(8):2352–2358
64. Faccioli N et al (2010) Evaluation of colonic involvement in endometriosis: double-contrast barium enema vs. magnetic resonance imaging. Abdom Imaging 35(4):414–421
65. Olive DL, Schwartz LB (1993) Endometriosis. N Engl J Med 328(24):1759–1769
66. Bazot M et al (2007) Accuracy of magnetic resonance imaging and rectal endoscopic sonography for the prediction of location of deep pelvic endometriosis. Hum Reprod 22(5):1457–1463
67. Chapron C et al (2004) Accuracy of rectal endoscopic ultrasonography and magnetic resonance imaging in the diagnosis of rectal involvement for patients presenting with deeply infiltrating endometriosis. Ultrasound Obstet Gynecol 24(2):175–179

68. Ascher SM et al (1995) Endometriosis: appearance and detection with conventional and contrast-enhanced fat-suppressed spin-echo techniques. J Magn Reson Imaging 5(3):251–257
69. Zanardi R et al (2003) Staging of pelvic endometriosis based on MRI findings versus laparoscopic classification according to the American Fertility Society. Abdom Imaging 28(5):733–742
70. Bazot M et al (2011) Deep pelvic endometriosis: limited additional diagnostic value of postcontrast in comparison with conventional MR images. Eur J Radiol 80(3):e331–e339
71. Scardapane A et al (2013) Deep pelvic endometriosis: accuracy of pelvic MRI completed by MR colonography. Radiol Med 118(2):323–338
72. Bis KG et al (1997) Pelvic endometriosis: MR imaging spectrum with laparoscopic correlation and diagnostic pitfalls. Radiographics 17(3):639–655
73. Sonavane SK, Kantawala KP, Menias CO (2011) Beyond the boundaries-endometriosis: typical and atypical locations. Curr Probl Diagn Radiol 40(6): 219–232
74. Tokue H, Tsushima Y, Endo K (2009) Magnetic resonance imaging findings of extrapelvic endometriosis of the round ligament. Jpn J Radiol 27(1):45–47
75. Novellas S et al (2010) Anterior pelvic endometriosis: MRI features. Abdom Imaging 35(6):742–749
76. Ideyi SC et al (2003) Spontaneous endometriosis of the abdominal wall. Dig Surg 20(3):246–248
77. Crespo R, Puig F, Marquina I (2005) Pyramidalis muscle endometriosis in absence of previous surgery. Int J Gynaecol Obstet 89(2):148–149
78. Hassanin-Negila A et al (2006) Endometriomas of the abdominal wall: imaging findings. J Radiol 87(11 Pt 1): 1691–1695
79. Zhao X et al (2005) Abdominal wall endometriomas. Int J Gynaecol Obstet 90(3):218–222
80. Gougoutas CA et al (2000) Pelvic endometriosis: various manifestations and MR imaging findings. AJR Am J Roentgenol 175(2):353–358
81. Gunes M et al (2005) Incisional endometriosis after cesarean section, episiotomy and other gynecologic procedures. J Obstet Gynaecol Res 31(5):471–475
82. Choudhary S et al (2009) Unusual imaging appearances of endometriosis. AJR Am J Roentgenol 192(6):1632–1644
83. Kirkpatrick A et al (2006) Radiologic-pathologic conference of Brooke Army Medical Center: endometriosis of the canal of Nuck. AJR Am J Roentgenol 186(1):56–57
84. Cervini P, Mahoney J, Wu L (2005) Endometriosis in the canal of Nuck: atypical manifestations in an unusual location. AJR Am J Roentgenol 185(1):284–285
85. Strasser EJ, Davis RM (1977) Extraperitoneal inguinal endometriosis. Am Surg 43(6):421–422
86. Mashfiqul MA, Tan YM, Chintana CW (2007) Endometriosis of the inguinal canal mimicking a hernia. Singapore Med J 48(6):e157–e159
87. Wadhwa V et al (2012) Sciatic nerve tumor and tumor-like lesions – uncommon pathologies. Skeletal Radiol 41(7):763–774
88. Goldsmith PJ et al (2009) Case hepatic endometriosis: a continuing diagnostic dilemma. HPB Surg 2009:407206
89. Keichel S et al (2011) Lymphangiogenesis in deep infiltrating endometriosis. Hum Reprod 26(10):2713–2720
90. Inal M et al (2000) Hepatic endometrioma: a case report and review of the literature. Eur Radiol 10(3): 431–434
91. Fluegen G et al (2013) Intrahepatic endometriosis as differential diagnosis: case report and literature review. World J Gastroenterol 19(29):4818–4822
92. Asran M, Rashid A, Szklaruk J (2010) Hepatic endometriosis mimicking metastatic disease: a case report and review of the literature. J Radiol Case Rep 4(11):26–31
93. Rousset-Jablonski C et al (2011) Catamenial pneumothorax and endometriosis-related pneumothorax: clinical features and risk factors. Hum Reprod 26(9): 2322–2329
94. Laghzaoui O, Laghzaoui M (2001) Nasal endometriosis: apropos of 1 case. J Gynecol Obstet Biol Reprod (Paris) 30(8):786–788
95. Mignemi G et al (2012) A case report of nasal endometriosis in a patient affected by Behcet's disease. J Minim Invasive Gynecol 19(4):514–516

5

Fibroids

Laura Pavanello, Stefano Cesari, Carlo Biasiutti,
Riccardo Manfredi, and Roberto Pozzi Mucelli

5.1 Pathology, Vascularization, and Symptoms

Fibroids, also known as leiomyomas or myomas, are the most common benign neoplasms of the uterus, which arise from one smooth muscle cell of the myometrium (Fig. 5.1). They are well-defined masses in the myometrium of the uterus, once surrounded by a pseudocapsule, and composed of smooth muscle with varying amount of fibrous connective tissue [1].

Leiomyomas occur more frequently in the body of the uterus (95 % of cases) (Fig. 5.3) and, rarely, in the cervix (<5 % of cases) (Fig. 5.10) and between the folds of the broad ligament (Fig. 5.9).

The incidence of fibroids is about 20–30 % among women of reproductive age, and it increases with age; by the age 50, myomas occur in 70 % of white women and in 80 % of black women, indeed [2]. This different incidence between white women and black women indicates the race as a factor that influences fibroids' onset. Prospective cohort studies have shown that also body mass index, parity, birth control pill usage, and cigarette smoking are all factors affecting the prevalence and incidence of fibroids. These studies have also shown that the susceptibility to fibroids has a genetic component: there is a higher risk of leiomyomas in monozygous twins than in dizygotic ones [2–4]. Although the cause of fibroids is still unknown, there is an important familiar predisposition to fibroids and some factors that affect the incidence and prevalence.

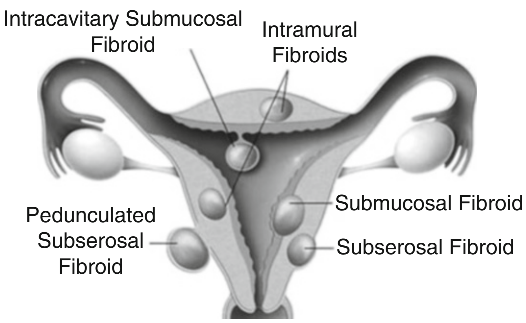

Fig. 5.1 Schematic shows the uterus demonstrating the different locations of fibroids (image from the web)

L. Pavanello (✉)
Department of Radiology,
G.B. Rossi University Hospital, Verona, Italy

Istituto di Radiologia,
Policlinico G.B. Rossi – Università di Verona,
via Mantovana, Porto Viro, RO 45014, Italy
e-mail: laura-pav@libero.it

S. Cesari • C. Biasiutti
Department of Radiology,
S.Giacomo apostolo Hospital,
Castelfranco Veneto, TV, Italy

U.O. Radiologia, Ospedale San Giacomo,
Via dei Carpani 16/Z, Castelfranco Veneto,
TV 31033, Italy
e-mail: scesari@live.it

R. Manfredi • R.P. Mucelli
Department of Radiology,
G.B. Rossi University Hospital, Verona, Italy

R. Manfredi, R. Pozzi Mucelli (eds.), *MRI of the Female and Male Pelvis*,
DOI 10.1007/978-3-319-09659-9_5, © Springer International Publishing Switzerland 2015

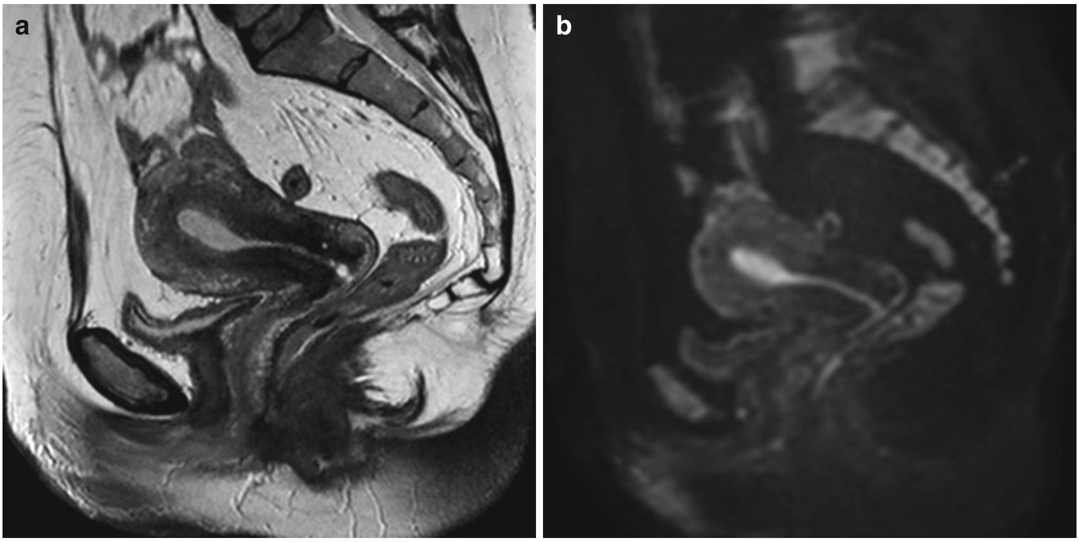

Fig. 5.2 Sagittal T2-weighted (TR 3,250 ms, TE 80 ms) (**a**) and sagittal DWI with *b*-Factor 800 ms (TR 4,000 ms, TE 75 ms) (**b**) of a normal uterus. We can see very well the distinction between the endometrium, which has low signal intensity on T2-weighted and on DWI images, and the myometrium, which has a higher signal intensity than the endometrium in both images

Estrogens and progesterone affect the growth and maintenance of fibroid, because fibroids have not been described before menarche and because they regress after a woman reaches in menopause [5]. Furthermore, some studies have shown that most fibroids neither grow nor become smaller during pregnancy [6].

Microscopically, fibroids are composed by smooth muscle spindle-shaped cells, orientated by various directions. Among these cells, there is varying amount of fibrous connective tissue.

The cut surface has a characteristic whorl-like, trabeculated appearance, by whitish to reddish color according to the prevalence of fibrous connective tissue or the prevalence of smooth muscle cells.

Macroscopically, fibroids may be singular, but more often, in the same uterus at the same time, there are multiple fibroids, very variable in size, in structural composition, and in location (Figs. 5.3 and 5.4). This great variability of fibroids in the same uterus is due to the fact that each one arises from one cell in the myometrium and so there is not a clonal relation [7].

The variation in size of fibroids is enormous, ranging from microscopic size (1–2 mm in diameter that are not detectable with imaging) to a quite large size (10–20 cm in diameter). Fibroid growth is a balance between mitosis, which produces more fibroid cells, and necrosis or apoptosis, which kills fibroid cells. As fibroids enlarge, they may outgrow blood supply and they may degenerate. The type of degenerative change depends on the degree and rapidity of the onset of the vascular insufficiency. Often fibroids >5–8 cm in diameter degenerate. Types of degeneration include hyaline degeneration, myxoid or cystic degeneration, necrotic degeneration, red (hemorrhagic) degeneration, calcification or fatty degeneration, and sarcomatous transformation (very rarely, <0.05 % of resected fibroids) [1].

According to their location (Fig. 5.1), fibroids are distinguished in:

- *Submucosal,* when they originate from the myometrium underlying the endometrium; they may be sessile or pedunculated and may protrude into the uterine cavity (Fig. 5.5).
- *Intramural,* when they grow entirely within the wall of the uterus (Fig. 5.6).
- *Subserosal,* when they originate beneath the uterine serosa and distort the contour of the outer face of the uterus; they may be sessile (Fig. 5.7) or pedunculated (Fig. 5.8).

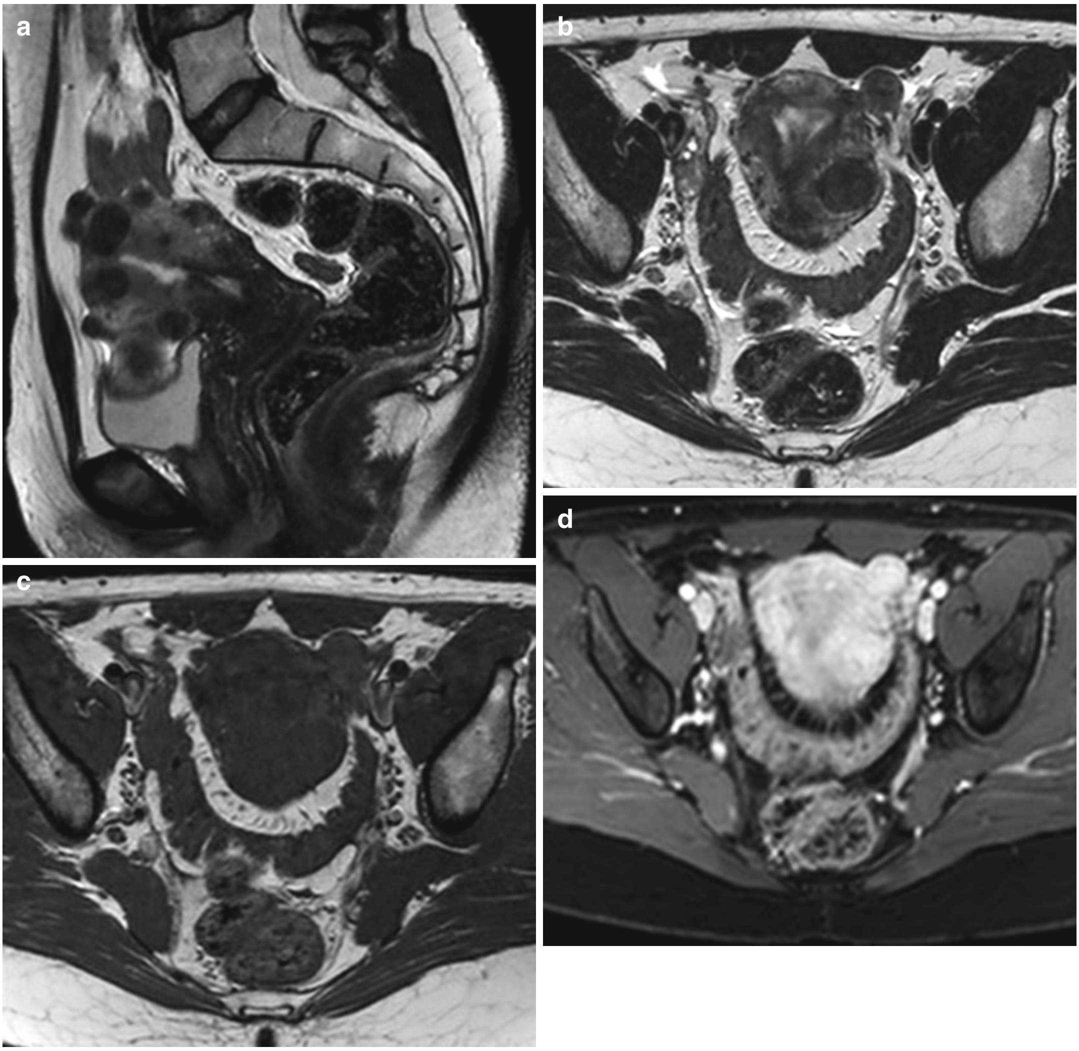

Fig. 5.3 Multiple uterine leiomyomas. Uterine leiomyomas are well-defined masses in the myometrium, with a homogeneous low signal intensity on T2-weighted images (TR 4,000 ms, TE 100 ms) (**a**, **b**) and a homogeneous isointense signal on T1-weighted image (TR 590 ms, TE 12 ms) (**c**), compared with that of the normal myometrium. On T1-weighted contrast-enhanced image (TR 4 ms, TE 2 ms) (**d**), they are homogeneous enhancing masses, but less than normal myometrium

- *Intraligamentous,* when they grow by lateral side of the uterus and may extend between the folds of the broad ligament (Fig. 5.9).
- *Cervical,* when they grow by the cervix of the uterus (Fig. 5.10).

We define submucosal or subserosal pedunculated leiomyomas when they protrude into the uterine cavity or out of the uterus through a stalk.

The most common fibroid location is intramural (40 % of women after age 35) [8].

This classification has clinical significance because the symptoms and the treatment vary among the subtypes of leiomyomas.

Uterine leiomyomas are generally less vascular in comparison to adjacent myometrial tissue [9] (Fig. 5.11).

Fibroids derive their main blood supply almost exclusively directly from branches of the arcuate (intramural) arteries. The arcuate arteries course through the outer third of the myometrium

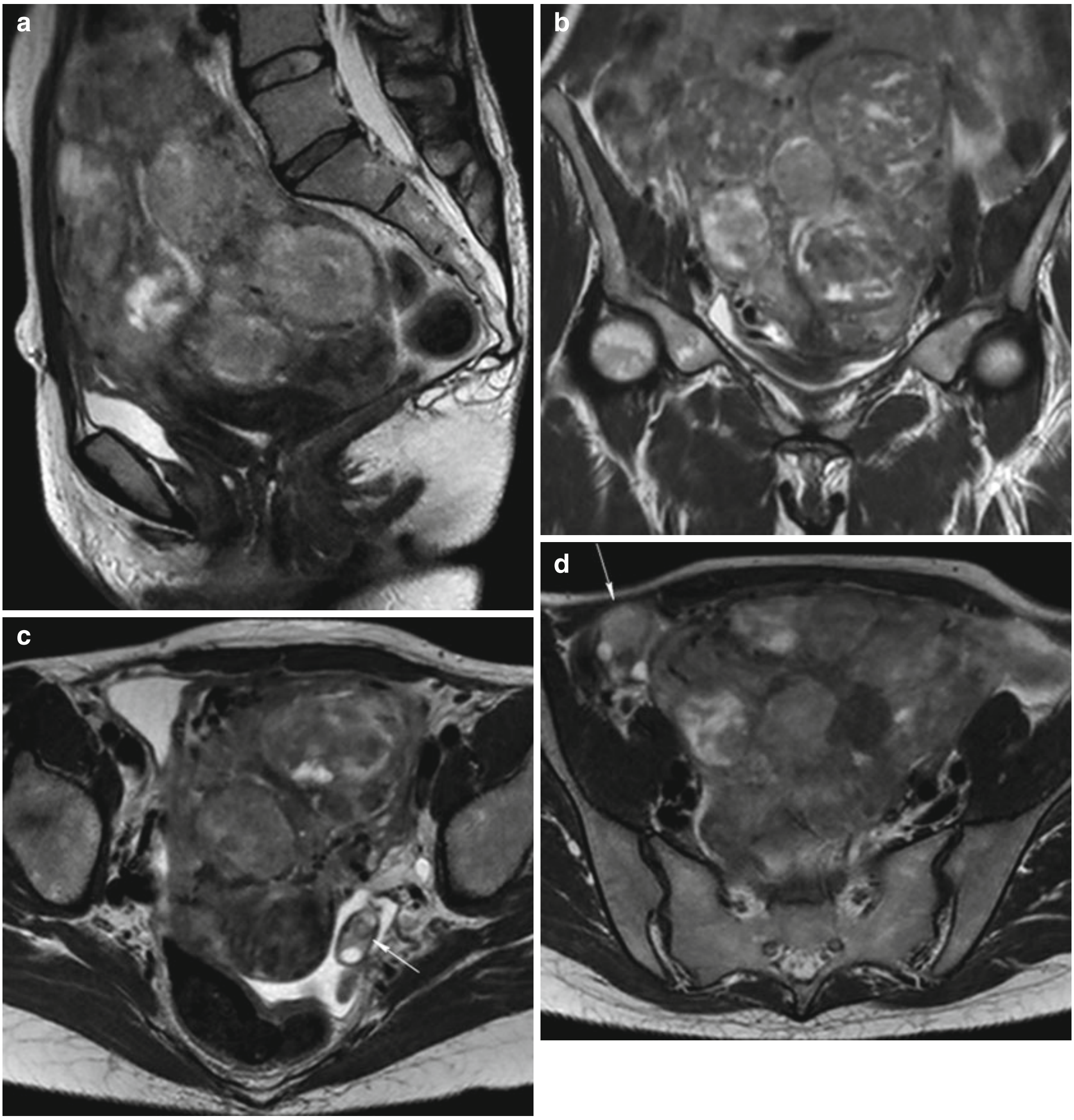

Fig. 5.4 Multiple uterine leiomyomatosis. Sagittal (TR 4,800 ms, TE 80 ms) (**a**), coronal (TR 4,800 ms, TE 80 ms) (**b**), and axial (TR 5,800 ms, TE 80 ms) (**c**, **d**) T2-weighted images show a bulky and deformed uterus by the presence of multiple voluminous intramural fibroids, with heterogeneous signal intensity and with multiple hyperintensity areas (degeneration areas). The enlarged uterus determines pressure on the bladder and rectum (**a**, **b**) and displaces the adnexa (*arrow* in **c**, **d**)

and are branches of the uterine artery. The uterine artery is the first or the second branch of the anterior division of the internal iliac artery (also called the hypogastric artery) in 51 % of cases, and it has several branches: the cervicovaginal artery and the arcuate arteries. The uterine artery may be replaced by small arterial branches or may be absent; it is often replaced by the ipsilateral ovarian artery. In 80–90 % of cases, the ovarian artery originates directly anteromedially from the abdominal aorta a few centimeters below the renal arteries; rarely, they can originate from the renal, lumbar, adrenal, or iliac arteries [10, 11].

The arcuate arteries give rise to peripheral arteries that course toward the serosal surface of

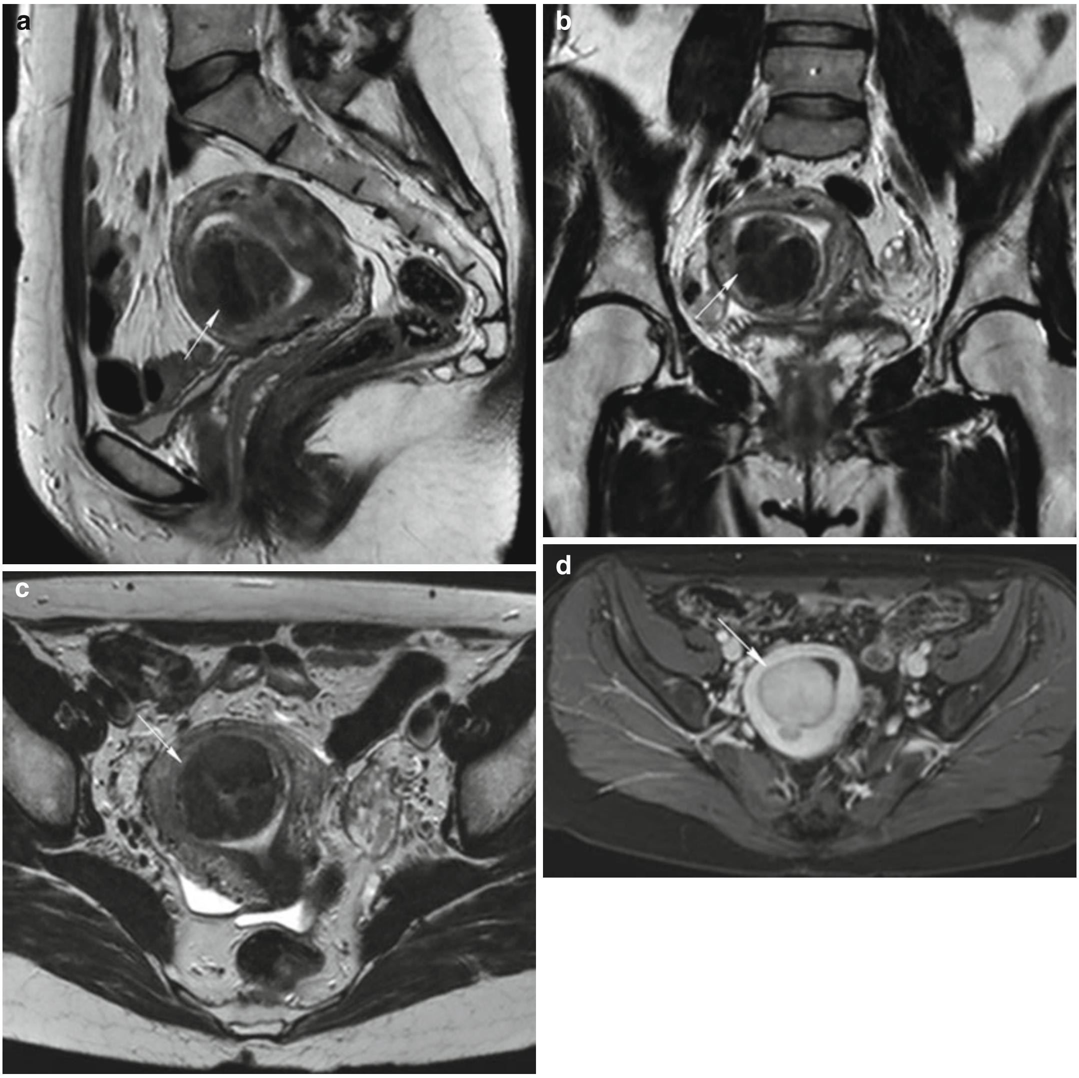

Fig. 5.5 Pedunculated submucosal fibroid (*arrow* in all images). Sagittal (TR 3,400 ms, TE 80 ms) (**a**), coronal (TR 3,700 ms, TE 100 ms) (**b**), axial (TR 4,800 ms, TE 120 ms) (**c**) T2-weighted, and axial contrast-enhanced fat-suppressed T1-weighted (TR 4 ms, TE 2 ms) (**d**) images show a pedunculated submucosal fibroid which protrudes into the uterine cavity. Fibroid demonstrates homogeneous low signal intensity on T2-weighted images and homogeneous high signal enhancement on T1-weighted images, but lower than of adjacent myometrium

the uterus and radial arteries that course toward the endometrial cavity. The radial arteries terminate at the endometrial junctional zone border by giving off multiple branches that enter and supply the endometrium. Longer, tortuous branches are described as “spiral arterioles.” Arterial blood from the spiral arterioles can pass directly into veins through arteriovenous anastomoses at multiple levels.

The perifibroid plexus is composed of terminal arteries, and it has any type of vascular anastomosis. These arteries have a diameter of 500–1,000 μm in most cases; instead, the arcuate and radial arteries, the spiral arterioles, and the utero-ovarian anastomosis have usually a diameter less than 500 μm.

The fibroid region next to the periphery, the most biologically active zone, has a higher density of vessels than the central region, where,

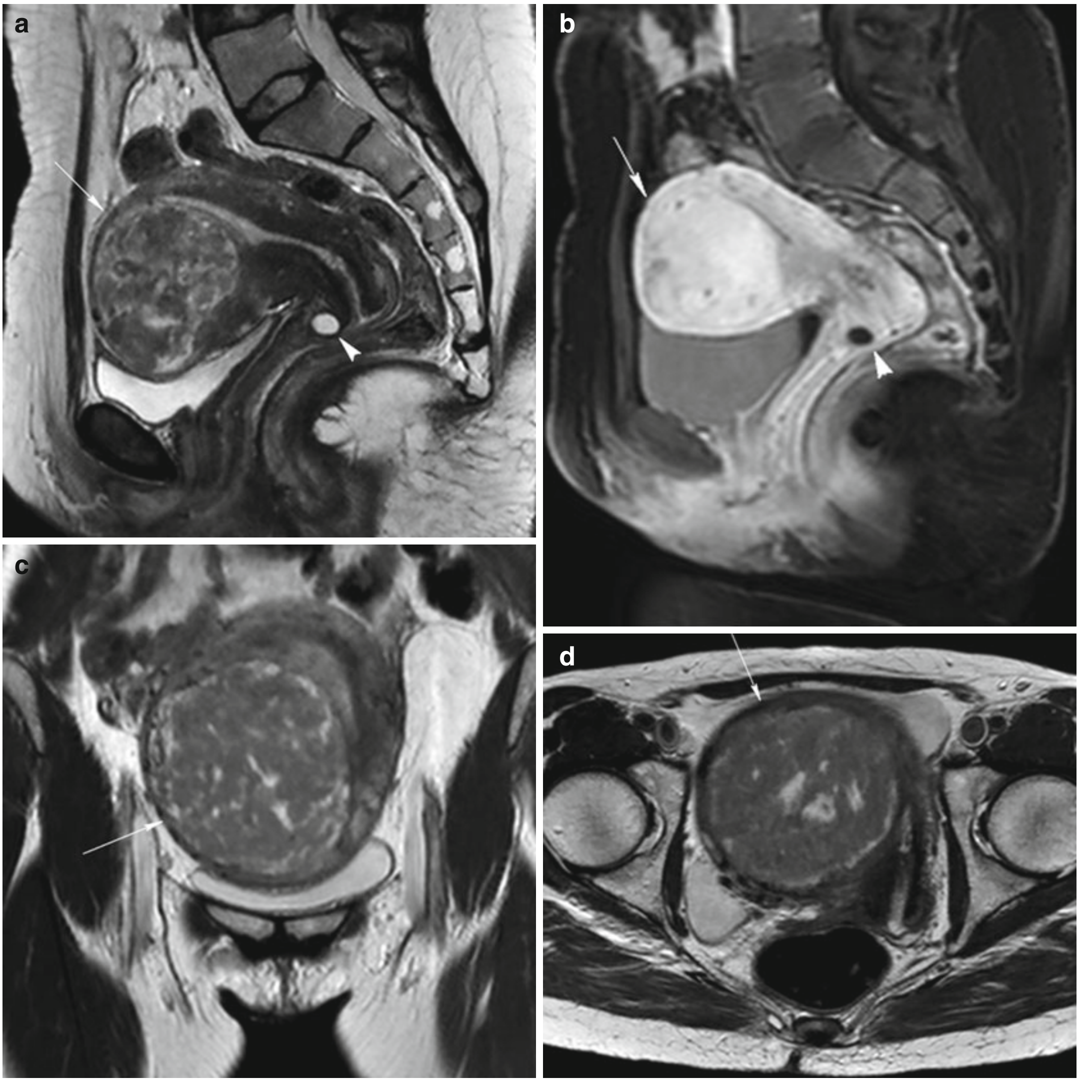

Fig. 5.6 Intramural uterine fibroid (*arrow* in all images). Sagittal T2-weighted images (TR 2,900 ms, TE 80 ms) (**a**) show an intramural fibroid (*arrow*) with heterogeneous low signal intensity. Sagittal contrast-enhanced fat-suppressed T1-weighted images (TR 4 ms, TE 2 ms) (**b**) show heterogeneous high signal enhancement of the fibroid. Naboth's cyst in the cervix of the uterus (*arrowhead* in **a** and **b**). Coronal (TR 3,500 ms, TE 80 ms) (**c**) and axial (TR 3,250 ms, TE 80 ms) (**d**) T2-weighted images of another woman show a voluminous intramural fibroid that displaces laterally the uterus. This fibroid demonstrates a heterogeneous low signal intensity on T2-weighted images, with some hyperintense areas that correspond to myxoid degeneration areas

as a consequence, frequently there is a necrotic area. Differences in vascularization between fibroids' periphery and central zone are more evident when fibroids are great in size. In support of this, there is the observation that large fibroids are more hypoxic than small ones [12].

As leiomyomas enlarge, they may outgrow blood supply, and they may have degenerative changes.

Degeneration occurs primarily in large leiomyomas and causes an increase of the symptoms or the onset of new symptoms (abdominal pain, menorrhagia, and bulk-related symptoms such as pelvic heaviness, palpable mass, urinary urgency, constipation, and bowel obstruction).

Types of degeneration are:

- *Hyaline degeneration,* a smooth homogeneous translucent zone in the fibroid.

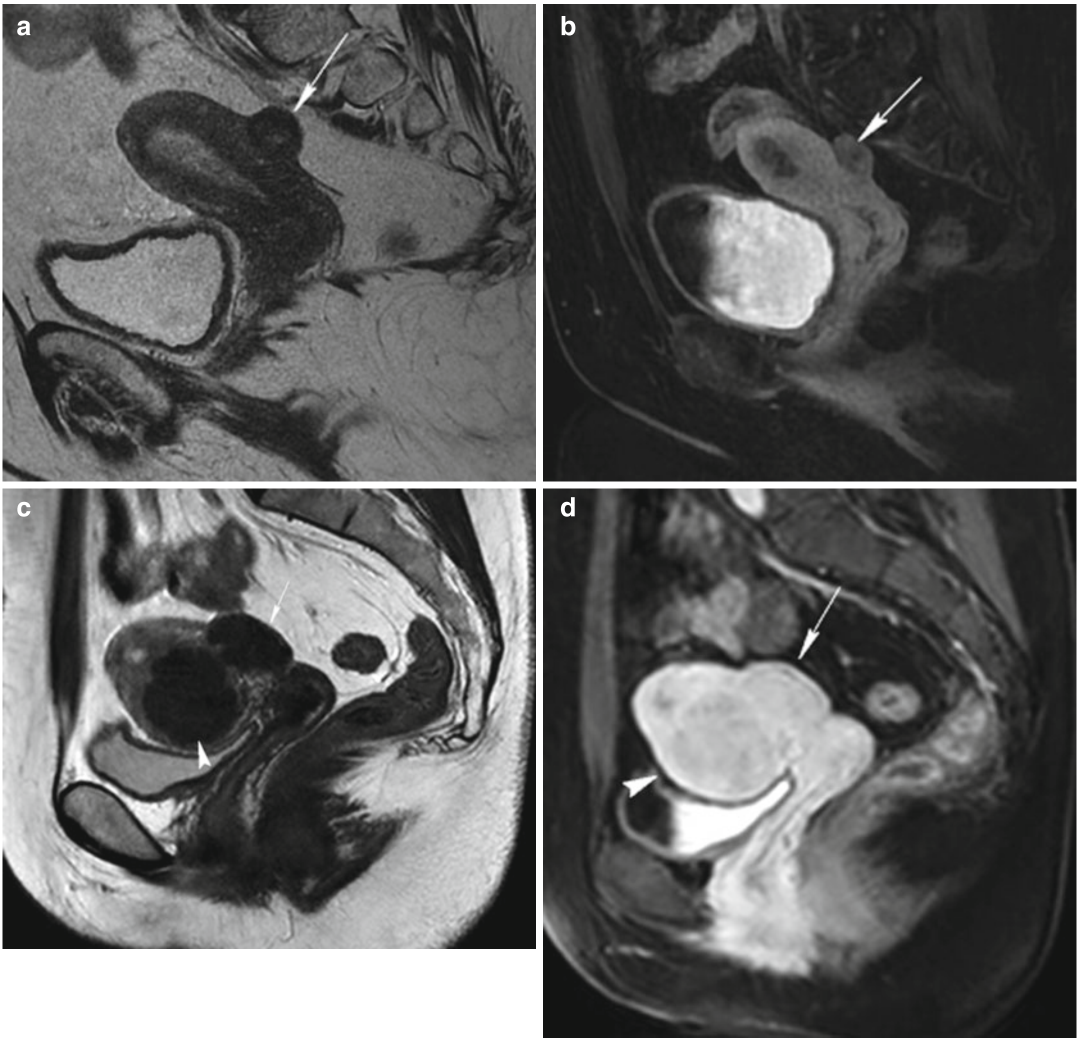

Fig. 5.7 Sessile subserosal fibroids. A little sessile subserosal fibroid on the superior face of the uterus (*arrow*) with heterogeneous low signal intensity on sagittal T2-weighted image (TR 4,500 ms, TE 90 ms) (**a**) and with low signal enhancement on contrast-enhanced fat-suppressed T1-weighted image (TR 4 ms, TE 2 ms) (**b**). Another woman (**c** and **d**) with a sessile subserosal fibroid on the posterior face of the uterus (*arrow*) and with an intramural fibroid on the inferior region of the uterus (*arrowhead*); both the fibroids have homogeneous low signal intensity on T2-weighted image (TR 2,900 ms, TE 80 ms) (**c**) and homogeneous high signal enhancement on contrast-enhanced fat-suppressed T1-weighted image (TR 4 ms, TE 2 ms) (**d**). Both these patients are eligible to uterine fibroid embolization, because the sessile subserosal fibroids have a large attachment to the uterus (larger than one third of the diameter of the fibroid)

- *Myxoid (or cystic) degeneration,* a gelatinous zone with small cystic cavities that may be a consequence to hyaline degeneration.
- *Fatty degeneration,* it may be a consequence to hyaline degeneration or due to lipomatous metaplasia, and it is more frequent during puerperium.
- *Fibroid's calcification,* more frequent in subserosal fibroids.
- *Red degeneration,* it is a hemorrhagic infarction of the uterine leiomyoma, due to venous obstruction at the periphery of the lesion.
- *Necrotic degeneration.*
- *Sarcomatous transformation* (very anecdotic), it begins in the center of the lesion and causes rapid important growth of the fibroid that becomes fixed and painful.

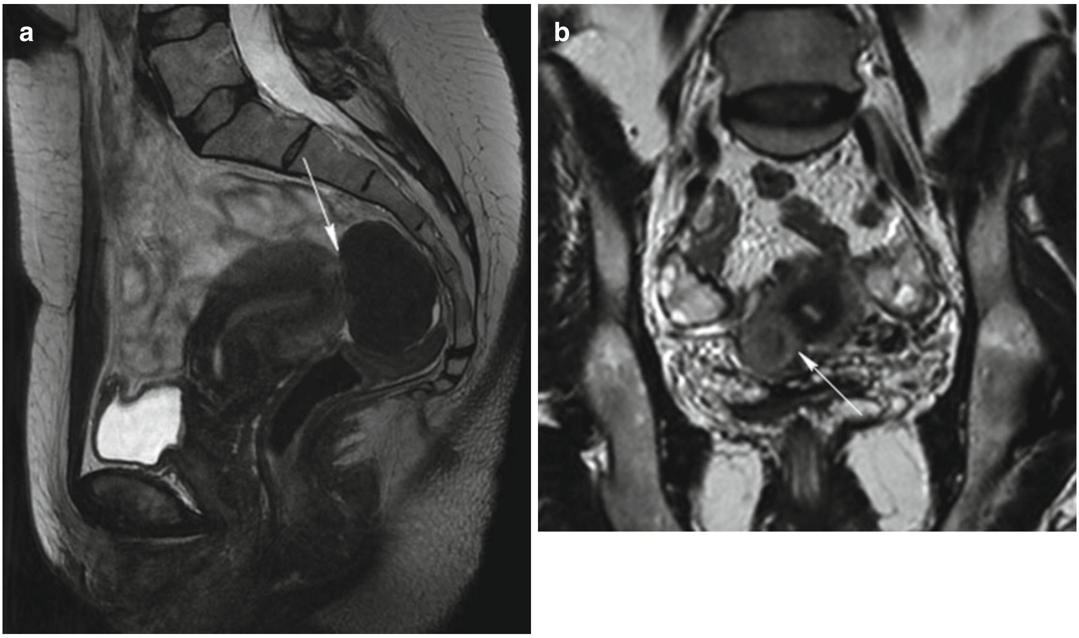

Fig. 5.8 Pedunculated subserosal fibroids. Sagittal T2-weighted image (TR 4,700 ms, TE 90 ms) (**a**) shows a homogeneous hypointense well-defined mass at the fundus of the uterus that is a pedunculated subserosal fibroid with a little stalk (*arrow*). Coronal T2-weighted image (TR 3,700 ms, TE 100 ms) (**b**) of another woman shows a isointense well-defined mass within a hypointense area at the inferior region of the uterus that is a pedunculated subserosal fibroid with a large stalk (*arrow*) and a little degenerated area within. The patient (**a**) is not eligible to uterine artery embolization, because the base of the stalk of the fibroid is less than one third of the diameter of the fibroid (this is a contraindication to UFE), while the patient (**b**) is eligible too

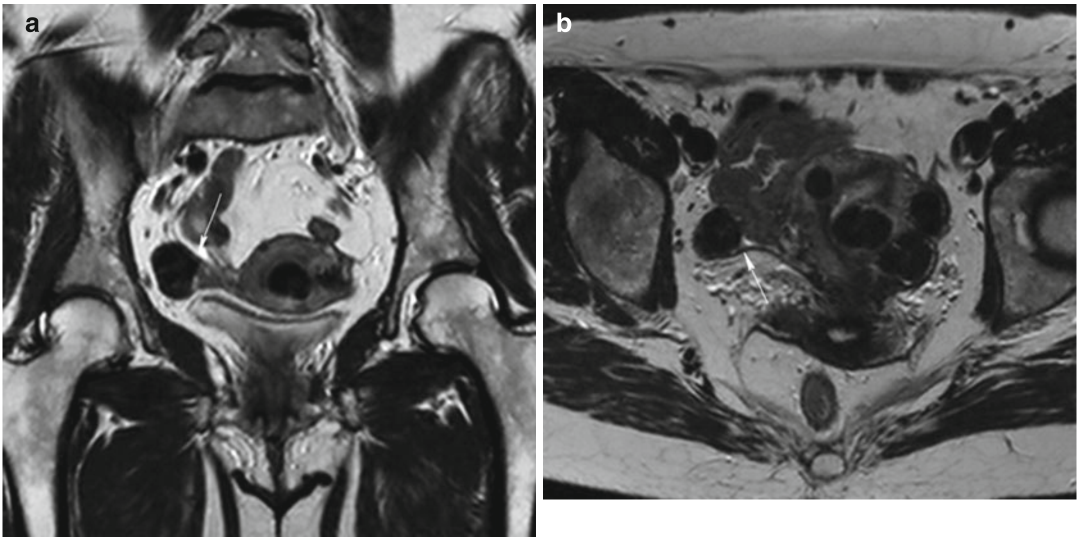

Fig. 5.9 Intraligamentous fibroid. Coronal (TR 3,700 ms, TE 100 ms) (**a**) and axial (TR 4,800 ms, TE 120 ms) (**b**) T2-weighted images show multiple hypointense well-defined uterine masses with different locations (submucosal, intramural, subserosal fibroids). One of them (*arrow*) is located between the folds of the right broad ligament

Fig. 5.10 Cervix leiomyoma with duplicity of the uterus. Sagittal T2-weighted (TR 4,900 ms, TE 90 ms) (**a**), sagittal DWI with b-Factor 800 ms (TR 5,000 ms, TE 70 ms) (**b**), and sagittal contrast-enhanced fat-suppressed T1-weighted (TR 4 ms, TE 2 ms) (**c**) images show a leiomyoma in the cervix of the uterus (*arrowhead*). On the posterior site of the uterus, there is an embryonic residue that represents a second little uterus (*arrow*). In both the uteri, endometrium is shown, and there is a little intracavitary fluid (exam obtained during menstrual phase)

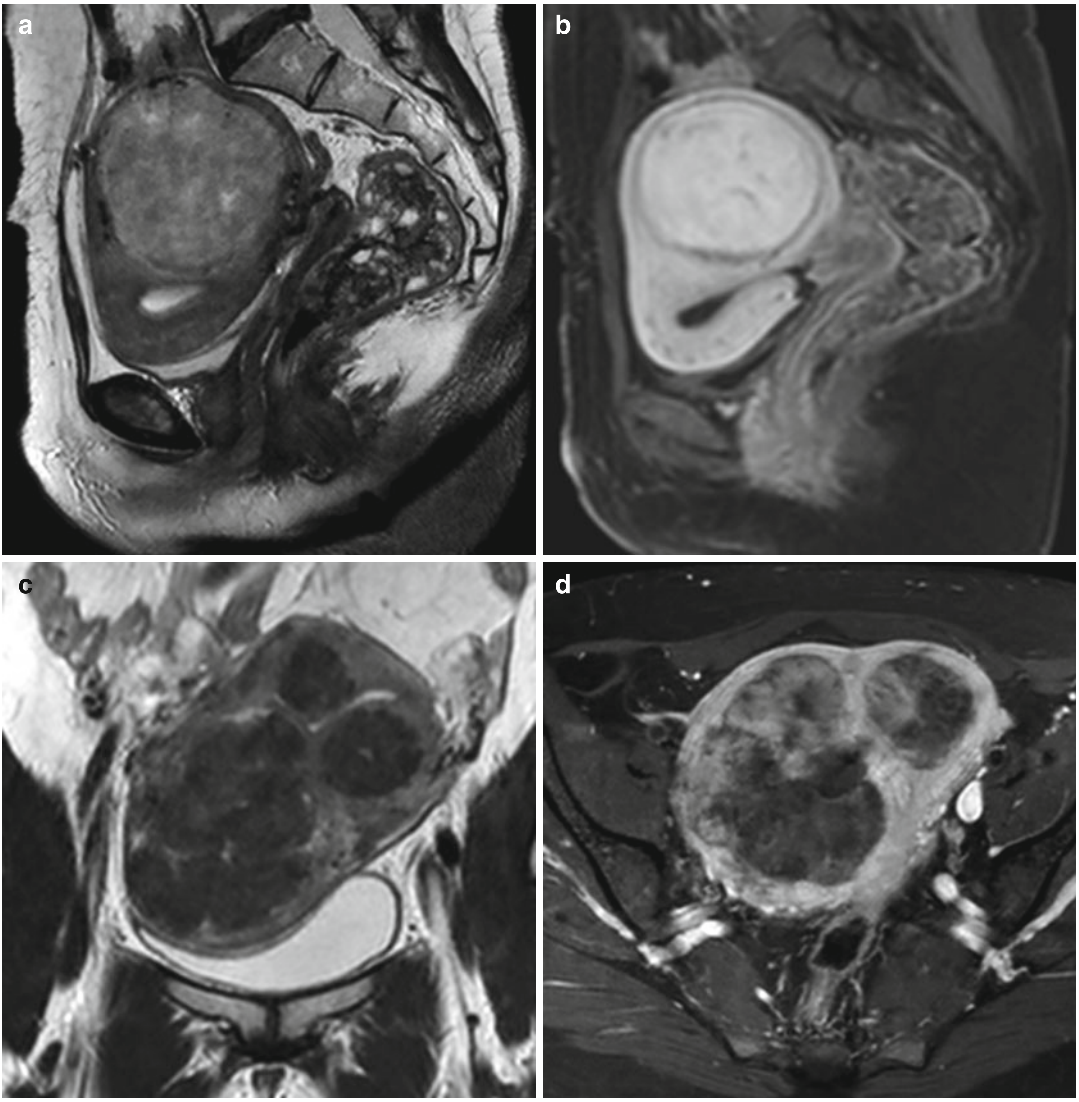

Fig. 5.11 Leiomyomas with different vascularization. *First patient.* Sagittal T2-weighted image (TR 3,250 ms, TE 80 ms) (**a**) shows a heterogeneous iso-hypointense intramural voluminous leiomyoma, which deforms the uterus; on sagittal contrast-enhanced fat-suppressed T1-weighted image (TR 4 ms, TE 2 ms) (**b**), it shows high signal intensity, similar to that of adjacent myometrium, and low-signal-intensity rim enhancement. *Second patient.* Coronal T2-weighted image (TR 3,700 ms, TE 80 ms) (**c**) shows a uterus with multiple heterogeneous hypointense signal intensity leiomyomas that, on axial contrast-enhanced fat-suppressed T1-weighted image (TR 450 ms, TE 12 ms) (**d**), show heterogeneous low-signal-intensity enhancement to that of adjacent myometrium

The clinical presentation is variable, depending on the size, location, and number of fibroids.

The most frequent symptoms of fibroids are abnormal uterine bleeding (menorrhagia or menometrorrhagia) and pelvic pain and discomfort (due to “mass effect”). As fibroids enlarge, they may produce pressure on surrounding structures (Fig. 5.12). When the fibroid uterus presses on the bladder, urinary urgency and frequency occur. When the rectum is pushed and displaced, symptoms are referable to the bowel. Acute pain occurs in 30 % of women with uterine fibroids, usually due to acute degeneration or torsion of pedunculated subserosal myomas or prolapse of pedunculated submucosal ones.

Fig. 5.12 Sagittal T2-weighted image (TR 3,400 ms, TE 80 ms) shows a bulky uterus with two heterogeneous low-signal-intensity fibroids that press on the bladder (*arrowheads*) and push the rectum (*arrow*)

Submucosal and intramural fibroids may also cause infertility, spontaneous abortions, or premature placental abruption.

5.2 Role of Imaging (US and MRI)

Ultrasonography is often the first method to detect the presence of leiomyomas due to its availability and low cost. Transvaginal ultrasound provides better visualization of the endometrium and submucosal leiomyomas than abdominal ultrasound, especially in obese women. Limitations of transvaginal ultrasound include operator-dependent variability, failure to detect small uterine fibroids, and difficulty in mapping large uteri, particularly when there are multiple fibroids. Transabdominal ultrasound is able to locate large leiomyomas, while transvaginal ultrasound is better at detecting leiomyomas that are near to the cervix. Larger fibroids may be evaluated best using a combination of abdominal and transvaginal ultrasound techniques. At US, leiomyomas typically appear as symmetrical, well-defined, heterogeneous, solid masses. The uterus may appear bulky or enlarged, with an abnormality in the normal contour. Degenerative fibroids may have a complex appearance. Doppler US shows fibroids' circumferential vascularity, but some of them have great vascularization, while necrotic fibroids have an absence of flow.

However, pelvic MR imaging provides better soft-tissue contrast resolution, lack of operator dependence, and decreased variability in interpretation of images when compared with transvaginal US. MRI can visualize fibroids as small as 5 mm in diameter, and it is capable of differentiating adenomyosis from uterine leiomyomas. Thus, MRI is the most accurate imaging technique for detection and measuring fibroids (number, volume, and location of each fibroid; its signal intensity characteristics; and its enhancement characteristics), measuring uterine volume, and excluding whatever concomitant pathology that may increase the symptoms or may be the real cause of the symptomatology (Figs. 5.13 and 5.14).

MR imaging is a noninvasive procedure that allows the diagnosis of fibroids to be established with a great degree of confidence and affects patient treatment by reducing the number of unnecessary surgeries [1]. Accurate detection and localization of leiomyomas with MR imaging can result in planned therapies being changed or obviated [13].

For these reasons, MR imaging has become the preferred imaging modality choice for evaluating the potential candidates for uterine artery embolization, assessing the success of UFE and potential risks for complications [14, 15].

5.3 MRI Protocol

Our MR images are obtained with a 1.5-T Philips Insignia (Philips Healthcare) using a torso phased-array coil. In order to minimize artifacts caused by bowel motion, each patient receives 20 mg of butylscopolamine bromide (Buscopan, Boehringer Ingelheim) in a single dose, with an intramuscular injection. The patient is restricted to clear fluids 4 h before the examination and voided immediately before the study.

Our protocol includes imaging sequences before and after administration of an intravenous bolus of gadolinium-based contrast (0.1 mmol/kg, gadobutrol, Gadovist, Bayer):

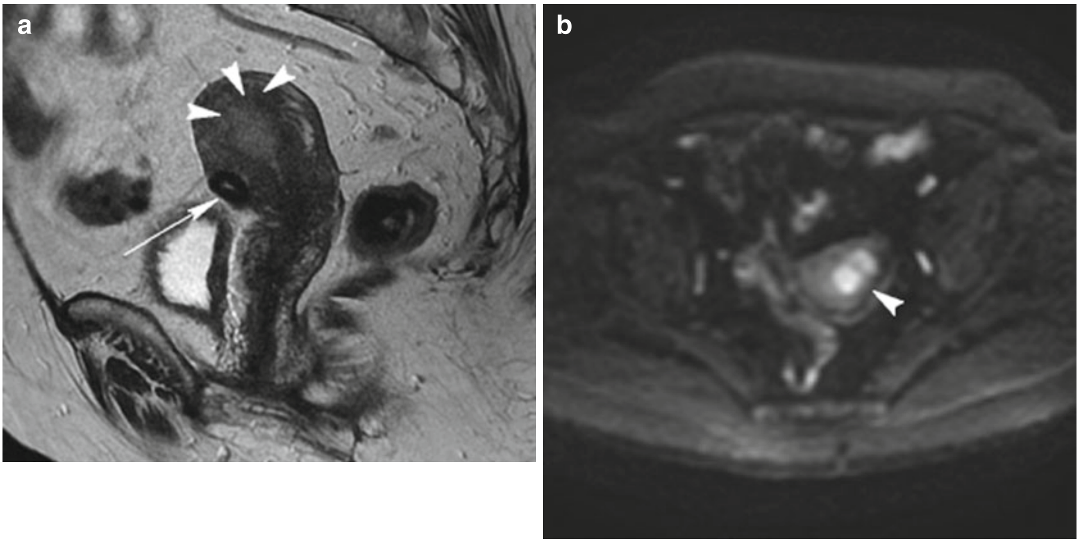

Fig. 5.13 Endometrial tumor. Patient with abnormal uterine bleeding. Sagittal T2-weighted image (TR 4,500 ms, TE 90 ms) (**a**) shows a little subserosal fibroid (*arrow*) on the inferior face of the uterus, but it shows also the loss of junctional zone at the fundus of the uterus, where there is an ill-defined homogeneous slightly hyperintense signal mass that penetrates into the myometrial wall (*arrowheads*). On axial DWI with b-Factor 800 ms image (TR 4,000 ms, TE 70 ms) (**b**), this mass (*arrowhead*) has a high restriction of signal intensity that confirms its malignant origin. Symptoms referred by the patient are due to endometrial malignant lesion

Fig. 5.14 Patient with abnormal uterine bleeding and with lumbar pain. Sagittal T2-weighted image (TR 4,400 ms, TE 90 ms) shows an intramural heterogeneous intermediate signal intensity fibroid, which is probably the cause of abnormal uterine bleeding. There is also the presence of two posterior bulgings between the two last lumbar vertebras and the first sacral ones (*arrowheads*); probably this is the cause of lumbar pain referred by the patient

- Sagittal T2-weighted turbo spin echo (TR 1,000 ms, TE 80 ms, turbo factor 22, flip angle 90°, matrix 200 × 190, slice thickness 2.5 mm, acquisition time 2.5 min)
- Coronal T2-weighted turbo spin echo (TR 3,000/5,000 ms, TE 100 ms, turbo factor 30, flip angle 90°, matrix 180 × 176, 3 mm slices, acquisition time ±2 min)
- Axial T2-weighted turbo spin echo (TR shortest automatic, TE 100 ms, turbo factor 22, flip angle 90°, matrix 200 × 196, 2.5 mm slices, acquisition time 3.5/4 min)
- Axial T1-weighted turbo spin echo (TR 400–600 ms, TE 12 ms, turbo factor 4, flip angle 95°, matrix 184 × 182, 2.5 mm slices, acquisition time ±2 min)
- Axial diffusion-weighted imaging (DWI) with b-Factor at time 0 ms and 800 ms (TR shortest automatic, TE shortest automatic, flip angle 90°, matrix 88 × 72, 5 mm slices, acquisition time ±1 min, with fat suppression SPIR)
- Sagittal DWI with b-Factor at time 0 ms and 800 ms (TR shortest automatic, TE shortest automatic, flip angle 90°, matrix 84 × 80, 3 mm slices, acquisition time ±3.5 min, with fat suppression SPIR)

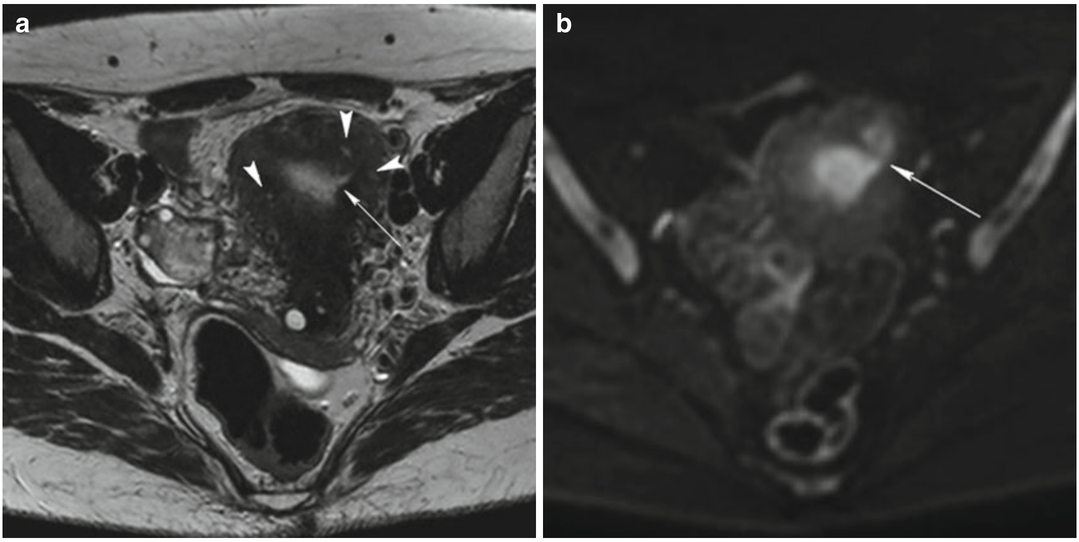

Fig. 5.15 Adenomyosis. Adenomyosis is characterized by the presence of ectopic endometrial glands and stroma within the myometrium, which results on axial T2-weighted image (**a**) as various hyperintense signal foci in the myometrium (*arrowheads*). Benign invasion of the basal endometrium into the myometrium is shown as introflection of the endometrium into the myometrium (*arrow*) on T2-weighted image (TR 4,300 ms, TE 120 ms) (**a**), but, very well, as high restriction signal intensity (*arrow*) on axial DWI with b-Factor 800 ms image (TR 2,600 ms, TE 70 ms) (**b**)

- Apparent diffusion coefficient map (ADC Map)
- Coronal THRIVE (T1 high-resolution isotropic volume excitation) (TR shortest automatic, TE shortest automatic, flip angle 10°, matrix 208 × 164, multislice 3D, acquisition time 1.5 min, with fat suppression SPAIR)
- Coronal CE-MRA, an angiographic sequence with contrast enhancement, it is a T1-TFE 3D sequence (T1-weighted fast gradient-echo) (TR shortest automatic, TE shortest automatic, flip angle 35°, matrix 360 × 360, acquisition time 22 s)
- Axial e-THRIVE (Enhanced T1 high-resolution isotropic volume excitation) (TR shortest automatic, TE shortest automatic, flip angle 10°, matrix 208 × 164, acquisition time 55 s, with fat suppression SPAIR)
- Sagittal e-THRIVE (TR shortest automatic, TE shortest automatic, flip angle 10°, matrix 208 × 164, acquisition time 1 min, with fat suppression SPAIR)
- Coronal-THRIVE (TR shortest automatic, TE shortest automatic, flip angle, matrix, acquisition time 1.5 min, with fat suppression SPAIR)

THRIVE is a T1-TFE 3D sequence (T1-weighted fast gradient-echo) with spectral fat suppression that produces isotropic voxels, and it may be useful for dynamic studies and multiplanar reconstructions.

We use this MRI protocol, which is rather complex, not exclusively for diagnosing the presence of fibroids, because the diagnosis is often clinical or with ultrasonography, but especially for evaluating potential candidates for uterine artery embolization rather for other therapeutic solutions as myomectomy or hysterectomy. Thus, our MRI protocol includes all these sequences for these reasons:

- Sagittal, axial, and coronal T2w TSE for a volumetric uterus and fibroids' study, for evaluating their relationship with other pelvic structures and for excluding whatever concomitant pathology.
- Axial T1w TSE and coronal T1w with fat suppression for evaluating the presence of fatty degeneration and of hemorrhagic intratumoral areas.
- DWI for excluding malignant pathology and for evaluating possible presence of adenomyosis, because this sequence outlines very well the endometrium and so it is possible to visualize the introflections of endometrium in this pathologic condition (Fig. 5.15); with DWI

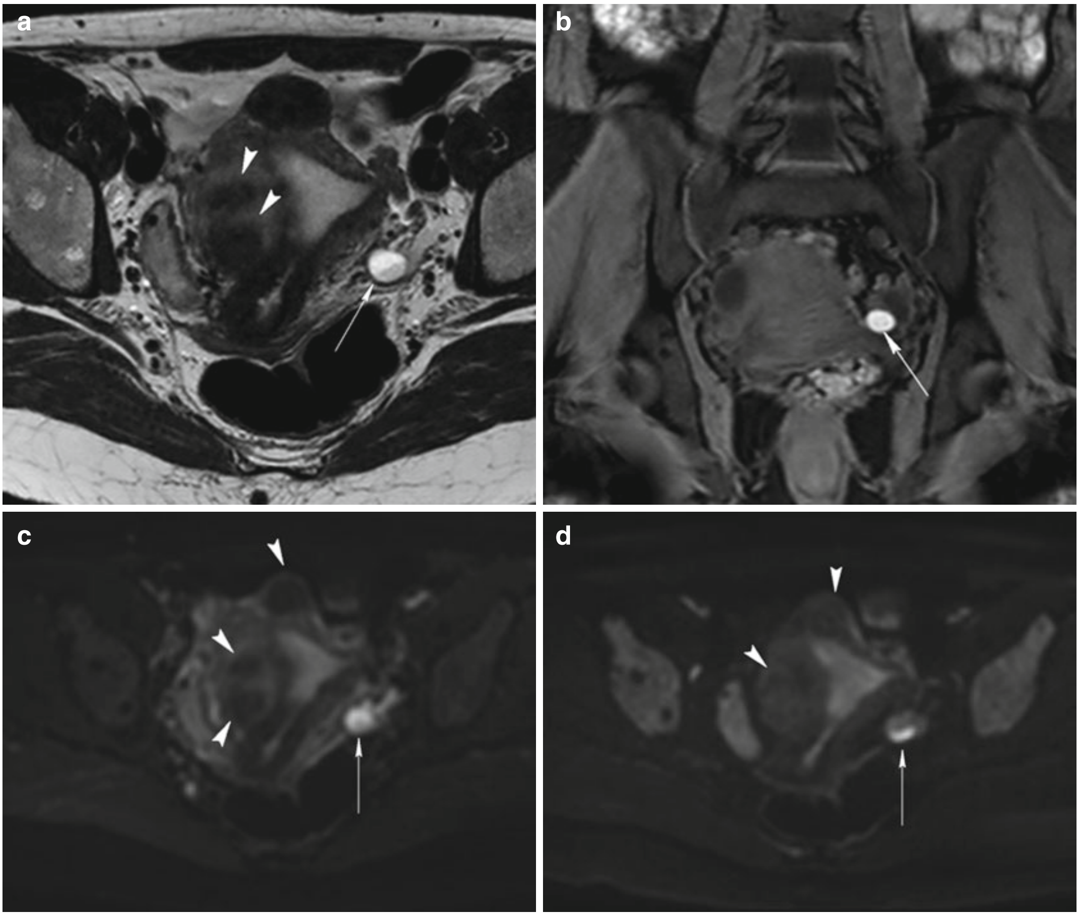

Fig. 5.16 Endometriosic adnexal cyst. Axial T2-weighted image (TR 2,900 ms, TE 80 ms) (**a**) shows a high hyperintense signal intensity area into left adnexa, with a slightly low-signal-intensity level into (*arrow*) and two heterogeneous low-signal-intensity leiomyomas (*arrowheads*). Coronal fat-suppressed T1-weighted image (TR 4 ms, TE 2 ms) (**b**) confirms hyperintense signal intensity adnexal lesion (*arrow*). Axial DWI with b-Factor 0 ms (TR 2,600 ms, TE 70 ms) (**c**) and with b-Factor 800 ms (TR 2,600 ms, TE 70 ms) (**d**) images show increased high restriction of signal intensity in left adnexa 8 (*arrow*) and moderate restriction of signal intensity of the leiomyomas (*arrowheads*). Fat-suppressed T1-weighted image and high restriction of signal intensity on DWI images demonstrate presence of hemoglobin's degradation products (endometriosic left adnexal cyst or endometrioma)

we may also evaluate whatever concomitant endometriosic focus in the pelvis (Fig. 5.16).

- Angiographic images are helpful to obtain a better understanding of the arterial anatomy of the uterus and of the fibroids before embolization and may enable detection of variations in the vascularization of uterine fibroids (Fig. 5.25).
- Axial, sagittal, and coronal T1w contrast-enhanced images with fat suppression for a volumetric evaluation of the uterus and fibroids' enhancement characteristics, and for evaluating enhancement characteristics of possible other concomitant pelvic lesions.

5.4 MR Imaging Appearance of Leiomyomas

The signal intensity of leiomyomas depends on the proportion of cellular fascicles and extracellular matrix [16].

5.4.1 Nondegenerated Fibroids

Nondegenerated fibroids have a typical appearance at MR imaging: well-circumscribed masses with homogeneously decreased signal intensity

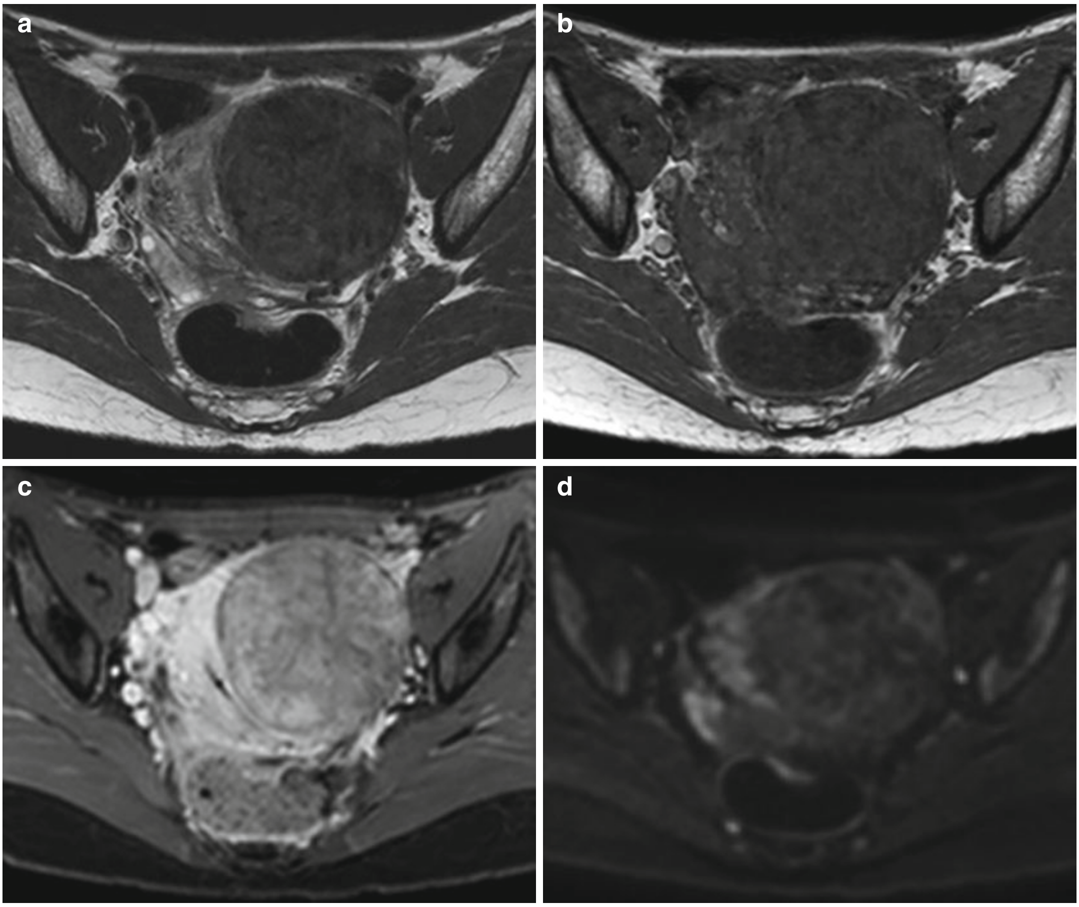

Fig. 5.17 Nondegenerated massive intramural fibroid. Well-circumscribed masses with homogeneously decreased signal intensity compared with that of the outer myometrium on T2-weighted image (TR 3,250 ms, TE 80 ms) (**a**), with homogeneously isointense signal intensity compared with that of the outer myometrium on T1-weighted image (TR 590 ms, TE 12 ms) (**b**), and with heterogeneous signal contrast-enhancement lower than that of adjacent myometrium on contrast-enhanced fat-suppressed T1-weighted image (TR 2,900 ms, TE 0 ms) (**c**). On DWI with b-Factor 800 ms image (TR 4 ms, TE 2 ms) (**d**) fibroid shows no restriction of signal intensity

compared with that of the normal myometrium on T2-weighted images [8, 17] and with homogeneously isointense signal compared with that of the normal myometrium on T1-weighted images. On T1-weighted contrast-enhanced images, they are homogeneous enhancing masses, but less than normal myometrium (Fig. 5.17).

Fibroids with hypointense signal intensity on T2-weighted images are characterized by a predominant extracellular matrix composed of vascularized connective tissue with whorl-ring bundles of smooth muscle cells. Fibroids with relatively increased T2-weighted signal intensity and homogeneous enhancement on early contrast-enhanced images are usually cellular fibroids, which are composed of densely packed cellular fascicles of smooth muscle with little intervening collagen. Cellular leiomyomas can be distinguished from other types of leiomyomas by the abundance of its cellular content and proliferative cells [8, 16, 17].

Some fibroids have a high-signal-intensity rim on T2-weighted images, which represents a pseudocapsule of dilated lymphatic vessels, dilated veins, or edema and correspond to peritumoral rim enhancement [9].

On DWI images, fibroids have variable signal intensity. In our experience, we have seen that DWI signal intensity of each fibroid is very well correlated with the symptomatology of the patient. We have seen that, after uterine fibroid embolization, there is a good correlation between fibroids' decreased signal intensity on DWI images and symptoms' resolution.

5.4.2 Degenerated Fibroids

Degenerated fibroids have variable appearance on T1-weighted, T2-weighted, and contrast-enhanced images.

Interstitial edema, the initial sign of degeneration, is detected as a high-signal-intensity region on T2-weighted images and shows enhancement with Gd-DTPA.

5.4.2.1 Hyaline Degeneration

Fibroids with hyaline, not liquefied, degeneration have a variable signal intensity on T1-weighted images (they may have increased signal intensity) and a decreased signal intensity on T2-weighted images. Thus, they could not be distinguished from smooth muscle whorls on T1- and T2-weighted images. However, undegenerated leiomyoma could be distinguished from hyaline degeneration, because the former is slightly enhanced by Gd-DTPA, but the latter is not.

5.4.2.2 Cystic Degeneration

Leiomyomas with cystic degeneration show low signal intensity on T1-weighted images and high signal on T2-weighted images, and the cystic areas do not enhance after intravenous administration of gadolinium contrast material (Fig. 5.18).

5.4.2.3 Myxoid Degeneration

Leiomyomas with myxoid degeneration have components of both low signal intensity and extremely high signal intensity on T2-weighted images and heterogeneous low signal intensity on T1-weighted images; hyperintensity signal foci on T2-weighted images have minimal contrast enhancement (Fig. 5.19).

5.4.2.4 Red Degeneration (Hemorrhagic Necrosis)

Fibroids with red degeneration have peripheral or diffuse high signal intensity on T1-weighted images and variable signal intensity with or without a low-signal-intensity rim on T2-weighted images. These findings correspond with numerous dilated vessels filled with red blood cells at the periphery of the lesion. The high signal intensity on T1-weighted images is secondary to proteinaceous content of the blood or the T1-shortening effects of methemoglobin. When the high signal intensity is isolated to the rim of the fibroid, it has been hypothesized that the blood products are confined to thrombosed vessels that surround the lesion [18]. Coagulative necrosis does not enhance after intravenous administration of gadolinium contrast material (Fig. 5.20).

5.4.2.5 Fatty Degeneration

Fat is usually microscopic, and it is associated with advanced hyaline degeneration.

5.4.2.6 Fibroid's Calcification

Fibroids with calcific degeneration have low signal intensity on T1- and on T2-weighted images, and they do not enhance.

5.4.2.7 Necrotic Degeneration

Necrotic areas have variable T1-weighted signal intensity, low T2-weighted signal intensity, and they do not enhance.

5.4.2.8 Sarcomatous Transformation

The prevalence of sarcomatous transformation in a preexisting benign uterine leiomyoma is extremely rare (<0.05 % of resected leiomyomas). Although it has been suggested that a heterogeneous, irregular, not well-defined leiomyoma on T2-weighted images is suggestive of sarcomatous transformation [19], the specificity of this finding has not been established, and the diagnosis is often first established by a pathologist after surgical removal of the suspected mass.

5.5 Differential Diagnosis

Other entities can have similar clinical presentations, such as pelvic pain and/or abnormal uterine bleeding, and need to be distinguished

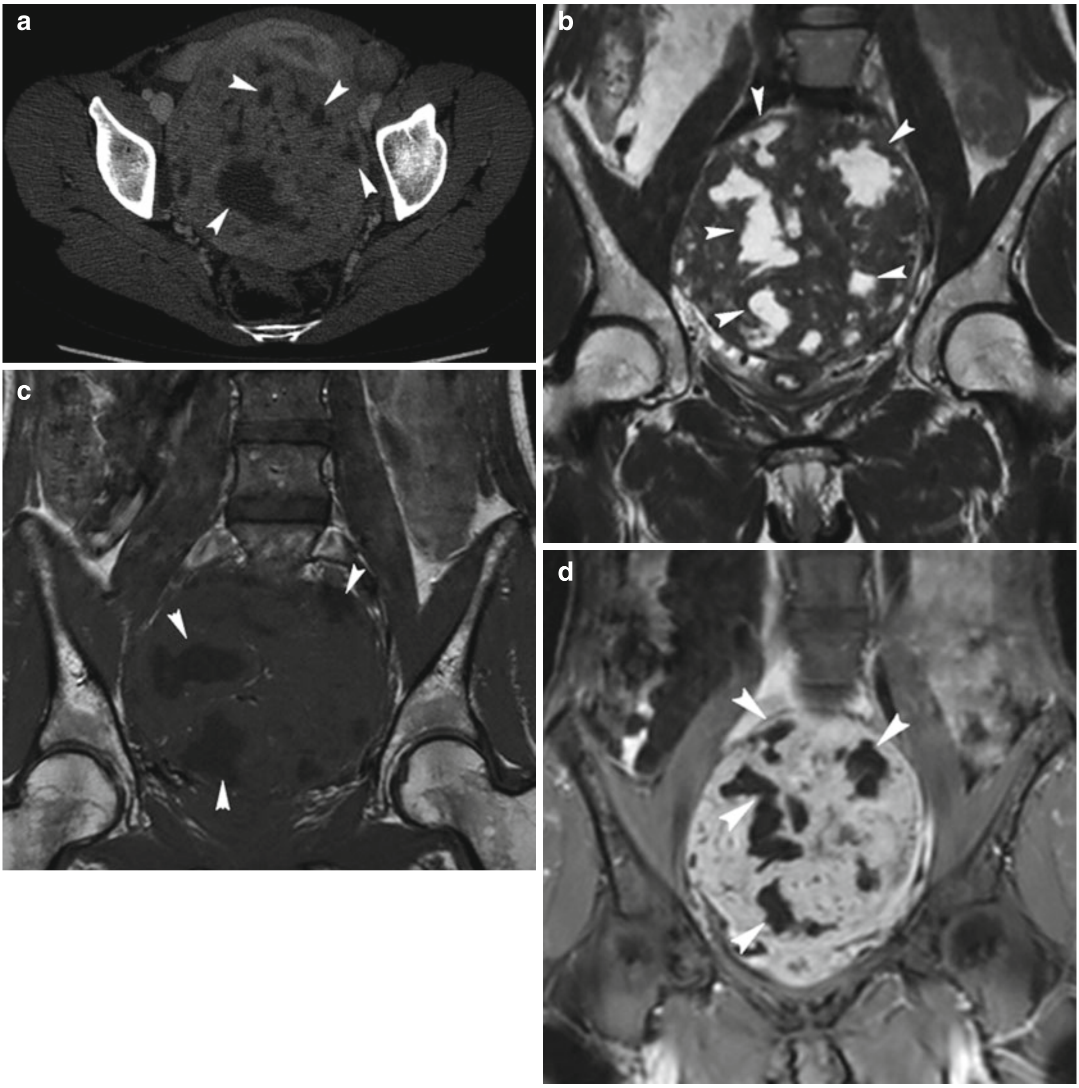

Fig. 5.18 Fibroid with cystic degeneration. Axial CT scan (**a**) shows a large uterine mass with some not-enhancing liquid areas. MRI confirms the presence of a large intramural fibroid with several areas in cystic degeneration; these areas demonstrate very high signal intensity on T2-weighted image (TR 4,300 ms, TE 80 ms) (**b**), low signal intensity on T1-weighted image (TR 530 ms, TE 12 ms) (**c**), and no enhancement on contrast-enhanced fat-suppressed T1-weighted image (TR 4 ms, TE 2 ms) (**d**). Areas in cystic degeneration are marked with *arrowheads* in all images.

from leiomyomas, because of the necessity of differential therapeutic strategies. MR imaging is superior than US for differential diagnosis of adenomyosis and evaluation of the adnexa and endometrium for potential disease, especially when the uterus is bulky and also when leiomyomas coexist and distort pelvic anatomy.

5.5.1 Adenomyosis

Adenomyosis is characterized by a benign invasion of the basal endometrium into the myometrium, which results in the presence of ectopic endometrial glands and stroma within the myometrium, with reactive hypertrophy of the surrounding myometrial smooth muscle.

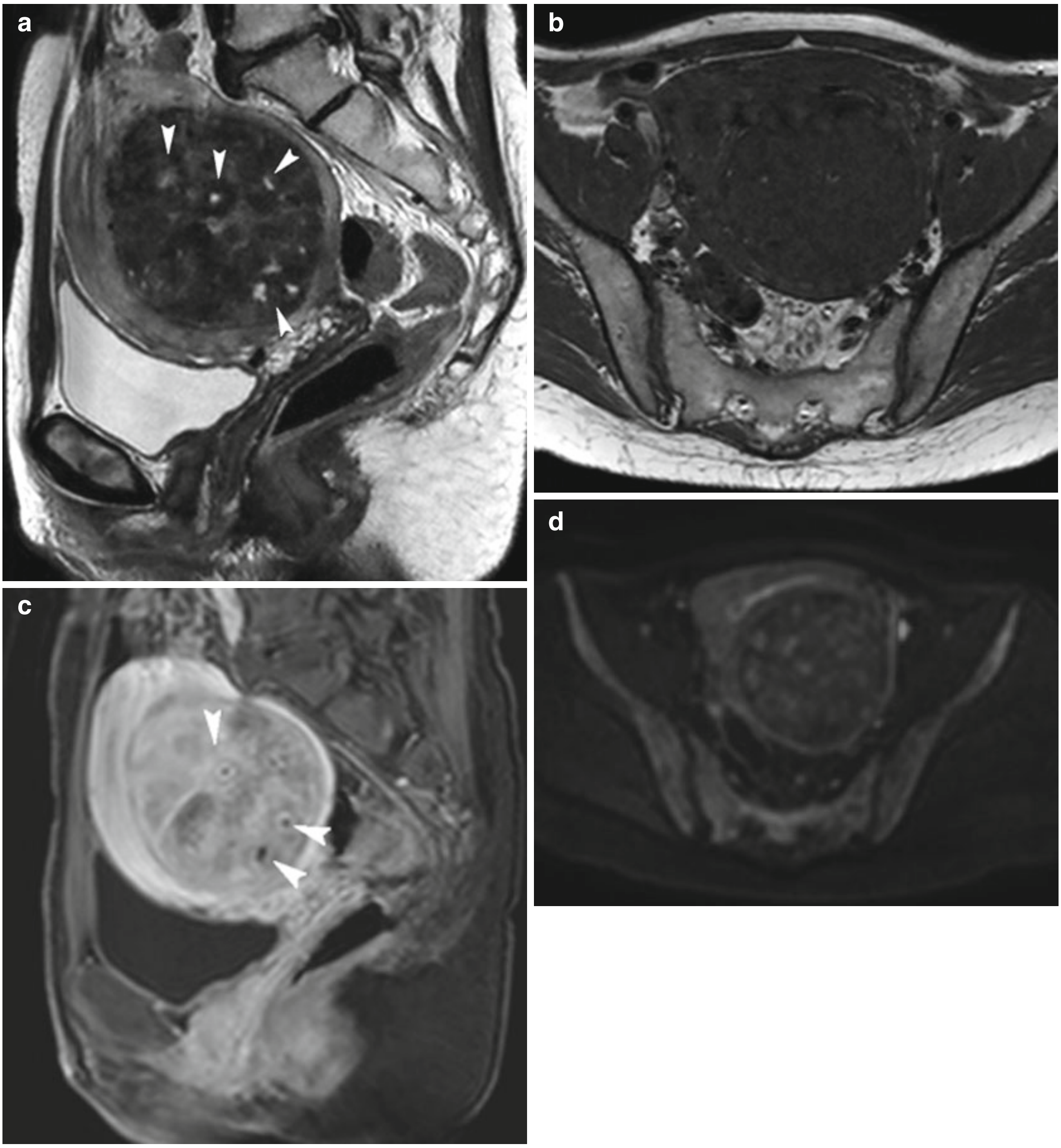

Fig. 5.19 Fibroid with myxoid degeneration. A large intramural low-signal-intensity fibroid with several hyperintensity foci (*arrowheads*) on sagittal T2-weighted image (TR 3,600 ms, TE 80 ms) (**a**). On axial T1-weighted image (TR 530 ms, TE 12 ms) (**b**), fibroid demonstrates heterogeneous low signal intensity, also in degenerated foci. On sagittal contrast-enhanced fat-suppressed T1-weighted image (TR 4 ms, TE 2 ms) (**c**), fibroid has high signal enhancement, but slightly lower than that of adjacent myometrium, and some intratumoral tissue with high signal intensity on T2-weighted image enhances, while others are not (*arrowheads*). The enhancement of these degenerated foci indicates that tissue does not represent intratumoral cyst or necrosis. On axial DWI with b-Factor 800 ms image (TR 2,800 ms, TE 70 ms) (**d**), we may see a slightly restriction signal intensity in degenerated tissue. The bladder and rectum are pressed by voluminous fibroid

Adenomyosis occurs in focal and diffuse forms, the latter being the more common appearance, and may coexist with fibroids (Fig. 5.21).

In contrast to fibroids, adenomyosis appears as a diffuse, ill-defined lesion extending subjacent to the endometrium. On T2-weighted images, the lesion shows a relatively homogeneous low

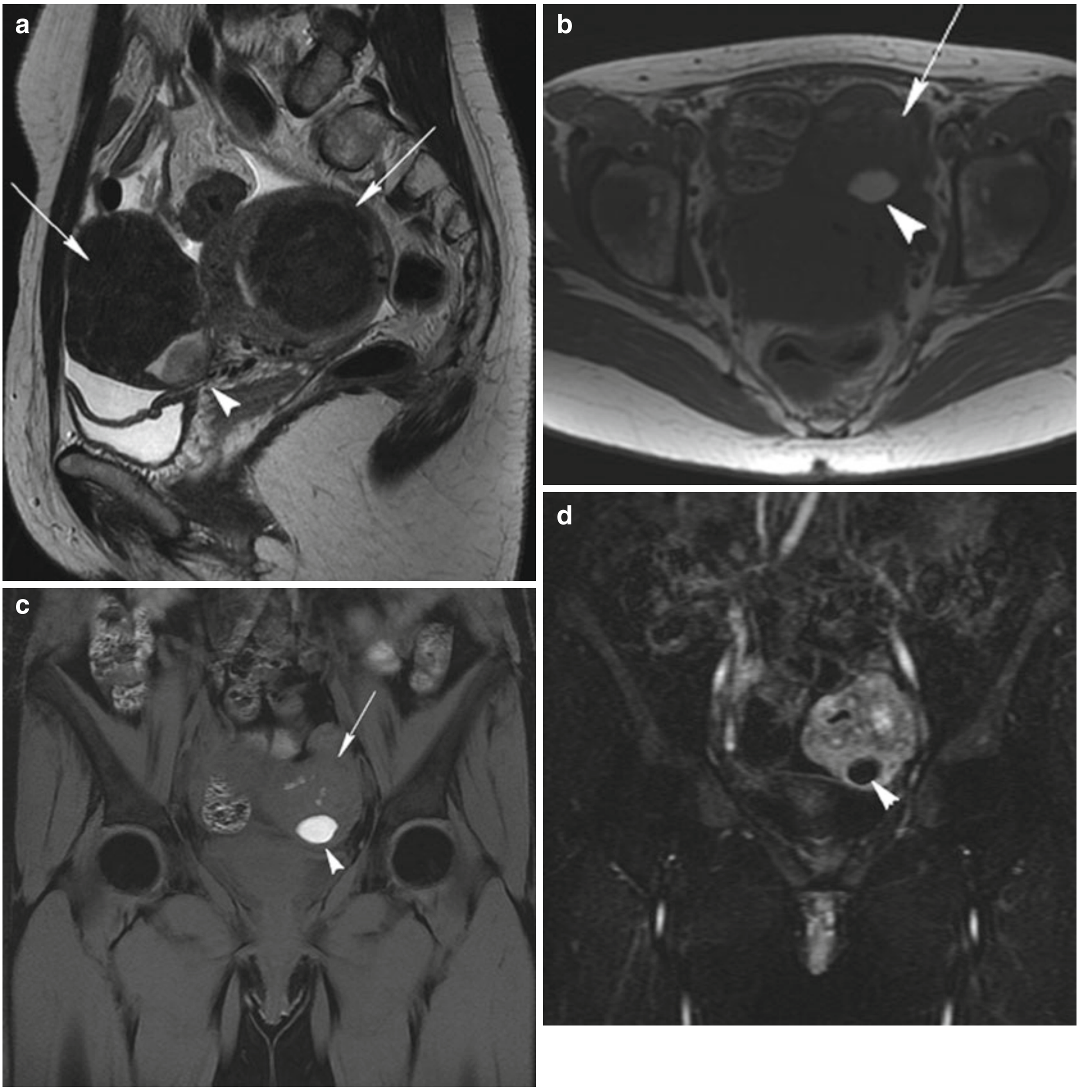

Fig. 5.20 Fibroid with red degeneration. Sagittal T2-weighted image (TR 4,500 ms, TE 90 ms) (**a**) shows two hypointense well-defined uterine masses (*arrows* in **a**, **b** and **c**), one is an intramural non-degenerated fibroid, and the other is a subserosal pedunculated fibroid with a well-defined hyperintense area, which has some content with intermediate signal intensity (*arrowhead* in all images) that is a degenerated focus. This degenerated area has very high signal intensity on axial T1-weighted (TR 600 ms, TE 10 ms) (**b**), and coronal fat-suppressed T1-weighted (TR 280 ms, TE 2 ms) (**c**) images, and it does not enhance on coronal contrast-enhanced fat-suppressed T1-weighted image (TR 6 ms, TE 2 ms) (**d**). The high signal intensity on T1-weighted images is secondary to proteinaceous content of the blood or the T1-shortening effects of methemoglobin. Subserosal fibroid has an area of hemorrhagic degeneration ("red degeneration"). Because of the presence of a pedunculated subserosal fibroid with a narrow stalk and an area with hemorrhagic degeneration, this patient is not eligible to UFE

intensity signal, embedded with sparse, tiny high-intensity spots. On T1-weighted images, it is isointense with the surrounding myometrium, but some of high-intensity spots are clearly visible. Small foci of high signal intensity on T2-weighted images represent the ectopic endometrial glands; some of these, that have also high signal intensity on T1-weighted images, correspond to hemorrhage, and thus they may cause magnetic susceptibility pitfalls [20, 21].

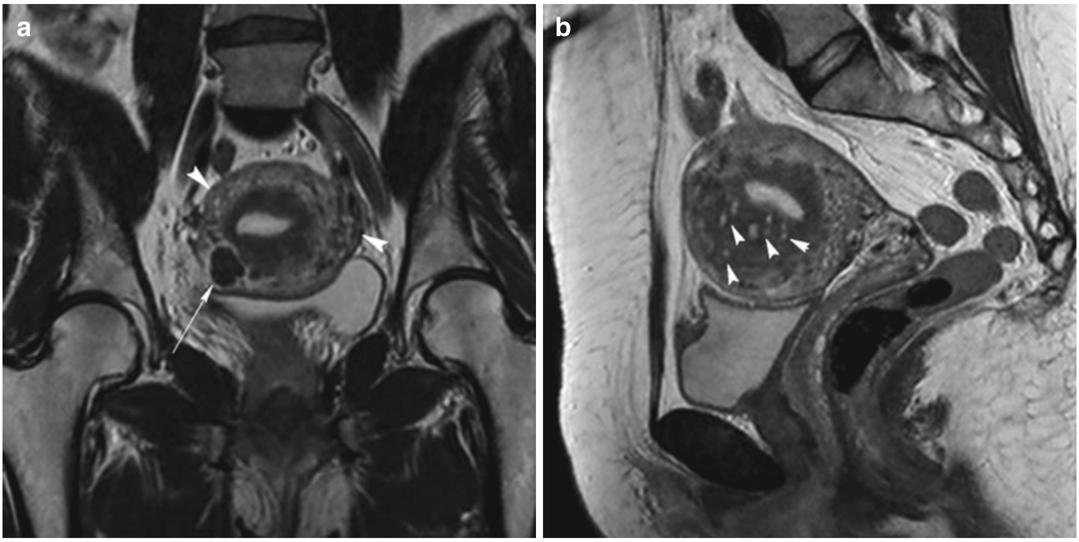

Fig. 5.21 Diffuse adenomyosis coexists with intramural leiomyoma. Coronal (TR 3,700 ms, TE 100 ms) (**a**) and sagittal (TR 3,250 ms, TE 80 ms) (**b**) T2-weighted images show several punctate foci of high signal intensity (*arrowheads*) in the myometrium. Region of junctional zone is widened and demonstrates intermediate low-signal-intensity characteristics of diffuse adenomyosis. An intramural homogeneous low-signal-intensity leiomyoma coexists (*arrow* in **a**)

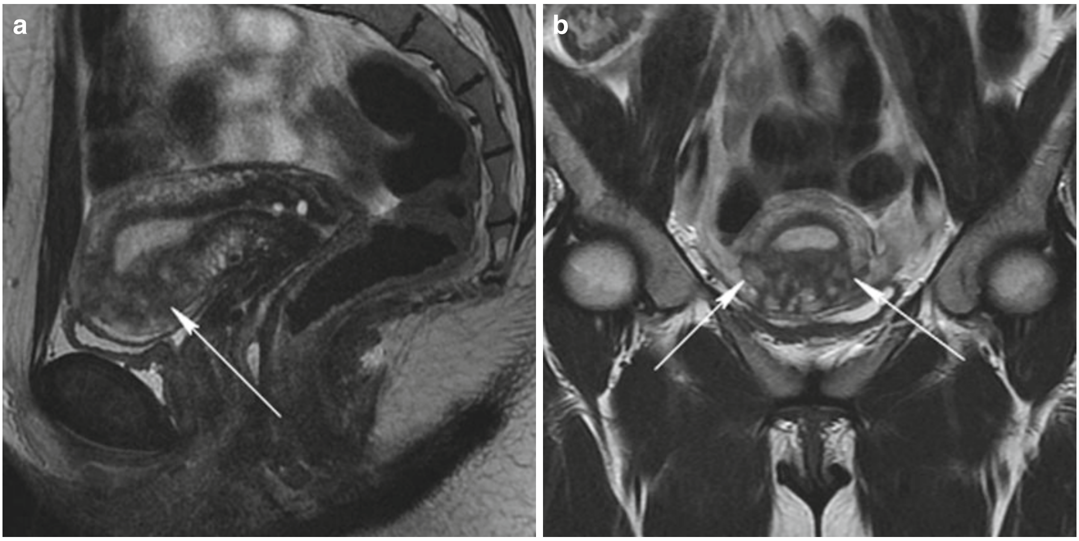

Fig. 5.22 Adenomyosis. Sagittal (TR 4,500 ms, TE 90 ms) (**a**) and coronal (TR 4,300 ms, TE 110 ms) (**b**) T2-weighted images show an ill-defined low-signal-intensity area in the inferior uterine region, with several punctate foci of high signal intensity (*arrows*). Endometrium is thickened and it has an irregular contour; junctional zone is lost. Small hyperintense foci represent ectopic endometrial glands

In its focal form, adenomyosis appears an ill-defined, poorly marginated area of low signal intensity within the myometrium on T2-weighted images.

Extensive involvement of adenomyosis distorts endometrium that appears with an irregular contour and with the loss of the junctional zone (Fig. 5.22).

5.5.2 Solid Adnexal Mass

Ovarian fibromas and Brenner tumors are benign ovarian neoplasms that have a large fibrous component and can have signal intensity similar to that of a pedunculated leiomyoma. If MR imaging can demonstrate continuity of an adnexal mass with the adjacent myometrium, then a diagnosis of leiomyoma can be established, but, if MR imaging can show fibromas or Brenner tumors surrounded by ovarian stroma and follicles, thus the ovarian origin of the mass is established.

5.5.3 Focal Myometrial Contraction

Uterine contractions can appear as transient hypointense T2-weighted masses and may simulate fibroids or focal adenomyosis on MR imaging. Because the contractions are transient, resolution of the mass at subsequent imaging allows the diagnosis to be established [22].

5.5.4 Uterine Leiomyosarcoma

Leiomyosarcoma may arise in a previously existing benign leiomyoma (sarcomatous transformation) or independently from the smooth muscle cells of the myometrium. Although it has been suggested that an irregular margin of a leiomyoma at MR imaging is suggestive of sarcomatous transformation, the specificity of this finding has not been established. The diagnosis of leiomyosarcoma is often established by a pathologist after surgical removal.

5.5.5 Malignant Perivascular Epithelioid Cell Tumor

Perivascular epithelioid cell tumors (PEComas) are a rare group of mesenchymal neoplasms composed of distinctive cells that show a focal association with blood vessel walls and usually express melanocytic and smooth muscle markers. The cell of origin of these tumors is unknown. Malignant PEComas most often arise in the kidneys and uterus and metastasize to the lungs, liver, or peritoneum. Because this malignant tumor tends to be well-circumscribed large mass with no infiltration of the adjacent organs, characterized by high signal intensity on T2-weighted images and by homogeneous enhancement, it mimics fibroids on imaging; thus, it should be considered in the differential diagnosis of fibroids [23].

5.6 Role of MR Imaging in Uterine Fibroid Embolization

5.6.1 Pre-procedure MR Imaging

Uterine fibroid embolization has become an accepted method for the treatment of symptomatic uterine fibroids. It has been shown to reduce the hospital stay and the rate of major complications when compared with myomectomy or hysterectomy. Although the minimally invasive, uterus-sparing nature of this technique is appealing, the chances of satisfactory symptomatic improvement and the risk of significant complications are affected by a number of anatomic factors. For these reasons, it is very important to identify the number, size, and location of the fibroids and the presence of coexisting uterine and adnexal disorders with an adequate pre-procedure imaging in order to determine the suitability of women who have uterine fibroids for uterine fibroid embolization.

Ultrasonography is widely available, can accurately confirm the presence of leiomyomas and uterine enlargement, and should be the first line of imaging, but, the pre-procedure evaluation can be made with much greater accuracy using pelvic MR imaging as compared with ultrasonography. MRI reveals also additional informations, such as the presence of adenomyosis and other pelvic disorders [24]. So, in our practice, pelvic MRI is routinely performed for pre-procedure evaluation.

In pre-procedure pelvic MRI, we must evaluate all these factors:

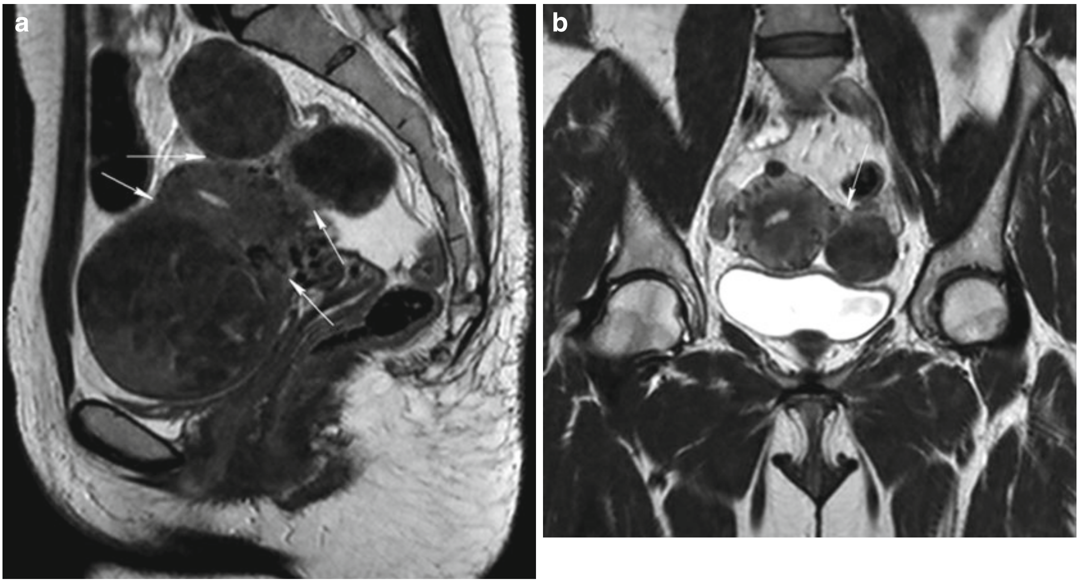

Fig. 5.23 Pedunculated subserosal fibroids with a narrow stalk. Sagittal (TR 3,000 ms, TE 80 ms) (**a**) and coronal (TR 3,700 ms, TE 80 ms) (**b**) T2-weighted images show two cases of multiple pedunculated subserosal hypointense signal fibroids with a fibroid's junction zone to uterine wall less than one third of the entire fibroid's circumference (*arrows*). In these patients, uterine fibroid embolization is contraindicated because of high risk of infarction of the stalk of the fibroid and the subsequent migration of the fibroid into the peritoneal cavity

- Size of uterus
- Number of fibroids and size of the greatest
- Location of each fibroid (submucosal, intramural, subserosal, or rare locations)
- Size of the base of the stalk, if pedunculated
- Size of submucosal interface, if intracavitary
- Signal intensity and enhancement characteristics
- Arterial anatomy of the uterus and of the greater fibroids (with MIP reconstructions of angiographic MR images)
- Presence of adenomyosis
- Presence of concomitant pelvic pathologies

There are some anatomic considerations in patient selection for eligibility for embolization. Although both single and multiple fibroids can be treated with UFE, patients with very large uteri or fibroids (size >20 cm) have less uterine and fibroid shrinkage after UFE than others and tend to have less symptom improvement [1, 25]. Also women with hypervascular leiomyomas have less symptom improvement than others.

Certain anatomic fibroid subtypes deserve special consideration. Submucosal or subserosal pedunculated fibroids may be predictors of complications after UFE. Patients with intracavitary fibroids treated with UFE have an increased risk for the vaginal passage of necrotic tissue, which results in important abdominal pain, increased cramping, bleeding, or infection.

Pedunculated subserosal fibroids are considered a relative contraindication to uterine fibroid embolization, depending on the fibroid size and the size of the stalk, although the inclusion criteria for UFE vary considerably among institutions [24]. In some studies, it has been shown that presence of pedunculated subserosal fibroids in which the diameter of the stalk is 50 % narrower than the diameter of the fibroid is a contraindication to uterine fibroid embolization [15]. In other studies, it has been shown that pedunculated subserosal fibroid with a stalk diameter inferior to 2 cm is not candidable to UFE [15]. In our experience, when the base of the stalk is less than one third of the entire fibroid's diameter, it is critical, because there is a high risk of infarction of the stalk of the fibroid and subsequent detachment of the fibroid, and its migration into the peritoneal cavity, which could lead to peritonitis, persistent pain, or infection (Figs. 5.23 and 5.24).

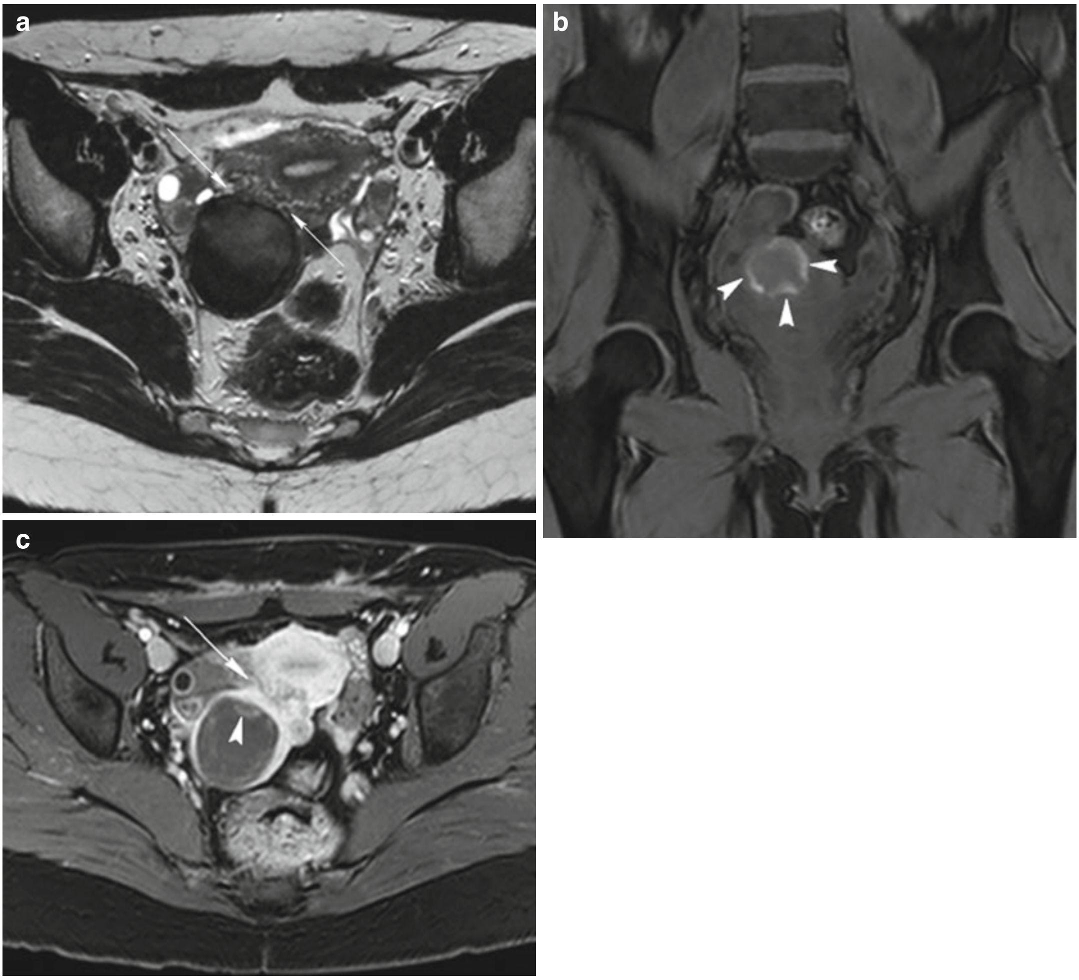

Fig. 5.24 Pedunculated subserosal fibroid with intratumoral hemorrhage. Axial T2-weighted image (TR 4,800 ms, TE 120 ms) (**a**) shows a large well-defined pedunculated subserosal fibroid with heterogeneous low signal intensity; it has a narrow stalk (*arrow* in **a** and **c**). Coronal fat-suppressed T1-weighted (TR 4 ms, TE 2 ms) (**b**) and axial contrast-enhanced fat-suppressed T1-weighted (TR 4 ms, TE 2 ms) (**c**) images demonstrate some little areas with high signal intensity (*arrowheads*), which are hemorrhagic intratumoral foci. In this patient, uterine fibroid embolization is contraindicated because of high risk of infarction of the stalk of the fibroid and the intratumoral hemorrhagic foci

Cervical fibroids may not become devascularized after UFE, probably because of an additional or alternative blood supply to the cervix (Fig. 5.10).

Another contraindication to UFE is the presence of intratumoral hemorrhagic foci, which are areas with high signal intensity on fat-suppressed T1-weighted images (Fig. 5.24).

Identification of blood vessels' anomalies is very important before the procedure, and it is possible with angiographic MR images and MIP reconstructions, which show uterine arteries and provide a "road map" prior the embolization (Fig. 5.25).

Knowledge of the presence of adenomyosis before the procedure is important in order to inform the patient that the response can be more variable in this situation (Fig. 5.21).

The presence of concurrent uterine, ovarian, or pelvic disorders is significant in the pre-procedure evaluation of patients for UFE. Not only can symptoms of other disorders such as endometriosis, ovarian tumor, or chronic pelvic infection mimic those of uterine fibroids, but also

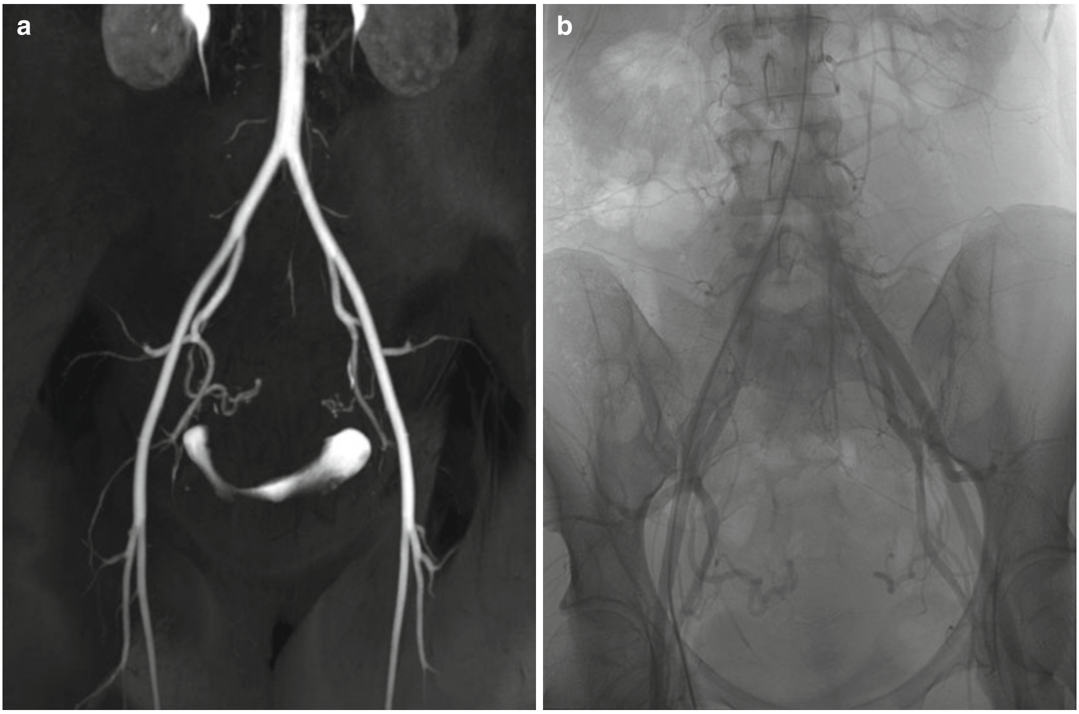

Fig. 5.25 Pelvic arterial vascularization and fibroid's arterial vessels. Note agreement of representation of pelvic vessels between MIP reconstruction of MRI angiographic arterial phase image (TR 4 ms, TE 1.5 ms) (**a**) and flush pelvic aortogram (**b**)

other disease processes may be incidentally found in the initial workup. Thus, the therapeutic options may be altered if another significant disorder is present [24] (Fig. 5.13).

5.6.2 Procedure

UFE is an angiographic procedure that is typically performed by using a unilateral femoral artery approach. Some operators use a bilateral femoral artery approach. In almost all cases, bilateral uterine artery catheterization and embolization are needed, since most uterine fibroids receive blood supply from both uterine arteries. After uterine arteriography, embolic material is injected into both uterine arteries to occlude the vessels of the fibroid. In our institution, we use acrylic polymer microspheres impregnated with porcine gelatine (Embosphere, Biosphere Medical S.A., Roissy, France) of range size 500–700 μm or 700–900 μm. The goal is to occlude the vessels of the fibroid but not to completely occlude the uterine artery (Fig. 5.26). It is appropriate to stop embolization when the fibroid branch arteries have become occluded, even if antegrade flow is still present in the main uterine artery.

Fig. 5.26 Uterine fibroid embolization (UFE). Digital subtraction of pelvic aortogram (**a**). Digital subtraction angiograms obtained with selective left (**b**) and right (**c**) uterine artery (*arrow*) injection show the characteristic arterial course and numerous intramural spiral arterioles (*arrowheads*). In (**d**) image we see that the fibroid branch arteries have become occluded, but the uterine artery has become not completely occlude (*arrow*): this is the goal of UFE. Digital subtraction subsequent angiograms obtained with selective right uterine artery injection in another woman (**e**, **f**) show progression of embospheres (*arrows*) into fibroid's vessels

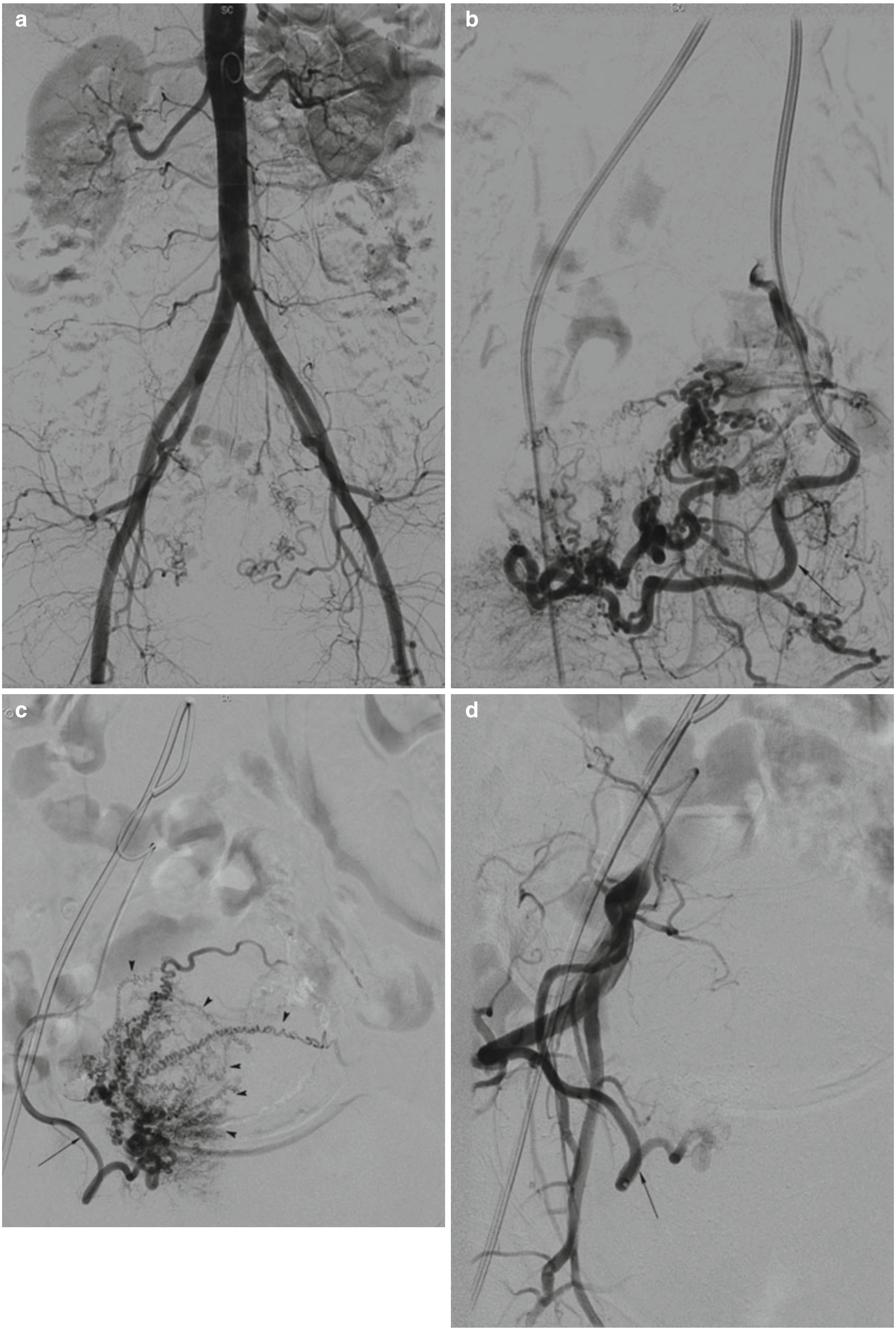
a
SC
b
SC
c
SC
d

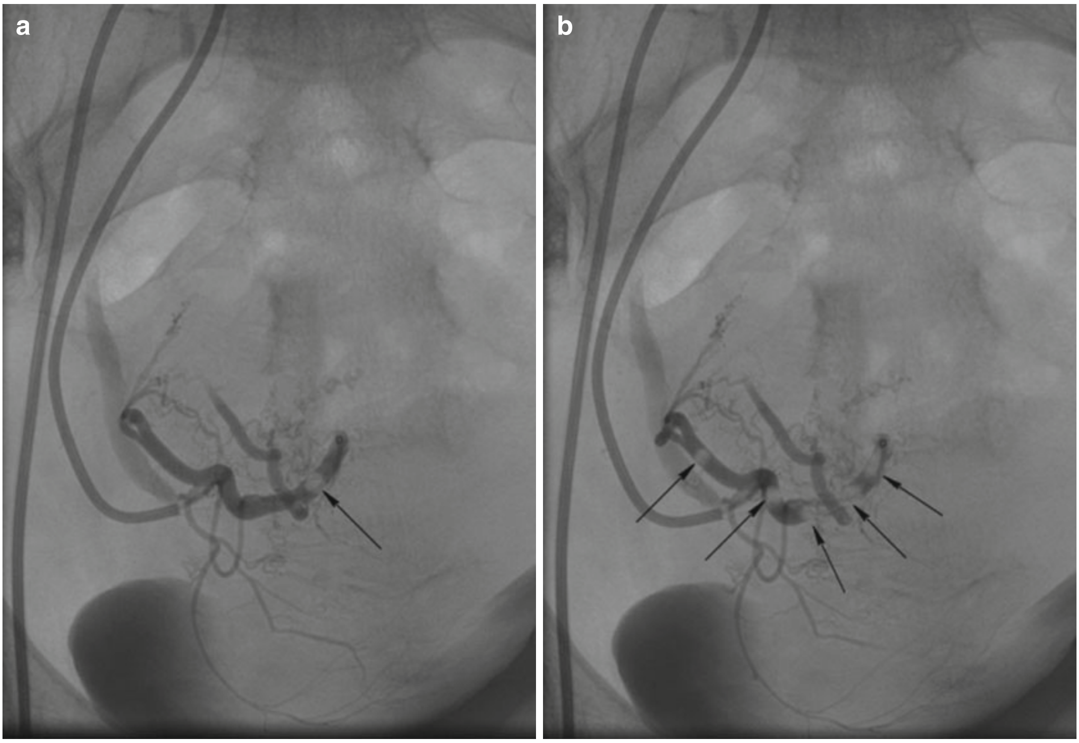

Fig. 5.26 (continued)

As a percutaneous interventional technique, this procedure may offer the advantages of avoidance of surgical risks, potential preservation of fertility, and shorter hospitalization [26].

5.6.3 Post-procedure MR Imaging

Although rare, complications after uterine fibroid embolization have been reported, and MR imaging may aid in diagnosis or exclusion of several post-procedure complications.

Minor complications include hematoma, transient pain, or post-embolization syndrome (pelvic pain, cramping, nausea and vomiting, low-grade fever, and general malaise), and transcervical expulsion of necrotic tissue (Fig. 5.27). Potential major complications include premature menopause (loss of ovarian function), bladder necrosis, and infection (tubo-ovarian abscess, endometritis, pyomyoma, and uterine necrosis) [1].

In patients who have no complications and have symptomatic improvement, we perform a pelvic contrast enhancement ultrasonography after 6 months since the procedure and a follow-up MR imaging after 1 year since procedure, which can be used to monitor the results of embolization by demonstrating the degree of shrinkage and the loss of enhancement of the leiomyomas. The success of UFE is characterized by a significant reduction in mean uterine and fibroid volumes, and by fibroids' infarction, while residual myometrium demonstrates reperfusion and enhances vividly (Fig. 5.28).

The treated leiomyomas show similar changes in signal intensity after UFE, that is, high signal intensity on T1-weighted images, homogeneous

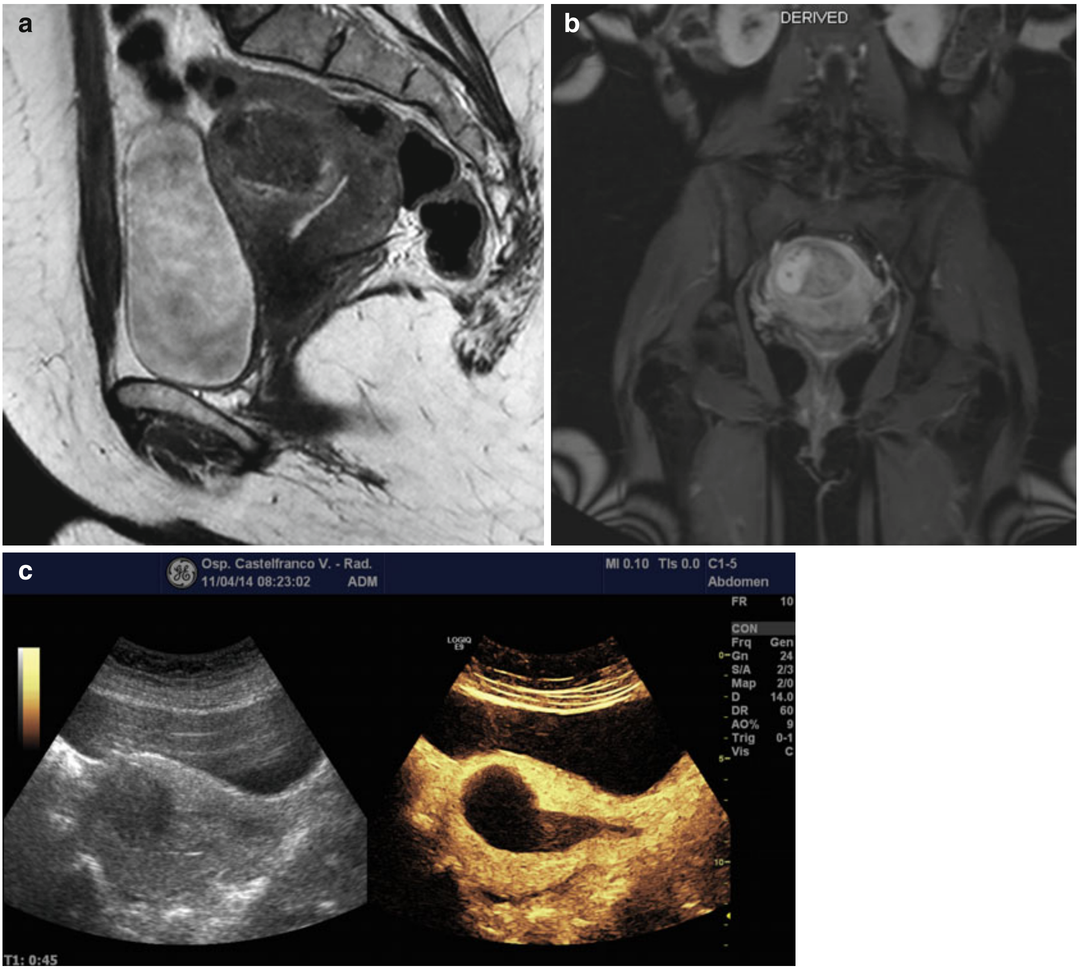

Fig. 5.27 MR images of an intramural uterine fibroid pre-procedure and 2 months post-procedure CEUS image. Sagittal T2-weighted image (TR 3,700 ms, TE 80 ms) (**a**) shows a large intramural heterogeneous low-signal-intensity fibroid; sagittal contrast-enhanced fat-suppressed T1-weighted image (TR 4 ms, TE 2 ms) (**b**) shows dishomogeneous low signal intensity of the fibroid, with a region with high signal intensity. This patient complains small continuous uterine bleeding after UFE. CEUS image (**c**) 2-month post-procedure of uterine fibroid embolization shows necrotic tissue in the uterine cavity

low signal intensity on T2-weighted images, and no detectable enhancement after gadolinium contrast material administration [14]. These signal intensity changes are typical of blood products and depend on the age of hemorrhage within the fibroid; this condition is known as "hemorrhagic infarction." As already explained, in our experience, we have seen that, after uterine fibroid embolization, there is a good correlation between fibroids' decreased signal intensity on DWI images and symptomatic improvement (Fig. 5.29).

However, in some cases, the fibroid may not be completely infarcted after embolization, and, thus, there may be residual areas of perfusion (Fig. 5.30).

Images of follow-up must be always interpreted in conjunction with clinical symptoms.

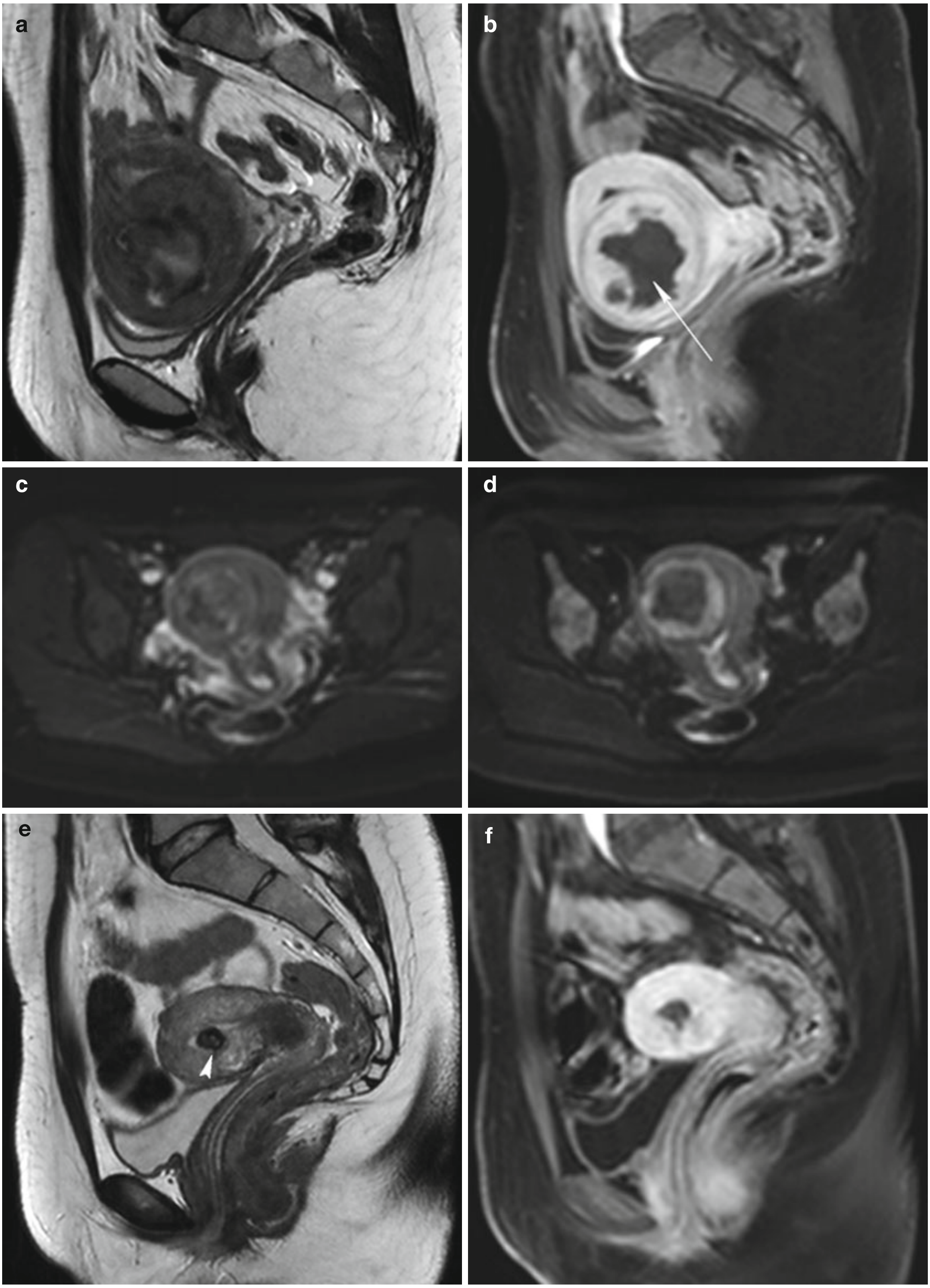
a
b
c
d
e
f

Fig. 5.28 Voluminous intramural fibroid pre-procedure and 1-year post-procedure of uterine fibroid embolization. Sagittal T2-weighted image (TR 2,900 ms, TE 80 ms) (**a**) shows a large intramural heterogeneous low signal intensity on T2-weighted fibroid in myxoid degeneration, which has a peripheral high signal enhancement and a central no enhancement area (*arrow*) on contrast-enhanced fat-suppressed T1-weighted image (TR 4 ms, TE 2 ms) (**b**); bladder is pressed. Axial DWI with b-Factor 0 ms (TR 2,600 ms, TE 70 ms) (**c**) and with b-Factor 800 ms (TR 2,600 ms, TE 70 ms) (**d**) demonstrate an intermediate signal restriction in the peripheral area of the leiomyoma fibroid, which corresponds to the well-vascularized area, and no signal restriction of the central degenerated area, which has no contrast-enhancement. Sagittal T2 (TR 3,600 ms, TE 80 ms) (**e**) and sagittal contrast-enhanced fat-suppressed T1-weighted (TR 4 ms, TE 2 ms) (**f**) images post-UFE show a very significant shrinkage of uterine and fibroid volumes. Fibroid demonstrates a homogeneous low signal intensity on T2-weighted image (*arrowhead* in **e**), and it is completely devascularized after gadolinium administration. The uterus is regular and bladder is not pressed. Patient refers complete symptomatic resolution

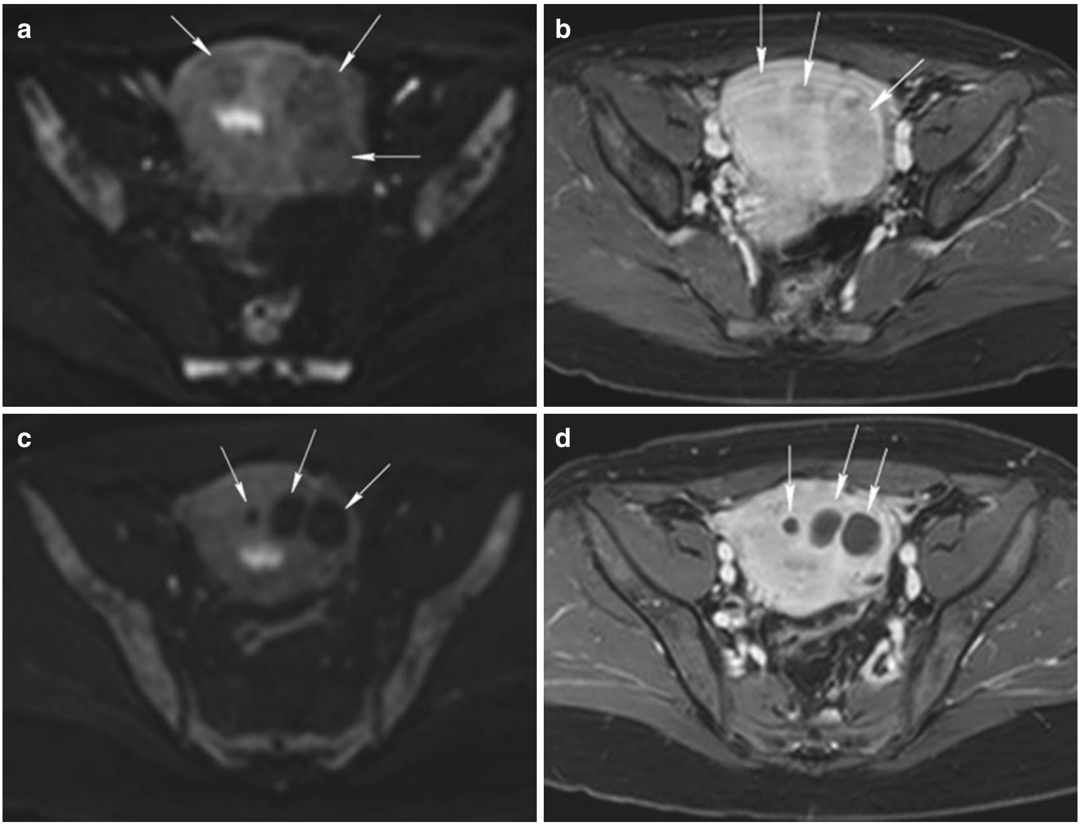

Fig. 5.29 Intramural fibroids (*arrows* in all images) pre-procedure (**a**, **b**) and 1 year after procedure (**c**, **d**) of uterine fibroid embolization. Axial DWI with b-Factor 800 ms (TR 2,600 ms, TE 70 ms) (**a**) and contrast-enhanced fat-suppressed T1-weighted (TR 4 ms, TE 2 ms) (**b**) images show three intramural fibroids with an intermediate signal restriction on DWI image and with high signal enhancement, similar to that of adjacent myometrium. Axial DWI with b-Factor 800 ms (TR 3,100 ms, TE 70 ms) (**c**) and contrast-enhanced fat-suppressed T1-weighted (TR 4 ms, TE 2 ms) (**d**) images, obtained 1 year after UFE, show moderate shrinkage of the fibroids that have no signal restriction on DWI image and are completely devascularized. Patient refers satisfactory symptomatic improvement

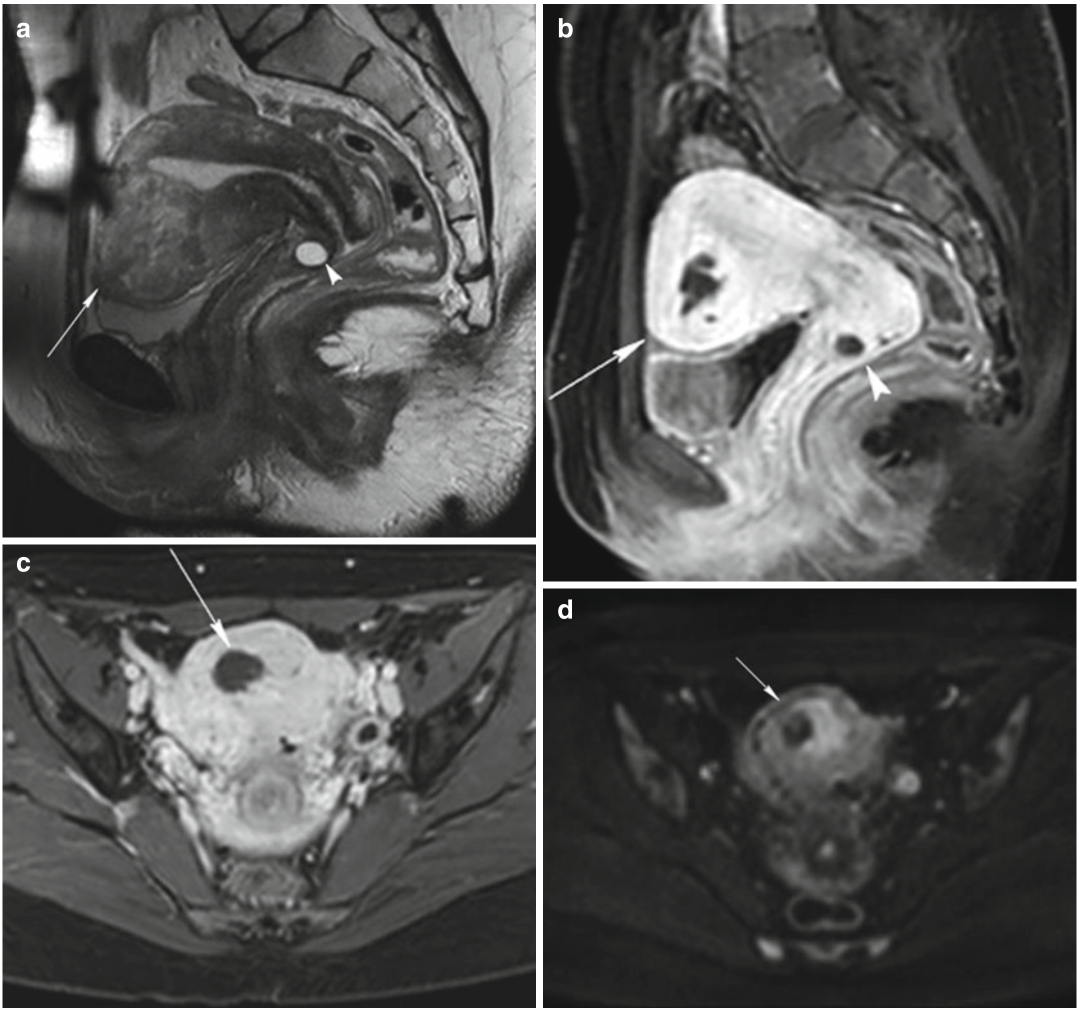

Fig. 5.30 MR imaging of the same patient of Fig. 5.6a, b obtained 1 year since UFE. Sagittal T2 (TR 3,250 ms, TE 80 ms) (**a**), sagittal (TR 4 ms, TE 2 ms) (**b**), and axial (TR 4 ms, TE 2 ms) (**c**) contrast-enhanced fat-suppressed T1-weighted images show shrinkage of fibroid volume and partial loss of contrast enhancement of the fibroid (*arrow*). Axial DWI with b-Factor 800 ms (TR 2,600 ms, TE 70 ms) (**d**) demonstrates no signal intensity restriction in the central area of the fibroid, which corresponds to devascularized area. Residual myometrium demonstrates reperfusion and enhances vividly. Patient refers satisfactory symptomatic improvement. Naboth's cyst in the cervix of the uterus (*arrowhead*)

References

1. Deshmukh SP, Gonsalves CF, Guglielmo FF, Mitchell DG (2012) Role of MR imaging of uterine leiomyomas before and after embolization. Radiographics 32:E251–E281
2. Baird DD, Dunson DD, Hill MC et al (2003) High cumulative incidence of uterine leiomyoma in black and white women: ultrasound evidence. Am J Obstet Gynecol 188(1):100–107
3. Wise LA, Palmer JR, Harlow BL et al (2004) Reproductive factors, hormonal contraception and risk of uterine leiomyomata in African-American women: a prospective study. Am J Epidemiol 159(2):113–123
4. Cramer DW (1992) Epidemiology of myomas. Semin Reprod Endocrinol 10:320–324
5. Stewart EA (2001) Uterine fibroids. Lancet 357: 293–298
6. Farquhar C, Arroll B et al (2001) A evidence-based guideline for the management of uterine fibroids. Aust N Z J Obstet Gynaecol 41:125–140

7. Speroff L, Glass RH, Kase NG (1994) Clinical gynecologic endocrinology and infertility, 5th edn. Williams & Wilkins, Baltimore
8. Murase E et al (1999) Uterine leiomyomas: histopathologic features, MR imaging findings, differential diagnosis and treatment. Radiographics 19:1179–1197
9. Hricak H, Finck S et al (1992) MR imaging in the evaluation of benign uterine masses: value of gadopentetate dimeglumine- enhanced T1-weighted images. AJR Am J Roentgenol 158:1043–1050
10. Pelage JP, Le Dref O, Soyer P et al (1999) Arterial anatomy of the female genital tract: variations and relevance to transcatheter embolization of the uterus. AJR Am J Roentgenol 172:989–994
11. Pelage JP, Walker WJ (2003) Ovarian artery angiographic appearance, embolization and relevance to uterine fibroid embolization. Cardiovasc Intervent Radiol 26(3):227–233
12. Wei JJ, Zhang XM et al (2006) Spatial differences in biologic activity of large uterine leiomyomata. Fertil Steril 85(1):179–187
13. Weinreb JC, Barkoff ND, Megibow A, Demopoulos R (1990) The value of MR imaging in distinguishing leiomyomas from other solid pelvic masses when sonography is indeterminate. AJR Am J Roentgenol 154(2):295–299
14. Jha RC, Ascher SM, Imaoka I, Spies JB (2000) Symptomatic fibroleiomyomata: MR imaging of the uterus before and after uterine arterial embolization. Radiology 217(1):228–235
15. Katsumori T, Akazawa K, Mihara T (2005) Uterine artery embolization for pedunculated subserosal fibroids. AJR Am J Roentgenol 184(2):399–402
16. Matsuno Y, Yamashita Y, Takahasni M et al (1999) Predicting the effect of gonadotropin-releasing-hormone (GnRH) analogue treatment on uterine leiomyomas based on MR imaging. Acta Radiol 40:656–662
17. Hricak H, Tscholakoff D, Heinrichs L et al (1986) Uterine leiomyomas: correlation of MR, histopathologic findings, and symptoms. Radiology 158(2):385–391
18. Kawakami S, Togashi K, Konishi I et al (1994) Red degeneration of uterine leiomyoma MR appearance. J Comput Assist Tomogr 18:925–928
19. Pattani SJ, Kier R, Deal R, Luchansky E (1995) MRI of uterine leiomyosarcoma. Magn Reson Imaging 13:331–333
20. Togashi K, Ozasa H, Konishi I et al (1989) Enlarged uterus: differentiation between adenomyosis and leiomyoma with MR imaging. Radiology 171(2):531–534
21. Togashi K, Nishimura K, Itoh K et al (1988) Adenomyosis: diagnosis with MR imaging. Radiology 166:11–114
22. Togashi K, Kawakami S, Kimura I et al (1993) Sustained uterine contractions: a cause of hypointense myometrial bulging. Radiology 187(3):707–710
23. Harsha Tirumani S, Shinagare AB, Hargreaves J et al (2014) Imaging features of primary and metastatic malignant perivascular epithelioid cell tumors. AJR Am J Roentgenol 202:252–258
24. Spielmann AL, Keogh C, Forster BB et al (2006) Comparison of MRI and sonography in the preliminary evaluation for fibroid embolization. AJR Am J Roentgenol 187:1499–1504
25. Bulman JC, Ascher SM, Spies JB (2012) Current concepts in uterine fibroid embolization. Radiographics 32:1735–1750
26. Goodwin SC, Vedantham S, McLucas B et al (1997) Preliminary experience with uterine artery embolization for uterine fibroids. J Vasc Interv Radiol 8: 517–526

Neoplasms of the Ovary

6

Maria Chiara Ambrosetti, Livia Bernardin,
Riccardo De Robertis Lombardi, Stefano Crosara,
Federica Castelli, Andrea Rockall, Riccardo Manfredi,
and Roberto Pozzi Mucelli

6.1 Introduction

6.1.1 Anatomy and Pathology

Ovaries are paired nodular structures located laterally to the uterus in relation to the lateral pelvic wall. They are the female reproductive internal organs and can produce gonadal cells and secrete hormones – mainly estrogen and progesterone. Their exact localization is highly variable, but they are typically found below the bifurcation of the common iliac vessels lateral to the uterine cornua. Histologically, the ovaries consist of several vesicular follicles embedded within a mixed connective tissue and spindle cell stroma. An adnexal mass is an enlarged structure in the uterine adnexa that can be palpated on bimanual pelvic examination or visualized with diagnostic imaging techniques [1, 2]. Adnexal masses are common findings among both premenopausal and postmenopausal women – nearly 10 % of women will undergo surgical evaluation for an adnexal mass or a suspected ovarian neoplasm at some point in their life [1, 2]. The majority of adnexal masses in the overall population are benign, with a small percentage of patients harboring an ovarian malignancy. The main goals of an initial diagnostic work-up for an adnexal mass are to rule out malignancy and to differentiate between adnexal masses requiring surgical intervention and those that can be managed conservatively. The differential diagnosis of an adnexal mass includes both gynecological and non-gynecological entities. Among the gynecological sources, diagnostic entities can be broadly separated into functional or physiological lesions, inflammatory lesions, or neoplastic lesions (Table 6.1) [3].

The latter category can be split into the following sub-categories:

(a) Surface epithelial–stromal tumors
(b) Sex cord–stromal tumors
(c) Germ cell tumors
(d) Secondary (metastatic) tumors

These latter are also important as treatment options differ from those for primary ovarian malignancies.

Overall, it is widely accepted that if an adnexal mass is considered to have an appreciable risk of malignancy, surgery should be recommended. It is nevertheless crucial to consider the clinical context of each individual patient diagnosed with an adnexal mass when determining the most

M.C. Ambrosetti (✉) • R. De Robertis Lombardi
S. Crosara • F. Castelli • R. Manfredi • R. Pozzi Mucelli
Istituto di Radiologia, Università di Verona,
Verona, Italy
e-mail: mchiara.ambrosetti@gmail.com;
riccardo.derobertis@hotmail.it

L. Bernardin
Istituto di Radiologia, Ospedale Fracastoro,
San Bonifacio, Verona, Italy
e-mail: liviabernardin@yahoo.it

A. Rockall
Department of Radiology,
Imperial College Healthcare, London, UK

R. Manfredi, R. Pozzi Mucelli (eds.), *MRI of the Female and Male Pelvis*,
DOI 10.1007/978-3-319-09659-9_6, © Springer International Publishing Switzerland 2015

Table 6.1 The most common etiologies of adnexal mass

- Functional and physiologic
  - Follicles
  - Hemorrhagic
  - Corpus luteum
- Inflammatory
  - Pelvic inflammatory disease
  - Endometrioma
- Other benign
  - Paratubal cysts
  - Hydrosalpinx
  - Ectopic pregnancy
  - Ovarian torsion
- Benign neoplasms
  - Germ cell
    - Mature cystic teratoma
  - Sex cord–stromal
    - Fibroma
  - Epithelial
    - Serous or mucinous cystadenoma
- Malignant neoplasms
  - Germ cell tumor
    - Dysgerminoma
    - Immature teratoma
  - Sex cord–stromal tumor
    - Granulosa cell tumor
    - Epithelial ovarian carcinoma
  - Borderline or low malignant potential
    - Invasive epithelial
    - Fallopian tube carcinoma

appropriate diagnostic and therapeutic strategy. Partly because of the low incidence of ovarian cancer in the general population, there are no accepted effective screening tests to early identify women with ovarian cancer [4] – unless there is a strong family history or a known gene mutation (e.g., BRCA).

There are three main clinical routes by which an adnexal mass may be detected: (1) symptomatic women diagnosed with an adnexal mass by physical exam or imaging, (2) adnexal mass detected during bimanual pelvic examination, and (3) asymptomatic adnexal mass detected incidentally on imaging performed for another indication [2].

In premenopausal women, the most likely scenario is an ultrasound evaluation during the pregnancy – even though the incidence of a malignancy is rare in this case. In peri- or postmenopausal women, the most common scenario would be while performing an evaluation for pelvic–vaginal (PV) bleeding. Since PV bleeding is not a common symptom of ovarian cancer, an adnexal mass found during evaluation for bleeding is an incidental finding [2].

6.1.2 Imaging

Multimodality imaging assessment plays a key role in the management of adnexal masses. Imaging helps to plan the most appropriate therapeutic approach. Since benign ovarian lesions are nowadays treated with laparoscopy, pretreatment imaging findings associated with proper characterization of an ovarian lesion are crucial [5]. The following parameters should be assessed by imaging preoperatively: (a) exact origin of the mass, (b) likelihood of malignancy, and (c), when surgery is needed, the feasibility of laparoscopy versus laparotomy [6].

Transabdominal and transvaginal ultrasonography (TVUS) represents the first-line imaging technique currently used to evaluate ovarian masses [7]. TVUS has been the foremost modality for detection and characterization of ovarian tumors. Especially with the advent of high-frequency transvaginal probes, the quality of images allows description of the lesion's gross anatomical features, hence making TVUS the method of choice in studying ovarian lesions. This is, however, limited by the great variability of macroscopic characteristics of both benign and malignant masses. Furthermore, the technique is operator dependent. To overcome these limitations, morphological scoring systems have been developed – this being based on specific ultrasound parameters each with several scores according to determined imaging features of the lesion and clinical data. The color Doppler scanning allows the assessment of tumor vascularity. Overall, malignancies display an increased vascularity with decreased peripheral blood flow resistance and increased blood flow velocity compared with benign tissue [2, 8–10]. Nevertheless, a significant proportion of adnexal masses (up to 20 %) remain indeterminate after TVUS.

Magnetic resonance (MR) imaging is now widely accepted as the "problem-solving technique" for the characterization of an indeterminate ovarian mass having both high sensitivity and specificity in discriminating benign versus malignant lesions. Moreover, thanks to its exquisite soft tissue contrast definition, it can address specific diagnosis for certain pathological types [7] (e.g., teratomas, endometriomas).

Computed tomography is commonly performed in preoperative disease burden assessment of a suspected ovarian malignancy [11–13].

6.1.2.1 MRI Assessment of an Adnexal Mass

Patient Preparation and Coil Selection for MRI Assessment

Patients undergoing MRI examination should have fasted for at least 4 h to limit artifacts due to bowel peristalsis. Further reduction of motion artifacts can be achieved with the use of antiperistaltic agents. Imaging is performed with the patient in supine position using a multichannel phase array coil. Endorectal and endovaginal coils have a limited field of view for the assessment of lateral pelvic structures and are therefore not routinely used.

Conventional MRI Sequences

A typical imaging protocol includes T1-weighted images (T1WI) in the axial plane and T2-weighted images (T2WI) in the axial, sagittal, and coronal planes using a small field of view (20 cm), a high resolution matrix (e.g., 256 × 256), and thin section images (3 mm). Fat-saturated T1-weighted images (T1W FS) are used to evaluate the presence of fat or hemorrhage, especially when high signal intensity is seen within the adnexa on T1WI and a dermoid tumor or endometriosis is suspected. In patients undergoing ovarian cancer staging, axial T1WI or fast spin-echo T2WI with a large field of view up to the renal pelvis should be included to evaluate the presence of metastatic disease (e.g., lymph node, liver, or bone metastases).

Contrast-Enhanced MRI Sequences

Gadolinium-enhanced images are useful for the evaluation of complex lesions as they may help differentiating solid components or papillary projections from clots and debris. Multiphase contrast-enhanced MRI is performed by using a three-dimensional gradient echo T1-weighted sequence after administration of 0.1 mmol gadolinium per kg of body weight. Dynamic contrast-enhanced MRI (DCE-MRI) involves repeatedly imaging a predetermined volume of interest every few seconds over 5–10 min during the passage of the contrast agent through the tissue of interest, so that changes in signal intensity can be assessed as a function of time. Semi-quantitative analysis can be performed through several parameters derived from contrast enhancement/time curves.

Diffusion-Weighted MRI (DW-MRI)

DW-MRI is performed using two or more *b-values*, which include one or more low *b*-values (50–100 s/mm^2) and a high *b*-value (750–1,000 s/mm^2). The apparent diffusion coefficient (ADC) is measured in mm^2/s and is calculated by the slope of the line of the natural logarithm of signal intensity versus *b*-values. The ADC maps are usually displayed as gray-scale images. Areas of restricted diffusion have lower ADC values and appear as a darker shade of gray on the ADC maps compared with areas of freely moving water such as cysts or bladder, which appear as a lighter shade of gray. Areas of restricted diffusion appear bright in the high-*b*-value images (*b*-value 750–1,000 s/mm^2).

Role of MRI in Characterizing Ovarian Masses

The greatest strength of MRI lies in its ability to characterize the physical and biochemical properties of different tissues (e.g., water, iron, fat, and extravascular blood and its breakdown products) through the use of multiple imaging sequences. There are no MRI signal intensity characteristics that are specific for malignant epithelial tumor, and these tumors should be distinguished based on morphologic criteria. The MRI features most predictive of malignancy are an enhancing solid component or vegetations within a cystic lesion, presence of necrosis within a solid lesion, as well as presence of ascites and peritoneal deposits [14, 15].

6.1.3 Defining the Origin of a Pelvic Mass: Adnexal, Extra-adnexal, and Extraperitoneal

Defining the correct origin of a mass is the first diagnostic step in setting up a treatment strategy. The size, architecture, and location may appear similar in adnexal, extra-adnexal peritoneal masses and even in extraperitoneal lesions. However, special features determining the anatomical relationship of the mass and the surrounding pelvic anatomical structures can help in their differentiation [16]. These parameters include visualization of ovarian structures, the type of contour deformity at the interface between the ovary and the pelvic mass, and the displacement pattern of the vessels, ureters, and other pelvic organs. Particularly in large pelvic lesions, the ovary may often be obscured or totally invaded by the mass [8]. In smaller lesions, when the ovary is not completely obscured, identifying ovarian structures – such as follicles – indicates its ovarian origin. Specific signs such as the "beak" sign and the "embedded organ" sign can aid in better defining the mass relationship with the ovary. When a mass deforms the edge of the ovary into a beak shape, it is likely arising from the ovary. In contrast, dull edges at the interface with the adjacent ovary suggest that the tumor compresses the ovary but does not arise from this [16]. Large ovarian masses typically displace the ureter posteriorly or posterolaterally. However other intraperitoneal lesions (e.g., those originating from the bladder, the uterus, or the bowel) can cause the same pattern of displacement [17]. An adnexal lesion typically displaces iliac vessels laterally. In contrast, extraovarian masses arising from the pelvic wall or lymphadenopathies displace the iliac vessels medially. The mass origin may be further elucidated by tracking the vascular pedicle or the ovarian suspensory ligament [16]. Because of their close anatomical relationship, masses arising from the fallopian tubes often cannot be distinguished from ovarian ones. However, incomplete septa emerging from the wall of a cystic "sausage-like" adnexal mass indicate its fallopian origin [18].

6.1.4 Differentiating Benign from Malignant Lesions

The clinical significance of discriminating benign from malignant masses differs depending on the clinical setting in which the mass is initially detected. For women with symptoms, in whom surgical management may be appropriate whether or not the mass is malignant, the main reason to discriminate between benign and malignant lesions is to set up the correct management. For asymptomatic women, discriminating benign from malignant disease is important both to ensure appropriate management in the setting of malignancy and to avoid unnecessary diagnostic procedures, including surgery.

Several MR imaging findings suggestive of malignancy have been reported in the literature. These can be summarized as follows: complex solid–cystic appearance, presence of wall irregularity and thickening, multiple (>5) septations with nodularity, and vegetations and solid enhancing components after contrast medium administration [19]. Predominantly cystic appearance with thin wall and septa and presence of strong hypointensity on T2-weighted images are more often associated with benign lesions. Secondary features of malignancy representing disease involvement of surrounding/distant structures consist of peritoneal, mesenteric, or omental deposits, pelvic side wall invasion, and lymphadenopathy, although pelvic ascites can also be seen in ovarian torsion, pelvic inflammatory disease, and benign ovarian fibroma [3, 4]. When these criteria are applied, the method sensitivity in detecting malignancy is 91–100 % and the specificity is 91–92 % [19, 20]. More recently, functional MRI techniques such as diffusion-weighted MRI (DW-MRI) and dynamic contrast-enhanced MRI (DCE-MRI) have demonstrated a valid contribution in ovarian masses' characterization. DW-MRI indirectly informs about tumor cellularity and tumor membrane integrity via apparent diffusion coefficient (ADC) calculation. The ADC value has been reported as useful in discriminating between benign and malignant ovarian surface epithelial tumors [20], although there is still no evidence that DW-MRI can independently characterize an ovarian mass [21–25]. DCE-MRI characterizes the leakage of contrast agent from capillaries into the extravascular extracellular space allowing quantitative measurements that reflect blood flow and vascular permeability. Quantitative DCE-MRI parameters have been shown to correlate to tumor angiogenesis status [26]. Semi-quantitative DCE-MRI parameters and curve analyses have also demonstrated a role in predicting malignancy with an increased specificity compared with conventional MRI [27]. Specifically a relationship between early enhancement of solid tumor components and malignancy has been postulated [5, 28, 29].

The probability of malignancy is also related to the patient's age. In young women less than 9 years of age, 80 % of ovarian masses are malignant, with the vast majority consisting of germ cell tumors. In women of reproductive age, the overall chance that an ovarian tumor will be malignant is 1 in 15 compared to 1 in 3 by 45 years of age [30].

6.1.4.1 Low-Risk Adnexal Masses

If both pre-assessment probability and imaging studies demonstrate low probability of malignancy, additional tests can be avoided [3].

6.1.4.2 Intermediate-Risk Adnexal Masses

The most challenging decision-making cases are the ones with intermediate risk for malignancy. A large proportion of intermediate-risk adnexal masses represent benign entities. Tests with greater specificity allow point-of-care triage that may obviate the need for surgery that would otherwise be purely for diagnostic purposes. However, in case of malignancy they would potentially offer a more timely diagnosis than a "watch and wait" strategy with interval ultrasound reassessment [3]. Tumor markers such as CA125 may be selectively performed, particularly in the postmenopausal population in which specificity is higher. Alternatively, surgical evaluation can be considered if the perceived risk for malignancy justifies this intervention [3].

6.1.4.3 High-Risk Adnexal Masses

If there is sufficiently high risk, then additional diagnostic studies may not be necessary, and clinicians may wish to proceed with studies most relevant to surgical planning and gyne-oncology referral [3].

6.1.5 Ovarian Tumors by Morphologic Characteristics

Morphological characteristics of adnexal masses provide important information for determining the pathological group of a tumor. Although MR imaging findings are not specific for any particular pathological group, some imaging features are more characteristic of one pathological group than another. Ovarian tumors are usually classified into three groups: cystic masses (unilocular or multilocular), cystic and solid masses, and predominantly solid masses.

6.1.5.1 Cystic Masses

Cystic masses may include nonneoplastic cysts, benign neoplasms, and borderline neoplasms. Functional cysts, para-ovarian cysts, hydrosalpinx, endometriotic cysts, serous cystadenomas, mucinous cystadenomas, and mucinous cystic tumors of borderline malignancy are the ovarian cystic lesions most frequently found.

6.1.5.2 Cystic and Solid Masses

In general, a combined cystic and solid mass strongly supports the diagnosis of ovarian malignancy. Primary epithelial carcinomas and metastatic tumors often show a cystic and solid appearance. Mature cystic teratoma is the important exception to this appearance.

6.1.5.3 Solid Masses

Predominantly solid ovarian masses include benign, borderline, and malignant tumors. The main entities are fibrothecomas, Brenner tumors, granulosa cell tumors, dysgerminomas, epithelial ovarian carcinomas, and metastatic carcinomas.

6.2 Benign Ovarian Lesions

Benign adnexal lesions constitute about 80 % of all ovarian tumors. They mostly occur in young women (<45 years). As for malignant tumors, benign neoplasms arise from one of the three ovarian components: surface epithelium, germ cells, or sex cord–stroma [31].

6.2.1 Physiologic Ovarian Cysts

Ovarian cysts below 3 cm are generally considered physiological. These entities can be divided into functional (associated with hormone production) or nonfunctional [32]. Functional cysts comprise follicular cysts, corpus luteum cysts, and uncommon cysts such as the theca–lutein cysts [33] (Fig. 6.1). Simple cysts are thin-walled (<3 mm), unilocular, and below 3 cm in diameter, but can occasionally grow larger. They usually develop during reproductive age, but may also be found in postmenopausal age and are almost always asymptomatic. The majority are follicular cysts and result from failure of rupture or of regression of the Graafian follicle. They are usually self-limiting and usually regress spontaneously within 2 months. Sometimes they are complicated by rupture and may cause abdominal pain and hemoperitoneum [7]. Most functional cysts appear as unilocular small cystic lesions with high signal intensity on T2-weighted images and intermediate to low signal intensity on T1-weighted images, reflecting simple fluid content. Hemorrhagic cysts usually present high signal on T1-weighted images [10, 34]. The thin wall of functional cysts is best depicted on T2-weighted images as a hypointense structure and on contrast-enhanced images as hypervascular in respect to ovarian stroma [11, 35, 36]. When below 3 cm of diameter, they cannot be differentiated from mature follicles. Unilocular cystadenomas may mimic functional cysts, but a follow-up that shows regression over 2–3 ovarian cycles allow the diagnosis of functional cyst. Corpus luteum cysts may get bigger in size because of internal hemorrhage [2, 37, 38]. Hemorrhagic and corpus luteum cysts usually have thicker walls with relatively higher signal intensity on T1-weighted images and intermediate to high signal intensity on T2-weighted images [11]. Among nonpregnant women, corpus luteum cysts derive from failure of regression or hemorrhage into the corpus luteum [2]. Theca–lutein cysts develop when choriogonadotropin levels are abnormally increased – e.g., in the

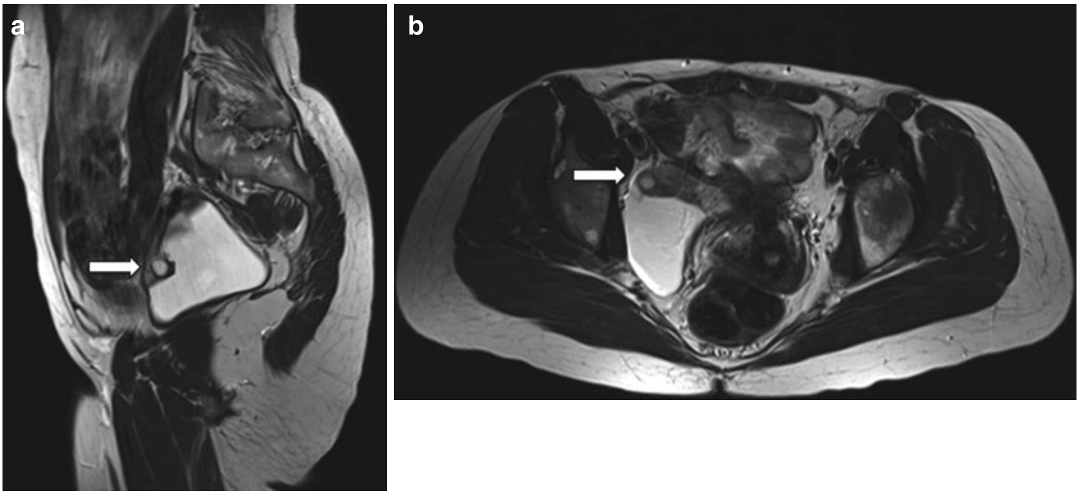

Fig. 6.1 Inclusion cyst. Follow-up scan in a 44-year-old woman with history of endometriosis. Sagittal and axial spin-echo T2-weighted images (TR:4361, TE:80; **a**, **b**): right-sided pelvic collection containing the right ovary anteriorly (*arrows*). There are no suspicious solid components

gestational trophoblastic disease or in the ovarian hyperstimulation syndrome [31, 39]. Progesterone production may persist in corpus luteum cysts, therefore resulting in dysmenorrhea. When these cysts are large in size, they can cause abdominal pain because of rupture, hemorrhage, or torsion. Corpus luteum cysts often require indeed up to 3 months to regress [2, 7]. Both corpus luteum cysts and endometriomas may show hemorrhagic content; however, a prominent T2 shading can be observed only in endometriomas, while corpus luteum cysts contain less concentrated hemoglobin, so the T2 shading is less common [32, 40]. Internal debris and fibrin clots can be differentiated from papillary projections of epithelial tumors by their lack of enhancement [32].

6.2.2 Endometriomas

External endometriosis is defined as the condition in which endometrial tissue is found in extrauterine sites [40, 41]. Endometrioid cysts, or endometriomas, are benign entities that can reach fairly large dimensions [40]. Malignant transformation is a rare complication (less than 1 %), and the most common histological subtypes include endometrioid and clear cell carcinoma [42].

External endometriosis mainly affects ovaries [41] and bilateral ovarian involvement occurs in 30–50 % of patients [43]. Endometriomas contain an obliterated loculus, lined by endometrial glands [44, 45]. These lesions range from cystic to solid appearance, depending on cyclic modifications under hormonal stimulation – likewise the normal endometrium. As a result, endometriomas may enlarge [7] and their walls can become fibrotic and thickened and may present an irregular external border [46]. These aspects have been explained with the attitude of endometrial loculi to perforate, producing a severe fibrosis as a result of the irritating effect of blood, with subsequent adhesion to the surrounding structures. Another hypothesis is that endometrial cysts have a free exit to the peritoneal cavity and are necessarily sealed off by organized blood or adhesions to surrounding organs [7]. Malignant transformation is a rare complication (less than 1 %); the most common histological subtypes include endometrioid and clear cell carcinoma [42, 47].

On MRI endometriomas usually present as multiple hemorrhagic cysts [34, 48–50]. They have an iron concentration many times higher than even the whole blood [51–53], and this characteristic gives them their typical very high signal intensity on T1-weighted fat-suppressed images and low signal intensity on T2-weighted images [54]. Homogeneous T2 shading, defined as signal loss on T2-weighted images [55], is a characteristic feature of endometriomas, and it mainly depends on their age and the amount of hemosiderin [56]. Other MRI findings include: adhesion to surrounding organs, a distinct low-intensity zone surrounding a cyst loculus on both T1- and T2-weighted images (thick fibrous capsule), loculus content with short T1 and T2 values (recent hemorrhagic content), dependent layering and a T2-hypointense fluid level representing different-aged blood products, and a hypointense peripheral ring caused by hemosiderin staining in chronic lesions [7, 34]. Non-cystic endometriomas may be difficult to identify due to their small size. Nevertheless, these implants are obviously more evident on fat-saturated T1-weighted images and show low signal intensity on T2-weighted images due to fibrosis surrounding glandular islands [57–60]. DW imaging may aid in differentiation between clots and clear cell cancer development within almost-solid endometriomas [48, 60, 61].

6.2.3 Cystadenomas

Cystadenomas are common epithelial ovarian tumors. Two main histological cystadenomas subtypes have been identified: serous and mucinous [33]. Although an overlap exists, imaging features may aid in the differentiation of serous from mucinous cystadenomas [5].

They account for 40–50 % of benign ovarian tumors in the reproductive age, with an increasing frequency with age, so that after menopause cystadenomas account for up to 80 % of the benign ovarian tumors [5, 32]. Cystadenomas are

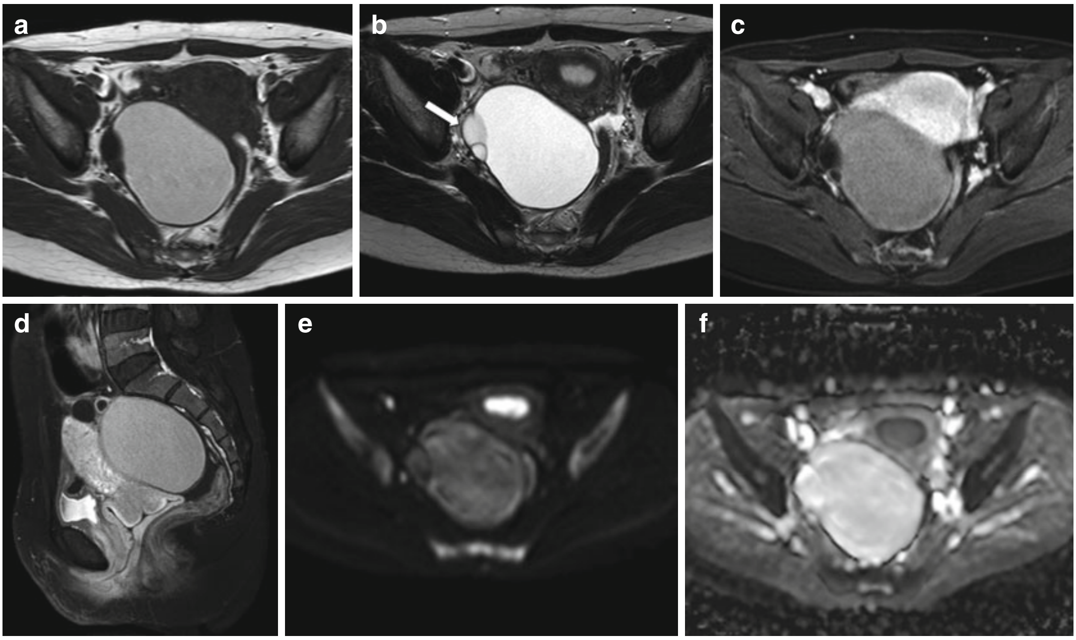

Fig. 6.2 Benign serous cystadenoma. A 32-year-old woman with a right adnexal cystic lesion showing thin septa on the right wall (*arrow*). The largest component shows high signal on T1-weighted (TR:519, TE:10; **a**) and T2-weighted imaging (TR:4361, TE:80; **b**) suggestive of hemorrhagic and/or proteinaceous contents. The remainder of the complex lesion shows low signal on T1-weighted imaging (TR:519, TE:10) and high on T2-weighted imaging (TR:4361, TE:80). There is no significant enhancement following gadolinium (axial and sagittal T1 fat-sat imaging, TR:519, TE:10; **c**, **d**). No pathological areas of restricted diffusion ($b = 1{,}000$ imaging, **e**; corresponding ADC map, **f**)

thin-walled unilocular or multilocular cystic lesions filled with serous or mucinous content, sometimes showing hemorrhagic content [22]. Papillary projections within cystic walls are rarely found; therefore, these findings should raise the suspicion of malignancy [22, 62, 63]. Serous and mucinous cystadenomas differ in pathology and prognosis. Serous cystadenomas account for 20–40 % of all benign ovarian neoplasms, with a peak incidence in the 4th to 5th decade of life, and up to 20 % of them are bilateral. They are often unilocular and the inner lining may be smooth or have gross papillary projections [5, 33, 64] (Fig. 6.2). Mucinous cystadenomas account for 20–25 % of benign ovarian neoplasms. They are more common during the 3rd to 5th decade of life and are bilateral in only 2–5 % of cases. They tend to be larger at the time of presentation and are more frequently multilocular, with different contents of the loculi. Mucinous cystadenomas are lined by a single layer of tall, columnar epithelial cells and contain a sticky gelatinous fluid; rupture of a mucinous cystadenoma can result in pseudomyxoma peritonei [5, 22, 25]. At MRI serous cystadenomas have simple fluid signal and hypointense on T1- and hyperintense on T2-weighted images. In contrast, mucinous cystadenomas have often various signal intensities depending on the content of different loculi, varying from simple fluid to proteinaceous to hemorrhagic. Mucin has lower intensity than serum on T2-weighted images. Rarely, mucinous cystadenoma can present as a simple cyst [5].

6.2.4 Adenofibroma and Cystadenofibroma

Adenofibromas and cystadenofibromas are classified as surface epithelial–stromal tumors. They represent about half of all benign ovarian cystic

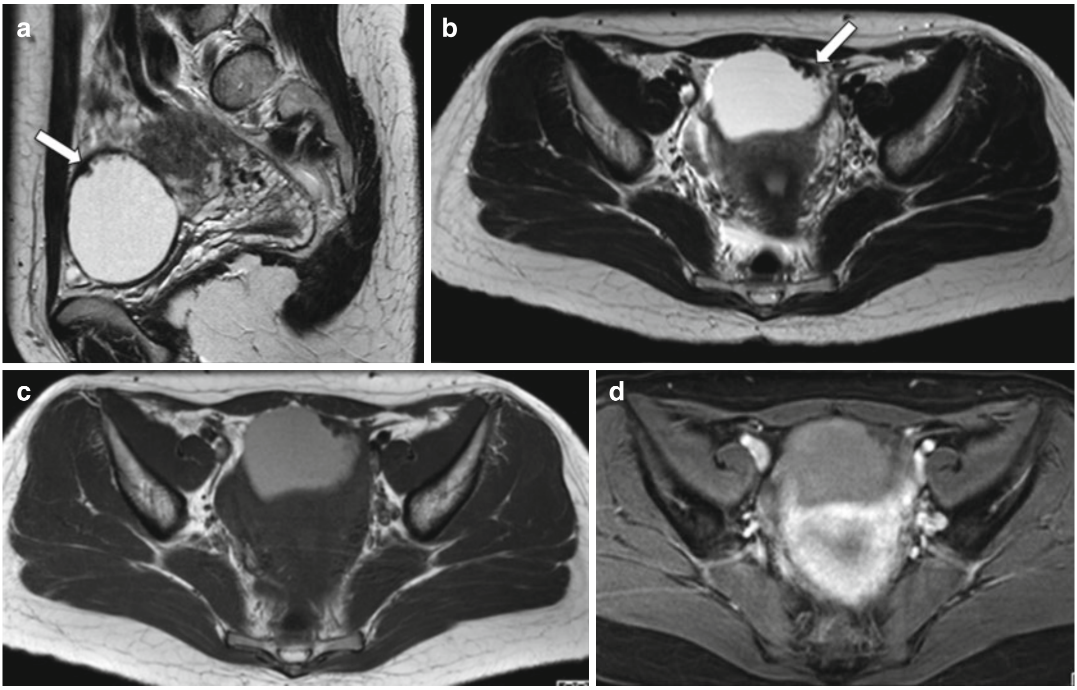

Fig. 6.3 Cystadenofibroma. A 39-year-old woman with normal CA125. Pelvic MRI demonstrates a left-sided complex, predominantly cystic, adnexal mass. The fluid contents are of high signal intensity on T2-weighted (TR:4361, TE:80; **a**, **b**) and T1-weighted images (TR:519, TE:10; **c**) with no signal loss on the fat-sat images (TR:519, TE:10; **d**) in keeping with proteinaceous/hemorrhagic materials. There is a papillary "carpet-like" wall thickening on the left anterior aspect of the mass with a very low signal intensity on T1- and T2-weighted images (*arrows*); this demonstrates mild, delayed contrast medium enhancement (post-gadolinium T1-weighted fat-sat image, **d**)

serous tumors and are usually found in women aged 15–65 years [65]. Imaging features are nonspecific and may be similar to malignant or borderline tumors [66]. In fact, the variable amount of fibrous stroma determines various aspects, from oligocystic to complex cystic with solid components or even totally solid, that can mimic ovarian cancer [22, 67]. Almost half of the patients with cystadenofibroma have an abnormal contralateral ovary [68]. Adenofibromas and cystadenofibromas are histologically characterized by fibrous tissue components with epithelial elements, similar to those of ovarian cystadenomas. They can also be completely cystic, with microscopic stromal foci, and their margins are usually well defined and smooth [22, 59, 69]. A black spongelike appearance on T2-weighted images is characteristic of these tumors, consisting of tiny high T2 signal intensity foci within very hypointense solid components, reflecting small cystic glandular structures within a dense fibrous stroma [60]. The majority of solid components shows very low T2 signal intensity and minimal enhancement [5, 6, 33, 60, 70]. Low signal intensity and diffusely or partially thickened cystic wall on T2-weighted images are features suggestive of cystadenofibroma [62] (Fig. 6.3). On DW images, the majority of fibromas and fibrothecomas show both low signal intensity on high-*b*-value images and low corresponding ADC values (mean 1.156×10^{-3} mm^2/s) owing to collagen-producing fibroblasts and a dense network of collagen fibers and also to the T2 blackout effect [24, 25, 60]. Fibrothecomas with degeneration may display intermediate to high signal intensity on high-*b*-value images [33, 64, 65, 71]. The presence of prominent solid components with high T2 signal intensity and strong enhancement are typical for cystadenocarcinofibroma [62].

6.2.5 Brenner Tumor

Brenner tumors are rare (1–3 %), mostly benign and incidentally found solid tumors, belonging to the epithelial surface derived tumors. They are composed of transitional cells with dense stroma, and a malignant component is rare [54]. They represent about 2–3 % of ovarian tumors and usually occur at a mean age of 50 years. They are usually small (<2 cm), solid, and unilateral [54]. Cystic components can be found in Brenner tumors, and in 20–30 % of cases they are associated with mucinous cystadenomas or other epithelial neoplasm [32, 54, 72, 73]. Brenner tumors may rarely produce estrogen; therefore, they can be associated with endometrial thickening [67]. On T2-weighted MR imaging, the dense fibrous stroma presents low signal intensity, similar to that of a fibroma. Extensive amorphous calcification is often present within the solid component [62, 67, 68]. On DW images, Brenner tumors show both low signal intensity on high-*b*-value images and low corresponding ADC values (mean 1.156×10^{-3} mm^2/s) owing to collagen-producing fibroblasts, to a dense network of collagen fibers, and also to the T2 blackout effect [64, 65]. The combination of a multi-septated ovarian tumor with a solid part with extensive calcifications may suggest the presence of a collision tumor consisting of a Brenner tumor and a cystic ovarian neoplasm, like cystadenoma [54].

6.2.6 Dermoid Cyst/Mature Teratoma

These are relatively common benign ovarian lesions, containing structures derived from the three germ cell layers. At imaging, the presence of fat within a cystic ovarian mass is pathognomonic for a mature cystic teratoma [74]. They are the most common ovarian neoplasms below 45 years of age, accounting for up to 70 % of tumors in women below 19 years of age [75]. They are usually unilateral, with only 10–15 % of dermoids found bilaterally [54]. They can be divided into three categories, among which mature cystic teratomas account for 99 %; less common types are the monodermal, which include struma ovarii and carcinoid tumors [54]. Although all three germ cell layers are present, ectodermal components predominate [63]. In the vast majority (88 %), dermoids are unilocular cystic lesions; a protuberance, called Rokitansky nodule or dermoid plug, projects into the cavity and is the hallmark of dermoids. Mature teratomas typically have a lipid content (90 %), consisting of sebaceous fluid, or adipose tissue within the cystic wall or the dermoid plug [73]. The Rokitansky nodule contains a variety of tissues, often including fat and calcifications, which represent teeth (31 %) or abortive bone [54, 74, 76]. A minority (8 %) of dermoid cysts do not demonstrate fat [74]. Dermoids are usually asymptomatic, incidentally discovered, and tend to grow slowly [77, 78]. Malignant degeneration, torsion and rupture, which can cause acute abdomen due to granulomatous peritonitis caused by leakage of the fatty content, can be present [79]; in particular, malignant degeneration, mainly arising from the dermoid plug, occurs in up to 2 % and is usually found in the 6th to 7th decades of life. The risk of malignancy is associated with larger size (>10 cm) and postmenopausal age [80]. Capsule perforation is a sign for malignant transformation of a mature teratoma [81]. At MRI mature teratomas are usually round or oval and sharply delineated; the lipid-laden cyst fluid shows high signal intensity on T1-weighted images and intermediate signal intensity on T2-weighted images (Fig. 6.4). Fat has a high signal intensity on T1- and T2-weighted fast spin-echo images and loss of signal on fat-saturated T1-weighted images. Chemical shift artifacts can be observed, differentiating fat from hemorrhage. There are some typical internal patterns, such as palm tree-like protrusions or dermoid nipples [40, 82, 83]. Calcifications can be missed on MRI due to the low signal intensity on both T1- and T2-weighted images. The presence of sebaceous fluid floating in the peritoneal cavity can suggest rupture [72]. Low ADC values caused by keratin may be useful in differentiation of mature teratomas with little fat from other cystic tumors; despite this, chemical shift imaging seems a better alternative

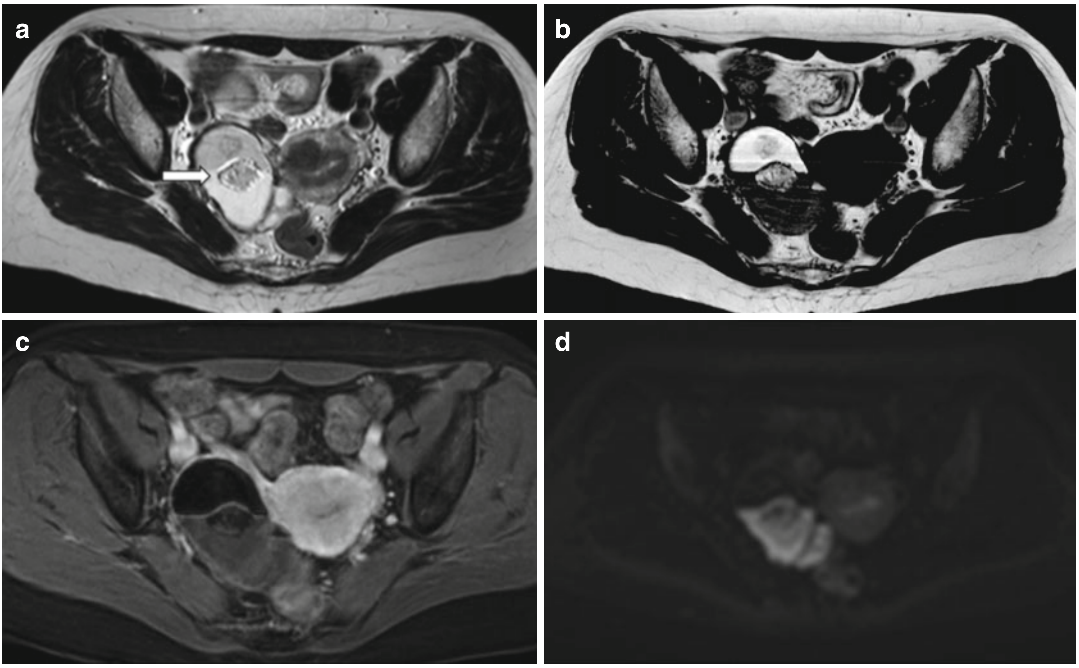

Fig. 6.4 Mature teratoma. A 47-year-old woman with ovarian enlargement on US and normal CA125. Pelvic MRI shows a right-sided complex adnexal mass. There is a fluid–fluid level, as depicted on axial T2-weigted image (TR:4361, TE:80; **a**) with hyperintense material on the top on axial T1-weighted image (TR:519, TE:10; **b**), the signal of which is suppressed on fat-saturated T1-weighted pulse sequence (TR:519, TE:10; **c**) indicative of the presence of fat. There are central areas which are of intermediate signal intensity suggestive of soft tissue (**a**, *arrow*) consistent with the typical Rokitansky nodule. These components demonstrate restricted diffusion (hyperintense on the b1000 – **d**) but do not demonstrate contrast enhancement (**c**)

[22, 35, 51]. MR fat-suppressed or chemical shift images are reliable for the differentiation of fat from hemorrhage [84]. In particular, when no or small amounts of fat are present, dermoids cannot be distinguishable from benign cystic ovarian tumors or ovarian cancer [79]. Monodermal teratomas are solid lesions, mainly or exclusively composed of one tissue type. They include struma ovarii, ovarian carcinoid tumors, and tumors with neural differentiation. Monodermal teratomas are typically solid lesions [22]. Struma ovarii is the most common type (3 %); it consists of mature thyroid tissue, but a mixed morphology with acini filled with thyroid colloid, hemorrhage, fibrosis, and necrosis can be found. Rarely, struma ovarii may produce thyrotoxicosis. They present as cystic or multilocular lesions with loculi displaying high signal intensity on T1- and T2-weighted images, without fat [85].

6.2.7 Fibroma, Thecoma, and Fibrothecoma

They are sex cord–stromal tumors, composed of spindle cells forming a variable amount of fibrosis and other cells [33] and can occur in both pre- and postmenopausal women. They are solid tumors accounting for 3–4 % of all ovarian tumors, typically unilateral (90 %), occurring in middle-aged and peri- and postmenopausal women. Fibromas are composed of whorled bundles of spindle-shaped fibroblasts with abundant collagen [18, 22, 86]. Fibromas are important from an imaging standpoint because they mimic malignant neoplasms. They can also be associated with ascites and rarely with pleural effusion [87, 88]. The association of an ovarian fibroma, ascites, and pleural effusion is known as Meigs syndrome. Thecomas and fibrothecomas can have estrogenic activity [63]. Bilateral fibromas are

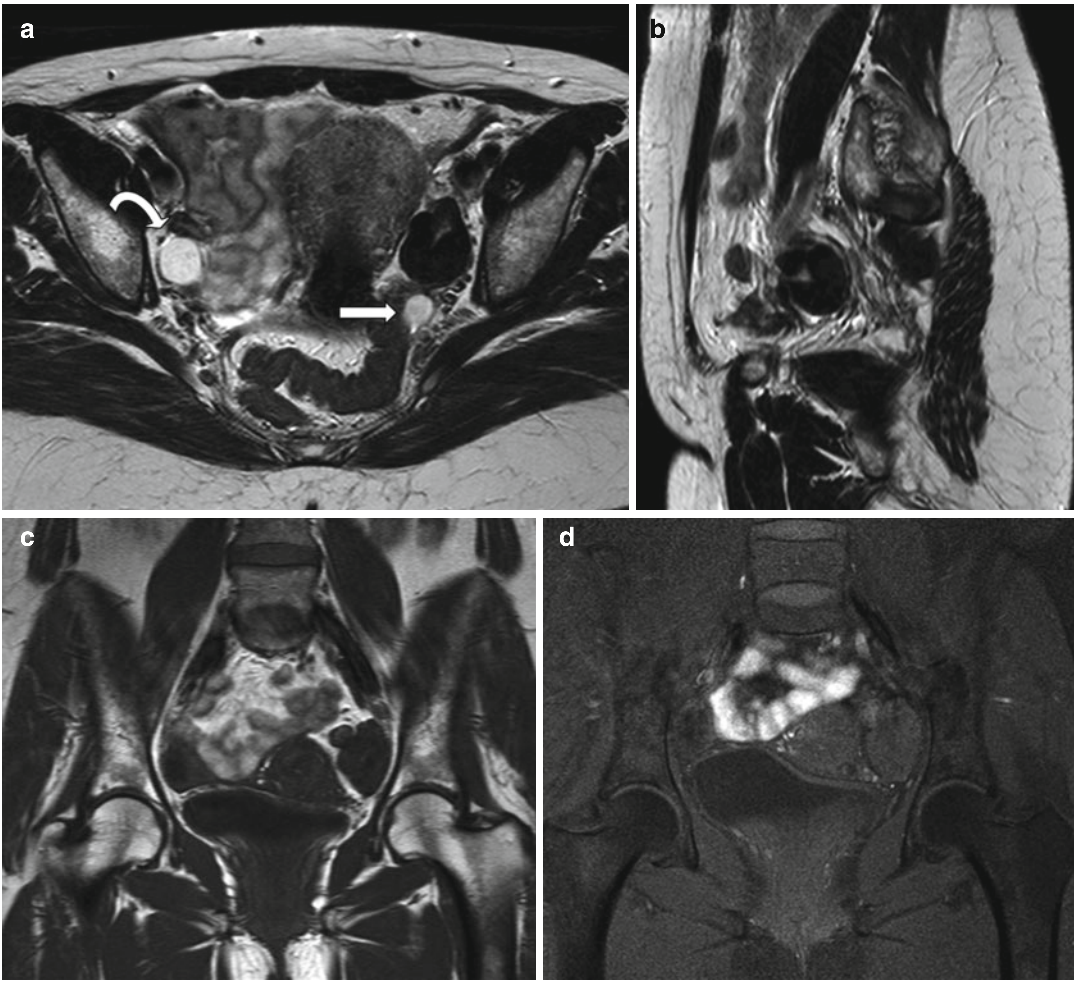

Fig. 6.5 Ovarian fibroma. A 55-year-old lady with pain on the left pelvis. Left ovarian mass showing very low signal intensity on T2-weighted images (axial and sagittal T2-weighted images, TR:4361, TE:80; **a**, **b**) and low signal intensity on T1-weighted image (coronal T1-weighted imaging without and with fat saturation, TR:519, TE:10; **c**, **d**) in keeping with a fibroma. There is a further small cyst at the posterior margin of the fibroma (*arrow*). The right ovary shows a small follicular cyst (*curved arrow*)

also present in basal cell nevus syndrome, along with basal cell carcinomas, bony, ocular, and brain abnormalities as well as other tumors [63].

Fibrothecomas are composed of thecal cells with abundant fibrosis. Unlike fibromas, they can have estrogenic activity and may present with uterine bleeding. In more than 20 %, endometrial carcinomas may be present concomitantly [63]. Because of their abundant collagen content, small fibromas and fibrothecomas have imaging features similar to uterine leiomyomas, with intermediate to low signal intensity on T1-weighted images and hypointensity on T2-weighted images. Larger lesions may have an inhomogenous structure with high signal intensity foci within the low signal intensity lesion, representing edema or cystic degeneration [22, 83, 89] (Fig. 6.5). In larger lesions, dense amorphous calcifications are present but not well appreciated because of their low signal intensity on T2-weighted images. Fibromas and fibrothecomas tend to show mild or delayed gadolinium enhancement [22, 83]. Differential diagnosis should be made with ovarian lesions with fibrous components other than fibroma and fibrothecomas that are cystadenofibroma and Brenner tumor [35, 82]. Pedunculated uterine leiomyomas and broad-ligament leiomyomas can appear as ovarian masses and have the same signal intensity features of fibromas and fibrothecomas. The recognition of the interface vessels between the uterus and adnexal mass is a useful tool in differentiating leiomyomas from ovarian fibromas [90, 91].

6.2.8 Sclerosing Stromal Tumor

Sclerosing stromal tumors are rare benign ovarian tumors occurring in young women [92]. They present as large masses with cystic and solid components. On MRI, they show a mixed hyper- and hypointense appearance on T2-weighted images. On dynamic images, the tumors show early peripheral enhancement with centripetal progression. A central area of prolonged enhancement of the mass represents fibrous hypocellular areas. The appearance after contrast medium administration is useful to differentiate sclerosing stromal tumors from fibromas [85, 93, 94].

6.3 Malignant Neoplasms

6.3.1 Epidemiology and Clinical Features

Worldwide, ovarian cancer accounts for 4 % of all female cancers and is the most frequent cause of death from gynecological malignancy with 239 new cases/year. In the majority of cases, it is a sporadic tumor and presents over the age of 30 years. There is a correlation between age distribution and tumor histology. Epithelial ovarian carcinomas usually present in postmenopausal women, whereas sex cord–stromal tumors and germ cell tumors are prevalent in young women around the age of 20–30 years. Several risk factors for ovarian cancer have been identified: increasing age, nulliparity, early menarche, late menopause, and long-term hormone replacement therapy. There are three recognized hereditary forms of ovarian cancer: breast–ovarian familial cancer syndrome (related to BRCA1 gene mutation), multiple site cancer family syndrome (Lynch II syndrome) and site-specific ovarian cancer. These tumors account for 5–10 % of the total cases; they tend to present mostly in premenopausal women and cause an increased –around 50 % – lifetime risk of developing ovarian carcinoma [95].

The most frequent clinical presentation of all ovarian malignancies consists of abdominal pain and swelling due to the fact that the tumor tends to manifest itself only when it has reached a large size. Functional ovarian neoplasms may present with specific endocrine and non-endocrine syndromes [96]. CA125 is currently the most commonly used serum marker for ovarian cancer, particularly in monitoring treated patients. Its role for initial diagnosis and staging is limited due to low sensitivity and specificity, particularly for stage I ovarian carcinoma. It also has a high false-positive rate in premenopausal women [97].

6.3.2 Staging

The gold standard for staging ovarian cancer remains surgery according to the International Federation of Gynaecology and Obstetrics (FIGO) guidelines. Those are based on the concept that ovarian cancer spreads centrifugally from the pelvis into the peritoneal cavity metastasizing outside the peritoneum only in advanced disease (National Comprehensive Cancer Network - NCCN guidelines for ovarian cancer). A TNM classification has also been defined [98] (Table 6.2).

Cross-sectional imaging staging is warranted for complex adnexal mass highly suggestive of malignancy (after US and/or CE-MRI) or for a noninflammatory complex adnexal mass with associated ascites. The main targets of preoperative staging are:

- Confirmation of malignant adnexal mass
- Tumor burden assessment with metastatic site determination and possible complication assessment (bowel obstruction, hydronephrosis, or venous thrombosis)
- Exclusion of a different primary site (GI tract, pancreas)

Table 6.2 TNM staging of ovarian cancer

TNM	FIGO	Imaging findings	Additional findings in surgical/histopathological findings
T1	*Stage I*	*Tumor limited to the ovaries*	
T1a	IA	Limited to one ovary, no ascites	Intact capsule and no tumor on the external surface
T1b	IB	Limited to both ovaries, no ascites	Intact capsule and no tumor on the external surface
T1c	IC	Stage IA or IB with ascites	With tumor on surface or capsule ruptured, or ascites or peritoneal washing positive for malignant cells
T2	*Stage II*	*Growth involving one or both ovaries, pelvic extension*	
T2a	IIA	Extension and/or metastases to the uterus and/or fallopian tubes	Ascites or peritoneal washing positive for malignant cells
T2b	IIB	Extension to other pelvic tissues	
T2c	IIC	Tumor either IIA or IIB with ascites	
T3 and/or N1	*Stage III*	*Tumor involving one or both ovaries, peritoneal implants (including small bowel and omentum) outside the pelvis including liver surface implants and/or metastases of retroperitoneal or inguinal lymph nodes*	
T3a	IIIA	Tumor grossly limited to the true pelvis, large volumes of ascites	
T3b	IIIB	≤2 cm implants of abdominal peritoneal surfaces, large volume of ascites	
T3c and/or N1	IIIC	≥2 cm implants of abdominal peritoneal surfaces and/or retroperitoneal or inguinal lymph nodes; large volume of ascites	
M1	Stage IV	Growth involving one or both ovaries, distant metastases, parenchymal liver metastases, pleural effusion with pleural abnormalities	Pleural effusion with positive cytology

Multidetector computer tomography (MDCT) is the imaging technique of choice in ovarian cancer staging and follow-up. MRI is a second-line technique for staging mainly due to the long examination time and limitations covering large field of view. Despite this MRI becomes first line for preoperative staging in specific situations:

- Contraindication to contrast medium administration (allergy)
- Pregnancy
- Young age

When MRI is used to assess disease burden, DWI with high *b*-values should always be included to assess peritoneal deposits due to its high sensitivity [99].

PET/CT may also be used for staging as an alternative to CT or MRI, particularly in patients presenting with pleural effusion and/or suprarenal lymphadenopathy [100]. Nevertheless PET/CT should be used carefully in early-stage disease due to its high rate of false-positive results [101].

Finally, it should be kept in mind that the optimal coverage for staging ovarian cancer by CT or MRI includes imaging from lung bases to the inguinal region [102].

6.3.3 Pathology and MRI Correlation

Ovarian neoplasms were classified by the World Health Organization (WHO) according to the tissue of origin into surface epithelial tumors, germ cell tumors, and sex cord–stromal tumors. These are further divided into benign, borderline, or malignant, which reflects their clinical behavior and prognosis [103].

6.3.4 Surface Epithelial Tumors

6.3.4.1 Borderline Epithelial Tumors

Borderline tumors (BOTs) are a unique entity of ovarian neoplasms without infiltrative destructive growth or stromal invasion. They represent 15–20 % of all ovarian tumors and usually affect younger women when compared to invasive carcinoma. They occur in all types of epithelial ovarian tumors, but are more common in serous and mucinous subtypes. They are associated with normal or minimally elevated CA125 level and are usually diagnosed at early stage. Up to 30 % of cases are bilateral. Use of fertility drugs and contraceptives has been correlated to an increased incidence of these tumors in the past decades. Endometriosis is also a recognized precursor for endometrioid and clear cell borderline tumors. Peritoneal implants may be present at the diagnosis, particularly in the serous subtype. Nevertheless, prognosis is better than that of common invasive epithelial ovarian cancer.

As these tumors affect young women who should be offered fertility-sparing surgery, identification of BOTs is a critical challenge for imaging. Despite several authors' efforts in identifying morphological imaging features suggestive of borderline lesions [104, 105], no specific findings have been demonstrated so far. In fact there is still a significant overlap with imaging features of invasive malignancy.

As reported in the literature, disease assessment should include confirmation of ipsilateral normal-appearing ovarian stroma and examination of the contralateral ovary to allow clinical decision towards fertility-preserving surgery. Furthermore, since the presence of invasive peritoneal implants significantly affects prognosis, assessment of peritoneal/omental disease and lymphadenopathy using MRI with DWI and complete surgical staging are mandatory.

Serous Borderline Neoplasm of the Ovary

Serous borderline tumors are the most common accounting for approximately 65 % of all BOTs [106]. Mean age at presentation is 34–40 years. These are slowly growing lesions that may exhibit an aggressive behavior consistent with peritoneal implants and regional lymphadenopathy (35 and 27 %, respectively). These peritoneal implants are classified as noninvasive (serous papillae in cystic spaces or plastered on the peritoneal surface, without invasion of the underlying tissue) or invasive (with invasion by haphazardly distributed glands and small cell clusters accompanied by a dense stromal reaction) – the latter having a poorer prognosis.

On MRI borderline serous ovarian tumors manifest as complex predominantly cystic mass (bilateral in 30 % of cases) with thin septa and endocystic or exocystic vegetations showing moderate early enhancement on dynamic MR imaging [107]. DW-MRI should be included to improve peritoneal implant detection, even if at the diagnosis 70 % of serous BOT are confined to the ovary (Fig. 6.6).

Mucinous Borderline Neoplasm of the Ovary

Mucinous borderline tumors of the ovary comprise 32 % of all BOTs. Mean age at presentation is 45 years. There are two distinct subtypes: the intestinal (90 %) and the mullerian (10 %) histotypes. The first one is usually unilateral and associated with pseudomyxoma peritonei in up to 17 % of cases. The second one is bilateral in 40 % of cases and associated with endometriosis in one-third of cases. On MRI they manifest as multilocular cystic mass with numerous septa containing fluids of variable signal intensities on T1- and T2-weighted images (stained glass appearance). The endocystic vegetations usually show delayed uptake of contrast medium [108] on DCE-MRI. The mullerian subtype tends to present as uni- or paucilocular cyst with mural enhancing nodules. At diagnosis up to 82 % of mucinous BOTs are confined to the ovary with peritoneal implants less common compared to serous BOTs.

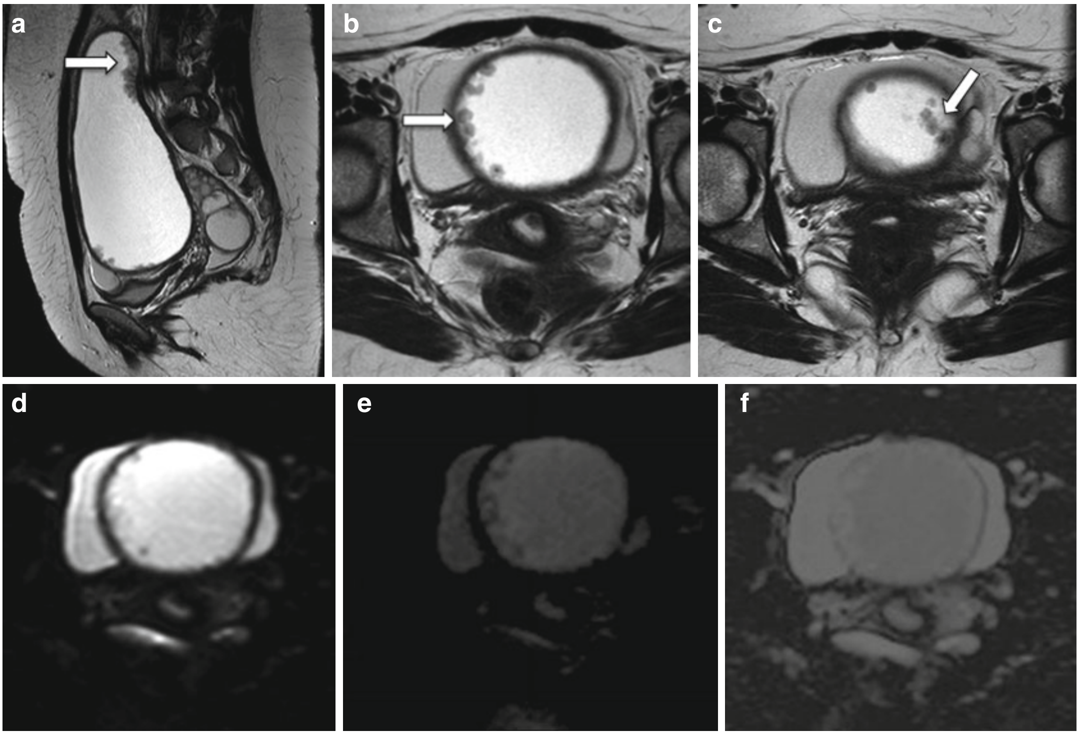

Fig. 6.6 Borderline serous cystadenoma low grade. A 30-year-old woman with bilateral complex cystic adnexal masses (sagittal and axial T2 images, TR:4361, TE:80; **a**–**c**); the largest on the right shows multiple papillary projections (*arrows*). No restricted diffusion is demonstrated (b0, b750, and ADC map, **d**–**f**)

6.3.4.2 Invasive Epithelial Tumors

Surface epithelial carcinomas represent 85–90 % of all ovarian malignancies. These consist in serous, mucinous, endometrioid, and clear cell carcinoma.

Serous Adenocarcinoma

Malignant serous tumors represent one-third of all ovarian serous neoplasms and approximately 50 % of all ovarian malignancies, with serous cystadenocarcinoma being the most common type of surface epithelial ovarian cancer [109]. More than 60 % of serous cystadenocarcinomas are bilateral. On MRI they usually manifest as predominantly cystic, unilocular or multilocular masses with multiple thick septations, mural nodules, and papillary projections avidly enhancing after contrast medium administration. Areas of hemorrhage (bright on T1- and variable on T2-weighted images with no signal drop on fat-sat images) or necrosis are common. Calcifications may be present – psammoma bodies with microscopic calcifications in 30 % of cases [110] (Fig. 6.7). Peritoneal implants are frequent in advanced stage disease. Bowel obstruction and hydronephrosis should always be considered as possible complications.

Mucinous Adenocarcinoma

Malignant mucinous tumors represent 5–10 % of all malignant ovarian tumors and are the second more common type of epithelial ovarian cancer. They tend to be larger than serous ones, but less frequently bilateral (only 20 %) [87]. On MRI they present as multilocular complex cystic masses, with honeycomb-like locules. Because of the variable protein and mucinous contents, these loculi show variable high signal on T1- and T2-weighted images configuring the so-called stained glass appearance (Fig. 6.8). Compared to borderline, invasive mucinous carcinomas have thick septa

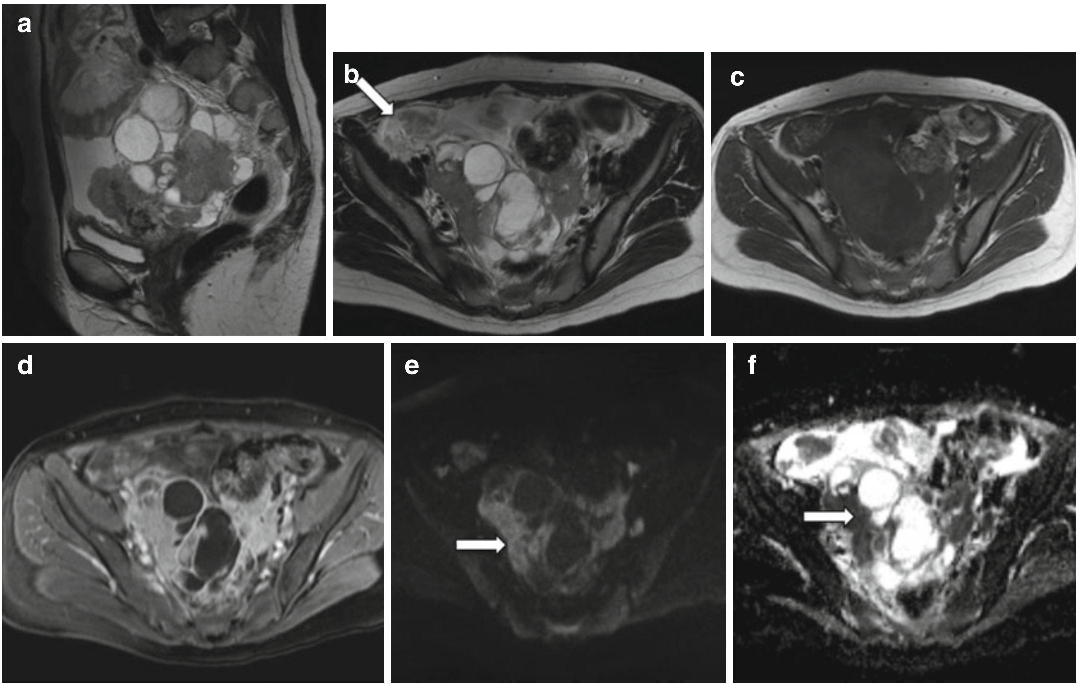

Fig. 6.7 High grade ovarian serous cystadenocarcinoma. A 33-year-old woman with a rapidly enlarging pelvic mass and elevated CA125. Pelvic MRI demonstrates bilateral adnexal masses with solid components of intermediate signal intensity on T2-weighted images (TR:4361, TE:80; **a**, **b**) and predominantly low signal intensity on T1-weighted image (TR:519, TE:10; **c**). The solid components are avidly enhancing post-contrast medium injection (**d**) and demonstrate marked hyperintensity on b1000 DWI (**e**) with restricted signal on the corresponding ADC map (**f**). There is ascites with peritoneal disease (*arrows*). Note the high sensitivity of the high-b-value DWI for peritoneal implant detection

and avidly enhancing solid components. Pseudomyxoma peritonei may be associated with the intestinal subtype with large amount of fluid-like (mucoid) material throughout the abdomen surrounding mesentery, bowel, and solid organs [29].

Endometrioid Adenocarcinoma

Endometrioid adenocarcinoma of the ovary is a primary ovarian surface epithelial carcinoma histologically identical to a typical adenocarcinoma arising from the endometrium. It represents 5.7 % of ovarian surface epithelial neoplasms, 17.5 % of all ovarian carcinomas, and the third most common type of ovarian malignancy after serous and mucinous cystadenocarcinomas. It can be bilateral in up to 30 % of cases. There is a well-established correlation between endometrioid adenocarcinoma, endometriosis, and endometrioid hyperplasia. Simultaneous manifestation of endometriomas and ovarian endometrioid adenocarcinoma occurs in 15–25 % of cases [111]. Kitajima et al compared contrast-enhanced MRI appearance of ovarian endometrioid adenocarcinoma arising or not arising from endometrioma, and they found interesting differences. Tumors arising from endometriomas usually present on T1-weighted imaging as low to intermediate nodules within a predominantly cystic mass. They also have a lower nuclear grade and are diagnosed at a less advanced clinical stage (Fig. 6.9). On the other hand, tumors not arising from endometriomas present as solid masses with a higher nuclear grade and more advanced clinical stage. Furthermore, endometrioid adenocarcinoma arising from endometriomas does not show the characteristic “shading effect” of benign endometriomas consistent in T1

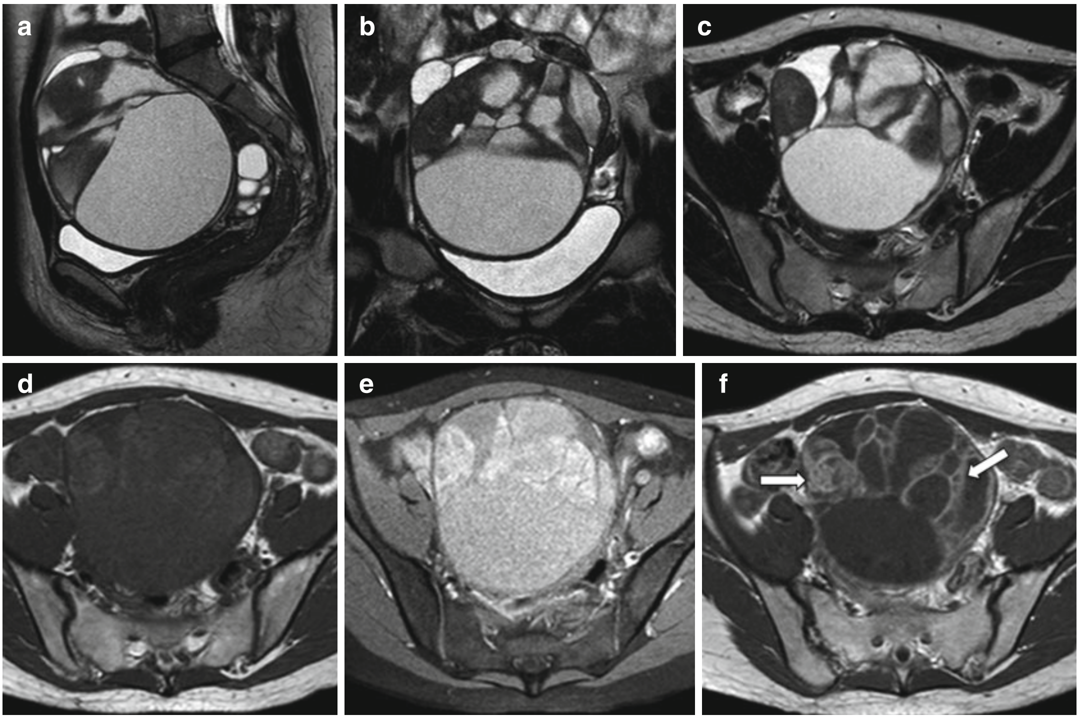

Fig. 6.8 Mucinous adenocarcinoma. A 25-year-old lady with abdominal pain and elevated CA125. There is a large multiloculated, predominantly cystic pelvic mass. The locules contain variable hyperintense fluid on T2-weighted images (TR:4361, TE:80; images **a**–**c**), while others contain mildly hyperintense components on T1-weighted image, suggestive of hemorrhage/mucin (TR:519, TE:10; **d**). No areas of fat saturation (**e**). There are numerous thick septa and enhancing solid components (**f**, *arrows*)

hyperintensity with layering T2 hyper-/hypointensity due to the magnetic susceptibility effect of old hemorrhage or densely concentrated fluid/fibrosis [40, 112].

Clear Cell Carcinoma

Clear cell carcinoma (CCC) represents approximately 5 % of all ovarian carcinomas and usually affects women in peri–postmenopausal age (around the age of 50 years). Up to 20 % of cases are bilateral. Despite the fact that this tumor is almost always malignant, the overall prognosis is good, as it tends to remain confined to the ovary with up to 75 % of patients presenting with stage I disease [113]. The survival rate is of 50 % at 5 years from the diagnosis. Recurrent CCC is more aggressive with distant organs and lymph node involvement occurring in 40 % of cases. There is a correlation with nulliparity and endometriosis; when arising within benign endometriomas, CCC tends to have a worse prognosis. On MRI CCCs usually appear as unilocular cystic masses with smooth margins, larger than 4 cm with cystic contents from low to very high T1 signal intensity and always high T2 signal. They can be either predominantly solid or cystic with one or more solid protrusions [114].

Brenner Tumor

Brenner tumors are uncommon transitional cell tumors of the ovary, accounting for about 2 % of ovarian neoplasms. The majority of them are benign, but borderline and malignant types can also arise. When malignant they tend to present later (around the age of 60 years) compared to the benign form (mean age at presentation of 40–60 years). They are usually discovered as incidental findings during surgery, transvaginal ultrasound, or MRI (over 90 % of them) [115]. While benign Brenner tumors are cured by local excision, the

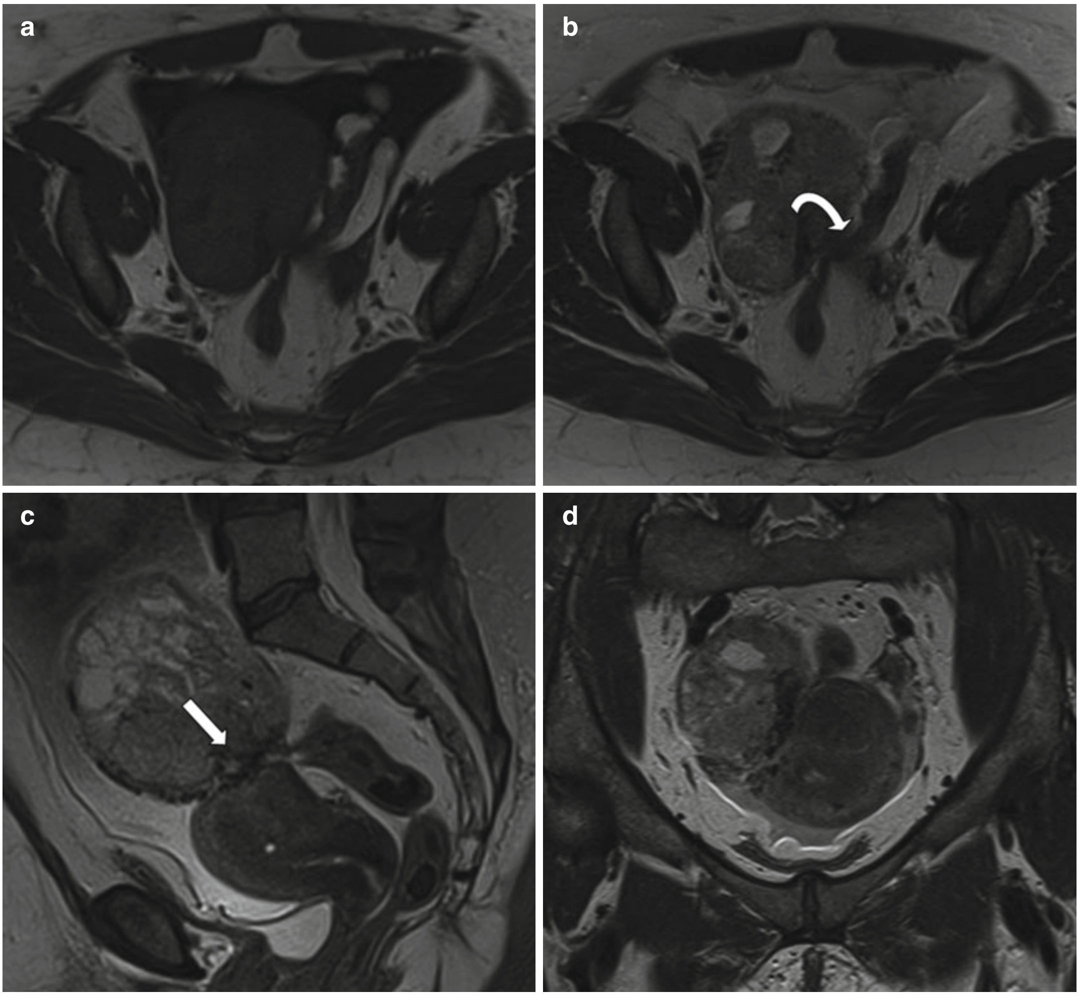

Fig. 6.9 Grade 1 endometrioid carcinoma in a background of diffuse endometriosis. A 52-year-old lady with a large right-sided predominantly solid pelvic mass. This demonstrates low signal intensity on T1-weighted image (TR:519, TE:10; **a**) and heterogeneous signal intensity on T2-weighted images (TR:4361, TE:80; **b**–**d**). Note large feeding vessels, best seen on sagittal image (**c**, *arrow*). There is a fibrotic plaque tethering the sigmoid bowel as a result of previous endometriosis (*curved arrow*)

malignant ones are incurable with a very poor prognosis. Borderline Brenner tumors have intermediate histological appearance and aggressiveness compared to the benign and malignant types. Malignant tumors are usually larger than the benign ones, with an average of 8–10 cm in diameter. They may present with nonspecific symptoms including abdominal distention, pain, and PV bleeding. On MRI, malignant Brenner tumors may appear as multiloculated cystic masses with heterogeneously enhancing solid components and papillary projections. The cystic components are of high signal intensity on T2-weighted imaging. Interestingly, the benign form tends to appear as predominantly solid mass of low signal intensity on both T1- and T2-weighted imaging with calcifications and rapid enhancement after contrast medium administration [72, 116, 117]. Differential diagnosis should include solid ovarian masses with or without calcification on CT and MRI, such as benign teratoma, fibroma–thecoma, granulosa cell tumor, Krukenberg tumor, and primary lymphoma. About 30 % of Brenner tumors occur in association with ipsilateral ovarian tumors such as mucinous cystadenomas [118].

6.3.5 Sex Cord–Stromal Tumors

Sex cord tumors account for 5–10 % of all ovarian malignancies and derive from sex cord and specialized stroma of the developing gonads [119]. They can differentiate into an ovarian direction (granulosa–theca cells), into a testicular direction (Sertoli–Leydig), or into a stromal–fibromatous direction. They may occur from childhood (5 % of all malignancies in this age) to reproductive age and postmenopausal phase, being more common after menarche. These tumors are also the most common functional neoplasms of the ovary [3].

6.3.5.1 Granulosa Cell Tumor

Granulosa cell tumors (GCT) derive from the cells surrounding the developing follicles. There are two different histological types: adult and juvenile. The adult type is of low malignant potential and occurs usually in peri- and postmenopausal age, with a peak of prevalence in 50–55-year-old women. It accounts for 95 % of all GCT and represents 5–10 % of solid ovarian tumors. The adult type is far more common than the juvenile type [120, 121]. Because these tumors produce estrogen, they are associated with endometrial hyperplasia, polyps, or carcinoma (usually well differentiated, occurring in 3–25 % of patients) and can manifest with irregular bleeding in premenopausal patients or postmenopausal bleeding [122]. There is a rare form that can produce androgen and is usually associated with purely cystic tumors [16]. Juvenile GCT constitutes only 5 % of all GCTs with a mean age of 13 years. Only 3 % of these tumors occur in women older than 30 years. In the most frequent case, it occurs in premenarchal girls causing sexual precocity because of the estrogen production [123]. Adult and juvenile GCTs have similar appearance on imaging. They are commonly unilateral solid or mostly solid masses and rarely cystic. Because of hemorrhage within the tumor, they usually show hyperintensity on T1-weighted images. When cystic they tend to be multilocular with a typical "sponge-like" appearance on T2-weighted imaging [124, 125]. Solid components demonstrate enhancement on post-gadolinium images. The histological features are not related to an accurate prediction of clinical behavior. Around 90 % of adult GCTs are found at stage I with a consequent excellent prognosis. Metastases and recurrences commonly occur long after surgery with a slow growth rate [126].

6.3.5.2 Sertoli–Stromal Tumor

Sertoli–stromal tumors are classified into Sertoli, stromal–Leydig, and Sertoli–Leydig cell tumors. Sertoli cell tumors account for only 4 % of these tumors and are usually non-functioning. Stromal–Leydig cell tumors are extremely rare (0.5 % of all ovarian tumors). They usually occur in women around the age of 30 years or younger. Less than 10 % of affected patients are over the age of 50 years. About 30 % of patients show virilization, manifested by amenorrhea or virilized secondary sexual characteristics, while 50 % have no hormonal manifestations [127]. Only occasionally these tumors can produce estrogens. They are rarely bilateral and have a variable appearance being either solid, mixed solid–cystic, or purely cystic. They may appear as a well-defined enhancing solid mass with or without multiple variable-sized cystic areas [23]. When they cause virilization, they are commonly small and difficult to detect on MRI [128]. Usually these small steroid-secreting tumors show high signal intensity on T1-weighted images because of the lipid content and avid enhancement after contrast administration. Low signal intensity on T2-weighted imaging depends on the extent of fibrous stroma (Fig. 6.10). They are microscopically ranged from well differentiated to poorly differentiated with accordance to clinical behavior. Most of them are stage I at

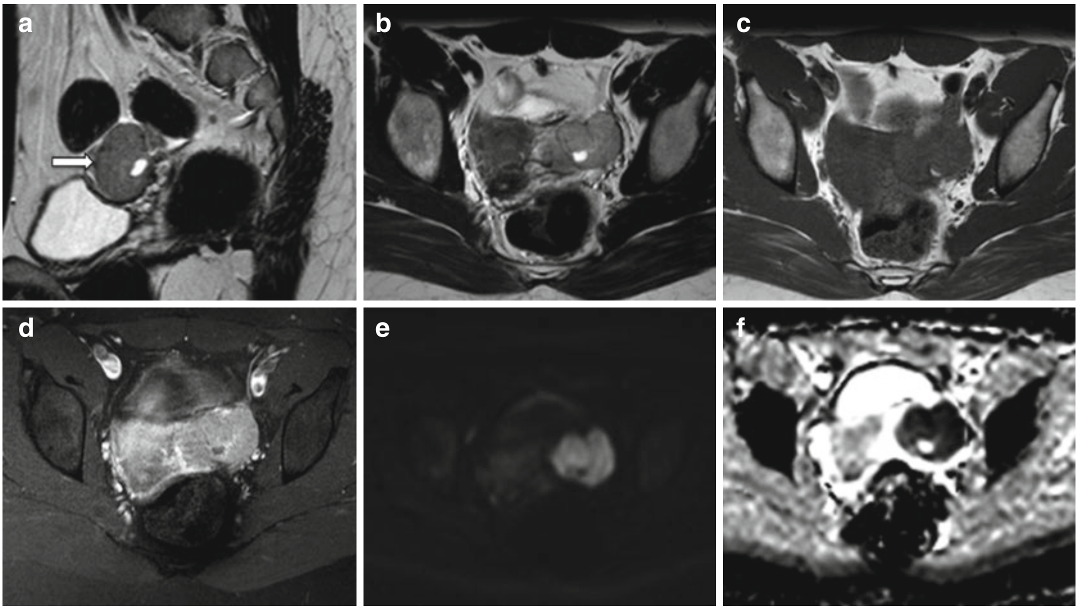

Fig. 6.10 Poorly differentiated Sertoli–Leydig ovarian tumor. Left-sided solid ovarian mass (*arrow*) in a 23-year-old patient with oligomenorrhea and excessive hair growth. The mass demonstrates intermediate signal intensity on T1- and T2-weighted images (TR:519, TE:10 and TR:4361, TE:80; **a**–**c**) and avid contrast medium enhancement (**d**). There is hyperintensity on the b1000 DWI (**e**) with hypointensity on the corresponding ADC map (**f**) indicating restricted diffusion

diagnoses and behave in a benign way [20]. Recurrence tends to occur soon after initial diagnosis.

6.3.5.3 Steroid Cell Tumor

Steroid cell tumors account for 0.1–0.2 % of all ovarian tumors and include three subtypes: stromal luteoma, Leydig (or hilus) cell tumor, and steroid cell tumor not otherwise specified [16]. They are all formed by typical steroid-secreting cells, including lutein cells, Leydig cells, and adrenocortical cells with abundant intracellular lipid. For these reasons these tumors are also called *lipid* or *lipoid cell* tumors. Mean age at presentation is around 50–60 years, but they can affect women of all ages. At imaging they usually appear as unilateral solid tumors, sometimes with small areas of cystic change or necrosis. When they cause virilization they are commonly small. Because of the presence of a high content of lipids, they show high signal intensity on T1-weighted imaging. Some authors suggested that chemical shift imaging can help in identifying the presence of intratumoral lipids [129]. After contrast administration they show intense enhancement because of the abundant blood vessels supplying the tumorous tissue. When they don't cause virilization, they are larger with a lobulated, solid appearance [8].

6.3.6 Germ Cell Tumors

6.3.6.1 Immature Teratoma

Immature teratoma represents less than 1 % of all teratomas and contains immature tissue from all three germ cell layers. It typically presents in the first two decades of life. In 26 % of cases it is associated with an ipsilateral mature teratoma

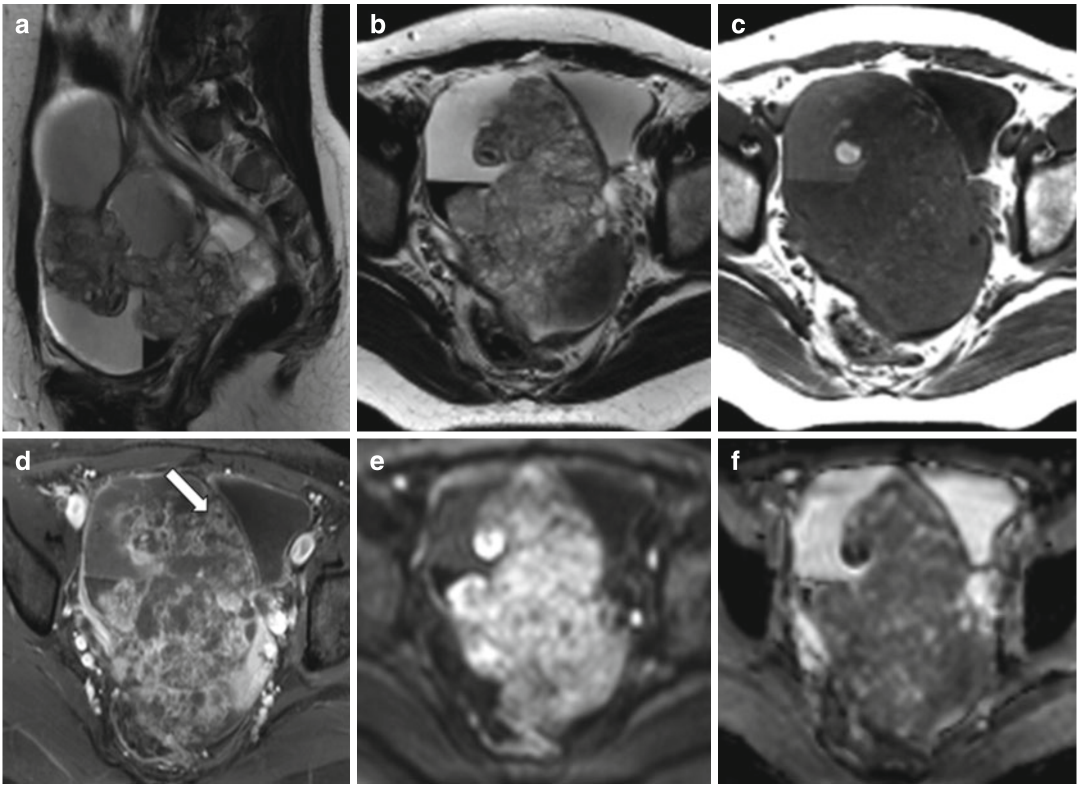

Fig. 6.11 Immature teratoma grade 2. A 27-year-old woman with a large, mixed cystic and solid, pelvic mass. The mass demonstrates heterogeneous T2/T1 signal intensity (TR:4361, TE:80 and TR:519, TE:10; **a**–**c**) and avid contrast medium enhancement (**d**). The solid components are hyperintense on b1000 image (**e**) and hypointense on the corresponding ADC map (**f**) indicating restricted diffusion. A few small areas of fat are present throughout the mass and best demonstrated on the T1-weighted, fat-saturated pulse sequence image (TR:519, TE:10; **d**, *arrow*)

and in 10 % of cases with an immature teratoma in the contralateral ovary [130]. Immature teratomas tend to present as large, complex masses with cystic and solid components and scattered calcifications, while mature teratomas tend to be smaller with calcifications usually associated to mural nodules [81]. The fat distribution is typical in immature teratomas with small, punctuated foci of fatty tissue scattered throughout the tumor; homogeneous larger fat deposits are present in benign lesions. Gradient echo sequences can be helpful in identifying small fat components in immature teratomas. Tumor capsule is not always well defined and can be perforated by rapid tumor growth. On MR solid tissue shows a wide variety of signal intensities on T2-weighted images (Fig. 6.11). Ascites and peritoneal dissemination can be observed [5, 131]. Despite several studies attempting to define specific features on conventional and functional MRI (DCE-MRI; DW-MRI) for the identification of immature teratomas, the differential diagnosis between the immature and the mature form remains challenging [71, 132].

6.3.6.2 Dysgerminoma

Dysgerminomas are rare ovarian tumors (3–5 % of all ovarian malignancies) that affect usually young women (less than 30 years old). They are usually not associated with endocrine hormone secretion. An elevated HCG serum level can be found in 5 % of cases: this is due to the presence of syncytiotrophoblastic giant cells able to produce HCG [26]. On MRI, they appear as multiloculated solid masses with prominent fibrovascular septa hypointense or isointense on

T2-weighted imaging, with avid enhancement after contrast administration on T1-weighted imaging. As recently demonstrated, these septa correspond to fibrovascular bundles at histologic examination [133]. Calcifications may be present in a speckled pattern together with necrosis and hemorrhage [27, 30], the latter appearing as high signal intensity on T1-weighted imaging.

6.3.6.3 Choriocarcinoma

Primary ovarian choriocarcinoma is an extremely rare germ cell tumor that occurs almost exclusively in patients younger than 20 years [134]. This is an aggressive tumor that usually has already metastasized to the lungs, liver, and bones by the time of presentation. In patients of reproductive age, a metastatic origin from uterine malignancy or a tumor arising from an ectopic ovarian pregnancy should be considered. Other forms of malignant germ cell neoplasms such as immature teratoma may present in association with this tumor. On MRI, it is usually unilateral and predominantly solid with hemorrhage and necrosis [31]. The main biochemical feature is the concomitant elevated serum HCG level [26].

6.3.6.4 Carcinoid Tumor

Ovarian carcinoids are extremely rare neoplasms, accounting for 0.3 % of all carcinoid tumors and for 0.1 % of all malignant ovarian tumors [135]. They usually have a low grade malignant potential, being benign in 95 % of cases. They are classically diagnosed as unilateral enhancing solid nodules often within the wall of mature cystic teratomas. When presenting as isolated enhancing masses, it is not possible to discriminate from a solid malignancy. They can also be associated to mucinous neoplasms. In the majority of cases they are asymptomatic, but in some cases typical carcinoid syndrome or constipation due to secretion of peptide YY can occur. On MRI they typically show low signal on T2-weighted images as almost all benign fibrous neoplasms. These tumors also tend to exhibit high signal intensity on diffusion-weighted imaging with low ADC values and hypervascularity on dynamic studies after contrast medium administration [136].

6.3.7 Other Rare Tumors

6.3.7.1 Mixed Mullerian Tumor

Mixed Mullerian tumors represent less than 1 % of all ovarian neoplasms and contain both epithelial and sarcomatous elements [137, 138]. They can originate anywhere along the female genital tract and in the peritoneum; the most frequent location is the uterus, but they can be found in the ovary, vagina, cervix, and fallopian tubes [139]. They are always malignant with very poor prognosis and usually diagnosed at advanced stage (70 % at stage III and IV) in postmenopausal women. On MRI they appear as large (even more than 10 cm), well-encapsulated, multinodular, and multicystic masses with very heterogeneous appearance and enhancing solid elements (papillary projections). Fluid–fluid levels within multilocular cystic components may be present due to old hemorrhage. The enhancement patterns can be extremely variable as well [140]. Secondary signs of malignancy such as ascites and metastases are usual findings at presentation.

6.3.7.2 Lymphoma

Ovarian involvement by a malignant lymphoma is usually a manifestation of disseminated disease. Primary lymphoma of the ovary is very rare, likewise other primary lymphomas of the genital tract, and accounts for 0.5 % of all non-Hodgkin's lymphomas and 1.5 % of all malignant ovarian neoplasms. Since there is no lymphoid tissue within the ovary, the tumor may originate from lymphocytes surrounding blood vessels or related to the corpus luteum. Diagnosis of primary ovarian lymphoma should be suggested when the tumor is confined to the ovary and regional lymph nodes or adjacent organs with no abnormal cells found in bone marrow and peripheral blood [141–144]. Non-Hodgkin's large B cell lymphoma is the most common type of lymphoma involving the ovary. It manifests as a large solid mass with a very rapid growth that must be differentiated from other predominantly solid tumors such as thecoma, fibroma, Brenner tumor, immature germ cell tumor, or granulocytic sarcoma. They present as unilateral or bilateral homogeneous adnexal masses without ascites. On MRI, the solid masses appear of intermediate signal intensity on T1- and T2-weighted imaging, with homogeneous enhancement after contrast administration. Several small cysts in a linear arrangement at the periphery of the mass may be present consisting of preserved follicles at the periphery of the ovary [145, 146]. Prognosis is the same as that of a NHL arising in a different site of the body.

6.3.7.3 Sarcoma

Sarcomas of the ovary are very rare neoplasms. In the literature fibrosarcoma, leiomyosarcoma, malignant peripheral nerve sheath tumor, angiosarcoma, rhabdomyosarcoma, osteosarcoma, and chondrosarcoma have been described as sporadic cases [147–153]. At MRI they show as a large tumor mass with heterogeneous high intensity on T2-weighted images and low intensity on T1-weighted images, with laminar or stripe-like enhancement. Hemorrhage and necrosis can be displayed in these lesions [154].

6.3.8 Metastases

Metastatic tumors of the ovary represent about 5–10 % of ovarian neoplasms. The ovary is a relatively preferential site of metastatic disease, as neoplastic cells can easily reach the ovary through hematogenous, lymphatic, and transperitoneal spread and/or direct extension. About 7 % of lesions clinically presenting as primary ovarian tumors are metastatic in origin. The most common primary tumors that metastasize to the ovary are stomach (Krukenberg tumor), colon, breast, and endometrial malignancies. Less frequently tumors arising from the pancreas, biliary duct, and lung may spread to the adnexal [155, 156]. A detailed clinical history is mandatory as ovarian secondarism may occasionally be the only initial manifestation of the disease, particularly in cancers of the gastrointestinal tract [157].

6.3.8.1 Krukenberg Tumor

Krukenberg tumor refers to bilateral ovarian metastases characterized by mucin-producing signet ring cells, most commonly from gastric cancer. Metastatic cells from gastric cancer easily penetrate the ovary and tend to stimulate a dense stromal reaction with variable degree of luteinization mimicking a fibroma or another spindle cell tumor. Morphologically most of these tumors are lobulated and complex consisting of solid elements with cystic areas. On MRI the solid components typically show heterogeneous signal intensity at T2-weighted imaging, related to the degree of stromal overgrowth and the amount of mucin produced (Fig. 6.12). Low signal intensity areas correspond to increased cellularity of fibrous stroma, whereas high signal intensities correspond to edema within the connective tissue and mucin [158]. Intratumoral cysts can be occasionally associated. Signal voids can be observed within the tumors, those representing increased tumor vascularity. After contrast administration the solid component shows homogeneous enhancement [158].

6.3.9 Collision Tumors

Collision tumors represent the coexistence of two histologically distinct but not mixed tumors. These tumors have been reported in various organs such as the brain, esophagus, stomach, liver, lung, thyroid, bone, uterus, ovary, kidney, adrenal gland, skin, paranasal sinus, and lymph nodes. Ovarian collision tumors are rare entities, most commonly composed of teratomas in combination with benign, borderline, or invasive epithelial tumors. Prognosis and treatment depend on tumor types present. Preoperative suggestion of a collision tumor is crucial, leading the pathologist to perform a thorough examination of the mass to diagnose the composing tumor types. A correct definition of these is critical for further patient management and prognosis [159]. When an ovarian tumor demonstrates imaging findings that cannot be subsumed as one specific histological type, especially in cases of ovarian teratoma, a collision tumor should be considered [159].

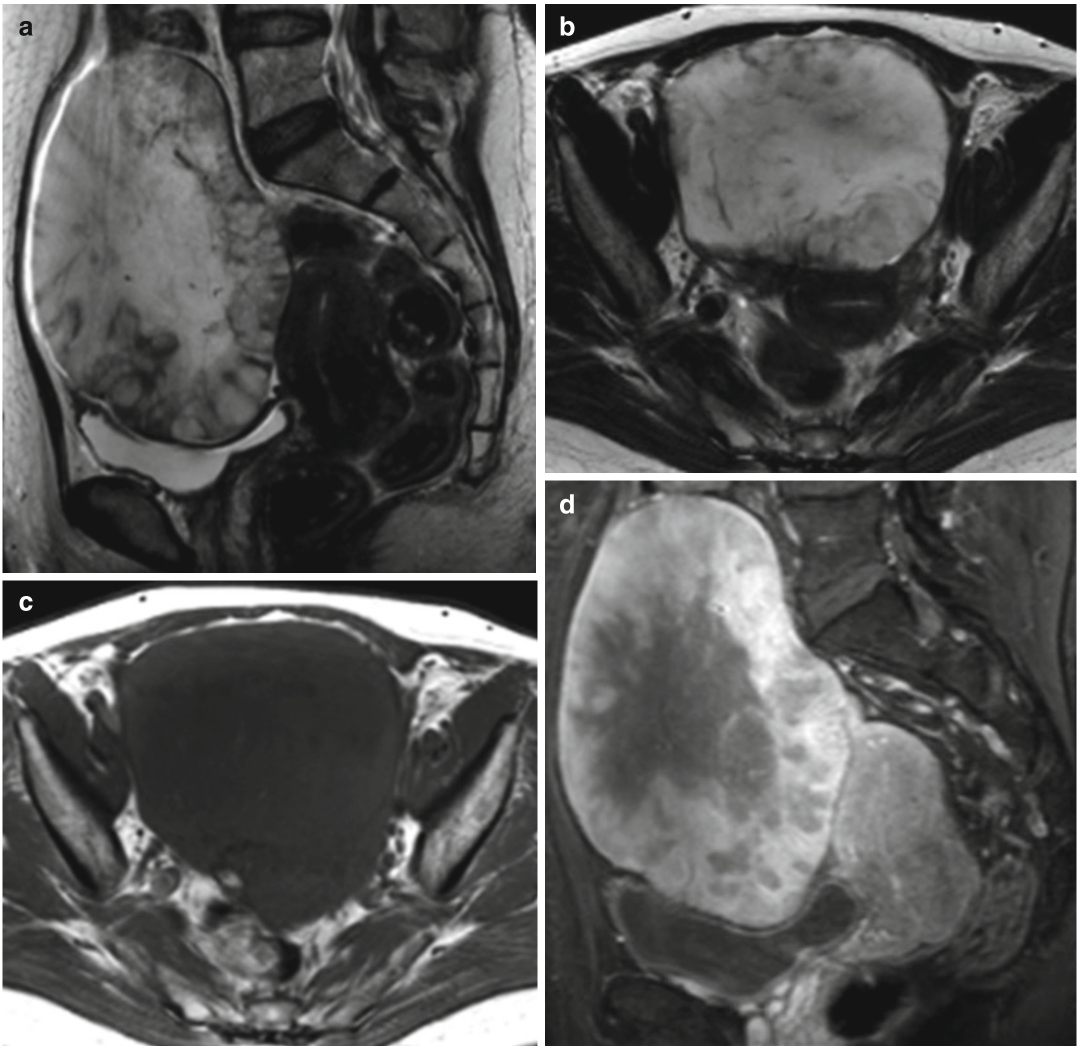

Fig. 6.12 Krukenberg. A 56-year-old patient with gastric adenocarcinoma and elevated CA125. There is a large pelvic mass with heterogeneous high signal intensity on T2-weighted images (TR:4361, TE:80; **a**, **b**) and low signal intensity on T1-weighted image (TR:519, TE:10; **c**). The mass is predominantly solid with avid peripheral enhancement after i.v. contrast medium administration (**d**)

References

1. Jemal A, Siegel R (2007) Cancer statistics cancer. J Clin 57:43–66
2. Myers ER et al (2006) Management of adnexal mass. Evid Rep Technol Assess (Full Rep) Feb;(130):1–145
3. Liu JH, Zanotti KM (2011) Management of the adnexal mass. Obstet Gynecol 117(6):1413–1428
4. Schorge JO et al (2010) SGO White Paper on ovarian cancer: etiology, screening and surveillance. Gynecol Oncol 119(1):7–17
5. Jung SE et al (2002) CT and MR imaging of ovarian tumors with emphasis on differential diagnosis. Radiographics 22(6):1305–1325
6. Sala EJ, Atri M (2003) Magnetic resonance imaging of benign adnexal disease. Top Magn Reson Imaging 14(4):305–327
7. Imaoka I et al (2006) Developing an MR imaging strategy for diagnosis of ovarian masses. Radiographics 26(5):1431–1448
8. Levine CD et al (1997) Benign extraovarian mimics of ovarian cancer. Distinction with imaging studies. Clin Imaging 21(5):350–358

9. Kurjak A et al (1993) Transvaginal color Doppler sonography in the assessment of pelvic tumor vascularity. Ultrasound Obstet Gynecol 3(2):137–154
10. Prompeler HJ, Madjar H, Sauerbrei W (1996) Classification of adnexal tumors by transvaginal color Doppler. Gynecol Oncol 61(3):354–363
11. Qayyum A et al (2005) Role of CT and MR imaging in predicting optimal cytoreduction of newly diagnosed primary epithelial ovarian cancer. Gynecol Oncol 96(2):301–306
12. Spencer JA, Forstner R, Hricak H (2008) Investigating women with suspected ovarian cancer. Gynecol Oncol 108(2):262–264
13. Spencer JA, Ghattamaneni S (2010) MR imaging of the sonographically indeterminate adnexal mass. Radiology 256(3):677–694
14. Hricak H et al (2000) Complex adnexal masses: detection and characterization with MR imaging–multivariate analysis. Radiology 214(1):39–46
15. Tempany CM et al (2000) Staging of advanced ovarian cancer: comparison of imaging modalities–report from the Radiological Diagnostic Oncology Group. Radiology 215(3):761–767
16. Saksouk FA, Johnson SC (2004) Recognition of the ovaries and ovarian origin of pelvic masses with CT. Radiographics 24(Suppl 1):S133–S146
17. Foshager MC, Hood LL, Walsh JW (1996) Masses simulating gynecologic diseases at CT and MR imaging. Radiographics 16(5):1085–1099
18. Outwater EK et al (1998) Dilated fallopian tubes: MR imaging characteristics. Radiology 208(2):463–469
19. Sohaib SA et al (2003) Characterization of adnexal mass lesions on MR imaging. AJR Am J Roentgenol 180(5):1297–1304
20. Li W et al (2012) Diffusion-weighted MRI: a useful technique to discriminate benign versus malignant ovarian surface epithelial tumors with solid and cystic components. Abdom Imaging 37(5):897–903
21. Bakir B et al (2011) Diffusion-weighted imaging of solid or predominantly solid gynaecological adnexial masses: is it useful in the differential diagnosis? Br J Radiol 84(1003):600–611
22. Nakayama T et al (2005) Diffusion-weighted echo-planar MR imaging and ADC mapping in the differential diagnosis of ovarian cystic masses: usefulness of detecting keratinoid substances in mature cystic teratomas. J Magn Reson Imaging 22(2):271–278
23. Sarty GE et al (2004) Magnetic resonance diffusion imaging of ovarian masses: a first experience with 12 cases. MAGMA 16(4):182–193
24. Takeuchi M, Matsuzaki K, Nishitani H (2010) Diffusion-weighted magnetic resonance imaging of ovarian tumors: differentiation of benign and malignant solid components of ovarian masses. J Comput Assist Tomogr 34(2):173–176
25. Thomassin-Naggara I et al (2009) Contribution of diffusion-weighted MR imaging for predicting benignity of complex adnexal masses. Eur Radiol 19(6): 1544–1552
26. Thomassin-Naggara I et al (2008) Epithelial ovarian tumors: value of dynamic contrast-enhanced MR imaging and correlation with tumor angiogenesis. Radiology 248(1):148–159
27. Bernardin L et al (2012) Effectiveness of semi-quantitative multiphase dynamic contrast-enhanced MRI as a predictor of malignancy in complex adnexal masses: radiological and pathological correlation. Eur Radiol 22(4):880–890
28. Thomassin-Naggara I et al (2008) Dynamic contrast-enhanced magnetic resonance imaging: a useful tool for characterizing ovarian epithelial tumors. J Magn Reson Imaging 28(1):111–120
29. Thomassin-Naggara I et al (2007) Value of dynamic enhanced magnetic resonance imaging for distinguishing between ovarian fibroma and subserous uterine leiomyoma. J Comput Assist Tomogr 31(2):236–242
30. Occhipinti KA (1999) CT and MRI of the ovary. In: Anderson JC (ed) Gynecologic imaging. Churchill Livingston, London, pp 345–359
31. Sutton CL et al (1992) Ovarian masses revisited: radiologic and pathologic correlation. Radiographics 12(5):853–877
32. Forstner R (2007) Adnexal masses: characterization of benign ovarian lesions. In: Bernd H (ed) MRI and CT of the female pelvis. Springer, Berlin\New York, pp 197–232
33. Atri M et al (1994) Endovaginal sonographic appearance of benign ovarian masses. Radiographics 14(4):747–760; discussion 761–2
34. Outwater EK, Mitchell DG (1996) Normal ovaries and functional cysts: MR appearance. Radiology 198(2):397–402
35. Nishie A et al (2003) Presacral dermoid cyst with scanty fat component: usefulness of chemical shift and diffusion-weighted MR imaging. Comput Med Imaging Graph 27(4):293–296
36. Outwater E et al (1993) Characterization of hemorrhagic adnexal lesions with MR imaging: blinded reader study. Radiology 186(2):489–494
37. Young RH, Crum P, Scully RE (1989) The ovary. In: Stephen SS (ed) Diagnostic surgical pathology. Raven, New York, pp 1655–1734
38. Russell P, Bannatyne P (1989) Dysfunctional cysts. In: Surgical pathology of the ovaries. Churchill Livingstone, Edinburgh\New York, pp 97–107
39. Yeh HC, Futterweit W, Thornton JC (1987) Polycystic ovarian disease: US features in 104 patients. Radiology 163(1):111–116
40. Togashi K et al (1991) Endometrial cysts: diagnosis with MR imaging. Radiology 180(1):73–78
41. Nishimura K et al (1987) Endometrial cysts of the ovary: MR imaging. Radiology 162(2):315–318
42. Stern RC et al (2001) Malignancy in endometriosis: frequency and comparison of ovarian and extraovarian types. Int J Gynecol Pathol 20(2):133–139
43. Dmowski WP, Radwanska E (1984) Current concepts on pathology, histogenesis and etiology of endometriosis. Acta Obstet Gynecol Scand Suppl 123:29–33

44. Gerbie AB, Merrill JA (1988) Pathology of endometriosis. Clin Obstet Gynecol 31(4):779–786
45. Clement PB (1994) Pathology of endometriosis. In: Fechner R, Rosen PP (eds) Pathology annual. Appleton & Lange, Norwalk, pp 245–295
46. Patel MD et al (1999) Endometriomas: diagnostic performance of US. Radiology 210(3):739–745
47. Mostoufizadeh M, Scully RE (1980) Malignant tumors arising in endometriosis. Clin Obstet Gynecol 23(3):951–963
48. Jain KA et al (1993) Adnexal masses: comparison of specificity of endovaginal US and pelvic MR imaging. Radiology 186(3):697–704
49. Jain KA, Jeffrey RB (1994) Evaluation of pelvic masses with magnetic resonance imaging and ultrasonography. J Ultrasound Med 13(11):845–853
50. Sugimura K et al (1993) Pelvic endometriosis: detection and diagnosis with chemical shift MR imaging. Radiology 188(2):435–438
51. Sugimura K et al (1992) The value of magnetic resonance relaxation time in staging ovarian endometrial cysts. Br J Radiol 65(774):502–506
52. Takahashi K et al (1996) Magnetic resonance relaxation time in evaluating the cyst fluid characteristics of endometrioma. Hum Reprod 11(4):857–860
53. Iizuka M et al (1998) Chemical assay of iron in ovarian cysts: a new diagnostic method to evaluate endometriotic cysts. Gynecol Obstet Invest 46(1): 58–60
54. Yamashita Y et al (1995) Magnetic resonance characteristics of intrapelvic haematomas. Br J Radiol 68(813):979–985
55. Glastonbury CM (2002) The shading sign. Radiology 224(1):199–201
56. Khashper A et al (2012) T2-hypointense adnexal lesions: an imaging algorithm. Radiographics 32(4): 1047–1064
57. Bis KG et al (1997) Pelvic endometriosis: MR imaging spectrum with laparoscopic correlation and diagnostic pitfalls. Radiographics 17(3):639–655
58. Siegelman ES et al (1994) Solid pelvic masses caused by endometriosis: MR imaging features. AJR Am J Roentgenol 163(2):357–361
59. Tanaka YO et al (1996) MR staging of pelvic endometriosis: role of fat-suppression T1-weighted images. Radiat Med 14(3):111–116
60. Thoeny HC, Forstner R, De Keyzer F (2012) Genitourinary applications of diffusion-weighted MR imaging in the pelvis. Radiology 263(2):326–342
61. Sala E et al (2010) The role of dynamic contrast-enhanced and diffusion weighted magnetic resonance imaging in the female pelvis. Eur J Radiol 76(3): 367–385
62. Buy JN et al (1991) Epithelial tumors of the ovary: CT findings and correlation with US. Radiology 178(3): 811–818
63. Outwater EK et al (1997) Papillary projections in ovarian neoplasms: appearance on MRI. J Magn Reson Imaging 7(4):689–695
64. Kurman RJ (1987) Blaustein's pathology of the female genital tract, 3rd edn. Springer, New York/London
65. Czernobilsky B, Borenstein R, Lancet M (1974) Cystadenofibroma of the ovary. A clinicopathologic study of 34 cases and comparison with serous cystadenoma. Cancer 34(6):1971–1981
66. Takeuchi M, Matsuzaki K, Harada M (2013) Ovarian adenofibromas and cystadenofibromas: magnetic resonance imaging findings including diffusion-weighted imaging. Acta Radiol 54(2):231–236
67. Cho S-M et al (2004) CT and MRI findings of cystadenofibromas of the ovary. Eur Radiol 14(5):798–804
68. Tang YZ et al (2013) The MRI features of histologically proven ovarian cystadenofibromas-an assessment of the morphological and enhancement patterns. Eur Radiol 23(1):48–56
69. Seidman JD, Russell P, Kurman RJ (2002) In: Kurman RJ (ed) Pathology of the female genital tract, 5th edn. Springer, New York/London, pp 791–904
70. Outwater EK et al (1997) Ovarian fibromas and cystadenofibromas: MRI features of the fibrous component. J Magn Reson Imaging 7(3):465–471
71. Fujii S et al (2008) Diagnostic accuracy of diffusion-weighted imaging in differentiating benign from malignant ovarian lesions. J Magn Reson Imaging 28(5):1149–1156
72. Moon WJ et al (2000) Brenner tumor of the ovary: CT and MR findings. J Comput Assist Tomogr 24(1): 72–76
73. Outwater EK, Siegelman ES, Hunt JL (2001) Ovarian teratomas: tumor types and imaging characteristics. Radiographics 21(2):475–490
74. Yamashita Y et al (1994) Mature cystic teratomas of the ovary without fat in the cystic cavity: MR features in 12 cases. AJR Am J Roentgenol 163(3):613–616
75. Koonings PP et al (1989) Relative frequency of primary ovarian neoplasms: a 10-year review. Obstet Gynecol 74(6):921–926
76. Buy JN et al (1989) Cystic teratoma of the ovary: CT detection. Radiology 171(3):697–701
77. Caspi B et al (1997) The growth pattern of ovarian dermoid cysts: a prospective study in premenopausal and postmenopausal women. Fertil Steril 68(3):501–505
78. Herbst AL, Mishell D, Stenchever MA (1992) Comprehensive gynecology. Mosby-Year Book, St Louise, pp 960–972
79. Rha SE et al (2004) Atypical CT and MRI manifestations of mature ovarian cystic teratomas. AJR Am J Roentgenol 183(3):743–750
80. BM C (1991) The adnexae. In: Carrington B, Hricak H (eds) MRI of the pelvis: a text atlas, Martin Dunitz: London. pp 185
81. Brammer HM 3rd et al (1990) From the archives of the AFIP. Malignant germ cell tumors of the ovary: radiologic-pathologic correlation. Radiographics 10(4): 715–724
82. Quinn SF, Erickson S, Black WC (1985) Cystic ovarian teratomas: the sonographic appearance of the dermoid plug. Radiology 155(2):477–478

83. Woodward PJ, Gilfeather M (1998) Magnetic resonance imaging of the female pelvis. Semin Ultrasound CT MR 19(1):90–9103
84. Stevens SK, Hricak H, Campos Z (1993) Teratomas versus cystic hemorrhagic adnexal lesions: differentiation with proton-selective fat-saturation MR imaging. Radiology 186(2):481–488
85. Matsuki M et al (2000) Struma ovarii: MRI findings. Br J Radiol 73(865):87–90
86. Troiano RN et al (1997) Fibroma and fibrothecoma of the ovary: MR imaging findings. Radiology 204(3):795–798
87. Jeong YY, Outwater EK, Kang HK (2000) Imaging evaluation of ovarian masses. Radiographics 20(5): 1445–1470
88. Pretorius ES et al (2001) Magnetic resonance imaging of the ovary. Top Magn Reson Imaging 12(2):131–146
89. Bazot M et al (1993) Fibrothecomas of the ovary: CT and US findings. J Comput Assist Tomogr 17(5): 754–759
90. Kim SH, Sim JS, Seong CK (2001) Interface vessels on color/power Doppler US and MRI: a clue to differentiate subserosal uterine myomas from extrauterine tumors. J Comput Assist Tomogr 25(1):36–42
91. Torashima M et al (1998) The value of detection of flow voids between the uterus and the leiomyoma with MRI. J Magn Reson Imaging 8(2):427–431
92. Matsubayashi R et al (1999) Sclerosing stromal tumor of the ovary: radiologic findings. Eur Radiol 9(7):1335–1338
93. Joja I et al (2001) Sclerosing stromal tumor of the ovary: US, MR, and dynamic MR findings. J Comput Assist Tomogr 25(2):201–206
94. Ihara N et al (1999) Sclerosing stromal tumor of the ovary: MRI. J Comput Assist Tomogr 23(4): 555–557
95. Moyle P, Addley HC, Sala E (2010) Radiological staging of ovarian carcinoma. Semin Ultrasound CT MR 31(5):388–398
96. Shanbhogue AK et al (2010) Clinical syndromes associated with ovarian neoplasms: a comprehensive review. Radiographics 30(4):903–919
97. Togashi K (2003) Ovarian cancer: the clinical role of US, CT, and MRI. Eur Radiol 13(Suppl 4):L87–L104
98. Forstner R et al (2010) ESUR guidelines: ovarian cancer staging and follow-up. Eur Radiol 20(12): 2773–2780
99. Kyriazi S et al (2010) Diffusion-weighted imaging of peritoneal disease for noninvasive staging of advanced ovarian cancer. Radiographics 30(5): 1269–1285
100. Kitajima K et al (2008) Diagnostic accuracy of integrated FDG-PET/contrast-enhanced CT in staging ovarian cancer: comparison with enhanced CT. Eur J Nucl Med Mol Imaging 35(10):1912–1920
101. De Iaco P et al (2011) FDG-PET/CT in advanced ovarian cancer staging: value and pitfalls in detecting lesions in different abdominal and pelvic quadrants compared with laparoscopy. Eur J Radiol 80(2):e98–e103
102. Forstner R (2007) Radiological staging of ovarian cancer: imaging findings and contribution of CT and MRI. Eur Radiol 17(12):3223–3235
103. Scully RE (1975) World Health Organization classification and nomenclature of ovarian cancer. Natl Cancer Inst Monogr 42:5–7
104. Bent CL et al (2009) MRI appearances of borderline ovarian tumours. Clin Radiol 64(4):430–438
105. Van Vierzen PB et al (1998) Borderline ovarian malignancy: ultrasound and fast dynamic MR findings. Eur J Radiol 28(2):136–142
106. Lalwani N et al (2010) Current update on borderline ovarian neoplasms. AJR Am J Roentgenol 194(2): 330–336
107. Bazot M et al (2006) MR imaging compared with intraoperative frozen-section examination for the diagnosis of adnexal tumors; correlation with final histology. Eur Radiol 16(12):2687–2699
108. Ghossain MA et al (1991) Epithelial tumors of the ovary: comparison of MR and CT findings. Radiology 181(3):863–870
109. Griffin N, Grant LA, Sala E (2010) Adnexal Masses: Characterization and Imaging Strategies. Seminars in Ultrasound CT and MRI 31:330–346
110. Tornos C, Silva EG (1994) Pathology of epithelial ovarian cancer. Obstet Gynecol Clin North Am 21(1):63–77
111. Jimbo H et al (1997) Prevalence of ovarian endometriosis in epithelial ovarian cancer. Int J Gynaecol Obstet 59(3):245–250
112. Kitajima K et al (2007) Magnetic resonance imaging findings of endometrioid adenocarcinoma of the ovary. Radiat Med 25(7):346–354
113. Wagner BJ et al (1994) From the archives of the AFIP. Ovarian epithelial neoplasms: radiologic-pathologic correlation. Radiographics 14(6):1351–1374; quiz 1375–6
114. Matsuoka Y et al (2001) MR imaging of clear cell carcinoma of the ovary. Eur Radiol 11(6):946–951
115. Russell P (1994) Surface epithelial-stromal tumors of the ovary. In: Kurman RJ (ed) Blaustein's pathology of the female genital tract, 4th edn. Springer, New York, pp 705–782
116. Sugimura K, Okizuka H, Imaoka I (1991) Malignant Brenner tumor: MR findings. AJR Am J Roentgenol 157(6):1355–1356
117. Takahama J et al (2004) Borderline Brenner tumor of the ovary: MRI findings. Abdom Imaging 29(4): 528–530
118. van der Westhuizen NG, Tiltman AJ (1988) Brenner tumours–a clinicopathological study. S Afr Med J 73(2):98–101
119. Reznek H (2010) Imaging in oncology. 3rd edn. Informa Healthcare, London
120. Young RH, Scully R (1994) Sex cord-stromal, steroid cell, and other ovarian tumors with endocrine, paraendocrine, and paraneoplastic manifestations. In: Kurman RJ (ed) Blaustein's pathology of the female genital tract, 4th edn. Springer, New York, pp 783–847

121. Outwater EK et al (1998) Sex cord-stromal and steroid cell tumors of the ovary. Radiographics 18(6): 1523–1546
122. Segal R, DePetrillo AD, Thomas G (1995) Clinical review of adult granulosa cell tumors of the ovary. Gynecol Oncol 56(3):338–344
123. Calaminus G et al (1997) Juvenile granulosa cell tumors of the ovary in children and adolescents: results from 33 patients registered in a prospective cooperative study. Gynecol Oncol 65(3): 447–452
124. Jung SE et al (2005) CT and MRI findings of sex cord-stromal tumor of the ovary. AJR Am J Roentgenol 185(1):207–215
125. Morikawa K et al (1997) Granulosa cell tumor of the ovary: MR findings. J Comput Assist Tomogr 21(6):1001–1004
126. Stenwig JT, Hazekamp JT, Beecham JB (1979) Granulosa cell tumors of the ovary. A clinicopathological study of 118 cases with long-term follow-up. Gynecol Oncol 7(2):136–152
127. Young RH, Scully RE (1985) Ovarian Sertoli-Leydig cell tumors. A clinicopathological analysis of 207 cases. Am J Surg Pathol 9(8):543–569
128. Tanaka YO et al (2007) MR findings of ovarian tumors with hormonal activity, with emphasis on tumors other than sex cord-stromal tumors. Eur J Radiol 62(3):317–327
129. Sakamoto K et al (2009) MR diagnosis of steroid cell tumor of the ovary: value of chemical shift imaging. Magn Reson Med Sci 8(4):193–195
130. Yanai-Inbar I, Scully RE (1987) Relation of ovarian dermoid cysts and immature teratomas: an analysis of 350 cases of immature teratoma and 10 cases of dermoid cyst with microscopic foci of immature tissue. Int J Gynecol Pathol 6(3):203–212
131. Choudhary S et al (2009) Imaging of ovarian teratomas: appearances and complications. J Med Imaging Radiat Oncol 53(5):480–488
132. Poncelet E et al (2013) Value of dynamic contrast-enhanced MRI for tissue characterization of ovarian teratomas: correlation with histopathology. Clin Radiol 68(9):909–916
133. Tanaka YO et al (1994) Ovarian dysgerminoma: MR and CT appearance. J Comput Assist Tomogr 18(3): 443–448
134. Gershenson DM (1985) Malignant germ-cell tumors of the ovary. Clin Obstet Gynecol 28(4):824–838
135. Athavale RD, Davies-Humphreys JD, Cruickshank DJ (2004) Primary carcinoid tumours of the ovary. J Obstet Gynaecol 24(1):99–101
136. Takeuchi M, Matsuzaki K, Uehara H (2011) Primary carcinoid tumor of the ovary: MR imaging characteristics with pathologic correlation. Magn Reson Med Sci 10(3):205–209
137. Cho SB et al (2001) Malignant mixed mullerian tumor of the ovary: imaging findings. Eur Radiol 11(7):1147–1150
138. Dass KK et al (1993) Malignant mixed mullerian tumors of the ovary. An analysis of two long-term survivors. Am J Clin Oncol 16(4):346–349
139. Navarini R, Pineda RL (2006) Malignant mixed mullerian tumors of the ovary. Curr Opin Obstet Gynecol 18(1):20–23
140. Yoon JH et al (2010) Magnetic resonance imaging findings in extrauterine malignant mixed Mullerian tumors: report of two cases. J Magn Reson Imaging 32(5):1238–1241
141. Fox H et al (1988) Malignant lymphoma presenting as an ovarian tumour: a clinicopathological analysis of 34 cases. Br J Obstet Gynaecol 95(4):386–390
142. Islimye Taskin M, Gokgozoglu L, Kandemir B (2013) Primary ovarian large B-cell lymphoma. Case Rep Obstet Gynecol 2013:493836
143. Yadav R et al (2013) Natural history of primary precursor B lymphoblastic lymphoma of the ovary: report of a rare case. J Obstet Gynaecol Res 39(2):611–616
144. Yildirim Y (2005) Primary ovarian large B-cell lymphoma in patient with juvenile rheumatoid arthritis treated with low dose Methotrexate. Gynecol Oncol 97(1):249–252
145. Crawshaw J et al (2007) Primary non-Hodgkin's lymphoma of the ovaries: imaging findings. Br J Radiol 80(956):e155–e158
146. Mitsumori A, Joja I, Hiraki Y (1999) MR appearance of non-Hodgkin's lymphoma of the ovary. AJR Am J Roentgenol 173(1):245
147. Friedman HD, Mazur MT (1991) Primary ovarian leiomyosarcoma. An immunohistochemical and ultrastructural study. Arch Pathol Lab Med 115(9): 941–945
148. Kraemer BB, Silva EG, Sneige N (1984) Fibrosarcoma of ovary. A new component in the nevoid basal-cell carcinoma syndrome. Am J Surg Pathol 8(3):231–236
149. Nucci MR et al (1998) Angiosarcoma of the ovary: clinicopathologic and immunohistochemical analysis of four cases with a broad morphologic spectrum. Am J Surg Pathol 22(5):620–630
150. Stone GC et al (1986) Malignant schwannoma of the ovary. Report of a case. Cancer 58(7):1575–1582
151. Hirakawa T et al (1988) Ovarian sarcoma with histologic features of telangiectatic osteosarcoma of the bone. Am J Surg Pathol 12(7):567–572
152. Nielsen GP et al (1998) Primary ovarian rhabdomyosarcoma: a report of 13 cases. Int J Gynecol Pathol 17(2):113–119
153. Talerman A, Auerbach WM, van Meurs AJ (1981) Primary chondrosarcoma of the ovary. Histopathology 5(3):319–324
154. Saito A et al (1999) MR images of ovarian carcinosarcoma. Radiat Med 17(6):447–450
155. McCluggage WG, Wilkinson N (2005) Metastatic neoplasms involving the ovary: a review with an emphasis on morphological and immunohistochemical features. Histopathology 47(3):231–247

156. Young RH, Scully R (2002) Metastatic tumors of the ovary. In: Kurman RJ (ed) Blaustein's pathology of the female genital tract, 5th edn. Springer, New York
157. Koyama T et al (2007) Secondary ovarian tumors: spectrum of CT and MR features with pathologic correlation. Abdom Imaging 32(6):784–795
158. Ha HK et al (1995) Krukenberg's tumor of the ovary: MR imaging features. AJR Am J Roentgenol 164(6): 1435–1439
159. Kim SH et al (1999) Collision tumors of the ovary associated with teratoma: clues to the correct preoperative diagnosis. J Comput Assist Tomogr 23(6): 929–933

Benign Prostatic Pathology

7

Teresa Milazzo, Federica Castelli, Beatrice Pedrinolla,
Emanuele Demozzi, Riccardo Manfredi,
and Roberto Pozzi Mucelli

7.1 Benign Prostatic Hyperplasia

7.1.1 Anatomy

The prostate gland is the male organ most commonly afflicted with either benign or malignant neoplasms. It comprises the most proximal aspect of the urethra. Anatomically, it resides in the true pelvis, separated from the pubic symphysis anteriorly by the retropubic space (space of Retzius). The posterior surface of the prostate is separated from the rectal ampulla by Denonvilliers' fascia. The base of the prostate is continuous with the bladder neck, and the apex of the prostate rests on the upper surface of the urogenital diaphragm. Laterally, the prostate is related to the levator ani musculature. Its arterial blood supply is derived from branches of the internal iliac artery (inferior vesical and middle rectal arteries). Venous drainage is via the dorsal venous complex, which receives the deep dorsal vein of the penis and vesical branches before draining into the internal iliac veins. Innervation is from the pelvic plexus. The normal prostate measures 3–4 cm at the base, 4–6 cm in cephalocaudad, and 2–3 cm in anteroposterior dimensions.

McNeal has popularized the concept of zonal anatomy of the prostate. Three distinct zones have been identified (Diagram 1). The peripheral zone accounts for 70 % of the volume of the young adult prostate, the central zone accounts for 25 %, and the transition zone accounts for 5 %. These anatomic zones have distinct ductal systems but, more important, are differentially afflicted with neoplastic processes. Sixty to seventy percent of carcinomas of the prostate (CaP) originate in the peripheral zone, 10–20 % in the transition zone, and 5–10 % in the central zone. Benign prostatic hyperplasia (BPH) uniformly originates in the transition zone [1].

7.1.2 Introduction and Pathogenesis

Benign prostatic hyperplasia (BPH) represents the most commonly diagnosed urological disease in men after the fifth decade. Although BPH etiology remains uncertain in some aspects, several mechanisms have been proposed to be involved in the pathogenesis and progression of BPH.

First, aging represents the most significant risk factor for the development of BPH and the compliant of lower urinary tract symptoms (LUTS). In aging men, an interference in growth factor

---

T. Milazzo (✉) • F. Castelli • B. Pedrinolla
E. Demozzi • R. Manfredi • R.P. Mucelli
Institute of Radiology, University of Verona,
Policlinico G.B. Rossi,
Piazzale Ludovico Antonio Scuro 10,
Verona 37134, Italy
e-mail: terrymilazz84@hotmail.it;
fedicastelli@gmail.com;
beatrice.pedrinolla@gmail.com;
e.demozzi@gmail.com; Riccardo.manfredi@univr.it;
roberto.pozzimucelli@univr.it

R. Manfredi, R. Pozzi Mucelli (eds.), *MRI of the Female and Male Pelvis*,
DOI 10.1007/978-3-319-09659-9_7, © Springer International Publishing Switzerland 2015

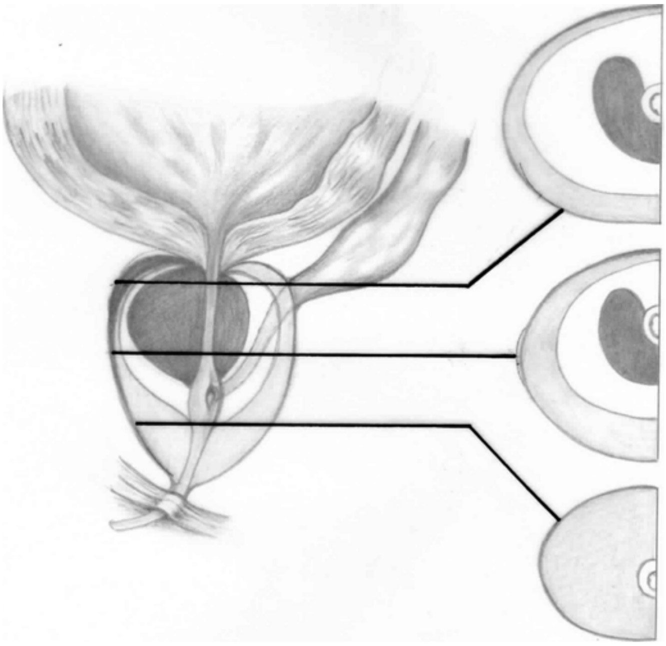

Diagram 1 Distribution and proportions of the tissue layers composing the prostate. Diagram of the prostate shows its zonal anatomy in the sagittal plane and corresponding axial sections from the base (*upper line*), midgland (*medium line*), and apex (*lower line*). Note the anterior fibromuscular stroma (*dark gray* part in the anterior portion), peripheral zone (*light gray*), central zone (*white*), and transition zone (*dark gray*)

pathway occurs and a significant tissue-remodeling process takes place, leading to prostatic enlargement. Second, hormonal alterations have been proposed to be involved in BPH pathogenesis and progression. Indeed, the development of BPH requires the presence of testicular androgens, and BPH tissue has higher dihydrotestosterone activity than normal prostate gland tissue.

Additionally, insulin resistance with secondary hyperinsulinemia has been proposed to be involved in the development of BPH. Third, a role of increased sympathetic nerve activity has also been proposed. Finally, in the last few years, the role of prostatic inflammation as a crucial part of BPH pathogenesis and progression has emerged. The chronic inflammatory condition may contribute to tissue injury, activating cytokine release and increasing the concentration of growth factors, creating a local vicious cycle. In this context, the upregulation of proinflammatory cytokines has been widely reported in prostatic tissues of patients with BPH. Concluding, all these data support the hypothesis that tissue damage, hypoxia, and chronic process of wound healing lead to a persistent process of stimulation of stromal and epithelial prostatic tissues, potentially resulting in BPH [2, 3].

Risk factors for the development of BPH are poorly understood. Some studies have suggested a genetic predisposition, and some have noted racial differences. Approximately 50 % of men under the age of 60 who undergo surgery for BPH may have a heritable form of the disease. This form is most likely an autosomal dominant trait, and first-degree male relatives of such patients carry an increased relative risk of approximately fourfold.

Interestingly, it has been hypothesized that inflammatory infiltrate leads to tissue damage and to a chronic process of wound healing that might subsequently determinate prostatic enlargement [4].

7.1.3 Epidemiology

BPH is the most common benign tumor in men, and its incidence is age related. The prevalence of histological BPH in autopsy studies rises from approximately 20 % in men aged 41–50 to 50 % in men aged 51–60 and to >90 % in men older than 80. Although clinical evidence of disease occurs less commonly, symptoms of prostatic obstruction are also age related. At age 55, approximately 25 % of men report obstructive voiding symptoms. At age 75, 50 % of men complain of a decrease in the force and caliber of their urinary stream [5, 6].

7.1.4 Clinical and Laboratory Findings

The symptoms of BPH can be divided into obstructive and irritative complaints. Obstructive symptoms include hesitancy, decreased force and caliber of stream, sensation of incomplete bladder emptying, double voiding (urinating a second time within 2 h of the previous void), straining to urinate, and post-void dribbling. Irritative symptoms include urgency, frequency, and nocturia. A detailed history focusing on the urinary tract excludes other possible causes of symptoms that may not result from the prostate, such as urinary tract infection, neurogenic bladder, urethral stricture, or prostate cancer.

A physical examination, digital rectal examination (DRE), and focused neurologic examination are performed on all patients. The size and consistency of the prostate is noted, even though prostate size, as determined by DRE, does not correlate with severity of symptoms or degree of obstruction. BPH usually results in a smooth, firm, elastic enlargement of the prostate. Induration, if detected, must alert the physician to the possibility of cancer and the need for further evaluation (i.e., prostate-specific antigen (PSA), transrectal ultrasound (TRUS), and biopsy) [7].

A urinalysis to exclude infection or hematuria and serum creatinine measurement to assess renal function are required. Renal insufficiency may be observed in 10 % of patients with prostatism and warrants upper-tract imaging. Patients with renal insufficiency are at an increased risk of developing postoperative complications following surgical intervention for BPH.

Serum PSA is considered optional, but most physicians will include it in the initial evaluation [8].

In some cases of benign prostatic hyperplasia are also observed high levels of PSA, but they are not considered index of malignant progression, but rather are due to the increase in prostate volume, consequently the most production of the antigen itself. PSA, compared with DRE alone, certainly increases the ability to detect CaP, but because there is much overlap between levels seen in BPH and CaP, its use remains controversial (see Screening for CaP) [9].

7.1.5 Pathological Findings

Benign prostatic hyperplasia is a disease characterized by an enlargement (hyperplasia or hypertrophy) of the prostate, more specifically in the prostatic epithelial cells and stromal cells, which leads to the formation of nodules in the periurethral region of the prostate. When these nodules become large enough to compress the urethral canal, causing a partial obstruction of the same, they interfere with normal urinary flow.

The hyperplastic prostate may consist of pure fibroleiomyomatous nodules or of pure glandular or of mixed glandular-atrophic-cystic areas. Frequently, these structures are intermixed. The smooth muscle fiber content of the prostate changes when concomitant chronic inflammatory processes are present. If, after transurethral resection in a recurrent hyperplastic gland, chronic transurethral resection (TUR)-prostatitis has developed, the fibromatous portion increases with little or no nodule formation. Vascularization and cellular content also change.

The prostate is an immunocompetent organ, and it is normally populated by a small number of inflammatory cells (i.e., T and B lymphocytes, macrophages, and mast cells).

Prostate tissue inflammatory patterns have been also widely assessed in patients with BPH. Robert et al. recently characterized the inflammatory infiltrate in a large cohort of patients surgically treated for BPH. Interestingly, 81 % of patients had T-lymphocytes infiltrates (CD-3), 52 % B cells (CD-20), and 82 % macrophage markers (CD-163) in BPH tissues. Thus, T cells represented the major component of the inflammatory infiltrate seen within the prostate gland. Moreover, an increased expression of B lymphocytes and macrophages was reported.

These antigen-presenting cells play an important role in the activation of T lymphocytes and in the subsequent onset of an inflammatory state.

Prostatic calcifications are common in men with BPH and their incidence increases with age. Interestingly, calcifications were also seen in 47.2 % of younger men aged <50 years with urological complaints. In some studies [10], the incidence and significance of calcifications in patients with chronic pelvic pain syndrome were evaluated. In these patients, calcifications detected at TRUS were significantly associated with greater inflammation and longer symptoms duration. Other authors found that patients with larger stones were at higher risk of developing LUTS or prostatitis [11]. It could be speculated that in young patients, alterations in the prostatic fluid related to infections or inflammatory diseases might result in prostatic calcifications, which may obstruct intraprostatic ducts and subsequently enhance the inflammatory process. Particularly, calcifications could be the expression of previous infections leading to a chronic inflammatory process, with higher risk of subsequent BPH development over time.

7.1.6 MR Imaging

In the last few years, magnetic resonance imaging (MRI) has been shown to be of great value in the imaging of the pelvis. Its advantages derive from the capability to obtain sections in direct axial, sagittal, and coronal planes and to show greater soft-tissue contrast than any other imaging modality [12]. In fact, CT does not easily provide direct coronal and sagittal images and does not visualize the internal architecture of prostate and seminal vesicles. Transrectal US is widely used as a first-choice exam in the study of prostatic pathology and gives a clear demonstration of the glandular texture. However, its limitation, when compared with MRI, is that it provides only a limited view of the pelvic structures surrounding the prostate and seminal vesicles.

T2-weighted MR imaging is the workhorse of prostate MR imaging. T2-weighted MR images have high spatial resolution and, thus, can clearly differentiate the normal intermediate- to high-signal-intensity peripheral zone (PZ) from the low-signal-intensity central and transition zones in young male subjects. In the aging man, owing to variable extension of the transition zone due to benign prostatic hyperplasia (BNH), the size and signal intensity of the prostate transition zone may vary. BPH itself is a round, well-defined, inhomogeneous area with (variable) intermediate signal intensity and a low-signal-intensity rim that surrounds the expanded transition zone. Because of transition zone expansion, the remainder of the compressed central zone is often indefinable on MR images (Fig. 7.1) [13, 14].

High-spatial-resolution T2-weighted rapid acquisition with refocused echo sequences with a small field of view, performed with endorectal and/or external body phased-array coils, is generally used to depict prostate anatomy. T1-weighted contrast in the prostate is very low. Therefore, it is not possible to appreciate the different anatomic zones on T1-weighted images. Therefore, a suggestion for minimal requirements for multiparametric MR imaging is a combination of T1- and T2-weighted imaging with DW or dynamic contrast-enhanced MR imaging. Owing to the presence of BPH, cancer in central and transition zones is more difficult to discern, BPH may have signal intensity similar to that of prostate cancer on T2-weighted images. However, it has been reported that features such as low-signal-intensity lesions with a wedge shape and a diffuse extension without mass may be reliable signs of benignity. Dynamic contrast-enhanced (DCE) MR imaging consists of a series of fast T1-weighted sequences covering the entire prostate before and after rapid injection (2–4 mL/s) of a bolus of a low-molecular-weight gadolinium chelate. A fast and direct method of characterizing prostatic vascular pharmacokinetic features is high temporal resolution DCE-MRI (<10 s). DCE-MRI consists of a series of axial T1WI gradient echo sequences covering the entire prostate during and after IV bolus injection of gadolinium contrast medium [15]. Diffusion-weighted imaging (DWI) is a powerful clinical tool, as it allows apparent diffusion coefficient (ADC) maps to be calculated, enabling qualitative and quantitative assessment of the prostate. Diffusion-weighted imaging

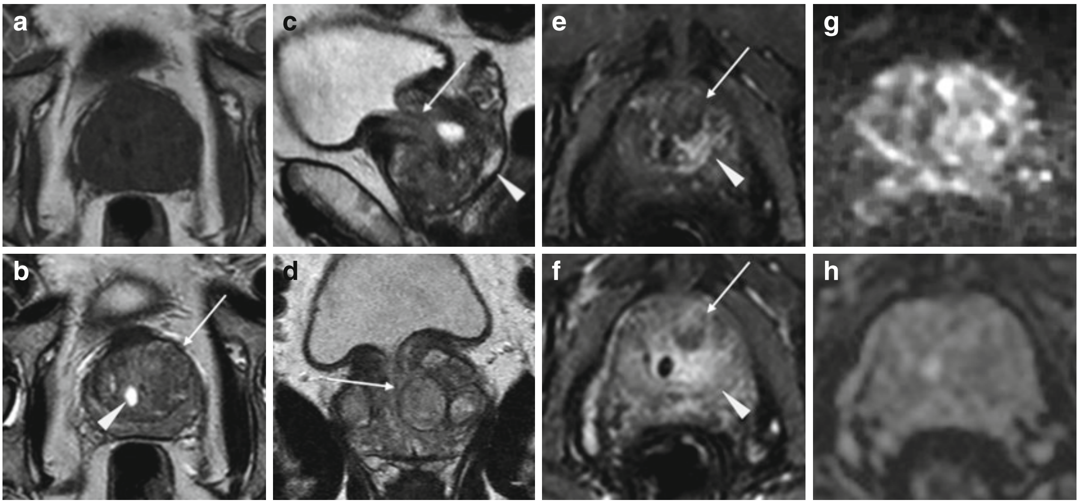

Fig. 7.1 Benign prostatic hyperplasia: signal intensity of adenomas; compression of urethra and peripheral zone. (**a**) Axial T1WI (TR 519/TE 10) shows an enlargement of prostate gland. (**b**) Axial T2WI (TR 3072/TE 100) depicts the presence of multiple adenomatous nodules that subvert the normal signal intensity of the transition zone (*arrow*). These nodules have inhomogeneous signal intensity but well-defined hypointense margins as we can determine their size and morphology. A cystic formation is recognizable in periurethral space on the right side (*arrowhead*). (**c**, **d**) Sagittal (TR 5712/TE 120) and coronal T2WI (TR 3000/TE 100) show very well the increase in the size of the central area, responsible of compression of the urethra (*arrow*) and of peripheral zone (*arrowhead*). (**e**) Early dynamic contrast-enhanced gradient-echo image (TR 4.02/TE 1.91) shows no enhancement of prostatic adenomas (*arrow*) because of their high fibrous component but depicts an early irregular enhancement in the left side of the central zone (*arrowhead*). (**f**) Later dynamic contrast-enhanced gradient-echo image (TR 4.01/TE 1.91) shows a normal progressive enhancement of prostatic adenomas (*arrow*) and does not show any washout in the left region of the central zone (*arrowhead*) indicating that it is an inflammation zone. (**g**, **h**) DWI (b800) and ADC image does not show significant restricted diffusion in the examined areas

should be acquired in the axial plane with an echo planar imaging sequence employing parallel imaging [16].

The MRI appearance of BPH is characteristic, though no tissue-specific diagnosis of benign disease can be made with certainty. The prostate is usually enlarged but can also be of normal size. On T1WI, the gland has a homogeneous intermediate-low signal intensity with no evidence of intraglandular zonal abnormalities. On T2WI, the appearance is that of a nonhomogeneous texture, mainly in the central gland, with alternating areas of intermediate and high signal (Fig. 7.1). The different signals of the various nodules are related to their relative stromal or epithelial components. The benign central gland is composed of two histologically distinct types of tissue: glandular tissue, which is hyperintense on T2-weighted images (Fig. 7.2), and stromal tissue, which is hypointense and can mimic CG cancer (Fig. 7.3). Like CG cancer, the majority of stromal hyperplastic foci could also demonstrate homogeneously low signal intensity and had ill-defined margins. The majority of glandular tissue foci are homogeneously hyperintense.

Sometimes each individual adenomatous nodule is surrounded by a hypointense rim of tissue (Figs. 7.1 and 7.4). MR images are usually obtained in more than one plane to allow accurate evaluation of prostatic volume. In addition, sagittal images are particularly suited to demonstrate impingement on the base of the bladder and the effect of the adenomatous nodules on the bladder neck and prostatic urethra. Stromal and sclerotic nodules of benign hyperplasia, if located in the peripheral zone where malignancy and inflammation usually occur, can appear the same as prostatitis or carcinoma.

Dynamic contrast-enhanced MRI in BPH can show accentuation of contrast already in the early

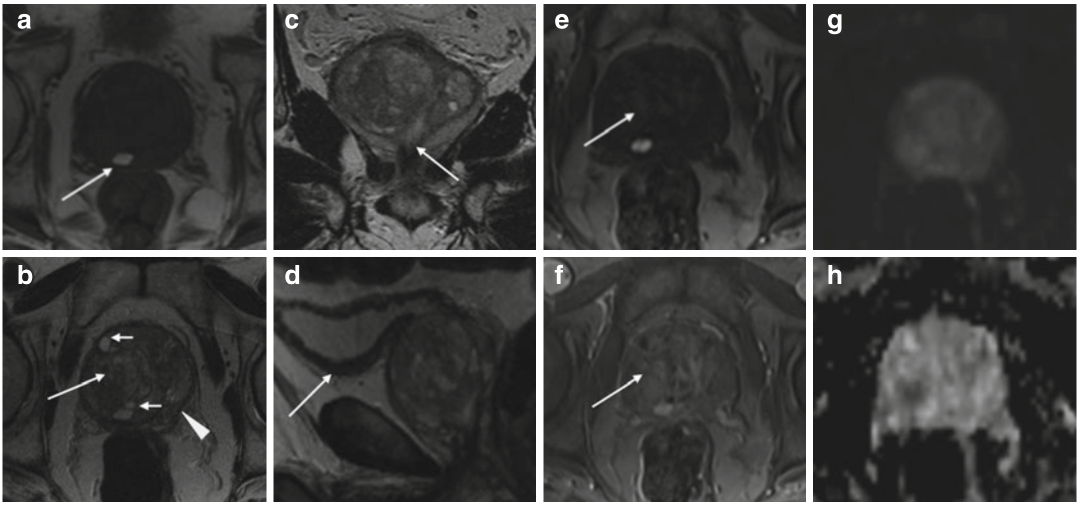

Fig. 7.2 Benign prostatic hyperplasia, normal pattern of adenomas enhancement. (**a**) Axial T1WI (TR 520/TE 12) shows an enlargement of the prostate gland, and a hyperintense cyst with proteinaceous content is evident in the right posterior region of the peripheral zone (*arrow*). (**b**) Axial T2WI (TR 3072/TE 100) shows a heterogeneous signal intensity in the transition zone for the adenomatous changes of the gland (*arrow*), with compression of the peripheral zone that appears thinned (*arrowhead*). There are also some small retention cysts of the gland (*short arrow*). (**c**) Coronal T2WI (TR 3000/TE 100) shows the compression/deflection of intraprostatic urethra by adenomatous hyperplasia. (**d**) Sagittal T2WI (TR5000/TE120) in which we can see a diffuse thickening of the bladder (*arrow*) wall because of chronic outflow obstruction. (**e**) Early dynamic contrast-enhanced gradient-echo image (TR 4.02/TE 1.91) (30 s) shows a slight and diffuse enhancement of the adenomatous central zone (*arrow*). (**f**) Later dynamic contrast-enhanced gradient-echo image (TR 4.02/TE 1.91) shows a greater and progressive enhancement of central gland adenomas without any washout (*arrow*) (no characteristics of pathology). (**g**, **h**) DWI (b800) and ADC images do not show significant restricted diffusion areas in the gland

phase after contrast administration but more frequently has a more delayed enhancement that increases progressively up to a plateau, reflecting the increased microvessel density in BPH (Figs. 7.2 and 7.5) [13].

Diffusion MR imaging parameters of central gland hyperplasia change according to the presence of stromal (ADC 1.27×10^{-3} mm^2/s) or glandular hyperplasia (ADC: 1.73×10^{-3} mm^2/s); therefore, it can be misleading to calculate a single diffusion parameter to represent the entire benign central gland. There is a considerable overlap between central gland carcinoma and stromal hyperplastic foci (Fig. 7.4).

7.1.7 Differential Diagnosis

7.1.7.1 Prostate Cancer

Prostate cancer (PC) may be detected by abnormalities on the DRE or an elevated PSA.

PSA, compared with DRE alone, certainly increases the ability to detect PC, but because there is much overlap between levels seen in BPH and PC, its use remains controversial. Conventional MR imaging is generally considered inadequate for evaluating CG cancers because of the heterogeneous T2 signal intensity in the normal transition zone. It has been suggested that homogeneous low T2 signal intensity, ill-defined margins, and lack of a capsule can be useful in the identification of PC. Lenticular shape and invasion of the anterior fibromuscular stroma can help differentiate cancer from benign central gland (CG).

In small studies, CG cancers demonstrated restricted diffusion, with smaller ADCs (0.93–1.37×10^{-3} mm^2/s) compared with BPH in the CG (1.34–1.79×10^{-3} mm^2/s), but other studies are discordant with these values. Despite a consensus in multiple series of restricted diffusion in CG cancers, there is substantial variation in reported ADCs of benign CG tissue [17]. Often, it is very hard to distinguish this pattern from that of a gland carcinoma central, which however enhances more and wash out faster than benign tissue [13].

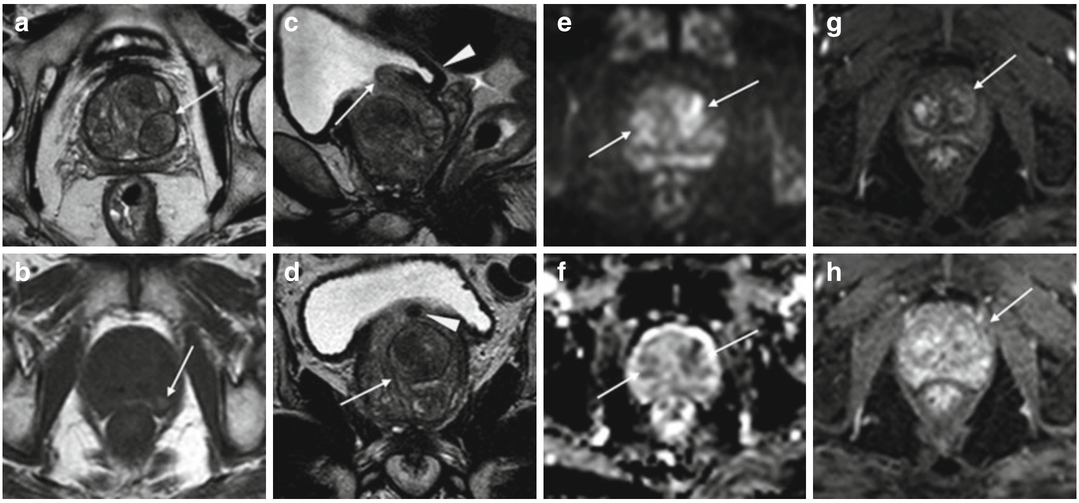

Fig. 7.3 Benign prostatic hyperplasia, diffusion restriction in stromal hyperplastic foci. Presence of post-biopsy hemorrhagic foci. (**a**) Axial T2WI (TR 3027/TE 100) shows an increase in volume of the transition zone in which context are appreciable (referred to nodules) multiple large hyperplastic nodules, typically surrounded by a hypointense rim of tissue (*arrow*). (**b**) Axial T1WI (TR 600/TE 13) shows some hyperintense foci in the peripheral zone attributable to post-biopsy hemorrhagic foci (*arrow*). (**c**) Sagittal T2WI (TR 5700/TE 130) shows the imprint of the transition zone of the prostate on bladder floor (*arrow*). Bladder walls are slightly thickened for detrusorial hypertrophy (*arrowhead*). (**d**) Coronal T2WI (TR 3000/TE 100) in which we can see the compression/deflection of intraprostatic urethra by adenomas (*arrow*). There is also a little calcification in the anterosuperior portion of the transitional region (*arrowhead*). (**e**, **f**) DWI (b800) and ADC show in this case some hyperintense and hypointense areas respectively, a sign of restricted diffusion, corresponding to some adenomatous nodules of the gland (*arrows*). (**g**) Early dynamic contrast-enhanced gradient-echo image (TR 3.8/TE 2) (30 s) shows a slight and diffuse enhancement of the adenomatous central zone (*arrow*). (**h**) Later dynamic contrast-enhanced gradient-echo image (TR 3.8/TE 2) (1.30 min) shows a progressive enhancement of central gland adenomas (*arrow*) without any washout (no characteristics of pathology)

7.1.7.2 Prostatitis

A urinary tract infection, which can mimic the irritative symptoms of BPH, can be readily identified by urinalysis and culture; however, a urinary tract infection can also be a complication of BPH (see other chapter).

7.1.7.3 Other Obstructive Conditions

Other obstructive conditions of the lower urinary tract, such as urethral stricture, bladder neck contracture, and bladder stone, must be entertained when evaluating men with presumptive BPH. A history of previous urethral instrumentation, urethritis, or trauma should be elucidated to exclude urethral stricture or bladder neck contracture.

Although irritative voiding complaints are also associated with carcinoma of the bladder, especially carcinoma in situ, the urinalysis usually shows evidence of hematuria. Likewise, patients with neurogenic bladder disorders may have many of the signs and symptoms of BPH, but a history of neurologic disease, stroke, diabetes mellitus, or back injury may be present as well. In addition, examination may show diminished perineal or lower extremity sensation or alterations in rectal sphincter tone or the bulbocavernosus reflex. Simultaneous alterations in bowel function (constipation) might also alert one to the possibility of a neurologic origin.

7.1.8 Treatment

After patients have been evaluated, they should be informed of the various therapeutic options for BPH. It is advisable for patients to consult with their physicians to make an educated decision on the basis of the relative efficacy and side effects of the treatment options.

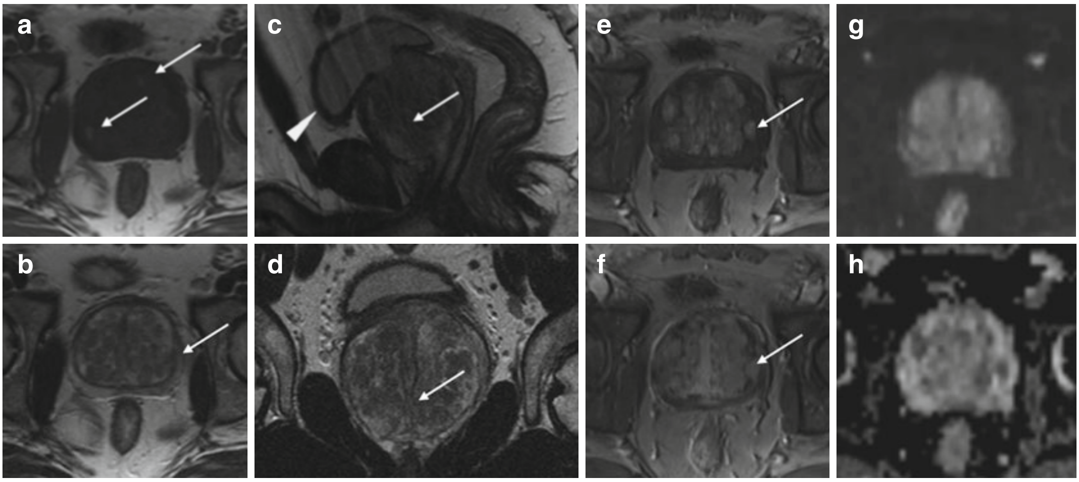

Fig. 7.4 Benign prostatic hyperplasia, normal pattern of adenomas enhancement. (**a**) Axial T1WI (TR 550/TE 9.3) shows an enlargement of prostate gland, and some slight hyperintense areas compatible with proteinaceous content cysts are evident in the right and posterior region of the peripheral zone (*arrows*). (**b**) Axial T2WI (TR 4480/TE 108) shows a heterogeneous signal intensity in the transition zone for the adenomatous changes of the gland, with compression of the peripheral zone which appears thinned (*arrow*). (**c**, **d**) Sagittal T2WI (TR 3000/TE 114) and coronal T2WI (TR 2860/TE 116) show very well the increase in the size of the central area, responsible of compression/deflection of intraprostatic urethra (*arrow*) and a diffuse thickening of the bladder wall because of chronic outflow obstruction (*arrowhead*). (**e**) Early dynamic contrast-enhanced gradient-echo image (TR 12/TE 15.76) shows a slight and diffuse enhancement of the adenomatous central zone (*arrow*). (**f**) Later dynamic contrast-enhanced gradient-echo image (TR 12/TE 5.76) shows a greater and progressive enhancement of central gland adenomas without any washout (*arrow*) (no characteristics of pathology). (**g**, **h**) DWI (b800) and ADC images do not show significant restricted diffusion areas in the gland

Specific treatment recommendations can be offered for certain groups of patients. For those with mild symptoms (symptom score 0–7), watchful waiting only is advised.

On the other end of the therapeutic spectrum, absolute surgical indications include refractory urinary retention (failing at least one attempt at catheter removal), recurrent urinary tract infection from BPH, recurrent gross hematuria from BPH, bladder stones from BPH, renal insufficiency from BPH, or large bladder diverticula [18, 19].

A. *Watchful Waiting*

   Watchful waiting is the appropriate management of men with mild symptom scores.

B. *Medical Therapy*

   1. *Alpha-blockers*—The human prostate and bladder base contains alpha-1-adrenoreceptors, and the prostate shows a contractile response to corresponding agonists. The contractile properties of the prostate and bladder neck seem to be mediated primarily by the subtype alpha-1a receptors. Alpha-blockade has been shown to result in both objective and subjective degrees of improvement in the symptoms and signs of BPH in some patients.
   2. *5-Alpha-reductase inhibitors*—Finasteride is a 5-alpha-reductase inhibitor that blocks the conversion of testosterone to dihydrotestosterone. This drug affects the epithelial component of the prostate, resulting in a reduction in the size of the gland and improvement in symptoms.

      Dutasteride differs from finasteride as it inhibits both isoenzymes of 5-alpha reductase. Similar to finasteride, it reduces serum prostatic-specific antigen and total prostate volume.
   3. *Combination therapy*—The reduction in risk associated with combination therapy (66 % risk reduction) is significantly greater than that associated with doxazosin or finasteride alone. Patients most likely to benefit from combination therapy

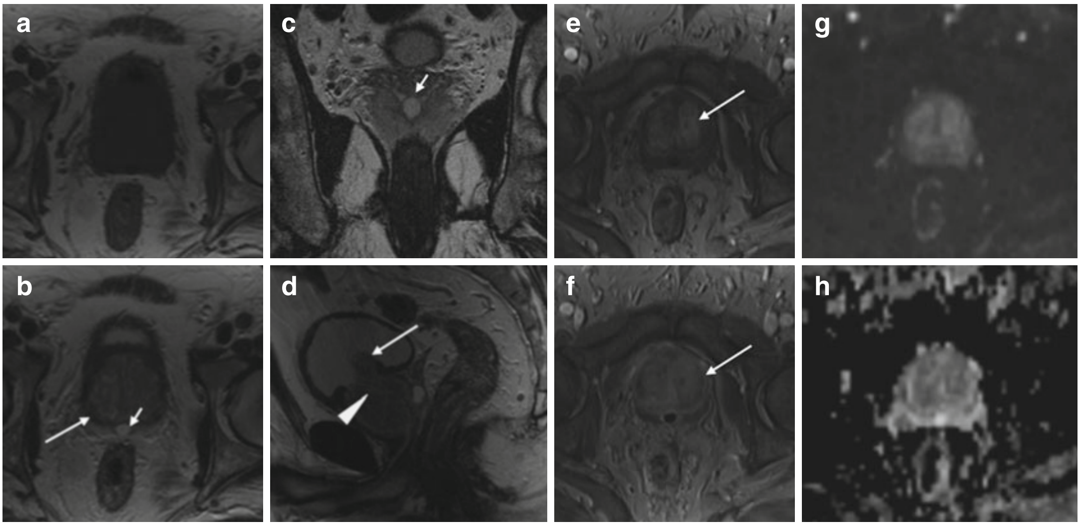

Fig. 7.5 Benign prostatic hyperplasia, normal pattern of adenomas enhancement. Presence of ejaculatory duct cyst. (**a**) Axial T1WI (TR 550/TE 9.3) shows an enlargement of the prostate. The gland has a homogeneous intermediate-low signal intensity with no evidence of intraglandular zonal abnormalities. (**b**) Axial T2WI (TR 5130/TE 108) shows a heterogeneous signal intensity in the transition zone for the adenomatous changes of the gland, with compression of the peripheral zone that appears thinned (*arrow*). There is also an ejaculatory duct cyst of 9 mm (*short arrow*). (**c**) Coronal T2WI (TR 3600/TE 116) shows the ejaculatory duct cyst behind the gland (*short arrow*). (**d**) Sagittal T2WI (TR3600/TE114) shows the imprint of the transition zone of the prostate on bladder floor (*arrow*) and the compression/deflection of intraprostatic urethra by adenomatous hyperplasia (*arrowhead*). (**e**, **f**) Early and later dynamic contrast-enhanced gradient-echo images (TR 12/TE 5.7) show a slight and diffuse enhancement of the adenomatous central zone and a greater and progressive enhancement of central gland adenomas without any washout (*arrow*). (**g**, **h**) DWI (b800) and ADC images do not show significant restricted diffusion areas in the gland

are those in whom baseline risk of progression is very high, generally patients with larger glands and higher PSA values.

C. *Conventional Surgical Therapy*
   1. *Transurethral resection of the prostate*—Symptom score and flow rate improvement with transurethral resection of the prostate (TURP) is superior to that of any minimally invasive therapy. Much controversy revolves around possible higher rates of morbidity and mortality associated with TURP in comparison with those of open surgery, but the higher rates observed in one study were probably related to more significant comorbidities in the TURP patients than in the patients undergoing open surgery. Several other studies could not confirm the difference in mortality when results were controlled for age and comorbidities.
   2. *Transurethral incision of the prostate*—Men with moderate to severe symptoms and a small prostate often have posterior commissure hyperplasia (elevated bladder neck). These patients will often benefit from an incision of the prostate. This procedure is more rapid and less morbid than TURP. Outcomes in well-selected patients are comparable, although a lower rate of retrograde ejaculation with transurethral incision has been reported (25 %).
   3. *Open simple prostatectomy*—When the prostate is too large to be removed endoscopically, an open enucleation is necessary. What constitutes "too large" is subjective and will vary depending upon the surgeon's experience with TURP. Glands >100 g are usually considered for open enucleation. Open prostatectomy may also be initiated when

concomitant bladder diverticulum or a bladder stone is present or if dorsal lithotomy positioning is not possible.

Open prostatectomies can be done with either a suprapubic or retropubic approach.

D. *Minimally Invasive Therapy*

1. *Laser therapy*—Many different techniques of laser surgery for the prostate have been described. Two main energy sources of lasers have been utilized—Nd:YAG and holmium:YAG.

   Several different *coagulation necrosis* techniques have been described. Transurethral laser-induced prostatectomy (TULIP) is done with TRUS guidance. The TULIP device is placed in the urethra, and TRUS is used to direct the device as it is slowly pulled from the bladder neck to the apex. The depth of treatment is monitored with ultrasound [20].
2. *Transurethral electrovaporization of the prostate*—Transurethral electrovaporization uses the standard resectoscope but replaces a conventional loop with a variation of a grooved rollerball. High current densities cause heat vaporization of the tissue, resulting in a cavity in the prostatic urethra.
3. *Hyperthermia*—Microwave hyperthermia is most commonly delivered with a transurethral catheter. Some devices cool the urethral mucosa to decrease the risk of injury. However, if temperatures are not >45 °C, cooling is unnecessary. Improvement in symptom score and flow rate is obtained, but as with laser surgery, large-scale, randomized studies with long-term follow-up are needed to assess durability and cost-effectiveness [21].
4. *Transurethral needle ablation of the prostate*—Transurethral needle ablation uses a specially designed urethral catheter that is passed into the urethra. Interstitial radiofrequency needles are then deployed from the tip of the catheter, piercing the mucosa of the prostatic urethra. The use of radio frequencies to heat the tissue results in a coagulative necrosis.
5. *High-intensity focused ultrasound*—High-intensity focused ultrasound is another means of performing thermal tissue ablation. A specially designed dual-function ultrasound probe is placed in the rectum. This probe allows transrectal imaging of the prostate and also delivers short bursts of high-intensity focused ultrasound energy, which heats the prostate tissue and results in coagulative necrosis.
6. *Intraurethral stents*—Intraurethral stents are devices that are endoscopically placed in the prostatic fossa and are designed to keep the prostatic urethra patent. They are usually covered by urothelium within 4–6 months after insertion. These devices are typically used for patients with limited life expectancy who are not deemed to be appropriate candidates for surgery or anesthesia.

7.2 Prostatitis

7.2.1 Introduction

The term prostatitis encompasses a broad spectrum of nonspecific symptoms of lower genitourinary tract mainly characterized by perineal or genital pain, urinary symptoms such as dysuria or urinary frequency, and sexual dysfunction in its various manifestations.

Prostatitis is a highly prevalent nosologic entity and hence has an enormous financial impact on health systems as well as negative repercussions on patients' quality of life.

The symptoms are ambiguous, diagnostic methods are controversial, and treatments are long and often produce inconsistent results; consequently, although not life threatening, prostatitis has become one of those diseases that is difficult both for the patient and for the physician who attempts to help, sometimes without success.

Although an infectious etiology is accepted in most cases, there are major controversies about both the diagnostic methods used and their interpretation. Recently, the National Institutes of Health in the USA has proposed a new

Table1

Categories	Definition	Description
I	Acute bacterial prostatitis	Bacterial infection of the prostate gland that requires urgent medical treatment
II	Chronic bacterial prostatitis	Chronic bacterial infection, rare condition usually present as intermittent urinary tract infections
III	Chronic prostatitis	Chronic pelvic pain for more than 3 months, without detection of bacterial agents
IIIA	Inflammatory chronic prostatitis	Patients with leukocytes in their prostatic fluid
IIIB	Non-inflammatory chronic prostatitis	Patients without leukocytes in their prostatic fluid
IV	Asymptomatic inflammatory prostatitis	Patients have no history of genitourinary pain but leukocytosis is noted, usually during evaluation for other conditions

classification of this disease to substitute that used for the last 20 years. This new classification may provide a more effective approach to the diagnosis and treatment of this insidious disease (Table 1), and it is better explained in the next paragraph.

7.2.2 Pathogenesis

Prostatitis is considered an inflammation of the prostate gland, which can be infectious or noninfectious in origin. The infective prostatitis is in most cases bacterial prostatitis, which is further divided into acute bacterial prostatitis (ABP) and chronic bacterial prostatitis (CBP) form.

ABP (Category I) refers to inflammation of the prostate associated with a urinary tract infection (UTI). In response to bacterial invasion, leukocytes (polymorphonuclear leukocytes, lymphocytes, plasma cells, and macrophages) are seen within and surrounding the acini of the prostate. Edema and hyperemia of the prostatic stroma frequently develop. With prolonged infection, variable degree of necrosis and abscess formation can occur.

In CBP (Category II), the bacteria colonize the prostate, which then serves as a nidus for recurrent UTI. It is thought that infection can result from ascending urethral infection or reflux of infected urine from the bladder into the prostatic ducts or direct hematogenous infection or spread from the rectum. Ascending urethral infection may occur following sexual intercourse. Inoculation may occur during cystoscopy, other instrumentation, prolonged catheterization, or unprotected anal intercourse. In the intraprostatic urinary reflux, the infected urine refluxes into the ejaculatory and prostatic ducts that empty into the posterior urethra. Urine reflux also may occur in urethral stricture disease. Because of the anatomy of the prostate gland, ducts that drain glands in the peripheral zone are positioned more horizontally than other prostatic ducts and, thus, facilitate the reflux of urine into the prostate. Consequently, most infections occur in the peripheral zone. Refluxing urine, even when sterile, may cause chemical irritation and initiate tubule fibrosis and prostatic stone formation, which then leads to intraductal obstruction and stagnation of intraductal secretions. Bacterial colonies can serve as a nidus for relapsing infections. The direct invasion or lymphogenous spread from the rectum may be facilitated by injury to the rectal wall by constipation or trauma (e.g., in prostate biopsy). The direct hematogenous infection is caused by a systemic infection, but it is a rare cause of prostatitis. Most infections involve only a single bacterial organism. Occasionally, two or three strains of bacteria may be involved. The organisms primarily responsible for bacterial prostatitis are also those responsible for most UTI: *Escherichia coli* (about 80 %), *Klebsiella* species, *Pseudomonas aeruginosa*, *Enterococcus faecalis*, gram-positive microorganisms, *Mycoplasma*, and *Chlamydia*. Nosocomial strains of bacteria are often cultured from the prostates of men with CBP or ABP after hospitalization and genitourinary manipulation.

In addition to infectious causes of prostatitis, there are also the noninfectious causes, and in this topic, there is an open discussion in the literature [22]. Bacterial prostatitis is a common problem, but the well-documented infections of the prostate are exceedingly uncommon especially in chronic bacterial prostatitis (7 %). The uropathogens that cause bacteriuria in these patients are identified in very few cases. Most patients with prostatitis do not have history of bacteriuria and have very little evidence of bacterial infection; in these patients, we talk about "no bacterial prostatitis" or "prostatodynia" or "chronic pelvic pain" (Category III). Patients of this group are classified basing on the presence or absence of leukocytes as "inflammatory prostatitis" (Category IIIA) for patients with leukocytes in their prostatic fluid or as "noninflammatory prostatitis" (Category IIIB) for patients without leukocytes in their prostatic fluid.

In many studies [23] about chronic pelvic pain and chronic prostatitis, some microbiological investigations found DNA of less common microorganism like *C. trachomatis*, *T. vaginalis*, and *M. genitalium* despite having no evidence of infection and negative urine cultures. Therefore, also in the classified noninfectious prostatitis, the infection could have a role as residue of previous infections or a process of reactivated infection that triggers a process of inflammation.

And finally, we can include in the list of prostatitis the asymptomatic inflammatory prostatitis (Category IV), in which we have an evidence of inflammation in biopsy or analysis of prostatic secretion in absence of symptoms.

7.2.3 Epidemiology

Together, the two forms of bacterial prostatitis (ABP and CBP) comprise less than 10 % of all prostatitis syndromes. The incidence of ABP and CBP in the USA is 102,000 cases per year (about 0.33 %) [22].

The incidence of bacterial prostatitis in the European Countries is 10–14 % [24].

Nonbacterial chronic prostatitis is a significant health problem with a prevalence between 2 and 16 % depending on the population studied, the epidemiological method and the definitions of prostatitis [25]. This underlines a significant burden on the health system in which prostatitis is a diagnosis in two million physician visits annually.

Talking about the asymptomatic prostatitis, histological evidence of prostatitis in asymptomatic men appears to be very common.

Recent studies [26, 27] showed the presence of histological evidence of chronic prostatitis in 78 % of the surgical specimens of patients who had undergone treatment (TURP) for prostatic hyperplasia and did not have prostatic symptoms. And there was not any statistical differences in the mean PSA density between the two groups with and without prostatitis.

7.2.4 Clinical and Laboratory Findings

Patients with acute bacterial prostatitis usually present with an abrupt onset of constitutional (fever, chills, malaise, arthralgia, myalgia, lower back/rectal/perineal pain) and urinary symptoms (frequency, urgency, dysuria). They may also present with urinary retention due to swelling of the prostate. Digital rectal examination reveals tender, enlarged glands that are irregular and warm.

Urine analysis usually demonstrates WBCs and occasionally hematuria. Serum blood analysis typically demonstrates leukocytosis. Prostate-specific antigen levels are often elevated [22]. With both Category I and Category II prostatitis, the acute and chronic bacterial forms of the condition, prostate-specific antigen (PSA) may leak from prostate cells into the bloodstream, boosting PSA levels on screening tests and raising fears about prostate cancer. If an increase in PSA is due to an infection, PSA levels will fall after the infection has cleared, but this can take 3–6 months.

In ABP, the diagnosis of prostatitis is finally made with microscopic examination and culture of the prostatic expressate and culture of urine obtained before and after prostate massage. In patients with acute prostatitis, fluid from the prostate massage often contains leukocytes with fat-laden macrophages. However, at the onset of acute prostatitis, prostatic massage is usually not suggested because the prostate is quite tender and the massage may lead to bacteremia. Similarly, urethral catheterization should be avoided. Culture of urine and prostate secretion usually identifies a single organism, but occasionally, polymicrobial infection may occur. *E. coli* is the most common causative organism in patients with acute prostatitis. Other gram-negative bacteria (*Proteus*, *Klebsiella*, *Enterobacter*, *Pseudomonas* and *Serratia* spp.) and enterococci are less frequent pathogens. Anaerobic and other gram-positive bacteria are rarely a cause of acute prostatitis.

In contrast to the acute form, chronic bacterial prostatitis has a more insidious onset, characterized by relapsing, recurrent UTI caused by the persistence of pathogen in the prostatic fluid despite antibiotic therapy. Most patients with chronic bacterial prostatitis typically present with dysuria, urgency, frequency, nocturia and low back/perineal pain. These patients usually are afebrile and do not uncommonly have a history of recurrent or relapsing UTI, urethritis or epididymitis caused by the same organism. In patients with chronic bacterial prostatitis, digital rectal examination of the prostate is often normal; occasionally, tenderness, firmness or prostatic calculi may be found on examination. The diagnosis is made after investigation for bacteriuria. Urine analysis demonstrates a variable degree of WBCs and bacteria in the urine, depending on the extent of the disease. Serum blood analysis normally does not show any evidence of leukocytosis. Prostate-specific antigen levels may be elevated. Finally, diagnosis is made after identification of bacteria from prostate expressate or urine specimen after a prostatic massage, using the 4-cup test. The causative organisms are similar to those of acute bacterial prostatitis.

When we have the suspect of chronic prostatitis but the culture of prostate expressate or urine analysis is negative, it could be a prostatitis of Category III [28]. It is also currently believed that other gram-positive bacteria, *Mycoplasma*, *Ureaplasma*, and *Chlamydia* are not causative pathogens in chronic bacterial prostatitis, but it is difficult to have a confirmative test of their presence.

A particular type of chronic inflammation is the granulomatous prostatitis, an uncommon benign lesion which can be basically classified into four types: infective, iatrogenic, allergic and idiopathic. Infective type is caused by *Mycobacterium tuberculosis*, *Treponema pallid*um, fungi, parasites, and *Escherichia coli*. Among them, *M. tuberculosis* is the most common causative agent. In the urological field, intravesical bacillus Calmette-Guerin (BCG) therapy is often applied to reduce the recurrence of bladder cancer. Iatrogenic type is usually related to transurethral resection of the prostate (TURP). Allergic type occurs usually simultaneously with systemic allergic reaction, such as asthma and vasculitis. Idiopathic type does not show evident causes and it is the most common type of GP [29].

7.2.5 Pathological Findings

Acute prostatitis is characterized by the presence of a purulent exudate inside the acinus with edema and inflammatory reaction in periacinus and periductal site; the exudate, together with the products of glandular epithelial desquamation, is poured into the urethra. If the infection does not resolve spontaneously or as a result of therapy, the inflammation tends to reach the periacinus interstitium and subsequently the pericapsular cells forming a prostatic and periprostatic phlegmon that can create a fistula in various directions.

Characteristic of chronic forms is the presence of one or more abscesses, mostly small in size, surrounded by a thick fibrous reactive capsule and sometimes communicating with the posterior urethra. This communication, on one hand promotes emptying of the abscessual cavity; on the other allows urine to reach the residual cavity and to stagnate in it, resulting, species if infected, to the formation of prostatic calculi. The typical histological appearance of chronic prostatitis is defined by the invasion of leukocytes, especially

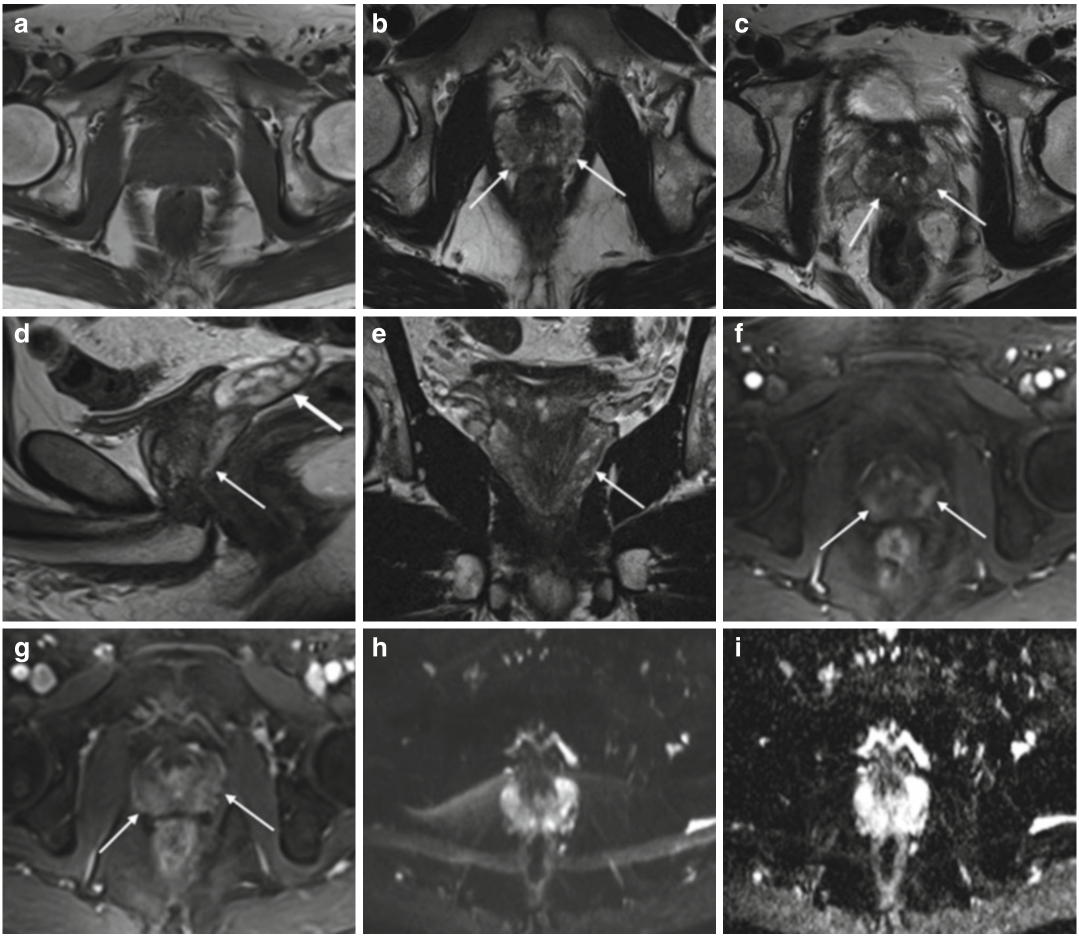

Fig. 7.6 Bacterial prostatitis. A 37-year-old man with hematospermia. (**a**) Axial T1WI (TR 550/TE 9.30) shows a normal signal intensity of the prostate gland. No high T1 is present to suggest blood. (**b**, **c**) Axial T2WI (TR 3600/TE 116) show a diffuse ill-defined intermediate T2 signal intensity throughout the peripheral zone (PZ) bilaterally (*arrows*). No focal area of significant low T2 signal intensity is identified. There is no significant enlargement of the transition zone or central zone. (**d**, **e**) Sagittal and coronal T2WI (TR 3600/TE 116) show the diffuse PZ hypointensity (*thin arrows*). The seminal vesicles are relatively distended (*thick arrow*) suggesting a degree of obstruction of the ejaculatory ducts. (**f**) Early dynamic contrast-enhanced (30 s) gradient-echo fat-saturated T1WI image (TR 12/TE 5.76) shows an early enhancement in PZ bilaterally (*arrows*). (**g**) Later dynamic contrast-enhanced (2 min) gradient-echo fat-saturated T1WI (TR 12/TE 5.76) image shows a progressive enhancement without any washout in these areas (*arrow*) with a plateau curve. (H-I) b800 DWI and ADC map images do not show significant restricted diffusion in the examined areas

polymorphonuclear leukocytes, into prostatic ducts and the periprostatic tissue.

The histological characteristics of granulomatous prostatitis include palisaded histiocytoid granulomas (composed by neutrophils, eosinophils, histiocytes) with a central fibrinoid necrosis and adjacent eosinophilic infiltration.

The xanthogranulomatous prostatitis [30] (XGP) is an even more rare cause of granulomatous prostatitis which consists pathologically of prominent foamy histiocyte infiltrates.

7.2.6 Magnetic Resonance Imaging

Until now, in the study of nonneoplastic prostatic disease, MRI does not appear to be an examination of the first instance. This also applies to the

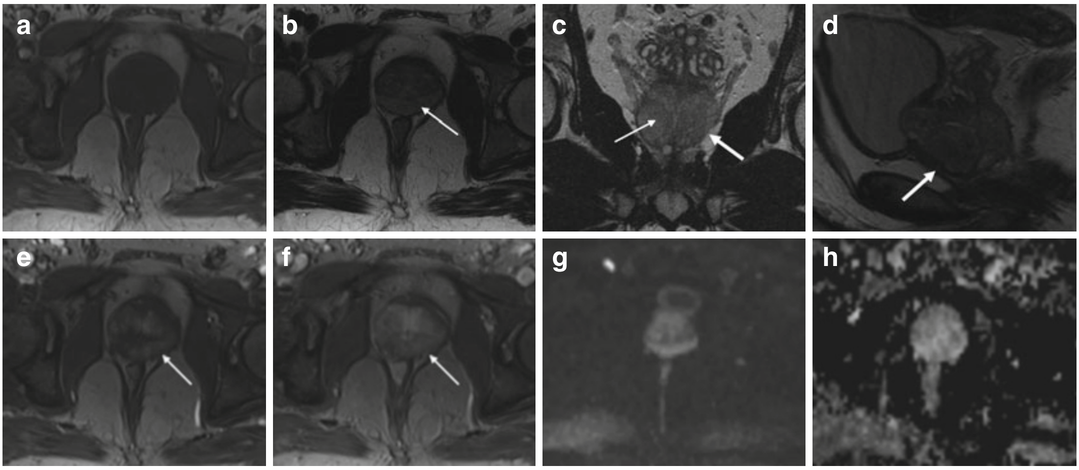

Fig. 7.7 Patient with prostatic hyperplasia and recent rise in the PSA. Detection of acute inflammatory foci in PZ. (**a**, **b**) Axial T1WI (TR 550/TE 9.30) and T2WI (TR 3600/TE 116) show an enlargement of the prostate gland with a normal signal intensity of the peripheral zone of the prostate gland (*arrow*). (**c**, **d**) Coronal and sagittal T2WI (TR 3600/TE 116) show an increase in the size of the central area (*thin arrow*) responsible for compression of the urethra and compression of the peripheral zone (*thick arrow*). (**e**) Early dynamic contrast-enhanced (30 s) gradient-echo image (TR 12/TE 5.76) shows a slight early enhancement in the peripheral zone of the left lobe (*arrow*) and also in the central zone. (**f**) Later dynamic contrast-enhanced (2 min) gradient-echo (TR 12/TE 5.76) image shows a progressive enhancement without any washout (*arrow*). (**g**, **h**) b800 DWI and ADC images do not show areas with significantly restricted diffusion

inflammatory disease, for which the patient is asked to undergo ultrasonography by transrectal ultrasound (TRUS), after the digital-rectal exploration (DRE) and urine analysis in three samples before and after prostatic massage.

The ultrasound allows us to assess gland volume, capsular profile, the presence of fibrocalcific areas and regularity of the bladder floor. However, in selected cases with elevated PSA, doubtful DRE and not diagnostic TRUS, RM with morphological evaluation, dynamic perfusion and eventually spectroscopic scans can be used.

Acute prostatitis (Fig. 7.6) is not a usual indication for this type of exam; usually the clinical presentation, analysis and ultrasound make diagnosis in these cases. However, RM can discover prostatic areas of acute inflammation in asymptomatic patients. These patients usually perform RM exam for elevated value of PSA and a suspected lesion seen on ultrasound (Fig. 7.7). Often, RM can show inflammation areas in patients who recently underwent transrectal prostatic biopsy.

In acute prostatitis, the gland becomes swollen, appearance characterized by abnormal homogeneous signal intensity (Fig. 7.6). The peripheral and the periurethral portions, more frequently affected by the inflammatory process, can have T1 hypointensity and T2 hyperintensity in relation to the presence of edema or they can present a T2 hypointense site of inflammation with focal or diffuse increased vascularization visualized on post-contrast dynamic sequences (Fig. 7.6). Starting from the rational that in acute inflammatory phase there be an increase in capillary permeability and vasodilation, in the dynamic study after administration of paramagnetic contrast agent, post-contrast enhancement of the areas of parenchyma affected by inflammation is showed, with the typical pattern of vascularization that demonstrates marked and early and widespread enhancement, in the absence of washout (Figs. 7.6 and 7.7). Infiltration of the periprostatic fat, involvement of the seminal vesicles, and enlarged venous plexus are the frequent associated findings. In this context, also abscesses could be identified, which sometimes originate from nodules of secretions themselves, represented by T2 hyperintensity and T1 hyperintensity, expression of the high protein content

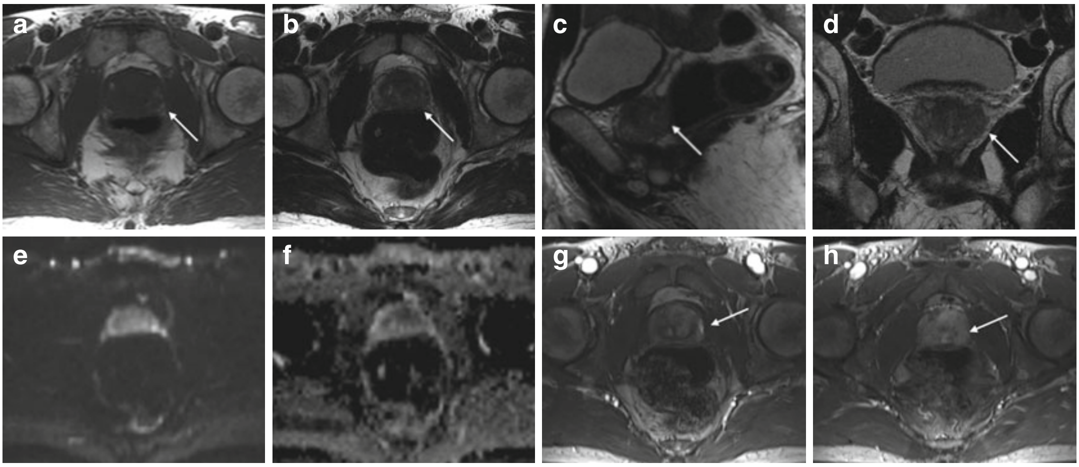

Fig. 7.8 Chronic inflammatory prostatitis. (**a**) Axial T1WI (TR 550/TE 9.30) shows some focal hyperintense lesions in the peripheral zone in keeping with previous biopsy (*arrows*). (**b**) Axial T2WI (TR 3600/TE 116) shows a not well-defined area of hypointensity signal in the peripheral zone of the left lobe of the prostate at the level of the middle third of the gland (*arrow*). (**c**, **d**) Sagittal and coronal T2WI (TR 3600/TE 116) show a low signal intensity in left posterior PZ (*arrow*). (**e**, **f**) b800 DWI and ADC images do not show significant restricted diffusion in the examined area. (**g**) Early dynamic contrast-enhanced (30 s) gradient-echo image (TR 12/TE 5.76) shows an area with striated morphology with early enhancement in the peripheral zone of left prostatic lobe (*arrow*). (**h**) Later dynamic contrast-enhanced (2 min) gradient-echo image (TR 12/TE 5.76) shows a progressive enhancement without any washout (*arrow*)

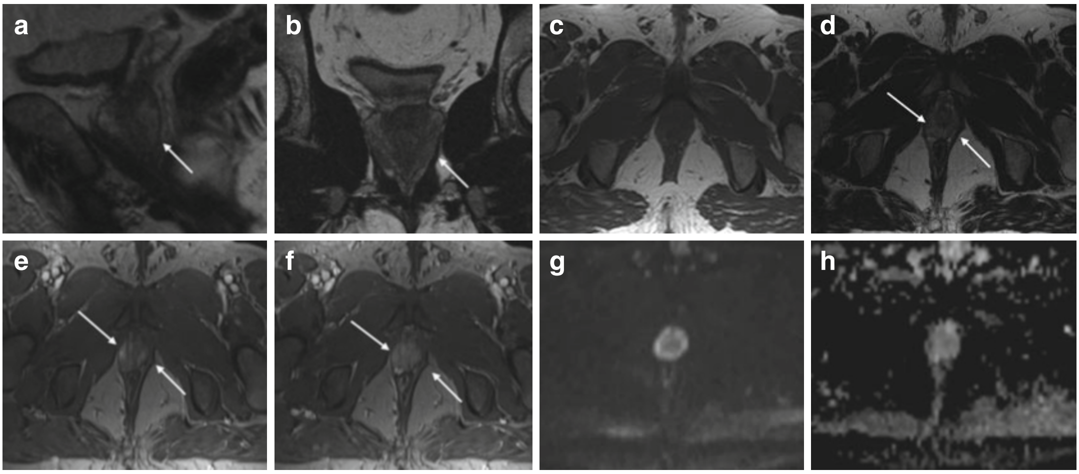

Fig. 7.9 Chronic prostatitis involving the whole peripheral zone. (**a**, **b**) Sagittal and coronal T2WI (TR 3600/TE 116) show a slightly hypointensity of all the peripheral zone (*arrows*); there are no irregularities in the prostatic capsule. (**c**) Axial T1WI (TR 550/TE 9.30) shows normal signal intensity of the prostatic apex. (**d**) Axial T2WI shows two foci of vague low signal intensity in the peripheral zone of the prostatic apex (*arrows*). (**e**) Early dynamic contrast-enhanced gradient-echo image (TR 12/TE 5.76) shows an early enhancement with striated morphology in the right and left PZ of prostatic apex (*arrows*). (**f**) Later dynamic contrast-enhanced gradient-echo image (TR 12/TE 5.76) shows a progressive enhancement without any washout (*arrow*). (**g**, **h**) b800 DWI and ADC images do not show areas of significantly restricted diffusion

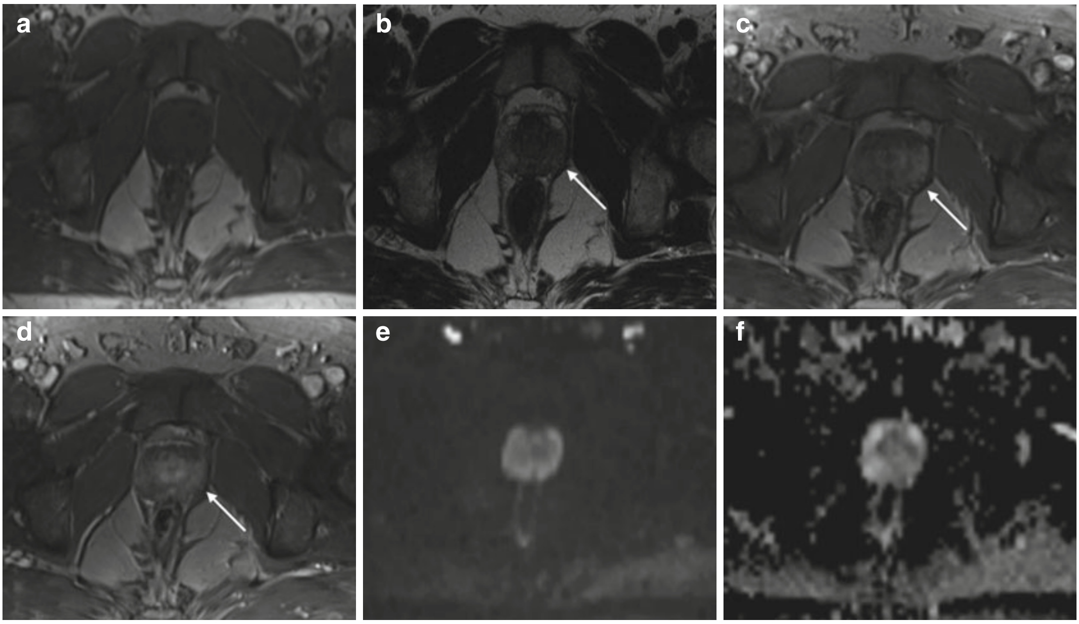

Fig. 7.10 Chronic prostatitis involving the whole peripheral zone (same patient of Fig. 7.9). (**a**) Axial T1 W (TR 550/TE 9.30) at midgland level of the prostate. (**b**) Axial T2WI (TR 3600/TE 116) shows a wide low-signal-intensity area in the peripheral zone of the left lobe (*arrow*). (**c**) Early dynamic contrast-enhanced gradient-echo image (TR 12/TE 5.76) shows a focal area with early enhancement in the peripheral zone of the left prostatic lobe (*arrow*). (**d**) Later dynamic contrast-enhanced gradient-echo image (TR 12/TE 5.76) shows a progressive enhancement without any washout (*arrow*). (**e**, **f**) b800 DWI and ADC image do not show significative diffusion restriction in the examined area

of the abscess, often surrounded by a rim characterized by marked enhancement.

In chronic prostatitis, areas of hypointense signal on T2 sequences may be present in the context of the peripheral skirt of the prostate gland, which does not exhibit nodular morphological characteristics. The lesions of the peripheral zone have not usually defined margins (Fig. 7.8) and sometimes they can appear as a diffuse thickening and homogeneous lowering of signal intensity of all the peripheral zone (Figs. 7.9, 7.10, and 7.11). In most cases in the context of these areas of altered signal, we can identify in post-contrast dynamic sequences linear or lozenge-like-appearance lesions (Figs. 7.8 and 7.9).

It is also possible to notice a chronic inflammation with nodular aspect characterized by abundant fibrotic component, as in the case of granulomatous prostatitis that presents RM pattern similar to that of a nodule of prostate cancer, with a focal round or oval hypointensity in T2 in the context of the peripheral zone (Figs. 7.12, 7.13, and 7.14).

In the dynamic-perfusional study, acquired during intravenous administration of paramagnetic contrast agent, bands of enhancement have been found in chronic prostatitis for increased vascularization pattern, typical of the inflammatory process, with modest late and progressive enhancement and absence of washout, which expresses fibrotic evolution of alteration (Figs. 7.8, 7.9, 7.10, and 7.11).

It is not rare to find patients with both chronic inflammation and benign prostatic hyperplasia [3] that show to have larger prostate volumes, more severe lower urinary tract symptoms and a higher probability of acute urinary retention than their counterparts without inflammation. Also, chronic inflammation could be a predictor of poor response to BPH medical treatment. Thus, the ability to identify patients with chronic inflammation would be crucial to prevent BPH progression and develop target therapies. In these cases, it may be difficult to distinguish a defined area of inflammation

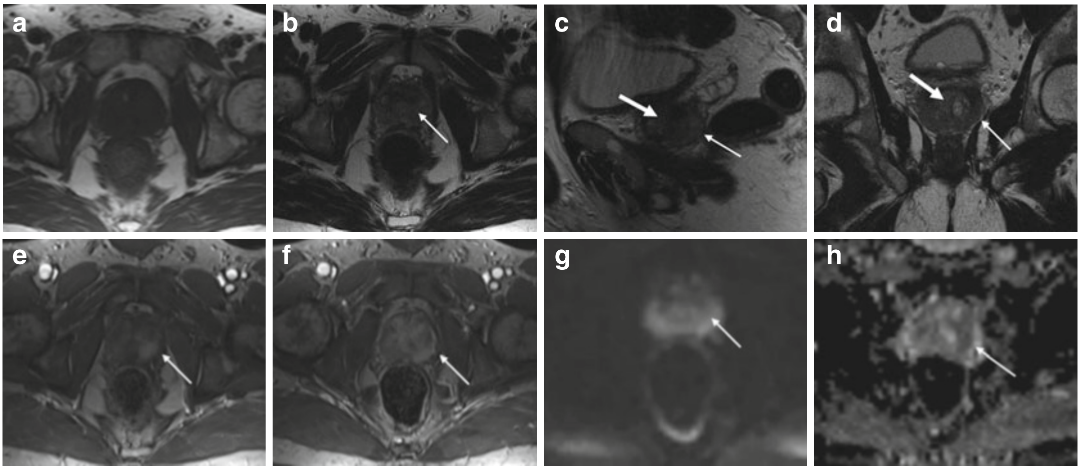

Fig. 7.11 Chronic prostatitis involving the peripheral zone (PZ) and the central zone (CZ). (**a**) Axial T1WI (TR 550/TE 9.30) reveals only a slight increase in size of the prostate gland. (**b**) Axial T2WI (TR 3600/TE 116) at the midgland level shows a poor differentiation of the peripheral zone with the central zone (*arrow*). The peripheral zone assumes a homogeneous alteration of its normal signal intensity without pointing out any focal lesions. (**c**, **d**) Sagittal and coronal T2WI (TR 3600/TE 116) confirm an ill definition of the zonal anatomy of the gland, with diffuse thickening and hypointensity of the peripheral posterior prostatic zone (*thin arrow*). Interstitial hyperplasia of the transitional zone (*thick arrow*) is seen. (**e**) Early dynamic contrast-enhanced gradient-echo image (TR 12/TE 5.76) shows a focal area with early enhancement in the peripheral zone of the left prostatic lobe (*arrow*). (**f**) Later dynamic contrast-enhanced gradient-echo image (TR 12/TE 5.76) shows a progressive enhancement without any washout (*arrow*). (**g**, **h**) b800 DWI and ADC images show an alteration of the diffusion coefficient with low ADC value in the focus described before (*arrow*)

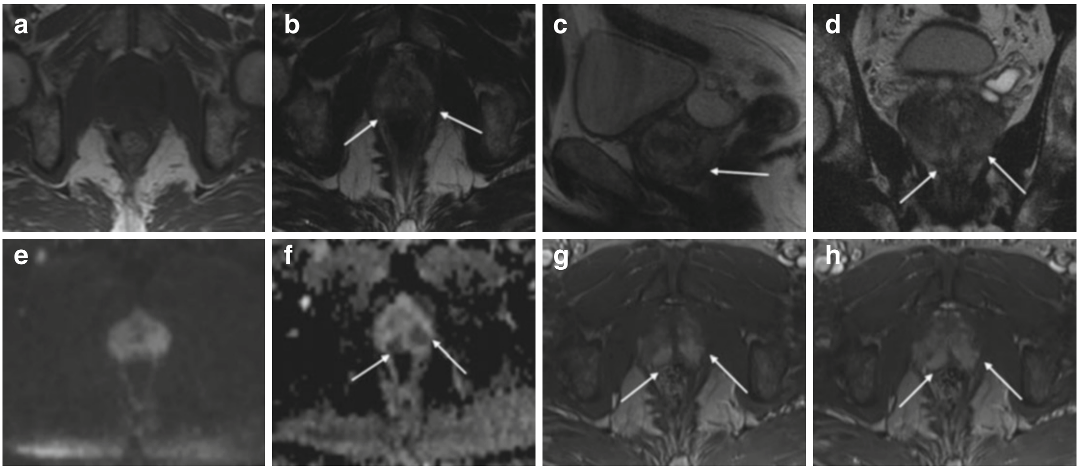

Fig. 7.12 Granulomatous prostatitis. (**a**) Axial T1WI (TR 550/TE 9.30) at the level of the apex of the prostate gland does not reveal any abnormality. (**b**) Axial T2WI (TR 3600/TE 116) at the same level shows two low-signal-intensity foci involving the posteromedial peripheral zone of the right and left prostatic lobes (*arrows*). (**c**, **d**) Sagittal and coronal T2WI (TR 3600/TE 116) confirm the low signal intensity areas in the posteromedial peripheral zone of the apex bilaterally (*arrows*). (**e**) DWI b800 at the apex does not reveal important changes of signal intensity. (**f**) ADC image better demonstrates a low ADC value in the previous described areas (*arrows*). (**g**, **h**) Early and later dynamic contrast-enhanced gradient-echo images (TR 12/TE 5.76) show a marked early enhancement in the peripheral areas of the apex without later washout (*arrows*)

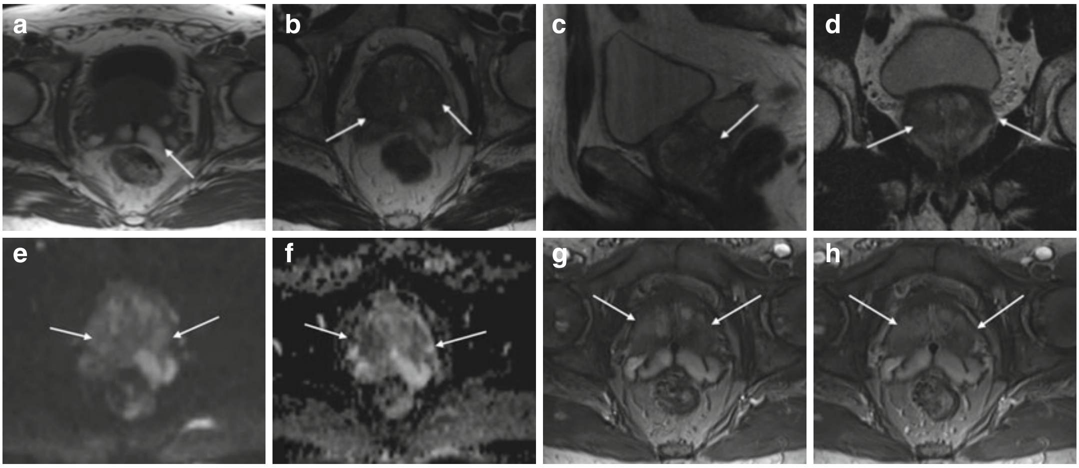

Fig. 7.13 Granulomatous prostatitis. (**a**) Axial T1WI (TR 550/TE 9.30) shows an increase in prostate volume with distension of seminal vesicles (*arrow*) which have hyperintense endoluminal content due to methemoglobin for previous biopsy. (**b**) Axial T2WI (TR 3600/TE 116) shows two low-signal regions in the right and in the left peripheral zone of the prostatic base with indistinct margins (*arrows*). (**c**, **d**) Sagittal and coronal T2WI (TR 3600/TE 116) confirm the low-signal-intensity foci in the base of prostate gland (*arrows*). (**e**, **f**) b600 DWI and ADC image show a restricted diffusion in the same zones (*arrows*). (**g**) Early dynamic contrast-enhanced gradient-echo image (TR 12/TE 5.76) shows diffuse early enhancement in the peripheral zone of the prostatic base (*arrows*). (**h**) Later dynamic contrast-enhanced gradient-echo image (TR 12/TE 5.76) does not show any washout (*arrows*)

in the context of the peripheral zone because this is compressed by hyperplasia or because the inflammatory process may involve both the peripheral zone and the transition zone causing a poor differentiation of the peripheral areas with the central and transitional areas (Figs. 7.7, 7.8, 7.9, and 7.10).

In DWI, areas of prostatitis could show a normal or a lower mean ADC value than the normal prostatic peripheral gland. Some studies demonstrate a difference in mean ADC between prostatitis and prostate cancer by using MR-guided biopsy specimens as standard of reference, although its usability in clinical practice is limited due to a high degree of overlap. In our experience in prostatitis lesions DWI was negative in most cases and the diagnosis was based mostly on hypointensity on T2-weighted and on pattern of vascularization typically characterized by early and progressive enhancement in the absence of washout (Figs. 7.7, 7.8, and 7.9).

Prostatic calcification is sometimes associated with inflammation when seen in young men [31]. Patients with chronic prostatitis are more likely to have calcified prostates. Some studies [11] correlated the presence of prostatic stones with presence of chronic prostatitis and showed that men with larger significant calcifications were much more likely to have symptoms of lower urinary tract symptoms or prostatitis. Calcifications can be an effect of repeated bouts of infection and inflammation (Fig. 7.15), or in contrast, they might indicate a switch from the early highly treatment-responsive phase of the prostatitis to the later chronic stage in which response to monotherapy is infrequent.

7.2.7 Differential Diagnosis

7.2.7.1 Prostatic Hyperplasia

Benign prostatic hyperplasia is the most common prostatic lesion found in men and frequently found in the age group of 60–70 years. The symptoms are often similar to prostatitis, but usually pain distinguishes chronic prostatitis from BPH better than any other urinary symptom [32].

Transitional zone prostatitis is difficult to distinguish from benign prostatic hyperplasia (BPH).

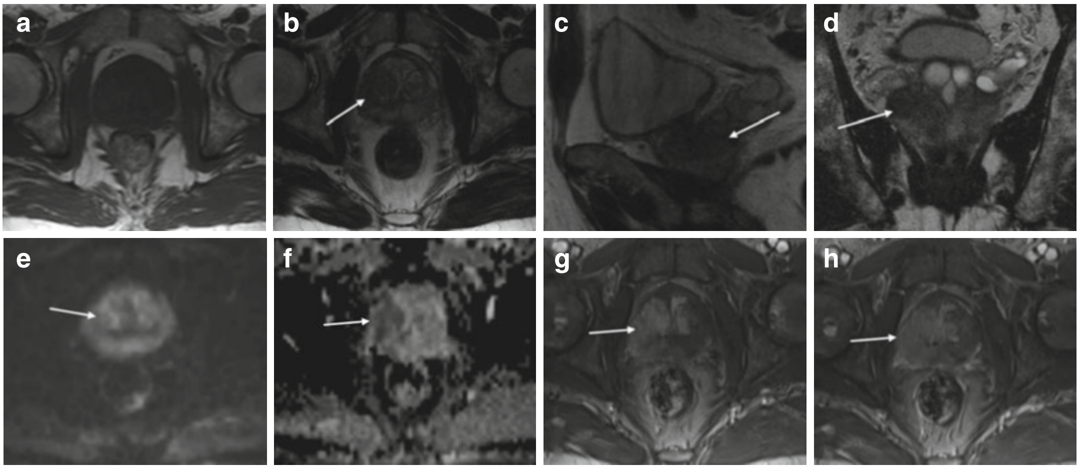

Fig. 7.14 Granulomatous prostatitis. (**a**) Axial T1WI (TR 550/TE 9.30) at the level of mid-third of the prostate gland does not reveal any alteration. (**b**) Axial T2WI (TR 3600/TE 116) at the same level shows a low signal intensity nodule involving the peripheral zone (PZ) and the central zone (CZ) of right prostatic lobe (*arrow*). (**c**, **d**) Sagittal and coronal T2WI (TR 3600/TE 116) confirm the low-signal-intensity lesion in the right prostatic lobe at midgland level (*arrow*). (**e**) DWI b800 shows a slight hyperintensity in the right prostatic lobe (*arrow*). (**f**) ADC image better demonstrates a low ADC value in the examined area (*arrow*). (**g**) Early dynamic contrast-enhanced gradient-echo image (TR 12/TE 5.76) shows a marked enhancement in the PZ and CZ of the right lobe (*arrow*). (**h**) Later dynamic contrast-enhanced gradient-echo image (TR 12/TE 5.76) shows a progressive enhancement without any washout of the granulomatous nodule (*arrow*)

7.2.7.2 Prostate Cancer

Prostatitis can be a cause of an elevated PSA level; in these cases, the differential diagnosis from prostate cancer could be difficult. As a consequence, prostatitis patients will undergo transrectal ultrasonography (US)-guided biopsy sessions. Moreover, prostate cancer can still be present in patients with biopsy-proved prostatitis.

Magnetic resonance imaging of the prostate is the imaging modality of choice in prostate cancer detection, localization, and staging. The diagnostic value of anatomic T2-weighted MR imaging in discriminating prostate cancer from benign prostate tissue is limited. The interpretation of these images can be affected by false-positive findings such as prostatitis, post-biopsy hemorrhage, and fibrosis.

DW imaging is a noninvasive technique that demonstrates a difference in mean ADC between prostatitis and prostate cancer [17] by using MR-guided biopsy specimens as standard of reference, although its usability in clinical practice is limited due to a high degree of overlap.

The median apparent diffusion coefficient (ADC) of prostatitis was higher than prostate cancer for both the peripheral zone and central gland; however, substantial overlap exists. Diffusion-weighted imaging may help reduce the number of false-positive findings at prostate cancer MR imaging.

To improve the diagnostic accuracy of prostate MR imaging, functional imaging techniques have been applied, such as dynamic contrast-enhanced MR imaging, proton MR spectroscopic imaging and diffusion-weighted MR imaging. From the dynamic-perfusional analysis, different patterns of vascularization between inflammation and cancer come out. While in presence of an inflammatory outcome a diffuse progressive enhancement without washout is documented, in the tumor you have strong early enhancement with subsequent washout.

In some studies [33], the perfusion parameters were investigated, and a statistically significant differentiation of chronic prostatitis from high-grade cancer was showed. High-grade cancer showed higher perfusion than chronic prostatitis. There were no statistically significant differences between low-grade and high-grade cancer or between low-grade cancer and chronic prostatitis.

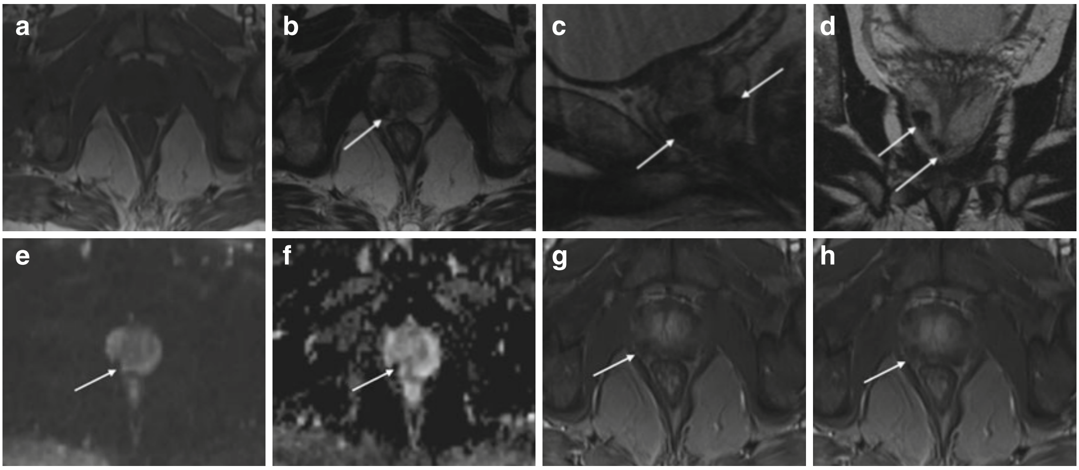

Fig. 7.15 Outcomes of previous recurrent prostatitis. Prostatic peripheral zone (PZ) calcification. (**a**) Axial T1WI (TR 550/TE 9.30) at midgland level does not show alterations. (**b**) Axial T2WI (TR 3600/TE 116) shows a marked hypointense focal round lesion in the right posterior PZ (*arrow*). (**c**, **d**) Sagittal and coronal T2WI (TR 3600/TE 116) show the presence of more diffuse lesions in the peripheral area (*arrows*) of prostate gland with round-like morphology and marked hypointensity. (**e**, **f**) In DWI b600 and ADC images, we recognize an absence of signal in one of the lesions previously described (*arrow*). (**g**, **h**) Early and later dynamic contrast-enhanced gradient-echo images confirm the absence of signal in the lesion of the peripheral prostatic zone (*arrow*) without any enhancement

Often, little neoplastic infiltration can be found adjacent to and in the context of inflammatory processes in the same patient. This overlap cannot be detected in the biopsies by random sampling because the frustules may not contain both lesions. MRI has the ability, thanks to the dynamic and spectroscopic study, to isolate individual voxel altered in neoplastic and/or in inflammatory sense, according to different metabolic characteristics.

7.2.8 Prognosis and Management

Category I: Acute bacterial prostatitis

Antibiotics are the standard treatment and are highly effective for this form of prostatitis. Typical choices include fluoroquinolones, such as ciprofloxacin (Cipro), levofloxacin (Levaquin), and ofloxacin (Floxin), and trimethoprim/sulfamethoxazole (Bactrim, Septra, Cotrim). It is important to continue medication for the entire prescribed course, even if the patient is feeling better. This will help prevent infection from returning.

Category II: Chronic bacterial prostatitis

Treatment requires the same antibiotics used for the acute form, usually for 1–3 months, but even with the prolonged treatment, the infection often recurs. If this happens, the recurrence can usually be controlled with another course of antibiotics.

Category III: Chronic prostatitis/chronic pelvic pain syndrome

Category III prostatitis has two variants, distinguished by the presence or absence of inflammation. In Category IIIA (inflammatory) prostatitis, white blood cells, a sign of infection, are found in the urine and in prostate secretions. Antibiotics are useful for Category IIIA prostatitis in case there is an undetected bacterial infection, but such treatment is generally ineffective. Because there is no known cause, most other therapies aim to reduce discomfort rather than address the cause of the condition. Pain medications that reduce inflammation, such as aspirin, ibuprofen, or other nonsteroidal anti-inflammatory drugs (NSAIDs), may be helpful and so may hot baths. In addition, anticholinergic drugs can be used, such as tolterodine (Detrol) and oxybutynin (Ditropan), which reduce urinary symptoms by decreasing bladder contractions. Also an alpha-blocker drug, which relaxes the muscles at the neck of the bladder, eases the flow of urine.

Category IIIB (no inflammatory) prostatitis is often referred to as prostatodynia. This term means "pain in the prostate" and, not surprisingly, that is the main symptom of the condition. But what is causing this pain is not clear; the prostate feels normal when it is examined, the urine is free of infection, and prostate secretions do not contain white blood cells. The pain can be persistent and debilitating and is often accompanied by depression, anxiety, or sexual dysfunction. Urine flow can also be abnormal, with an interrupted or weak stream, an urge to urinate (even when you can produce little urine), or frequent urination (often in small amounts). Although it can occur at any age, prostatodynia is most common in young to middle-aged men. Alpha-blockers medications most likely are used to reduce such symptoms and are useful more in men who were newly diagnosed with chronic pelvic pain syndrome; an extended course of treatment (3–6 months) is more effective than a shorter course; and broader alpha-blockers such as doxazosin (Cardura) and terazosin (Hytrin) are more effective than the more selective agents.

References

1. McNeal JE et al (1988) Zonal distribution of prostatic adenocarcinoma. Correlation with histologic pattern and direction of spread. Am J Surg Pathol 12(12): 897–906
2. Nelson WG et al (2004) The role of inflammation in the pathogenesis of prostate cancer. J Urol 172 (5 Pt 2):S6–S11; discussion S11–S12
3. Gandaglia G et al (2013) The role of chronic prostatic inflammation in the pathogenesis and progression of benign prostatic hyperplasia (BPH). BJU Int 112(4): 432–441
4. Hughes C et al (2005) Molecular pathology of prostate cancer. J Clin Pathol 58(7):673–684
5. Jemal A et al (2005) Cancer statistics, 2005. CA Cancer J Clin 55(1):10–30
6. Barqawi AB et al (2005) Observed effect of age and body mass index on total and complexed PSA: analysis from a national screening program. Urology 65(4):708–712
7. Grossfeld GD, Coakley FV (2000) Benign prostatic hyperplasia: clinical overview and value of diagnostic imaging. Radiol Clin North Am 38(1):31–47
8. Roddam AW et al (2005) Use of prostate-specific antigen (PSA) isoforms for the detection of prostate cancer in men with a PSA level of 2-10 ng/ml: systematic review and meta-analysis. Eur Urol 48(3): 386–399; discussion 398–399
9. Berger AP et al (2005) Longitudinal PSA changes in men with and without prostate cancer: assessment of prostate cancer risk. Prostate 64(3):240–245
10. Shoskes DA et al (2003) Long-term results of multimodal therapy for chronic prostatitis/chronic pelvic pain syndrome. J Urol 169(4):1406–1410
11. Geramoutsos I et al (2004) Clinical correlation of prostatic lithiasis with chronic pelvic pain syndromes in young adults. Eur Urol 45(3):333–337; discussion 337–338
12. Murphy G et al (2013) The expanding role of MRI in prostate cancer. AJR Am J Roentgenol 201(6): 1229–1238
13. Oto A et al (2010) Prostate cancer: differentiation of central gland cancer from benign prostatic hyperplasia by using diffusion-weighted and dynamic contrast-enhanced MR imaging. Radiology 257(3): 715–723
14. Barentsz JO et al (2012) ESUR prostate MR guidelines 2012. Eur Radiol 22(4):746–757
15. Huisman C et al (2001) Accelerated cisplatin and high-dose epirubicin with G-CSF support in patients with relapsed non-small-cell lung cancer: feasibility and efficacy. Br J Cancer 85(10):1456–1461
16. Saremi F et al (2009) Characterization of genitourinary lesions with diffusion-weighted imaging. Radiographics 29(5):1295–1317
17. Nagel KN et al (2013) Differentiation of prostatitis and prostate cancer by using diffusion-weighted MR imaging and MR-guided biopsy at 3 T. Radiology 267(1):164–172
18. McConnell JD (1994) Benign prostatic hyperplasia. J Urol 152(2 Pt 1):459–460
19. McConnell JD et al (2003) The long-term effect of doxazosin, finasteride, and combination therapy on the clinical progression of benign prostatic hyperplasia. N Engl J Med 349(25):2387–2398
20. Hoffman RM, MacDonald R, Wilt TJ (2004) Laser prostatectomy for benign prostatic obstruction. Cochrane Database Syst Rev (1):CD001987
21. Hoffman RM et al (2004) Transurethral microwave thermotherapy vs transurethral resection for treating benign prostatic hyperplasia: a systematic review. BJU Int 94(7):1031–1036

22. Duclos A et al (2008) Genitourinary pain and inflammation: diagnosis and management. vol 2, pp 175–199
23. Krieger JN, Riley DE (2002) Prostatitis: what is the role of infection. Int J Antimicrob Agents 19(6):475–479
24. Mehik A et al (2000) Epidemiology of prostatitis in Finnish men: a population-based cross-sectional study. BJU Int 86(4):443–448
25. Krieger JN, Ross SO, Riley DE (2002) Chronic prostatitis: epidemiology and role of infection. Urology 60(6 Suppl):8–12; discussion 13
26. Piovesan AC et al (2009) Incidence of histological prostatitis and its correlation with PSA density. Clinics (Sao Paulo) 64(11):1049–1051
27. Edlin RS et al (2012) Prevalence of histological prostatitis in men with benign prostatic hyperplasia or adenocarcinoma of the prostate presenting without urinary retention. S Afr J Surg 50(4):127–130
28. Jiménez-Cruz JF, Broseta-Rico E (2005) Clasificaciòn, etiologìa, diagnostico y tratamiento de las prostatitis. Otros tipos de prostatitis. Enferm Infecc Microbiol Clin 23(4):47–56
29. Warrick J, Humphrey PA (2012) Nonspecific granulomatous prostatitis. J Urol 187(6):2209–2210
30. Lee HY et al (2012) Xanthogranulomatous prostatitis: a rare entity resembling prostate adenocarcinoma with magnetic resonance image picture. Clin Imaging 36(6):858–860
31. Shoskes DA et al (2007) Incidence and significance of prostatic stones in men with chronic prostatitis/chronic pelvic pain syndrome. Urology 70(2):235–238
32. Collins MM et al (1999) Distinguishing chronic prostatitis and benign prostatic hyperplasia symptoms: results of a national survey of physician visits. Urology 53(5):921–925
33. Franiel T et al (2008) Evaluation of normal prostate tissue, chronic prostatitis, and prostate cancer by quantitative perfusion analysis using a dynamic contrast-enhanced inversion-prepared dual-contrast gradient echo sequence. Invest Radiol 43(7):481–487

Adenocarcinoma of the Prostate

8

Ugolino Alfonsi, Anna Ventriglia, Riccardo Manfredi,
and Roberto Pozzi Mucelli

8.1 Introduction

With an estimated 5-year prevalence of 2.3 million patients in the world, prostate cancer is a major global health problem [1]. In particular, prostate cancer is the most frequently diagnosed cancer in males, accounting for 25 % of all cancers in males (192,280 of 766,130 newly diagnosed cancers in males in 2009), compared with 15 % for lung cancer. It is the second leading cause of cancer-related death in men, making up 9 % of cancer deaths in males (27,360 of 292,540 cancer-related deaths in males in 2009), a value exceeded only by the death rate from lung cancer in males (30 %) [2]. In the United States, the lifetime probability of developing prostate cancer is 1 in 6 [3]. The prevalence of prostate cancer increases with age; 34 % of men in the 5th decade of life and up to 70 % aged 80 years or older have histologic evidence of prostate cancer.

Because of the advent of prostate-specific antigen (PSA) screening, most prostate cancers are now diagnosed at an earlier stage. At present, 86 % of newly diagnosed prostate cancers are localized within the gland, and patients have a 5-year relative (i.e., adjusted for life expectancy) survival rate of 100 %. The 5-year relative survival rate for all stages of prostate cancer is 98 %, while the corresponding 10-year survival rate is 93 %, and the 15-year survival rate is 79 %. That indicates that most prostate cancers grow slowly [4, 5] and allow for prolonged survival, even in patients with metastases at diagnosis [6]. An early detection can lead to a complete cure; however, in more than 85 % of cases of prostate cancer, multiple cancer foci are found in the prostate [7–9].

Prostate cancer screening consists of *(a)* the measurement of PSA concentration in serum and *(b)* a digital rectal examination. The various conflicting guidelines and recommendations regarding prostate cancer screening reflect the controversies surrounding the potential benefits and limitations of PSA testing [10, 11]. PSA measurement has yielded higher detection rates than has digital rectal examination [12], but its specificity is low (36 %) owing to false-positive PSA elevation under benign circumstances, such as inflammation or benign prostatic hyperplasia (BPH) [13]; digital rectal examination has a low overall sensitivity (37 %) and low positive predictive value when lower PSA ranges of 0–3 ng/mL are encountered [11]. Therefore, some groups, including the American Urologic Association, have recommended that a baseline PSA serum measurement be obtained in men between the ages of 40 and 50 years, whereas others remain unconvinced of a need for, or

---

U. Alfonsi (✉) • A. Ventriglia • R. Manfredi
R.P. Mucelli
Department of Radiology, University of Verona,
Piazzale L.A. Scuro, 10, Verona 37134, Italy
e-mail: ugolinoalfonsi@yahoo.it;
ven_anna@libero.it; riccardo.manfredi@univr.it;
roberto.pozzimucelli@univr.it

R. Manfredi, R. Pozzi Mucelli (eds.), *MRI of the Female and Male Pelvis*,
DOI 10.1007/978-3-319-09659-9_8,

benefit from, a routine PSA measurement [10]. Conversely, the American Cancer Society recommends that PSA screening be offered to men aged 50 years or older who have an average prostate cancer risk and an estimated life expectancy of at least 10 years.

Patients with an elevated PSA level or with abnormal findings at digital rectal examination are candidates for further diagnostic evaluation with a transrectal ultrasonography (US)-guided prostate biopsy: because of the low accuracy of US for prostate cancer detection and localization, a random biopsy is usually performed instead of a targeted biopsy of lesions encountered during the US exam. The systematic random sextant biopsy involves the acquisition of a minimum of four extra cores from lateral peripheral zones or from a region that is suspicious for cancer [14]. Histopathologic analysis of these biopsy samples provides the clinician with information on the Gleason score. However, a random biopsy has several disadvantages. For example, it may lead to an increase in complications because of the unnecessary sampling of normal prostate tissue. Moreover, a biopsy-determined Gleason grade, although valuable, is subject to undersampling (35 % cancers missed on first biopsy for locations outside the routine biopsy) [15] or underestimation of the Gleason grade [16, 17]. In addition, there may be difficulty in determining the site of a previous biopsy when repeating biopsy in a patient with a previous negative result and continuously high prostate-specific antigen levels.

Because these diagnostic methods all have their limitations, there is a need for improved prostate cancer diagnosis with improved detection, localization, and staging [18]. Improvements in all three of these dimensions are prerequisites for optimal clinical management and therapy selection; also, an imaging modality is needed as adequate follow-up after treatment. Moreover, promising new focal treatment modalities (e.g., high-intensity focused ultrasound ablation, cryotherapy, and laser ablation) require accurate detection, localization, and sampling of regions of aggressive prostate cancer [19]. Thus, a technique that noninvasively demonstrates the presence, extent, and aggressiveness of prostate cancer could make a substantial contribution to the decision-making process for individualized treatment. Magnetic resonance (MR) imaging enable the noninvasive evaluation of anatomic and biologic tumor features and, thus, may play an important role in the detection, localization, and staging of prostate cancer and help guide treatment selection and planning [20–22].

MR imaging can provide functional tissue information along with anatomic information. To increase the accuracy, anatomic T2-weighted MR imaging and functional MR imaging techniques such as dynamic contrast agent-enhanced MR imaging, diffusion-weighted (DW) imaging, and MR spectroscopic imaging can be combined in an integrated multiparametric MR imaging examination. Dynamic contrast material-enhanced (DCE) MR imaging dynamically captures the distribution of intravenously administered gadolinium-based contrast agents between tissue and the blood pool, allowing characterization of alterations in the microvascular environment resulting from tumor angiogenesis. Diffusion-weighted imaging interrogates the tissue microstructure at the microscopic scale of water self-diffusion (Brownian motion). MR spectroscopy probes the concentration of biochemical disease markers in tissues. All of these techniques benefit from continuing improvements in imaging unit hardware and software. Also, MR-compatible devices have been developed for diagnostic and therapeutic interventions and for minimally invasive procedures. These multiparametric MR techniques will contribute to prostate cancer diagnostics, although results for detection, localization, and local staging of prostate cancer vary greatly among the studies performed.

8.2 Pathology

The most widely used grading scheme for prostatic carcinoma is the Gleason system [7, 23–25], which is designed for application to all untreated prostatic glandular carcinomas, representing almost all prostatic tumor cases developing in adult males.

The Gleason system is based entirely on the growth patterns of the architectural arrangement of the cancer cells, consolidated into five classes; a score from 1 to 5 is assigned to these five classes. The Gleason grade is generated by adding two more common classes, or, if only one grade is in the tissue sample, that grade is multiplied by two to give the score: the result is that the Gleason score ranges from 2 to 10. A first limit is that the Gleason grading system considers only two separate grade patterns, but the histomorphological appearance of prostatic carcinoma is usually more heterogeneous than this [26–28]. Secondly, the prediction of pathologic stage by needle biopsy Gleason grade alone is possible but is not accurate: the Gleason grade in needle biopsy agrees with that in the matched whole prostate gland in only 43 % of cases and to within +/− 1 score unit in 77 % of cases [29]. Undergrading of a tumor in needle biopsy occurs in 42 % of all cases, while overgrading in needle biopsy occurs 15 % of all cases. Moreover, the Gleason grading system possesses an inherent degree of subjectivity [29, 30].

Increasing Gleason grade is directly related to the pathological stage, including the tumor size, the risk of extraprostatic and lymphovascular extension, and metastasis. So patients with lower-grade (Gleason score 2–6) carcinomas usually, but not always, have cancer limited inside the prostate, while patients with a high-grade carcinoma component (Gleason score 7–10) have cancer with a greater risk of extending outside the prostate. The needle biopsy Gleason grade is combined with serum PSA and clinical stage to predict pathologic stage, most commonly using the “Partin tables” [31], a tool routinely used to determine the eligibility of different treatment plans, choosing between types of radiation therapy alone or administering hormonal therapy, radical prostatectomy, or watchful waiting [32].

The Gleason system identifies three variants: ductal (the so-called endometrioid in the past), signet ring cell, and small cell carcinoma. The rare variations in histology did not receive specific designations, including mucinous and sarcomatoid carcinomas, but this does not have practical implications; nonetheless, some variants have specific clinical features and differential diagnoses. Squamous cell and urothelial (transitional) cell carcinomas of the prostate should not be graded by the Gleason method.

8.3 MR Anatomy

MR imaging depicts the zonal anatomy of the prostate with exquisite detail because of its high spatial resolution, superior contrast resolution, multiplanar capability, and large field of view. The prostate is subdivided into the base, mid-gland, and apex from superior to inferior. Approximately 70 % of the prostate is composed of glandular tissue, and 30 % consists of nonglandular tissue.

The major nonglandular elements are the prostatic urethra and the anterior fibromuscular band. The glandular prostate consists of outer and inner components, which are differentiated by location, duct anatomy, and histologic characteristics. Although the zones of the prostate gland were first described in the 1960s, the terms were not commonly used in clinical practice until the 1980s; for anatomic division of the prostate, the zonal compartment system developed by McNeal is widely accepted [33–36]. According to this system, glandular tissue is subdivided into *central gland* (which refers collectively to the periurethral, central, and transition zones) and *peripheral gland* (which includes only the peripheral zone) (Fig. 8.1). In clinical practice, other terms used frequently are those describing the anatomic division of the prostate into sextants. The sextant description of the prostate refers to the systematic biopsy of the right and left base, mid-gland, and apex of the prostate gland.

The peripheral zone envelops the posterior, lateral, and apical portions of the prostate and shows high signal intensity on T2-weighted MR images, constituting 70 % of the glandular tissue. The central zone is located superiorly, just posterior to the proximal urethra, and constitutes 25 % of the glandular tissue. Just anterior and lateral to the proximal urethra is the transition zone, which

Fig. 8.1 (**a**–**f**) Normal prostate anatomy depicted with T2-weighted MR images; in coronal plane (TR: 2300; TE: 116) (**a**); in axial plane (TR: 5130; TE: 108) at the level of the seminal vesicles (**b**), the mid-gland of the prostate (**c**) and the apex, and membranous urethra (**d**); in sagittal plane (TR: 3600; TE: 114), medially (**e**) and laterally (**f**). The letters (**a**–**f**) correspond to *b* urinary bladder, *c* central zone, *fs* anterior fibromuscular stroma, *p* peripheral zone, *r* rectum, *s* symphysis pubis, *sv* seminal vesicles, *u* urethra

constitutes 5 % of the glandular tissue. The urethra and periurethral glandular tissue represents less than 1 % of the glandular prostate and are located anteriorly in the prostate gland and are best seen in the inferior region (i.e., the apex) of the prostate. On MR images, the central and transition zones have similar signal intensities and are best differentiated by their respective anatomic locations; however, the transitional zone is often inseparable from the central zone due to benign prostatic hypertrophy (BPH), the incidence of which increases with age; the two zones together are referred to as the central gland. The signal intensities in the central and transition zones are lower than those in the peripheral zone on T2-weighted images; often heterogeneous, with a mixture of hyperintense glandular tissue and hypointense hypertrophic fibrotic nodules; and show less contrast enhancement [37–39]. The zones are not only defined histologically; many prostatic diseases have a zonal distribution: benign prostatic hyperplasia usually involves the transition zone, whereas prostate cancer arises in glandular tissue.

The junction of the transition and peripheral zones is marked by a visible linear boundary, which is often referred to as the prostate pseudocapsule or surgical capsule.

The true prostate capsule is an outer band of fibromuscular adherent tissue and appears as a thin layer of low-signal-intensity tissue surrounding the prostate on T2-weighted images. The capsule is most apparent posteriorly and posterolaterally because it contrasts with the higher, more uniform signal intensity of the peripheral zone of the gland. This capsule is an important landmark in the assessment of extraprostatic extension (EPE) of the tumor.

The seminal vesicles (Fig. 8.1) are located posterosuperiorly to the prostate and secrete seminal fluid into the bilateral ductus deferentes, which become the ejaculatory ducts. These ducts traverse the prostate and join the urethra at the verumontanum. A seminal vesicle filled with seminal fluid is typically T2 hyperintense.

Low-signal-intensity foci posterolateral to the capsule are indicative of neurovascular bundles, which course posterolateral to the prostate capsule bilaterally at the 5- and 7-o'clock positions. At the apex and base, the neurovascular bundles send penetrating branches through the capsule, providing a route for EPE.

In the most anterior part of the prostate, there is a region of nonglandular tissue known as the anterior fibromuscular stroma, which has low signal intensity on T2-weighted images.

The proximal urethra is rarely identifiable unless a Foley catheter is present or a transurethral resection has been performed. The distal prostatic urethra can be seen as a low-signal-intensity ring in the lower prostate. The genitourinary diaphragm is clearly definable on MR images. It consists of two layers of fascia enclosing deep transverse perineal muscle and the external sphincter of the urethra [40]. On MR images, the genitourinary diaphragm is seen as a flat plate of fibromuscular tissue suspended between the inferior pubic rami just below the symphysis pubis. The prostate is separated from the rectum posteriorly by the Denonvilliers fascia, which attaches to the peritoneal lining above and the genitourinary diaphragm below. This fascia restricts posterior extension of prostatic carcinoma into the rectum.

8.4 MR Imaging

As previously described, prostate cancer is most common in the peripheral zone (70 % of cases), followed by the transitional zone (25 %) and central zone (5 %) [41].

On T1-weighted MR images, the normal prostate gland demonstrates homogeneous intermediate-to-low signal intensity. As with computed tomography (CT), T1-weighted MR imaging has insufficient soft tissue contrast resolution for visualizing the intraprostatic anatomy or abnormality. Instead, the zonal anatomy of the prostate gland is best depicted on high-resolution T2-weighted images, of which the main application is precisely in local staging of prostate cancer. On T2-weighted images, prostate cancer usually demonstrates low signal intensity in contrast to the high signal intensity of the normal peripheral zone (Figs. 8.2 and 8.3). Low signal intensity in the peripheral zone, however, is not specific for cancer. It can also be seen in several benign conditions, such as hemorrhage, prostatitis, hyperplastic nodules, or posttreatment sequelae (e.g., as a result of irradiation or hormonal treatment). Furthermore, similar modifications can be formed as postbiopsy changes, as a result of hemorrhage: in general, MR imaging is performed at least 6 weeks after prostate biopsy to allow any hemorrhage to resolve (Figs. 8.4 and 8.5). Localization of a tumor in the central gland can be challenging because of the inhomogeneous nature of a benign central gland (Figs. 8.6 and 8.7). Important signs of a central gland tumor

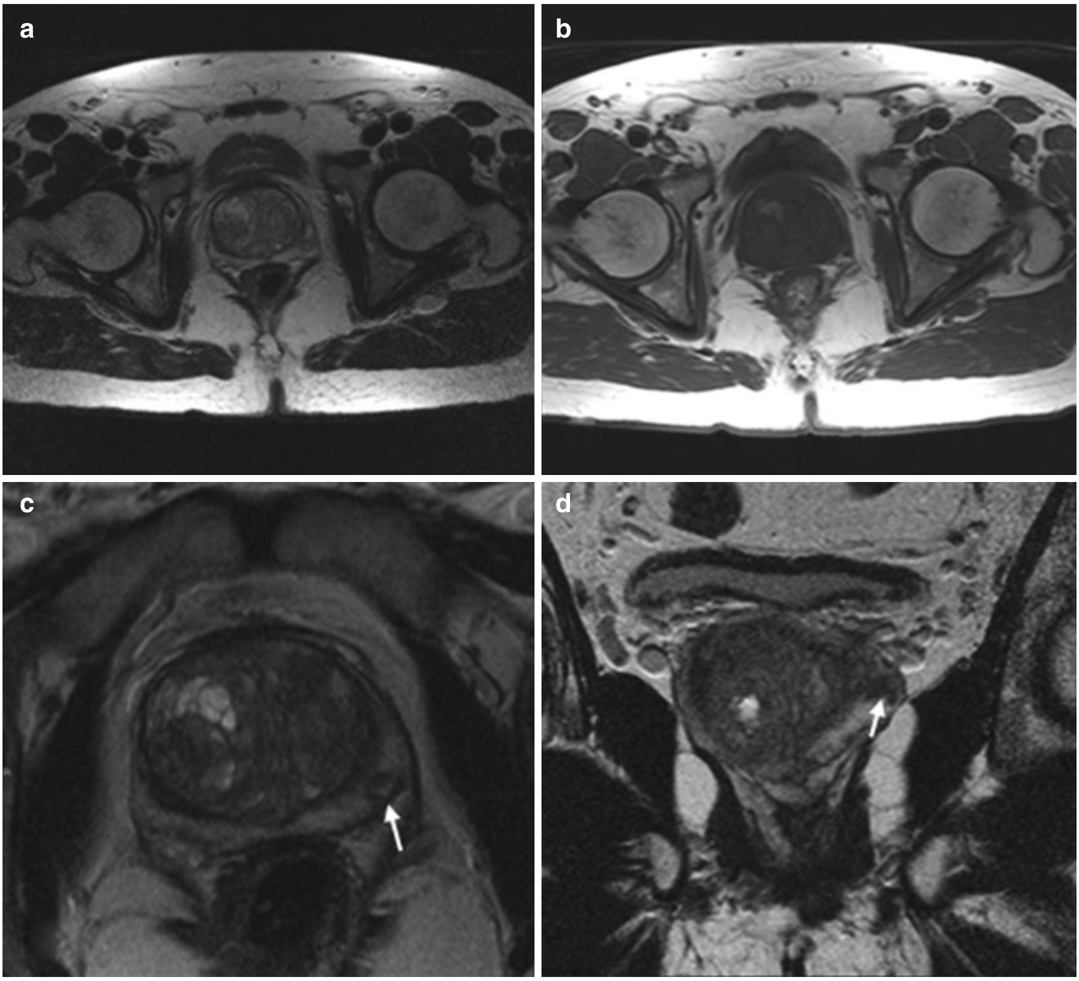

Fig. 8.2 (**a**–**f**) 59 years old, PSA 6.7 ng/ml, Gleason 7 (3+4). On axial T2-weighted (TR: 5130; TE: 108) (**a**) and T1-weighted (TR: 550; TE: 9.3) (**b**) sequences, the central zone of the prostate appears increased in volume, with inhomogeneous appearance, due to adenomatous hyperplasia (estimated volume of 53 ml, weight of all surgical specimen is 64 g). Axial T2-weighted (TR: 3600; TE: 116) sequence acquired with a narrower fov (Field Of View) and thinner layer for study of the prostate (**c**), at a lower level than in **a**, and a coronal T2-weighted (TR: 2300; TE: 116) sequence (**d**) allowed to document the presence of a small (diameter 6 mm) nodule (*arrows*), hypointense, in the periphery of the left lobe. On the ADC sequence (**e**), the nodule (*arrows*) appears hypointense while on the post-contrastographic phase sequence (**f**) appears hypervascularized (*arrows*). This lesion did not cause breaks in the prostatic capsule; no infiltration of the vascular nervous bundle and seminal vesicles is documented. No nodule in the right lobe. Pathologic analysis of the surgical specimen yielded neoplasm occupying 5 % of the prostate volume, with extension to both lobes, more to the left

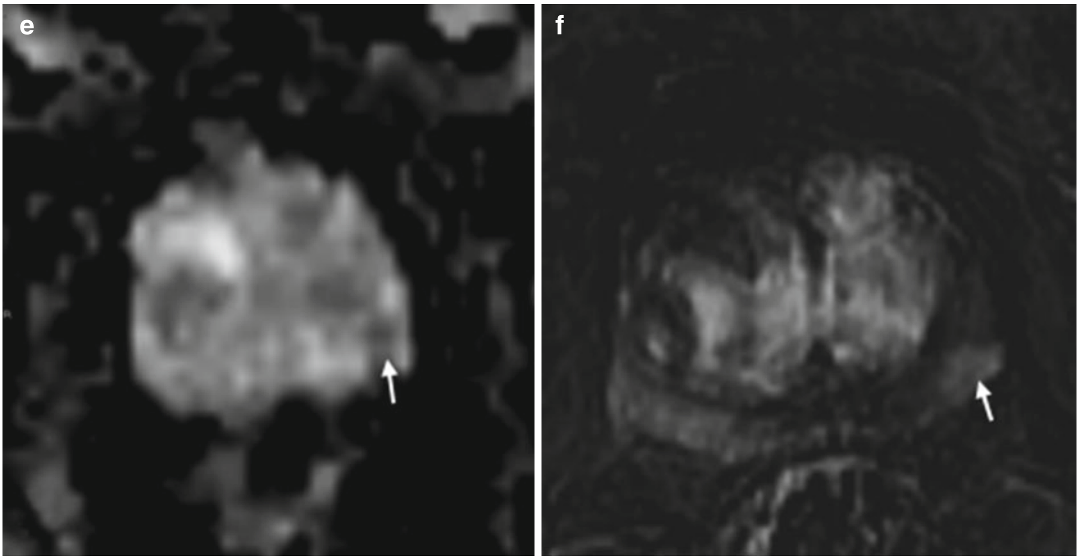

Fig. 8.2 (continued)

include homogeneous T2 hypointensity, disruption of the low-signal-intensity rim of a BPH nodule, and mass effect [42].

Sensitivity and especially specificity of T2-weighted MR imaging of prostate cancer localization vary, ranging from 54 to 91 % and 27 to 91 % [43–46]. Variation of results in these prospective studies might be partially explained by the fact that image analysis was based on different numbers of regions of interest, different cut-off points for a positive result, and inclusion or exclusion of prostate cancer localization in the transition zone. Moreover, results vary as the correlation of MR imaging findings with prostatectomy findings is difficult owing to different angles and section intervals of MR sections and prostatectomy slices and to deformation and shrinkage during histopathologic processing of the prostate specimens.

Therefore, findings on T2-weighted anatomic MR images are often nonspecific. The addition of functional MR imaging techniques to anatomic MR imaging has improved prostate tumor localization, particularly by improving the specificity [45, 47–50]. These functional MR imaging modalities include diffusion-weighted imaging, DCE imaging, and MR spectroscopy. The diagnostic accuracy of multiparametric MR imaging can vary depending on the image acquisition technique and diagnostic criteria used. In general, however, the more functional and anatomic MR imaging techniques are combined, the better the performance of MR imaging in tumor detection.

8.4.1 Diffusion-Weighted Imaging

Diffusion is Brownian motion of free water molecules at the cellular level. Diffusion-weighted imaging can add valuable information about a tissue at the cellular level to the information from conventional T1-weighted and T2-weighted imaging [51]. Because diffusion-weighted imaging measures the Brownian motion of water molecules, it provides important information about the functional environment of water in tissue and reflects the cellular status of normal and pathologic tissue. Furthermore, diffusion-weighted imaging is sensitive to changes in the microdiffusion of water within the intracellular space and extracellular space and cytotoxic edema due to alterations in the adenosine triphosphate-dependent sodium–potassium pumps. Diffusion can be quantitated in terms of the ADC on diffusion-weighted MR images. The ADC

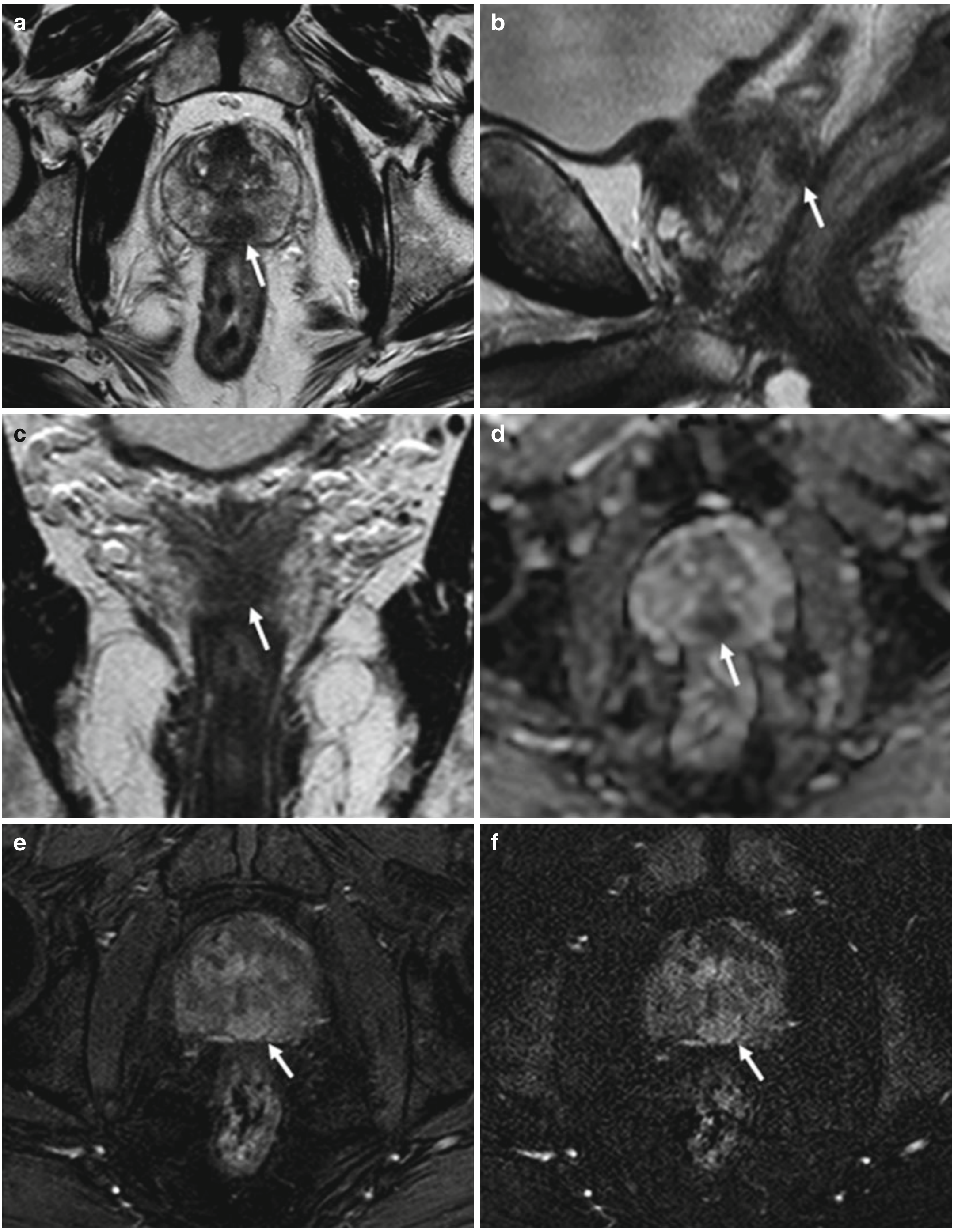

Fig. 8.3 (**a**–**f**) 74 years old, PSA 8.2 ng/ml, Gleason 9 (4+5). Axial (TR: 4074; TE: 100) (**a**), sagittal (TR: 4006; TE: 100) (**b**), and coronal (TR: 4013; TE: 100) (**c**) T2-weighted sequences show a hypointense nodule (*arrows*), with major axis of 18 mm, at the middle third, posteriorly and medially, involving both lobes. On ADC sequence (**d**), the nodule (*arrow*) appears hypointense, while on post-contrastographic phase (**e**) and subtractive perfusion image (**f**) the nodule (*arrows*) appears hypervascularized (not shown pre-contrastographic phase, in which the nodule is isointense). This lesion did not extend to the vascular nervous bundles and seminal vesicles, in relation to the medial position, and did not break the prostatic capsule. After prostatectomy, tumor is documented occupying both lobes, with infiltration of the prostatic capsule, but without extracapsular extension

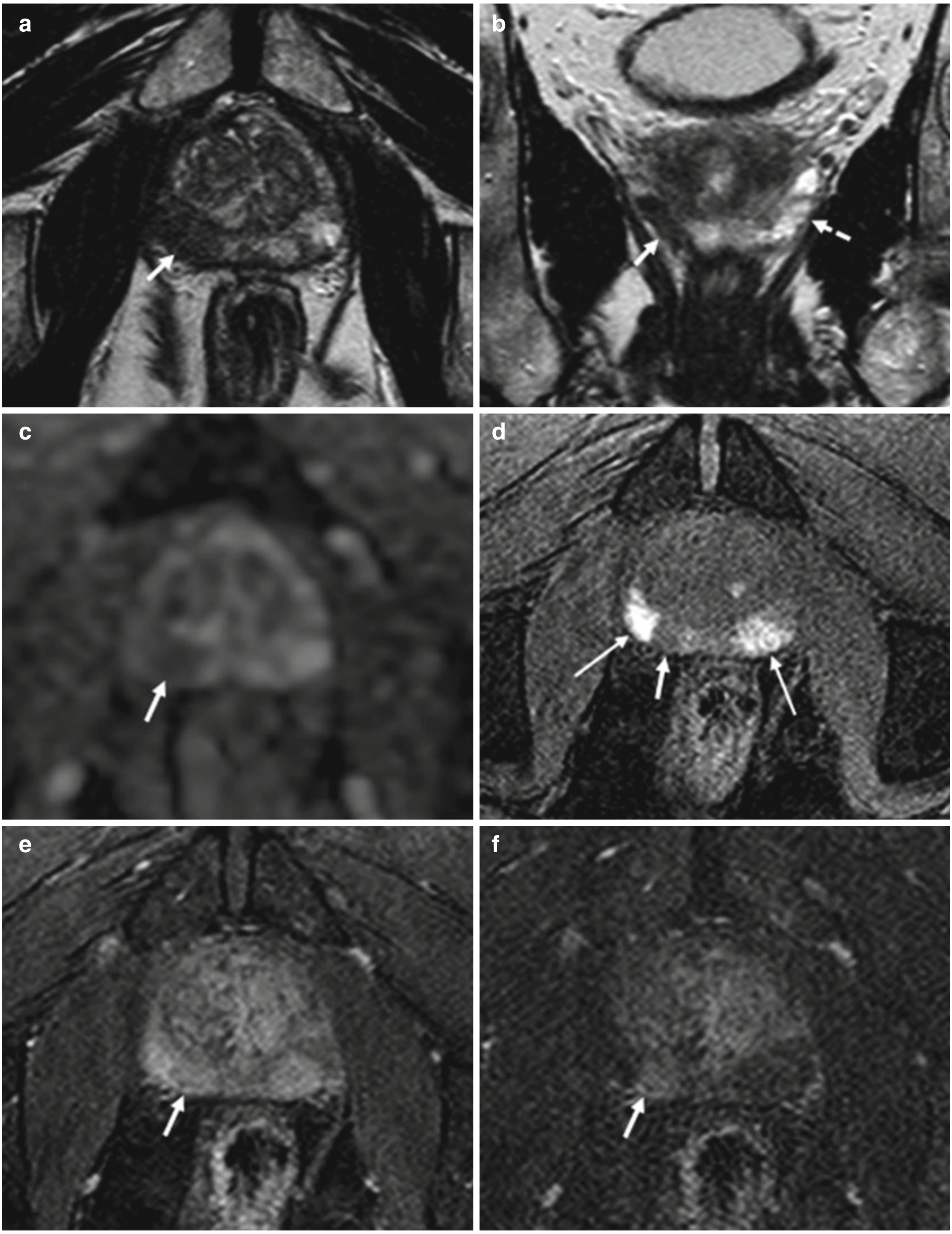

Fig. 8.4 (**a**–**f**) 64 years old, recently underwent prostate biopsy. Axial (TR: 4074; TE: 100) (**a**) and coronal (TR: 4013; TE: 100) (**b**) T2-weighted sequences show hypointense area in the peripheral zone of the right lobe (*arrows*), more appreciable when compared to the physiologic hyperintensity in the left lobe (*dashed arrow*). On ADC sequence (**c**), the nodule (*arrow*) appears hypointense while on axial T1-weighted (TR: 8,9; TE: 4,3) sequence (**d**) is more hypointense than the remaining peripheral zone (*long arrow*) that appears diffusely hyperintense, as a consequence of recent biopsy: if a patient underwent biopsy, the MR exam should be performed at a distance of at least 2 months. On postcontrastographic phase sequence (**e**), eventual hypervascularized nodules are masked by diffuse hyperintensity. However, on subtractive perfusion image (**f**), the hypointense area on ADC and T2-weighted sequences is more easily recognizable as hypervascularized (*arrow*). The patient underwent prostatectomy that confirmed the presence of a tumor

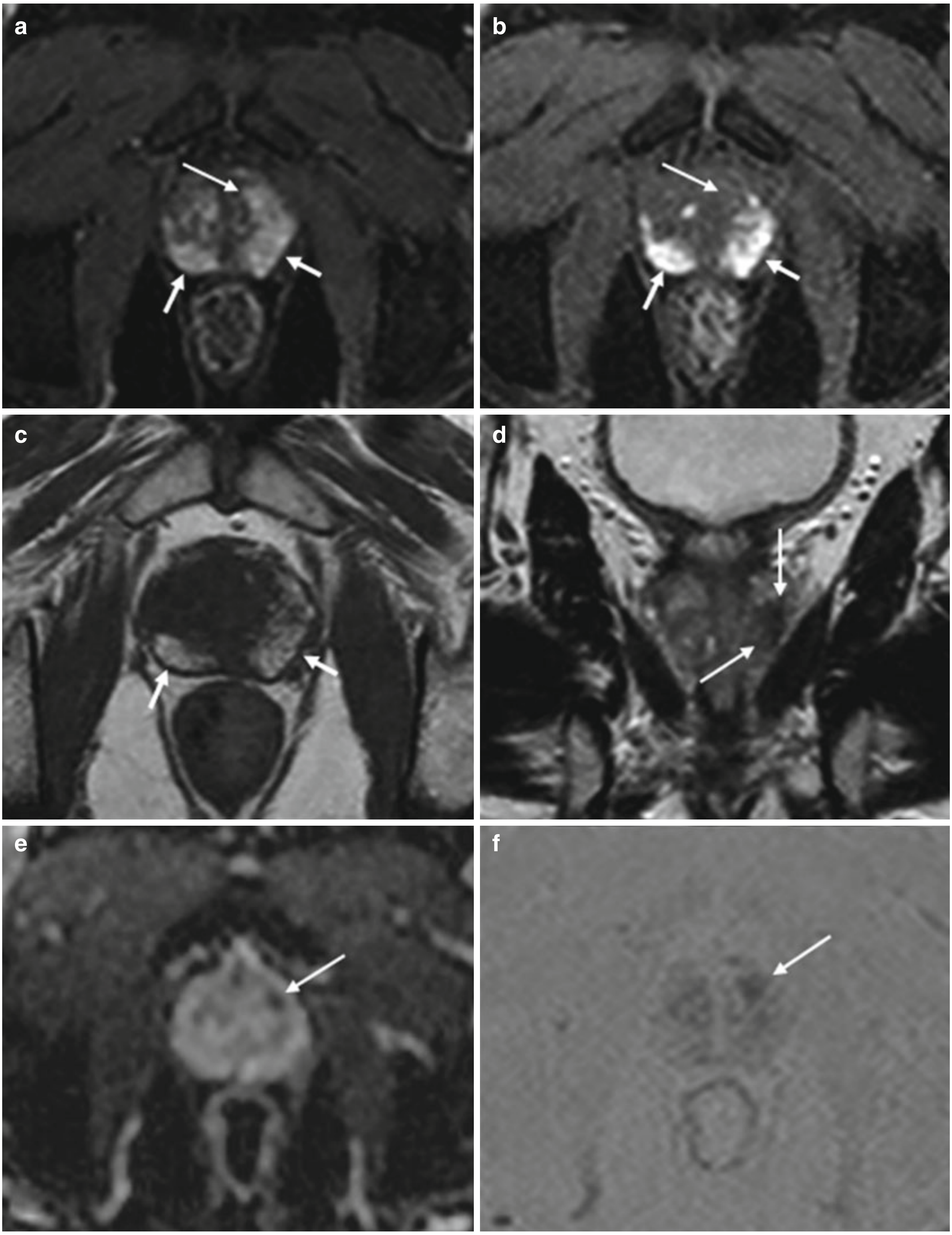

Fig. 8.5 (**a**–**f**) 68 years old, PSA 5.6 ng/ml, Gleason 6 (3+3), recently underwent prostate biopsy. On axial post-contrastographic (TR: 8.9; TE: 4.3) sequence (**a**), hyperintensity is appreciable in the entire peripheral zone of the prostate (*arrows*), extending to both lobes, especially to the left. However, this is not due to the presence of a diffuse lesion. In fact, on pre-contrastographic phase (**b**), the peripheral zone appears already diffusely hyperintense (*arrows*); this is evident also in the corresponding (**c**) T1 TSE (TR: 550; TE: 10). This hyperintensity in T-1 sequences is secondary to paramagnetic phenomenon due to the presence of methemoglobin (recent biopsy). On coronal T2-weighted (TR: 4013; TE: 100) sequence (**d**), appreciable is a hypointense area at the middle third that corresponds on ADC sequence (**e**) to a hypointense area (*arrows*). Also on dynamic sequence (**a**), a hypervascularized lesion is recognizable (*long arrow*), not corresponding to a hyperintense area in basal image: using subtractive perfusion image (**f**), the lesion is more easily appreciable (*long arrow*)

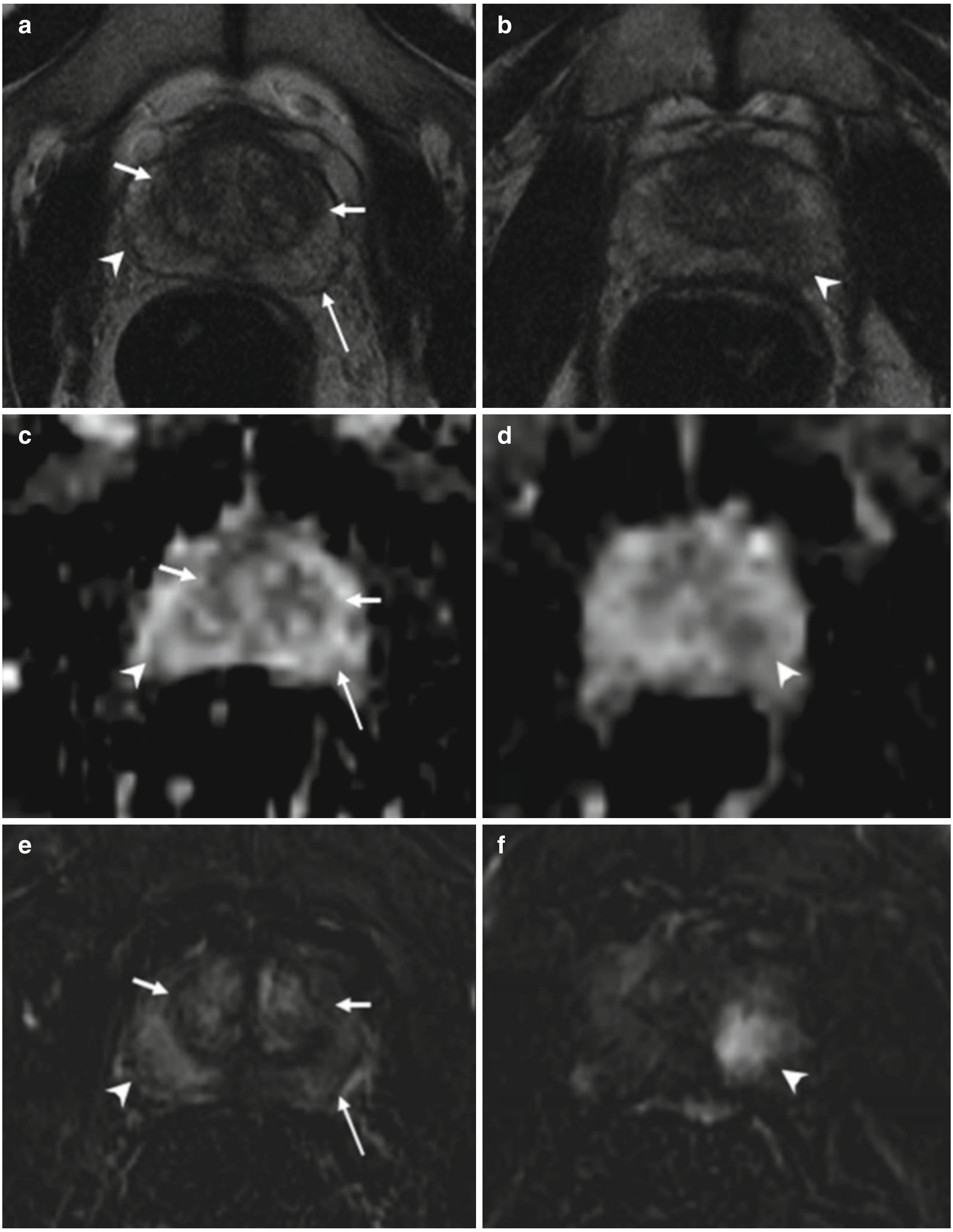

Fig. 8.6 (**a**–**f**) 58 years old, PSA 6 ng/ml, Gleason 6 (3+3). (**a**, **c**, **e**) axial sections at the lower third. (**b**, **d**, **f**) axial sections at the middle third. (**a**, **b**) T2-weighted images; (**c**, **d**) ADC images; (**e**, **f**) post-contrastographic phase images. Central zone of the prostate (*short arrows*); peripheral zone of the prostate (*long arrows*); abnormal finding (*arrowheads*). (**a**, **c**, **e**) T2-weighted (TR: 3600; TE: 116) (**a**) and ADC (**c**) sequences show increased volume of the central zone of the prostate (estimated volume of 35 ml), with inhomogeneous hypointense appearance; the peripheral zone of the prostate appears homogeneous hyperintense. Both T2-weighted and ADC sequence prove no abnormal finding. On post-contrastographic phase (TR: 12; TE: 5.8) sequence (**e**), inhomogeneous enhancement of the central zone (normal finding); homogeneous hypovascularized enhancement of the peripheral zone (normal finding) except for a focal hypervascularized area in the right lobe (*arrowhead*), not confirmed on T2 and ADC: these characteristics are ascribable to inflammation. (**b**, **d**, **f**) the *arrowheads* point to a hypervascularized area (**f**) of 13 mm in the left lobe; however, unlike in **e**, this area is hypointense in T2-weighted (**b**) and ADC (**d**) sequence; therefore, in this case the lesion is a neoplastic lesion. The patient underwent prostatectomy that confirmed the diagnosis

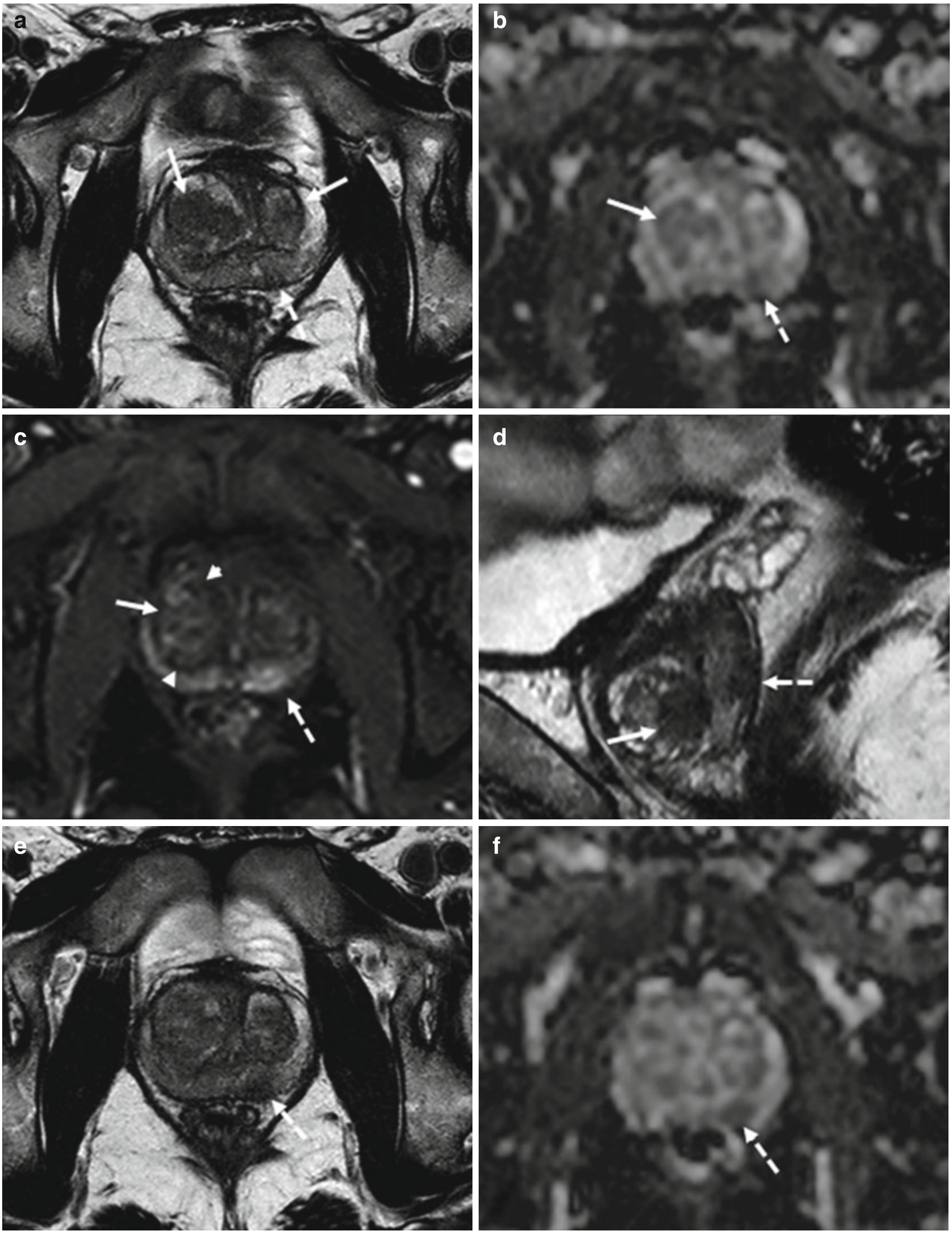

Fig. 8.7 (**a**–**f**) 56 years old, PSA 9.2 ng/ml, Gleason 6 (3 + 3). On axial T2-weighted (TR: 4074; TE: 100) sequence (**a**), the transition zone appears inhomogeneous because of the presence of two large hypointense nodules (*arrows*). On ADC sequence (**b**), the right nodule is clearly recognizable, appearing hypointense (*arrow*), while is quite vascularized on post-contrastographic phase (**c**), bounded by a hypointense edge (*arrowheads*). The left nodule is better appreciable at a lower axial plane (not shown) and on sagittal (**d**) T2-weighted (TR: 4006; TE: 100) sequence (*arrow*). Nevertheless, although these signal features in the peripheral zone are suspected for cancer, in the central gland these are the consequences of adenomatous hyperplasia. However, a neoplastic lesion is recognizable in the peripheral zone of the left lobe, at the middle third, posteriorly (*dashed arrows* in **a**–**d**): on axial T2-weighted and ADC sequences (respectively in **e** and **f**), just lower than in **a**–**c**, the lesion is well visible (*dashed arrows*)

quantifies the combined effects of both diffusion and capillary perfusion. A decreased ADC is interpreted as reduced motion of water molecules or diffusion, whereas in tissue with an increased ADC there is less restriction of water molecule motion. In prostate tumors, as in other solid tumors, the motion of water molecules is restricted because of their increased cellular density, with reduction of the extracellular space and restriction of the motion of a larger portion of water molecules to the intracellular space, resulting in decreased ADC. Therefore, diffusion-weighted imaging and ADC provide powerful indicators for characterization of prostate tissue, particularly in differentiation between benign and malignant lesions [52].

To optimize the ability of diffusion-weighted imaging to allow characterization of the diffusion properties of a tissue, imaging parameters should be optimized according to the imaging unit and magnetic field strength used. Selection of the correct b value is particularly important for prostate tissue with a prolonged T2 relaxation time. The b value specifies the sensitivity of diffusion. Use of high b values increases diffusion sensitivity by diminishing the hyperintensity of tissues with long T2 relaxation times (thus avoiding T2 shine-through). In general, a high b value (>700 s/mm^2 at 1.5 T and >1,000 s/mm^2 at 3 T) is recommended for prostate diffusion-weighted imaging, and a postprocessed ADC map is absolutely necessary for identifying and evaluating prostate tumors both objectively and subjectively. The higher the b value, the lower the signal-to-noise ratio; thus, an incremental increase in the number of excitations is required for optimization of image quality. Although studies have shown significant differences between cancerous and normal prostatic tissue in ADC [52, 53], this should be interpreted carefully in clinical patient care due to the current technical variability and lack of consensus. The advantages of diffusion-weighted imaging are a relatively short acquisition time and high contrast resolution between tumors and normal tissue. In general, regional ADC map values differ depending on location and tissue composition. Malignant lesions have lower ADC values (about 20–40 %) than benign or normal prostatic tissue; also, there are regional variations in the normal tissue values for different zones of the prostate (Fig. 8.8). Some authors have stratified ADC values into benign and malignant and demonstrated that diffusion-weighted imaging and ADC mapping can increase the sensitivity of MR imaging in detection of prostate cancer when diffusion-weighted imaging is used in conjunction with T2-weighted imaging [45] (Fig. 8.9); in particular, the addition of DWI imaging to T2-weighted MR imaging significantly improved sensitivity to 81 % (sensitivity for T2-weighted MR imaging alone, 54 %), whereas specificity was slightly lower for T2-weighted MR imaging combined with DWI (84 %) than for T2-weighted MR imaging alone (91 %). Also, in other prospective studies [54, 55], the addition of DW imaging to T2-weighted MR imaging improved prostate cancer localization performance. However, in a recent retrospective 3-T study in 51 patients, with prostatectomy specimens as reference standard [56], DW imaging did not add value to T2-weighted MR imaging for prostate cancer localization. Preliminary results suggest that diffusion-weighted imaging has the potential to support prediction of tumor aggressiveness [57].

The location of prostate cancer affects the sensitivity of diffusion-weighted imaging. Noncancerous peripheral zone tissue has been found to have higher average ADC (less overlap with cancerous tissue) than the transition zone and prostate base. Overlap limits the ability to differentiate prostate cancer from noncancerous tissue [58]. The high prevalence of BPH in elderly men significantly contributes to this difficulty. The stromal form of BPH in particular exhibits lower ADC and low T2 signal intensity, mimicking prostate cancer, whereas glandular BPH and prostatic intraepithelial neoplasia can be more readily distinguished because of their higher average ADC and higher T2 signal intensity [59] (Figs. 8.7 and 8.10). A higher Gleason score has repeatedly been shown to be associated with decreased ADC, likely due to the dedifferentiated infiltrative growth of these tumors, as opposed to the glandular organization of a more well-differentiated prostate cancer, which more closely resembles normal prostatic tissue [60, 61] (Fig. 8.11).

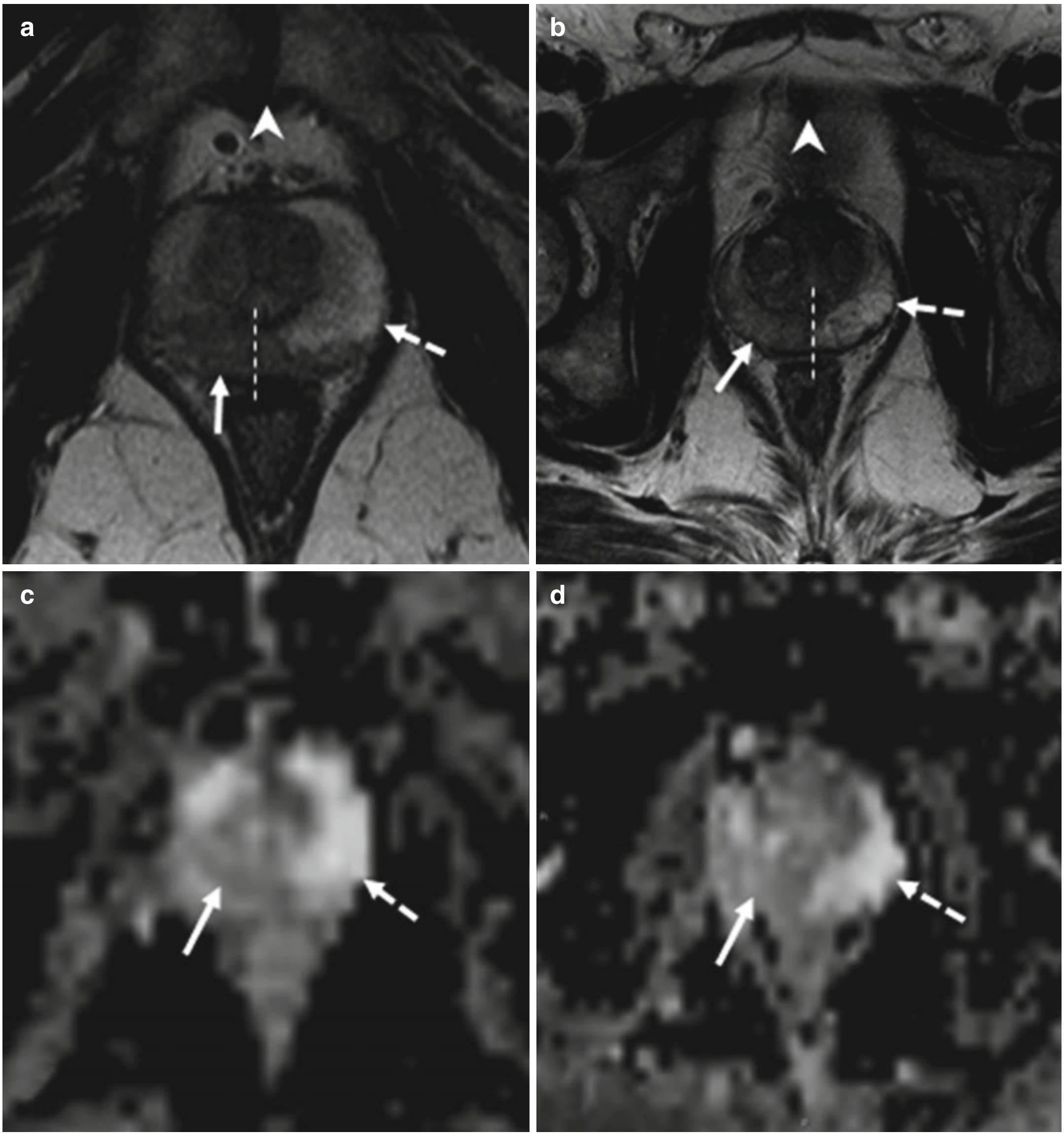

Fig. 8.8 (**a**–**f**) 58 years old, PSA 6.7 ng/ml, Gleason 7 (3+4). (**a**, **c**, **e**) axial sections at the lower third; on **a**, the symphysis pubis can be identified (*arrowhead* in **a**). (**b**, **d**, **f**) axial sections at the middle third, just above the symphysis pubis, that are not identifiable (*arrowhead* in **b**). (**a**, **b**) T2-weighted images (TR: 3600; TE: 100); (**c**, **d**) ADC images; (**e**, **f**) post-contrastographic images (TR: 12; TE: 5,8). On T2-weighted sequence at the lower third (**a**), a hypointense area (*arrow*) can be documented at the right lobe of the prostate, with extension to the left lobe (the *dashed line* represents the limit of the two lobe). On ADC sequence (**c**), the same nodule appears hypointense while on post-contrastographic sequence (**e**) appears hypervascularized. On all three sequences, the lesion is clearly visible and has different signal features than the contralateral healthy lobe (*dashed arrows*). At the middle third, an area with the same signal features but confined in the right lobe (*dashed line*). Patient underwent prostatectomy that confirmed a tumor occupying 50 % of the prostate volume, with extension to both lobes, more to the right, without break in the prostatic capsule or infiltration of the vascular nervous bundles and seminal vesicles

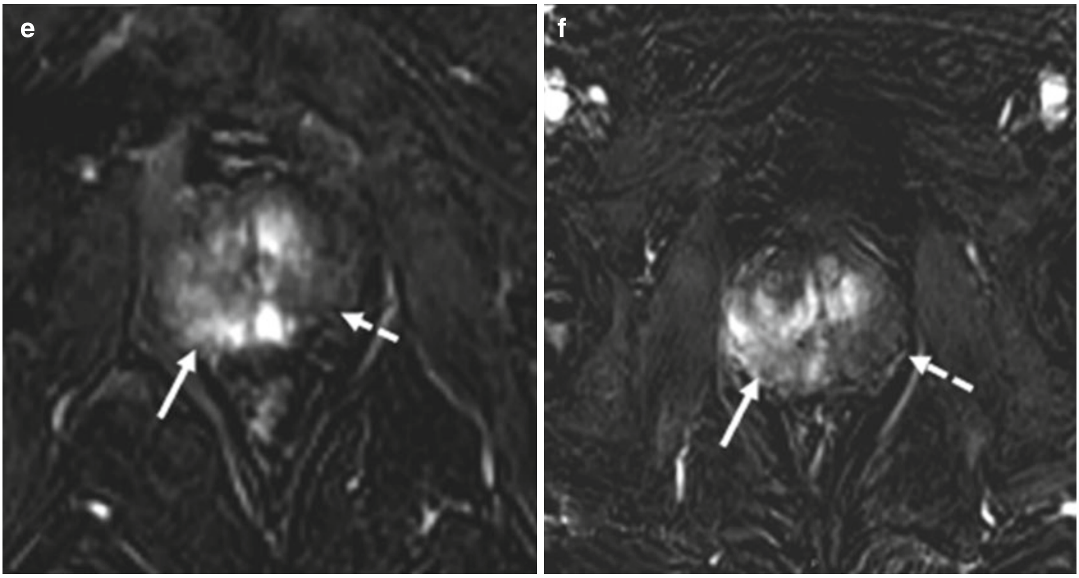

Fig. 8.8 (continued)

The principal pitfall of diffusion-weighted imaging includes a potential for false-positive findings of tumor related to postbiopsy hemorrhage: it has been reported that postbiopsy hemorrhage lowers the ADC of benign peripheral zone tissue and therefore limits the usefulness of diffusion-weighted imaging in this setting [60]. However, more recent data demonstrated excellent ability of the ADC in differentiation of prostate cancer from hemorrhage in the peripheral zone, and it was suggested that delayed imaging after biopsy may not be necessary [61] (Figs. 8.4 and 8.5).

The shortcomings include susceptibility-induced distortions, which are caused by susceptibility effects from an air-filled rectum or endorectal coil balloon, bone–tissue interfaces, poor local magnetic field homogeneity, and chemical shift artifacts caused by periprostatic fat.

8.4.2 DCE MR Imaging

Dynamic contrast-enhanced MR imaging was developed to help achieve a higher accuracy in prostate cancer localization and staging than that obtained with conventional T2-weighted MR imaging. DCE MR imaging is an advanced, fast, dynamic imaging technique (e.g., temporal resolution <5–10 s) that allows derivation of parameters that are closely related to microvascular properties and angiogenesis in tissues. As a response to the tumor hypoxia, there is a strong expression of angiogenesis-inducing factors, such as vascular endothelial growth factor and fibroblast growth factor receptor in their endothelial cells [62], with budding of new blood vessels from existing blood vessels (angiogenesis) or de novo formation of blood vessels (vasculogenesis). Tumor neovessels are in general more permeable

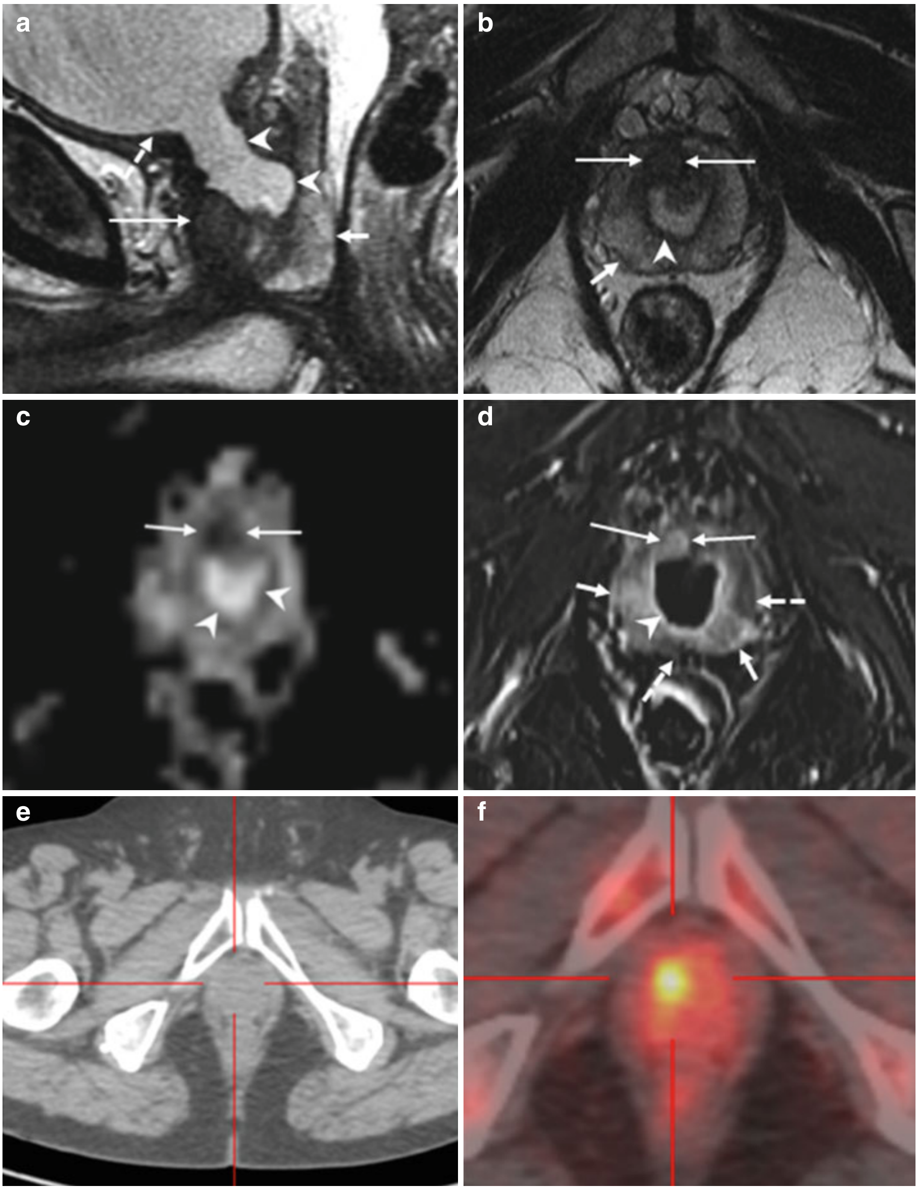

Fig. 8.9 (**a**–**f**) 68 years old, undergone TURP 3 years ago for BPH (PSA: 4–5 ng/ml; free-to-total ratio: 18 %); in the next years, the PSA values increased and free-to-total PSA ratio dropped (last values: respectively, 11–2 ng/ml; 7 %); these values are suspected for neoplastic lesion. The patient underwent prostate biopsy that revealed a prostatic cancer (Gleason 3 + 3). On sagittal T2-weighted sequence (TR: 3600; TE: 114) (**a**), the prostate (*short arrow*) appears regularly hyperintense, with the exception of a hypointense lesion anteriorly (*long arrow*); appreciable in this plane is a large bladder neck (*arrowheads*), consequence of a previous resection of the median lobe, just below the bladder (*dashed arrow*). Axial T2-weighted (TR: 3600; TE: 116) sequence (**b**) shows the hypointense lesion (*long arrow*), anteriorly, just to the right of the midline, while the remaining prostate is hyperintense (*short arrow*); within the prostate, the bladder neck is homogeneous and markedly hyperintense (*arrowhead*). At the same plane in **b**, ADC sequence (**c**) shows the hypointense lesion (*long arrows*) and the urine in the bladder neck, markedly hyperintense (*arrowhead*). On post-contrastographic phase (**d**), the lesion appears hypervascularized (*long arrows*) while the prostate is less vascularized (*dashed arrows*); however, some hypervascularized areas are recognizable (*short arrows*), not significantly hypointense on T2-weighted and ADC sequence, therefore to refer to inflammation. Urine is regularly markedly hypointense (*arrowhead*). On axial landmark CT image (**e**) and choline PET–CT scan (**f**), a hypermetabolic lesion is clearly visible. Patient underwent prostatectomy that confirmed presence of tumor occupying 50 % of the prostate volume, with extension to both lobes (Gleason 4 + 3)

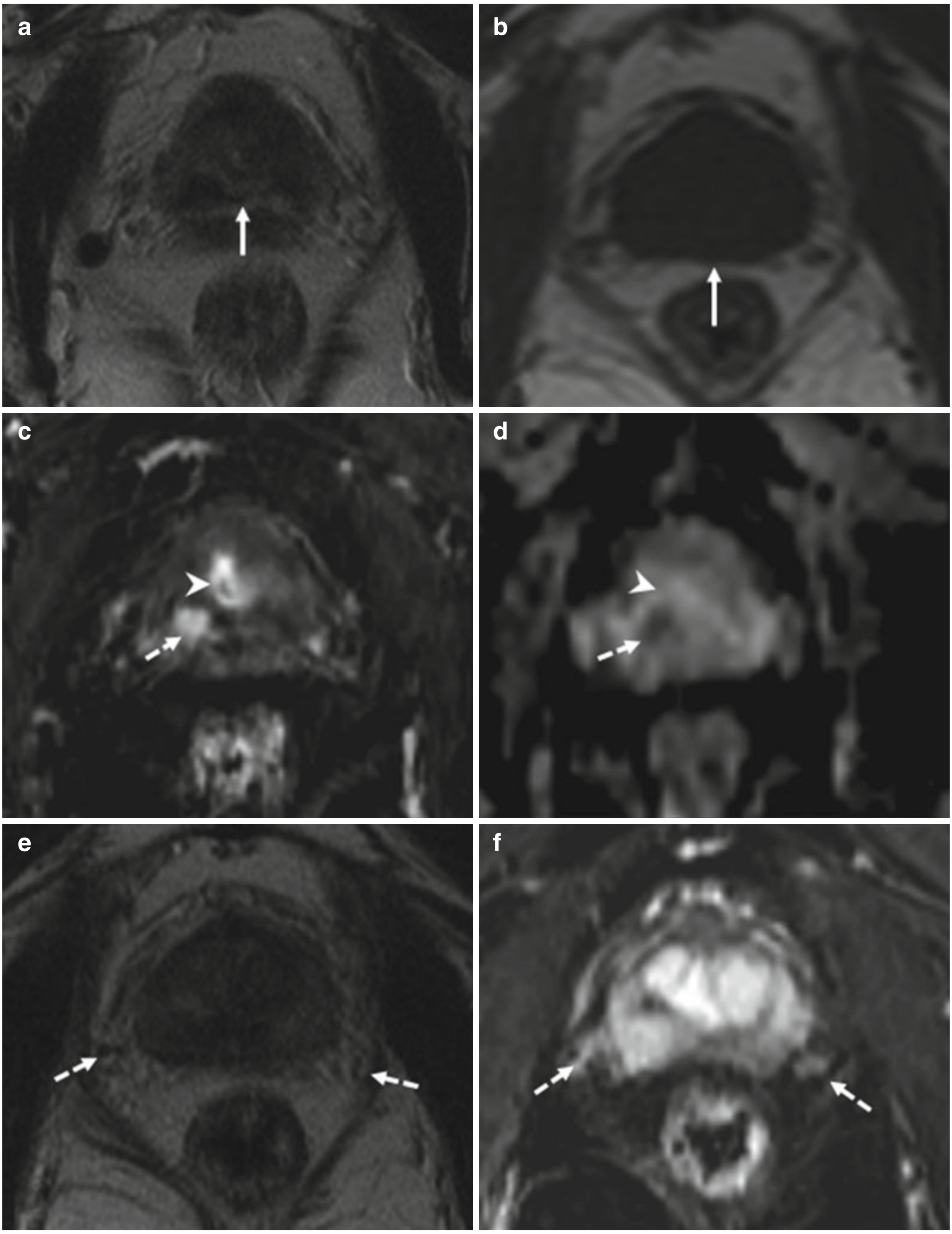

Fig. 8.10 (**a**–**f**) 72 years old, previous diagnosis of prostate cancer 8 years ago, treated with hormonotherapy and radiotherapy. Recent PSA 1.4 ng/ml. On axial T2-weighted (TR: 5130; TE: 108) (**a**) and T1-weighted (TR: 550; TE: 9.3) (**b**) sequences, the prostate (*arrows*) appears to have a regular volume (estimated volume of 14 ml, surgical specimen weight 27 g), inhomogeneous, and diffusely hypointense on T2-weighted sequence (consequence of both hormonotherapy and radiotherapy). On axial post-contrastographic sequence (**c**), a hypervascularized lesion of 9 mm (*dashed arrow*) can be observed in the right lobe, at the middle third, in the posterior zone; on ADC sequence (**d**), lesion is hypointense (*dashed arrow*). In the central zone, in the post-contrastographic sequence (**c**), a hypervascularized area is identified, not confirmed in ADC sequence (**d**) (*arrowheads* both in **c** and **d**); the presence of hypervascularized areas is frequent in the central zone, but it is not suggestive of neoplastic lesions. On axial T2-weighted sequence (**e**), at a lower plane than in **a**–**d**, the vascular nervous bundles can be identified as areas of low signal (*dashed arrows*), while on post-contrastographic sequence (**f**) the right is surrounded by hypervascularized tissue (sign of infiltration). After prostatectomy, histopathological examination confirmed presence of tumor occupying 50 % of the prostate volume, with extension to both lobes

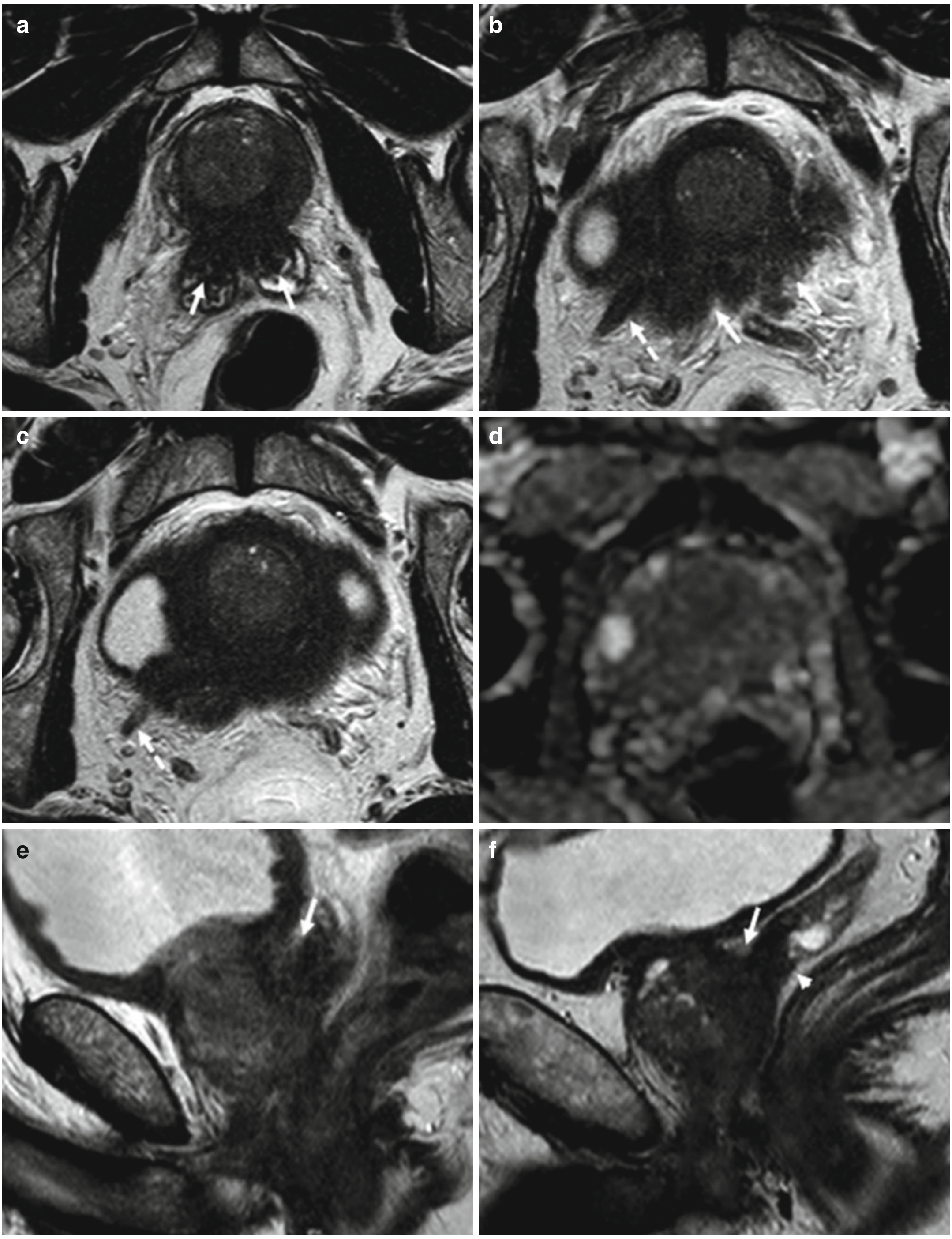

Fig. 8.11 (**a**–**f**) 70 years old, Gleason 6 (3+3). (**a**–**c**) Axial T2-weighted (TR: 4074; TR: 100) MR images, obtained at the middle third (**a**) and at the upper third (**b**, **c**), show a low-signal-intensity tumor which infiltrates both seminal vesicles (*arrows* in **a**), breaks capsule (*arrows* in **b**), with extension and envelopment of the right neurovascular bundle (*dashed arrows*), and asymmetry of the two neurovascular bundles. On ADC sequence (**d**), at the same level in (**b**), the prostate appears diffusely hypointense. On sagittal T2-weighted (TR: 4006; TE: 100) sequence (**e**), the fat plane between the seminal vesicle and the posterior urinary bladder is obliterated (*arrow*) in relation to local extension; conversely, in another patient (**f**), although the seminal vesicles are involved (*arrowhead*), the fat plane (*arrow*) is maintained

than normal vessels, more heterogeneous in size and branching pattern, and more disorganized, making prostate tumors highly vascular and manifesting early hyperenhancement (higher and earlier peak enhancement than in normal tissue) and rapid washout of contrast material from the tumor, in comparison with normal prostate tissue. Microvascular alterations and neovascularity are in general most severe in prostate cancer, in comparison with other processes in the prostate such as BPH or prostatic intraepithelial neoplasia [63].

Numerous contrast enhancement parameters can be used to differentiate cancerous from benign tissue, including onset time, time to peak enhancement, peak enhancement, relative peak enhancement, and washout time; results of numerous studies suggest that the peak enhancement of cancer relative to that of surrounding benign tissue is the most accurate parameter for cancer localization [64] (Fig. 8.12). Typically, prostate cancer appears as an early and rapidly enhancing lesion with fast washout of contrast material in comparison with that of normal prostate tissue. The presence of rapid washout is highly indicative of prostate cancer [65], even in the absence of low T2 signal intensity. On contrast-enhanced MR images, the peripheral zone enhances more than the transition or central zone. In prostate cancer, onset time and time to peak enhancement are lower and peak enhancement is higher than in high-grade prostatic intraepithelial neoplasia and chronic inflammation, and abnormalities are more distinct in high-grade prostate cancer [66]. All DCE MR imaging parameters can be converted into pseudocolor parametric maps and overlaid on the anatomic T1- and T2-weighted images for interpretation. The contrast resolution is similar to that seen on T2-weighted images.

Results of studies indicated that dynamic contrast-enhanced MR imaging can help improve the accuracy of prostate cancer staging. Localization accuracy with dynamic contrast-enhanced MR imaging increased to 72–91 %, as compared with 69–72 % for anatomic T2-weighted MR imaging only [49, 67–69]. DCE MR imaging in combination with MR spectroscopy allows detection of prostate cancer in 46 % of patients with prior negative transrectal US-guided biopsy results and a persistently elevated PSA level (4–10 ng/mL) versus a prostate cancer detection rate of 24 % with repeat transrectal US-guided biopsy in these patients [66] (Fig. 8.13). Although much progress has been made, challenges for DCE MR imaging remain. Benign prostate tissue (e.g., some BPH nodules) is also highly vascular, limiting the overall accuracy of DCE MR imaging in tumor detection, in particular the differentiation of prostatitis from cancer in the peripheral zone and BPH from transition zone tumors [63].

Prostatic intraepithelial neoplasia and well-differentiated prostate cancer demonstrate less neovascularity and permeability changes than higher-grade prostate cancer, therefore representing a source of false-negative results at DCE MR imaging. Differentiation of chronic prostatitis from low-grade prostate cancer may not be possible, while differences were found in DCE MR imaging parameters between high-grade prostate cancer and chronic prostatitis [70]. In addition, low tumor volumes and infiltrative prostate cancer are affected by partial volume effects and are more difficult to detect. However, continuous evolution of rapid imaging techniques has allowed well-designed DCE MR imaging to improve the accuracy of intraprostatic detection of prostate cancer [47–49].

Criteria for extracapsular extension or seminal vesicle invasion at DCE MR imaging include abnormally high or asymmetric peak enhancement, contrast agent washout, and short onset time and time to peak enhancement. In the case of extracapsular extension, these findings are detected near the neurovascular bundle or rectoprostatic angle, broadly abutting the capsule, or in an extracapsular location. In seminal vesicle invasion, these abnormalities are found in the lumen of the ejaculatory ducts or in the seminal vesicles themselves and are associated with wall thickening of the ejaculatory ducts (Fig. 8.14). DCE MR imaging can improve the staging accuracy of less-experienced readers for detection of capsular penetration and seminal vesicle invasion and can allow detection of cancers that are not apparent on T2-weighted images. In addition, in multifocal cancers, DCE MR imaging may demonstrate additional foci of higher stage than

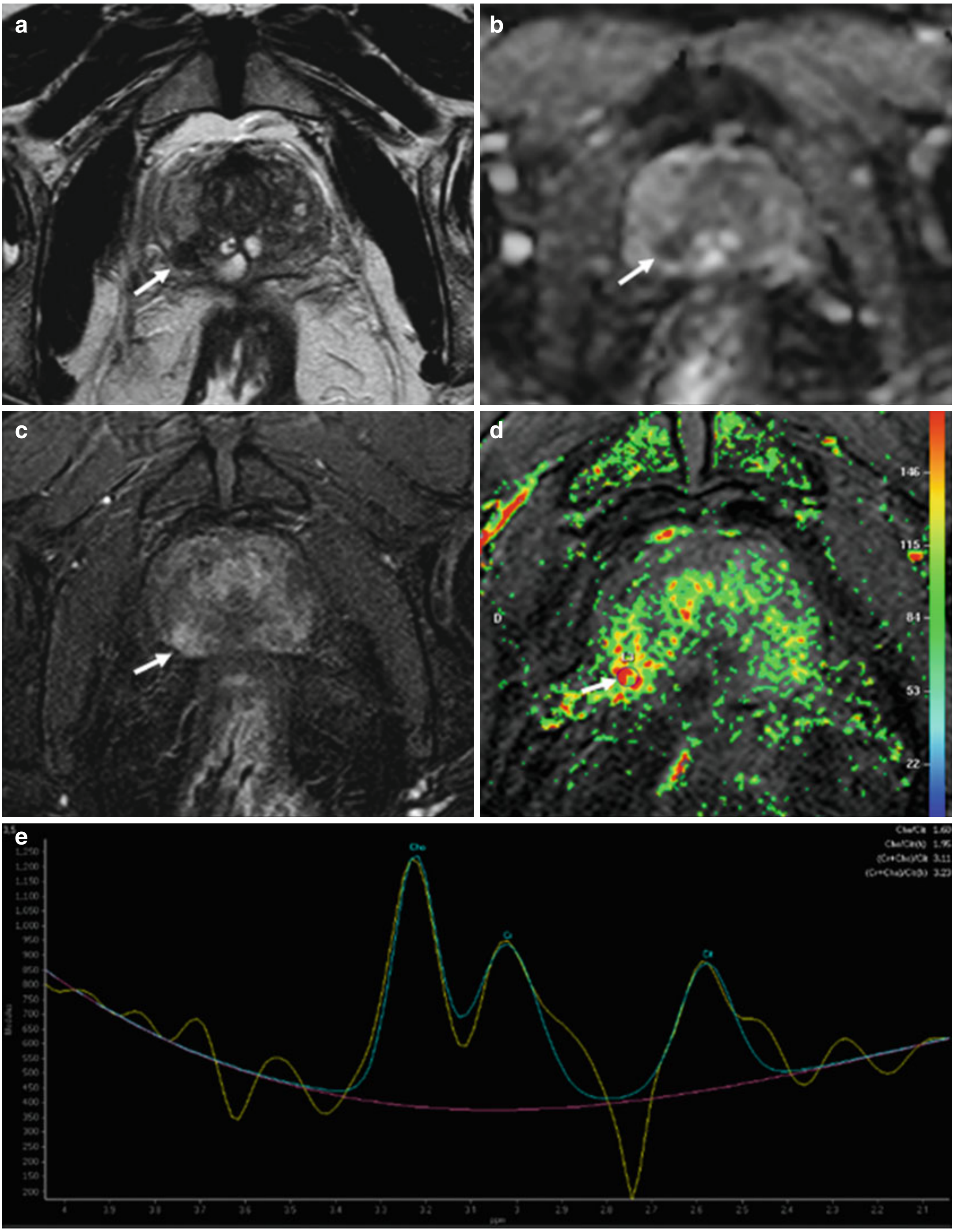

Fig. 8.12 (**a**–**e**) 68 years old, Gleason 7 (3+4). On axial T2-weighted (TR: 4074; TE: 100) sequence (**a**), a small hypointense nodule (*arrow*) is appreciable in the right peripheral zone, posteriorly. On ADC sequence (**b**), the lesion (*arrow*) appears hypointense while on post-contrastographic phase (TR: 8.9; TE: 4.4) (**c**) hypervascularized. Although these features allow to diagnose a neoplastic lesion, the exam was completed with a color map from DCE and MR spectroscopy. The color map from DCE MR imaging (**d**) shows that the area of highest permeability is the suspicious lesion (*arrow*), while an MR spectrum (**e**) obtained in the abnormal area shows an elevated ratio (in arbitrary units) of choline (*Ch*) and creatine (*Cr*) to citrate (*Ci*). Both findings are indicative of prostate cancer

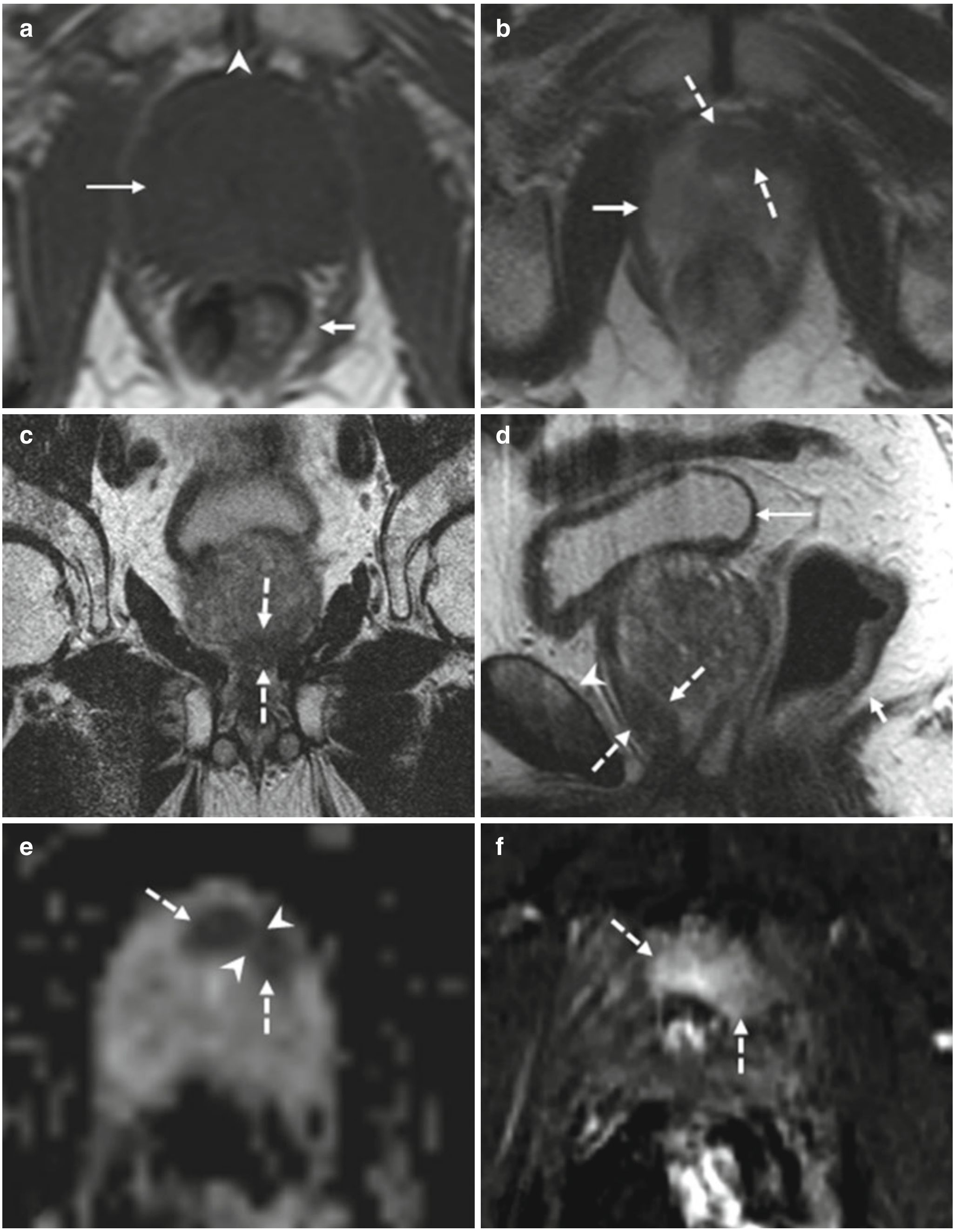

Fig. 8.13 (**a**–**f**) 74 years old, underwent randomized prostate biopsy both 2 years ago and 3 months ago because of increasing PSA (last value 15.6 ng/ml). Axial T1-weighted (TR: 550; TE: 9.3) sequence (**a**) shows a prostate (*long arrow*), homogeneously and regularly hypointense, with increased volume (estimated 89 ml). In this plane the rectum (*short arrow*) and symphysis pubis (*arrowhead*) can be recognized. On axial T2-weighted (TR: 3600; TE: 116) sequence (**b**), acquired just below **a**, the prostate (*continued arrow*) appears homogeneously hyperintense with the exception of an hypointense nodule, 10 mm long, at level of the anterior apex, mostly included in the left lobe (*dashed arrows*); on coronal (TR: 2300; TE: 116) (**c**) and sagittal (TR: 3600; TE: 114) (**d**) T2-weighted sequences, its position anteriorly in the apex is better appreciable (*dashed arrows*); in **d**, the rectum (*short arrow*), the symphysis pubis (*arrowhead*), and the bladder is recognizable (*long arrow*). On ADC sequence (**e**), the hypointense area on the T2-weighted sequences corresponds to two markedly hypointense contiguous nodules, but divided (*arrowheads*). On post-contrastographic sequence (**f**), the area appears hypervascularized. The identified lesion underwent targeted biopsy that revealed a prostatic cancer. This case shows the difficulty to detect cancer during randomized biopsy, if localized in the apex

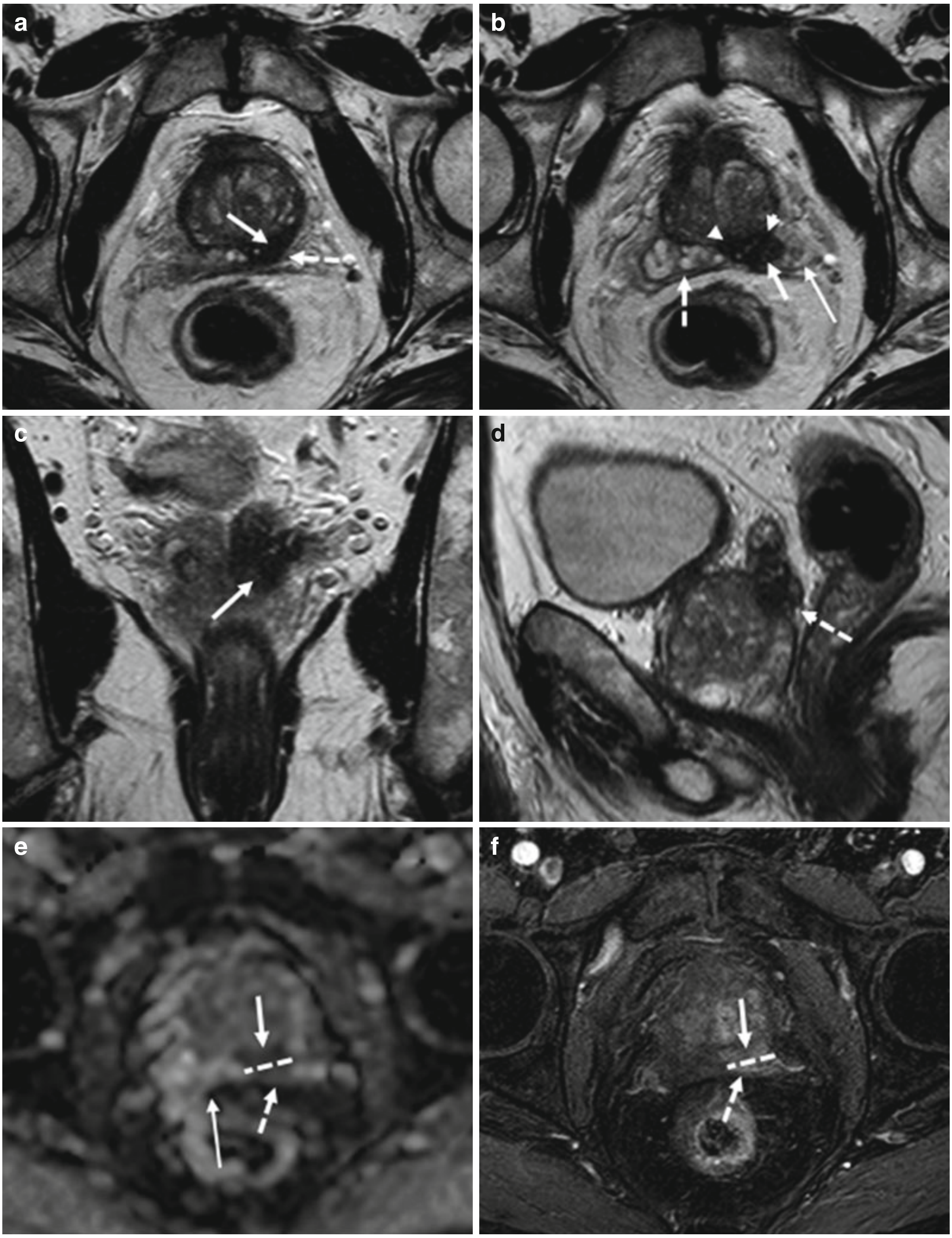

Fig. 8.14 (**a**–**f**) 72 years old, PSA 12.8 ng/ml, Gleason 9 (4+5). Axial T2-weighted (TR: 4074; TE: 100) sequence (**a**) shows a nodule, hypointense (*arrow*), in the posterior left lobe, at the upper third; at this level, the prostatic capsule appears diffuse thickening (*dashed arrow*). On the same sequence than in **a**, just at a upper plane (**b**), the anterior border (*arrow*) of the left seminal vesicle (*long arrow*) is not clearly definable because of an hypointense nodule (*arrowheads*) extending from the prostate: this is a sign of infiltration of the seminal vesicle. The right vesicle (*dashed arrow*) appears regularly hyperintense; however its medial border is close near the nodule. Coronal (TR: 4013; TE: 100) (**c**) and sagittal (TR 4006; TE: 100) (**d**) T2-weighted sequences show the nodule (*arrow*) with diffuse hypointensity of the left vesicle (*dashed arrow*). On ADC sequence (**e**), the nodule (*arrow*) and the infiltrated part of the seminal vesicle (*dashed arrow*) appear hypointense while on post-contrastographic phase sequence (**f**) hypervascularized; *dashed lines* show the border between the prostatic capsule and seminal vesicle, while the *long arrow* shows the right vesicle, hyperintense on ADC sequence, in relation to the physiological high level of water. Analysis of surgical specimen documented the presence of a tumor occupying both lobes, with involvement of the prostatic capsule and extension to both seminal vesicles

the known lesions, leading to adequate upstaging of tumors [71].

8.4.3 MR Spectroscopy

Because MR spectroscopy provides metabolic information about prostatic tissue by displaying the relative concentrations of chemical compounds within contiguous small volumes of interest (voxels), it is increasingly being used as a biomarker for detection of cancers, including prostate cancer [72]. MR spectroscopy is also known as chemical shift imaging. Chemical shift is the physical phenomenon in which the electron cloud surrounding the imaged nucleus (in prostate MR spectroscopy, hydrogen nuclei = protons) shields the nucleus partially from the external field and is highly dependent on the chemical environment (chemical bond, adjacent molecules, or atoms) and the molecule the proton is located in. Some chemical compounds have simple spectra (a singlet or single spectral peak) while others possess highly coupled spectra with multiple spectral main peaks, each of which may be composed of multiplets (doublet, triplet, etc.). The analyzed metabolites are choline, citrate, creatine, and polyamine.

Choline is represented by its distinct methyl proton resonance, which forms a composite peak of phospholipid cell membrane components (e.g., phosphocholine, glycerophosphocholine, and free choline) at 3.2 ppm. Owing to elevated cell membrane turnover (phospholipid synthesis and degradation) and increased cell surface compared with cell volume in cellular tumors, the choline level is elevated in the proliferating malignant tissue. Increased choline signal or concentration is considered the spectroscopic hallmark of cancer [73]; however, it has also been found in benign conditions of the prostate such as prostatitis [74].

Citrate is a normal secretion of the healthy prostatic glandular epithelium, and normal prostate tissue contains high levels of citrate (higher in the peripheral zone than in the central and transition zones) [75]; glandular hyperplastic nodules, however, can demonstrate citrate levels as high as those observed in the peripheral zone. The normal prostate has an MR spectrum with a prominent citrate peak at 2.6 ppm, which is usually seen as a doublet with occasional visualization of small additional side peaks. In the presence of prostate cancer, the citrate level is diminished or undetectable because of a conversion from citrate-producing to citrate-oxidating metabolism, but reduced levels can be found also in prostatitis and hemorrhage.

Creatine resonates at 3.0 ppm and is related to energy metabolism. Normal prostatic tissue contains high polyamine levels, of which spermine is a predominant component. Polyamines are represented by a relatively broad spectral peak between creatine and choline (3.1 ppm) that shows significant overlap with creatine and choline. Polyamine levels are reduced in prostate cancer because of higher metabolism.

Lipids cause signal in a broad range at the lower end of the citrate peak (typically 1.3 ppm). Adequate placement of saturation bands around the prostate is important to avoid contamination of the spectra by inclusion of extraprostatic fat, which causes large lipid signals.

Typically, the method for depicting tumors is based on an increased choline/citrate ratio. Because the creatine peak is very close to the choline peak in the spectral trace, the two may be inseparable; therefore, for practical purposes, the (choline + creatine)/citrate ratio is used as a biomarker in prostate tumor detection. An increase in the choline-to-citrate ratio or the (choline + creatine)/citrate ratio is often used as a marker of malignancy in prostate cancer and increases the specificity of diagnosis; however, it is most reliable in the peripheral zone (Figs. 8.12 and 8.15).

There is no consensus about spectral interpretation. The classification system described by Kurhanewicz et al. [76] is often used. In that system, a voxel is classified as normal, suspicious for cancer, or very suspicious for cancer. Furthermore, a voxel may contain nondiagnostic levels of metabolites or artifacts that obscure the metabolite frequency range. Voxels are considered suspicious for cancer if the ratio of choline and creatine to citrate is at least 2 standard deviations (SDs) higher than the average ratio for the normal peripheral zone. Voxels are considered very suspicious for cancer if the ratio of choline and creatine to citrate is higher than 3 SDs above the average ratio [77]. Voxels considered nondiagnostic

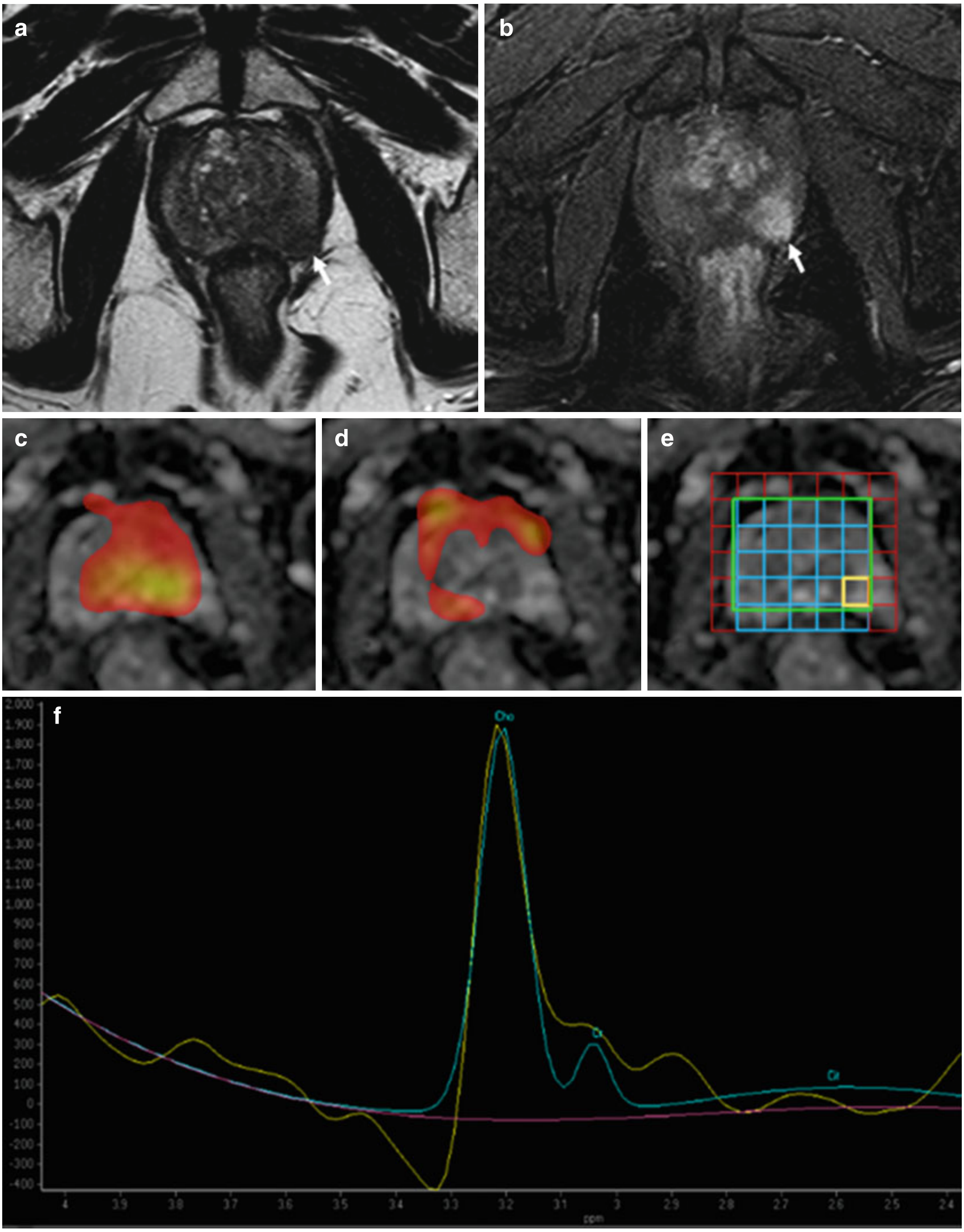

Fig. 8.15 (**a**–**f**) Axial T2-weighted (TR: 4074; TE: 100) MR image (**a**) shows a low-signal-intensity lesion in the left lobe of the prostate (*arrow*), which appears hypervascularized on post-contrastographic phase (*arrow* in **b**). MR spectroscopic images (**c**, **d**) demonstrate the areas respectively rich in choline (**c**) and citrate (**d**): the zone with suspected nodule is rich in choline and poor in citrate. MR spectrum (**f**) at the level of the lesion (*yellow square* in **e**) shows high ratios (in arbitrary units) of choline *(Ch)* and creatine *(Cr)* to citrate *(Ci)*. The findings are indicative of cancer, which was confirmed with targeted biopsy

contain no metabolites with signal-to-noise ratios greater than 5. In voxels in which only one metabolite is detectable, the other metabolites are assigned a value equivalent to the SD of noise.

Although MR spectroscopy shows promise as a problem-solving modality with high specificity, it is limited by low sensitivity. Partial volume effects may obscure the presence of prostate cancer, especially small or infiltrative lesions, which are obscured by strong signals from glandular BPH or surrounding normal tissue present in the MR spectroscopic voxels. By shifting the MR spectroscopic voxels to a position centered on the area of suspected abnormality, a voxel containing the highest possible partition of abnormal tissue can be generated; with this method, some of the lost information can occasionally be recovered.

The combined use of MR imaging and MR spectroscopy improves detection of tumors within the peripheral zone [44, 77, 78]; it has also been shown to increase the specificity in the localization of prostate cancer in the peripheral zone. MR spectroscopic imaging has shown higher specificity (68–99 %) and lower sensitivity (25–80 %) for prostate cancer localization, when compared with anatomic T2-weighted MR imaging (specificity, 61–90 %; sensitivity, 68–87 %) in prospective studies with prostatectomy specimens as reference standard [44, 46, 49, 79]; however, a multicenter trial that included 110 patients, with prostatectomy findings as reference standard, did not show any benefit for the addition of 1.5-T MR spectroscopic imaging to T2-weighted MR imaging in prostate cancer localization [80].

It has been recommended that the maximum ratio of choline and creatine to citrate combined with tumor volume at MR spectroscopy be used as an index to help predict tumor aggressiveness [81]: some studies found that the ratio of choline and creatine to citrate in the lesion shows correlation with the Gleason grade, with the elevation of choline and reduction of citrate indicative of increased cancer aggressiveness [82].

Despite the relatively high specificity of MR spectroscopy, false-positive MR spectroscopic findings can occur due to contamination from the seminal vesicle and prostatitis [83]. The metabolite ratio in cancerous tissue in the transitional zone can overlap with that of benign tissue or stromal BPH [81]: although the (choline + creatine)/citrate ratio can be low or normal in BPH, in stromal BPH, however, citrate and polyamine levels can be strongly suppressed and there may be elevation of choline due to the presence of proliferative elements, leading to significant overlap with the findings of prostate cancer. This leads to possible significant difficulty in distinguishing prostate cancer from prostatitis and stromal BPH, especially in the transition zone.

MR spectroscopic imaging, as for the other T2-weighted, can be often false-negative in the aggressive mucinous subtype of prostate cancer, presumably due to the large extracellular lakes of mucin [84]. However, this subtype is rare and represents only approximately 0.4 % of all prostate adenocarcinomas.

When combined with anatomic imaging, MR spectroscopy has been found to increase the accuracy of tumor volume estimation in prostate cancer [85], although other data have shown lack of an additional advantage. More recent data have shown significantly increased choline-to-citrate ratios and larger tumor volumes in stage T2b or higher tumors than in stage T2a or lower tumors, further suggesting a potential of MR spectroscopy for tumor volume estimation and staging [86].

The main pitfall of MR spectroscopy is the long acquisition time, with consequent possible motion artifacts; other problems are the susceptibility effects from endorectal balloon air, air in the rectum, that may decrease spectral quality and limit the ability to acquire high-quality data. The lower resolution of MR spectroscopy demands minimization of diagnostically decisive partial volume effects: a significant number of spectral voxels acquired may contain nondiagnostic levels of metabolites. Postbiopsy hemorrhage is known to degrade MR spectra [87]. However, it was shown that MR spectroscopy may improve diagnostic accuracy for cancer in the presence of postbiopsy hemorrhage, when findings on T2-weighted images are nondiagnostic [88].

8.5 Technique

8.5.1 Prostate MR Imaging Using an Endorectal Coil Versus Pelvic Coil

There has been a long-standing debate on whether or not to use an endorectal coil for prostate cancer staging since its use results in a more labor-intensive and costly examination. In a meta-analysis, Engelbrecht et al. [89] reported on 146 studies performed at 1.5 T and found that the use of turbo spin-echo sequences, an endorectal coil, and multiplanar acquisitions all significantly increased staging performance. The application of an integrated endorectal–pelvic phased-array coil significantly improved staging performance, particularly sensitivity, compared with that of a pelvic phased-array coil alone [90]; although, in the largest prospective prostate cancer staging study performed at 1.5 T [91] comparing MR imaging with a body coil only and with an endorectal coil only, body coil imaging performed better (accuracy, 62 %) than did endorectal coil imaging (accuracy, 52 %). However, in the past years since this trial, technologic developments such as the use of higher field strengths improved pelvic phased-array coils, and multiparametric MR imaging techniques have improved staging accuracy considerably.

8.5.2 Prostate MR Imaging at 3 T Versus 1.5 T

With the growing availability of 3-T whole-body MR imaging units, new opportunities arise for clinical and research applications in prostate imaging. In comparison with 1.5-T imaging, improvements in spatial or temporal resolution and in patient comfort (when no endorectal coil is used) are possible. Both conventional T1- and T2-weighted imaging techniques and the new multiparametric MR imaging protocols benefit significantly from imaging at higher field strength.

First, diffusion-weighted imaging inherently benefits from higher field strengths, allowing higher-quality imaging and higher spatial resolution [92], however including increased susceptibility artifacts and greater chemical shifts. Because the sensitivity of diffusion-weighted imaging to susceptibility artifacts and distortions is increased at 3 T, significant motion artifacts need to be avoided by limiting gross motion of the patient and suppressing rectal peristalsis (e.g., by intravenous administration of glucagon before the examination). Separation of tumor from healthy parenchyma is improved with 3-T diffusion-weighted imaging in comparison with 1.5-T diffusion-weighted imaging, and the ADC has been found to be significantly lower in prostate cancer than in normal tissue [93].

Second, DCE MR imaging achieves its highest potential at higher field strengths such as 3 T. In DCE MR imaging at 1.5 T, the temporal resolution is often a limiting factor to preserve spatial resolution. At 3 T, instead, the increased spatial resolution reduces volume averaging and allows detection of smaller tumor foci and more precise tumor volume assessment.

Third, MR spectroscopy is another technique that benefits from higher field strengths, as a result of the inability to increase the spectral resolution with other methods; both better spatial resolution and better spectral resolution improve the ability to detect and characterize tumors with MR spectroscopy. The faster data acquisition and imaging at smaller voxel sizes (at higher resolution) permits to reduce volume averaging of tumors with periprostatic fat, the seminal vesicles, postbiopsy hemorrhage, or periurethral tissues. At 1.5 T, the spectral quality may prohibit routine separation of closely adjacent peaks such as the choline, polyamine, and creatine peaks, which are therefore often combined into a single parameter (e.g., the [choline + creatine]/citrate ratio) for analysis.

Therefore the detection, the localization, and the staging of prostate cancer should benefit from the use of 3 T; however, conclusions on the effects of higher field strength on MR staging of prostate cancer remain difficult to infer because research on this topic is still immature. In particular, there are few studies comparing directly 3-T and 1.5-T MR staging of prostate cancer, and these studies are not fully comparable, using a pelvic phased-array coil at 3 T compared with a pelvic phased-array coil and/or an endorectal coil at 1.5 T.

8.6 Role of Choline PET–CT

Another functional imaging technique which offers the possibility to reflect biological tissue characteristics is positron-emission tomography (PET) [94]. PET uses compounds labeled with positron-emitting radioisotopes to detect pathologic processes. Relatively recently, carbon 11 (11 C)- or 18 F-labeled choline PET has been used in the assessment of patients with prostate cancer [95]: the first is preferred over the second because of its lower urinary excretion (excreted tracer in the urinary bladder that caused obscuration of the pelvis). However, the value of PET with radiolabeled choline in the staging of prostate cancer has been a subject of controversy, and varying results have been reported.

In particular, in the evaluation of primary prostate cancer, choline PET–CT is currently not suitable for patient selection for primary treatment due to its low sensitivity and specificity in localizing tumor lesions both at the level of the prostate gland and the lymph nodes. For local T staging, choline PET–CT seems to be of limited value since there is no difference in tracer accumulation between benign prostate hyperplasia and prostate carcinoma [96, 97]; some studies performed in patients with advanced clinical stage and more aggressive cancers reported higher sensitivity for the detection of primary prostate cancer [98]. Therefore, there is no additional value of choline PET–CT to MRI for the detection of tumor nodules within the prostate [99] (Fig. 8.9).

In contrast, its potential use is the detection of recurrent tumor tissue in patients with biochemical evidence of recurrence of prostate cancer, distinguishing those with local versus distant relapse (Fig. 8.16), thus providing an attractive tool to guide irradiation of local recurrences [100, 101].

8.7 Staging

Prostate cancer localization is the most important clinical indication for multiparametric MR imaging of the prostate. First, accurate definition of prostate cancer location helps improve cancer detection in targeting prostate biopsies with MR imaging guidance. Second, accurate definition of a prostate cancer location also helps improve prostate cancer staging, because better assessment of prostate cancer location(s) near the neurovascular bundle is possible in patients in whom nerve-sparing surgery is planned. Third, improved evaluation of prostate cancer location helps improve and support focused intensity-modulated radiation therapy planning of the dominant prostatic lesion and improves guidance of minimally invasive focal therapies.

Compared with CT, US, systematic random biopsy, and digital rectal examination, MR imaging localization of prostate cancer was significantly more accurate. The literature, however, shows a wide range (50–92 %) in the accuracy of local staging with MR imaging [89]. Despite its high specificity in the identification of organ-confined disease and extracapsular extension, owing to lower sensitivity and substantial interobserver variability, the routine use of MR imaging in the local staging of prostate cancer remains controversial.

Historically, the stage of prostate cancer was based on the Jewett classification; only in the past 10 years has the TNM system prevailed. At present, however, both staging systems are in common use. The Jewett classification system (stages A–D) was described in 1975 and has since been modified. In 1997, the American Joint Committee on Cancer and the International Union Against Cancer adopted a revised TNM system that uses the same broad T-stage categories as in the Jewett system but includes subcategories of T stage, including a stage to describe disease diagnosed by means of PSA screening. In 2002, the American Joint Committee on Cancer further revised the TNM classification system [102]. This revised TNM system is clinically useful and more precisely stratifies newly diagnosed cancer.

In this classification, prostate cancer is divided in four stages. Stage T1 is only clinical, because the tumor is neither palpable nor visible with imaging. In stage T2, tumor is confined within the prostate and is further divided second to uni- or bilobar disease—respectively, T2a involving one-half of one lobe or less (Figs. 8.2, 8.6, and 8.7), T2b more than one-half of one lobe but not both lobes, and T2c both lobes (Figs. 8.3, 8.8, and 8.13). In stage T3, tumor extends through the prostate capsule and is further divided into T3a (extracapsular extension unilateral or bilateral) (Figs. 8.10 and 8.17) and

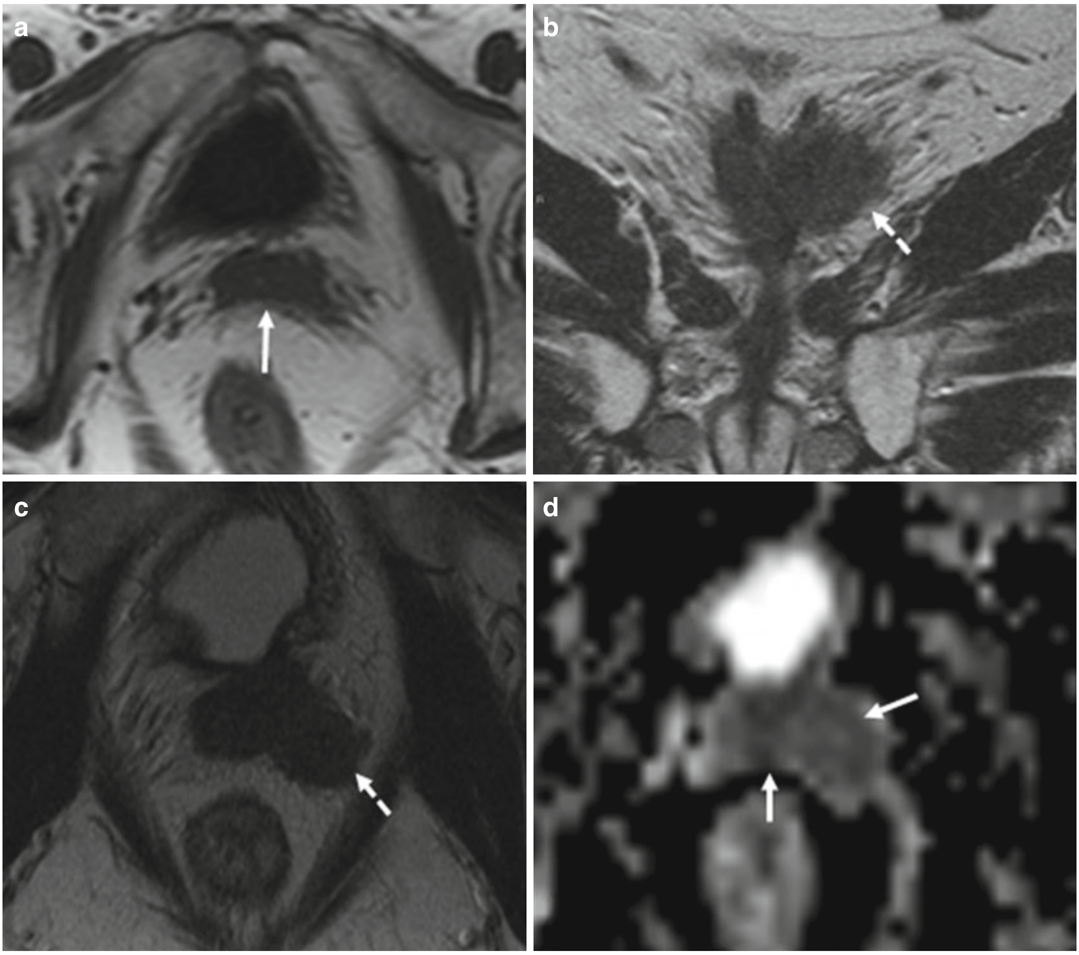

Fig. 8.16 (**a**–**j**) 68 years old, previous diagnosis of prostate cancer 8 years ago, underwent treatment with HIFU and subsequently hormonotherapy. PSA annulled for the first 4 years, then progressively rising (last PSA 4 ng/ml). Axial T1-weighted (TR: 550; TE: 9.3) sequence (**a**) shows the prostate (*arrow*) with reduced volume; on coronal T2-weighted (TR: 2300: TE: 116) sequence (**b**), an asymmetry of the two lobes is visible, with prevalence of the left lobe (*dashed arrow*). Axial T2-weighted sequence (**c**), acquired at a lower level than in (**a**), confirms prevalence of the left lobe (*dashed arrow*), documenting a diffuse hypointensity of both lobes. On ADC sequence (**d**), the prostate appears hypointense (*arrows*), while on post-contrastographic phase sequence (**e**) the whole prostate appears hypervascularized, with a more vascularized nodule visible in the left lobe (*dashed arrows*). On **e**, within the prostate, a homogeneous markedly hypointense area (*arrow*), the bladder neck. On fusion choline PET–CT image (**f**), in the same point on previous axial MRI sequences (**c**–**e**), a hypermetabolic lesion is visible (*dashed arrows*); the hypermetabolic area extends to the left lobe (*arrow*); anteriorly, the bladder (*arrowhead*). On post-contrastographic phase (**g**), acquired at apex, a nodule is recognizable too in the right lobe (*arrow*). Sagittal T2-weighted (TR: 3600; TE: 114) sequence (**h**) confirms diffuse hypointensity of all prostatic gland (*dashed arrow*). Lastly, both on T1-weighted sequence (**i**) and on fusion choline PET–CT image (**j**), a pathological external iliac lymph node (major axes: 11 × 8 mm) is identified (*arrowheads*), appearing hypointense on T1-weighted sequence and hypermetabolic on PET. Histopathological analysis of the surgical specimens confirmed a tumor, Gleason 9 (4 + 5), occupying 80 % of the prostate volume, with extension to both seminal vesicles. Metastases in three iliac–obturator lymph nodes

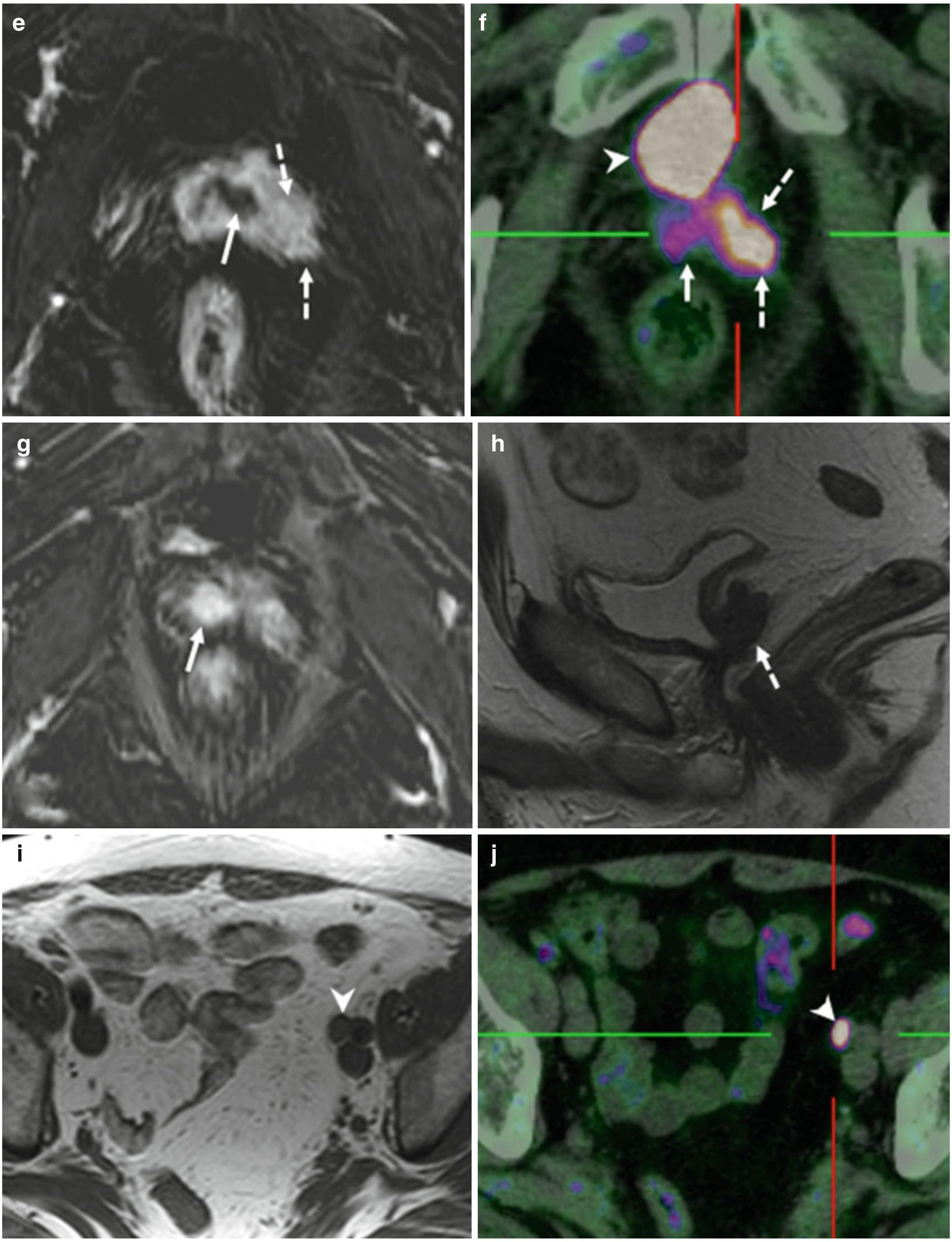

Fig. 8.16 (continued)

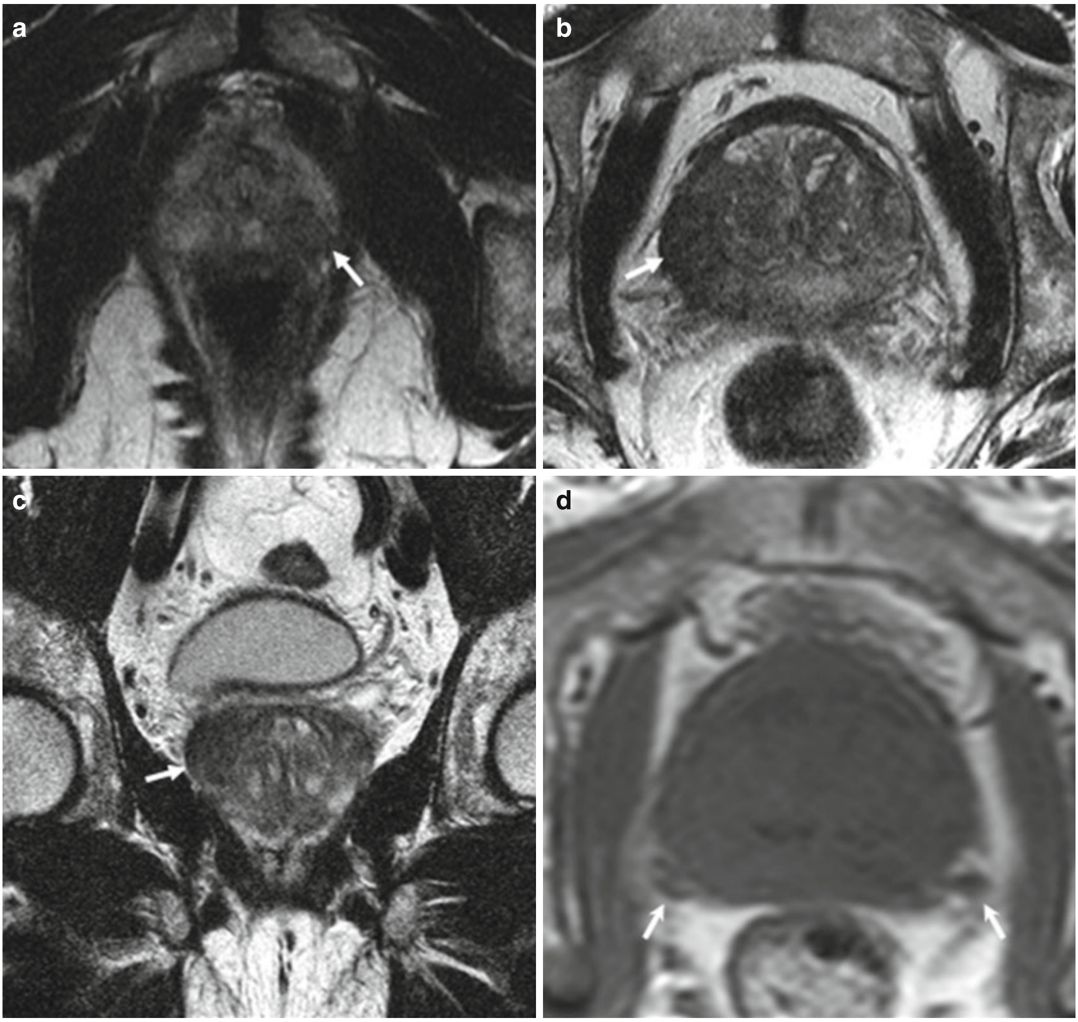

Fig. 8.17 (**a**–**j**) 58 years old, PSA 10.2 ng/ml. Axial T2-weighted (TR: 3600; TE: 116) sequences at the apex (**a**) and at the upper third (**b**) document the presence of two hypointense nodule (*arrows*)—respectively, 12 and 27 mm—interrupting the regular hyperintensity of the peripheral zone; on coronal T2-weighted (TR: 2300; TE: 116) sequence (**c**), the same lesion in **b** (*arrow*). On axial T1-weighted (TR: 550; TE: 9.3) sequence at the middle third (**d**), both the vascular nervous bundles (*short arrows*) are recognizable, but the right presents a limit with the prostatic capsule less clear (sign of initial involvement). Sagittal T2-weighted (TR: 3600; TE: 114) sequences at the left lobe (**e**) and at the right lobe (**f**) show, respectively, the small lesion in **a** at the apex, posteriorly, and the bigger lesion in **b** and **c**, at the upper two thirds (*arrows*); the prostatic capsule (*dashed arrows*), posteriorly, at the level of the second lesion, is irregular, with obliteration of fat tissue (*arrowhead*). On axial ADC sequence (**g**), at the apex level but lower than in **a**, in addition to the nodule in the left lobe (*arrow*), another lesion is recognizable in the posterior right lobe (*dashed arrow*), both markedly hypointense. On ADC sequence at the upper third (**h**), at the same level than in **b**, the lesion (*arrows*) appears similar to the lesions at the lower third. On post-contrastographic phase sequences (**i** and **j**, respectively, at the same level of **g** and **h**), the lesions are very vascularized (*arrows*). All three nodules present signal features typical of neoplastic lesions, confirmed with surgery

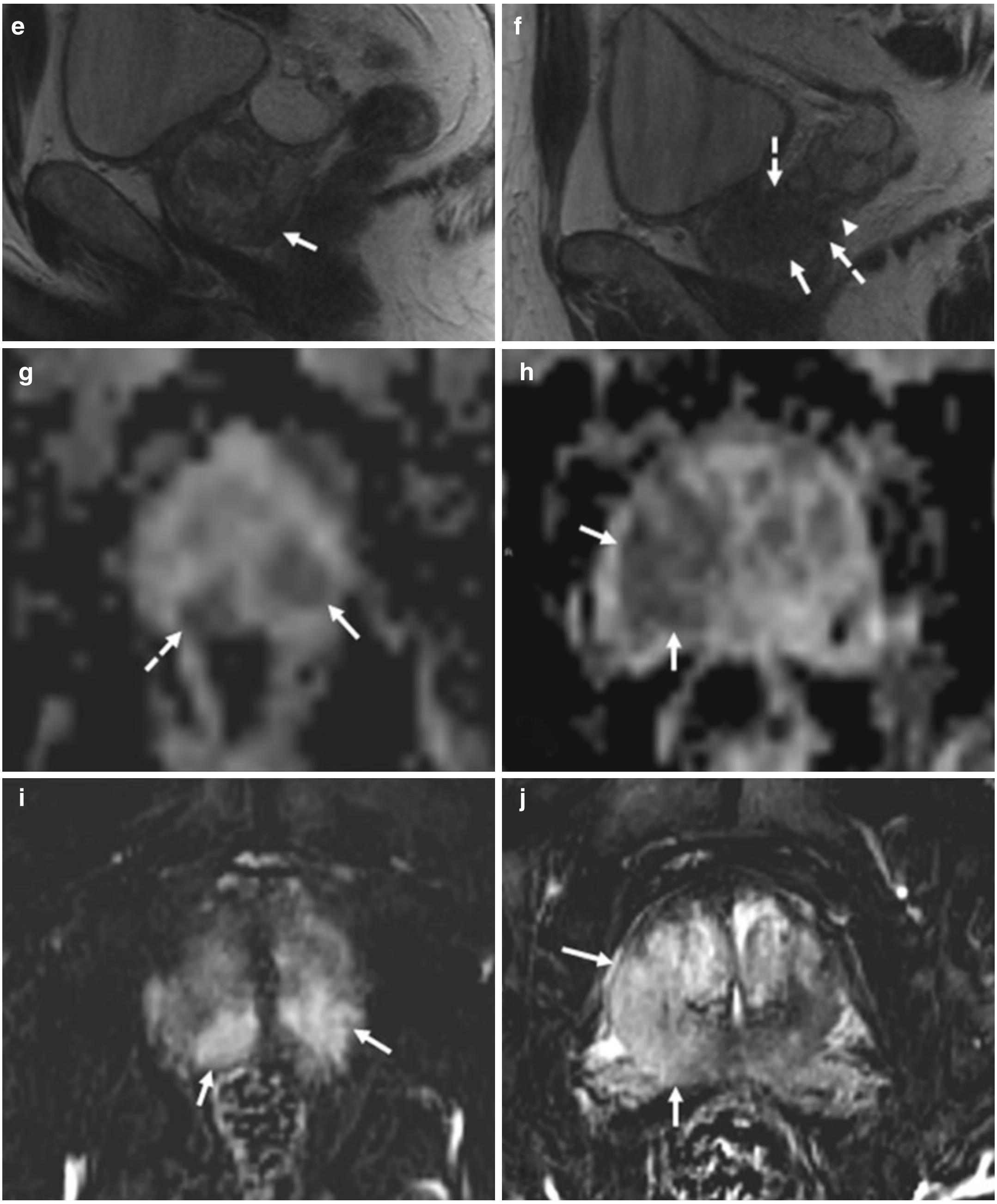

Fig. 8.17 (continued)

T3b (if a seminal vesicle is invaded) (Figs. 8.11, 8.14, and 8.18). In stage T4, tumor is fixed or invades adjacent structures other than the seminal vesicles: bladder neck, external sphincter, rectum, levator muscles, and/or pelvic wall (Fig. 8.19). In the evaluation of lymph node metastases, the two stages are N0 (no regional lymph node metastasis) and N1, if there are metastases in regional lymph nodes (internal iliac, obturator, external iliac, perirectal, and presacral) (Figs. 8.16, 8.18, and 8.19). The metastases are classified into M0 (absence of distant metastases) and M1 (presence of distant

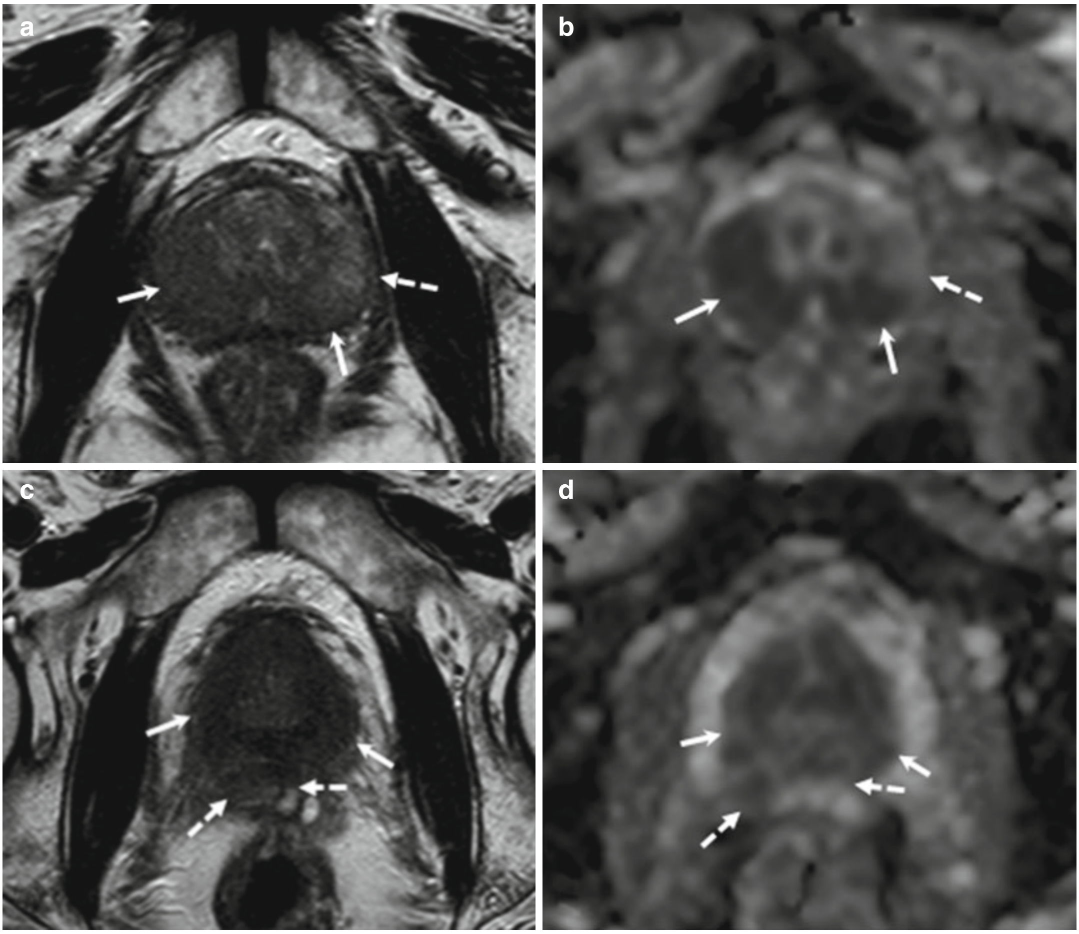

Fig. 8.18 (**a**–**j**) 52 years old, Gleason 7 (3+4). On axial T2-weighted (TR: 4074; TE: 100) (**a**) and ADC (**b**) sequences, acquired at the middle third, a diffuse hypointensity of the peripheral zone (*arrows*) is observed, with the exception of the peripheral zone of the left lobe (*dashed arrows*). On the same sequences (respectively, **c** and **d**), at the upper third, the hypointensity involves the entire peripheral zone (*arrows*), spreading posteriorly and infiltrating both seminal vesicles (*dashed arrows*), which appear irregularly hypointense, more evident in the right. On axial post-contrastographic phase sequence (**e**), at the level in **c** and **d**, the entire peripheral zone is hypervascularized (*arrows*). On coronal T2-weighted (TR: 4013; TE: 100) sequence (**f**), the entire upper third of the prostate is markedly more hypointense than the two lower thirds. On axial T2-weighted (**g**), ADC (**h**), and post-contrastographic phase (**i**) sequences, acquired at an upper level than in **c**–**e**, the diffuse hypointense and hypervascularized area of the peripheral zone (*arrows*) is recognizable. At this level, the hypointensity of the seminal vesicles is better visible (*dashed arrows*); not clearly identifiable is the posterior border of the prostate, because the surrounding tissues are diffusely slightly hypointense and vascularized (*long arrows*). In **j**, a hypointense external iliac lymph node (*arrow*), with major axes of 10×6 mm (suspicious for pathological). After prostatectomy, histopathological analysis confirmed the infiltration of both seminal vesicles and metastases in an external right iliac lymph node and revealed a second metastatic left lymph node, which did not have suspicious MRI features

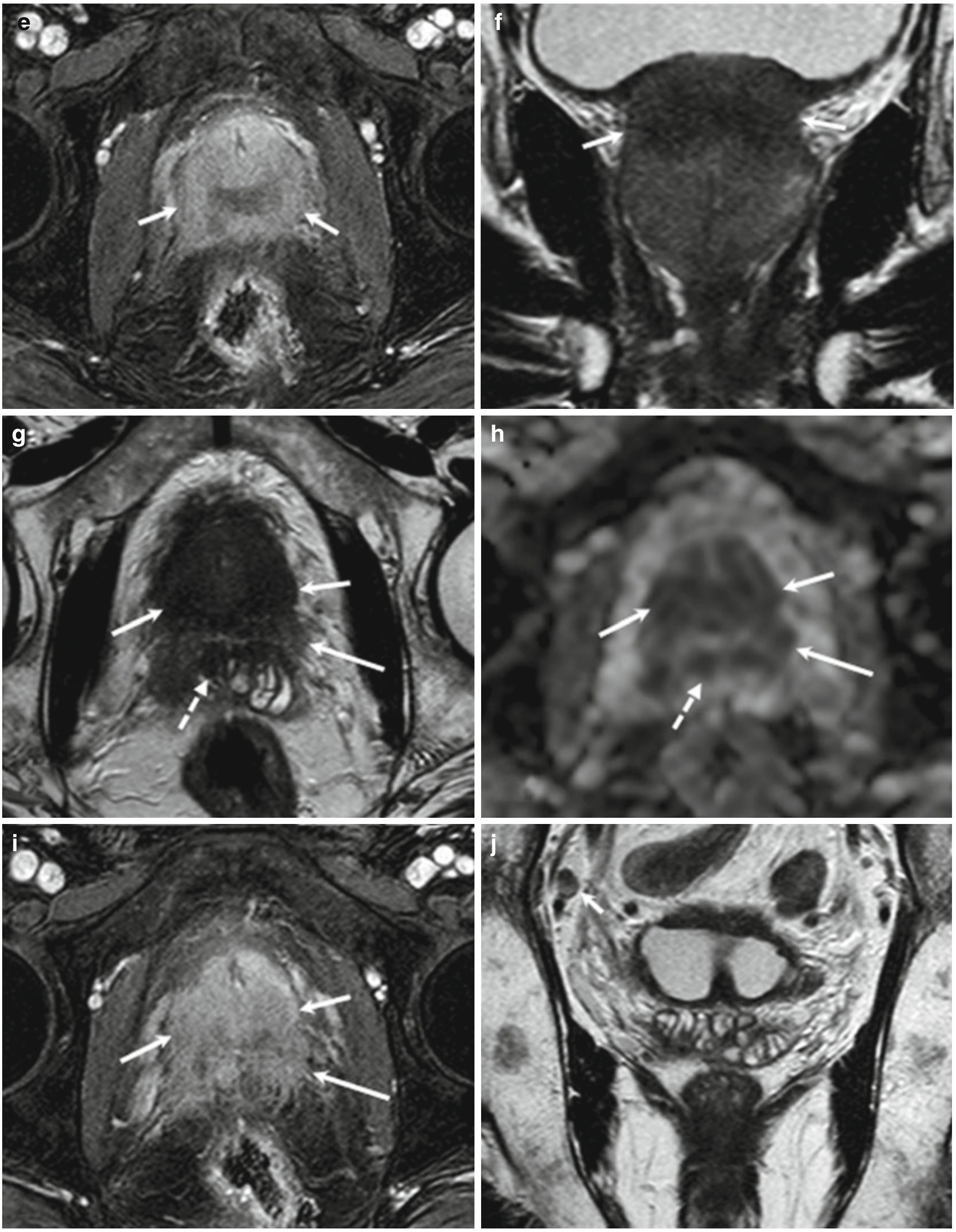

Fig. 8.18 (continued)

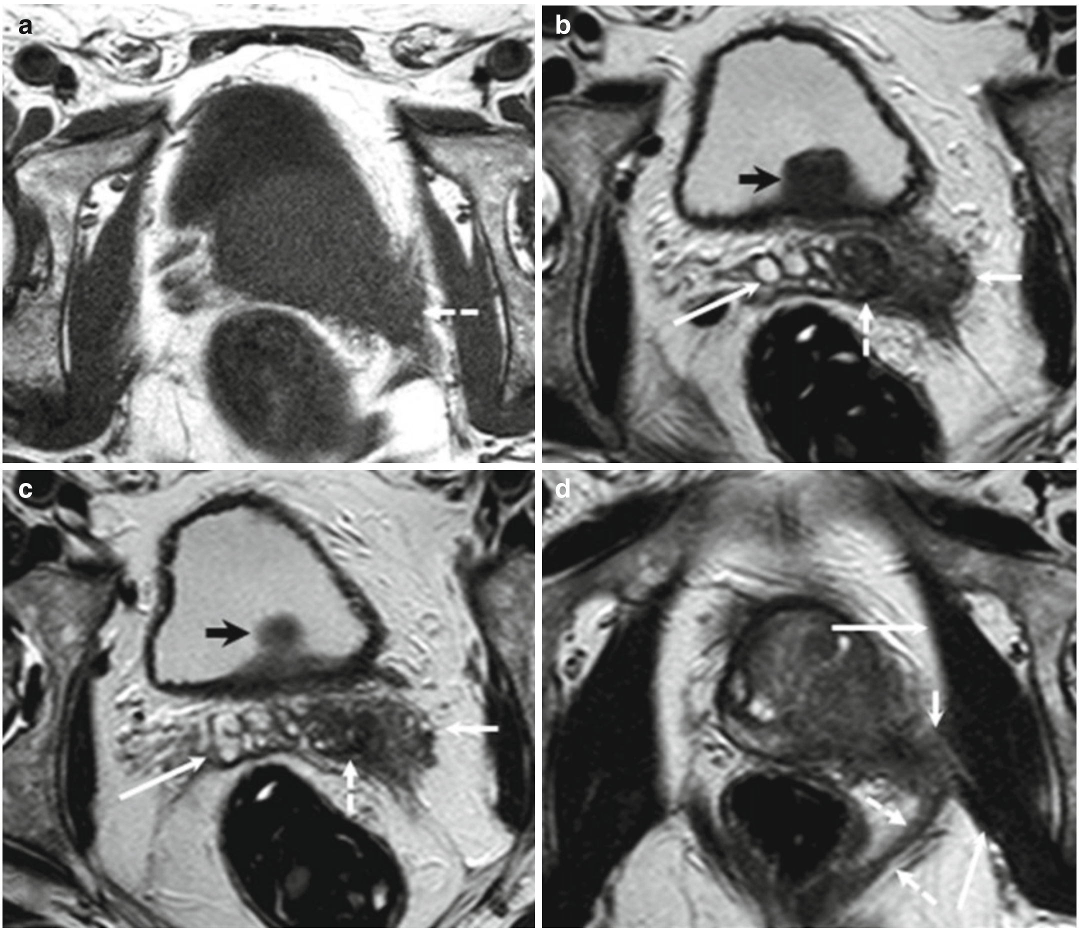

Fig. 8.19 (**a**–**j**) 68 years old, PSA 50.8 ng/ml, underwent biopsy 8 weeks before, Gleason 7 (4+3). On axial T1-weighted (TR: 500; TE: 10) sequence (**a**), at the upper third, asymmetry of the prostate, with prevalence of the left lobe (*dashed arrow*). On axial T2-weighted (TR: 4072; TE: 100) sequence (**b** and **c**), at a higher level than in **a**, diffuse inhomogeneous hypointensity of fat adjacent the border of the left lobe (*white arrows*); the seminal vesicle appears markedly hypointense (*dashed arrows*) compared with the contralateral (*long arrows*). Anteriorly, the median lobe is bulging upwards (*black arrows*). Still, axial T2-weighted sequence (**d**), at the middle third, confirms the presence of hypointense tissue (*white arrow*) extending in the bordering fat, involving the levator ani muscle (*dashed arrows*) and the obturator internus muscle (*long arrows*). On coronal T2-weighted (TR: 4013; TE: 100) sequences (**e** more anteriorly than **f**), the hypointense tissue spreads and invades the surrounding fat and the levator ani muscle (*dashed arrows*) and obturator internus muscle (*long arrows*); appreciable are two hypointense pathological (major axes: 20×12 and 16×12 mm) external iliac lymph nodes (*white arrows*). Sagittal T2-weighted (TR: 4013; TE: 100) sequences (**g** in right part of the pelvis, **h** in left): physiologic hyperintensity of right vesicle (**g**, *arrow*), while left vesicle appears markedly hypointense (**h**, *arrow*), surrounded and invaded by hypointense tissue (*dashed arrow*), spreading from the left lobe. On axial post-contrastographic phase sequence (**i** and, more caudally, **j**), the tissue in the left lobe appears hypervascularized (*arrows*); confirmed invasion of the levator ani muscle (*dashed arrows*) and obturator internus muscle (*long arrows*)

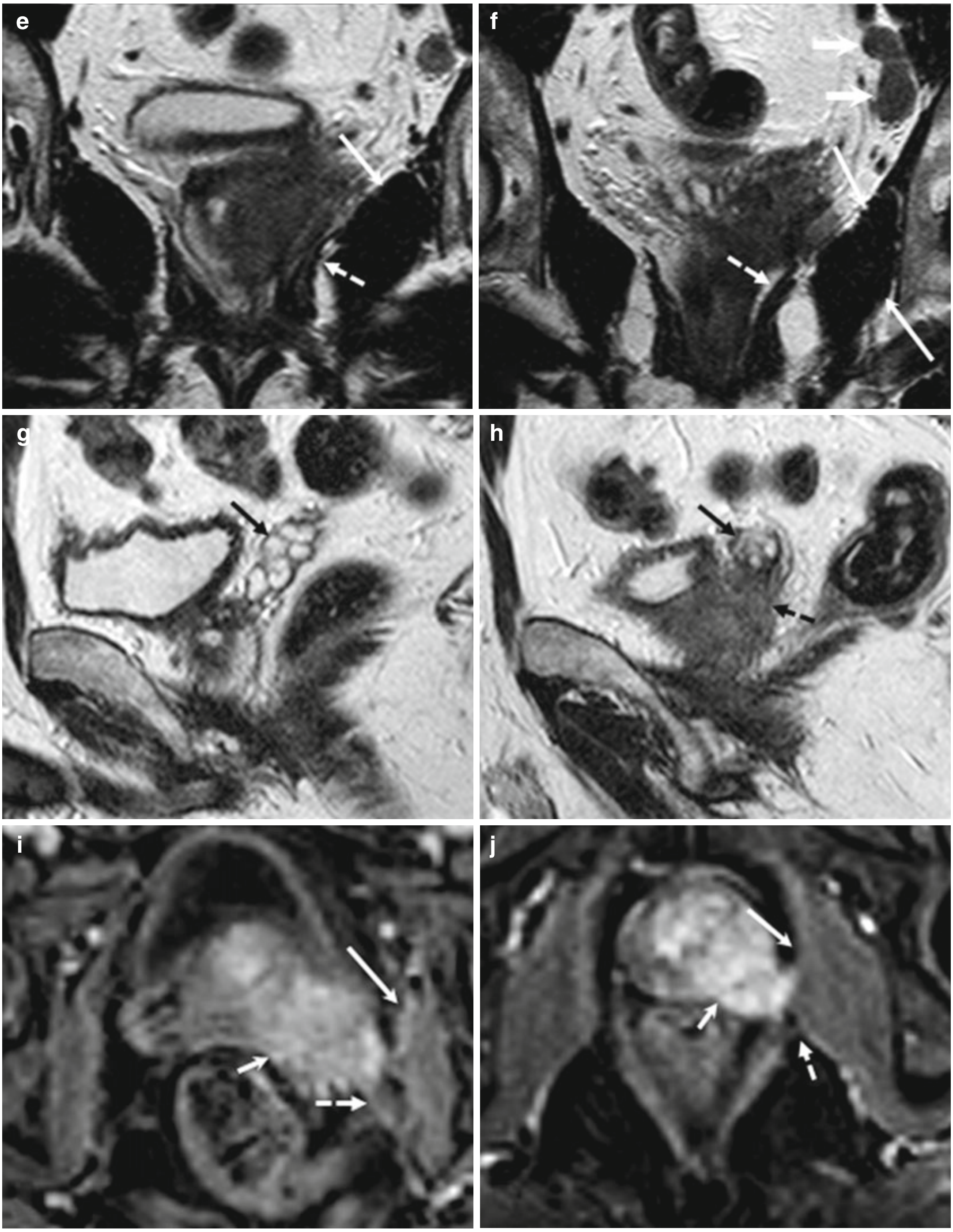

Fig. 8.19 (continued)

metastases); M1 is divided in M1a (involvement of nonregional lymph nodes, and the more frequent sites are the common iliac and para-aortic), M1b (bone), and M1c (other site).

For appropriate therapy planning it is important to differentiate between organ-confined disease (stage T1 or T2) and early advanced disease in the form of extracapsular extension or seminal vesicle invasion (stages T3 and T4). Advanced MR imaging techniques have been repeatedly shown to be more accurate in differentiating between stage T2 and T3 prostate cancer than other imaging modalities and are preferred for local staging: in particular, the current clinical staging, generally based on digital rectal examination, PSA, and transrectal US findings, results in frequent understaging (59 %) and some overstaging (5 %) [103]. The most widely used criteria for extracapsular spread are asymmetry of the neurovascular bundle, tumor encasement of the neurovascular bundle, a bulging prostatic contour, an irregular or spiculated margin, obliteration of the rectoprostatic angle, capsular retraction, a tumor–capsule interface of greater than 1 cm, and a breach of the capsule with evidence of direct tumor extension [42]. At multivariate feature analysis, the following MR imaging criteria were most predictive of extracapsular extension: a focal irregular capsular bulge, asymmetry or invasion of the neurovascular bundles, and obliteration of the rectoprostatic angle [104] (Figs. 8.10 and 8.17). In addition to extracapsular extension, seminal vesicle invasion is an important prognostic clinical parameter because it is associated with the highest rates of treatment failure—second only to lymph node metastases [105, 106]. The combination of images obtained in the axial, coronal, and sagittal planes facilitates the diagnosis of both extracapsular extension and seminal vesicle invasion. The features of seminal vesicle invasion include focal low signal intensity within and along the seminal vesicle, an enlarged low-signal-intensity seminal vesicle, enlarged low-signal-intensity ejaculatory ducts, obliteration of the angle between the prostate and the seminal vesicle, and demonstration of direct tumor extension from the base of the prostate into and around the seminal vesicle [42] (Figs. 8.11, 8.14, and 8.18). MR imaging has been reported to have a wide range of sensitivities (13–95 %) and specificities (49–97 %) for detection of extracapsular extension, with a similarly wide range of sensitivities (23–80 %) and specificities (81–99 %) for detection of seminal vesicle invasion [42, 107]. Limitations of conventional morphologic MR imaging of the prostate highlight the need for a combined anatomic and functional imaging approach.

In a large prospective study with 99 patients [71], dynamic contrast-enhanced MR imaging combined with T2-weighted MR imaging significantly improved the accuracy of prostate cancer staging compared with that of T2-weighted MR imaging alone, and this improvement was major for less-experienced readers; in a prospective study with 53 patients [108], the addition of three-dimensional MR spectroscopic imaging results to T2-weighted MR imaging results significantly improved accuracy for predicting extracapsular extension for both experienced and less-experienced readers. Drawbacks of T2-weighted MR imaging for prostate cancer localization and local staging include differentiation of inflammatory changes from cancer. Furthermore, high inter- and intraobserver variability may lead to under- or overestimation of cancer stage [109]. Also, postbiopsy hemorrhage can decrease staging accuracy. Finally, T2-weighted MR imaging cannot be used to detect microscopic capsular invasion. Increased experience in interpretation and a better understanding of morphologic criteria used to diagnose extraprostatic disease are key to further improving the role and accuracy of MR imaging in staging. The combined use of multiparametric MR imaging substantially improves the evaluation of extracapsular extension and decreases interobserver variability. As mentioned earlier, pitfalls of multiparametric MR techniques also affect the ability to facilitate prostate cancer localization and local staging. Of all clinical indications for multiparametric MR imaging, localization is the most important. Accurate prostate cancer localization results in more accurate prostate cancer staging and in more accurate MR guidance of prostate biopsy and therapy.

MR imaging is also helpful for diagnosing the invasion of adjacent organs, for example, the urinary bladder and rectum (stage T4): in particular, the sagittal imaging plane optimizes the evaluation of tumor extension into the bladder and rectum.

In the evaluation of lymph node metastases, efficacy data for MR imaging and CT are similar, with both modalities having low sensitivity.

Radionuclide bone scanning is the initial imaging modality recommended for detecting bone metastases. Although MR imaging is more sensitive than radionuclide scanning, evaluation of the entire skeletal system has not been critically analyzed. Reported cutoff values of PSA level used to identify patients at high risk for lymph node and bone metastases are around 15 and 20 ng/mL, respectively; however, there is considerable variation in cutoff values among different series in the literature [110, 111].

Although no specific staging system for prostatic tumors different from adenocarcinoma exists, imaging should analyze the same parameters: in particular, differentiating between organ-confined disease (stage T2 adenocarcinoma) and extraprostatic extension (T3 and T4) [112] (Fig. 8.20).

8.8 Treatment

Controversy exists with regard to the appropriate management of prostate cancer. The choice of treatment depends on the patient's age at diagnosis, the stage and aggressiveness of the tumor, the potential side effects of the treatment, and patient comorbidity [113, 114]. The thrust of cancer care is risk-adjusted, patient-specific therapy designed to maximize cancer control while minimizing the risks of complications. Risk-adjusted, patient-specific treatment of prostate cancer necessitates the accurate characterization of the location and extent of cancer.

The optimal therapeutic approach varies widely; options include watchful waiting, androgen ablation (chemical or surgical castration), hormone therapy, radical surgery, and various forms of radiation therapy (brachytherapy, external beam irradiation). The optimal treatment for prostate cancer is best selected on the basis of clinical TNM stage, Gleason grade, and the level of the circulating tumor marker, PSA. The decision to treat should also take into account patient age, disease stage, associated medical illnesses, and the patient's personal preferences. The inclusion of multiparametric MR imaging helps improve the prediction of cancer extent, thereby improving patient selection for local therapy. Other advantages include the possibility of monitoring the progress of patients who select watchful waiting or other minimally aggressive cancer management options and the guidance and assessment of emerging local prostate cancer therapies. Selection of the optimal treatment modality is based primarily on the initial clinical stage and the risk of biochemical failure (the likelihood of recurrence after locoregional treatment) [115, 116] (Figs. 8.10 and 8.16).

Radical treatment options for patients with prostate cancer include prostatectomy (for organ-confined T1 and T2 disease) and hormone ablation combined with radiation therapy (for advanced extraprostatic T3 and T4 disease). In certain situations, expectant management (watchful waiting) is a legitimate choice for patients with small-volume, low-grade, low-risk disease without any additional morbidity; however, the selection of treatment has to consider estimated life expectancy, comorbidities, potential side effects, and patient preferences. In general, patients should have a life expectancy of greater than 10 years to recommend definitive treatment.

The most common treatment side effects are erectile dysfunction and urinary incontinence. Efforts to reduce treatment morbidity while maximizing treatment effects have led to the demand for patient-specific and disease-targeted therapies. Recently, local and minimally invasive therapies such as cryoablation, radiofrequency ablation, brachytherapy, photodynamic therapy, and high-intensity focused ultrasonography (US) (Fig. 8.16) have been introduced for organ-confined prostate cancer; however, these therapies require exact localization of the cancer. With accurate staging and localization of prostate cancer, minimally invasive therapies can provide uncompromised oncologic outcome with significantly less comorbidity. However, patient selection for such treatments remains a challenge, since the tumor biology of prostate cancer still remains poorly understood. Most patients in whom prostate

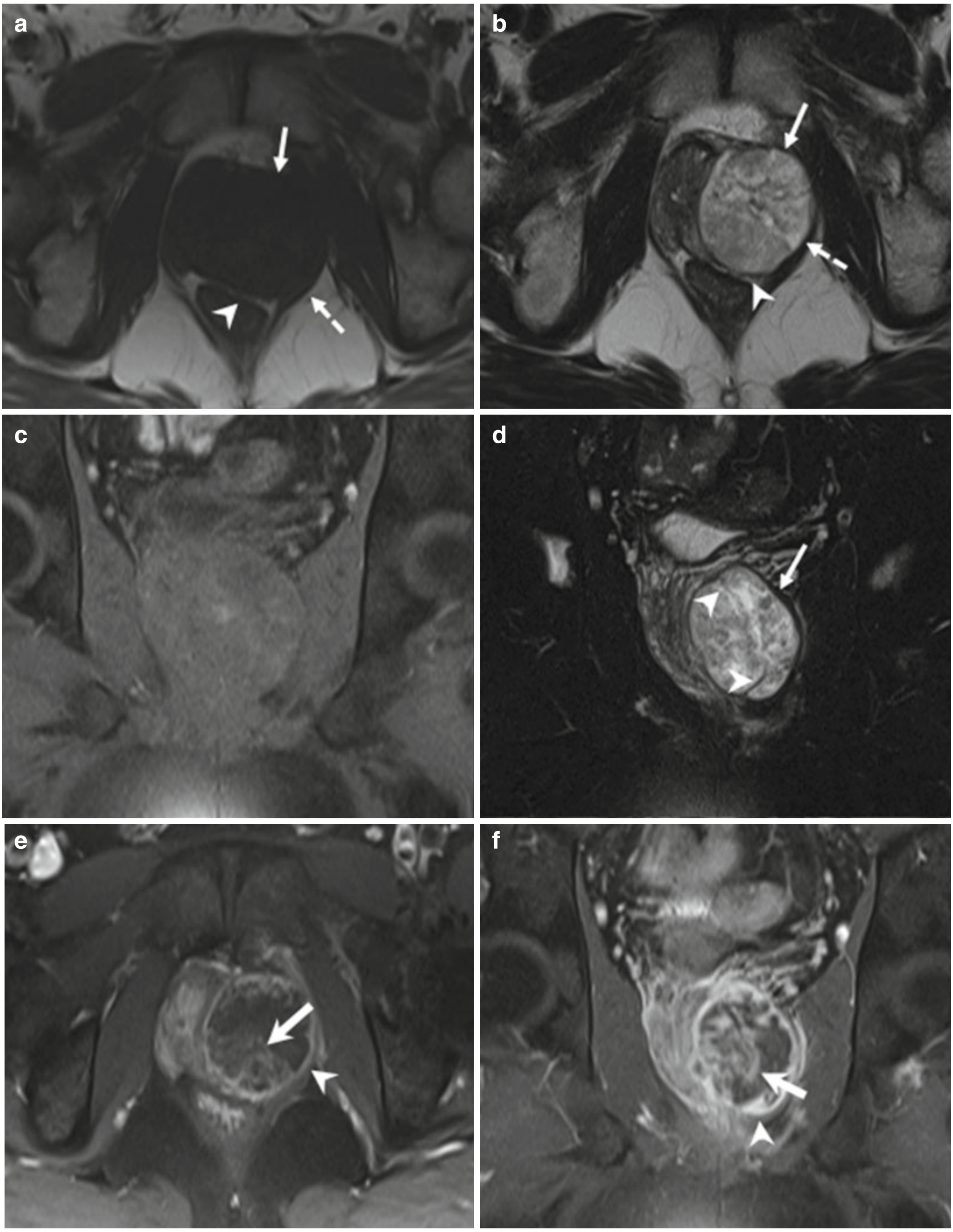

Fig. 8.20 (**a**–**f**) 38 years old. Axial T1-weighted (TR: 550; TE: 9,3) sequence (**a**) shows the prostate increased in volume, especially the left lobes (*arrow*), with lateral dislocation of left levator ani muscle (*dashed arrow*). On axial T2-weighted (TR: 5130; TE: 108) sequence (**b**), in the left lobe a lesion is recognizable (*arrow*), inhomogeneous hyperintense, with regular margins and a hypointense capsule (*dashed arrow*); the left lobe appears compressed and displaced to the right. Both in **a** and **b**, the posterior fat tissue is regular (*arrowhead*) and no sign of infiltration is appreciable. On coronal fat saturated T1-weighted (TR: 400; TE: 10) sequence (**c**), the lesion is not visible, while on coronal fat saturated T2-weighted (TR: 3000; TE: 80) sequence (**d**), the lesion (*arrow*) appears bilobed (*arrowheads*). On axial (**e**) and coronal (**f**) post-contrastographic phase sequences, the capsule and the internal septa show rich enhancement (*arrowheads*), while the lesion shows enhancement only in the posterior, medial portion (*arrows*) due to the rich necrotic component in the external portion. After prostatectomy, pathological analysis documented a highly malignant sarcoma (high cellularity, elevated mitotic index, and presence of necrosis)

cancer is diagnosed die with the disease rather than of the disease. Although several methods have been developed to predict patients' outcome [117], it is still difficult to project which patients will experience progression of the disease.

8.8.1 Surgery

Most cancers treated today are not palpable, and apart from the information obtained with US and biopsy, the surgeon has limited information about the size, location, and extent of the cancer. MR imaging can help refine the surgical plan, thus maximizing the preservation of periprostatic tissues (important for the recovery of urinary and sexual function) and minimizing the risk of positive surgical margins. MR imaging before radical prostatectomy can have an influence on the surgical decision to spare or resect the neurovascular bundles; this is especially valuable in high-risk patient groups. MR imaging can also be useful for predicting intraoperative blood loss during radical retropubic prostatectomy (i.e., a cutoff value of 4-mm separation from tumor to apical periprostatic veins at MR imaging has been shown to correlate with greater blood loss) [118]. In addition, MR imaging can help predict urinary incontinence after radical retropubic prostatectomy: patients with a longer membranous urethra regain urinary continence more easily and quickly [119] (Fig. 8.21).

8.8.2 Radiotherapy

Radiotherapy (RT) is one of the principal treatment modalities for both localized and locally advanced prostate cancer. RT may be delivered externally with either external beam radiotherapy (EBRT) or proton therapy or delivered internally with radioactive seeds (brachytherapy). Patients with intermediate- or high-risk localized disease may be treated with a combination of both external and internal RT to maximize the radiation dose to the prostate cancer. The guidelines for the optimal choice of treatment are not well established, and the choices are often empirical. The results of several retrospective analyses and the early results of clinical trials indicate that an increased radiation dose is associated with reduced rates of biochemical failure and may, therefore, increase local control rates and decrease the risk for distant metastasis and the rate of overall mortality [120–122]. This observation is important in the treatment of intermediate- or high-risk prostate cancer patients; however, increased radiation doses may be associated with a risk of treatment morbidity [123].

Advantages of RT over surgery include a very low risk of urinary incontinence or urethral stricture and no surgery-related complications. In addition, erectile dysfunction is less common after RT than after surgery; however, the risk of bowel side effects is higher after RT than after surgery. Contraindications to RT include any prior pelvic irradiation, active inflammatory disease of the rectum, and active prostatitis. Relative contraindications include very low bladder capacity; chronic, moderate, or severe diarrhea; bladder outlet obstruction requiring use of a suprapubic catheter; and inactive ulcerative colitis [116].

MR imaging is more accurate than CT in defining the prostate volume, with the highest nonagreement in the apex and posterior parts of the gland and the seminal vesicles [124–126], and in the anatomic delineation of surrounding structures, such as the rectal wall, the sigmoid, the urethra, and the penile bulb, which are at risk for radiation-induced tissue damage. The dose delivered to the rectal wall and bulb of the penis is substantially reduced with treatment plans based on the MR imaging-delineated prostate anatomy compared with treatment plans based on the CT-delineated prostate anatomy, decreasing the risk of rectal and urologic complications [127].

Despite the precise delivery of radiation dose to the whole prostate, intraprostatic tumor recurrences do occur, particularly at the sites of dominant intraprostatic tumors [128, 129] (Fig. 8.10). Because of its ability to show tumor location and extent, MR imaging can be of tremendous help to radiation therapy planning, permitting to map tumor volume or to localize a visible dominant tumor or more aggressive regions within the tumor, such as highly proliferating or hypoxic foci, so that very high radiation doses are combined in areas of high tumor cell density within the prostate gland without substantially increasing the risk of normal tissue damage, minimizing the risk of recurrences [130–132] (Fig. 8.22).

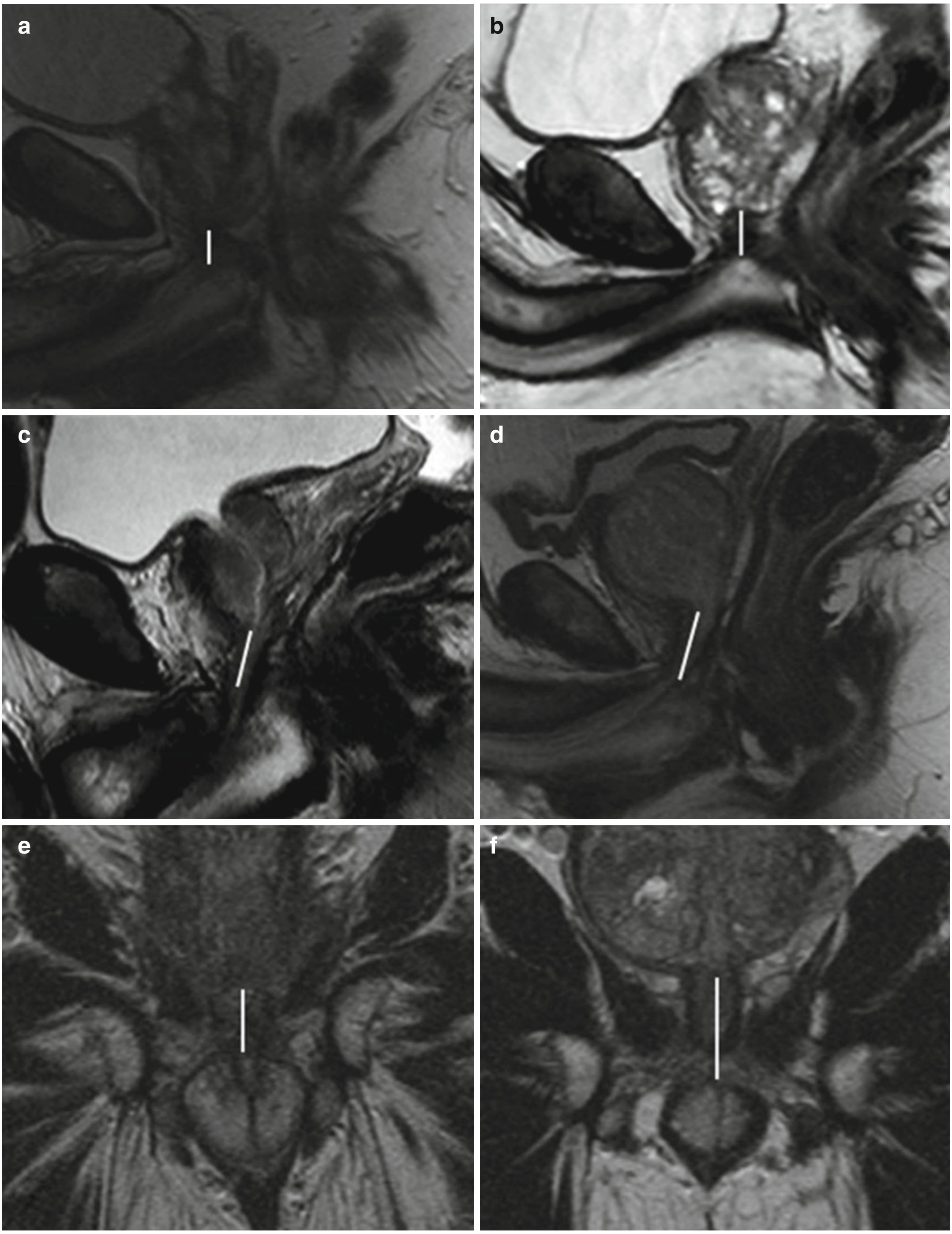

Fig. 8.21 (**a**–**f**) Preoperative sagittal T2-weighted (TR: 3600; TE: 114) sequences (**a**–**d**) of four different patients; **e** and **f**, coronal view (TR: 2300; TE: 116), respectively, of **a** and **d**. The preoperative membranous urethral length (the distance from the prostatic apex to the level of the urethra at the penile bulb, *white line* in a–f) is measured in the coronal and sagittal planes. A longer rather than a shorter (**c**, **d**) preoperative membranous urethra is associated with a faster and more frequent recovery of continence (**a**, **b**)

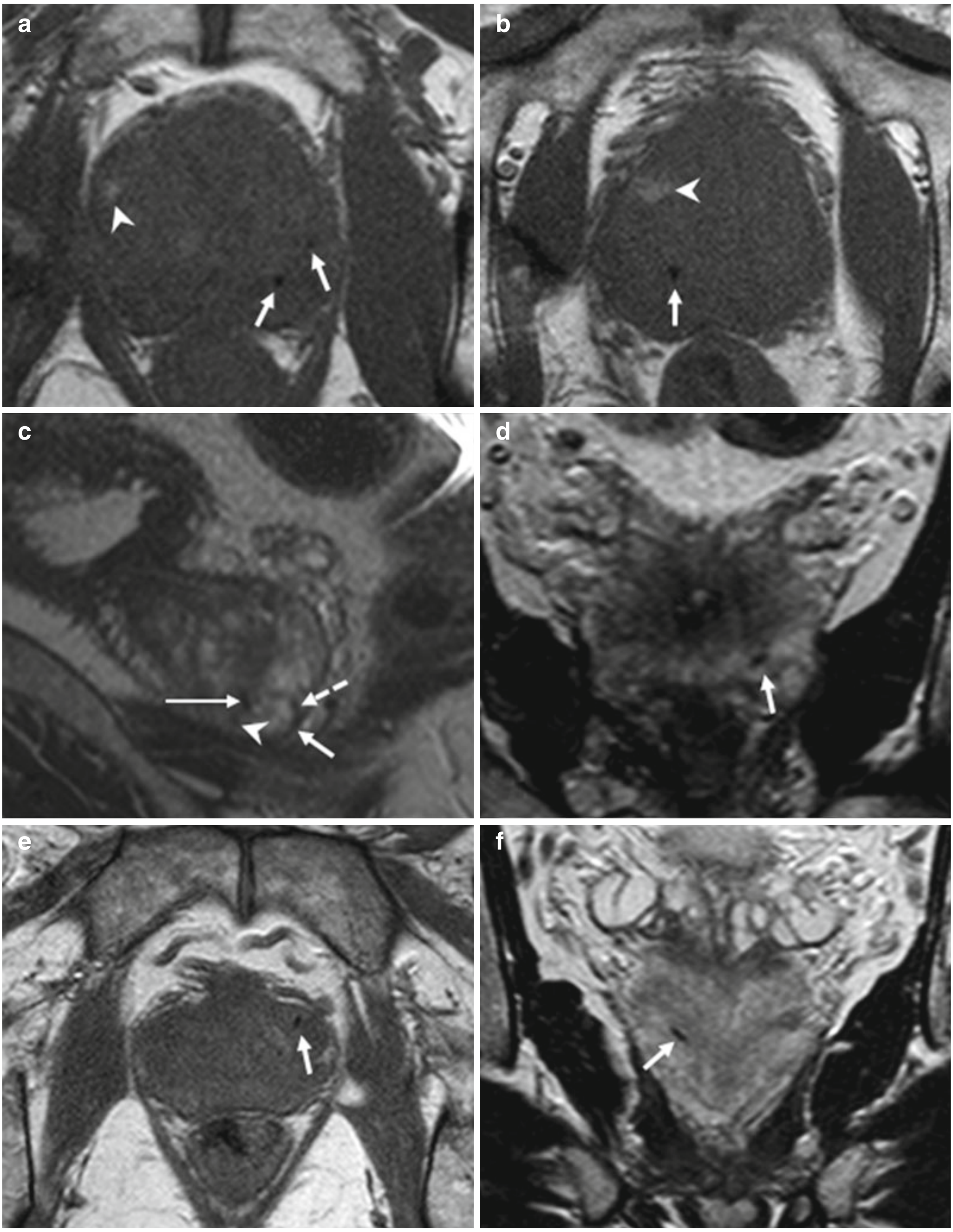

Fig. 8.22 (**a**–**f**) 62 years old, PSA 7.8 ng/ml, diagnosis of prostate tumor 3 months ago (Gleason 6, 3+3), candidate for radiotherapy. (**a**, **b**) axial T1-weighted (TR: 500; TE: 10) sequences. (**c**, **d**) sagittal (TR: 4006; TE: 100) (**c**) and coronal (TR: 4013; TE: 100) (**d**) T2-weighted sequences, respectively. The subject underwent placement of gold fiducial marker seeds that are used as a fixed standard of reference during radiation treatment. The markers are inserted by performing a transrectal ultrasound: three markers are inserted through a needle which is passed through the ultrasound probe. The markers correspond to the very low signal intensity images (*arrows* **a**–**d**) seen edgeways (**a**, **b**) or along the major axis (**c**, **d**). In particular, in **c**, a marker (*long arrow*) is in the central zone, at the border with peripheral zone (*arrowhead*), another (*dashed arrow*) is in peripheral zone, in close contact with the prostatic capsule (*short arrow*) while in **d** in the peripheral zone (*arrow*), in the left lobe. Furthermore, in **a** and **b**, an area of high signal intensity in the right lobe (*arrowhead*), hemorrhage in recent procedure of placement of markers. In a second subject, on axial T1-weighted (**e**) and coronal T2-weighted (**f**) sequences, other examples of fiducial markers (*arrows*)

References

1. Parkin DM et al (2005) Global cancer statistics, 2002. CA Cancer J Clin 55(2):74–108
2. American Cancer Society (2009) Prostate cancer fact. Cancer fact and figures. American Cancer Society, Atlanta, pp 19–20
3. Mazhar D, Waxman J (2002) Prostate cancer. Postgrad Med J 78(924):590–595
4. Pound CR et al (1999) Natural history of progression after PSA elevation following radical prostatectomy. JAMA 281(17):1591–1597
5. Johansson JE et al (1997) Fifteen-year survival in prostate cancer. A prospective, population-based study in Sweden. JAMA 277(6):467–471
6. Byar DP, Mostofi FK (1972) Carcinoma of the prostate: prognostic evaluation of certain pathologic features in 208 radical prostatectomies. Examined by the step-section technique. Cancer 30(1):5–13
7. Gleason DF (1992) Histologic grading of prostate cancer: a perspective. Hum Pathol 23(3):273–279
8. Egevad L et al (2002) Prognostic value of the Gleason score in prostate cancer. BJU Int 89(6):538–542
9. Partin AW et al (2001) Contemporary update of prostate cancer staging nomograms (Partin Tables) for the new millennium. Urology 58(6):843–848
10. Albertsen PC (2010) The unintended burden of increased prostate cancer detection associated with prostate cancer screening and diagnosis. Urology 75(2):399–405
11. Schroder FH et al (1998) Evaluation of the digital rectal examination as a screening test for prostate cancer. Rotterdam section of the European Randomized Study of Screening for Prostate Cancer. J Natl Cancer Inst 90(23):1817–1823
12. Catalona WJ et al (1994) Comparison of digital rectal examination and serum prostate specific antigen in the early detection of prostate cancer: results of a multicenter clinical trial of 6,630 men. J Urol 151(5):1283–1290
13. Schroder FH et al (2008) Early detection of prostate cancer in 2007. Part 1: PSA and PSA kinetics. Eur Urol 53(3):468–477
14. Donovan J et al (2003) Prostate Testing for Cancer and Treatment (ProtecT) feasibility study. Health Technol Assess 7(14):1–88
15. Djavan B et al (2001) Prospective evaluation of prostate cancer detected on biopsies 1, 2, 3 and 4: when should we stop? J Urol 166(5):1679–1683
16. Noguchi M et al (2001) Relationship between systematic biopsies and histological features of 222 radical prostatectomy specimens: lack of prediction of tumor significance for men with nonpalpable prostate cancer. J Urol 166(1):104–109; discussion 109–110
17. Cookson MS et al (1997) Correlation between Gleason score of needle biopsy and radical prostatectomy specimen: accuracy and clinical implications. J Urol 157(2):559–562
18. Hoeks CM et al (2011) Prostate cancer: multiparametric MR imaging for detection, localization, and staging. Radiology 261(1):46–66
19. Yacoub JH et al (2012) Imaging-guided prostate biopsy: conventional and emerging techniques. Radiographics 32(3):819–837
20. Coakley FV, Qayyum A, Kurhanewicz J (2003) Magnetic resonance imaging and spectroscopic imaging of prostate cancer. J Urol 170(6 Pt 2):S69–S75; discussion S75–S76
21. Steyn JH, Smith FW (1982) Nuclear magnetic resonance imaging of the prostate. Br J Urol 54(6):726–728
22. Hricak H et al (1983) Anatomy and pathology of the male pelvis by magnetic resonance imaging. AJR Am J Roentgenol 141(6):1101–1110
23. Gleason DF (1966) Classification of prostatic carcinomas. Cancer Chemother Rep 50(3):125–128
24. Mellinger GT, Gleason D, Bailar J 3rd (1967) The histology and prognosis of prostatic cancer. J Urol 97(2):331–337
25. Gleason DF, Mellinger GT (1974) Prediction of prognosis for prostatic adenocarcinoma by combined histological grading and clinical staging. J Urol 111(1):58–64
26. Aihara M et al (1994) Heterogeneity of prostate cancer in radical prostatectomy specimens. Urology 43(1):60–66; discussion 66–67
27. McGowan DG, Bain GO, Hanson J (1983) Evaluation of histological grading (Gleason) in carcinoma of the prostate: adverse influence of highest grade. Prostate 4(2):111–118
28. Ruijter ET et al (1996) Histological grade heterogeneity in multifocal prostate cancer. Biological and clinical implications. J Pathol 180(3):295–299
29. Humphrey PA (2003) Grading of prostatic carcinoma. In: Prostate pathology. ASCP Press, Chicago, pp 338–374
30. Allsbrook WC Jr et al (2001) Interobserver reproducibility of Gleason grading of prostatic carcinoma: general pathologist. Hum Pathol 32(1):81–88
31. Partin AW et al (1997) Combination of prostate-specific antigen, clinical stage, and Gleason score to predict pathological stage of localized prostate cancer. A multi-institutional update. JAMA 277(18):1445–1451
32. Koppie TM et al (2000) Patterns of treatment of patients with prostate cancer initially managed with surveillance: results from The CaPSURE database. Cancer of the Prostate Strategic Urological Research Endeavor. J Urol 164(1):81–88
33. McNeal JE (1981) The zonal anatomy of the prostate. Prostate 2(1):35–49
34. Hricak H et al (1987) MR imaging of the prostate gland: normal anatomy. AJR Am J Roentgenol 148(1):51–58
35. Villers A, Steg A, Boccon-Gibod L (1991) Anatomy of the prostate: review of the different models. Eur Urol 20(4):261–268
36. Coakley FV, Hricak H (2000) Radiologic anatomy of the prostate gland: a clinical approach. Radiol Clin North Am 38(1):15–30
37. Hambrock T et al (2008) Thirty-two-channel coil 3T magnetic resonance-guided biopsies of prostate tumor suspicious regions identified on multimodality 3T

magnetic resonance imaging: technique and feasibility. Invest Radiol 43(10):686–694
38. Takashima R et al (2002) Anterior distribution of Stage T1c nonpalpable tumors in radical prostatectomy specimens. Urology 59(5):692–697
39. Franiel T et al (2011) Areas suspicious for prostate cancer: MR-guided biopsy in patients with at least one transrectal US-guided biopsy with a negative finding–multiparametric MR imaging for detection and biopsy planning. Radiology 259(1):162–172
40. Mirilas P, Skandalakis JE (2004) Urogenital diaphragm: an erroneous concept casting its shadow over the sphincter urethrae and deep perineal space. J Am Coll Surg 198(2):279–290
41. Kundra V et al (2007) Imaging in oncology from the University of Texas M. D. Anderson Cancer Center: diagnosis, staging, and surveillance of prostate cancer. AJR Am J Roentgenol 189(4):830–844
42. Hricak H et al (2007) Imaging prostate cancer: a multidisciplinary perspective. Radiology 243(1):28–53
43. Hricak H et al (1994) Carcinoma of the prostate gland: MR imaging with pelvic phased-array coils versus integrated endorectal–pelvic phased-array coils. Radiology 193(3):703–709
44. Scheidler J et al (1999) Prostate cancer: localization with three-dimensional proton MR spectroscopic imaging–clinicopathologic study. Radiology 213(2): 473–480
45. Haider MA et al (2007) Combined T2-weighted and diffusion-weighted MRI for localization of prostate cancer. AJR Am J Roentgenol 189(2):323–328
46. Turkbey B et al (2010) Prostate cancer: value of multiparametric MR imaging at 3 T for detection–histopathologic correlation. Radiology 255(1):89–99
47. Delongchamps NB et al (2011) Multiparametric magnetic resonance imaging for the detection and localization of prostate cancer: combination of T2-weighted, dynamic contrast-enhanced and diffusion-weighted imaging. BJU Int 107(9):1411–1418
48. Chen M et al (2008) Prostate cancer detection: comparison of T2-weighted imaging, diffusion-weighted imaging, proton magnetic resonance spectroscopic imaging, and the three techniques combined. Acta Radiol 49(5):602–610
49. Futterer JJ et al (2006) Prostate cancer localization with dynamic contrast-enhanced MR imaging and proton MR spectroscopic imaging. Radiology 241(2):449–458
50. Tanimoto A et al (2007) Prostate cancer screening: the clinical value of diffusion-weighted imaging and dynamic MR imaging in combination with T2-weighted imaging. J Magn Reson Imaging 25(1):146–152
51. Moseley ME et al (1990) Diffusion-weighted MR imaging of acute stroke: correlation with T2-weighted and magnetic susceptibility-enhanced MR imaging in cats. AJNR Am J Neuroradiol 11(3):423–429
52. Hosseinzadeh K, Schwarz SD (2004) Endorectal diffusion-weighted imaging in prostate cancer to differentiate malignant and benign peripheral zone tissue. J Magn Reson Imaging 20(4):654–661
53. Sato C et al (2005) Differentiation of noncancerous tissue and cancer lesions by apparent diffusion coefficient values in transition and peripheral zones of the prostate. J Magn Reson Imaging 21(3):258–262
54. Kim CK et al (2007) Value of diffusion-weighted imaging for the prediction of prostate cancer location at 3T using a phased-array coil: preliminary results. Invest Radiol 42(12):842–847
55. Lim HK et al (2009) Prostate cancer: apparent diffusion coefficient map with T2-weighted images for detection–a multireader study. Radiology 250(1):145–151
56. Vargas HA et al (2011) Diffusion-weighted endorectal MR imaging at 3 T for prostate cancer: tumor detection and assessment of aggressiveness. Radiology 259(3):775–784
57. Desouza NM et al (2007) Magnetic resonance imaging in prostate cancer: the value of apparent diffusion coefficients for identifying malignant nodules. Br J Radiol 80(950):90–95
58. Kim JH et al (2008) Apparent diffusion coefficient: prostate cancer versus noncancerous tissue according to anatomical region. J Magn Reson Imaging 28(5): 1173–1179
59. Noworolski SM et al (2008) Dynamic contrast-enhanced MRI and MR diffusion imaging to distinguish between glandular and stromal prostatic tissues. Magn Reson Imaging 26(8):1071–1080
60. Tamada T et al (2008) Apparent diffusion coefficient values in peripheral and transition zones of the prostate: comparison between normal and malignant prostatic tissues and correlation with histologic grade. J Magn Reson Imaging 28(3):720–726
61. Rosenkrantz AB et al (2010) Prostate cancer vs. post-biopsy hemorrhage: diagnosis with T2- and diffusion-weighted imaging. J Magn Reson Imaging 31(6): 1387–1394
62. Jackson MW, Bentel JM, Tilley WD (1997) Vascular endothelial growth factor (VEGF) expression in prostate cancer and benign prostatic hyperplasia. J Urol 157(6):2323–2328
63. Padhani AR, Harvey CJ, Cosgrove DO (2005) Angiogenesis imaging in the management of prostate cancer. Nat Clin Pract Urol 2(12):596–607
64. Engelbrecht MR et al (2003) Discrimination of prostate cancer from normal peripheral zone and central gland tissue by using dynamic contrast-enhanced MR imaging. Radiology 229(1):248–254
65. Alonzi R, Padhani AR, Allen C (2007) Dynamic contrast enhanced MRI in prostate cancer. Eur J Radiol 63(3):335–350
66. Sciarra A et al (2010) Magnetic resonance spectroscopic imaging (1H-MRSI) and dynamic contrast-enhanced magnetic resonance (DCE-MRI): pattern changes from inflammation to prostate cancer. Cancer Invest 28(4):424–432
67. Ogura K et al (2001) Dynamic endorectal magnetic resonance imaging for local staging and detection of neurovascular bundle involvement of prostate cancer: correlation with histopathologic results. Urology 57(4):721–726

68. Jager GJ et al (1997) Dynamic TurboFLASH subtraction technique for contrast-enhanced MR imaging of the prostate: correlation with histopathologic results. Radiology 203(3):645–652
69. Kim CK, Park BK, Kim B (2006) Localization of prostate cancer using 3 T MRI: comparison of T2-weighted and dynamic contrast-enhanced imaging. J Comput Assist Tomogr 30(1):7–11
70. Franiel T et al (2008) Evaluation of normal prostate tissue, chronic prostatitis, and prostate cancer by quantitative perfusion analysis using a dynamic contrast-enhanced inversion-prepared dual-contrast gradient echo sequence. Invest Radiol 43(7):481–487
71. Futterer JJ et al (2005) Staging prostate cancer with dynamic contrast-enhanced endorectal MR imaging prior to radical prostatectomy: experienced versus less experienced readers. Radiology 237(2):541–549
72. Heerschap A et al (1997) Proton MR spectroscopy of the normal human prostate with an endorectal coil and a double spin-echo pulse sequence. Magn Reson Med 37(2):204–213
73. Podo F (1999) Tumour phospholipid metabolism. NMR Biomed 12(7):413–439
74. Shukla-Dave A et al (2004) Chronic prostatitis: MR imaging and 1H MR spectroscopic imaging findings–initial observations. Radiology 231(3):717–724
75. Yacoe ME, Sommer G, Peehl D (1991) In vitro proton spectroscopy of normal and abnormal prostate. Magn Reson Med 19(2):429–438
76. Kurhanewicz J et al (1996) Three-dimensional H-1 MR spectroscopic imaging of the in situ human prostate with high (0.24–0.7-cm3) spatial resolution. Radiology 198(3):795–805
77. Males RG et al (2000) Clinical application of BASING and spectral/spatial water and lipid suppression pulses for prostate cancer staging and localization by in vivo 3D 1H magnetic resonance spectroscopic imaging. Magn Reson Med 43(1):17–22
78. Obek C et al (1999) Comparison of digital rectal examination and biopsy results with the radical prostatectomy specimen. J Urol 161(2):494–498; discussion 498–499
79. Wefer AE et al (2000) Sextant localization of prostate cancer: comparison of sextant biopsy, magnetic resonance imaging and magnetic resonance spectroscopic imaging with step section histology. J Urol 164(2): 400–404
80. Weinreb JC et al (2009) Prostate cancer: sextant localization at MR imaging and MR spectroscopic imaging before prostatectomy–results of ACRIN prospective multi-institutional clinicopathologic study. Radiology 251(1):122–133
81. Zakian KL et al (2003) Transition zone prostate cancer: metabolic characteristics at 1H MR spectroscopic imaging–initial results. Radiology 229(1):241–247
82. Zakian KL et al (2005) Correlation of proton MR spectroscopic imaging with gleason score based on step-section pathologic analysis after radical prostatectomy. Radiology 234(3):804–814
83. Bonekamp D et al (2011) Advancements in MR imaging of the prostate: from diagnosis to interventions. Radiographics 31(3):677–703
84. Westphalen AC et al (2009) Mucinous adenocarcinoma of the prostate: MRI and MR spectroscopy features. AJR Am J Roentgenol 193(3):W238–W243
85. Coakley FV et al (2002) Prostate cancer tumor volume: measurement with endorectal MR and MR spectroscopic imaging. Radiology 223(1): 91–97
86. Crehange G et al (2010) Tumor volume and metabolism of prostate cancer determined by proton magnetic resonance spectroscopic imaging at 3 T without endorectal coil reveal potential clinical implications in the context of radiation oncology. Int J Radiat Oncol Biol Phys 80(4):1087–1094
87. Qayyum A et al (2004) Organ-confined prostate cancer: effect of prior transrectal biopsy on endorectal MRI and MR spectroscopic imaging. AJR Am J Roentgenol 183(4):1079–1083
88. Kaji Y et al (1998) Localizing prostate cancer in the presence of postbiopsy changes on MR images: role of proton MR spectroscopic imaging. Radiology 206(3):785–790
89. Engelbrecht MR et al (2002) Local staging of prostate cancer using magnetic resonance imaging: a meta-analysis. Eur Radiol 12(9):2294–2302
90. Futterer JJ et al (2007) Prostate cancer: comparison of local staging accuracy of pelvic phased-array coil alone versus integrated endorectal-pelvic phased-array coils. Local staging accuracy of prostate cancer using endorectal coil MR imaging. Eur Radiol 17(4):1055–1065
91. Tempany CM et al (1994) Staging of prostate cancer: results of Radiology Diagnostic Oncology Group project comparison of three MR imaging techniques. Radiology 192(1):47–54
92. Barker PB, Hearshen DO, Boska MD (2001) Single-voxel proton MRS of the human brain at 1.5 T and 3.0 T. Magn Reson Med 45(5):765–769
93. Gibbs P, Pickles MD, Turnbull LW (2006) Diffusion imaging of the prostate at 3.0 tesla. Invest Radiol 41(2):185–188
94. Picchio M et al (2003) Value of [11C]choline-positron emission tomography for re-staging prostate cancer: a comparison with [18 F]fluorodeoxyglucose-positron emission tomography. J Urol 169(4): 1337–1340
95. Jadvar H (2011) Prostate cancer: PET with 18F-FDG, 18F- or 11C-acetate, and 18F- or 11C-choline. J Nucl Med 52(1):81–89
96. Hofer C et al (1999) Fluorine-18-fluorodeoxyglucose positron emission tomography is useless for the detection of local recurrence after radical prostatectomy. Eur Urol 36(1):31–35
97. Liu IJ et al (2001) Fluorodeoxyglucose positron emission tomography studies in diagnosis and staging of clinically organ-confined prostate cancer. Urology 57(1):108–111

98. Oyama N et al (2002) Prognostic value of 2-deoxy-2-[F-18]fluoro-D-glucose positron emission tomography imaging for patients with prostate cancer. Mol Imaging Biol 4(1):99–104
99. Van den Bergh L et al (2013) Does 11C-choline PET-CT contribute to multiparametric MRI for prostate cancer localisation? Strahlenther Onkol 189(9):789–795
100. Grosu AL et al (2005) Positron emission tomography for radiation treatment planning. Strahlenther Onkol 181(8):483–499
101. Picchio M et al (2010) Clinical evidence on PET/CT for radiation therapy planning in prostate cancer. Radiother Oncol 96(3):347–350
102. Greene FI, Balch CM, Fleming ID, et al (2002) In: The American Joint Committee on Cancer (ed) AJCC cancer staging manual. Springer, New York, pp 309–316
103. Bostwick DG (1997) Staging prostate cancer–1997: current methods and limitations. Eur Urol 32(Suppl 3):2–14
104. Yu KK et al (1997) Detection of extracapsular extension of prostate carcinoma with endorectal and phased-array coil MR imaging: multivariate feature analysis. Radiology 202(3):697–702
105. Hull GW et al (2002) Cancer control with radical prostatectomy alone in 1,000 consecutive patients. J Urol 167(2 Pt 1):528–534
106. Catalona WJ, Ramos CG, Carvalhal GF (1999) Contemporary results of anatomic radical prostatectomy. CA Cancer J Clin 49(5):282–296
107. Bonekamp D, Macura KJ (2008) Dynamic contrast-enhanced magnetic resonance imaging in the evaluation of the prostate. Top Magn Reson Imaging 19(6):273–284
108. Yu KK et al (1999) Prostate cancer: prediction of extracapsular extension with endorectal MR imaging and three-dimensional proton MR spectroscopic imaging. Radiology 213(2):481–488
109. Masterson TA, Touijer K (2008) The role of endorectal coil MRI in preoperative staging and decision-making for the treatment of clinically localized prostate cancer. MAGMA 21(6):371–377
110. Naya Y, Babaian RJ (2003) The predictors of pelvic lymph node metastasis at radical retropubic prostatectomy. J Urol 170(6 Pt 1):2306–2310
111. Wymenga LF et al (2001) Routine bone scans in patients with prostate cancer related to serum prostate-specific antigen and alkaline phosphatase. BJU Int 88(3):226–230
112. Tamada T et al (2011) MRI appearance of prostatic stromal sarcoma in a young adult. Korean J Radiol 12(4):519–523
113. Lu-Yao GL, Yao SL (1997) Population-based study of long-term survival in patients with clinically localised prostate cancer. Lancet 349(9056):906–910
114. Holmberg L et al (2002) A randomized trial comparing radical prostatectomy with watchful waiting in early prostate cancer. N Engl J Med 347(11): 781–789
115. Edge SB et al (2010) Prostate. In: AJCC cancer staging handbook. Springer, New York, pp 525–538
116. National Comprehensive Cancer Network (NCCN) (2012) Clinical practice guidelines in oncology: prostate cancer. National Comprehensive Cancer Network, Fort Washington
117. Slawin KM, Diblasio CJ, Kattan MW (2004) Minimally invasive therapy for prostate cancer: use of nomograms to counsel patients about the choice and probable outcome of therapy. Rev Urol 6(Suppl 4):S3–S8
118. Coakley FV et al (2002) Blood loss during radical retropubic prostatectomy: relationship to morphologic features on preoperative endorectal magnetic resonance imaging. Urology 59(6):884–888
119. Paparel P et al (2009) Recovery of urinary continence after radical prostatectomy: association with urethral length and urethral fibrosis measured by preoperative and postoperative endorectal magnetic resonance imaging. Eur Urol 55(3):629–637
120. Leibel SA et al (2002) Intensity-modulated radiotherapy. Cancer J 8(2):164–176
121. Pollack A et al (2003) Radiation therapy dose escalation for prostate cancer: a rationale for IMRT. World J Urol 21(4):200–208
122. Pollack A et al (2004) Prostate cancer radiotherapy dose response: an update of the fox chase experience. J Urol 171(3):1132–1136
123. Kuban D et al (2003) Hazards of dose escalation in prostate cancer radiotherapy. Int J Radiat Oncol Biol Phys 57(5):1260–1268
124. Roach M 3rd et al (1996) Prostate volumes defined by magnetic resonance imaging and computerized tomographic scans for three-dimensional conformal radiotherapy. Int J Radiat Oncol Biol Phys 35(5): 1011–1018
125. Debois M et al (1999) The contribution of magnetic resonance imaging to the three-dimensional treatment planning of localized prostate cancer. Int J Radiat Oncol Biol Phys 45(4):857–865
126. Rasch C et al (1999) Definition of the prostate in CT and MRI: a multi-observer study. Int J Radiat Oncol Biol Phys 43(1):57–66
127. Steenbakkers RJ et al (2003) Reduction of dose delivered to the rectum and bulb of the penis using MRI delineation for radiotherapy of the prostate. Int J Radiat Oncol Biol Phys 57(5):1269–1279
128. Cellini N et al (2002) Analysis of intraprostatic failures in patients treated with hormonal therapy and radiotherapy: implications for conformal therapy planning. Int J Radiat Oncol Biol Phys 53(3): 595–599
129. Pucar D, Sella T, Schoder H (2008) The role of imaging in the detection of prostate cancer local recurrence after radiation therapy and surgery. Curr Opin Urol 18(1):87–97
130. Pickett B et al (1999) Static field intensity modulation to treat a dominant intra-prostatic lesion to 90 Gy compared to seven field 3-dimensional

radiotherapy. Int J Radiat Oncol Biol Phys 44(4): 921–929

131. De Meerleer G et al (2005) The magnetic resonance detected intraprostatic lesion in prostate cancer: planning and delivery of intensity-modulated radiotherapy. Radiother Oncol 75(3):325–333
132. van Lin EN et al (2006) IMRT boost dose planning on dominant intraprostatic lesions: gold marker-based three-dimensional fusion of CT with dynamic contrast-enhanced and 1H-spectroscopic MRI. Int J Radiat Oncol Biol Phys 65(1): 291–303

9

MR Imaging of the Scrotum

Michele Bertolotto, Francesca Cacciato,
Matilde Cazzagon, and Lorenzo E. Derchi

9.1 Introduction

Although ultrasonography remains the primary imaging modality in the diagnosis of scrotal pathology, magnetic resonance (MR) imaging may provide valuable additional information. Due to its increased panoramicity, it performs better with very large lesions, which are difficult to image in the limited field of view of the ultrasonographic probe. Another major strength over conventional ultrasound and Doppler modes is improved tissue characterization. Moreover, MR imaging can investigate heavily fibrotic or calcified testes, in which ultrasonography is inconclusive, and can detect flow in hypovascular lesions with a sensitivity rivaling that of contrast-enhanced ultrasonography [1].

9.2 Examination Technique

Scrotal MR imaging [2, 3] can be implemented with virtually every MR unit, even though image quality and signal-to-noise ratio is better with high-field-strength equipment. Susceptibility artifacts, which cause signal loss and image distortion at the air-tissue interface, are especially found at high field strength. To minimize this problem, it is recommended to use fast spin-echo instead of gradient echo sequences. Relatively low specific absorption rates (SAR) are used to minimize heating of the scrotum which, however, in a clinical setting is well below the threshold known to affect spermatogenesis in mammals [4].

9.2.1 Coil Selection

A circular surface coil can be used placed on the patient's lower pelvis and centered over the scrotum [5]. In our clinical practice, however, we prefer multichannel phased-array coils for parallel imaging, such as cardiac coils, which provide high-definition images with excellent signal-to-noise ratio and increased panoramicity. Appropriate positioning of the scrotum is important. The testes should be arranged to maintain nearly equal distance from the coil [5, 6]. The penis is kept upward and taped against the abdominal wall. Towels or sponges are placed between the thighs to minimize motion artifact. Respiratory compensation may be used to reduce motion artifact, but image quality obtained without respiratory compensation is high enough for the diagnosis with reduced acquisition time [7].

M. Bertolotto, MD (✉) • F. Cacciato • M. Cazzagon
Department of Radiology, University of Trieste,
Ospedale di Cattinara, Strada di Fiume 447,
Trieste 34149, Italy
e-mail: bertolot@units.it

L.E. Derchi
Dicmi-Radiologia, University of Genova,
Largo R. Benzi 8, Genoa 16132, Italy

R. Manfredi, R. Pozzi Mucelli (eds.), *MRI of the Female and Male Pelvis*,
DOI 10.1007/978-3-319-09659-9_9,

9.2.2 Imaging Planes and Pulse Sequences

The testes are usually examined along the longitudinal and transverse axes. Coronal and axial acquisitions allow direct comparison of the two testes and evaluation of the spermatic cord [6]. Scanning along sagittal and oblique planes may be indicated in selected cases.

The scanning protocol varies depending on the clinical setting. In general, non-contrast-enhanced T1- and T2-weighted images are first obtained followed by contrast-enhanced T1-weighted images or dynamic contrast-enhanced scans if necessary. We commonly obtain high-resolution thin contiguous sections of 3–4 mm. Parallel imaging techniques are applied to reduce scan time by accelerating image acquisition. This eventually results in increased patient comfort and acceptability, decreased patient movement, and better image quality.

T1-weighted images provide anatomical information of the testis, epididymis, and spermatic cord. T2-weighted images are usually the most informative; they show a variety of tissue contrast depending on the echo time [2, 8]. A standard T2 contrast between the testes, epididymis, spermatic cord, and surrounding fat tissue is obtained with an echo time of about 100 ms; long echo times (250–350 ms) produce heavily T2-weighted images in which fluid displays very high signal intensity while the testes and epididymis have intermediate signal intensity. Diffusion-weighted imaging (DWI) of the scrotum is still on a stage of investigation [9–13]. It is usually performed along the axial plane using a single-shot, multislice, spin-echo planar sequence with b-values of 0 and 800–1,000 s/mm^2.

Contrast-enhanced MR imaging gives information on tissue perfusion. Comparison between the contrast enhancement of the right and left testes facilitates the evaluation of the affected-side testis with the unaffected-side testis serving as a normal control. Usually, high-resolution T1-weighted images with fat suppression are obtained before and after gadolinium contrast administration and image subtraction [14]. Dynamic contrast-enhanced imaging is indicated in selected cases only. It can be obtained in the coronal plane using fat-suppressed fast spin-echo images or ultrafast spoiled gradient echo sequences when a high temporal resolution is required, with the disadvantage of lower spatial resolution and increased artifacts. Image subtraction is recommended.

9.3 Normal Anatomy

The normal adult testes show intermediate- and high signal intensity on T1- and T2-weighted images, respectively [5, 6]. Intermediate signal intensity is displayed on heavily T2-weighted images. On DWI images the normal testes present homogeneous high signal intensity (Fig. 9.1). Aging is associated with structural and functional alterations resulting in decreased signal restriction [15]. The mediastinum testis appears as a low-signal-intensity band along the long axis of the testis. On heavily T2-weighted images, fine fibrous septa are often seen as thin linear structures of low signal intensity extending from the mediastinum testis and dividing the lobules. The tunica albuginea and the visceral layer of the tunica vaginalis are stuck together showing low signal intensity in all sequences [5, 6, 16]. The signal intensity of the epididymis is similar to that of the testis on T1-weighted images but lower on T2-weighted images [5, 6, 17]. The vas deferens can be traced from the tail of the epididymis to the spermatic cord on T2-weighted images.

The fluid between the visceral and the parietal layers of the tunica vaginalis shows high and very high signal intensity on T2- and heavily T2-weighted images, respectively [5, 6].

9.4 Congenital Abnormalities

MR imaging is the imaging modality of choice in investigating patients with ambiguous genitalia, which are usually associated with complex malformations of the genitourinary tract. The most common isolated abnormalities of the scrotal content are undescended testis and congenital hydro-

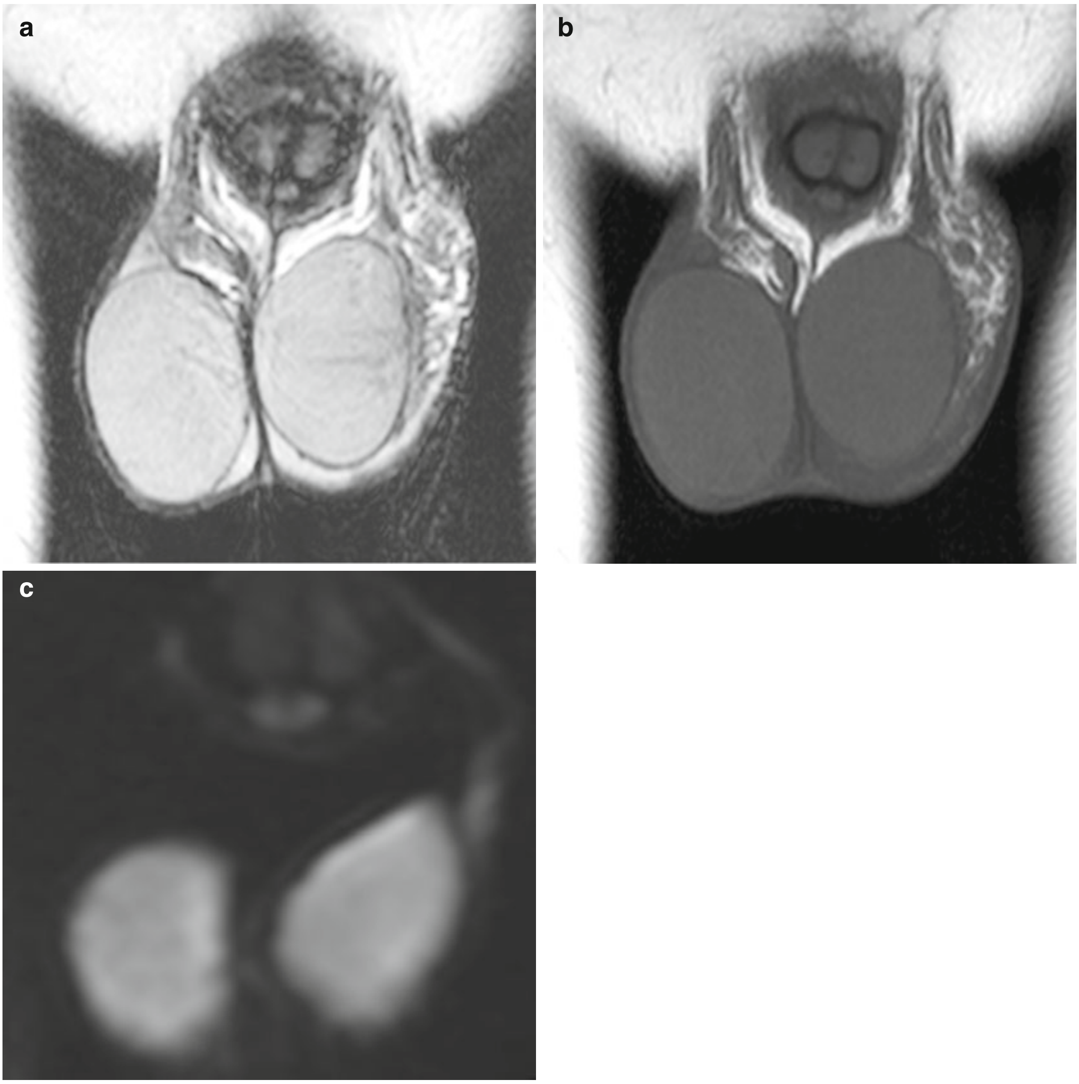

Fig. 9.1 Appearance of the normal testes on MR imaging. Coronal images. (**a**, **b**) The testes show high signal intensity on T2- and intermediate signal intensity on T1-weighted images, respectively. The tunica albuginea has low signal intensity in all sequences. (**c**) Diffusion-weighted image ($b = 1{,}000$ s/mm^2) shows signal restriction of the testicular parenchyma

celes. Bell-clapper deformity is difficult to be detected. Polyorchidism and adrenal rests are rare.

9.4.1 Undescended Testis

Undescended testis is the most common genitourinary anomaly with a prevalence at birth of 2–5 % and up to 30 % in preterm infants. Approximately 2:3 undescended testes will spontaneously descend within the first months of life, with a prevalence at the age of 1 year of 0.8 %. The testis may be located at any point along the descent route from the retroperitoneum to the external inguinal ring [18]. It can be ectopic, but in general it is found along the normal path of descent: approximately 70 % in the inguinal canal, 20 % in the prescrotal region just beyond the external inguinal ring, and the remaining in the abdomen. About 3–5 % of patients with undescended testis

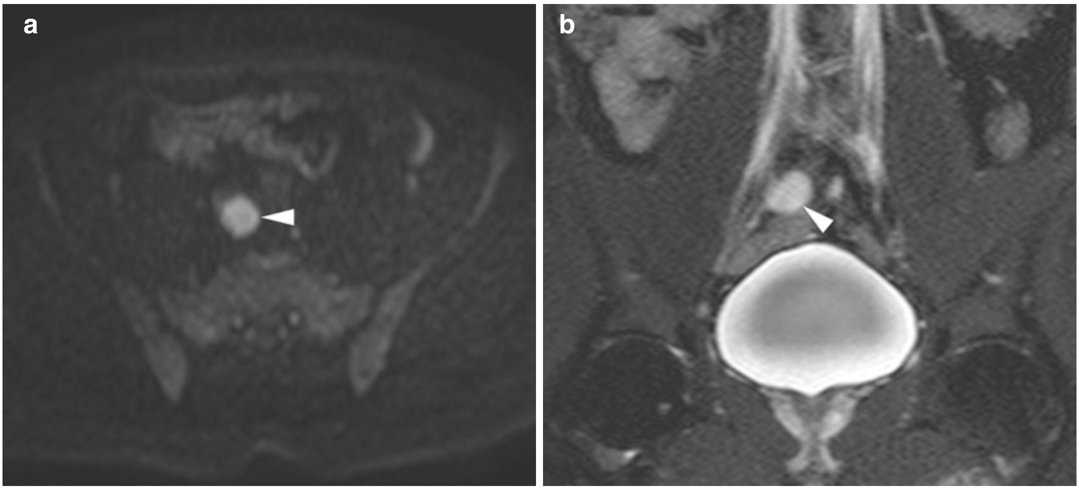

Fig. 9.2 An undescended testis located in the abdomen near the right iliac vessels. (**a**) Axial diffusion-weighted image ($b = 800$ s/mm^2) identifies the retained testis as a lesion with signal restriction (*arrowhead*). (**b**) Coronal T2-weighted image confirming the location of the testis adjacent to the right iliac vessels (*arrowhead*)

have congenital absence of the testis. It is conceivable that in most cases, the testis was originally present during fetal life and then regressed.

The major complications of cryptorchism are malignant degeneration, infertility, torsion, and bowel incarceration because of an associated indirect inguinal hernia. Tumors are far more common in an undescended testis than in a normally positioned testis.

Imaging is indicated to search for the location of the cryptorchid testis to evaluate its size and to seek for parenchymal lesions. The cryptorchid testis is usually smaller relative to the normally located testis because of testicular dystrophy and degeneration [19].

Ultrasonography can reliably detect testicles located in the inguinal canal or between the external inguinal ring and the scrotal neck. Detecting the testicle in intra-abdominal locations is often difficult or even impossible. MR imaging allows detecting the testis not only in the inguinal canal but also in the abdomen. High abdominal testes, however, may be difficult to identify, and a recent meta-analysis of an American pediatric group shows a low sensitivity [20]. DWI performed at high b-values (800–1,000 s/mm^2) improves visualization of the undescended testis which appears hyperintense in most of cases [13] (Fig. 9.2). Severely atrophic testes, however, may show low signal intensity on diffusion-weighted imaging [21] (Fig. 9.3).

9.4.2 Congenital Hydrocele

Congenital hydrocele occurs when there is incomplete closure of the processus vaginalis. It is very common in newborn but is encountered in less than 1 % of adults. The patent processus vaginalis permits flow of peritoneal fluid into the scrotum. Indirect inguinal hernias can be associated. There are two subtypes of congenital hydrocele: the encysted type, also called spermatic cord cyst, with no communication with the peritoneum and with the tunica vaginalis, and the funicular type, also called funiculocele, which communicates with the peritoneum at the internal ring but does not surround the testis.

Either ultrasonography or MR imaging can be used to evaluate congenital hydrocele. On ultrasound, it appears as an anechoic fluid collection surrounding the anterolateral aspects of the testis extending to the inguinal canal or as a well-demarcated anechoic mass, associated with either a patent or a closed internal ring, separated from the testis and epididymis which are displaced inferiorly. On MR imaging hydrocele is homogeneous and hypointense on T1-weighted images

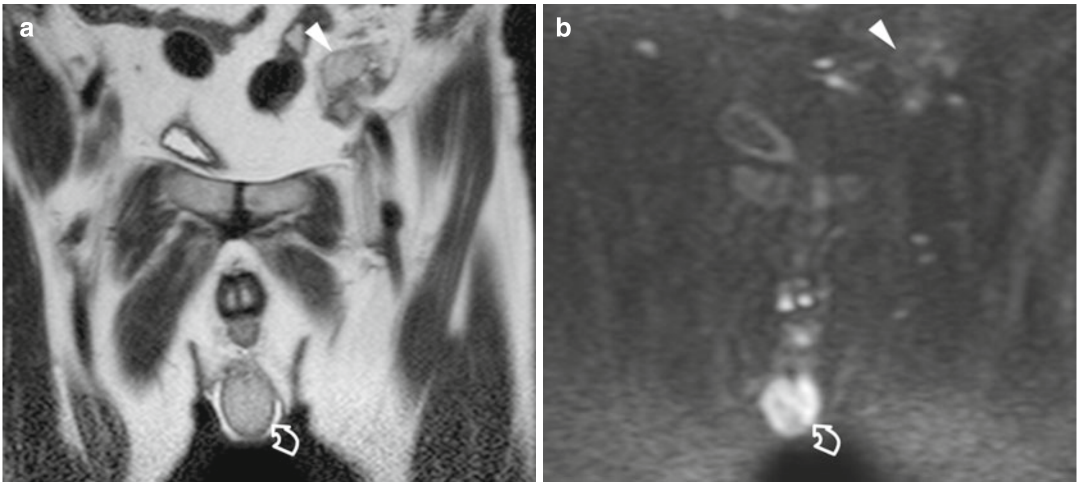

Fig. 9.3 An undescended testis located in the abdomen near the left iliac vessels. (**a**) Coronal T2-weighted image showing a normally descended right testis (*curved arrow*) and a small left testis adjacent to the left iliac vessels (*arrowhead*). (**b**) Coronal diffusion-weighted image ($b = 1{,}000$ s/mm^2) fails to show signal restriction of the retained testis (*arrowhead*), which was markedly dystrophic and poorly vascularized at surgery (*arrowhead*). The normally descended right testis (*curved arrow*) displays signal restriction

and hyperintense on T2-weighted images, characteristic of fluid. Occasionally, septations are identified, although prominent septations should suggest a hematocele or pyocele. Patency of the processus vaginalis with entry of peritoneal fluid into the scrotal sac is best demonstrated in heavily T2-weighted images.

9.4.3 Bell-Clapper Deformity

Failure of the normal posterior anchoring of the epididymis and testis is called bell-clapper deformity because it leaves the testis free to swing and rotate within the tunica vaginalis of the scrotum like the clapper inside of a bell. It is a common precondition for testicular torsion, with a 12 % incidence in an autopsy series.

Bell-clapper deformity itself is hard to be detected by imaging. A suggestive feature is the abnormal direction of the long axis of the testis on the axial plane, in the right-to-left or anterior-posterior direction with the epididymis right upon the testis (Fig. 9.4). The deformity is more often recognized in heavily T2-weighted images when hydrocele is present and the tunica vaginalis completely encircles the epididymis, distal spermatic cord, and testis rather than attaching to the posterolateral aspect of the testis.

9.4.4 Polyorchidism

Polyorchidism is a rare congenital abnormality where more than two testes are present which may have separate or common spermatic cords and epididymis. Although three testes is the most common form, as many as five have been reported. In approximately 75 % of cases, the supernumerary testes are intrascrotal. Of the remaining cases, 20 % of the supernumerary testes are inguinal and 5 % retroperitoneal. On ultrasonography the accessory testis presents with the same echogenicity, echotexture, and vascular pattern as the normal testes. On MR imaging it has the same signal characteristics as the normal testes: intermediate signal intensity on T1-weighted images, high signal intensity on T2-weighted images, and hyperintensity on DWI (Fig. 9.5). Thanks to its panoramicity and improved tissue characterization, MR imaging is helpful in making a definitive diagnosis in case of equivocal ultrasound findings or extrascrotal testes [22].

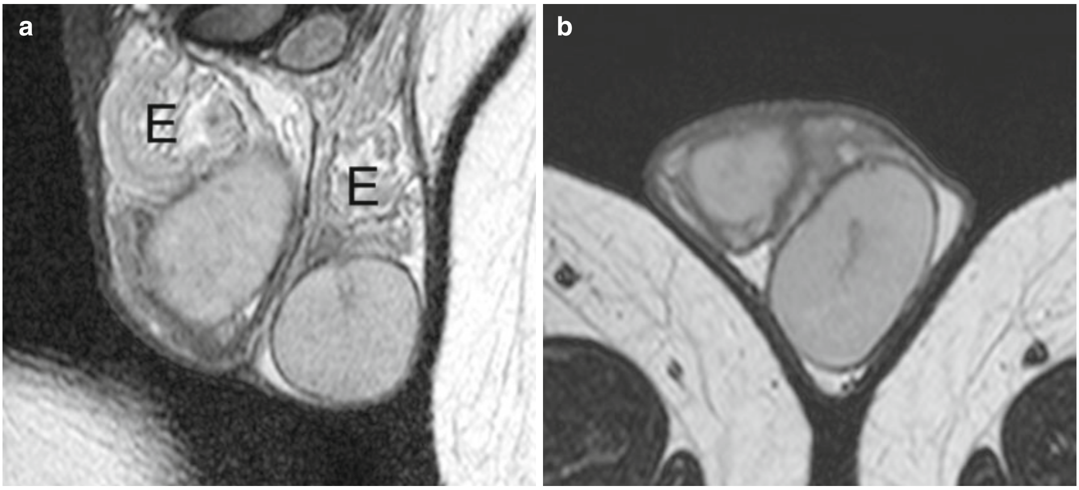

Fig. 9.4 Surgically proved bell-clapper deformity. The patient had several episodes of acute scrotal pain on both sides which released spontaneously, interpreted as recurrent episodes of low-degree torsion with spontaneous detorsion. Coronal (**a**) and axial (**b**) T2-weighted images show the major axis of the testes laying on an axial plane, the right testis in right-to-left direction, the left in anterior-posterior direction. The epididymis (*E*) is right upon the testes in both sides

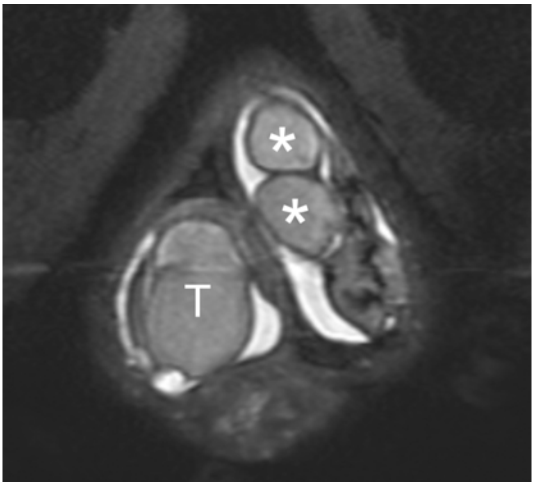

Fig. 9.5 Polyorchidism. Oblique-coronal T2-weighted image shows a single testis (*T*) on the right hemiscrotum and two testes (*asterisks*) in the left hemiscrotum

9.4.5 Testicular Adrenal Rests

Testicular adrenal rests derive from the hyperplasia of aberrant adrenal cortical tissue that descends during prenatal life with the testes or ovary. In approximately 8 % of patients with congenital adrenal hyperplasia, the elevated levels of serum adrenocorticotropic hormone stimulates these rests to grow. They are bilateral in more than 80 % of cases, usually presenting as palpable masses inside of or close to the mediastinum testis.

Testicular adrenal rests present on ultrasound as unilateral or bilateral lobulated masses with variable echogenicity located within or adjacent to the mediastinum testis. Acoustic shadowing may be due to fibrotic changes or calcifications. Lesions are isointense to the surrounding normal tissue of the testis on T1-weighted images and hypointense to the surrounding normal tissue of the testis on T2-weighted images with and without fat suppression. Strong enhancement is demonstrated after gadolinium administration.

9.5 Ischemic Disorders

The mainstay of imaging ischemic scrotal disorders is color Doppler ultrasonography. In high-degree torsion non-enhancement of the testis after gadolinium administration has been reported as highly sensitive and specific for torsion [14], but MR imaging is more expensive and time-consuming than color Doppler ultrasonography and therefore has no or minimum practical role in the setting of acute scrotal pain. In low-degree torsion perfusion is reduced compared with the healthy contralateral testis [23]. In acute

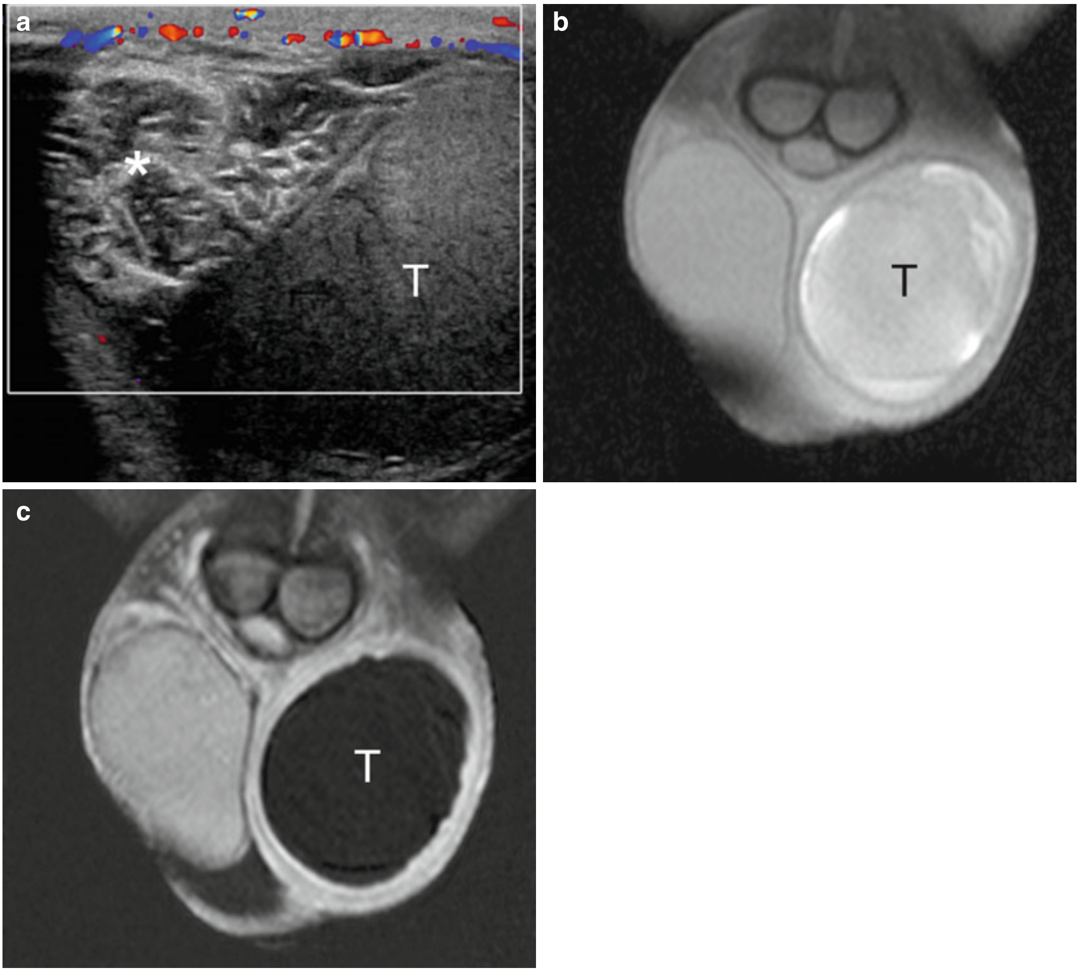

Fig. 9.6 Long-standing high-degree left testicular torsion. (**a**) Color Doppler interrogation shows an avascular left testis (*T*) and a twisted spermatic cord (*asterisk*). The paratesticular tissues display increased vascularization. (**b**) T1-weighted coronal image with fat suppression shows inhomogeneous left testis (*T*) with high signal intensity due to hemorrhagic changes. (**c**) Gadolinium-enhanced subtracted image showing complete lack of vascularization of the left testis (*T*) and slight hyperemia of the surrounding tissues

testicular torsion, the testis has normal signal intensity on both T1- and T2-weighted images and high signal intensity on DWI [9]. The twisted spermatic cord is best demonstrated on transaxial T2-weighted and contrast-enhanced images [24]. In the subacute and chronic stages, the signal intensity of the testis changes due to necrosis and hemorrhagic components (Fig. 9.6).

9.5.1 Torsion of the Appendages

The normal appendages are typically seen only when hydrocele is present [25–27]. They usually display intermediate signal intensity on T2-weighted images. In appendiceal torsion, a twisted and swollen appendage is usually seen as a hyperintense oval structure on T2-weighted images lacking intralesional enhancement with ring-like perilesional enhancement on dynamic subtraction contrast-enhanced images [2, 28].

9.5.2 Segmental Testicular Infarction

MR imaging has been claimed as a problem-solving technique in doubtful cases of segmental

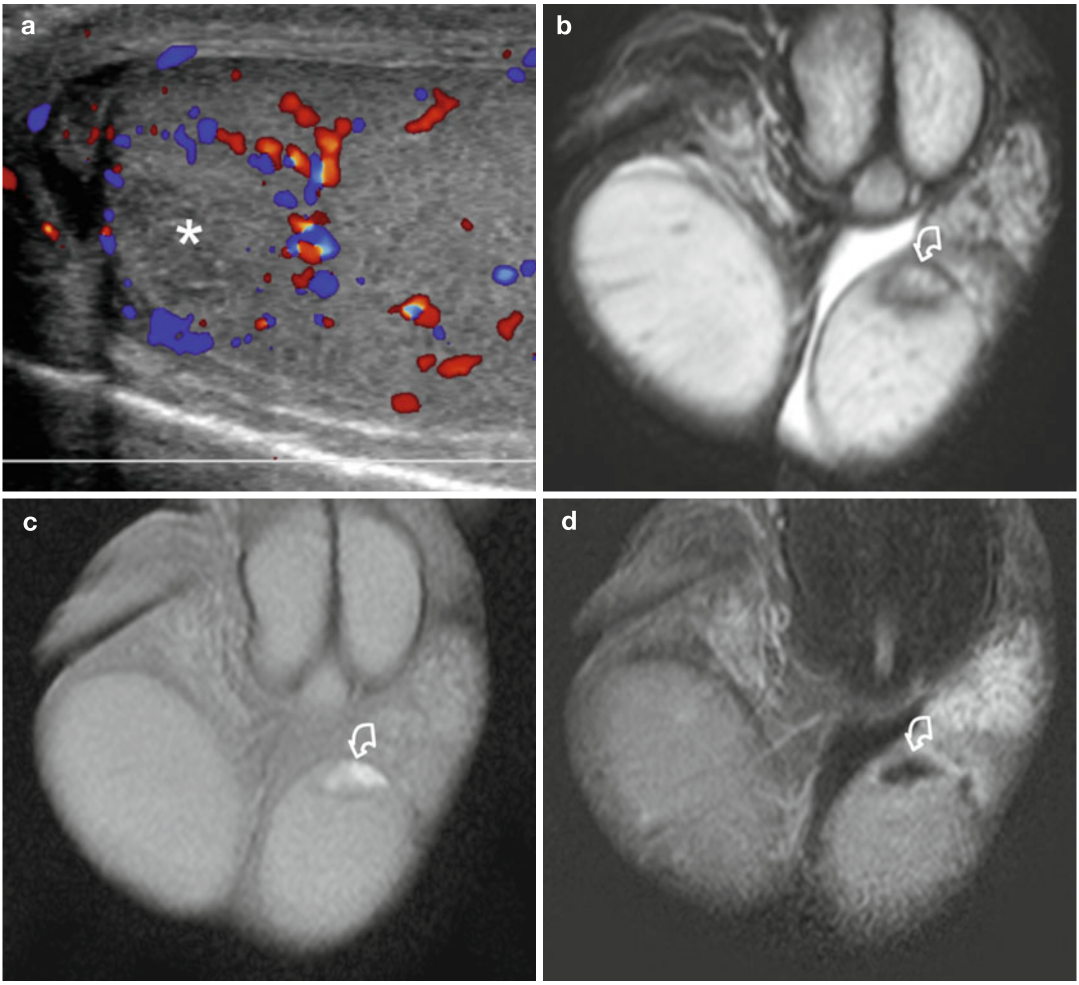

Fig. 9.7 Segmental testicular infarction. Patient presenting with acute left scrotal pain. (**a**) Color Doppler interrogation shows an avascular, slightly hypoechoic area (*asterisk*) in the upper pole of the left testis with perilesional hypervascularization. (**b**) T2-weighted coronal image showing the lesion (*curved arrow*) with inhomogeneous signal intensity. (**c**) T1-weighted image showing the hyperintense lesion (*curved arrow*) due to hemorrhagic changes. (**d**) Gadolinium-enhanced subtracted image shows lack of vascularization of the lesion (*curved arrow*) and slight perilesional hypervascularization

testicular infarction [29, 30]. On T1-weighted MR images, infarcts may appear isointense to the surrounding normal testicular parenchyma, occasionally with foci of high signal intensity due to hemorrhage.

On T2-weighted images, the signal intensity is variable. The lesion is avascular after gadolinium contrast administration (Fig. 9.7), often with an enhancing perilesional rim in subacute infarction [29, 31]. Although segmental testicular infarction presents with characteristic MR features, this investigation is not commonly performed in our clinical practice, as similar information is provided by contrast-enhanced ultrasonography which is quicker and with a lower cost [32].

9.6 Inflammation

MR imaging provides a panoramic view of the extension of the disease to adjacent organs in severe scrotal inflammation. Involvement of the perineum and/or abdominal region can be investigated. MR imaging enables a diagnosis of postinflammatory testicular ischemia, testicular hemorrhagic and necrotic changes, epididymo-orchitis with abscess formation, and intrascrotal fistulas [33]. In acute epididymitis the enlarged epididymis has increased signal intensity relative to the normal side on T2-weighted images and clearly shows intense contrast enhancement on dynamic subtraction contrast-enhanced images. Abscesses are typically hypointense on T1-weighted images, hyperintense on T2-weighted images, and display high signal intensity on DWI images. They do not enhance, while the surrounding tissues show avid enhancement.

9.7 Testicular Masses

Not all intratesticular lesions are tumors, and not all testicular tumors are malignant. Granulomata, focal orchitis, fibrous pseudotumors, and spontaneous hematomas are often difficult to differentiate from tumors on ultrasound examination. In many cases, however, it is suggested that the diagnosis integrates the history of the patient, clinical presentation, and the superior capability of MR imaging for tissue characterization and evaluation of intralesional flows.

The patient's age at presentation is important. Germ cell tumors are prevalent in the young while lymphomas in the elderly, and some histotypes are much more prevalent in prepuberal than in puberal boys. Clinical correlation is vital: many nonneoplastic intratesticular conditions are likely to manifest with acute scrotum. One needs to be cautious, however, because tumors can also occasionally manifest with pain. A history of fever or trauma may suggest a nonneoplastic origin as well. Tumor markers often help in the differential diagnosis between testicular tumors and nonneoplastic lesions. Normal serum tumor markers, however, do not rule out testicular neoplasms. In any case, traumatic and inflammatory changes evolve rapidly; if a nonneoplastic pathology is suspected, a short-term follow-up examination will likely allow differential diagnosis with tumor.

9.7.1 Dilated Rete Testis

Tubular ectasia of the rete testis is a benign nonneoplastic condition thought to result from partial or complete obliteration of the efferent ducts. It is more common in men over the age of 55 years, often bilateral, and frequently associated with spermatoceles.

Using modern ultrasonographic equipment, a tubular ectasia of the rete testis is characterized in virtually all patients; in case of doubt, however, MR can show the dilatation of multiple small tubules of the rete testis appearing hyperintense on T2-weighted and heavily T2-weighted images. After gadolinium administration no internal enhancement is seen [16].

9.7.2 Testicular Epidermoid Cyst

The classic ultrasonographic appearance of testicular epidermoid cyst is the "onion ring" pattern, consisting in alternating rings of low and high echogenicity, which represent layers of keratinized squamous epithelium. This appearance is virtually pathognomonic, but epidermoid cysts with an atypical appearance may be difficult to differentiate from tumors. On MR imaging an epidermoid cyst typically shows on T2-weighted images alternating zones of high- and low signal intensity [1, 34, 35] and signal restriction on DWI [11]. This appearance, however, is not constant (Fig. 9.8). Signal intensity on T1-weighted images is variable. No matter the imaging features, epidermoid cysts do not demonstrate internal flow on Doppler interrogation nor enhancement after gadolinium administration [16].

9.7.3 Spontaneous Testicular Hematoma

Spontaneous intratesticular hematoma is a rare entity with few reports in the literature, mimicking a neoplasm on grayscale ultrasonography. Diagnosis of a nonneoplastic condition, however, is suggested as the lesion lacks vascularization on color Doppler interrogation and contrast-enhanced

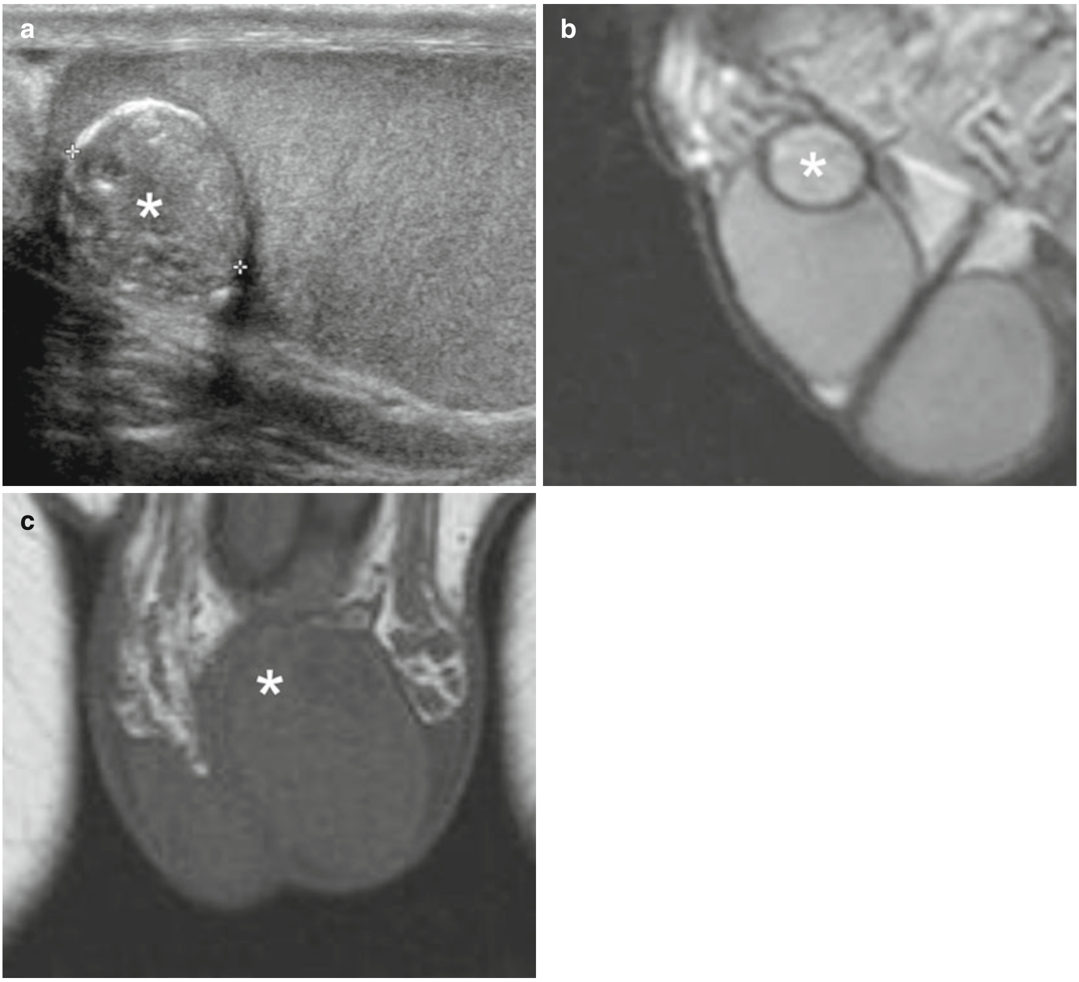

Fig. 9.8 Epidermoid cyst presenting as a palpable nodule of the left testis. (**a**) Grayscale ultrasonography showing a slightly inhomogeneous lesion isoechoic to the surrounding normal tissue of the testis, with a few wall calcifications (*asterisk*). (**b**) Sagittal T2-weighted image shows a slightly hyperintense nodule (*asterisk*) with hypointense wall. (**c**) Coronal T1-weighted image showing the lesion (*asterisk*) isointense to the surrounding normal tissue of the testis, which was completely avascular after gadolinium contrast administration (not shown)

ultrasonography [36, 37]. MR imaging confirms the diagnosis showing a lesion with the characteristic signal changes of blood. No enhancement is seen after gadolinium contrast administration (Fig. 9.9). Follow-up is recommended to ascertain lesion size reduction and signal intensity changes over time of the blood content.

9.7.4 Fat-Containing Masses

Testicular lipoma is a rare condition now being increasingly reported secondary to the widespread use of scrotal sonography [38–40]. On ultrasonography lipoma usually consists of a homogeneously hyperechoic non-shadowing lesion without flow on color Doppler interrogation. The diagnosis is confirmed on MR imaging which shows the signal intensity characteristics of fat in all sequences [22] (Fig. 9.10).

Testicular lipomatosis is a recently described entity occurring in patients with Cowden disease and in Bannayan-Riley-Ruvalcaba syndrome [41] in which nonneoplastic fat-containing hamartomas are seen. On ultrasonography testicular lipomatosis presents with multiple non-shadowing, uniformly hyperechoic small round foci of various sizes in both testes [42]. Although virtually

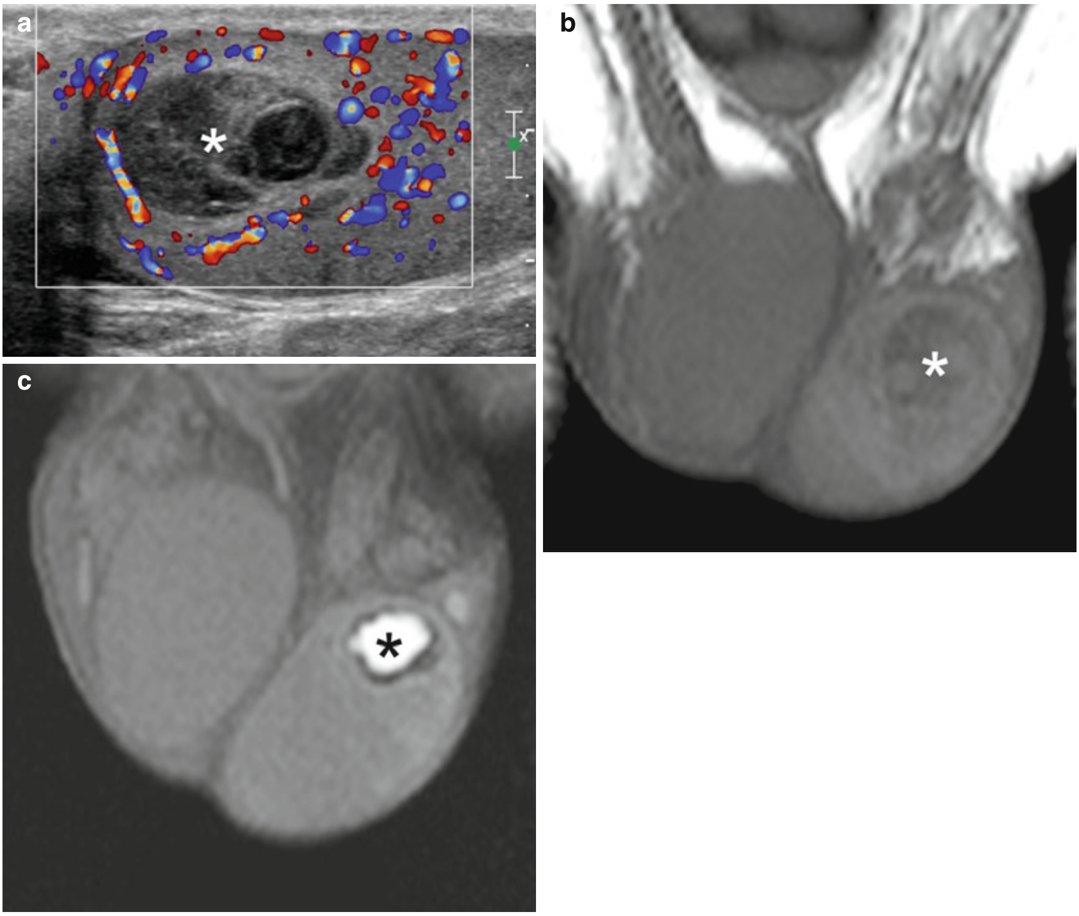

Fig. 9.9 Spontaneous testicular hematoma. The patient presented with acute left scrotal pain for 3 h with no history of trauma. (**a**) Color Doppler interrogation shows an inhomogeneously hypoechoic left testicular lesion lacking vascularization (*asterisk*). (**b**) Coronal T1-weighted image obtained within 24 h after ultrasonography shows an inhomogeneous isointense lesion (*asterisk*) which was avascular after gadolinium contrast administration (not shown). (**c**) Follow-up MR investigation obtained 2 months after the previous study. Coronal T1-weighted image shows a hyperintense lesion (*asterisk*) which is reduced in size, characterized by hypointense rim due to blood degradation

diagnostic of testicular lipomatosis in the context of known Cowden disease, this pattern may also be due to fibrotic changes and other conditions. MR imaging allows differential diagnosis showing multiple foci in both testes with the signal intensity characteristics of fat [43].

9.7.5 Calcifying, Sclerosing, and Fibrotic Lesions

Heavily calcified adrenal rests [3], epidermoid cysts with peripheral and intralesional calcifications, calcified intratesticular hematomas, and calcifying, sclerosing, and fibrotic tumors such as cavernous hemangioma [44], large-cell calcifying Sertoli cell tumor [34], and sclerosing Sertoli cell tumor [45] cannot be investigated effectively with ultrasonographic modes due to back attenuation. MR imaging is indicated in these patients to evaluate the lesion, attempt tissue characterization, and investigate whether it is vascularized or not [45].

9.7.6 Heavily Calcified and Strongly Heterogeneous Testes

MR imaging is indicated to rule out clinically suspected testicular lesions in patients with heterogeneous testicular parenchyma on

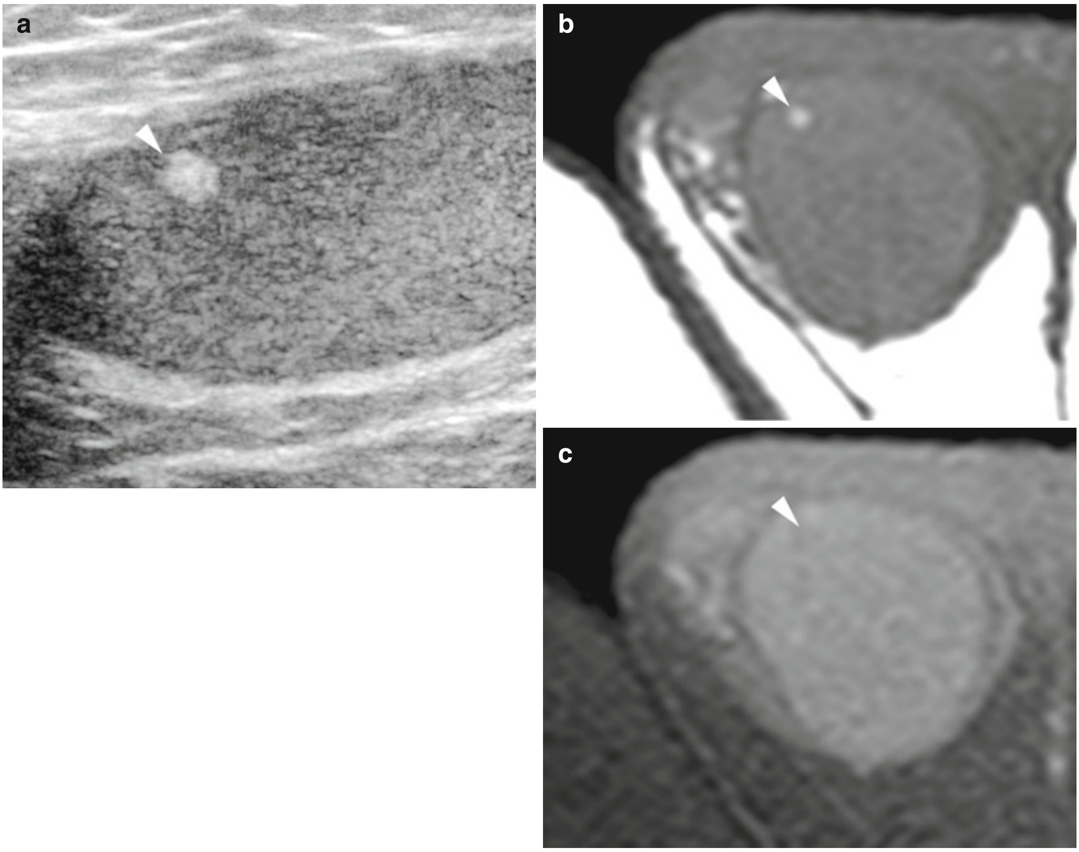

Fig. 9.10 Testicular lipoma. (**a**) Grayscale ultrasonography shows a small hyperechoic right testicular lesion (*arrowhead*). (**b**) The lesion (*arrowhead*) is hyperintense on axial T1-weighted image and displays signal loss in the T1-weighted fat-suppressed image (**c**)

ultrasonography (Fig. 9.11); testicular fibrotic changes either after inflammation, surgery, or trauma; multiple testicular calcifications; or microlithiasis with heavily calcified testes. Fibrosis, in particular, can be very worrisome on ultrasonography, but the low signal intensity in T1- and T2-weighted images, sometimes radiating from the mediastinum, is indicative of a benign lesion.

9.7.7 Other Testicular Neoplasms

A recent study shows that T2-weighted and contrast-enhanced T1-weighted images have the potential to characterize seminomatous from nonseminomatous testicular neoplasms [46]. A seminoma usually presents as a rounded or multinodular sharply defined lesion with predominantly low signal intensity on T2-weighted images. Fibrovascular septa showing greater enhancement than tumor tissue after gadolinium administration are typically detected. Nonseminomatous tumors usually appear as heterogeneous masses on T2-weighted images with heterogeneous enhancement after gadolinium administration. In our experience, however, this appearance is far from sensitive or specific. Dynamic contrast-enhanced MR imaging defines three different types of time-intensity curves. In type I the signal gradually continues to increase; in type II an initial upstroke is followed by either a plateau or a gradual increase in the late phase; in type III an initial upstroke is followed by gradual washout. The normal testis is characterized by an enhancement with a type I curve, while type II is prevailing in benign lesions and type III in

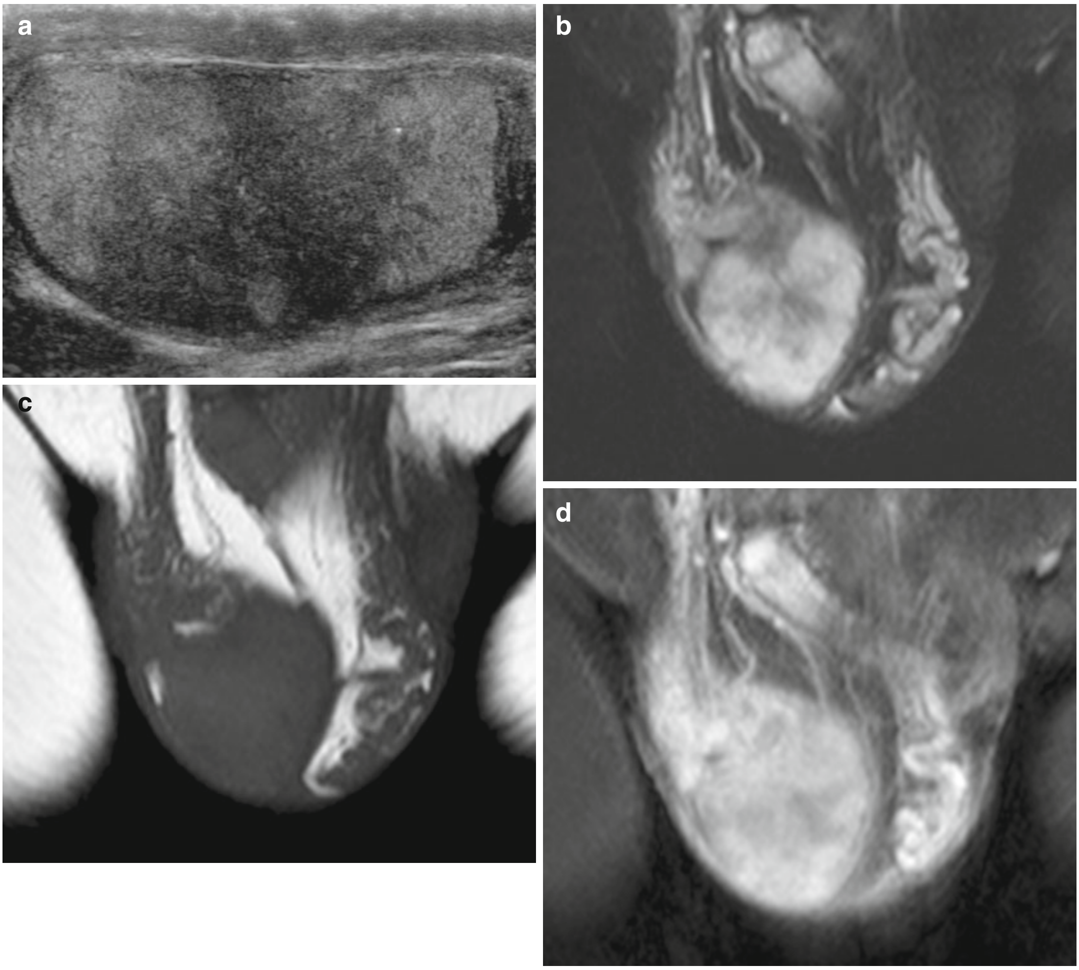

Fig. 9.11 MR investigation of a patient with inconclusive ultrasonographic scan. (**a**) Grayscale ultrasonography shows a markedly inhomogeneous right testis. (**b**–**d**) T2-weighted, T1-weighted, and T1-weighted fat-suppressed images obtained after gadolinium contrast administration allow to ruling testicular lesions

malignant lesions [47]. Malignant tumors often show increased signal restriction in DWI compared to the normal testis [10]. Despite these promising results, in the common clinical practice the evaluation of time-intensity curves and ADC values is unable to differentiate benign and malignant testicular lesions clearly.

9.8 Paratesticular Lesions

Approximately 70 % of paratesticular tumors are benign. Ninety percent are found in the spermatic cord followed by the epididymis and testicular tunicae. Lipoma is the most common tumor of the spermatic cord in adults followed by leiomyoma, lymphangioma, and angioleiomyoma [16]. While liposarcoma is the most common malignant neoplasm of the spermatic cord in adults, rhabdomyosarcoma is the most common paratesticular neoplasm in children and adolescents. Other sarcomas are rare. Adenomatoid tumor accounts for approximately one-third of all neoplasms of the paratesticular tissues. This benign lesion is more frequent in the tail of the epididymis but may develop anywhere in the epididymis and also in the spermatic cord and tunica albuginea, where it can mimic a testicular lesion.

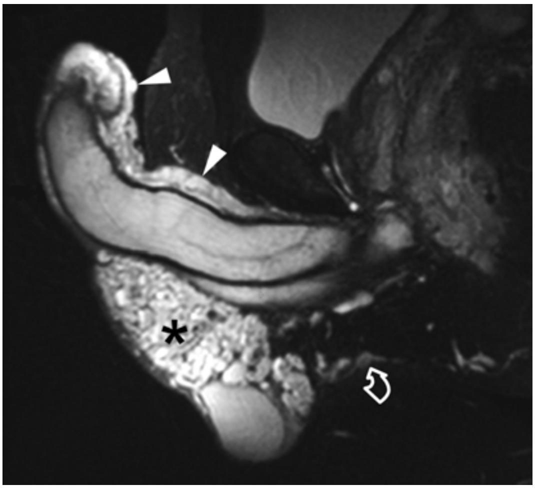

Fig. 9.12 Giant penoscrotal cavernous hemangioma. T2-weighted sagittal MR image showing a high-signal-intensity lesion involving the scrotum (*asterisk*), the anterior portion of the perineum (*curved arrow*), and the dorsal aspect of the penis (*arrowheads*)

Tumors of the tunicae and of the scrotal wall are very rare. The most common are malignant mesothelioma of the tunica vaginalis of the testis and scrotal hemangioma. Metastatic deposits are seen in patients with a known malignancy in an advanced stage.

9.8.1 Scrotal Hemangioma

In patients with large scrotal hemangiomas, MR imaging is indicated to determine the anatomic extension of the lesion to the penis, scrotum, and anterior perineum. The lesion appears as a lobulated scrotal mass with intermediate signal intensity on T1-weighted images and high signal intensity on T2-weighted images (Fig. 9.12). Focal areas of signal void consistent with a thrombus can be recognized.

9.8.2 Extratesticular Epidermoid Cysts

Extratesticular epidermoid cysts are rare [48]. Inflammation leads to calcification of the cystic wall with subsequent calcification of the content. Complete local excision is considered the treatment of choice.

At ultrasonography the appearance of extratesticular epidermoid cysts varies from anechoic to hyperechoic depending on their content. Calcified lesions are echogenic with back attenuation. On MR imaging extratesticular epidermoid cysts are usually thin-walled, hypointense on T1-weighted images, and hyperintense on T2-weighted images and show signal restriction on DWI images. However, they may show heterogenous intensity on both T1- and T2-weighted images due to inner dense keratinous materials. Signal intensity is low in heavily calcified lesions. Gadolinium-enhanced images usually show only peripheral wall enhancement (Fig. 9.13).

9.8.3 Fibrous Pseudotumor

Fibrous pseudotumor represents a benign reactive fibrous proliferation that results in one or several paratesticular nodules, usually arising from the tunica vaginalis. It is the third most common extratesticular mass after lipoma and adenomatoid tumor. Lesions as large as 8 cm have been reported. There is hydrocele in 50 % of cases. Local excision can be performed and orchiectomy avoided. On ultrasonography, the typical appearance of fibrous pseudotumor is a hypoechoic mass or several tunical masses, sometimes with internal calcifications. On MR imaging, fibrous pseudotumors show uniformly intermediate-to-low signal intensity on T1-weighted images and are markedly hypointense on T2-weighted images (Fig. 9.14), with slow but persistent enhancement [22].

9.8.4 Other Extratesticular Tumors

Fat-containing lesions can be characterized on MR imaging (Fig. 9.15), but lipoma may be difficult to differentiate from liposarcoma. Lymphoma is suspected when a diffuse infiltration of the spermatic cord by tumor tissue is seen, surrounding the spermatic vessels whose course and caliber are preserved. Tumor tissue is

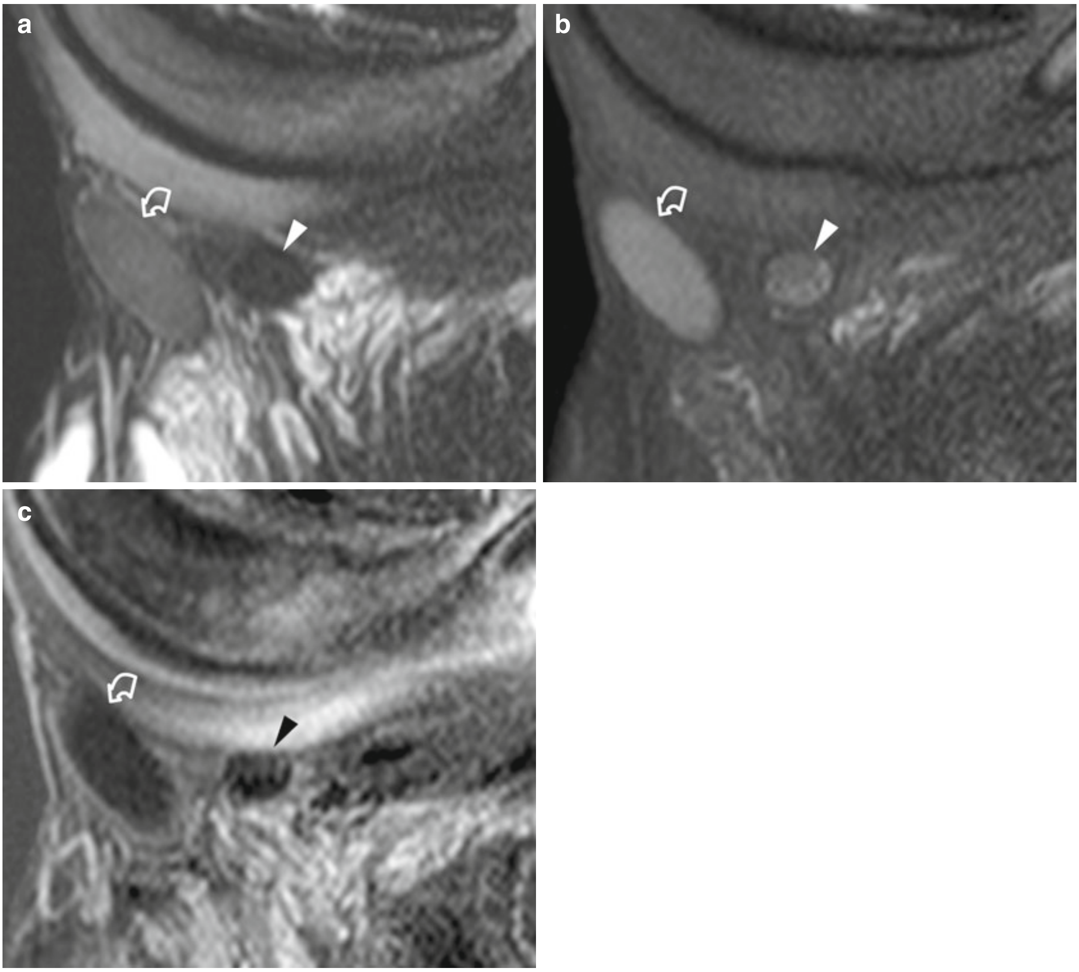

Fig. 9.13 Epidermoid cysts of the scrotal wall. T2-weighted (**a**) and T1-weighted sagittal images with fat suppression (**b**) show two well-demarcated masses, the larger with intermediate signal intensity on T2-weighted images (*curved arrow*) and the smaller with low signal intensity (*arrowhead*). Both lesions display relatively high signal intensity on T1-weighted images. (**c**) Subtraction images obtained after gadolinium contrast administration show no enhancement with minimum enhancement of the cystic wall (*curved arrow*). The smaller nodule (*arrowhead*) was partially calcified

markedly hypervascular after gadolinium contrast administration, homogeneously hypointense on T2-weighted images, isointense to the surrounding normal tissue of the testis on T1-weighed images, and lacking fat tissue [49]. High signal intensity is found on diffusion-weighted images (DWI), as occurs for lymphomas elsewhere in the body.

The MR imaging appearance of the other extratesticular scrotal tumors is not specific. Scrotal metastatic deposits are indistinguishable from primary neoplasms. A preliminary investigation suggests that hypointensity on DWI and increased ADC are in favor of benign paratesticular lesions [10].

9.9 Inguinal-Scrotal Hernia

Though physical examination and ultrasonography allow for accurate diagnosis in most cases, MR examination can be indicated in patients with inconclusive findings. Fat tissue such as the omentum and mesentery, protruding through the inguinal canal, usually shows high signal intensity on T1-weighted images and low signal

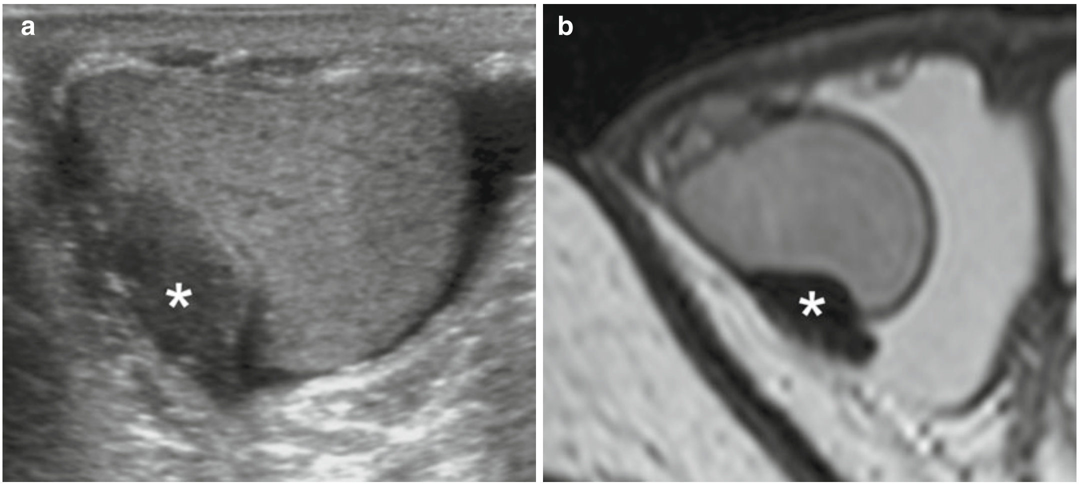

Fig. 9.14 Fibrous extratesticular pseudotumor. (**a**) Ultrasonography shows a hypoechoic lesion (*asterisk*) causing compression of the testicular parenchyma arising from the tunica albuginea or from the visceral lamina of the tunica vaginalis. (**b**) T2-weighted axial image confirms the extratesticular location of the low-signal-intensity lesion (*asterisk*)

intensity on T1- and T2-weighted images with fat suppression. Vessels of the omentum and/or mesentery appear as curvilinear structures. Herniation of bowel loops and of other viscera, such as the urinary bladder, can be investigated.

9.10 Varicocele

Although color Doppler ultrasonography is the modality of choice for imaging varicocele, this pathological condition may be an incidental finding on MR imaging in patients investigated for other purpose. The MR appearance of varicocele consists of multiple, serpiginous, tubular structures with varying sizes larger than 2 mm in diameter that are usually best visualized superior and lateral to the testis. Signal intensity characteristics may vary depending on the speed of flow within the dilated vessels. Slow-flowing varicoceles often have intermediate signal intensity on T1-weighted images and high signal intensity on T2-weighted images. A signal void may be seen in those with higher velocity flow. Enhancement is appreciable after gadolinium contrast administration. Since varicocele may affect testicular growth [50], testicular volumes should be systematically measured, and the signal intensity of the parenchyma should be investigated.

9.11 Trauma

If the tunica albuginea is intact, a testicular trauma can be managed conservatively, while immediate operation is usually necessary if albugineal disruption is suspected. MR imaging provides additional clinically useful information in patients with equivocal findings for albugineal disruption on ultrasound. The tunica albuginea is well visualized as a low-signal-intensity line which is interrupted in testicular rupture. In a series of seven patients with blunt scrotal traumas evaluated with MR imaging before surgical exploration, the presence or absence of albugineal rupture was identified correctly in all cases. Associated parenchymal ischemia and hematomas are identified as areas lacking vascularization after gadolinium contrast administration. In testicular hematomas characteristic signal changes with time are appreciated on T1- and T2-weighted images, as methemoglobin within subacute blood is hyperintense on T1-weighted images while hemosiderin deposition produces a low-signal-intensity rim on T2-weighted images. Lack of internal enhancement eases differential diagnosis with hypovascular tumors, which display contrast enhancement after administration of gadolinium contrast material in virtually all cases.

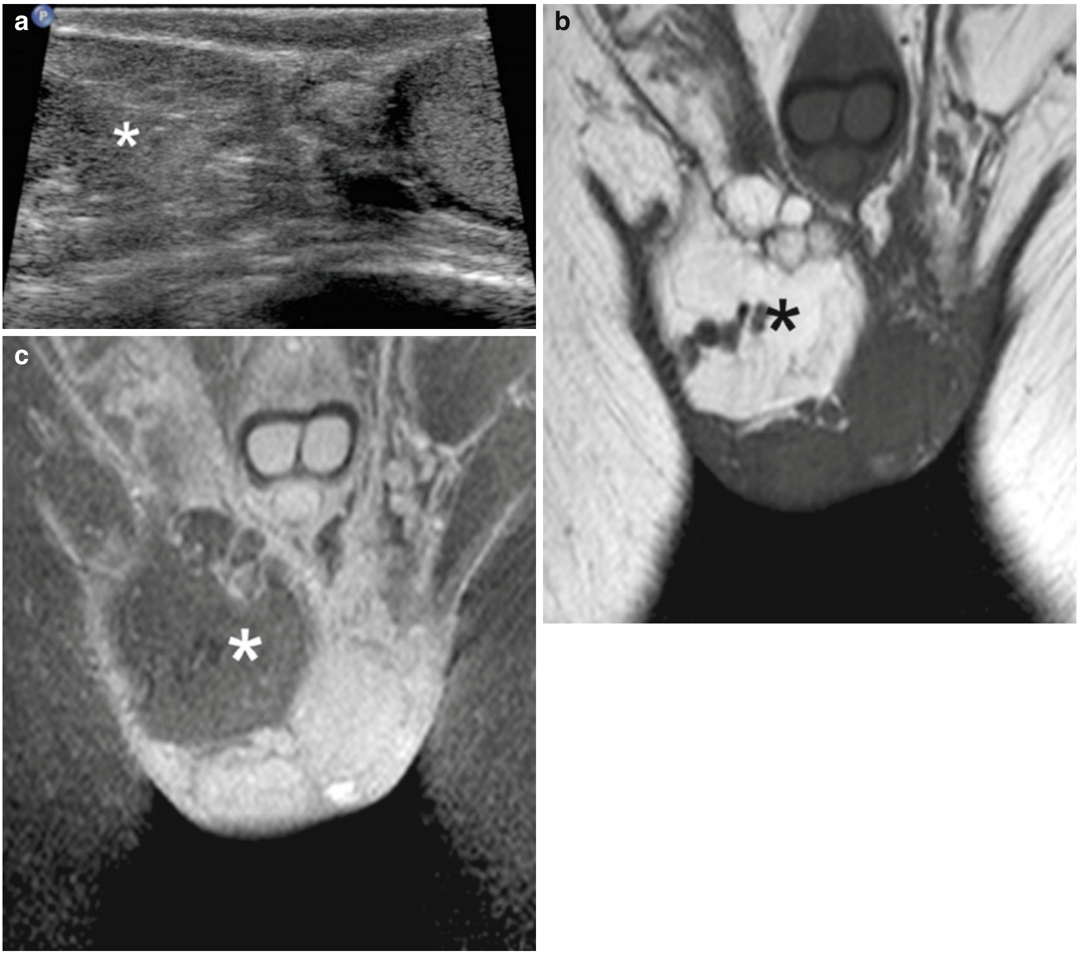

Fig. 9.15 Lipoma of the spermatic cord. (**a**) Grayscale ultrasonography shows a mass (*asterisk*) with intermediate echogenicity involving the spermatic cord. Due to the limited panoramicity, the relationships of the mass cannot be assessed accurately. The lesion (*asterisk*) shows a prevalence of fatty tissue on coronal T1-weighted (**b**) and T1-weighted image with fat suppression (**c**). An adequate evaluation of the relationships with the surrounding tissues is possible

Conclusion

Concern is rising that a variety of scrotal lesions are benign, and surgical exploration can be avoided in many cases, provided that a firm preoperative diagnosis is reached. Ultrasonographic modes have virtually absolute sensitivity for lesion identification, but characterization is limited. Moreover, situations exist in which ultrasonography is inconclusive. Although in the majority of cases the MR appearance of the different intratesticular and extratesticular tumors is not specific, in selected cases MR imaging allows a specific diagnosis based on the identification of fluid or of hematic, fibrotic, and fatty components. Avascular benign lesions can be differentiated effectively from hypovascular tumors due to higher sensitivity of flow compared to color Doppler interrogation.

References

1. Tsili AC, Giannakis D, Sylakos A, Ntorkou A, Sofikitis N, Argyropoulou MI (2014) MR imaging of scrotum. Magn Reson Imaging Clin N Am 22: 217–238, vi
2. Watanabe Y, Dohke M, Ohkubo K et al (2000) Scrotal disorders: evaluation of testicular enhancement patterns at dynamic contrast-enhanced subtraction MR imaging. Radiology 217:219–227

3. Andipa E, Liberopoulos K, Asvestis C (2004) Magnetic resonance imaging and ultrasound evaluation of penile and testicular masses. World J Urol 22:382–391
4. Shellock FG, Rothman B, Sarti D (1990) Heating of the scrotum by high-field-strength MR imaging. AJR Am J Roentgenol 154:1229–1232
5. Rholl KS, Lee JK, Ling D, Heiken JP, Glazer HS (1987) MR imaging of the scrotum with a high-resolution surface coil. Radiology 163:99–103
6. Baker LL, Hajek PC, Burkhard TK et al (1987) MR imaging of the scrotum: normal anatomy. Radiology 163:89–92
7. Frush DP, Sheldon CA (1998) Diagnostic imaging for pediatric scrotal disorders. Radiographics 18:969–985
8. Watanabe Y, Nagayama M, Okumura A et al (2007) MR imaging of testicular torsion: features of testicular hemorrhagic necrosis and clinical outcomes. J Magn Reson Imaging 26:100–108
9. Maki D, Watanabe Y, Nagayama M et al (2011) Diffusion-weighted magnetic resonance imaging in the detection of testicular torsion: feasibility study. J Magn Reson Imaging 34:1137–1142
10. Tsili AC, Argyropoulou MI, Giannakis D, Tsampalas S, Sofikitis N, Tsampoulas K (2012) Diffusion-weighted MR imaging of normal and abnormal scrotum: preliminary results. Asian J Androl 14:649–654
11. Kim MS, Kim KA, Chang SH (2011) Testicular epidermoid cyst on diffusion-weighted MR imaging and ADC map : a case report. J Korean Soc Magn Reson Med 15:154–159
12. Gulum M, Cece H, Yeni E et al (2012) Diffusion-weighted MRI of the testis in hydrocele: a pilot study. Urol Int 89:191–195
13. Kantarci M, Doganay S, Yalcin A, Aksoy Y, Yilmaz-Cankaya B, Salman B (2010) Diagnostic performance of diffusion-weighted MRI in the detection of nonpalpable undescended testes: comparison with conventional MRI and surgical findings. AJR Am J Roentgenol 195:W268–W273
14. Terai A, Yoshimura K, Ichioka K et al (2006) Dynamic contrast-enhanced subtraction magnetic resonance imaging in diagnostics of testicular torsion. Urology 67:1278–1282
15. Tsili AC, Giannakis D, Sylakos A et al (2014) Apparent diffusion coefficient values of normal testis and variations with age. Asian J Androl 16:493–497
16. Kim W, Rosen MA, Langer JE, Banner MP, Siegelman ES, Ramchandani P (2007) US MR imaging correlation in pathologic conditions of the scrotum. Radiographics 27:1239–1253
17. Hricak H, Hamm B, Kim B (1995) Imaging techniques, anatomy, artifacts and bioeffects: magnetic resonance imaging. Raven, New York
18. Nguyen HT, Coakley F, Hricak H (1999) Cryptorchidism: strategies in detection. Eur Radiol 9:336–343
19. Sijstermans K, Hack WW, van der Voort-Doedens LM, Meijer RW (2009) Long-term testicular growth and position after orchidopexy for congenital undescended testis. Urol Int 83:438–445
20. Krishnaswami S, Fonnesbeck C, Penson D, McPheeters ML (2013) Magnetic resonance imaging for locating nonpalpable undescended testicles: a meta-analysis. Pediatrics 131:e1908–e1916
21. Kaipia A, Ryymin P, Makela E, Aaltonen M, Kahara V, Kangasniemi M (2005) Magnetic resonance imaging of experimental testicular torsion. Int J Androl 28:355–359
22. Cassidy FH, Ishioka KM, McMahon CJ et al (2010) MR imaging of scrotal tumors and pseudotumors. Radiographics 30:665–683
23. Gotto GT, Chang SD, Nigro MK (2010) MRI in the diagnosis of incomplete testicular torsion. Br J Radiol 83:e105–e107
24. Baud C, Veyrac C, Couture A, Ferran JL (1998) Spiral twist of the spermatic cord: a reliable sign of testicular torsion. Pediatr Radiol 28:950–954
25. Aso C, Enriquez G, Fite M et al (2005) Gray-scale and color Doppler sonography of scrotal disorders in children: an update. Radiographics 25:1197–1214
26. Dogra VS, Gottlieb RH, Oka M, Rubens DJ (2003) Sonography of the scrotum. Radiology 227:18–36
27. Hricak H, Filly RA (1983) Sonography of the scrotum. Invest Radiol 18:112–121
28. Watanabe Y (2002) Scrotal imaging. Curr Opin Urol 12:149–153
29. Fernandez-Perez GC, Tardaguila FM, Velasco M et al (2005) Radiologic findings of segmental testicular infarction. AJR Am J Roentgenol 184:1587–1593
30. Kodama K, Yotsuyanagi S, Fuse H, Hirano S, Kitagawa K, Masuda S (2000) Magnetic resonance imaging to diagnose segmental testicular infarction. J Urol 163:910–911
31. Saxon P, Badler RL, Desser TS, Tublin ME, Katz DS (2012) Segmental testicular infarction: report of seven new cases and literature review. Emerg Radiol 19:217–223
32. Bertolotto M, Derchi LE, Sidhu PS et al (2011) Acute segmental testicular infarction at contrast-enhanced ultrasound: early features and changes during follow-up. AJR Am J Roentgenol 196:834–841
33. Parenti GC, Feletti F, Brandini F et al (2009) Imaging of the scrotum: role of MRI. Radiol Med 114:414–424
34. Woodward PJ, Sohaey R, O'Donoghue MJ, Green DE (2002) From the archives of the AFIP: tumors and tumorlike lesions of the testis: radiologic-pathologic correlation. Radiographics 22:189–216
35. Langer JE, Ramchandani P, Siegelman ES, Banner MP (1999) Epidermoid cysts of the testicle: sonographic and MR imaging features. AJR Am J Roentgenol 173:1295–1299
36. Park SB, Lee WC, Kim JK et al (2011) Imaging features of benign solid testicular and paratesticular lesions. Eur Radiol 21:2226–2234
37. Gaur S, Bhatt S, Derchi L, Dogra V (2011) Spontaneous intratesticular hemorrhage: two case descriptions and

brief review of the literature. J Ultrasound Med 30: 101–104
38. Hertzberg BS, Mahony BS, Bowie JD, Anderson EE (1985) Sonography of an intratesticular lipoma. J Ultrasound Med 4:619–621
39. Harper M, Arya M, Peters JL, Buckingham S, Freeman A, O'Donoghue EP (2002) Intratesticular lipoma. Scand J Urol Nephrol 36:223–224
40. Serra AD, Hricak H, Coakley FV et al (1998) Inconclusive clinical and ultrasound evaluation of the scrotum: impact of magnetic resonance imaging on patient management and cost. Urology 51: 1018–1021
41. Walker RN, Murphy TJ, Wilkerson ML (2008) Testicular hamartomas in a patient with Bannayan-Riley-Ruvalcaba syndrome. J Ultrasound Med 27: 1245–1248
42. Philips S, Nagar A, Dighe M, Vikram R, Sunnapwar A, Prasad S (2012) Benign non-cystic scrotal tumors and pseudotumors. Acta Radiol 53:102–111
43. Woodhouse J, Ferguson MM (2006) Multiple hyperechoic testicular lesions are a common finding on ultrasound in Cowden disease and represent lipomatosis of the testis. Br J Radiol 79:801–803
44. Liu B, Chen J, Luo J, Zhou F, Wang C, Xie L (2013) Cavernous hemangioma of the testis mimicking a testicular teratoma. Exp Ther Med 6:91–92
45. Tanaka U, Kitajima K, Fujisawa M, Hara S, Takahashi S (2013) Magnetic resonance imaging findings of sclerosing Sertoli cell tumor of the testis. Jpn J Radiol 31:286–288
46. Tsili AC, Tsampoulas C, Giannakopoulos X et al (2007) MRI in the histologic characterization of testicular neoplasms. AJR Am J Roentgenol 189:W331–W337
47. Tsili AC, Argyropoulou MI, Astrakas LG et al (2013) Dynamic contrast-enhanced subtraction MRI for characterizing intratesticular mass lesions. AJR Am J Roentgenol 200:578–585
48. Lee SJ, Lee JH, Jeon SH, Kim MJ (2010) Multiple epidermoid cysts arising from the extratesticular scrotal, spermatic cord and perineal area. Korean J Urol 51:505–507
49. Bertolotto M, Borsato A, Derchi LE (2014) Lymphoma of the spermatic cord: Sonographic appearance. J Clin Ultrasound 42:509-512
50. Thomas JC, Elder JS (2002) Testicular growth arrest and adolescent varicocele: does varicocele size make a difference? J Urol 168:1689–1691

Magnetic Resonance Urography

10

Maria Assunta Cova, Gabriele Poillucci,
Luca De Paoli, and Maja Ukmar

Magnetic resonance (MR) urography has become an integral part of the recently emerging advances that involve clinical uroradiology. MR urography has received a relatively lower attention than multidetector CT (MDCT) urography, being hampered by the low spatial resolution which is crucial for calyceal evaluation and by the requirement of updated MR units. However, excellent contrast resolution and lack of ionizing radiation make MR urography a technique to be considered for noninvasively evaluating the entire urinary tract, especially when ionizing radiation is to be avoided, such as in pediatric or pregnant patients.

The MR urographic techniques can be divided into two categories: static-fluid MR urography and excretory MR urography. The static-fluid MR urography utilizes unenhanced, heavily T2-weighted pulse sequences to image the urinary tract. On the heavily T2-weighted images, the urinary tract is hyperintense because of its long relaxation time, independent of the excretory renal function. This technique is ideally suited for patients with dilated or obstructed collecting system.

In excretory MR urography, intravenous gadolinium is combined with a T1-weighted 3D gradient echo (GRE) sequence. The practicability of excretory MR urography depends on the ability of the kidneys to excrete the intravenously administered gadolinium agent. Administration of low-dose furosemide can improve the quality of excretory MR urography by enhancing urine flow and therefore providing a uniform distribution of the contrast material inside the entire urinary tract. Excretory MR urography provides high-quality images of both non-dilated and obstructed collecting systems.

Beginners in MR urography are encouraged to try these new techniques, which are quite easy to put into operation. The various unenhanced T2-weighted and gadolinium-enhanced T1-weighted MR urographic techniques are described next in this chapter.

10.1 Technical Considerations

10.1.1 Equipment

Magnetic resonance urography requires high magnetic field magnets (1.5–3 T) with powerful gradients and fast slew rate. Different surface coils may be employed, and the body coil alone could also offer good images. However, the use of phased array coils is important to increase signal-to-noise ratio (SNR) and especially to obtain rapid imaging in order to avoid motion artifacts.

M.A. Cova (✉) • G. Poillucci • L. De Paoli
M. Ukmar
Department of Radiology, Cattinara Hospital,
University of Trieste, Strada di Fiume 447,
Trieste 34149, Italy
e-mail: cova@gnbts.univ.trieste.it

R. Manfredi, R. Pozzi Mucelli (eds.), *MRI of the Female and Male Pelvis*,
DOI 10.1007/978-3-319-09659-9_10, © Springer International Publishing Switzerland 2015

The use of 3 T magnets allows an increase in SNR or to study larger volumes even if there are no unambiguous data about a real improvement of diagnostic accuracy. The drawback of using 3 T MR scanner is the introduction of more magnetic susceptibility artifacts and problems related to the extension of T1 with possible repercussions on the contrast T1-weighted images [1].

10.1.2 Imaging Protocol

MR sequences for the study of the urinary tract are divided into (a) static-fluid MR urography sequences characterized by high T2W that exploit the long T2 relaxation time of urine [2] and (b) excretory MR urography (CE-MRU) sequences characterized by T1W which allow the evaluation of the excretory phase through the use of paramagnetic contrast agent.

Static-fluid MR images can be obtained with two types of sequences. The first is to perform a thick (6–8 cm) single-shot fast spin echo T2W (T2 SSFSE) sequence with coronal scanning planes with a large field of view (FOV) that includes the entire urinary tract from the upper renal pole to the bladder. The acquisition time for each slab is about 3–8 s. Usually are acquired 6–8 projections. The individual acquisitions must be at least 10–15 s in order to allow the saturation of the tissues.

SSFSE T2-weighted sequences take advantage of the long T2 relaxation time of urine (Fig. 10.1). They are characterized by a low spatial resolution and relatively low SNR. Multiple acquisitions repeated over time can improve the evaluation of the ureters and help distinguish between stenosis and peristaltic contractions. SSFSE T2-weighted sequences can be obtained in apnea or respiratory-triggered.

The second method consists in the acquisition of multiple thin layers (multislice technique, 3–5 mm thick) with 3D TSE (or SSFSE) T2W sequences subsequently processed with various algorithms including the most widely used MIP algorithm. For improved urographic image quality on oblique and lateral MIP images, a 50 % overlap between the source images is recommended and should be considered during the evaluation of both partition images and 3D reconstructions. Compared to the previous these sequences have the advantage of allowing an improved assessment of details. The longest duration and possible masking by other structures are among the disadvantages that should be remembered (e.g., ascites, bowel loops, etc.). The 3D TSE T2-weighted sequences are obtained with respiratory triggering (Fig. 10.2).

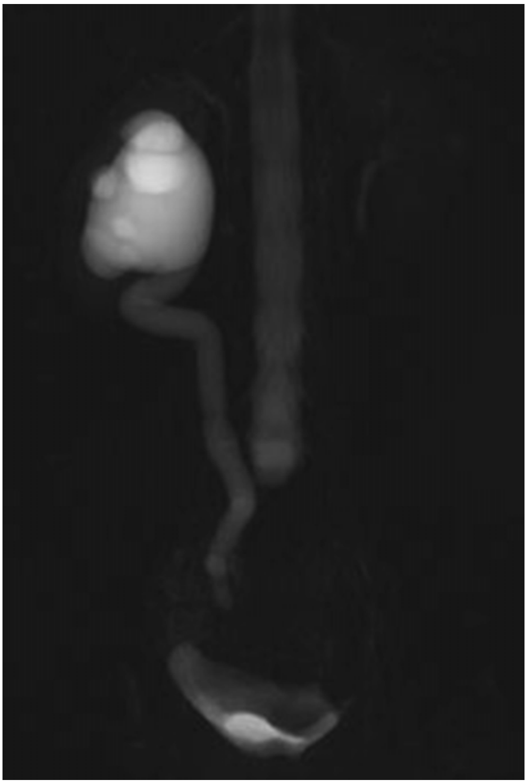

Fig. 10.1 Image of static-fluid MR urography (SSFSE T2) 8 cm thick which demonstrates considerable right hydroureteronephrosis (fibrous tissue due to multiple episodes of endometriosis in the distal third of the ureter)

T2-weighted sequences are indicated in particular for hydronephrosis assessment not allowing, however, to recognize the cause of the obstruction [3]. Static-fluid MR urography does not require the excretion of contrast agent and is therefore useful for demonstrating the collecting system of an obstructed, poorly excreting kidney [4]; it permits the assessment of the urinary tract

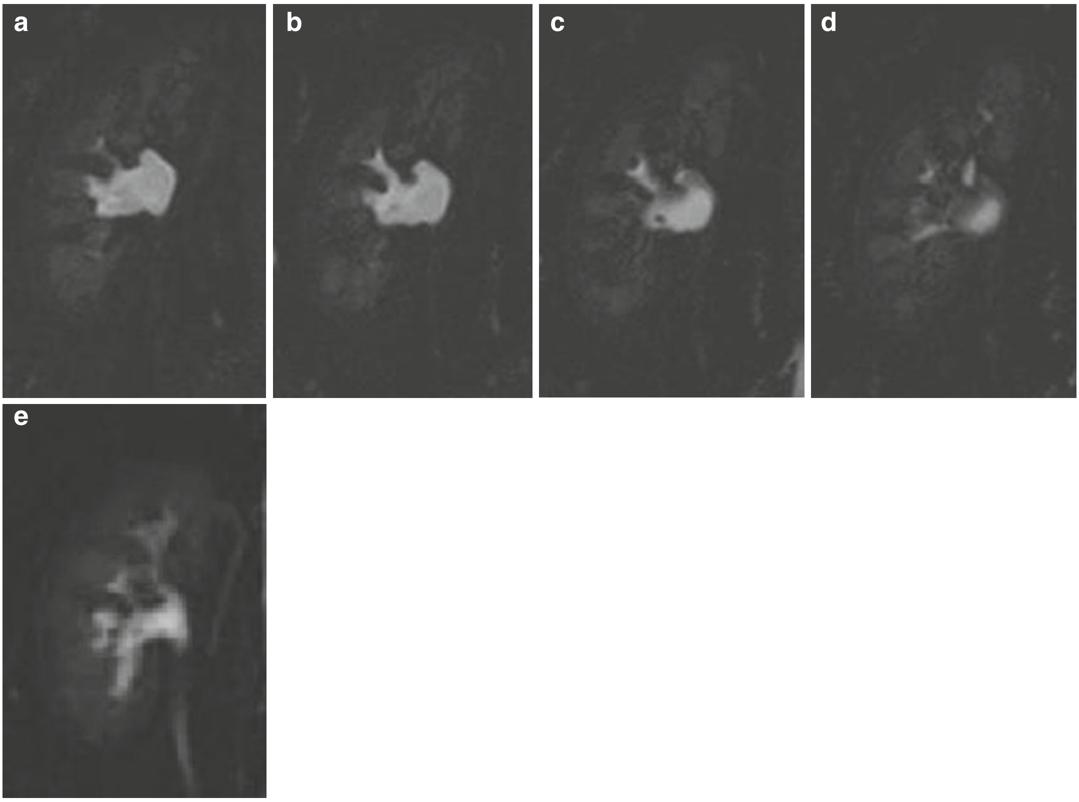

Fig. 10.2 Multislice acquisition partition images (**a**–**d**) (3D TSE T2W, 3 mm thick) that demonstrate a small hypointense area in the context of the renal pelvis, only intuitable in MIP elaborations (**e**). It refers to the presence of a millimetric calculi

in particular if it is dilated, while it is not accurate in the evaluation of the urinary tract in poor condition or just not dilated. In these latter cases (patients with non-dilated systems), the use of hydration, diuretics, and, according to some authors, compression may enhance the quality of MR urography [5].

CE-MRU images are obtained with fat-suppressed 3D GE T1W sequences (THRIVE, VIBE, LAVA, etc.) after the administration of intravenous contrast agent. The recommended acquisition plan is coronal with a wide FOV in order to allow the study of the entire urinary tract in one acquisition. To obtain a better spatial resolution, in particular for the study of the intrarenal urinary tract, it is good to use a kidney-targeted FOV. 3D sequences will result in about 70 layers of 1.5 mm, which have to be reconstructed with MIP algorithm (Fig. 10.3).

During reporting both partition and reconstruction images are evaluated. For patients with a limited capacity to hold their breath, the use of EPI sequence (reduced acquisition time) has been described; these techniques are characterized, however, by low spatial resolution [6]. The 3D GE T1W sequences are obtained with the breath-hold technique. It has been shown that the use of standard doses (0.1 mmol/kg) of gadolinium has as a consequence an excessive concentration of the latter in the urinary tract which reduces the signal intensity of the urine due to T2* effects. Best results are obtained with reduced doses (0.01–0.05 mmol/kg) [7]. Recently the use of a liver-specific contrast agent with minimal renal excretion (Gd-EOB-DTPA) which would allow adequate signal from the urinary tract in the absence of T2* artifacts has been proposed. The quality of MR urography

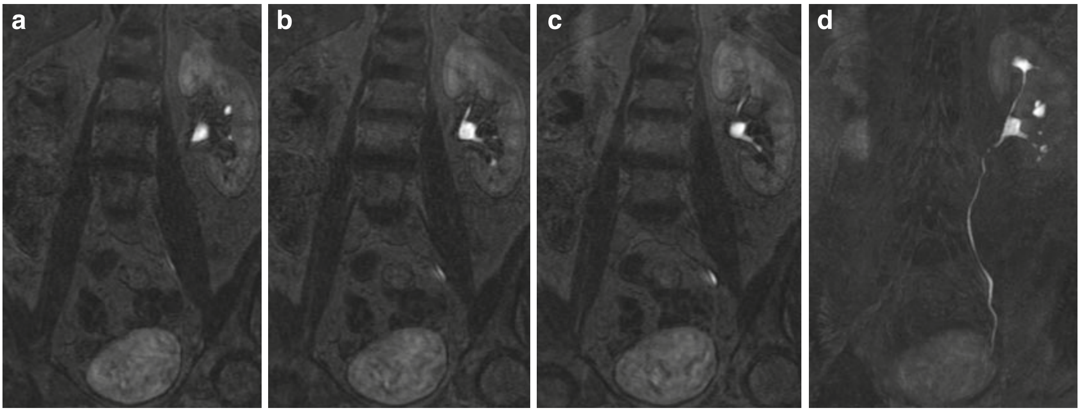

Fig. 10.3 3D GE T1 THRIVE partition images with 1.5 mm-thick (**a**–**c**) and relative MIP reconstruction (5 cm) (**d**) focused on the left kidney and urinary tract

Fig. 10.4 Patients with polycystic kidneys (APDK); static-fluid-MR urography SSFSE T2W 8 cm thick (**a**) where the pelvis and calyces are not properly evaluated in relation to the high signal intensity from multiple cysts; MIP processing sequence of excretory MR urography 3D GE T1 THRIVE (**b**) in which the intra- and extrarenal excretory pathways are the only ones appearing hyperintense (which do not exhibit expansion)

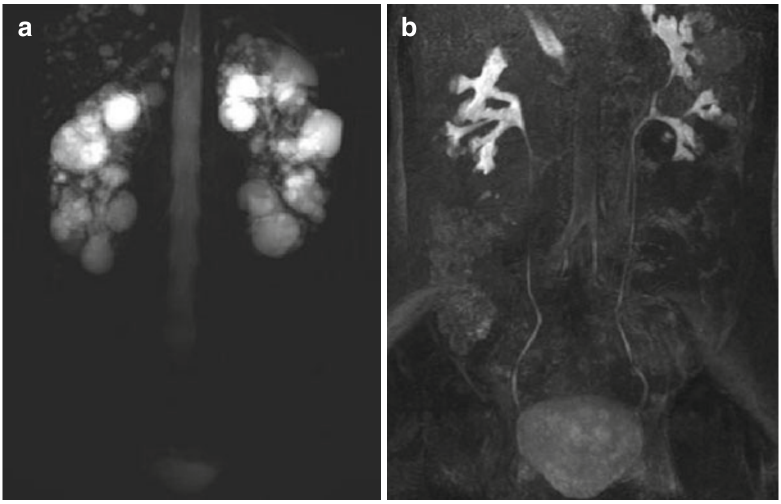

images is also improved by the administration of a diuretic (furosemide) at a relatively low dose of 0.05–0.1 mg/kg from 1 to 5 min before the administration of contrast agent. Furosemide leads to greater distension of the urinary tract, better distribution of contrast agent, and reduced concentration of the latter in the urine, thus reducing the T2* effect. The contraindications to the administration of furosemide are hypersensitivity to the drug, hypotension, and anuria, so there are no absolute contraindications (Fig. 10.4) [8–12].

Another possible MR study is the use of *diffusion-weighted imaging (DWI) sequences*, which provides functional but not anatomical information, in particular about the degree of freedom of movement of the water molecules inside cells and tissues. The sequences most commonly used are the echo planar (EPI) with selective saturation of fatty tissue, if possible optimized using respiratory gating; they are fast running, but with poor spatial resolution. We recommend the use of at least a pair of b-values (usually 0 and a b-values ranging between 800 and 1,000 $s/mm^2 \times 10^{-3}$ with 1.5 T magnets), in order to create a corresponding ADC map and to avoid, or at least resolve, typical artifacts as, e.g., “shine-through.” Tissues in which cells are

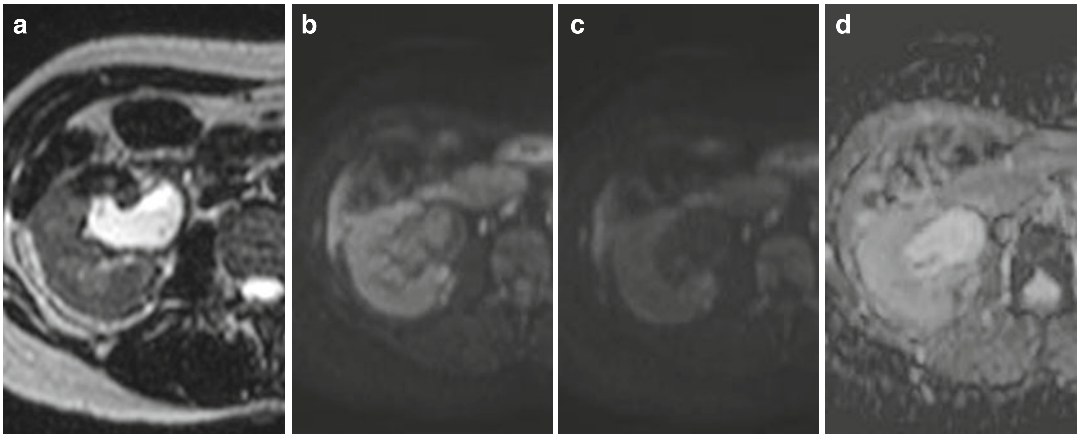

Fig. 10.5 SE breath-hold image T2W-SENSE with a thickness of 3 mm (**a**) that shows the presence of a moderate dilatation of the right renal pelvis in a context of hydronephrosis, with only a slight inhomogeneity of signal; DWI with b = 500 (**b**), signal intensity of the content of the renal pelvis comparable to that of the adjacent parenchyma, in relation to the T2* effect of urine that determines the permanence of high signal intensity in the sequences with DWI values b to medium–low; DWI with $b = 1{,}000$ (**c**) where you can appreciate the distinct hypointensity of the content of the renal pelvis, evidence of the high diffusibility of water molecules, confirmed in its ADC map that shows clear hyperintensity (**d**)

highly packed, or in which cells show a high nucleus-cytoplasm ratio, will tend to have a high signal in DWI sequences and consequently low intensity in ADC maps, as well as low numerical value of ADC, and vice versa. In clinical practice, these sequences may be useful, for example, in the differential diagnosis between hydronephrosis (Fig. 10.5) and pyonephrosis (the presence of purulent material determines signal restriction which can be seen as a hyperintensity in DWI and hypointensity on the ADC maps), in the evaluation of extension and especially in follow-up of pyelonephritis and abscesses without the need to use a contrast agent (e.g., pregnant women), as well as in the differential diagnosis between different masses (although there is still no uniqueness on the values of the ADC, often too similar between tumors histologically different), in which the neoplastic lesion tends to have higher signal restriction than that of the adjacent renal tissue, due to the high cellularity, usually seen in malignancies.

In addition to the sequences targeted for the study of the urinary tract are performed sequences for the study of renal parenchyma.

10.1.3 Patient Preparation

The patient usually lies supine with the arms raised above the head. Patients should empty the bladder before starting the exam. The use of oral negative contrast material to avoid hyperintense signal from intestinal loops may be useful even if not habitually used.

10.2 Clinical Applications

10.2.1 Congenital Anomalies

MRI is appropriate for the study of various congenital anomalies such as duplication of the excretory system, megaureter, and ureteropelvic junction (UPJ) obstruction syndromes [13, 14]. Duplication of the ureter may be incomplete or complete (Fig. 10.6a), and in the latter case the upper ureter pole typically inserts inferior and medial to the lower pole ureter and is more frequently the site of obstruction and may be associated with ureterocele (Fig. 10.7). MRI also allows evaluation of possible ectopic outlets.

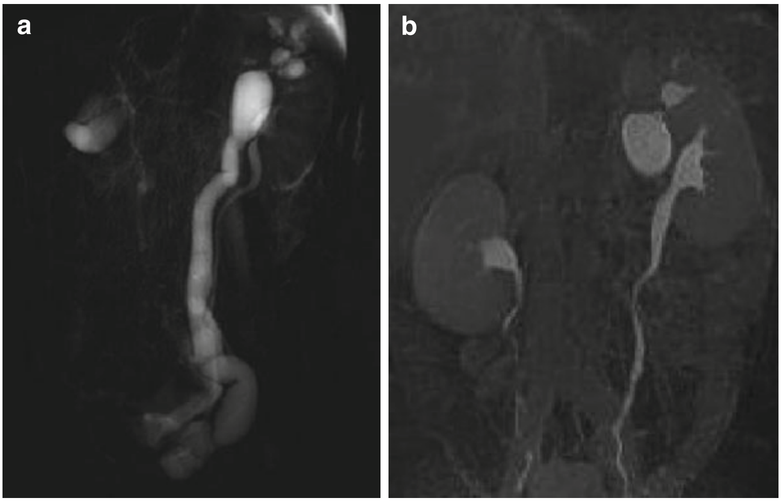

Fig. 10.6 (**a**) Static-fluid MR SSFSE T2W with a thickness of 8 cm which demonstrates a left double district with hydroureteronephrosis originating from the upper third of the kidney; (**b**) MIP processing of the excretory MR urography sequence 3D GE T1W THRIVE: it provides not only morphological but also functional information, demonstrating delayed opacification of the ureter originating from the upper third; it is possible to appreciate the dilatation of the renal pelvis and major calyces, attributable to reduced and delayed excretion capacity of that portion of the kidney; opacification of the urinary tract originating from the middle and lower third is normal

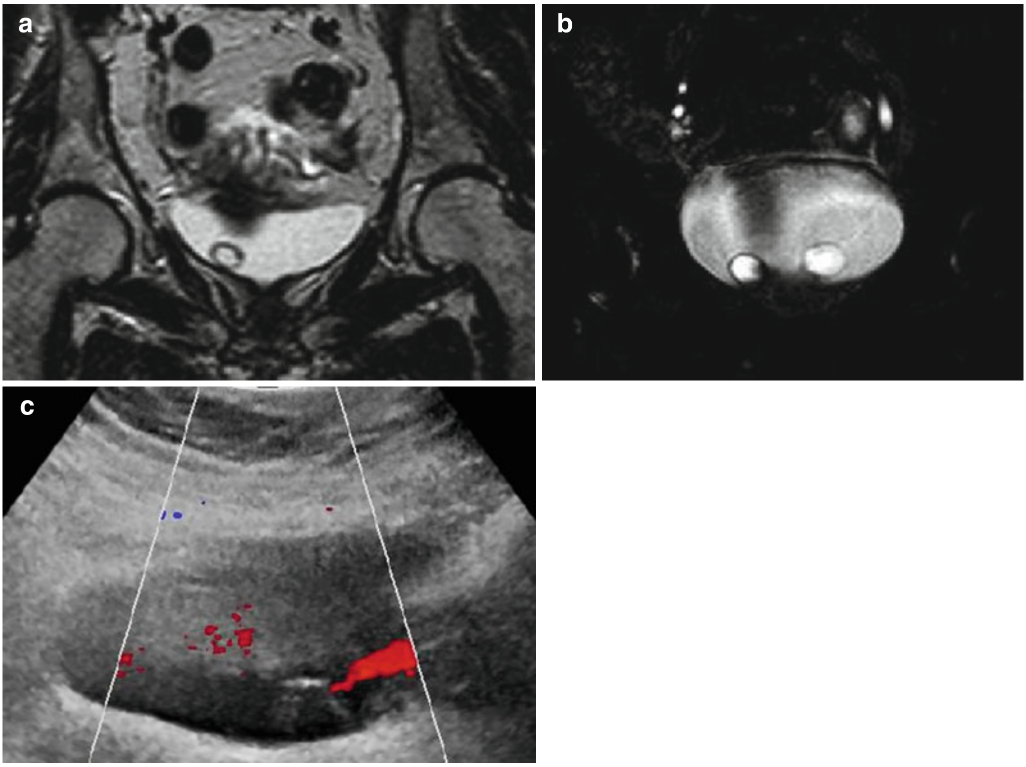

Fig. 10.7 SE T2W breath-hold image SENSE 3 mm thick (**a**), acquired on a coronal plane passing through the bladder, which demonstrates the presence of a round mass with well-recognizable walls, regular and hypointense, with internal signal intensity comparable to that of the bladder urine; in partition image (**b**) of multislice 3D TSE T2W acquisition (with a thickness of 3 mm), the presence of similar mass is observed also on the left, in a context of bilateral ureterocele, comparable to what is observed in the echo-Doppler imaging (**c**)

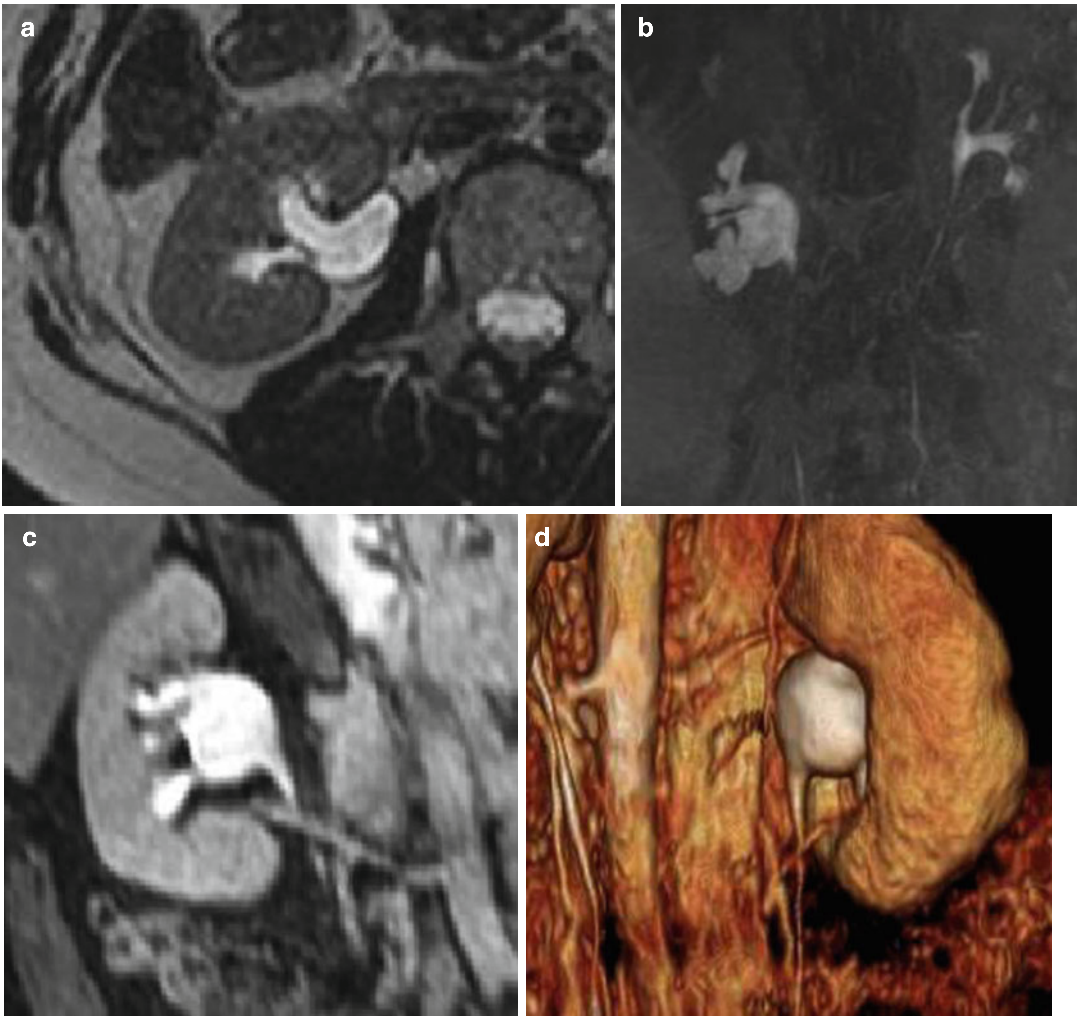

Fig. 10.8 A right kidney-targeted image SE T2W breath-hold SENSE with a thickness of 3 mm (**a**) acquired on the axial plane, which shows a moderate hydronephrosis of the pelvis and calyces. (**b**) MIP processing of excretory MR 3D GE T1W THRIVE sequence shows an abrupt change in caliber, on the right, between the renal pelvis and ureter at the ureteropelvic junction. Oblique MPR obtained from 3D GE T1W THRIVE sequences (**c**) and three-dimensional volume-rendered image (**d**) performed after injection of contrast material highlight the presence of a lower polar renal artery; in the segment below the ureter shows a normal caliber in a context to be referred to ureteropelvic junction syndrome

Ureteropelvic junction (UPJ) obstruction syndrome is the most frequent reason of urinary obstruction in children. There are many different causes, and among the more frequent we can list scars, vascular compressions, and impaired ureteral innervation. UPJ is the most common site of urinary obstruction in children. In vascular compression cases may be useful to perform an angiography sequence to clearly demonstrate the responsible vessel (Fig. 10.8).

10.2.2 Urolithiasis

MR imaging is useful, in second place than ultrasonography, especially in the evaluation of urolithiasis in pediatric patients and pregnant women [14]. Most urinary tract calculi appear as signal voids in both T1W and T2W sequences. At both static-fluid and excretory MR urographies, calculi appear as hypointense surrounded by urine or contrast material that is hyperintense

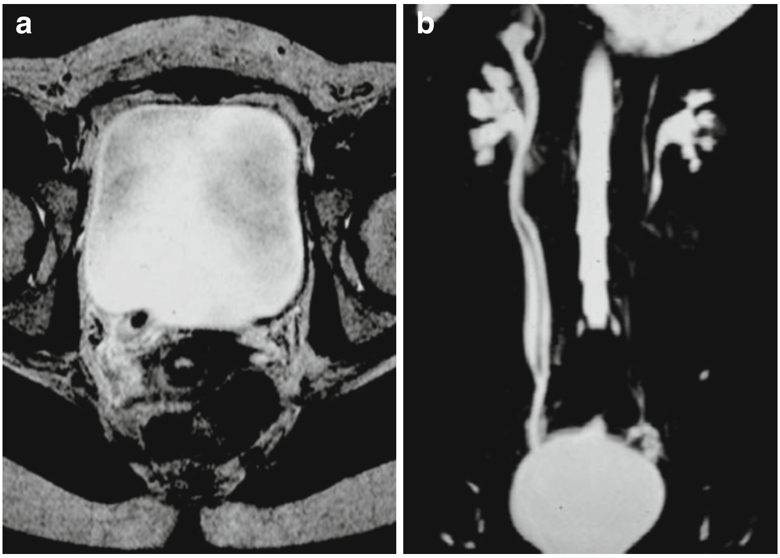

Fig. 10.9 SE T2W-SENSE image with a thickness of 3 mm (**a**) acquired in the axial plane that highlights the presence of a roundish hypointense signal of about 1 cm at the level of the right ureteral meatus, attributable to the presence of a calculus, which determines hydroureteronephrosis on the upper tract, as can be seen in the image of static-fluid MR (**b**), in a patient with double district ureter on the right

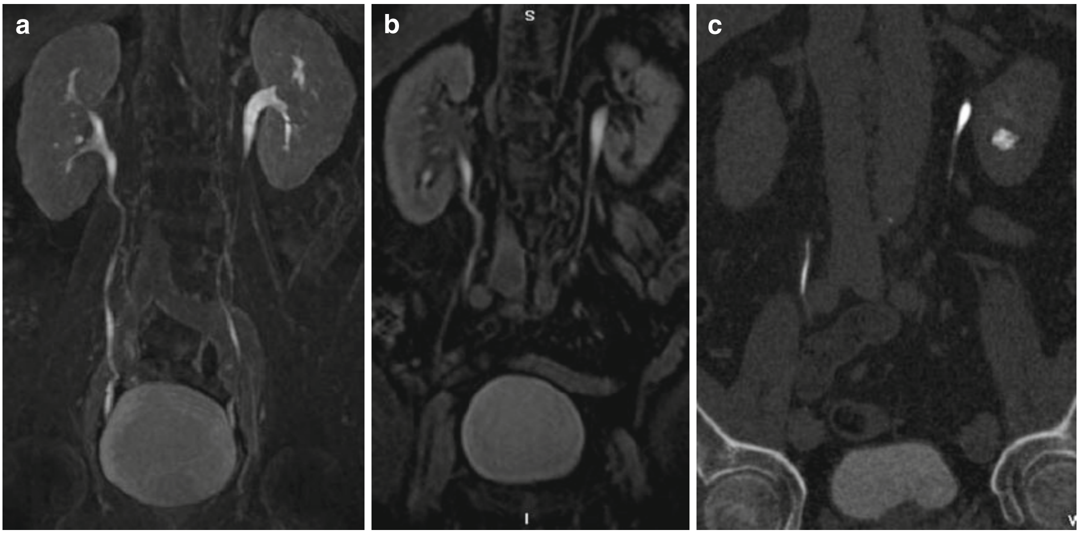

Fig. 10.10 Patient with a history of left renal colic; excretory RM images (**a**, **b**) demonstrate that there are neither dilation of the urinary tract nor particular images related to the presence of calculi; the CT image (**c**) instead shows the presence of a voluminous gallstone formation in the context of a calyx in the lower group of the left kidney

(Fig. 10.9). T2-weighted sequences also allow to highlight the ureteral edema and perinephric and periureteral fluid with suffusion of fat at these sites. Small stones can be misunderstood, especially in static-fluid MR images of large thickness. In this regard, the partition images of the 3D TSE sequences and conventional additional sequences at the site of the obstruction are useful (Figs. 10.9, 10.10, and 10.11).

Differential diagnoses to be considered are blood clots and cancer. The first are characterized by a high T1 signal, while neoplasms often have enhancement after administration of contrast agent.

10.2.3 Infections

When urinary infections involving the lower urinary tract often resolve spontaneously and

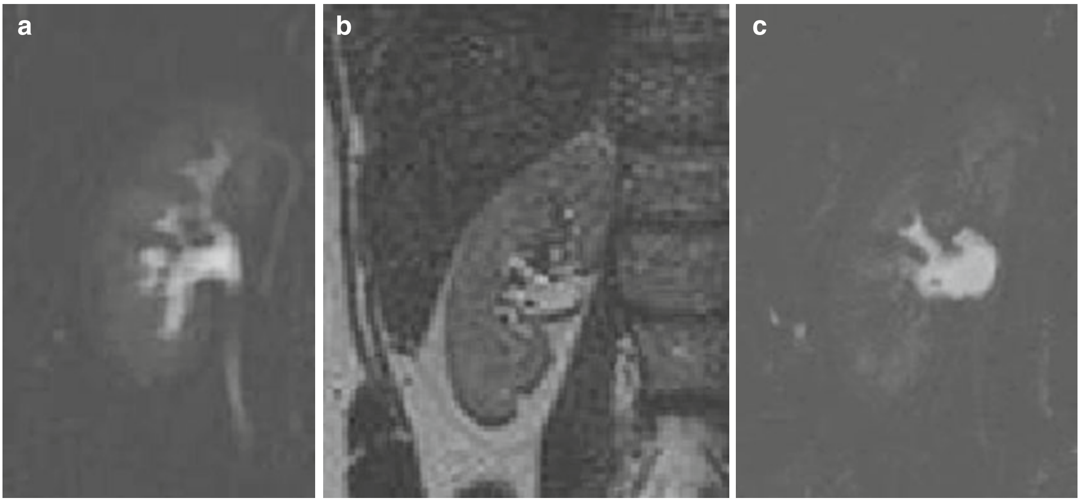

Fig. 10.11 Particular static-fluid MR SSFSE T2W image (**a**) of the right kidney (thickness of 5 cm) where it is possible to appreciate only a very small signal inhomogeneity in the context of the renal pelvis, possible expression of partial volume; a thin layer (thickness of 2.5 mm) SE T2 breath-hold SENSE image (**b**) and partition image (**c**) with a thickness of 2 mm from static-fluid MR multislice 3D TSE T2W acquisition show the same, the presence of millimetric roundish hypointensity attributable to the presence of small calculus

do not require recourse to imaging and when there is instead the involvement of both the renal parenchyma and urinary tract, particularly in cases of difficult healing, MRI may be particularly helpful. Vesicoureteral reflux (VUR) is present in approximately 1 % of children and is associated with an increased risk of pyelonephritis and renal scarring [15]. Voiding cystourethrography (VCUG) remains the gold standard for detecting vesicoureteral reflux (VUR). However, VCUG is an invasive examination causing huge distress to both patients and parents [16]. It is not our intention to treat this topic in this chapter, although it should be noted that there are new techniques (without the use of ionizing radiation) as MR voiding cystography that with a real-time interactive MR fluoroscopic technique on an open MRI magnet is feasible for the evaluation of VUR in children [17, 18].

In bacterial infections, static-fluid MR sequences may demonstrate dilation of the urinary tract. In the case of pyonephrosis, the T2 intensity is reduced compared to the one of hydronephrosis as a consequence of the presence of pus and cellular debris. In these cases DWI sequences may be useful to differentiate from hydronephrosis (accelerated diffusion) and pyonephrosis, which have restricted diffusion (Figs. 10.12 and 10.13).

In tubercular patterns of disease static-fluid and excretory MR urography sequences demonstrate the presence of dilated calyces with particles included (from papillary necrosis and calcifications), infundibular stenosis, and multiple level involvement of the ureter that shows stenotic stretches often interspersed by dilated segments. Conventional sequence association is fundamental to better characterize the stenosis that is usually represented by wall thickening without focal signs of mass.

10.2.4 Benign Strictures

They are often the result of intrinsic inflammatory diseases (e.g., appendicitis, endometriosis, Crohn disease, etc.), infections (e.g., tuberculosis), radiation therapy, and surgical or interventional procedures.

Benign strictures are characterized by ureteral wall thickening typically not associated with a soft tissue mass. Excretory MR urography sequences can distinguish between partial and total obstruction and are also helpful in gauging the severity (Fig. 10.14).

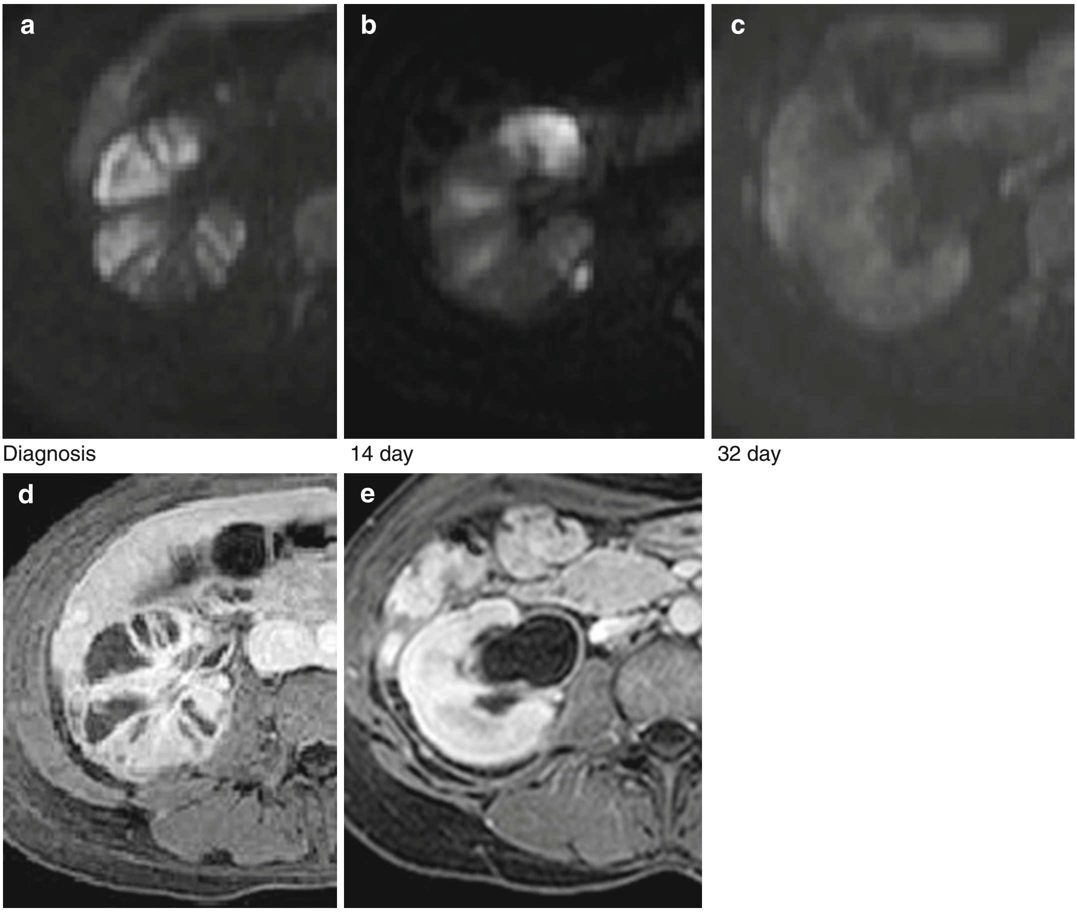

Fig. 10.12 DWI targeted on the right kidney with $b = 1{,}000$ (**c**) in patient with a history of pyelonephritis arising after childbirth; at diagnosis (**a**) multiple areas of intense signal restriction are visible, referring to multiple abscesses and ischemic parenchyma, which correspond to that detectable in 3D GE T1W THRIVE sequences after contrast agent injection (**d**); after 14 days (**b**) reduction of areas with restricted diffusion is seen, which disappear at control performed 1 month after (**c**); finding also confirmed by the gadolinium-enhanced sequences (**e**).

Extrinsic narrowing of the ureters may occur with numerous pathologies of the pelvis such as: fluid collections, uterine fibroids, etc.

10.2.5 Urothelial Carcinoma

Transitional cell carcinoma (TCC) is the most common urothelial tumor. Although it rises more frequently from the bladder, it occurs even in the upper urinary tract. TCCs can appear as sessile filling defects or wall thickening [19]. CT has to be considered as the technique of choice for the detection of urothelial carcinoma thanks to its higher spatial resolution. On the other hand, MRU and particularly static-fluid MRU could visualize collecting system without contrast medium administration thanks to the high intrinsic contrast resolution [20]. So it may be a useful tool in patients with renal function impairment or with a contrast excretion too limited to allow tumor detection. TCC appearance differs according to the dimension and the degree of invasion. Small TCC appears as filling defect, hypointense inside hyperintense urine on T2W, isointense to renal parenchyma on T1W, and with mild enhancement after contrast medium administration. Subtracted images may help in demonstrating

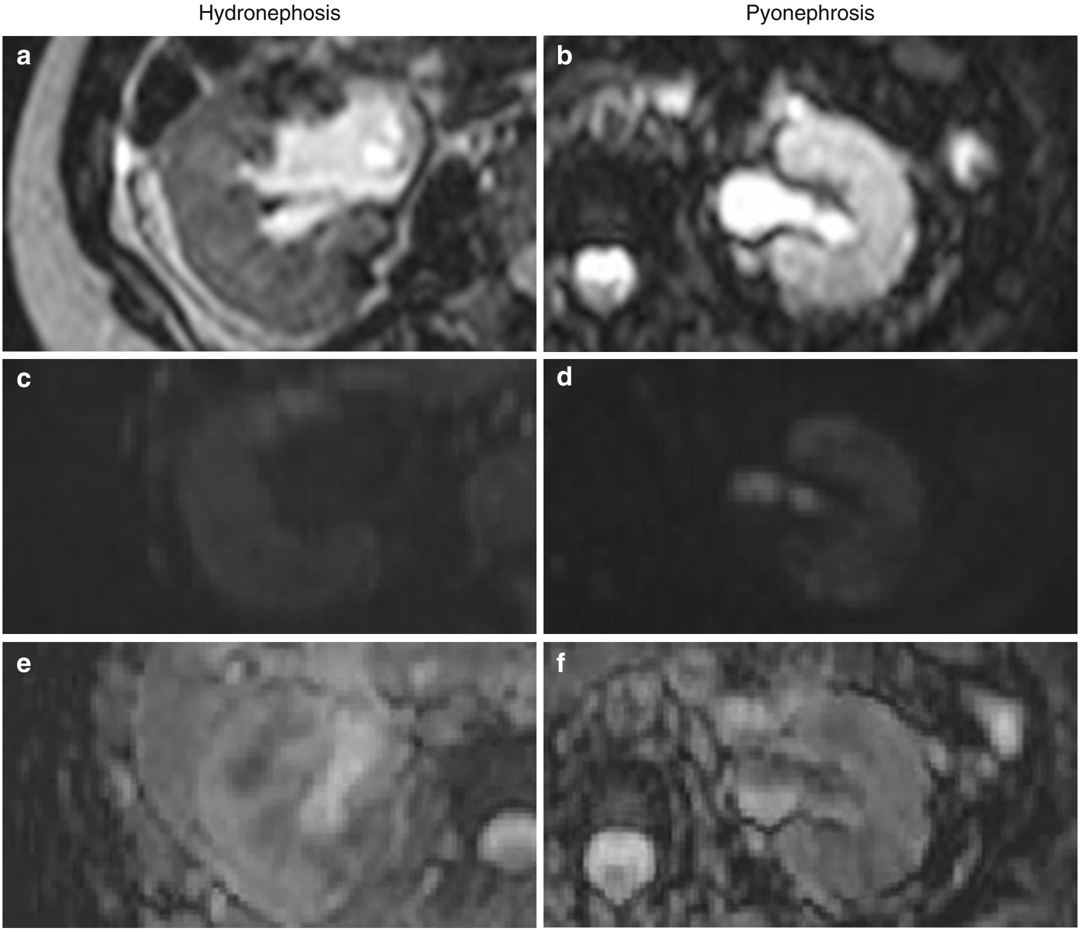

Fig. 10.13 T2-weighted (**a**, **b**) and DWI comparison with $b = 1{,}000$ (**c**, **d**), with relative ADC map $b = 0$–$1{,}000$ (**e**, **f**). Subtle signal inhomogeneity in the context of the renal pelvis in T2-weighted images (**a**, **b**); homogeneous hypointensity of the pelvis in DWI sequences in a case of hydronephrosis (**c**), sign of high diffusibility, in sharp contrast to the findings in the case of pyonephrosis, where it is possible to appreciate marked hyperintensity (**d**), the result of marked restriction; these characteristics are confirmed in the relative ADC map images (**e**, **f**), where the urine hyperintensity in hydronephrosis and the classical hypointensity of pyonephrosis associated with the purulent material

enhancement to differentiate TCC from other small filling defects, like clots (Fig. 10.15). TCC may appear as a focal enhancing urothelial thickening; in this case the differential diagnosis with inflammatory disease is difficult. Larger infiltrative masses may obliterate the renal sinus or invade the renal parenchyma, preserving renal shape, or may extend along the collecting system. In this case TCC is typically hypointense-isointense to renal parenchyma on T2W with a low-grade enhancement on postgadolinium T1W, but larger masses could heterogeneously enhance. DWI shows hyperintense signal, indicating restricted diffusion [21]. With increasing size ureteral neoplasms manifest as irregular wall thickening with focal enhancement after contrast medium.

10.2.6 Postoperative Lower Urinary Tract Fistulae and Leakages

Urinary leakages or fistulae are rare complications that can be seen following various surgical

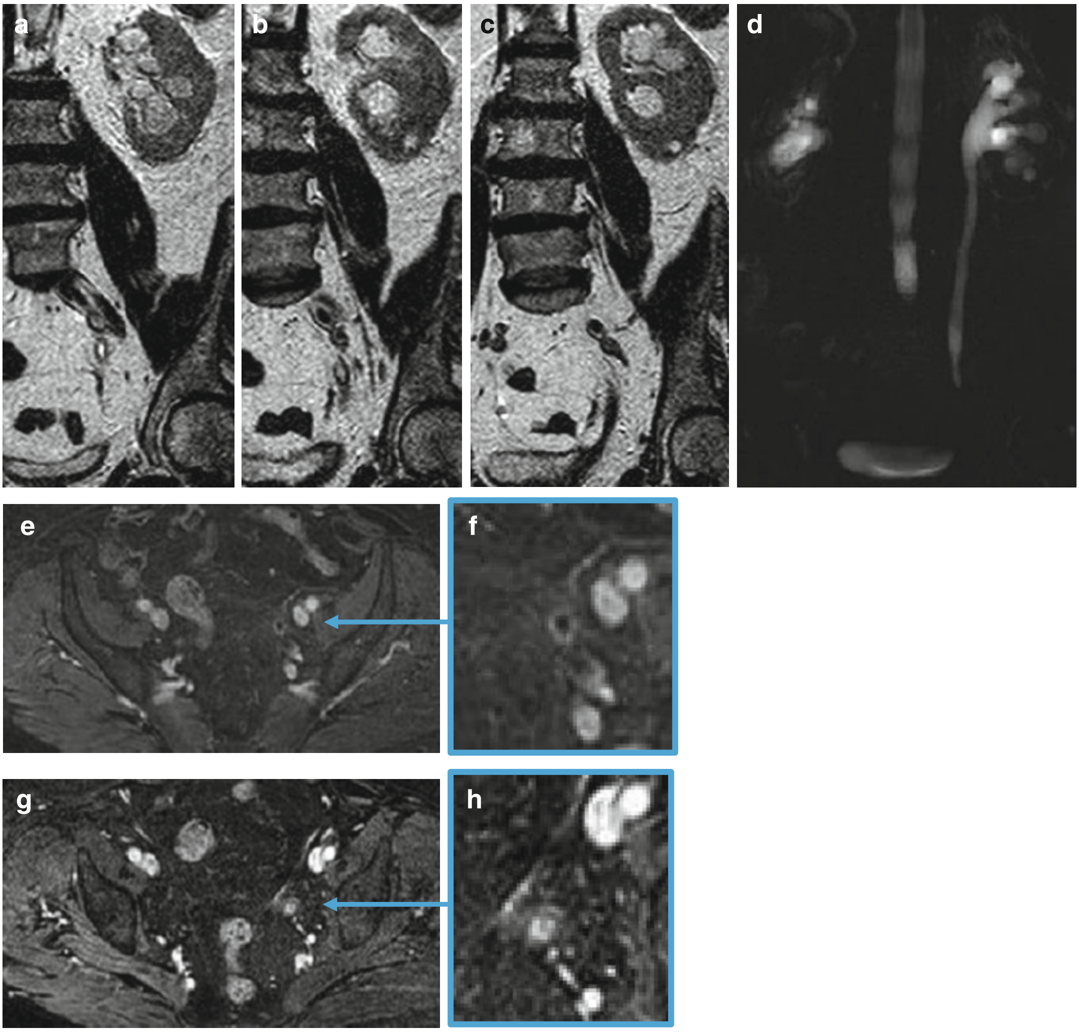

Fig. 10.14 SE breath-hold T2-SENSE images with a thickness of 3 mm (**a**–**c**) acquired on coronal plane, showing an abrupt caliber reduction of the left ureter at the transition point between the middle and distal third, with moderately thickened walls and discrete dilatation of the proximal ureter and intrarenal urinary tract, as can be seen also in the static-fluid MR image 8 cm thick (**d**). 3D GE T1W THRIVE sequences acquired after intravenous injection of contrast material (**e**–**h**), demonstrate a widespread enhancement of the walls of the left ureter, with slight enhancement of surrounding tissue at stenosis point; that was a pts. likely to have an inflammatory stenosis after repeated episodes of renal colic with calculi expulsions

procedures (from cesarean section to ureterectomy), trauma, tuberculosis of the genital tract, cryoablation, or radiotherapy with an incidence of approximately 1–4 % [22–24]. Urinary fistulae and leakages of the lower urinary tract are serious complications, and radiologists need to have enough information about these situations to perform precise diagnosis and treatment. Recent studies demonstrate that CE-MRU could show the existence and location of the urinary fistulae and leakages clearly without the need for another investigation technique. In addiction CE-MRU is a safe and relatively inexpensive technique that avoids exposure to radiation as well as nephrotoxic and more allergic contrast material administration [25].

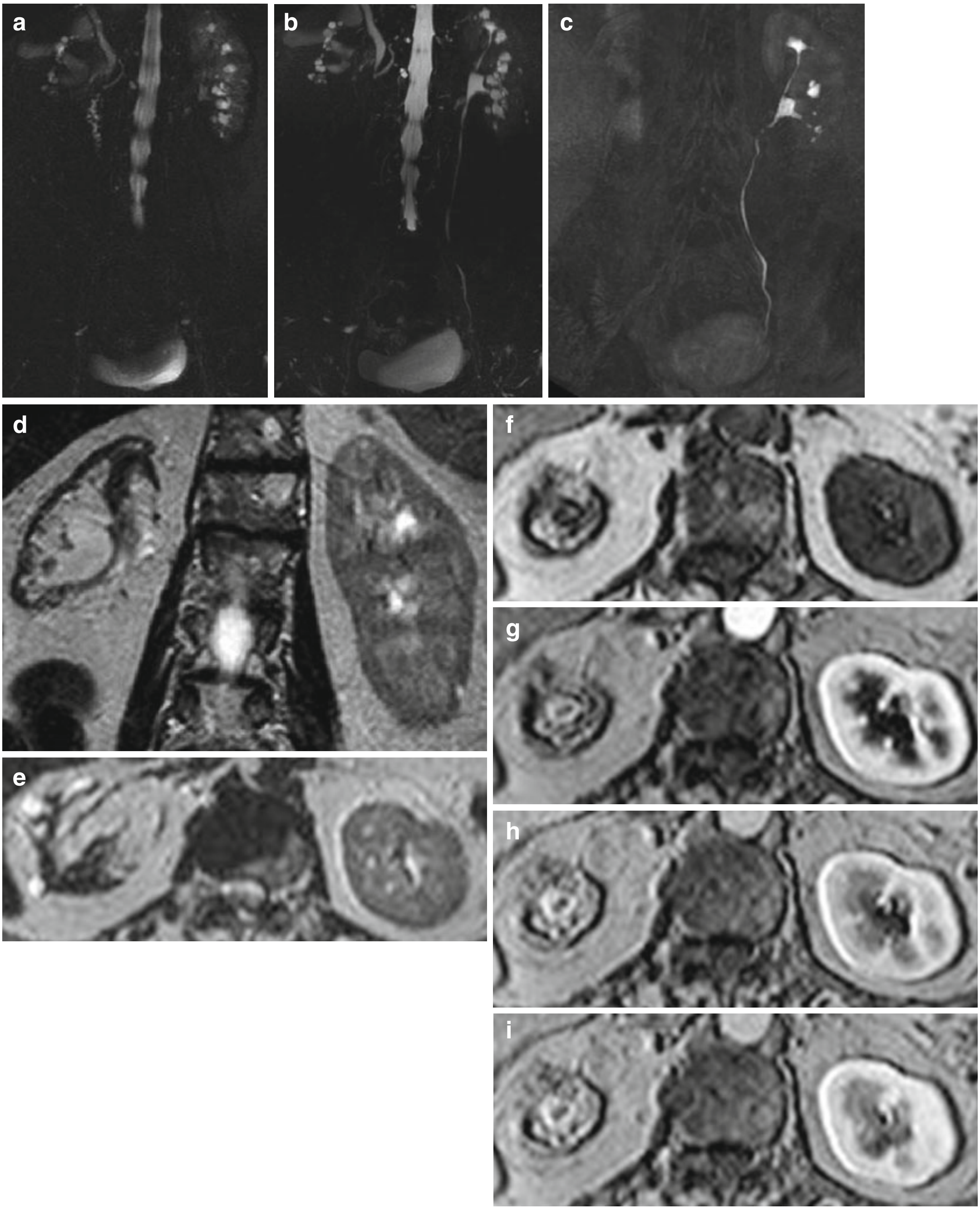

Fig. 10.15 Static-fluid MR images (**a**, **b**) and MIP reconstructions of excretory MR urography (**c**) demonstrating a normal representation of the urinary tract of the left and almost the complete lack of visualization of the right one; SE-T2W breath-hold SENSE 3 mm-thick images (**d**, **e**), acquired on coronal and axial planes, demonstrating right contracted kidney, with some cortical cysts, and mildely dilated lower-middle calyces group. In T1W images acquired before (**f**) and after intravenous injection of contrast medium (**g**–**i**) at 30, 60, and 100 s, there was a progressive and intense enhancement of the walls of the upper right group of the calyces, suggestive for urothelial origin neoplasm, subsequently confirmed at histological study

References

1. Childs DD, Leyendecker JR, Gianini J, Hall C (2013) Contrast-enhanced magnetic resonance urography at 3T: clinical feasibility. J Comput Assist Tomogr 37: 29–36
2. Merkle EM, Dale BM, Paulson EK (2006) Abdominal MR imaging at 3T. Magn Reson Imaging Clin N Am 14:17–26
3. Roy C, Saussine C, Guth S et al (1998) MR urography in the evaluation of urinary tract obstruction. Abdom Imaging 23:27–34
4. Regan F, Bohlman ME, Khazan R et al (1996) MR urography using HASTE imaging in the assessment of ureteric obstruction. AJR Am J Roentgenol 194: 125–130
5. Tang Y, Yamashita Y, Namimoto T et al (1996) The value of MR urography that uses HASTE sequences to reveal urinary tract disorders. AJR Am J Roentgenol 167:1497–1502
6. Rothpearl A, Frager D, Subramanian A et al (1995) MR urography: technique and application. Radiology 194:125–130
7. Roy C, Saussine C, Jahn C et al (1994) Evaluation of RARE-MR urography in the assessment of ureterohydronephrosis. J Comput Assist Tomogr 18:601–608
8. Aerts P, Van Hoe L, Bosmans H et al (1996) Breath hold MR urography using the HASTE technique. AJR Am J Roentgenol 166:543–545
9. Nolte-Ernsting CCA, Staatz G, Tacke J et al (2003) MR urography today. Abdom Imaging 28:191–209
10. Dym RJ, Chernyak V, Rozenblit AM (2013) MR imaging of renal collecting system with gadoxetate disodium: feasibility for MR urography. J Magn Reson Imaging 38:816–823
11. Karabacakoglu A, Karakose S, Ince O et al (2004) Diagnostic value of diuretic-enhanced excretory MR urography in patients with obstructive uropathy. Eur J Radiol 52:320–327
12. Nolte-Ernsting CCA, Tacke J, Adam GB et al (2001) Diuretic-enhanced gadolinium excretory MR urography: comparison of conventional gradient echo sequences and echo-planar imaging. Eur Radiol 11:18–27
13. Grattan-Smith JD, Jones RA (2006) MR urography in children. Pediatr Radiol 36:1119–1132
14. Mullins JK, Semins MJ, Hyams ES (2012) Half Fourier Single-shot turbo spin-echo magnetic resonance urography for the evaluation of suspected renal colic in pregnancy. Urology 79:1252–1255
15. Celik O, Ipekci T, Aydogdu O, Yucel S (2013) Current medical diagnosis and management of vesicoureteral reflux in children. Nephrourol Mon. 2013;6(1):e13534
16. Ellison JS, Maxfield CM, Wiener JS (2009) Voiding cystography practices and preferences of North American pediatric urologists. J Urol 182:299–304
17. Vasanawala SS, Kennedy WA, Ganguly A (2009) MR voiding cystography for evaluation of vesicoureteral reflux. AJR Am J Roentgenol 192:206–211
18. Riccabona M (2004) Pediatric MRU: its potential and its role in the diagnostic work-up of upper urinary tract dilatation in infants and children. World J Urol 22:79–87
19. Quaia E (ed) (2011) Radiological imaging of the kidney. Part II, Chapter 6: Magnetic resonance imaging of the kidney, Medical radiology. Springer, Berlin. doi:10.1007/978-3-540-87597-0_6, © Springer-Verlag Berlin Heidelberg
20. Blandino A, Gaeta M, Minutoli F et al (2002) MR urography of the ureter. AJR Am J Roentgenol 179:1307–1314
21. Yoshida S, Kobayashi S, Koga F (2013) Apparent diffusion coefficient as a prognostic biomarker of upper urinary tract cancer: a preliminary report. Eur Radiol 23:2206–2214
22. Yu NC, Raman SS, Patel M, Barbaric Z (2004) Fistulas of the genitourinary tract: a radiologic review. Radiographics 24:1331–1352
23. Narayanan P, Nobbenhuis M, Reynolds KM, Sahdev A, Reznek RH, Rockall AG (2009) Fistulas in malignant gynecologic disease: etiology, imaging, and management. Radiographics 29:1073–1083
24. Brown DB, Bhayani SB (2007) Persistent urine leak after cryoablation of a renal tumor in a patient with an ileal conduit. J Vasc Interv Radiol 18:1324–1327
25. Algin O, Ozmen E, Metin MR (2012) Contrast-material-enhanced MR urography in evaluation of postoperative lower urinary tract fistulae and leakages. Magn Reson Imaging 30:734–739

Fetal MRI

11

Alessia Adami, Sara Mehrabi, Alessandro Zaccarella,
Anna Ventriglia, Riccardo Manfredi,
and Roberto Pozzi Mucelli

11.1 MR Imaging Technique

Fetal MRI is a noninvasive method to study both fetal and maternal structures. Nowadays, ultrasonography is the standard screening modality (level 1) to detect possible fetal anomalies. If in the basic scan there is some suspect of fetal pathology, a more detailed ultrasonographic scan (level 2) must be performed to try to reach a diagnosis. Ultrasonography has a lot of advantages such as to obtain anatomic images with high resolution in real time or to visualize the fetus in different anatomic planes. It is furthermore a low-cost method, safe both for the mother and for the fetus. It has however some limits: poor visualization of the fetus because of maternal obesity or oligoanhydramnios, unfavorable fetal position, and twin fetuses [1].

MRI intervenes as a third-level exam, afterwards ultrasound imaging, with various aims: to confirm ultrasound diagnosis, to search for other possible associated anomalies, and to obtain the right information in order to do a prognostic prediction and give parents an adequate counseling. It offers several advantages over prenatal US. It has higher contrast resolution; it allows the direct visualization of both sides of the fetal brain, while in ultrasound imaging, the hemisphere underlying the transducer is often nonvisible and of the sulci, the cortex, and the structures situated in posterior fossa. It has a high sensibility for intracranial hemorrhages, and it overcomes some limits of ultrasounds such as maternal obesity, low amniotic fluid volume, or anomalous fetal position [2, 3].

Consequently, the results obtained with fetal MRI affect parental counseling and the management of pregnancy that includes the possibility to continue or interrupt pregnancy in later stages, to establish the modality of delivery, and to direct parents and newborn steps toward an adequate postnatal follow-up or postnatal therapeutic interventions.

Fetal MRI is nowadays performed with 1.5 T magnetic fields. There are many different limitations to fetal imaging, such as maternal and fetal motility. Simple rules are used to reduce the problem of maternal movement, such as to fast in the hours preceding the exam and to find the best position for the woman in the scanner. So patients that do not tolerate supine position could be positioned in left lateral decubitus [4].

The acquisition of images is particularly influenced by fetal motility, because the exam is not executed with maternal or fetal sedation. So fetal MRI is executed with ultrafast techniques, the so-called single-shot fast spin-echo (SS-FSE) or half-Fourier acquired single-shot turbo spin-echo (HASTE). Through such techniques, a single T2

A. Adami (✉) • S. Mehrabi • A. Zaccarella
A. Ventriglia • R. Manfredi • R.P. Mucelli
Department of Radiology,
G.B. Rossi University Hospital,
Piazzale Scuro 10, Verona 37134, Italy
e-mail: alessiaadami@hotmail.it

R. Manfredi, R. Pozzi Mucelli (eds.), *MRI of the Female and Male Pelvis*,
DOI 10.1007/978-3-319-09659-9_11, © Springer International Publishing Switzerland 2015

image can be acquired in less than a second, reducing the probability of artifacts due to fetal motion. Moreover, since every image is acquired separately, only the image acquired during the fetal movement is damaged, further reducing movement artifacts. Other limits of fetal MRI are the small size of the structure being imaged and the marked distance between the receiver coil (placed on maternal abdomen) and the structure being imaged, especially in earlier gestational ages. Therefore, fetal MRI is typically not performed before 22 gestational weeks. The examination protocol at first involves the acquisition of T2-weighted ultrafast sequences along the three planes, orthogonal to the maternal longitudinal axis: axial, sagittal, and coronal. These sequences have the main aim of analyzing relations between maternal-fetal structures and placental characteristics. T2-weighted ultrafast sequence images are then obtained of the fetal structures in the axial, coronal, and sagittal planes. The examination protocol can furthermore include the acquisition of sequences of the family of true fast imaging with steady-state precession (true-FISP), BALANCE or 2D FIESTA, that in some cases permits to obtain a higher spatial resolution, with thickness <3 mm for every slice.

Single-shot fluid-attenuated inversion recovery (single-shot FLAIR) sequences have a poor spatial resolution, but they can be used to identify intraventricular alterations or the normal cerebral stratification before the 25th week of gestation (GW).

In T1-weighted sequence areas of hyperintensity may be identified, such as cerebral hemorrhage, hematomas, meconium, and big clots. Such sequences have the disadvantage of long acquisition, times that require maternal apneas at least of 14 s in case of fast spin-echo T1 (FSE-T1) or at least of 20 s in case of gradient echo with short TR and TE. So T1-weighted images are more susceptible to fetal motion because of their longer acquisition times and they are of lower signal-to-noise image quality.

Advanced MR techniques such as diffusion-weighted imaging have also recently been successfully applied to fetal MR imaging. Diffusion-weighted imaging (DWI) provides quantitative information about water motion and tissue microstructure and can be used to identify focal areas of injury as well as to assess brain development. Diffusion MRI is useful when there is a suspect of acute ischemic lesion not correctly identifiable in T2-weighted images, because of the natural hyperintensity of cerebral tissue [4].

There is no accordance for what concerns the risks of fetal MR, because many studies have been executed on animal embryos, without homogeneity of methods and results; moreover, the studies on pregnant women are very few and not conclusive. So it is advisable not to execute the exam during the first trimester and not to administer contrast medium, to reduce potential risks for the developing fetus [5].

11.2 Maternal Imaging

MRI has been shown to be useful in the diagnosis of maternal complications during pregnancy. Physical examination in pregnancy is impaired by the presence of the gravid uterus, making assessment of abdominal or pelvic pathology difficult. Although CT is well established in the evaluation of acute abdominal pain, this exposes the fetus to ionizing radiation and should be avoided if possible. Ultrasonography remains the primary imaging modality; however, its value is limited by the enlarged uterus as well as lack of tissue specificity. MRI provides excellent anatomic detail without ionizing radiation and therefore is a useful adjunct in the characterization of abdominal and pelvic disease [6].

11.2.1 Gastrointestinal Causes

Acute appendicitis is the most common nonobstetric surgical condition in pregnant patients. Physical exam and imaging evaluation are made difficult by the enlarging uterus, which often displaces the appendix with the risk of a misdiagnosis because the location of pain is not typical and because symptoms and signs of appendicitis such as nausea, vomiting, and leukocytosis may occur physiologically during pregnancy.

The MR appearance of appendicitis includes an enlarged appendix, periappendiceal fluid, or inflammation or abscess formation.

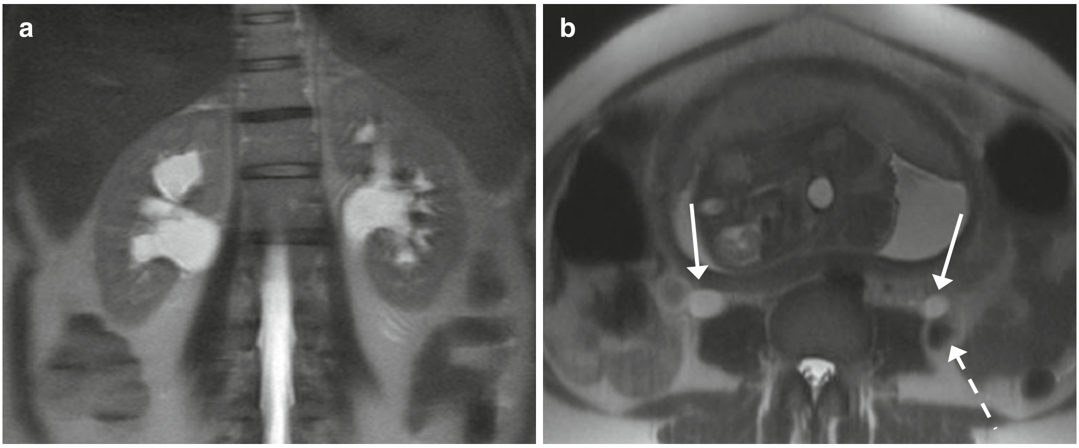

Fig. 11.1 Hydroureteronephrosis and deep venous thrombosis in a pregnant woman. (**a**, **b**) In the coronal (**a**) and axial (**b**) T2-weighted images (TR/TE ∞/95 ms), modest bilateral hydroureteronephrosis is visible, with dilated ureters that could be followed till the pelvis (*arrows*, **b**). A partial thrombosis of the left ovarian vein could be seen as a filling defect in the vascular lumen (*dashed arrow*, **b**)

MRI may also elucidate other gastrointestinal disorders as the cause of abdominal pain during pregnancy, such as bowel obstruction, abscess, toxic megacolon, bleeding, and cholelithiasis associated with choledocholithiasis and pancreatitis [7].

11.2.2 Renal Causes

Hydronephrosis is common during pregnancy, because of smooth muscle relaxation in the ureters and hormonal changes as well as extrinsic compression by the gravid uterus. This usually requires no intervention. It is occasionally necessary to exclude obstructing ureteral stone as the cause of hydronephrosis, and this may be difficult with ultrasound (Fig. 11.1).

Pyelonephritis is more common in pregnant than nonpregnant patients because of urinary stasis. While the diagnosis is usually made based on clinical parameters, MR imaging is useful to detect or exclude complications that require intervention such as perinephric abscess [8].

11.2.3 Gynecological Causes

Uterine leiomyomas demonstrate the same imaging characteristics during pregnancy as in the nongravid uterus. However, they may outgrow their vascular supply, resulting in degeneration, rapid growth, or torsion, leading to significant pain and premature labor. Most commonly, hemorrhagic infarction and necrosis will be seen with peripheral or diffuse high signal intensity on T1-weighted images and variable signal intensities with or without low signal intensity on T2-weighted images.

Subserosal fibroids can undergo torsion as well as degeneration during pregnancy.

When the gestational contents preclude accurate assessment with ultrasound, MRI is indicated. When multiple or large leiomyomas are present in the lower uterine segment, a decision may be made to perform cesarean section (Fig. 11.2) [9].

The diagnosis of an adnexal mass during pregnancy poses a diagnostic challenge. The most common adnexal mass in a pregnant patient is a corpus luteal cyst. It usually measures less than 6 cm in size and does not enlarge during pregnancy. MRI allows differentiation of simple cysts from more complex lesions, and the relationship between the mass and the pregnant uterus can be established. Because of the increased pressure in the pelvic cavity, adnexal masses may undergo extrinsic compression, hemorrhage, or torsion and lead to important abdominal pain (Fig. 11.3). Torsion is more common during pregnancy and

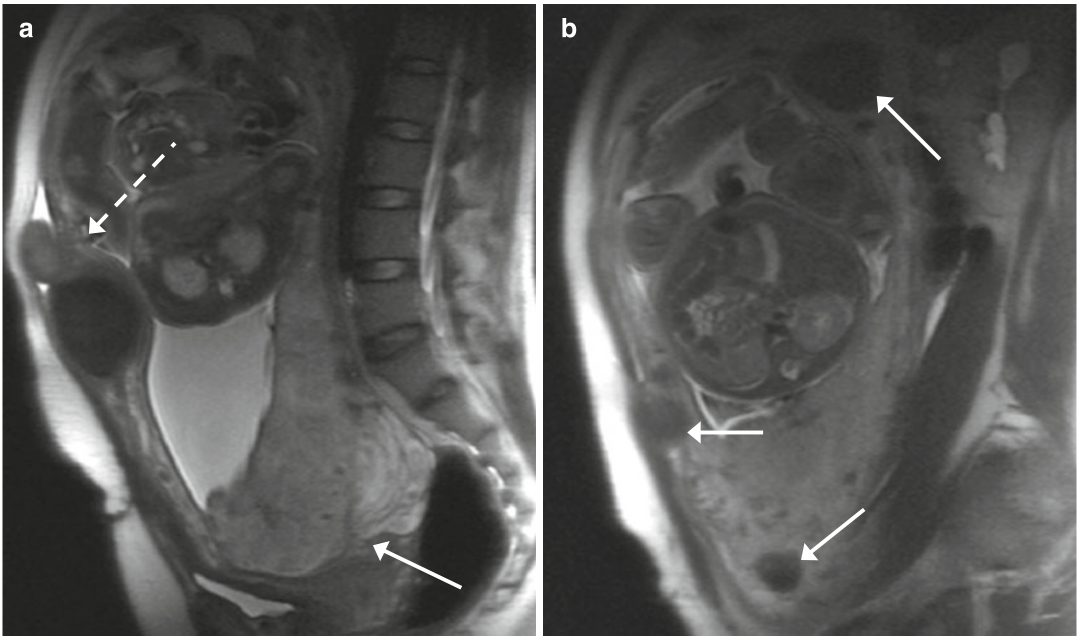

Fig. 11.2 Placenta previa and multiple fibroids in a pregnant woman (GW 32+4). (**a**, **b**) In the sagittal T2-weighted images (TR/TE ∞/95 ms), the placenta is inserted on the anterior and posterior wall of the uterus, and it covers the internal uterine orifice (*arrow*, **a**). Multiple fibroid intramural and submucosal tumors are visible (*arrows*, **b**). One subserosal pedunculated fibroid is localized in the ventral part of the body of the uterus (*dashed arrow*, **a**)

may occur with or without an underlying mass. On MR imaging, a torsed ovary appears enlarged and edematous with increased stromal signal intensity on T2-weighted images [10].

11.3 Placental Imaging

MRI, because of its multiplanar capabilities, allows exact assessment of the placental position size and volume. It has been shown to be highly accurate in the diagnosis of placenta previa and might thus be an important adjunct to ultrasound in inconclusive cases. Placenta previa is diagnosed when the placenta covers a portion or all of the internal cervical canal and usually presents with painless vaginal bleeding during the course of the third trimester (Figs. 11.2 and 11.4). A related placental condition is placenta accreta, which is a leading cause of emergent peripartum hysterectomy. Placenta accreta is caused by lack of decidua basalis, which normally prevents villous invasion of the myometrium; any cause of uterine scarring, such as cesarean section or myomectomy, can lead to abnormal placental attachment. Prior cesarean section is by far the most common risk factor (Fig. 11.4). Three types of placenta accreta are described: placenta accreta vera (adherence to the myometrium), placenta increta (invasion into the myometrium), and placenta percreta (invasion of the uterine serosa). Because emergency hysterectomy is associated with substantial maternal morbidity and mortality, the prenatal diagnosis of invasive placenta is important. MRI is particularly helpful to determine the extent of placental invasion, which is critical for presurgical planning. Diagnosis depends largely on multiplanar T2-weighted images where the placenta demonstrates moderately high signal intensity and fine internal architecture. MR findings suggestive of placenta accrete vera include myometrial thinning, irregularity, or focal disruption, but the findings may be subtle, since no frank myometrial invasion is present. MR findings of the more severe placenta percreta include dark placental bands on T2-weighted images, focal thinning of myometrium, disorganized architecture of the adjacent placenta, focal exophytic

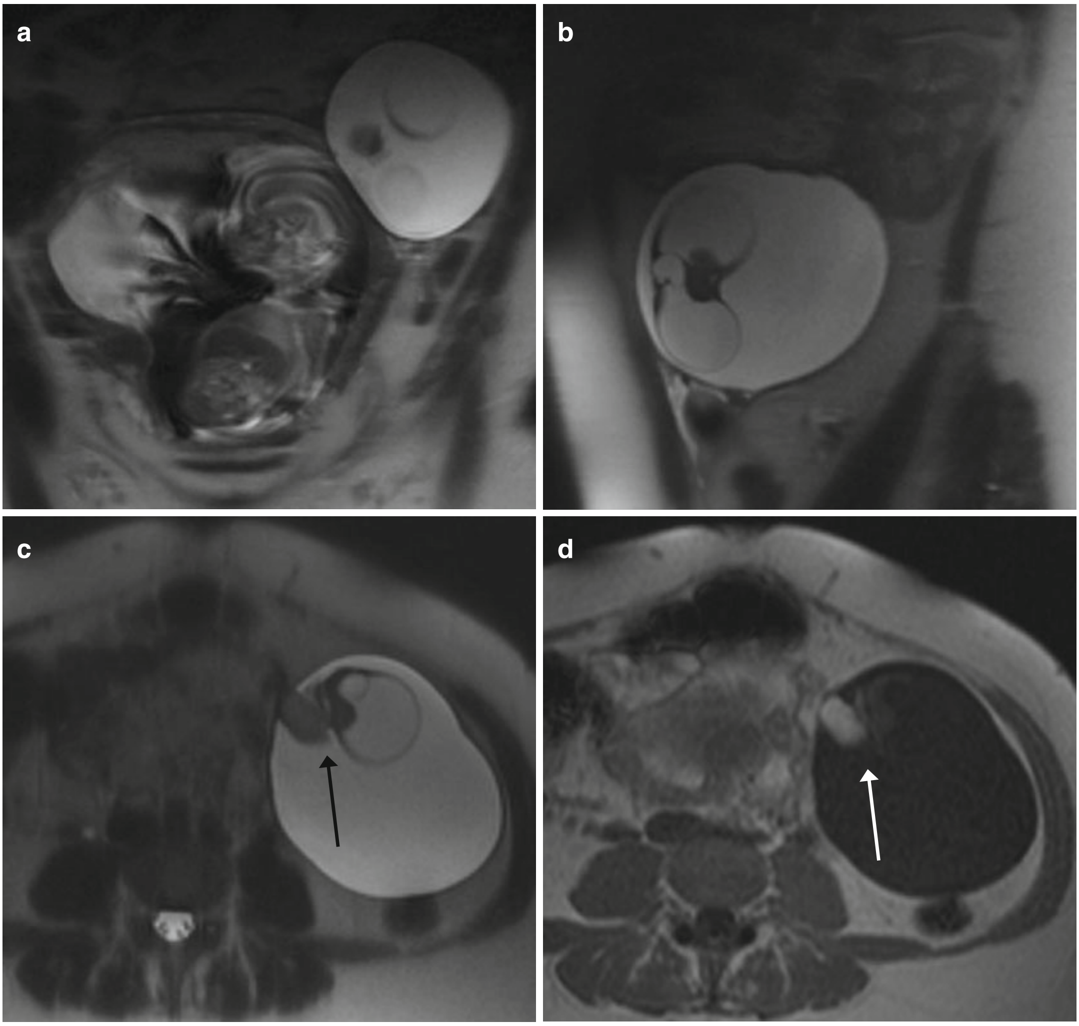

Fig. 11.3 Ovarian lesion in a pregnant woman. (**a**, **b**) Coronal (**a**) and sagittal (**b**) T2-weighted images (TR/TE 1,230/107 ms): the left ovary is entirely occupied by a cystic lesion. (**c**, **d**) Axial T2-weighted (**c**) and T1-weighted (**d**) images (TR/TE 141/4.7 ms): the lesion is well defined, with a prevalent cystic structure and an inner solid component (the Rokitansky nodule) (*arrow*, **c**) that presents the paramagnetic phenomenon (*arrow*, **d**). These characteristics permit the diagnosis of a dermoid cyst

mass, and in cases of anterior placental invasion involving the bladder, thinning of the uterine serosa-bladder interface [11, 12].

11.4 Fetal Imaging

11.4.1 Central Nervous System

Because the fetal brain is a dynamic structure, it is important for radiologists to familiarize themselves with the normal appearance of it at different gestational ages in order to be better able to identify and characterize abnormalities with fetal MRI. Changes in fetal brain maturation proceed through different stages in a predictable fashion: by gestational weeks (GW) 12–23, the brain demonstrates a smooth surface except for the interhemispheric fissure. Sulci appear with this order: Sylvian and interhemispheric (GW 10–15); calcarine, parieto-occipital, and cingulate (GW 16–19); central and superior temporal

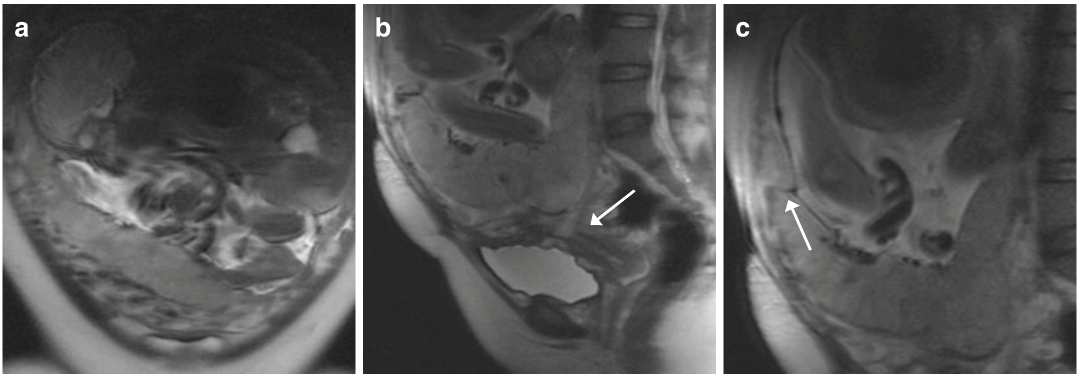

Fig. 11.4 Placenta previa and accreta (GW 30+5). (**a**–**c**) Coronal (**a**) and sagittal (**b**, **c**) T2-weighted images (TR/TE ∞/95 ms): unique fetus in podalic position and with his back turned toward the left side (**a**). The placenta is inserted on the anterior and posterior wall of the uterus, and it covers the internal uterine orifice (*arrow*, **b**). On the anterior wall of the uterus, the placenta shows an area of inhomogeneous signal (*arrow*, **c**) that corresponds to the site of previous caesarian sections. This is compatible with placenta accreta, confirmed after birth by the histological analysis of the uterus and placenta

(GW 20–23); precentral, postcentral, and superior frontal (GW 24–27); inferior frontal and inferior temporal (GW 28–31); insular, parietal, superior occipital, secondary frontal, secondary parietal, and secondary temporal (GW 32–35); and inferior occipital, tertiary frontal, and tertiary parietal (GW 36–39) (Fig. 11.5) [13]. Sulcation in the whole cerebral cortex is seen from GW 30 on, whereas infolding of the cortex and opercular formation will not be seen before GW 33. The developing nervous system has a multilayered appearance; till GW 28, from the surface to the depth, four layers could be recognized: the cortical plate, the subplate, and the intermediate and the ventricular zone that contains the germinal matrix. Afterwards, such distinction will fade away till the only distinction between white and gray matter (Fig. 11.6).

The germinal matrix appears as a band of T2 hypointensity/T1 hyperintensity, for the high density of cells and microvessels, surrounding the ventricles in early gestation until the third trimester, when it gradually regresses to be present only in the caudo-thalamic groove at term. The cortical plate is seen as a band of T2 hypointensity/T1 hyperintensity at the periphery of the brain. The intervening parenchyma is of higher signal intensity on T2-weighted images but contains two visible layers as well, usually discernable between GW 20 and 28 [14].

By GW 23, cerebral ventricles appear relatively large, corresponding to the normal fetal hydrocephalus, gradually becoming smaller thereafter. The atria of the lateral ventricles remain relatively stable in size from GW 15 to 35, and the size should be less than 10 mm at the level of the atria when measured in an axial plane both by ultrasound and MRI. The cavum septi pellucidi is situated between the two lateral ventricles. It is a transient structure that remains visible till the end of pregnancy, and it has the same signal characteristics of the ventricles. Sonographic measurements of the third ventricle in the axial plane have revealed an upper limit of normal ranging from 1.0–1.2 mm by GW 12 to 3.5–3.6 mm at term, although no MR correlation has yet been performed. The cisterna magna may be difficult to visualize in the third trimester with ultrasound because of attenuation from the calvarium at the skull base; however, this is well visualized with MRI throughout the second and third trimesters. The subarachnoid space overlying the cortical convexities is slightly dilated at all gestational ages, most markedly by GW 21–26. The corpus callosum develops between GW 8 and 20. With MR, it is normally visible by GW 20 as a subtle T2 hypointensity. It forms in an orderly progression from genu to splenium, with the rostrum being formed last. The cerebellum, as the cerebral hemispheres, has a progressive

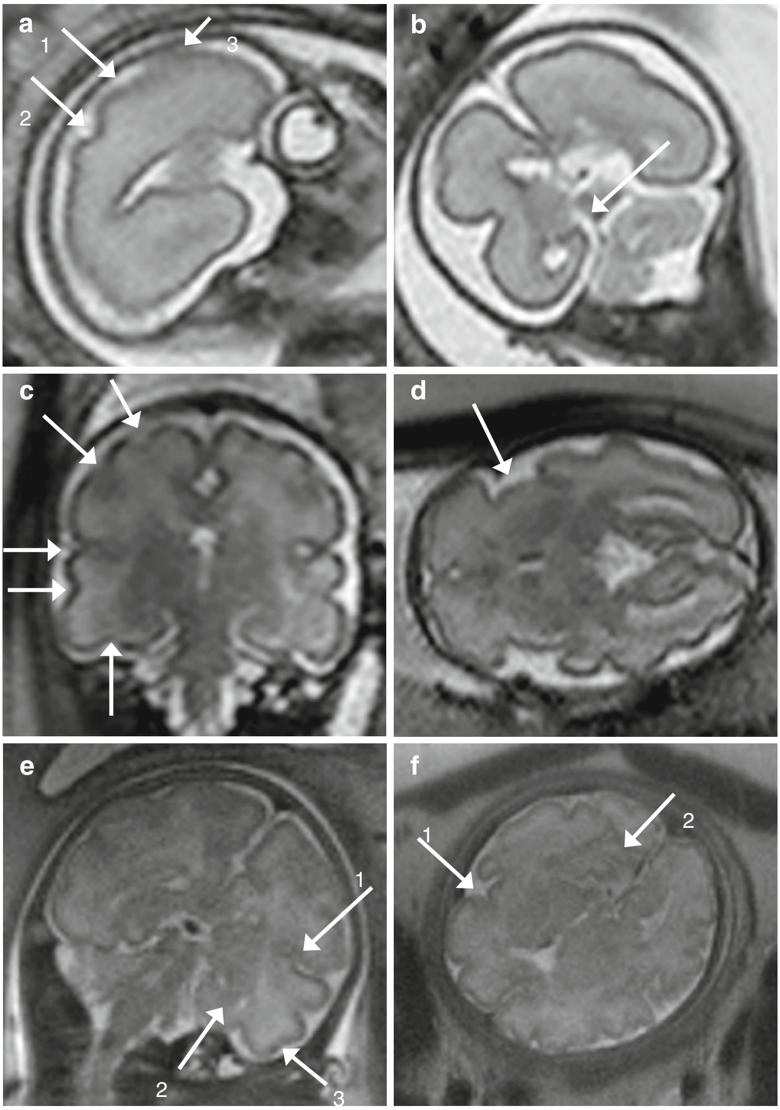

Fig. 11.5 Development of the sulci. (**a**, **b**) GW 24. In the sagittal (**a**) T2-weighted image (TR/TE ∞/95 ms), the central (*1*), the postcentral (*2*), and the precentral (*3*) sulci are visible. In the coronal (**b**) T2-weighted image, the calcarine sulcus (*arrow*) is visible. (**c, d**) GW 31. In the coronal (**c**) T2-weighted image (TR/TE ∞/95 ms), in counterclockwise direction, the precentral, the central, the lateral (of Sylvius), the superior temporal, and the occipito-temporal sulci are visible. In the axial (**d**) T2-weighted image (TR/TE ∞/95 ms), the Sylvian valley is visible. (**e**, **f**) GW 34. In the coronal (**e**) T2-weighted image (TR/TE ∞/95 ms), the inferior temporal sulcus is visible (3). The lateral (of Sylvius) (*1*) and the calcarine (*2*) sulci are also showed, as in the next axial (**f**) T2-weighted image (TR/TE ∞/95 ms)

development of the sulci. The first fissure that appears is the posterolateral one, by GW 12–13, and it divides the corpus cerebelli from the flocculonodular lobe. The development of the primary fissure that divides the anterior from the posterior lobe follows by GW 14–15, and subsequently, the prepyramidal, preculminate, and precentral fissures are seen by GW 15–16, and the horizontal fissure by GW 21. The foliation of the vermis starts in GW 14, and between 24 and 37 GW, the number of foliae in each lobule accounts for 50 % of the amount in adults. By GW 17, the primary fissure of the vermis should be visible, as should a normal fastigial point with an acute angle. The prepyramidal fissure is visible by GW 21, the preculminate fissure by GW 21–22, and the secondary fissure by GW 24. By GW 27, all vermian lobules and fissures are visible. The craniocaudal length of the vermis reaches that of the cerebellar hemispheres by GW 18–19. The vermis extends caudally to cover the roof of the fourth ventricle, completely covering it by GW 22–24.

The pons and the mesencefalus begin to differentiate themselves by GW 8. They appear hyperintense in T2-weighted images and hypointense in

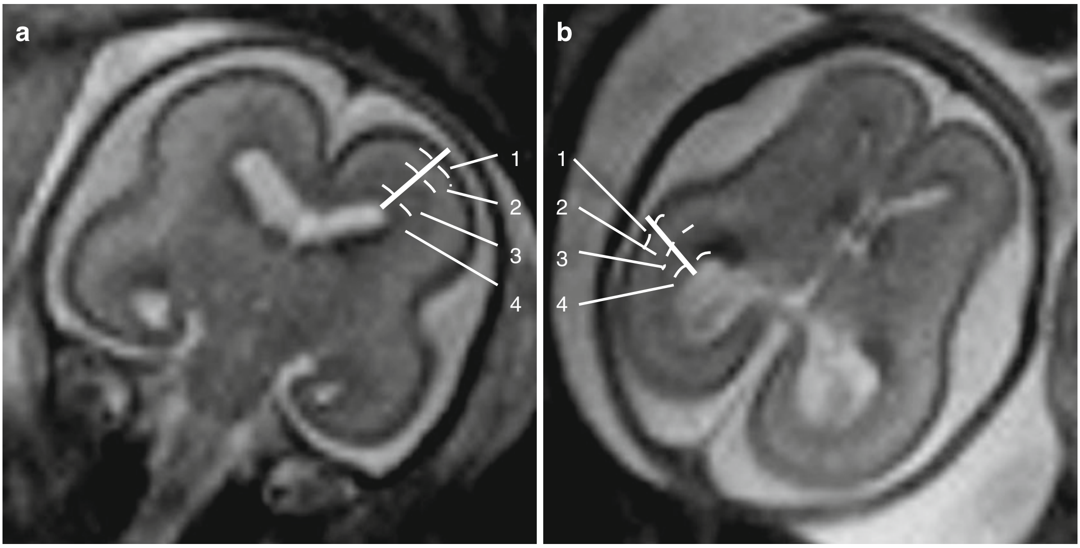

Fig. 11.6 Multilayered appearance of the developing nervous system at GW 24. (**a**, **b**) Coronal (**a**) and axial (**b**) T2-weighted images (TR/TE ∞/95 ms): from the surface to the depth, four layers could be recognized, the cortical plate (*1*), the subplate (*2*), the intermediate (*3*), and the ventricular zone (*4*) that contains the germinal matrix

T1-weighted images in their ventral portion, but they become more and more hypointense in T2 and hyperintense in T1 in their dorsal portion, because of the progressive myelination of the ascending tract. The medulla oblongata contains ascending myelinated sensitive tracts, hypointense in T2-weighted images, and pyramidal tracts, whose myelination will begin in the postnatal period, which appear hyperintense in T2-weighted images [15].

The first role of fetal MRI is to explore the fetal brain anatomy to ensure that every structure is correctly developing and to make measurements on the fetal brain to ascertain that its development corresponds to the gestational age (Fig. 11.7). The obtained measurements could be compared with brain normal linear biometric values extrapolated by literature (Tables) [16, 17].

11.4.2 Ventriculomegaly

Ventriculomegaly (VM) represents the most frequent encephalic anomaly seen at fetal magnetic resonance imaging (MRI), with an incidence varying between 0.5 and 2 per 1,000 births per year. The frequency of associated malformations, both cerebral and extracerebral, varies between 41 and 78 % [18]. The causes of VM are as follows:

- Anomalous turnover of cerebrospinal fluid caused by block to the ventricular system (i.e., expansive lesions, inflammatory and infective processes, hemorrhage) or by block to the reabsorption system (i.e., meningoencephalitis, subaracnoideal hemorrhage)
- Anomalous cerebral development (i.e., corpus callosum agenesis) or neuronal disorders of proliferation or migration
- Destructive processes (i.e., hemorrhages or infections)

Lateral ventricles are characterized by an anterior portion (frontal horn) and a posterior portion (atrium and occipital horn). In normal conditions, the ventricular cavity at the atrium is almost completely occupied by plexus choroid glomus. When a ventricle enlarges itself, the fluid accumulates between the choroid plexus and the medial wall, giving an image of dangling plexus. Ventricular measurement can be conducted on coronal images, placing calipers at the atrial level on the axis which is perpendicular to the ventricular one or on axial images

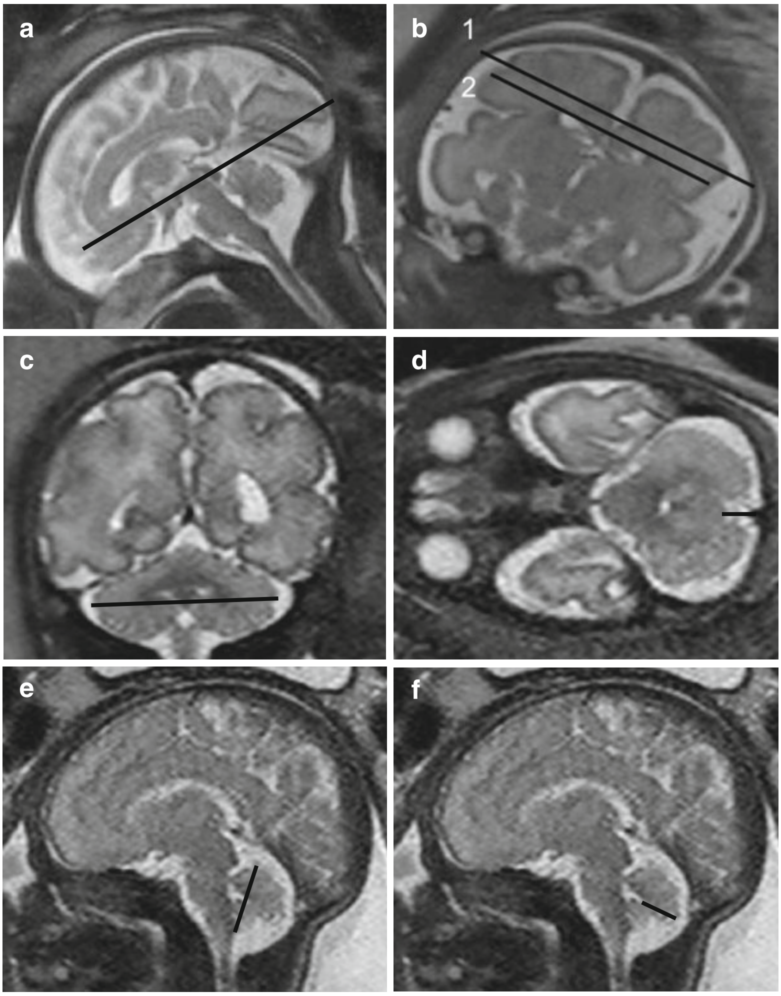

Fig. 11.7 Main linear measures useful to evaluate normal brain development. (**a**) Sagittal T2-weighted image (TR/TE ∞/95 ms): fronto-occipital diameter. (**b**) Coronal T2-weighted image (TR/TE ∞/95 ms): bone biparietal (*1*) and cerebral biparietal (*2*) diameter. (**c**) Coronal T2-weighted image (TR/TE ∞/95 ms): transverse cerebellar diameter. (**d**) Axial T2-weighted image (TR/TE ∞/95 ms): width of the cisterna magna. (**e**) Sagittal T2-weighted image (TR/TE ∞/95 ms): supero-inferior diameter of the vermis. (**f**) Sagittal T2-weighted image (TR/TE ∞/95 ms): anteroposterior diameter of the vermis

and placing calipers at the luminal margins of ventricular atria, perpendicular to the long axis of the ventricle, at the level of the glomus of the choroid plexus. The measure is stable during the second and third trimester, with a medium diameter of 6–8 mm, and it is normal till a limit value of 10 mm.

VM can be both monolateral and bilateral; s can be both monolateral and bilateral, symmetric or asymmetric, and it is diagnosed when the atrial diameter (AD) of one or both ventricles is ≥10 mm (corresponding to 4 standard deviations (SD) above the mean) from 14 weeks of gestational age to term (Fig. 11.8). It is classified into three degrees of severity depending on the width of dilatation [19]:

- Mild (or borderline): 10 mm ≤AD ≤12 mm
- Moderate: 13 mm ≤AD ≤15 mm
- Severe: AD >15 mm

The factors that most affect the prognosis of a fetus with VM are width of dilatation (mild, moderate, severe), presence of associated anomalies (structural, chromosomal), and an underlying etiological factor (i.e., infections, alloimmune thrombocytopenia) [20]. More than 60 % of cases of severe VM are associated with structural anomalies (Fig. 11.8). Prognosis for severe VM associated with other malformations is unfavorable, with a 2-year survival rate not exceeding 16 %. Prognosis of isolated severe VM is slightly better, with a 33 % survival rate at 2 years and normal neurological and physical

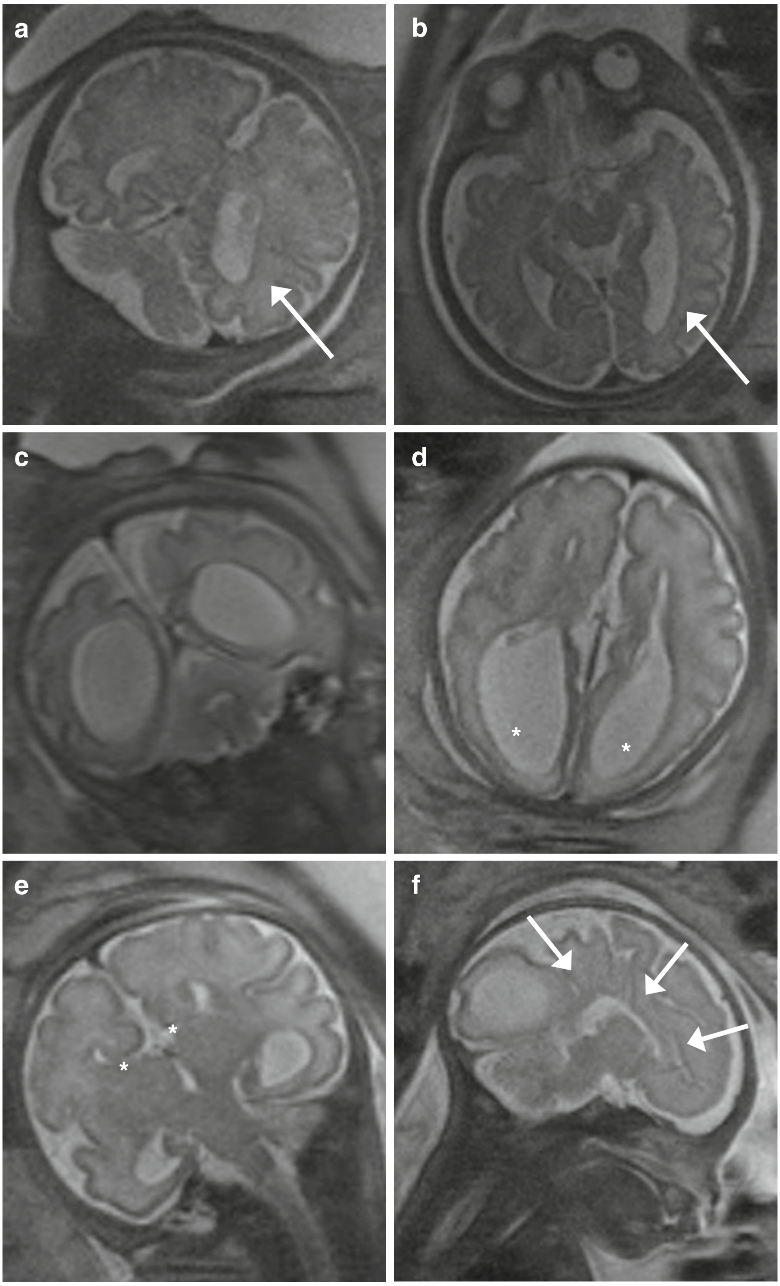

Fig. 11.8 (**a**, **b**) Mild ventriculomegaly (GW 35+2). In the coronal (**a**) and axial (**b**) T2-weighted images (TR/TE ∞/95 ms), mild unilateral dilatation of the left lateral ventricle is present (*arrows*), with an atrial diameter of 11 mm. The right one is normal, having a diameter of 9 mm. (**c**–**f**) Severe ventriculomegaly associated to complete agenesis of the corpus callosum (GW 32+1). Coronal (**c**, **e**), axial (**d**), and sagittal (**f**) T2-weighted images (TR/TE ∞/95 ms): severe bilateral dilatation of the lateral ventricles is present (**c**, **d**) with the right atrial diameter of 22 mm and the left one of 19 mm. The ventriculomegaly is associated to complete agenesis of the corpus callosum and of the cavum septi pellucidi, best demonstrable in the coronal image (**e**). Other secondary signs of corpus callosum agenesis are the parallel aspect of the lateral ventricles (**d**), the extreme distance between frontal horns (**d**) and their internal concavity (*asterisks*, **e**), the enlargement of atria and occipital horns (*asterisks*, **d**), and the radial disposition of the sulci on the mesial hemispheric surface (*arrows*, **f**)

development in 10–62.5 % of cases, depending on the study [21]. Moderate VM is associated with other anomalies in 10–50 % of the cases, whereas mild VM is associated in a very low percentage of cases. Prognosis is conditioned by the existing concomitant anomalies. Regarding the prognosis of isolated forms, a delay in neurological development can be found in 25 % of cases of moderate and in up to 7 % of cases of mild VM [22].

Another factor influencing the prognosis of isolated VM, either moderate or mild, is the evolution of dilatation over time. VM progression occurs in 16 % of cases, whereas stabilization is reported in 43 % of cases, and an in utero normalization occurs in 41 % of cases. Progression is associated with a 22 % rate of chromosomal anomalies and with a negative prognosis in 44 % of cases in comparison with 1 and 7 %, respectively, of the forms that do not progress (stabilization or regression) [23].

11.4.3 Medium Line Malformations

11.4.3.1 Holoprosencephaly and Absence of the Cavum Septi Pellucidi

Holoprosencephaly refers to a large group of cerebral malformation with a common embryogenesis, with an incomplete separation of the prosencephalus in right and left hemisphere. There are three principal forms:

- Lobar holoprosencephaly (separated lateral ventricles)
- Semilobar holoprosencephaly (partially separated lateral ventricles)
- Alobar holoprosencephaly (lateral ventricles fused in one)

There is another form, syntelencephaly, that involves parietal and frontal lobes, and it seems to have a different embryonal origin.

RM is especially useful in the evaluation of difficult cases of holoprosencephaly and syntelencephaly, to identify a small fusion of frontal lobes or to make the differential diagnosis between holoprosencephaly and microcephaly. RM is also useful to identify eventual associated anomalies [24].

Absence of the cavum septi pellucidi is seldom isolated; it is usually acquired, secondary to a disruptive process such as endoventricular hemorrhage or infective process, or associated to a malformative process, such as holoprosencephaly or septo-optic dysplasia. In cases of no visualization of the folders of the septi pellucidi in US, MRI can confirm the absence of such structures, which can be appreciated in every plane. The inferior dislocation of the fornices, a consequence of the absence of septi pellucidi, is better seen in sagittal sequences. MRI is especially indispensable to search eventual associated anomalies or possible causes of the malformation [25].

11.4.3.2 Abnormalities of the Corpus Callosum

The prevalence of abnormalities of corpus callosum is 0.3–0.7 % in general population and 2–3 % in population with developmental delay. They can be associated to other malformations, either cerebral or extracerebral, including at least 46 malformative syndromes and metabolic disorders.

Fetal MR is useful in the evaluation of sonographically suspected callosal anomalies because the corpus callosum can be directly visualized in the sagittal and coronal planes as a curvilinear T2 hypointense structure located at the superior margin of the lateral ventricles, superior to the fornices. Direct visualization of the callosum by sonography, however, is more difficult, and thus, sonography typically relies on indirect signs of abnormal callosal development (such as absence of the cavum septi pellucidi, colpocephaly, which is a selective ventriculomegaly of the occipital horns more than the frontal or temporal horns of the lateral ventricles and inferior orientation of the medial hemispheric sulci) to identify abnormalities of callosal formation. These indirect signs can also be seen with fetal MRI (Fig.11.8) [26]. On fetal MR, the corpus callosum is best assessed using thin (3 mm) midline sagittal images. Its length can be measured on midline sagittal images, and measurements can be compared with published normative data, especially in cases of suspected callosal hypogenesis [27].

Fetal MR has been reported to have a greater detection of callosal agenesis as compared with prenatal US. In addition, fetal MR can identify an intact corpus callosum in approximately 20 % of cases referred for sonographically suspected callosal agenesis or hypogenesis, which has significant implications for patient counseling. Additional callosal abnormalities, including hypogenesis (or partial agenesis), dysgenesis, and hypoplasia, can also be diagnosed by fetal MRI. Because of the normally thin appearance of the fetal corpus callosum, callosal hypoplasia is more difficult to diagnose, especially during the second trimester.

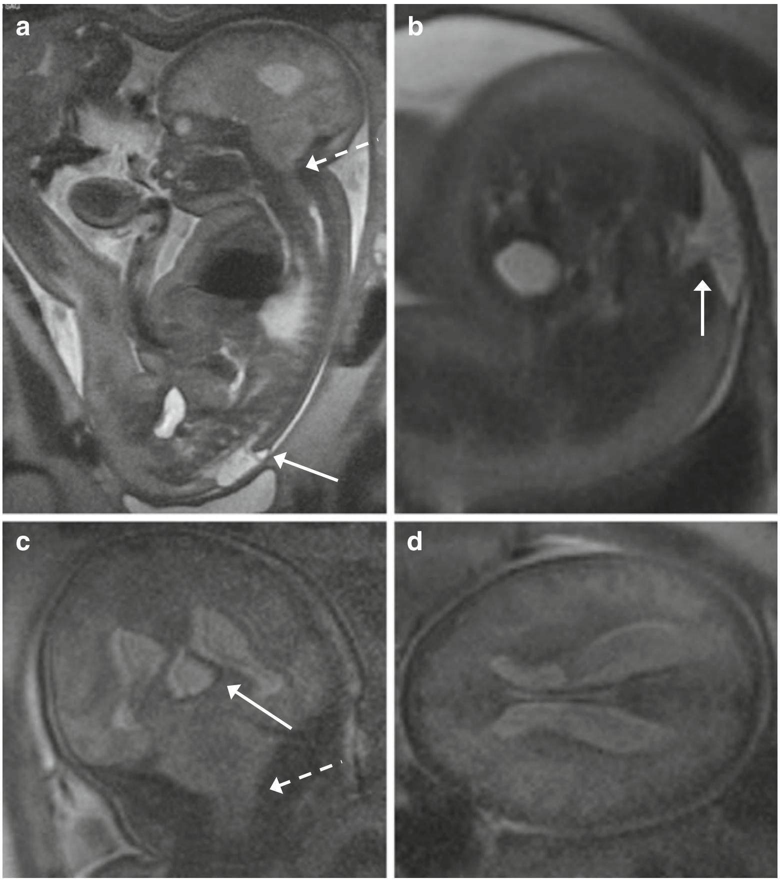

Fig. 11.9 Lumbosacral myelomeningocele with Chiari II and triventricular hydrocephalus (GW 35+3). (**a**–**d**) Sagittal (**a**), axial (**b**, **d**), and coronal (**c**) T2-weighted images (TR/TE ∞/95 ms): open spinal dysraphism at lumbosacral level, with herniation from the spinal canal of the meninges and nervous structures that come in touch with the cutaneous plane (*arrows*, **a**, **b**). A Chiari II malformation is also present, with herniation of the cerebellar tonsils and of the brainstem through the foramen magnum into the spinal canal (*dashed arrows*, **a**, **c**). This implies the reduction of the dimensions of the posterior cranial fossa, with more caudal insertion of the tentorium and disappearance of basal cisterns and of the fourth ventricle (**a**, **c**). An obliteration of the supratentorial subarachnoid spaces is also demonstrable (**a**, **c**, **d**). A secondary severe dilatation of the third ventricle (*arrow*, **c**) and of both the lateral ventricles is present

Fetal MRI is important in detecting additional abnormalities in cases of callosal agenesis. Indeed, detection of associated brain anomalies by fetal MR is greater than by prenatal sonography in these cases, and additional anomalies are detected by fetal MR in up to 93 % of cases. The identification of additional findings by fetal MRI may suggest a specific disorder or syndrome associated with callosal agenesis; this has implications both for the current pregnancy and for the recurrence risk in future pregnancies. Thus, when fetal MRI is performed for cases of suspected callosal agenesis, the supratentorial structures as well as the infratentorial structures should be carefully examined [28].

11.4.4 Posterior Fossa Abnormalities

11.4.4.1 Chiari II

Chiari II malformation is an important indirect sign of open spinal dysraphism (myelomeningocele and myelocele) (Fig. 11.9). Each of these can occur with or without spinal cord splitting with an incidence of 0.5–1 in 1,000 live births. The

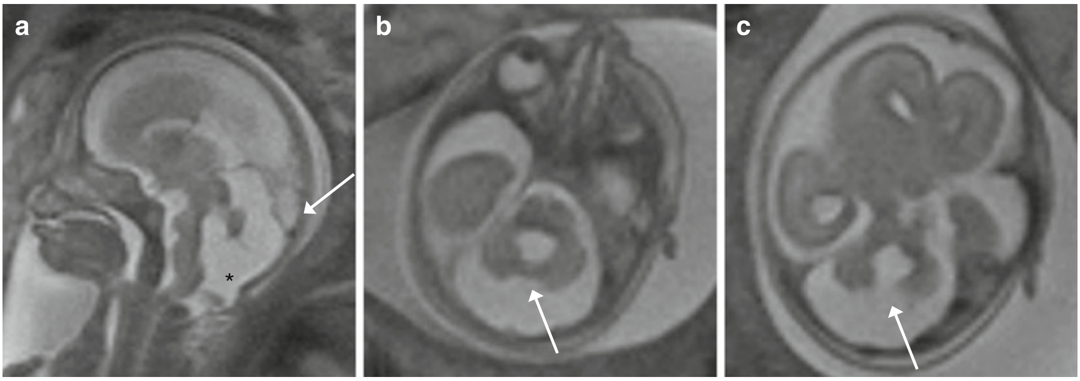

Fig. 11.10 Dandy-Walker malformation (GW 21+2). (**a**–**c**) Sagittal (**a**) and axial (**b**, **c**) T2-weighted images (TR/TE ∞/95 ms): enlargement of posterior cranial fossa with an expanded cisterna magna (*asterisk*, **a**) and with the upward displacement of the tentorial insertion (*arrow*, **a**) is visible. Partial vermian agenesis, with the presence of its superior part (*arrow*, **b**) and the absence of its inferior part, and direct communication between a dilated fourth ventricle and the cisterna magna (*arrow*, **c**) are also demonstrable

position of the neural placode with respect to the level of the skin surface differentiates myelomeningocele from myelocele. When there is elevation due to expansion of the subarachnoid space, the lesion is called a myelomeningocele (MMC). Axial images demonstrate the posterior osseous and skin defect, through which the neural placode protrudes, secondary to expansion of the underlying subarachnoid space that is covered by a thin membrane.

Myelocele (myeloschisis) is the term used when the placode is in plane with the level of the back without an overlying membrane-covered fluid-filled sac. This is much less common than the MMC but is embryologically similar. Only the expansion of the subarachnoid space distinguishes an MMC from a myelocele. The clinical manifestations and functional impairments are similar in these two entities. The localized failure of neural tube closure can occur anywhere along the spinal cord but is most common in the lumbosacral region [29].

The association between open spinal dysraphism and Chiari II is proposed to be due to the leakage of cerebrospinal fluid via the spinal defect that collapses the primitive ventricular system and prevents expansion of the rhombencephalic vesicle. This may result in a small posterior fossa with medulla, vermian, and cerebellar tonsil herniation. It is important to remember that in some cases, the findings may be mild and may progress; thus, close follow-up and correlation with alpha-fetoprotein and karyotype is important. With US, the so-called *banana sign* permits to discover the anomaly, but it cannot help to establish the entity of the problem. Through sagittal images, MRI is helpful to determine the entity of cerebellar herniation, which is directly correlated to the neurological outcome. MRI permits to identify other typical findings of Chiari II malformations, such as the *lemon sign* (which refers to the shape of the fetal skull when the frontal bones lose their normal convex contour and appear flattened in axial images at the level of the ventricles) and the *American eagle sign* (angled aspect of the lateral ventricles), to evaluate lateral ventricular dimensions and cerebral parenchyma. T2 signal is in fact increased in fetuses with Chiari II malformation, because of an increase of extracellular water, such as demonstrated by apparent diffusion coefficient calculation [30].

11.4.5 Cystic Anomalies

The Dandy-Walker (DW) malformation has an incidence of 1/25,000–35,000 live births. The classic DW malformation includes three criteria: (1) partial or complete vermian agenesis,

(2) cystic dilatation of the fourth ventricle, and (3) enlargement of posterior cranial fossa with upward displacement of the insertion of the tentorium (Fig. 11.10).

DW malformation can be isolated or associated to a chromosomal disorder or a polymalformative syndrome. Thus, it is important to search for other neurological and extraneurological anomalies and to do karyotype analysis. DW malformation is observed in 1–4 % of hydrocephalus prenatally diagnosed, and in such cases, the prognosis is poor.

Vermian agenesis is defined as partial or complete absence of vermis. When the agenesis is partial, the inferior portion of the vermis is usually absent. It is important to acquire both sagittal and axial images with thin slices, to avoid partial volume artifacts with the cerebellar hemispheres. It may be isolated or may be part of different syndromes, associating brain and visceral malformations [31].

Cerebellar hypoplasia is a small but proportionated cerebellum with short fissures, normally arranged. It can be considered the result of reduction or arrest of cell production. The diagnosis is based on a reduced transverse cerebellar diameter that can only be revealed in the third trimester of pregnancy. It is usually a secondary condition, but it may be primitive, and in such cases, we could have a pontocerebellar atrophy/hypoplasia [31].

Mega cisterna magna is subjectively estimated and corresponds to abundant retrocerebellar fluid. It is a normal anatomic variant so the normal features must be identified, without any ventricular enlargement [32].

Persistent Blake's pouch cyst represents an embryonic midline outpouching of a portion of the primitive fourth ventricle (superior medullary velum), which extends inferior and posterior to the vermis into the cisterna magna and may push the developing tentorium into an abnormal, relatively high position. Its appearance at imaging is that of a nonspecific retrocerebellar cyst [33].

Closed arachnoid cyst is a cystic pouch without communication with the fourth ventricle, and it may be localized in every cisternae space of the posterior fossa. It is usually associated with a good prognosis; however, if the cyst is large, the mass effect can blur cerebellar foliation, and it can be difficult to be completely sure of the diagnosis. Moreover, a large cyst can compress CSF pathways, leading to hydrocephalus. Cysts can increase in size in the few days or weeks after birth and thus require postnatal follow-up [32].

11.4.6 Ischemic and Hemorrhagic Cerebral and Cerebellar Disease

A wide variety of maternal, fetal, or placental pathological conditions resulting in circulatory impairment may lead to different types of lesions depending on the time of occurrence during gestation and the severity and the duration of the intrauterine insult. Examples of maternal conditions are systemic disorders (anemia, coagulopathy, cardiovascular collapse, anaphylactic reaction), alloimmune thrombocytopenia, eclampsia and preeclampsia, epileptic seizures, and trauma. Examples of fetal conditions are umbilical cord accident, death of one monochorionic twin, infection, arterial-venous malformations, and fistulae. Examples of placental conditions are placenta previa, abruptio placentae, intrauterine growth retardation, and polyhydramnios. There are also iatrogenic causes, such as amniocentesis and fetal blood sampling.

Imaging techniques, particularly fetal ultrasonography and, more recently, magnetic resonance imaging, have made it possible to detect these lesions in utero. Their morphological appearance depends on the time that has elapsed between the insult and examination of the fetal brain. In the acute phase (first 3–5 days), MRI can find parenchymal edema, alterations in cerebral stratification, and hyperintensity in T2 sequences (not always distinguishable from the normal parenchyma). The ischemic lesion appears hyperintense in diffusion-weighted images, and its apparent diffusion coefficient is lower than the one of normal parenchyma. In the subacute phase, it is characterized by hyperintensity in T2 and in T1 (intraparenchymal necrosis). Chronic phases are characterized by parenchymal atrophy, focal malacia, and distortion of ventricular shape; hyperintensity in T1 images stands for necrosis.

Differential diagnosis should be made with infective disease.

Both extra-axial posterior fossa hemorrhages and intraparenchymal cerebellar hemorrhages can be related to maternal/fetal trauma and to vascular malformations. Dural sinus malformations often appear as slightly T2 hypointense and T1 isointense mass-like lesions involving the torcula; thrombus within the dural venous sac appears as T1 hyperintensity and marked T2 hypointensity. Vascular causes of intraparenchymal cerebellar hemorrhage include germinal matrix hemorrhages and underlying vascular malformations such as cavernous malformations. Although uncommon, cerebellar hemorrhage has also been reported in cases of infection with cytomegalovirus and in both immune and nonimmune hydrops fetalis, presumably from associated hematological and hemodynamic abnormalities. When a cerebellar hemorrhage is identified, infection should be considered, and a careful search for other abnormalities (e.g., intrauterine growth retardation, microcephaly, calcifications, echogenic bowel, and hydrops fetalis) should be initiated.

11.4.7 Infections

Prenatal infection may be caused by ascending agents from the maternal vagina, or by hematogenous spread via the placenta, or iatrogenically (at amniocentesis). In case of congenital infection, both ultrasound and fetal MRI have a high sensitivity in detecting the nonspecific signs of fetal sufferance, such as ascites, pleural and pericardial effusion, subcutaneous edema, anomalies in amniotic fluid, placental thickening, and the possible implication of fetal organs, such as cardiomegaly, hepatosplenomegaly, hepatic calcifications, and intestinal hyperechogenicity. Fetal MRI has however a higher sensitivity in the study of the possible implication of the nervous system in the infective process, so it is indicated to execute an MRI exam in every case of fetal infection, even if there are no ultrasonographic alterations [34]. The most common infections are part of the TORCH complex (*Toxoplasma*, other HIV, rubella, *Cytomegalovirus*, herpes simplex virus), and the one from *Cytomegalovirus* (CMV) is the most frequent. Fifty percent of pregnant women are not immune to CMV, and 1 % of them will develop the primary infection (with 30 % of transmission to the fetus), while 5 % of immune pregnant women will develop secondary infection (with 3 % of transmission to the fetus). The entity of fetal damage corresponds with the time of infection: the earlier the infection, the more serious the cerebral damage. The alterations in the encephalon represent the results of a previous damage and not the acute phase of the infection. Both nonspecific and specific signs of CMV infection are to be searched. The nonspecific signs, common to other infections, are microcephaly, hydrocephalous, calcifications, subependymal cysts, and intraventricular septa. The specific signs of CMV infection are malformations of cortical development, cerebellar hypoplasia, focal lesions of periventricular white matter, and temporal horn alterations (focal enlargement, cysts situated anteriorly and separated by thin septa or white matter edema) [35].

11.4.8 Complications of Monochorionic Twin Pregnancies

11.4.8.1 Co-twin Demise

Monochorionic twins share a common placenta that often contains abnormal intertwin vascular connections. Because of the placental vascular anatomy, the overall morbidity and mortality of monochorionic twins is much higher than that of dichorionic twins.

In utero, death of a co-twin is associated with an increased risk of neurological impairment in

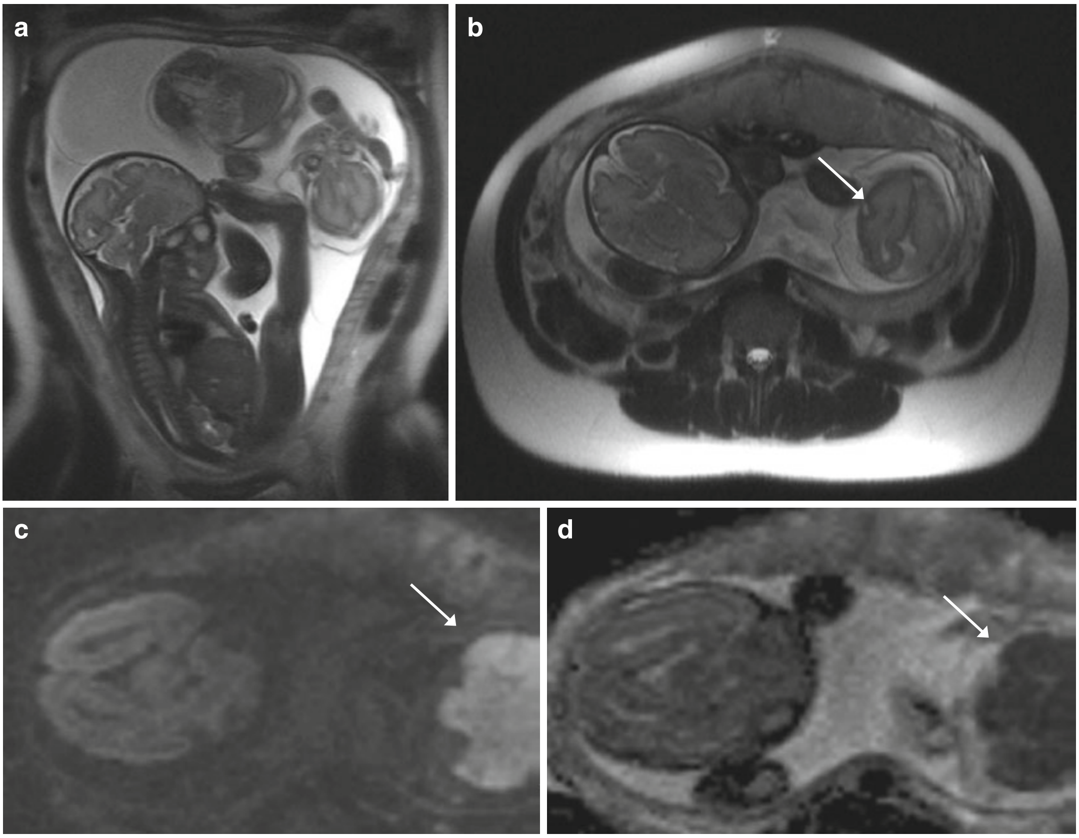

Fig. 11.11 Monochorionic diamniotic twin pregnancy, with intrauterine co-twin demise (GW 29+6). (**a**, **b**) Coronal (**a**) and axial (**b**) T2-weighted images (TR/TE ∞/95 ms): the alive twin is in podalic position on the right, with normal amount of amniotic fluid. The dead twin is in cephalic position on the left and he is smaller than the podalic fetus, with prominent areas of altered cerebral signal intensity and total subversion of cerebral parenchymal structure (*arrow*, **b**). (**c**, **d**) Axial diffusion-weighted image (DWI, TR/TE 3,700/94 ms, b-600) (**c**) and correspondent apparent diffusion coefficient (ADC) map (**d**): the brain of the alive fetus has normal signal intensity, while the dead fetus' one shows marked and diffuse DWI hyperintensity (*arrow*, **c**) that corresponds to a diffuse signal restriction in the ADC map (*arrow*, **d**)

the surviving co-twin, most likely a result of acute cerebral hypoperfusion at the time of demise or possibly thromboemboli. In cases of co-twin demise, fetal MRI (including DWI) should be performed as early as possible to identify acute injury and then repeated at least 2 weeks after the suspected demise to detect subacute/chronic sequelae of intracranial injury in the surviving fetus (Fig. 11.11). Fetal MR can in fact identify destructive parenchymal lesions that might not be detected by prenatal sonography in the surviving co-twin. Ischemic injuries can appear as focal or diffuse areas of increased signal on T2-weighted images in the germinal matrix, developing white matter, and/or cortex. Ischemic injury to the fetal brain can also result in other cortical malformations such as polymicrogyria, encephalomalacia, germinolytic cysts, hemorrhage, ventriculomegaly, and delayed sulcation [36].

11.4.8.2 Twin-Twin Transfusion Syndrome

It is characterized by abnormal blood flow from the smaller donor twin to the larger recipient twin via placental vascular connections. The recipient twin develops polyhydramnios because of volume overload, and the donor twin develops oligohydramnios resulting in a "stuck twin." The morbidity rate is very high, and both the recipient and the donor twin are at risk for cerebral ischemia and hemorrhage. Brain abnormalities detected by fetal MRI are similar to those seen in survivors of co-twin demise and include encephalomalacia, periventricular white matter injury, germinal matrix hemorrhages, intraventricular hemorrhage, intraparenchymal hemorrhage, and cortical malformation [37].

11.4.9 Head and Neck

11.4.9.1 Head

The combination of three imaging planes is required in the fetal MRI study of the head, which the primary purpose is the search of facial clefts: axial views at the level of the maxilla and coronal views at the level of the fetal lips and sagittal planes.

In the axial plane, the hard palate can be visualized in its entirety, as well as the soft tissue of the upper lip overlaying the maxilla and the alveolar ridge with the anterior six tooth buds. In the coronal plane, the continuity of the entire upper lip can be assessed. A sagittal section shows the soft tissue profile of the fetal face and the posterior palate as a continuous straight line. It is best visualized when amniotic fluid fills the fetal mouth. Twenty-five percent of clefts affect only the primary palate with good functional and aesthetic outcome. The cleft primary palate is best visualized on MRI in the axial and coronal planes. Approximately 30 % of fetuses with a complete cleft of the primary palate will also have a complete cleft of the secondary palate, whereas 45 % of clefts only affect the secondary palate. Clefts extending into the secondary palate are directly visible on MRI in the axial and sagittal planes. Amniotic fluid is of high signal on T2-weighted images and allows visualization of the external fetal contour. When amniotic fluid fills the fetal mouth, a clear identification of the oropharynx, tongue, and secondary palate as a curve of soft tissue signal intensity is possible [38].

11.4.9.2 Neck

Lymphangioma is a benign malformation of lymphatic vessels. It is localized in the posterior cervical triangle in 75 % of cases, and it appears both in microcystic and macrocystic form as a mass with thin septa filled with fluid and so hyperintense in T2-weighted images and hypointense in T1-weighted images [39].

Hemangioma is a benign malformation of small vessels. Most lesions are superficial, cutaneous, or subcutaneous, but they can originate also in internal organs (1/3 hepatic). They usually increase in size till the 6 month of life and then they slowly disappear. They appear homogeneously or heterogeneously hypointense in T1-weighted images and tenuously hyperintense in T2 [40].

Teratoma originates from the three embryonic tissues (ectoderm, mesoderm, and endoderm), and it is differentiated in mature and immature. It is frequently localized in the sacrococcygeal region (70–80 %), followed by the head and neck. It is a forming-mass lesion, with cystic and solid areas inside, often with calcifications. It appears inhomogeneous in T2-weighted images and tenuously hypointense in T1 [41].

11.4.10 Chest

The lungs are complex and highly specialized organs that are unnecessary for intrauterine existence. An optimal lung function needs a long and delicate development, extending from the embryonic period, through the fetal period up to birth. During the intrauterine life, the lung development is characterized by a series of accurately organized events that can be divided into five stages: embryonic, pseudoglandular, canalicular, saccular, and alveolar [42]. The embryogenic phase (3–6; 8 weeks of gestation) begins with the formation of a groove in the ventral lower pharynx. At the end, by a dichotomous division in a caudal direction, the growth of the tracheobronchial tree takes place. The further subdivision into the entire air-conduction bronchial tree arises in the pseudoglandular phase

(6; 8–16 weeks of gestation). At this time, the pulmonary vessels have formed themselves. At the canalicular stage (16–26; 28 weeks of gestation), the terminal bronchioles resemble the development of the acinus, which comprises respiratory bronchioles and acinar structures. The surfactant starts to be produced by the developing epithelium. In the saccular phase (26; 28–32; 36 weeks of gestation), the last generation of air spaces continues to divide and generates transitory ducts and terminal saccules; the end of each terminal saccule is coated with type I and type II pneumocytes. During the alveolar phase (32; 36 weeks of gestation – at birth) new sacculi and alveoli form [43].

The fetal thoracic abnormalities refer to a heterogeneous group of fetal lung diseases, including pulmonary hypoplasia, congenital pulmonary airway malformation (CPAM), bronchopulmonary sequestration (BPS), bronchogenic cyst, and congenital diaphragmatic hernia (CDH) [42]. In recent years, the prenatal magnetic resonance imaging has not only revolutionized the detection of these anomalies, it has also transformed the perinatal and postnatal management of this rare but significant spectrum of fetal malformations that are usually discovered incidentally on routine prenatal US examination [44]. In fact, the purpose of the fetal MR is to confirm the diagnosis and to evaluate the mass size, the compression of the normal lung parenchyma, and the shift of the mediastinal organs that may cause polyhydramnios and hydrops that are considered indicators of a poor prognosis in fetuses with these abnormalities [42]. When a thoracic abnormality is suspected during pregnancy, treatment is coordinated and decided through a multidisciplinary team. In most cases, the pregnancy will be closely monitored for its duration, and the surgical repair takes place after birth; but if any fetal complication develops, then antenatal surgical intervention will be required because mortality is high [45].

Pulmonary hypoplasia is an extremely rare condition characterized by an inadequate size and shape of the fetal lung, resulting in decreased pulmonary cell numbers, air space, and alveoli, due to pulmonary underdevelopment. It accounts from 9 to 11 per 10,000 live births, with a mortality rate of 50–70 % [46]. Pulmonary hypoplasia can be primary or secondary [42]. The secondary hypoplasia occurs when an intrathoracic or extrathoracic process limits the thoracic space for lung development. The most common intrathoracic causes are congenital diaphragmatic hernia (CDH), congenital pulmonary airway malformation (CPAM), bronchogenic cyst, bronchopulmonary sequestration (BPS), cardiac or mediastinal masses, pleural effusion, and skeletal dysplasias. The most common extrathoracic cause is severe oligohydramnios, secondary to either genitourinary anomalies or to prolonged rupture of membranes [42]. When a cause of a pulmonary underdevelopment cannot be elucidated, it should be considered the hypothesis of a primary pulmonary hypoplasia which is much less common that the secondary hypoplasia [46]. MRI can better assess the diagnosis of pulmonary hypoplasia by evaluating the changes of the volumes and the intensity of the lungs during the intrauterine life. The estimation of the fetal lung volume changes during the pulmonary development, but it is a direct marker of this condition [46]. On T2-weighted images, the normal fetal lung has homogeneous and moderate signal intensity between that of amniotic fluid and skeletal muscle. The increased alveolar fluid production during the fetal maturation is associated with a higher signal intensity. The pulmonary hypoplasia is suggested by an abnormal hypointensity of the lungs. Low intensity of the lungs is suggestive of pulmonary hypoplasia [47].

The congenital pulmonary airway malformation (CPAM) results from an early airway maldevelopment that forms a cystic and non-cystic tissue into the terminal airways. In this rare anomaly, the affected enlarged lung lobe resembles a tumor-like mass, often with small cysts and hamartomatous or dysplastic terminal bronchioles. Its pathogenesis is still unknown and the incidence is reported as of 1 in 10,000 to 1 in 35,000 live births [48]. Stocker et al. first divided this entity into five subtypes, as follows:

- Type 0, the acinar dysplasia is not compatible with life because the CPAM involves all the lung lobes.

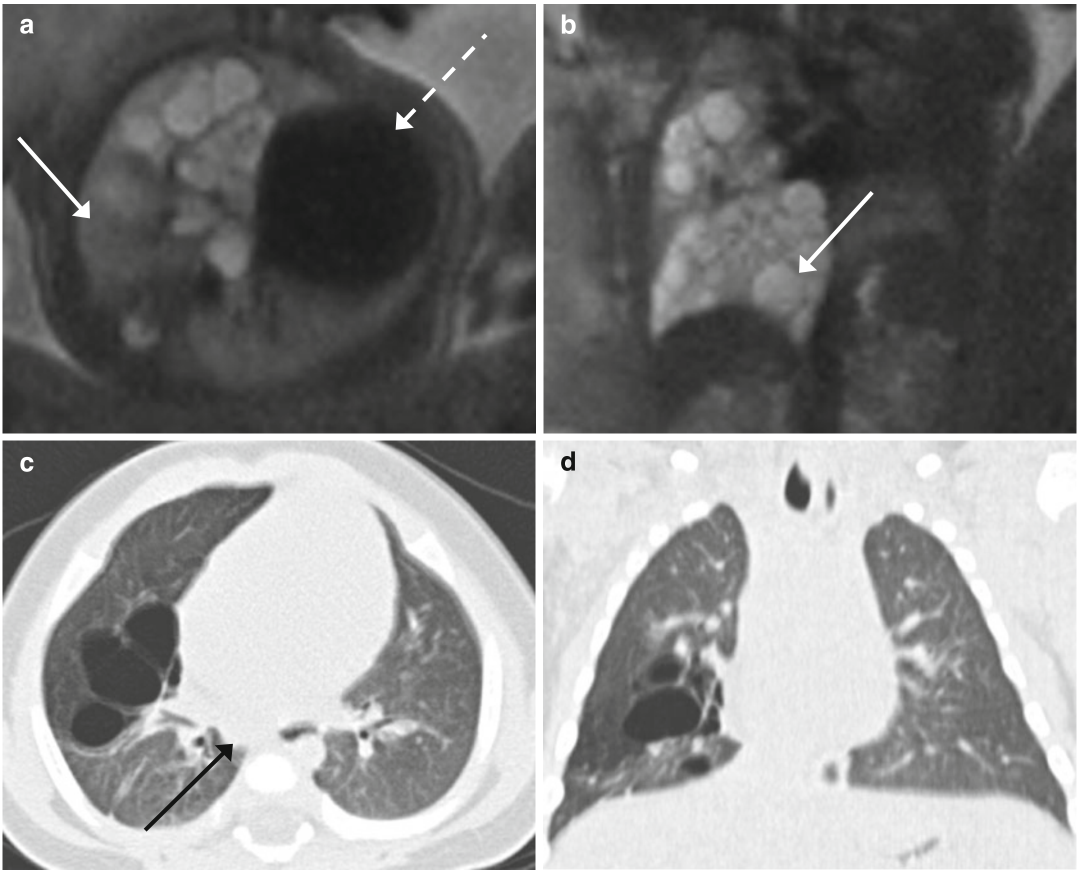

Fig. 11.12 Congenital pulmonary airway malformation (CPAM) of type II (GW 26+4); the lesion was already diagnosed at the ultrasonographic (US) screening of the second trimester. (**a, b**) Axial (**a**) and coronal (**b**) T2-weighted images (TR/TE ∞/95 ms): the lesion is localized in the medium and inferior right lobes, and it is characterized by many cysts of different sizes that appear hyperintense in comparison to the adjacent normal parenchyma (*arrow*, **a**). The major one measures 1.5 cm, and it is localized at the inferior lobe (*arrow*, **b**). Mild contralateral mediastinal dislocation is present (*dashed arrow*, **a**). (**c**, **d**) Postnatal axial (**c**) and coronal (**d**) images of computed tomography: the lesion has partially decreased in size and the mediastinum is no longer dislocated (*arrow*, **c**)

- Type I (50–65 %), a lesion with a single dominant cyst or multiple large cysts (diameter >2 cm), frequently producing mediastinal compression.
- Type II (10–40 %), the mass contains multiple small cysts (diameter between 0.5 and 2 cm); it is frequently associated with other abnormalities and therefore with a poor prognosis (Fig. 11.12).
- Type III (5–10 %), the malformation produces a solid or microcystic large mass, with cyst < of 0.5 cm, characterized by a high signal intensity on the T2-weighted images that depends on the predominantly microcystic pattern. This group often causes a mediastinal shift and has a very poor prognosis (Fig. 11.13).
- Type IV lesions are large peripheral and usually asymptomatic cysts [42, 48].

The MR imaging has a variable appearance due to the different cystic and solid components of the lesion. The unilocular or multilocular lesions usually appear hyperintense on T2-weighted images, with different thickness of the walls [42]. The fetal MR imaging may provide morphological and volumetric evaluation of the lesion especially describing the vascular component of the malformation that can guide the management of the fetus. In fact, CPAM

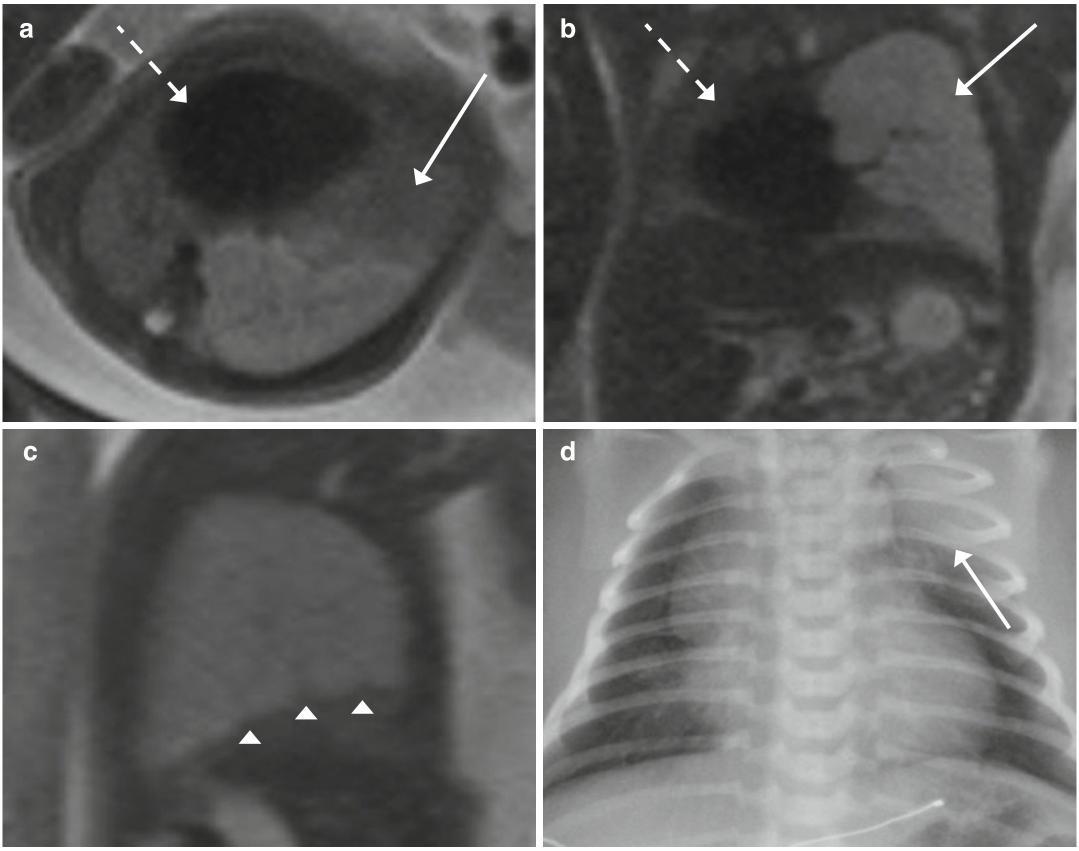

Fig. 11.13 CPAM of type III (GW 23+4); an isolated dextrocardia was described at the US screening of the second trimester. (**a**–**c**) Axial (**a**), coronal (**b**), and sagittal (**c**) T2-weighted images (TR/TE ∞/95 ms): the lesion is recognizable as hyperintensity of left superior pulmonary lobe (*arrow*, **b**), in comparison to the adjacent normal parenchyma (*arrow*, **a**), with scissural delimitation (*arrowheads*, **c**). Contralateral mediastinal dislocation is present (*dashed arrows*, **a**, **b**). (**d**) Postnatal image of conventional radiography: during pregnancy, the lesion has progressively decreased in volume, remaining visible at birth as a parenchymal densification at the left pulmonary apex (*arrow*), with complete resolution of the mediastinal dislocation

usually receives blood supply from the pulmonary arteries and has a venous drainage via the pulmonary veins. This vascular characteristic helps the different diagnosis between CPAM and the bronchopulmonary sequestration (BPS), even if sometimes there can be congenital mixed malformations with either BPS or CPAM components [49]. Even if the natural history of this pulmonary lesion is variable, the authors considered the prognosis for a fetus with CPAM generally good. In fact, the spontaneous in utero regression after 29 weeks of gestation is recognized in up to 43–86 % of lesions [50, 51].

A developmental mass of nonfunctioning bronchopulmonary tissue that lacks communication with the tracheobronchial tree and receives blood supply from the thoracic or abdominal aorta represents a bronchopulmonary sequestration (BPS) [52]. With an incidence of 1 per 1,000 live births, the sequestrations are divided anatomically into two different subtypes: intralobar or extralobar masses [51]. The intralobar mass that represents the 75 % of this anomaly is located within the parenchyma of a lung lobe, whereas the extralobar has its own pleural investment and may be associated with other congenital systemic anomalies, such as congenital diaphragmatic hernia, cardiac abnormalities, pulmonary hypoplasia, or foregut duplication cysts [44]. Both preserve a systemic vascularization. Bronchopulmonary sequestrations are so characterized as lung masses lacking communication with the rest of the airways with their own blood supply [51]. Typically on the prenatal MR imaging, this lesion demonstrates well-demarcated margins, high T2 signal intensity relative to the surrounding pulmonary parenchyma, and a systemic feeding artery [53]. The recommended treatment in case of BPS is removal of the lesion because of the risk of infection, bleeding, and pneumothorax and the risk of malignant transformation [54].

A bronchogenic cyst is a type of bronchopulmonary foregut malformation, occurring probably between the 26th and the 40th days of the embryogenesis [42]. This anomaly depends on the timing of the developmental abnormal ventral budding of the tracheobronchial tree, and it is usually classified anatomically. The mediastinum location is the most frequent site, and the lesion is commonly situated near the carina area. But when the developmental alteration occurs late in the fetal life, the lesion is located within the pulmonary parenchyma [54]. Unfortunately, there is a significant overlap between this malformation and other cystic congenital lesion such as the esophageal duplication cyst, usually located in the posterior mediastinum and the neurenteric cyst that is associated with a vertebral defect [43]. The prenatal MR imaging may demonstrate a unilocular cyst usually in the middle-posterior mediastinum with a high signal intensity on the T2-weighted images that corresponds to a high or low signal intensity on the T1-weighted images, depending on the cyst components [42].

Congenital lobar overinflation (CLO) refers to an overinflation with distension of one or more lung lobes, due to different factors including a secondary defect in the bronchial cartilage or an extrinsic compression of an airway by an abnormal artery or a bronchogenic cyst [55]. These causes bear a possible “check-valve mechanism” at a bronchial level resulting in air trapping that usually involves the left upper lobe or the middle-upper right lobes [44]. Antenatally, CLO can also be caused by a bronchial atresia that commonly causes a hyperinflation of the lower lobes. It is more common in males and can be associated with congenital heart defects, even if it rarely causes fetal complications [42]. CLO can be detected at MR imaging because the fluid-filled airways have high signal intensity on the T2-weighted images [42]. However, this homogeneous high signal intensity is indistinguishable from a microcystic CPAM at fetal MR examination [44].

Congenital diaphragmatic hernia (CDH) is a condition that leads to pulmonary hypoplasia, in which a hole in the diaphragm allows abdominal organs to move into the chest (Fig. 11.14). It occurs sporadically in about 1 in every 2,500/5,000 live births, and it can be associated with genetic and structural anomalies with poor prognosis [43, 56]. The discontinuity of the hypointense diaphragm on T2-weighted images identifies this congenital defect of the muscle that separates the abdominal organs from the chest. CDH also usually involves the left side of the lung (85 %) [43]. The prenatal MR may also help in measuring the total fetal volume by evaluating both the pathological and contralateral lung size and assessing lung maturity, and it should be used to exclude the presence of cardiac, renal, central system, or gastrointestinal anomalies [56]. The pulmonary hypoplasia and/or hypertension and the liver herniation are the most important causes of death and morbidity in fetuses with CDH [43].

11.4.11 Abdomen

Since most abdominal pathologies are easily seen on prenatal ultrasound, the role of MRI in the abdomen is less clear than in the brain and in the thorax. In each trimester of the pregnancy in fact, specific landmarks of the normal abdomen anatomy should be verified by obstetric ultrasound; but occasionally, additional imaging information is needed [55]. The magnetic resonance imaging can be used as a complementary imaging tool for the confirmation of the ultrasonography findings and as a guide for the clinical management of the fetus [56]. Thanks to the use of faster sequences and experience, the MR imaging of the fetal development is now more accurate and precise also in the prenatal diagnosis of the abdomen abnormalities (Fig. 11.15), especially in

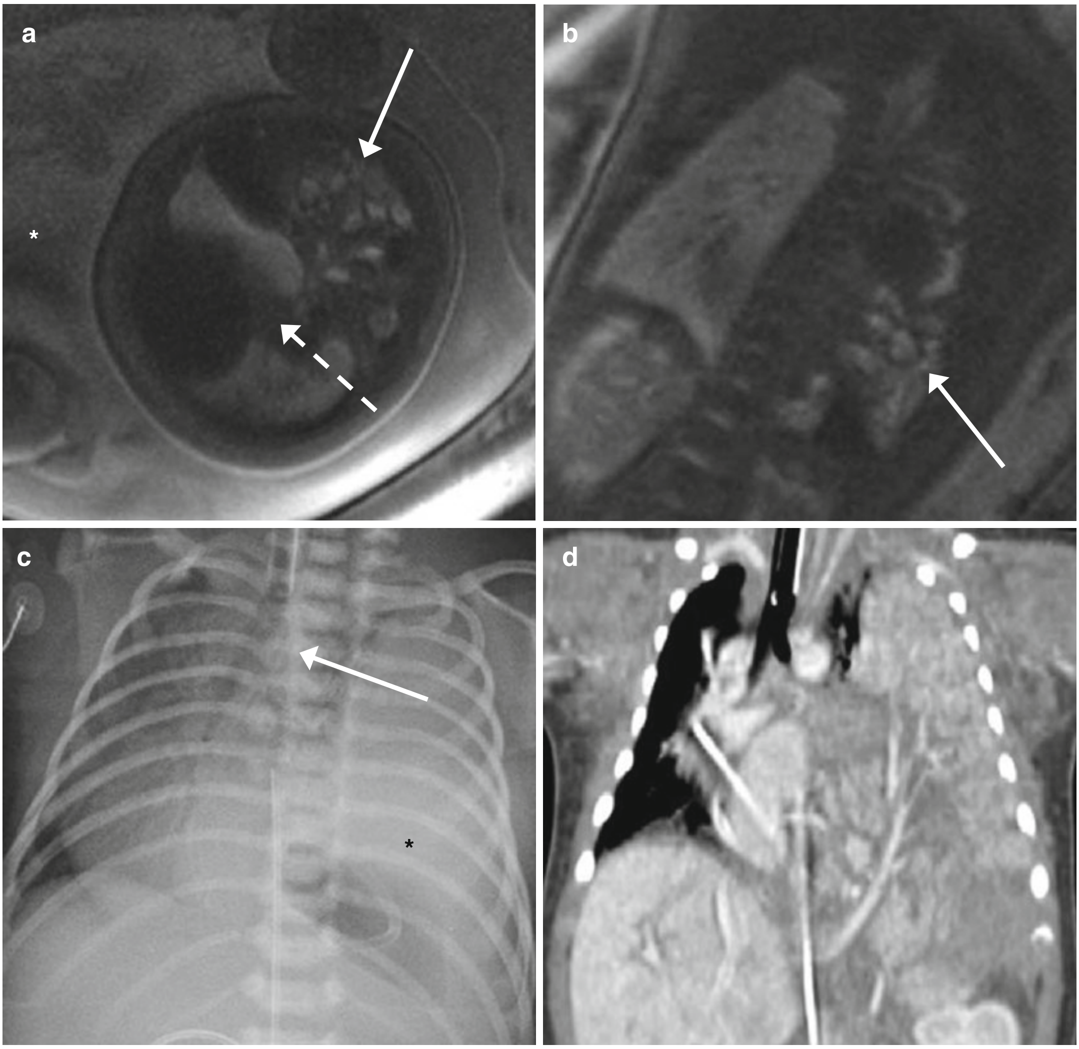

Fig. 11.14 Congenital diaphragmatic hernia (GW 35+3); the lesion was already diagnosed at the ultrasonographic (US) screening of the second trimester. (**a**, **b**) Axial (**a**) and coronal (**b**) T2-weighted images (TR/TE ∞/95 ms): bilateral pulmonary hypoplasia secondary to bulky herniation of stomach and intestinal loops in the left chest (*arrows*, **a**, **b**), with concomitant contralateral mediastinal shift (*dashed arrow*, **a**). Abundant amniotic fluid is also present (*asterisk*, **a**). (**c**) Postnatal image of conventional radiography: complete left pulmonary parenchymal densification (*asterisk*) and contralateral tracheal shift (*arrow*) are showed. (**d**) Postnatal coronal image of computed tomography (CT) of the lesion

the study of the genitourinary tract. The renal kidney develops from a complex series of successive phases of interactions between the Wolffian duct and the surrounding mesenchymal tissue [57]. Anomalies of the genitourinary system are common: accounting for 30 % of anomalies detected on prenatal sonography. The renal parenchymal disease might be recognized by cystic abnormalities and sometimes might present a genetic basis (Fig. 11.16) [57]. Although fetal genitourinary tract anomalies are frequent, the study of the urogenital tract is only one part of a thorough examination of the fetus [58]. Therefore, the fetal MR can be an excellent technique for revealing both: the standard anatomic assessment of the second or the third trimester and the possible abnormalities of all the abdominal organs [57, 58]. Another use of the MRI is the characterization of the sacrococcygeal teratomas, often incompletely visualized by ultrasound due to shading by the iliac bones (Fig. 11.17) [58].

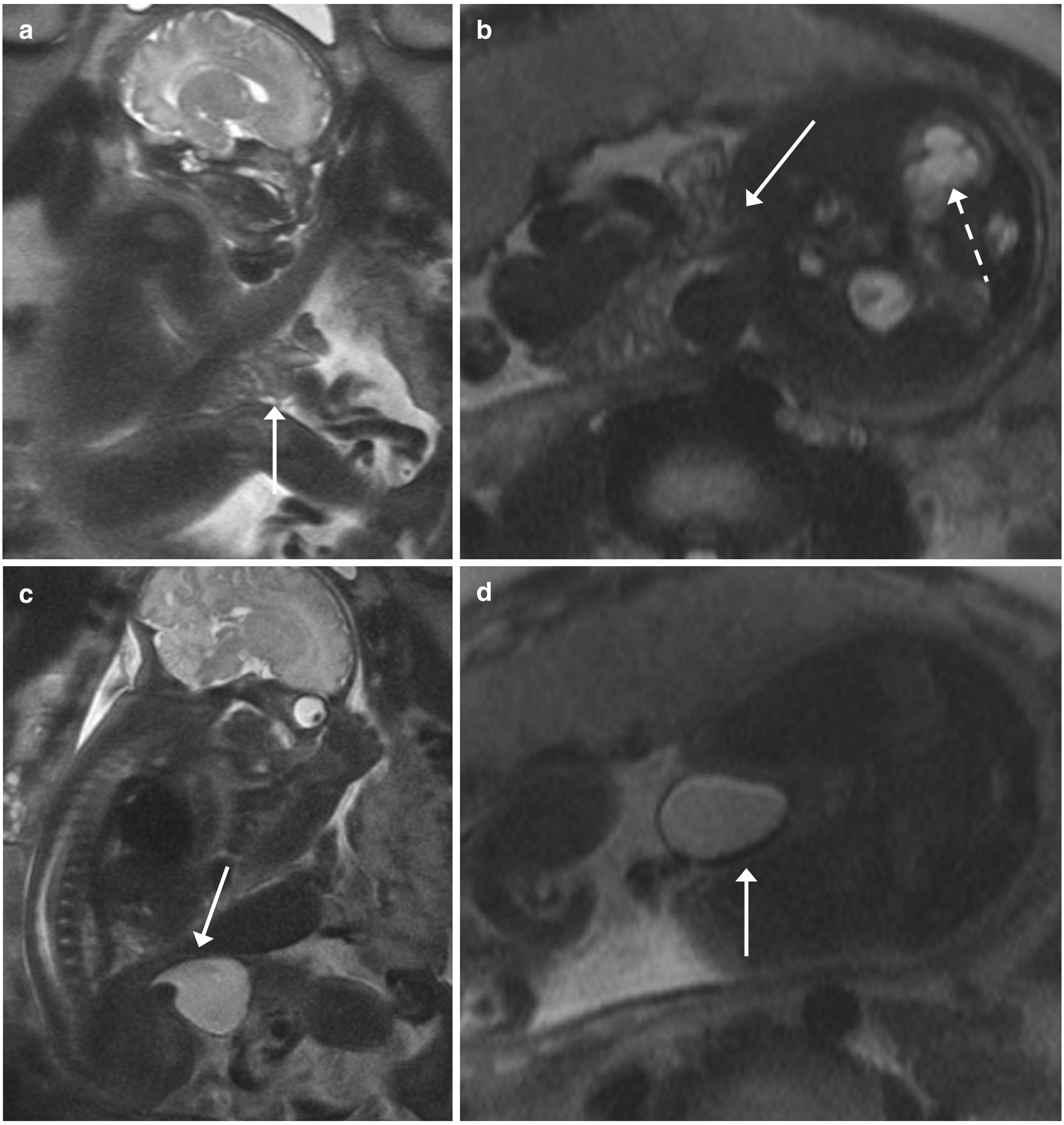

Fig. 11.15 Gastroschisis (GW 34). (**a**–**d**) Sagittal (**a**–**c**) and axial (**b**–**d**) T2-weighted images (TR/TE ∞/95 ms): a defect of the anterior abdominal wall is present (*arrow*, **b**). It is localized at the right side of the midline, at the height of the umbilicus, with herniation of intestinal loops that float in the amniotic cavity (*arrow*, **a**) and of the bladder (*arrow*, **c**, **d**). Right hydroureteronephrosis is also visible (*dashed arrow*, **b**). In all the images, oligohydramnios is also visible

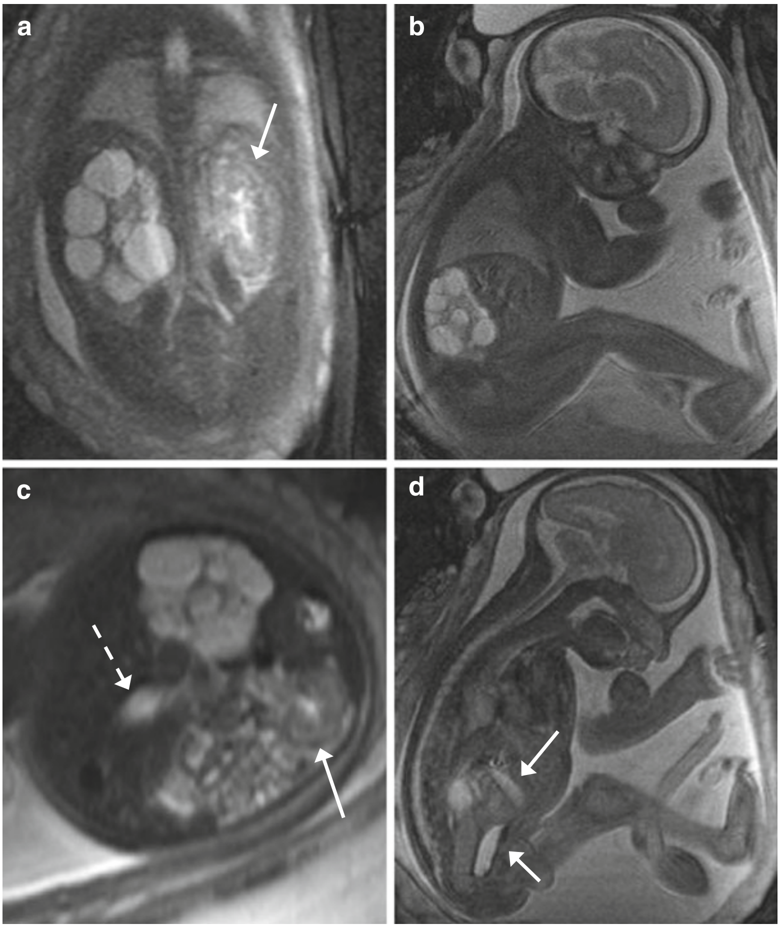

Fig. 11.16 Renal polycystic kidney (GW 27 + 3). (**a**–**d**) Coronal (**a**), sagittal (**b**, **d**), and axial (**c**) T2-weighted images (TR/TE ∞/95 ms): the right kidney is increased in volume and completely replaced by multiple hyperintense cysts of different sizes, while the left one is normal (*arrow*, **a**, **c**). Right renal parenchyma is not recognizable. Right hydroureteronephrosis is also visible (*dashed arrow*, **c**, *arrows*, **d**)

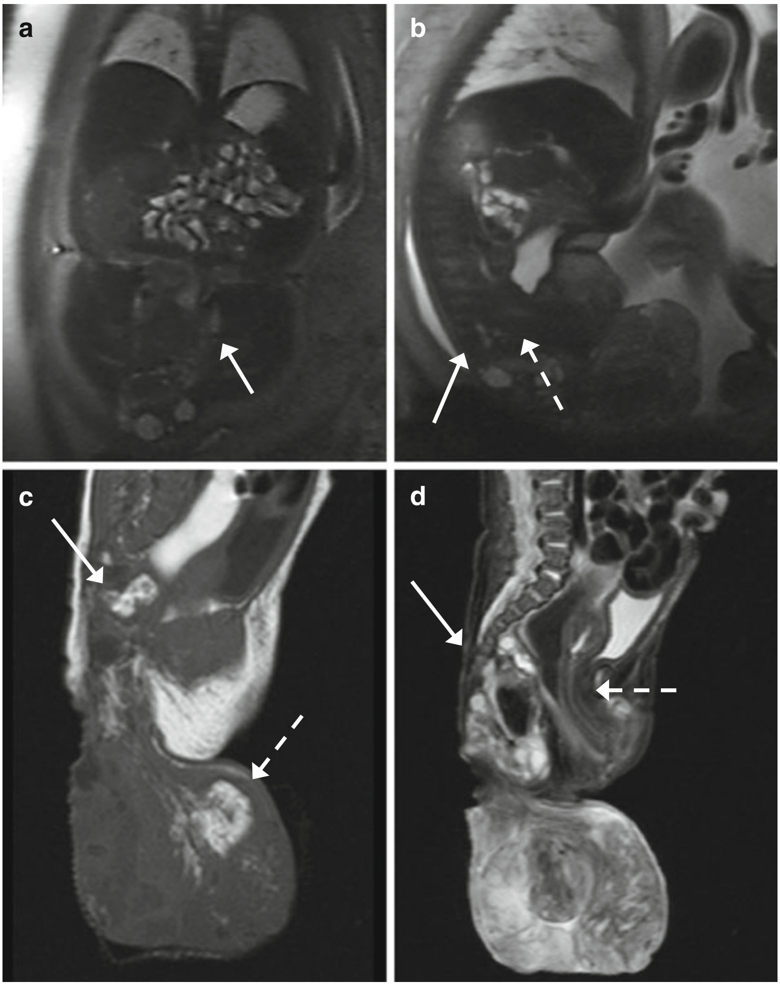

Fig. 11.17 Sacrococcygeal teratoma (GW 37 + 6). (**a**, **b**) Coronal (**a**) and sagittal (**b**) T2-weighted images (TR/TE ∞/95 ms): a sacrococcygeal mass, with an inhomogeneous structure, with solid and with cystic areas, is shown. It has a prevailingly exophytic growth but also a significantly intrapelvic portion (*arrow*, **a**). There are no signs of communication with the neural tube, which does not show cleft defects (*arrow*, **b**). The cleavage plane with the rectus and the bladder is preserved (*dashed arrow*, **b**). (**c**–**d**) Postnatal sagittal T1-weighted (TR/TE 593/8,4 ms) (**c**) and T2-weighted (TR/TE 4,590/103 ms) with fat saturation (**d**) *images*: no new information are added; the lesion, partially solid with fatty areas in it (*dashed arrow*, **c**) and partially cystic, has one exophytic portion and one that broadens in the right gluteus region (*arrow*, **c**). There are no signs of communication with the neural tube (*arrow*, **d**), the rectus, the bladder, and the vagina (*dashed arrow*, **d**)

References

1. Reddy UM et al (2008) Prenatal imaging: ultrasonography and magnetic resonance imaging. Obstet Gynecol 112(1):145–157
2. Wright C, Sibley CP, Baker PN (2010) The role of fetal magnetic resonance imaging. Arch Dis Child Fetal Neonatal Ed 95(2):F137–F141
3. Weston MJ (2010) Magnetic resonance imaging in fetal medicine: a pictorial review of current and developing indications. Postgrad Med J 86(1011): 42–51, quiz 50
4. Glenn OA, Barkovich AJ (2006) Magnetic resonance imaging of the fetal brain and spine: an increasingly important tool in prenatal diagnosis, part 1. AJNR Am J Neuroradiol 27(8):1604–1611
5. Shellock FG, Crues JV (2004) MR procedures: biologic effects, safety, and patient care. Radiology 232(3):635–652
6. Semelka RC (2010) Abdominal-pelvic MRI, 3rd edn. Wiley-Blackwell, Hoboken

7. Stone K (2002) Acute abdominal emergencies associated with pregnancy. Clin Obstet Gynecol 45(2):553–561
8. Spencer JA et al (2004) Evaluation of painful hydronephrosis in pregnancy: magnetic resonance urographic patterns in physiological dilatation versus calculous obstruction. J Urol 171(1):256–260
9. Coronado GD, Marshall LM, Schwartz SM (2000) Complications in pregnancy, labor, and delivery with uterine leiomyomas: a population-based study. Obstet Gynecol 95(5):764–769
10. Sherer DM et al (2000) Prenatal magnetic resonance imaging assisting in differentiating between large degenerating intramural leiomyoma and complex adnexal mass during pregnancy. J Matern Fetal Med 9(3):186–189
11. Levine D et al (1997) Placenta accreta: evaluation with color Doppler US, power Doppler US, and MR imaging. Radiology 205(3):773–776
12. Masselli G et al (2011) MR imaging in the evaluation of placental abruption: correlation with sonographic findings. Radiology 259(1):222–230
13. Levine D, Barnes PD (1999) Cortical maturation in normal and abnormal fetuses as assessed with prenatal MR imaging. Radiology 210(3):751–758
14. Prayer D et al (2006) MRI of normal fetal brain development. Eur J Radiol 57(2):199–216
15. Glenn OA (2009) Normal development of the fetal brain by MRI. Semin Perinatol 33(4):208–219
16. Garel C (2004) MRI of the fetal brain, Ith edn. Springer, Berlin
17. Parazzini C et al (2008) Prenatal magnetic resonance imaging: brain normal linear biometric values below 24 gestational weeks. Neuroradiology 50(10):877–883
18. Leitner Y et al (2009) The neurocognitive outcome of mild isolated fetal ventriculomegaly verified by prenatal magnetic resonance imaging. Am J Obstet Gynecol 201(2):215 e1–215 e6
19. Gaglioti P, Oberto M, Todros T (2009) The significance of fetal ventriculomegaly: etiology, short- and long-term outcomes. Prenat Diagn 29(4):381–388
20. Garel C et al (2003) Ventricular dilatations. Childs Nerv Syst 19(7–8):517–523
21. Mehta TS, Levine D (2005) Imaging of fetal cerebral ventriculomegaly: a guide to management and outcome. Semin Fetal Neonatal Med 10(5):421–428
22. Kelly EN et al (2001) Mild ventriculomegaly in the fetus, natural history, associated findings and outcome of isolated mild ventriculomegaly: a literature review. Prenat Diagn 21(8):697–700
23. Griffiths PD et al (2010) A prospective study of fetuses with isolated ventriculomegaly investigated by antenatal sonography and in utero MR imaging. AJNR Am J Neuroradiol 31(1):106–111
24. Dill P et al (2009) Fetal magnetic resonance imaging in midline malformations of the central nervous system and review of the literature. J Neuroradiol 36(3):138–146
25. Hosseinzadeh K et al (2013) Non-visualisation of cavum septi pellucidi: implication in prenatal diagnosis? Insights Imaging 4(3):357–367
26. Volpe P et al (2006) Characteristics, associations and outcome of partial agenesis of the corpus callosum in the fetus. Ultrasound Obstet Gynecol 27(5):509–516
27. Garel C et al (2003) Fetal MRI: normal gestational landmarks for cerebral biometry, gyration and myelination. Childs Nerv Syst 19(7–8):422–425
28. Tang PH et al (2009) Agenesis of the corpus callosum: an MR imaging analysis of associated abnormalities in the fetus. AJNR Am J Neuroradiol 30(2):257–263
29. Bulas D (2010) Fetal evaluation of spine dysraphism. Pediatr Radiol 40(6):1029–1037
30. Chao TT et al (2010) Central nervous system findings on fetal magnetic resonance imaging and outcomes in children with spina bifida. Obstet Gynecol 116(2 Pt 1):323–329
31. Adamsbaum C et al (2005) MRI of the fetal posterior fossa. Pediatr Radiol 35(2):124–140
32. Epelman M et al (2006) Differential diagnosis of intracranial cystic lesions at head US: correlation with CT and MR imaging. Radiographics 26(1):173–196
33. Tortori-Donati P et al (1996) Cystic malformations of the posterior cranial fossa originating from a defect of the posterior membranous area. Mega cisterna magna and persisting Blake's pouch: two separate entities. Childs Nerv Syst 12(6):303–308
34. Barkovich AJ, Girard N (2003) Fetal brain infections. Childs Nerv Syst 19(7–8):501–507
35. Soussotte C et al (2000) Contribution of transvaginal ultrasonography and fetal cerebral MRI in a case of congenital cytomegalovirus infection. Fetal Diagn Ther 15(4):219–223
36. Jelin AC et al (2008) Intracranial magnetic resonance imaging findings in the surviving fetus after spontaneous monochorionic cotwin demise. Am J Obstet Gynecol 199(4):398 e1–398 e5
37. Quarello E, Molho M, Ville Y (2007) Incidence, mechanisms, and patterns of fetal cerebral lesions in twin-to-twin transfusion syndrome. J Matern Fetal Neonatal Med 20(8):589–597
38. Stroustrup Smith A et al (2004) Prenatal diagnosis of cleft lip and cleft palate using MRI. AJR Am J Roentgenol 183(1):229–235
39. Teksam M et al (2005) MR imaging and ultrasound of fetal cervical cystic lymphangioma: utility in antepartum treatment planning. Diagn Interv Radiol 11(2):87–89
40. Shiraishi H et al (2000) Prenatal MRI in a fetus with a giant neck hemangioma: a case report. Prenat Diagn 20(12):1004–1007
41. Woodward PJ et al (2005) From the archives of the AFIP: a comprehensive review of fetal tumors with pathologic correlation. Radiographics 25(1):215–242
42. Biyyam DR et al (2010) Congenital lung abnormalities: embryologic features, prenatal diagnosis, and postnatal radiologic-pathologic correlation. Radiographics 30(6):1721–1738
43. Recio Rodriguez M et al (2012) MR imaging of thoracic abnormalities in the fetus. Radiographics 32(7): E305–E321

44. Barth RA (2012) Imaging of fetal chest masses. Pediatr Radiol 42(Suppl 1):S62–S73
45. Bush A (2009) Prenatal presentation and postnatal management of congenital thoracic malformations. Early Hum Dev 85(11):679–684
46. Vergani P (2012) Prenatal diagnosis of pulmonary hypoplasia. Curr Opin Obstet Gynecol 24(2):89–94
47. Sandrasegaran K, Lall CG, Aisen AA (2006) Fetal magnetic resonance imaging. Curr Opin Obstet Gynecol 18(6):605–612
48. Lakhoo K (2009) Management of congenital cystic adenomatous malformations of the lung. Arch Dis Child Fetal Neonatal Ed 94(1):F73–F76
49. Azizkhan RG, Crombleholme TM (2008) Congenital cystic lung disease: contemporary antenatal and postnatal management. Pediatr Surg Int 24(6):643–657
50. Kunisaki SM et al (2007) Large fetal congenital cystic adenomatoid malformations: growth trends and patient survival. J Pediatr Surg 42(2):404–410
51. Wilson RD et al (2006) Cystic adenomatoid malformation of the lung: review of genetics, prenatal diagnosis, and in utero treatment. Am J Med Genet A 140(2):151–155
52. Alamo L et al (2012) Prenatal diagnosis of congenital lung malformations. Pediatr Radiol 42(3):273–283
53. Liu YP et al (2010) Fetal cystic lung lesions: evaluation with magnetic resonance imaging. Pediatr Pulmonol 45(6):592–600
54. Williams HJ, Johnson KJ (2002) Imaging of congenital cystic lung lesions. Paediatr Respir Rev 3(2): 120–127
55. Winters WD, Effmann EL (2001) Congenital masses of the lung: prenatal and postnatal imaging evaluation. J Thorac Imaging 16(4):196–206
56. Done E et al (2008) Prenatal diagnosis, prediction of outcome and in utero therapy of isolated congenital diaphragmatic hernia. Prenat Diagn 28(7):581–591
57. Huisman TA, Kellenberger CJ (2008) MR imaging characteristics of the normal fetal gastrointestinal tract and abdomen. Eur J Radiol 65(1):170–181
58. Brugger PC, Prayer D (2006) Fetal abdominal magnetic resonance imaging. Eur J Radiol 57(2):278–293